Università degli Studi di Cagliari

DOTTORATO DI RICERCA

SCIENZE E TECNOLOGIE CHIMICHE

Ciclo XXVIII

TITOLO TESI

COMPLEX FORMATION EQUILIBRIA OF LIGANDS WITH METAL IONS OF BIOMEDICAL INTEREST

Settore/i scientifico disciplinari di afferenza

CHIM/01

Presentata da: María de Guadalupe Jaraquemada Peláez

Coordinatore Dottorato Prof. Mariano Casu

Tutor Prof.ssa. Valeria Marina Nurchi

Esame finale anno accademico 2014 – 2015

List of Figures

List of Tables

List of Schemes

List of Symbols and Abbreviations

%I.A	percent of Injected Activity
1,2-HP	1-Hydroxypyridin-2-one
3,2-HP	3-Hydroxypyridin-2-one
3,4-HP	3-Hydroxypyridin-4-one
Å	Angstrom
AAS	Atomic Absorption Spectroscopy
AD	Alzheimer's disease
Arg	Arginine
Asn	Asparagine
Asp	Aspartic acid
Aβ	β-Amyloid
BAL	2,3-Dimercaptopropanol, dimercaprol
BBB	Blood-Brain Barrier
BFCs	Bifunctional Chelators
β_{ML}	Cumulative complex formation constant
Bn	Benzyl
Bq	Becquerel
Caco-2	Human Colon Carcinoma
CcO	Cytochrome-c Oxidase
CQ	Clioquinol
Cyc	Cyclen
Cys	Cysteine
Da	Dalton
DCM	Dichloromethane
DFO	Deferrioxamine
DFP	Deferiprone, 1,2-dimethyl-3-hydroxypyridin-4-one
DFT	Density Functional Theory (*in silico* calculations)
DMSO	Dimethylsulfoxide
DNA	Deoxyribonucleic acid
DOTA	1,4,7,10-tetraazacyclododecane -*N*,*N'*,*N''*,*N'''*-tetraacetic acid
D-pen	D-penicillamine
DTPA	Diethylenetetraaminepentaacetic acid
EA	Elemental Analysis
EDTA	Ethylenediaminetetraacetic acid
EPR	Electron Paramagnetic Resonance
ESI-MS	Electrospray Ionization-Mass Spectrometry
EtOH	Ethanol
FALS	Familial Amyotrophic Lateral Sclerosis
FDA	Food and Drug Administration (USA)
Fosrenol	Lanthanum carbonate
Glu	Glutamine

HAP	Hydroxyapatite
HASAB	Hard-Soft Acid-Base Theory
His	Histidine
HPLC	High Performance Liquid Chromatography
HPOs	Hydroxypyridinones
HSQC	Heteronuclear Single Bond Correlation/Coherence (1H-13C NMR)
IC50	half maximal inhibitory concentration
$IDAPr(3,4\text{-}HP)_2$	2,2'-Azanediylbis(N-(3-(3-hydroxy-2-methyl-4-oxopyridin-1 (4H)-yl)propyl)acetamide)
IMPY	6-Iodo-2-(4-(Dimethylamino)phenyl)imidazol[1,2-a]pyridine
J	Joule
J	Coupling constant (NMR)
K0	2-(4-(Dimethylamino)phenyl)imidazol[1,2-a]pyridin-8-ol
KA	Kojic Acid
k'_d	Equilibrium dissociation constant
$KEMPBu(3,4\text{-}HP)_3$	1,3,5-Tris-[4-(3-hydroxy-2-methyl-4-oxo-4*H*-pyridin-1-yl)-butylcar bamoyl]-1,3,5-trimethylcyclohexane
$KEMPPr(3,4\text{-}HP)_3$	1,3,5-Tris-[3-(3-hydroxy-2-methyl-4-oxo-4*H*-pyridin-1-yl)-propylcar bamoyl]-1,3,5-trimethylcyclohexane
KLVFF	(2S,5S,8S,11S,14S)-14,18-Diamino-2,5-dibenzyl-11-isobutyl-8-isopropyl-4,7,10,13-tetraoxo-3,6,9,12-tetraazaoctadecan-1-oic acid
K_{sp}	Solubility Product
L	Ligand or Litre
L_b	Bidentate ligand
L-DOPA	L-3,4-dihydroxyphenylalanine
L_h	Hexadentate ligand
log BB	Blood-Brain partition coefficient
log P	Octanol/ water partition coefficient
LP	Lone pair
L_t	Tetradentate ligand
M	Molar
m	milli- or medium or multiplet
M.p.	Melting point
m/z	Mass per unit charge
MECAM	1,3,5-N,N',N"-tris-(2,3-dihydrobenzoyl)triaminomethylbenzene
MeOH	Methanol
Met	Methionine
MG-63	Cells derived from a human osteosarcoma
mol	Mole
MS	Mass Spectrometry
MTs	Metallothioneins
MW	Molecular weight
n	Nano (10^{-9}) or number of unit
nm	Nanometer

NMR	Nuclear Magnetic Resonance
NOTA	1,4,7-triazacyclononane-1,4,7-triacetic acid
NTA	Nitrilotriacetic acid
NTP	Nitrilopropionic acid
O-TRENSOX	7,7',7''-(2,2',2''-Nitrilotris(ethane-2,1-diyl)tris(azanediyl))tris (oxomethylene)tris(8-hydroxyquinoline-5-sulfonate)
PD	Parkinson's disease
Pd/C	Palladium on carbon (10% by weight)
PET	Positron Emission Tomography
Phe	Phenylalanine
pK_a	-log[K_a], K_a acid dissociation constant
pM^{n+}	the negative logarithm of the concentration of free metal (M^{+n}) in solution. [ligand]= 10^{-5} M, total [metal] =10^{-6} M at pH 7.4
ppm	Parts per million
Pro	Proline
ROS	Reactive Oxygen Species
rt	Room temperature
s	Singlet (NMR)
SD	Standard Deviation
SOD	Superoxide Dismutase
SOPTA	Second-Order Perturbation Theory Analysis
SPECT	Single Photon Emission Computed Tomography
t	Triplet (NMR) or time
$t_{1/2}$	half-life
TFA	Trifluoroacetic acid
TLC	Thin Layer Chromatography
TOCSY	Total Correlation Spectroscopy
TRAP	triazacyclononane-phosphinic acid
TETA, trientine or Trien	triethylenetetramine ((N,N' –bis(2-aminoethyl)-1,2-ethanediamina
TTM	Ammonium Tetrathiomolibdate
Tyr	Tyrosinase
TyrBm	tyrosinase from Bacillus megaterium
WD	Wilson Disease
XH1	2,2'-(2,2'(Carboxymethylazanediyl)bis(ethane-2,1-diyl) bis((2-(4-(benzo[d]thiazol-2-yl)phenylamino)-2-oxoethyl)azanediyl))
XRD	X-ray diffraction
δ	Chemical shift in ppm (NMR)
ε	Absorptivity

Acknowledgements

I want to take the time to acknowledge the many people who were important to me during this three-year period in my life. When I thought I couldn't work in chemistry any longer, these people were there to support and encourage me to start my PhD. Without them, I couldn't have completed the work presented in this thesis.

First, I want to thank my parents, Felipe and Teresa, who are examples for me and from whom I received not only an education, but above all, love, support and encouragement in all my life projects. I want to thank my three lovely sisters, Teresa, Inma and Blanca, because we grew together helping and loving each other and sharing great and difficult moments. My aunt, "Tia Mª Jesús", who was the best "grandmother" ever. From her, I learned many important things which are difficult to find within my generation. My partner, Luigi, for his understanding and love since we met almost ten years ago. My lovely friends in Cagliari, Carla, Francesca, Patrizia e Valentina.

I must also extend my thanks to my supervisor, Prof. Valeria Nurchi, and her husband, Prof. Guido Crisponi, first for their trust and second, for funding me during my PhD. Without their endless support and guidance, my work would never have been completed. My friend and collaborator, Dr. Joanna Lachowicz, for her generous support, for being the best colleague anyone could ever hope to work with, and for all our coffee times and funny moments in the lab. My friends in the Chemistry Department in Cagliari, including Prof. Claudia Caltagirone for her endless support and help, Dr. Andrea Scorciapino for solving my NMR doubts, and finally, for the good moments in the lunchroom with Cristina, Riccardo, Chiara and Merilin. Prof. Juan Niclós Gutiérrez, Prof. Josefa María González Pérez, Dr. Duane Choquesillo Lazarte, Prof. Alfonso Castiñeiras and all the people in the Inorganic Chemistry Department of Granada, for making me feeling at home during the three-month period I spent there. Prof. Maria Antonietta Zoroddu and Dr. Massimiliano Peana for their help with NMR titrations. Prof. Maurizio Remelli for his contribution with calorimetry measurements. Prof. Chris Orvig for giving me the chance to work in his labs and spend a very productive and beautiful time there. I would also like to thank all the Orvig group members, especially David, for involving me in his PhD project, and Sarah, Hunter and Tom.

I want also to thank my friends at Green College: Sana, Linh, Arya, Larissa and Anupama, for all the good moments shared during my stay in Vancouver.

Dedication

For my parents, sisters,"tia Mª Jesús" and Luigi, for endless support and encouragement.

1. Introduction

In a healthy situation, the body is provided with homeostatic mechanisms and buffers to maintain physiological concentrations of free metal ions, thus preventing their abnormal decompartmentalization, release and trafficking. The main reasons for the anomalous accumulation of non-essential metal ions in the body are environmental exposure and administration of metallodrugs for therapy or diagnosis, which may cause competition for biometals, generation of oxidative stress and disregulation of several metal-enzyme systems. Inorganic medicinal chemistry has to deal with the introduction of metal ions in the body, but also with their removal or passivation through the use of chelators. In these terms, thermodynamics and kinetics of complex formation are very important for a correct understanding of the role of metal ions in human diseases.

During my PhD work, some new ligands were synthesized and their complex formation equilibria with toxic, essential and other metal ions of biomedical interest were studied.

In particular, some derivatives of kojic acid have been synthesized and their protonation and chelating properties toward the target metal ions Fe^{3+} and Al^{3+}, and the two essential Cu^{2+} and Zn^{2+} have been characterized. Furthermore, the complex formation equilibria of some drugs actually in clinical use with the essential metal ions Cu^{2+} and Zn^{2+} were studied to give evidence of their possible implications in copper chelation. Moreover, the tyrosinase inhibitory properties of the kojic derivative[1] (5-hydroxy-4-oxo-4H-pyran-2-yl)methyl3-({[(5-hydroxy-4-oxo-4H-pyran-2yl)methoxy]carbonyl} amino)propanoate and its complex formation equilibria with copper have been studied, since the inhibitory effect may result from the interaction with copper ions in the active center of the enzyme.

This thesis is divided in an **Introduction**, dedicated to a description of metals, to their chemistry and their overload or deficiency, to chelation therapy, to the characteristics of chelators for metal overload treatment and to the improvements induced on some pathological conditions in diabetic patients. Further attention is devoted to tyrosinase inhibition and radiopharmaceutical labelling. An **Experimental** part describes the synthesis of new chelators and the methods used for a complete characterization. In the section **Results and Discussion** the determination of protonation constants for all ligands, together with that of their complex formation constants with metals of interest like Fe^{3+}, Al^{3+}, Ga^{3+}, Cu^{2+} and Zn^{2+}, is presented, in order to evaluate their therapeutic application in metal overload diseases. Complex stability studies of two new ligands with lanthanum to be used in the treatment of bone disorders are also presented as a part of a collaboration during my three month period at the University of British Columbia, Vancouver-Canada. A brief section **Conclusions** summarizes the presented results.

1.1. Metal homeostasis and chelation therapy.

A number of metal ions play a crucial role in living organisms. Metals can easily lose electrons from the elemental or metallic state to give cations, which are soluble in biological fluids, and can interact with biological molecules. Metal ions, which are electron deficient, can bind and interact with electron rich biological molecules such as proteins and DNA.

Natural evolution has incorporated many metal ions into essential biological functions. Haemoglobin, an iron-containing protein, binds to oxygen through its iron atom and carries it throughout the body. Calcium-containing minerals are the basis of bones, the structural framework of the human body. Zinc is a natural component of insulin, a substance crucial to the regulation of sugar metabolism. Metals such as copper, zinc, iron and manganese are incorporated into catalytic proteins (metalloenzymes) which facilitate a multitude of chemical reactions needed for life[2].

Nowadays in the industrial society, exposure to metal ions is ever increasing. Metal compounds are used in medicine for either therapeutic or diagnostic purposes, in alimentary industries, in water purification plants, in cosmetics, in painting and so on. According to the role that metal ions exert in the human physiology, at least three categories can be roughly distinguished: essential, inert and toxic[3].

Any metal ion or complex, or indeed any chemical compound, is subject to the potential limitations in the Bertrand diagram (Figure 1.1).

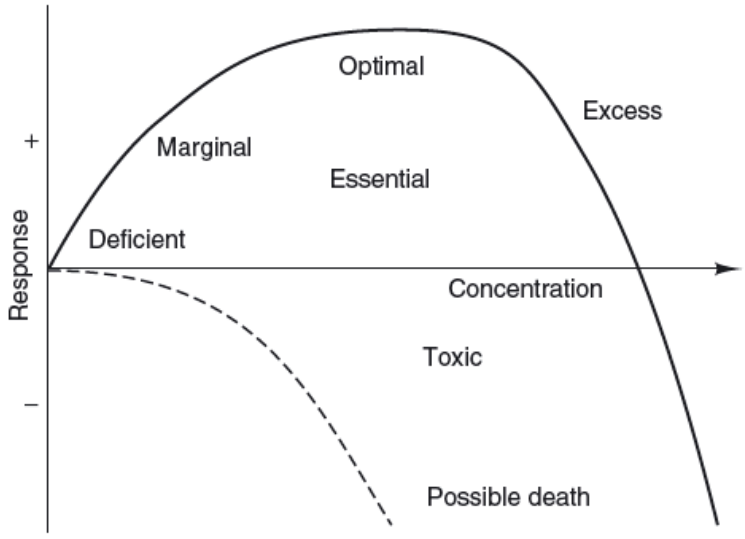

Figure 1.1. Bertrand diagram indicating the relationship between positive/negative effects from an element and its concentration[3].

Toxic compounds can be tolerated in low doses, at which may even exert therapeutic effects, and essential metals can become toxic at high concentrations[4]. For a true knowledge of the behavior of an element in the human body, it is important not only its range concentration, but also its speciation and oxidation state. One of the principal ways to counteract metal toxicity in humans consists in the treatment with metal chelators, which transform the toxic metal ion in a less dangerous species and favour its excretion from the organism.

1.2. Chelation therapy and metal chelators

The word "chelation" derives from the Greek χηλη - that means claw. Chelators have at least two binding atoms that form either two covalent, or one covalent and one coordinate, or two coordinate linkages. Atoms like S, N and O are the main binding atoms, in chemical groups like -SH, -S-S, $-NH_2$, =NH, -OH, $-OPO_3H$ or –C=O. Bidentate or multidentate chelators form ring structures that include the metal ion with at least two-ligand atoms attached to the metal (Figure 1.2). In the chelation therapy, metal binding molecules are most often organic compounds with suitable chelating properties. Metal chelators interact with metal ions and they can be used either to remove toxic metals from the body in metal overload conditions or for diagnostic and radionuclear therapeutic applications.

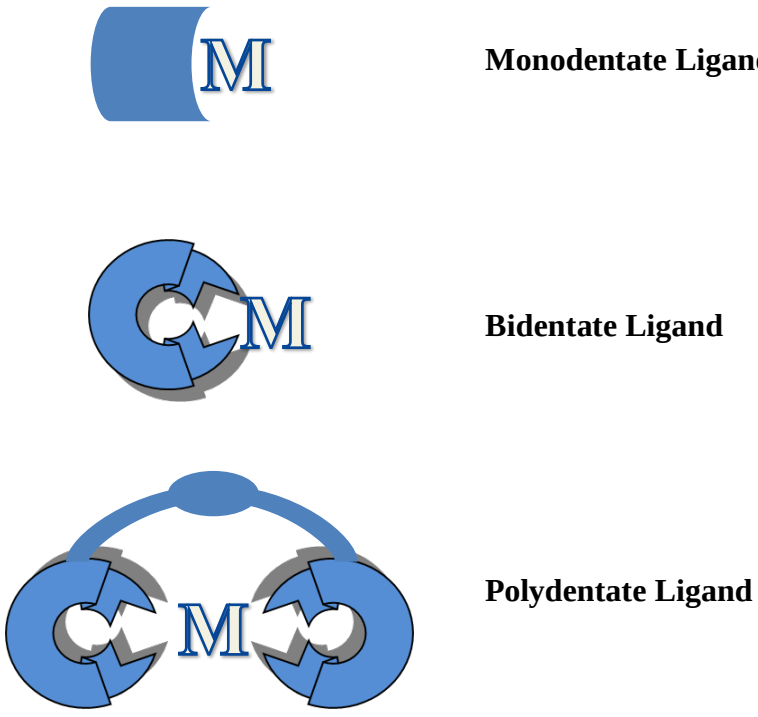

Figure 1.2. Metal-Ligand complex formation using mono, bi and polydentate ligands.

Many ligands act as bidentate ligands and five-membered chelate rings are especially stable. There are also examples of inorganic chelates which form five membered rings with metal ions. The complexation of metal ions with *i* molecules of a monodentate ligand, L, or with one molecule of an *i* dentate ligand λ can be expressed as:

$$M + iL \leftrightharpoons ML_i$$

$$M + \lambda \leftrightharpoons M\lambda$$

The overall stability constants can be expressed by the equations:

$$\beta_L = [ML_i] / [M][L]^i$$

$$\beta_\lambda = [M\lambda] / [M][\lambda]$$

The stability of the complex depends on the thermodynamic equation:

$$\Delta G^0 = \Delta H^0 - T\Delta S^0 = -RT \ln\beta$$

The formation of the ML_i complex depends in a larger extent on the concentration of the ligand (L is at the i^{th} power in β_{ML}) than does the formation of the Mλ complex (λ is at the first power in $\beta_{M\lambda}$). Especially at low ligand concentration, chelates are far more stable than the corresponding complexes with monodentate ligands. The change in log β for complexes with multidentate ligands with increasing numbers of identical donor groups gives evidence of the size of the *chelate effect* [5]. A favourable entropy change occurs upon the exchange of many monodentate ligands for fewer multidentate ligands to bind a given metal ion. The denticity of the ligands determines the number and stoichiometry of the formed complexes. As a general rule, hexadentate ligands are preferred because they form only one kind of complex. Ligands with low denticity form multiple complexes, whose speciation pattern depends on both ligand concentration and ligand/metal molar ratio. The stability of the complex respects the trend monodentate < bidentate < tridentate < tetradentate < …< hexadentate ligands.

1.2.1. Characteristics of chelating agents

In designing a therapeutic metal chelator, one must consider the hard-soft acid-base (HASAB) theory for the appropriate interaction of donor atoms with the target metal ion. Their interaction will determine the stability of the final complex and the selectivity of the ligand for the target metal ion, in an environment where many metal ions are free in solution, such as Ca^{2+}, Mg^{2+} and K^+.

The HASAB theory describes the propensity of electron acceptors (metal ions) to bind electron donors (coordinating molecules) preferentially of similar “hardness” or “softness”. For a metal ion, the term “hardness” or “softness” means how easily its empty orbitals accept electron density. For donor atoms this definition means how deformable are the outer electron orbitals[6]. “Hard” metal ions such as Fe^{3+} or Al^{3+} bind preferentially with “hard” donors such as oxygen in carboxylate groups. On the other

hand, “soft” metals ions such Hg^{2+} are well coordinated by ligands with “soft” donors atoms such as sulphur (Table 1.1).

Table 1.1. Acid and base classification according to the HASAB theory of Pearson.

Acids	
Hard	***Soft***
H^+, Li^+, Na^+, K^+, Be^{2+}, Mg^{2+}, Ca^{2+}, Sr^{2+}, Ba^{2+}, Al^{3+}, Sc^{3+}, Ga^{3+}, In^{3+}, La^{3+},Gd^{3+}, Lu^{3+}, Cr^{3+}, Co^{3+}, Fe^{3+}, As^{3+}, Si^{4+}, Ti^{4+}, Zr^{4+}, Hf^{4+}, Th^{4+}, U^{4+}, Pu^{4+}, Ce^{4+}, WO^{4+}, Sn^{4+}, UO^{2+}, VO^{2+}, MoO^{3+}	Cu^+, Ag^+, Au^+, Ti^+, Hg^+, Pd^{2+}, Cd^{2+}, Pt^{2+}, Hg^{2+}, CH_3Hg^+, $Co(CN)_5^{2-}$, Pt^{4+}, Te^{4+}, Br^+, I^+
Borderline	
Fe^{2+}, Co^{2+}, Ni^{2+}, Cu^{2+}, Zn^{2+}, Pb^{2+}, Sn^{2+}, Sb^{3+}, Bi^{3+}, Rh^{3+}, Ir^{3+}, $B(CH_3)^3$	
Bases	
Hard	***Soft***
H_2O, OH^-, F^-, $CH_3CO_2^-$, PO_4^{3-}, SO_4^{2-}, Cl, CO_3^{2-}, ClO_4^-, NO_3^-, ROH, RO^-, R_2O, NH_3,RNH_2, NH_2NH_2	R_2S, RSH, RS^-, I^-, SCN^-, $S_2O_3^{2-}$, R_3P, R_3As, CO, $(RO)_3P$, CN^-, RNC, C_2H_4, H^-, R^-
Borderline	
$C_5H_5NH_2$, C_5H_5N, N_3^-, Br^-, NO_2^-, N_2, SO_3^{2-}	

The introduction of chelating agents in biological systems requires the comparison between the affinity of the chelator for the target metal ion and that of endogenous ligands. This is because metal ions, especially those which are redox-active under physiological conditions, such as $Cu^{+/2+}$ or $Fe^{2+/3+}$, are generally bound to biomolecules such as proteins, nucleic acids or others, and the introduced chelating agent must participate in a series of ligand exchange competition reactions to form the stable desired complex that can be later dislocated or excreted. Complexation can further protect the metal ion from deleterious reactions, such as the reduction of Fe^{3+} to Fe^{2+}, which via Fenton reaction produces reactive oxygen species (ROS).

The stability constant of a complex $Me_pL_qH_r$ is related to its formation equilibrium, $pMe + qL + rH \leftrightharpoons Me_pL_qH_r$, starting from the completely deprotonated ligand. However, the complex formation *in vivo* occurs with the ligand in its prevailing form at physiological pH according to its speciation pattern determined by the protonation constants. Taking into consideration that complex formation is a competitive reaction between proton and metal for the same basic binding sites on the ligand, and that complexes of different stoichiometries can be formed depending on the denticity and kind of the ligand, stability constants cannot be used to compare the effectiveness of different ligands. A more useful standard comparison is the pM^{n+} value[7], defined as the

negative logarithm of the concentration of free metal (M^{+n}) in solution. Typically pM^{n+} values are calculated for total [ligand] = 10^{-5} M, total [metal] = 10^{-6} M at pH 7.4. The so calculated pM^{+n} values allow a direct comparison of ligands because they take into account the effects of ligand protonation, denticity and the differences in complex stoichiometries[8]. Iron chelators with high pFe^{+3} values are predicted not only to scavenge iron effectively at low ligand concentrations, but also to dissociate less readily, forming low concentrations of the partially coordinated complexes[7].

The requirements of chelating agents have been better and better defined on the bases of many chemical and biomedical considerations, and they are the starting point for the design of a successful metal chelator. These can be summarized:

- Low toxicity of the chelator itself and of the resulting complex. The side effects that often occur after a period of use require the suspension and/or substitution with a different chelator;
- High stability of the formed complex in comparison with the stability of those formed with endogenous ligands;
- High ligand selectivity, mainly determined by the hardness-softness character and by the *chelate effect*;
- Biochemical metabolism of the chelating agent once entered into the body;
- Kinetics of exchange with endogenous ligands;
- Factors affecting absorption and bioavailability;
- Absence of effects on the activity of metal ion-dependent enzymes;
- Kinetic stability of the complex to ensure efficient transport and excretion;

Selectivity toward the target metal ion is one of the main requisites of chelation therapy. For example, to counteract iron overload, iron binding should be not perturbed by the presence of other essential metal ions such as copper and zinc, and at the same time the ligand should not affect their homeostatic equilibrium. The design of the chelator should localize its activity in the target tissue or even in the cell compartment where the metal ion overload is located. Many research groups have tried different strategies to achieve this localization through the synthesis of specific pro-ligands that can be transformed inside the organism and can become active where it is needed, or by appending targeting molecules to the ligand, as is the case of the bifunctional chelators for radiopharmaceutical applications.

The ideal chelator should possess cell membrane permeability in order to be effectively absorbed, but the metal ion complex should not cross the blood-brain barrier (BBB) to prevent unexpected neurological damages. Chelators should be efficiently absorbed by the gastrointestinal tract, and this depends on membrane permeability through parameters like molecular size, lipophilicity and net charge[9]:

- Molecular weight < 500 g/mol;
- The octanol/ water partition coefficient (log P) > 5;

- Less than 10 hydrogen bond donors in the molecule (OH and NH) groups;
- Less than 10 hydrogen bond acceptors present in the molecule (N and O atoms);
- Ionisation state.

Uncharged molecules penetrates cell membranes more rapidly than charged molecules[10]. To achieve absorption greater than 70% subsequent to oral application, the chelator molecular weight needs to be less than 300, while non facilitated diffusion is generally considered to be dominant for drugs with molecular weights < 200.

It is important to remember that the ability of a compound to penetrate BBB critically depends on the partition coefficient as well as on the molecular weight[11]. The BBB permeability is predicted to be low for the most hexadentate compounds, by virtue of their molecular weight[8]. Compounds with molecular weight > 300, and log $P_{water/octanol}$ values less than -1.3 tend to penetrate inefficiently[12].

1.3. Iron

Iron is the second most abundant metal, after aluminium, and the fourth most abundant element in the earth's crust. Iron is a very important metal for a wide variety of cellular events, indeed no life form is possible without the presence of this element. This important role of iron resides on its facile redox chemistry and on its affinity for oxygen. Iron possesses incomplete filled d-orbitals and can exist in various valence states, the most common in aqueous media being Fe^{2+} and Fe^{3+}. Fe^{3+} is quite insoluble in neutral water ($K_{sp}=10^{-39}$M and at pH 7.0 $[Fe^{3+}]= 10^{-18}$ M), and significant concentrations of water-soluble Fe^{3+} species can be attained only when it is in a strong complexed form. In contrast, Fe^{2+} is extremely water soluble. High spin Fe^{3+} is a spherically symmetrical tripositive cation with an ionic radius of 0.067 nm and it is classified as a "hard" Lewis acid by virtue of its high charge density. It forms more stable bonds with "hard" oxygen ligands such as phenolate and carboxylate rather than with imidazole or thiolate. In contrast, the Fe^{2+} cation with an ionic radius of 0.083 nm has lower charge density and it is on the borderline between "hard" and "soft", favouring nitrogen (imidazole and pyrrole) and sulphur ligands (thiolate and methionine) over oxygen ligands.

The most frequent geometry associated with coordination number 6 is the octahedral, for both Fe^{2+} and Fe^{3+}, but also four coordinated complexes (tetrahedral) and five coordinated complexes (trigonal bipyramidal or square pyramidal) can be found. While low-spin complexes are obtained with strong-field ligands, such as F^- and OH^-, high-spin complexes are formed in the presence of weak-field binding groups, such as CO and CN^-. Changes of spin state affect ion size of both Fe^{2+} and Fe^{3+}, the high-spin ion being significantly larger that the low-spin ion. Both oxidation states are Lewis acids, particularly the ferric state[13].

The solution chemistry of iron is essentially characterized by the hydrolysis and polymerisation of aqueous Fe^{3+} to insoluble and potentially biologically inaccessible ferric hydroxides and oxyhydroxides. Living organisms have overcome this accessibility problem by excreting low molecular weight ligands (mainly derived from catechols, or from hydroxamic acids) designed as siderophores. These molecules can specifically sequester iron in a soluble form[14], allowing microorganisms to take up these complexes via specific transport systems. Once inside the cell the iron is released either by reduction to Fe^{2+} (for which the siderophore have little affinity) or by hydrolysis of the ferri-siderophore accompanied by release of its iron. In general multicellular organisms do not possess a system of siderophores with their appropriate receptors so they must find the required iron from alimentation. The role of the transport of iron to the different cell within the organism and its resorption from the dietary sources is assured by the serum globulin transferrin, which complexes iron, transports it in the circulation, and via specific receptors it is taken up by the cells of the organism. The release of iron is pH-dependent and the availability of proton pumps within specific intracellular compartments assures the intracellular release of iron; the iron-free protein is recycled from the cell and released into the circulation for reutilisation. Once the iron is released within the cell, either the iron which liberated from its soluble siderophore complex will be complexed by an intracellular chelator, or it will follow its inexorable hydrolysis and polymerisation towards biological inaccessibility. As an evolution of the capacity of living organisms to assimilate and utilize iron, there are intracellular iron storage compounds, which allow the cell in physiological conditions to dispose of a pool of bioavailable, soluble and non-toxic iron. The archetype of these compounds is the iron storage protein, ferritin.

The importance that such iron storage compounds should be non-toxic is because the potential toxicity of iron related to its redox chemistry. Iron ions, as other transition metal ions, are intimately associated with many of oxidative stress events, especially in the process of lipid peroxidations, which lead to the cells and tissues damage.

In the Fenton reaction a Fe^{2+} in presence of H_2O_2 produces the •OH radical:

$$Fe^{2+} + H_2O_2 \rightarrow Fe^{3+} + \bullet OH + OH^-$$

In the presence of trace amount of iron, superoxide can than reduce Fe^{3+} to molecular oxygen and Fe^{2+}.

$$Fe^{3+} + O_2^- \rightarrow Fe^{2+} + O_2$$

$$O_2^- + H_2O_2 \rightarrow O_2 + \bullet OH + OH^-$$

Since the oxidation of ferrous iron by molecular oxygen can be represented by the sequence of reactions below, it is immediately apparent that if 'free' iron exists within a cell, it could provoke the production of hydroxyl radicals, with disastrous consequences for the cell. The system is in fact used by macrophages in the killing of bacteria:

$$Fe^{2+} + O_2 \rightarrow Fe^{3+} + O_2\bullet^-$$

$$2O_2^- + 2H^+ \rightarrow H_2O_2 + O_2\bullet$$

Therefore the complexation of iron within a cell necessitates that the iron storage protein must guard its iron in a soluble, bio-available and non-toxic form as ferritin does. In fact iron metabolism in man is highly conservative, and since man lacks a physiological mechanism to eliminate iron, iron homeostasis in the normal individual is achieved by a tight regulation of iron absorption from the gastrointestinal tract.

However there are situations when the iron status can change, either locally as in ischaemic tissue, or systematically due to the genetic haemochromatosis or transfusion-induced iron overload. The most common iron overload is a genetically determined disorder, the homozygous state for hereditary hemochromatosis, occurring in as much as 0.5% of the population or as many as 1 million individuals[15]. There are other forms of iron overload, less frequent but affecting several thousand patients with iron-loading or transfusion-dependent anaemias such as thalassemia major and acquired refractory anaemias. Dietary iron-overload resulting from intake of iron in brewed beverages is a common problem affecting many populations in Sub-Saharan Africa[16]. In such circumstances, the elevated levels of iron ultimately accumulates in the heart, liver and joints, among other tissues, and can lead to free radical-mediated damage and eventual death[17].

1.3.1. Iron chelators

To prevent patients from iron toxicity, iron chelating agents have been introduced in clinical practices. Unfortunately an ideal chelator to overcome iron overload in humans has not been identified yet. Fe^{3+} forms stable bonds with hard ligands which contain oxoanions as a functional groups, such as catechols, hydroxamates, aminocarboxylates, hydroxycarboxilates, hydroxypyridinones (HPOs) and hydroxypyrones.

1.3.1.1. Catechols

Catechol, as a functional group is found in Enterobactin (Figure 1.3), which is a siderophore that binds iron for microbial systems. It is found mainly in Gram-negative bacteria, such as Escherichia coli and Salmonella typhimurium[18]. Molecules such as MECAM (1,3,5-N,N',N"-tris-(2,3-dihydrobenzoyl)triaminomethylbenzene, Figure 1.3) have been synthesized in order to mimic the natural siderophore molecule. This extremely strong interaction with tripositive metal cations is a result of the high electron density of both oxygen atoms. This high charge density is also associated with the high affinity for protons (pK_a values 12.1 and 8.4)[19]. The complexes forming at pH 7.0 bear a net charge and consequently are unlikely to permeate membranes by simple diffusion[20]. Such iron complexes tend to be trapped in intracellular compartments. Moreover, bidentate catechols form with Fe^{3+} the 2:1complexes (dominant form in the pH range 5.5-7.5), where iron atom being not completely protected from the solvent is

able to interact with hydrogen peroxide and oxygen to produce free radicals[8]. The main problem with the catechol-based ligands is their susceptibility towards oxidation.

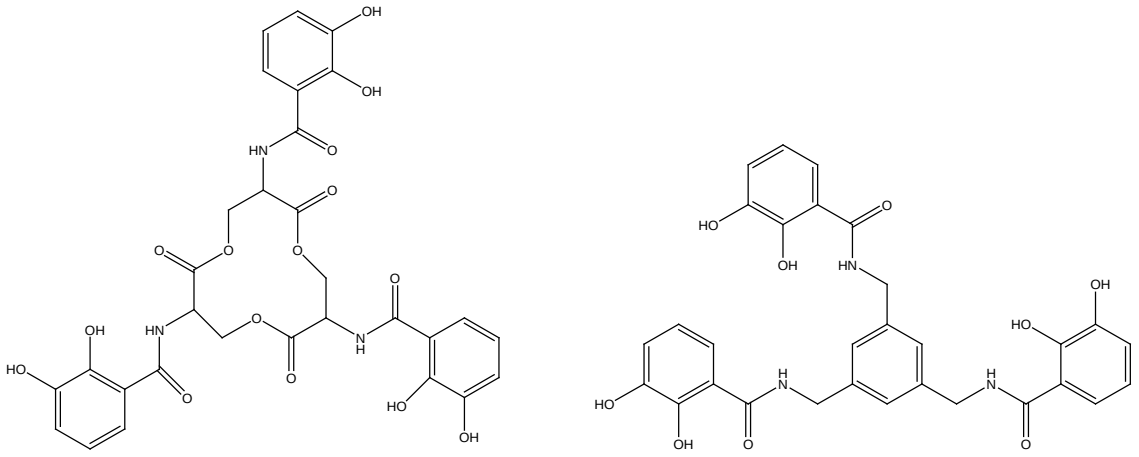

Enterobactin MECAM

Figure 1.3. Hexadentate catechols.

1.3.1.2. Hydroxamates

An important natural hexadentate ligand is deferrioxamine (DFO, Figure 1.4), a fungal siderophore. DFO is a hydroxamate-based hexadentate chelator isolated from *Streptomyces pilosus*, and it is the current clinical chelator of choice for the treatment of iron overload diseases such as β-thalassemia. Siderophores are natural product iron chelators, secreted by microbes as a response to the insoluble nature of iron in the environment[21]. These hydroxamates have a lower affinity for iron than catechols, but they have the advantage to form neutral *tris*-complexes with Fe^{3+} which are able to permeate membranes by non-facilitated diffusion[20]. The protonation constant (pK_a ~ 9) makes lower the proton competition for the binding sites on the ligand at physiological pH that in the case of catechol ligands, consequently 3:1 complex predominates at pH 7.4 and sufficient ligand concentration. Unfortunately, the affinity for a simple bidentate hydroxamate ligand (Figure 1.3) is insufficient to solubilize Fe^{3+} at pH 7.4 at clinical concentrations. For this reason, only tetradentate and hexadentate ligands are considered as possible Fe^{3+} scavengers under such conditions. The hexadentate DFO, displays very poor oral bioavailability and must be administered via long subcutaneous infusions, leading to high cost of treatment and low patient compliance. Many others hydroxamates are metabolically labile and poorly absorbed via the oral route[22]. However, more lipophilic DFO analogues have been synthesized by reacting the terminal primary amino group with fatty and aromatic acid chlorides or anhydrides, but none of them has been reported more efficient than DFO administered via subcutaneous route[23].

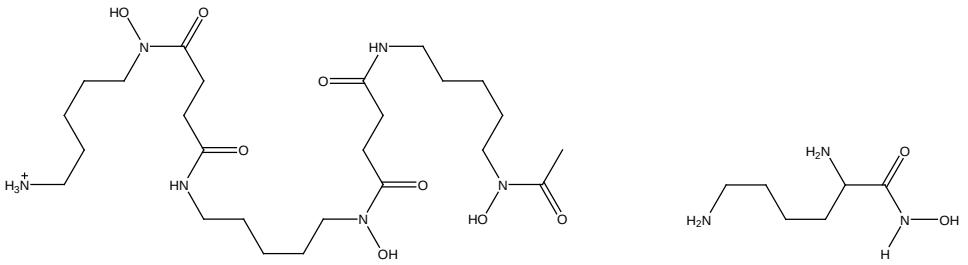

DFO **L-lysinehydroxamic acid**

Figure 1.4. Hexadentate deferrioxamine (DFO) and bidentate (L-lysinehydroxamic acid) hydroxamates.

1.3.1.3. Aminocarboxylates

Aminocarboxylates ligands are produced by cereals, for instance wheat, barley, rye and oat (i.e. mugineic acid in Figure 1.5). This category includes chelators such as EDTA and DTPA (Figure 1.5). They are able to chelate strongly iron. However they are not selective for iron and for this reason their use in medical treatment is limited because their lack of selectivity leads to zinc depletion in patients[10]. Moreover, the complexes formed with iron can catalyse redox reactions. Thus, EDTA is not able to shield the surface of the Fe^{3+} ion, but it forms an open complex. The exposition of the complex to the biological environment facilitates the interaction with the metal and consequently originates Fenton reactions with reactive oxygen species (ROS)[24].

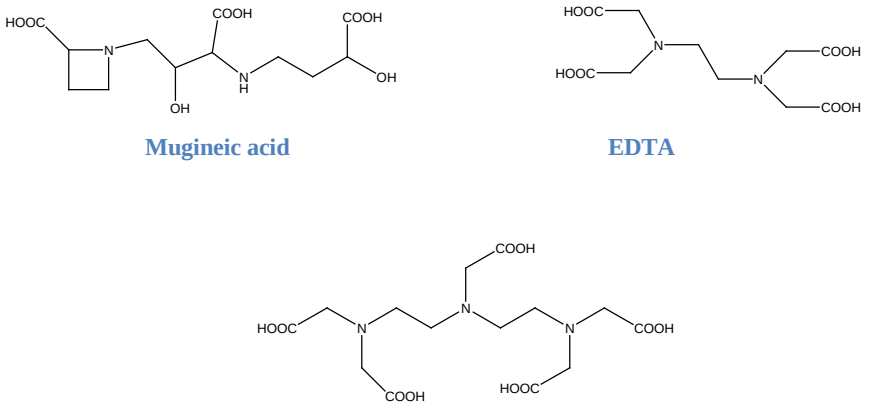

Mugineic acid **EDTA**

DPTA

Figure 1.5. Aminocarboxylates ligands.

1.3.1.4. Hydroxycarboxylates

The hydroxycarboxylate ligands such as citrate (Figure 1.6) are strong chelating agents. They only have oxygen coordinating atoms so they are more selective towards Fe^{3+} than aminocarboxylates. The interaction between Fe^{3+} and citrate has been well established, but by virtue of its tridentate nature, a large number of complexes have been identified

including iron/citrate polymers. In contrast, the hexadentate hydroxycarboxylate ligands, staphloferrin[25] and rhizoferrin (Figure 1.6) form simple 1:1 complexes, similarly to DFO[26].

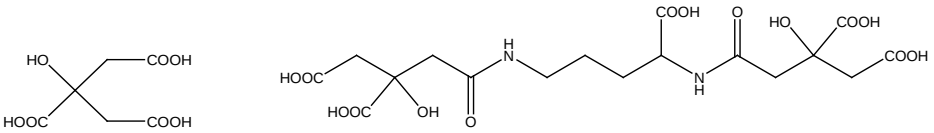

Citrate Rhizoferrin

Figure 1.6. Hydrocarboxylates.

1.3.1.5. Hydroxypyridinones

Hydroxypyridinones (HPOs) are acids, which form 5-membered chelate rings in which metal is coordinated by two vicinal oxygen atoms. This family of chelators combine the characteristics of the functional groups hydroxamates and catechols to chelate selectively tribasic metal cations over dibasic species. There are three classes of metal chelating HPOs, namely, 1-hydroxypyridin-2-one (1,2-HP), 3-hydroxypyridin-2-one (3,2-HP) and 3-hydroxypyridin-4-one (3,4-HP), shown in Figure 1.7. This family of ligands can be easily functionalized to improve their properties, above all the bioavailability and the chelating ability[27]. Deferiprone (1,2-dimethyl-3-hydroxypyridin-4-one, DFP) is a member of the bidentate hydroxypyridinone family of iron chelators, which is the first orally active treatment of β-thalassemia characterized by a value of pFe 20.67. The high pK_a value of hydroxyl function of 3-hydroxypyridin-4-one results from extensive delocalisation of the lone pair associated with the ring nitrogen atom. DFP forms neutral 3:1 complexes with Fe^{3+} that dominate the speciation profile in the millimolar concentration range at physiological pH. However, at micromolar concentrations at pH 7.4, the 2:1 complex is no more negligible (~10%) and the incomplete coordination of iron by deferiprone would enable the access of reductants to the iron core and may potentially lead to ROS production[28].

In order to reduce the presence of redox active complexes and increase complex stability[29], various derivatives have been synthesized containing two or three units of HPOs[30],[31],[32] (Figure 1.7). These enable the modulation of bioavailability and the possibility of interaction with several biological targets.

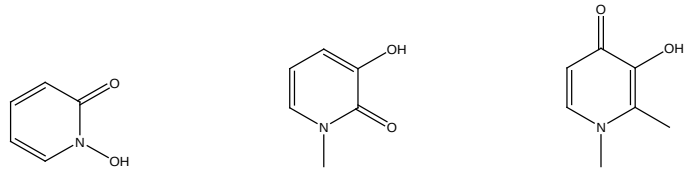

1,2-HP 3,2-HP 3,4-HP (Deferiprone)

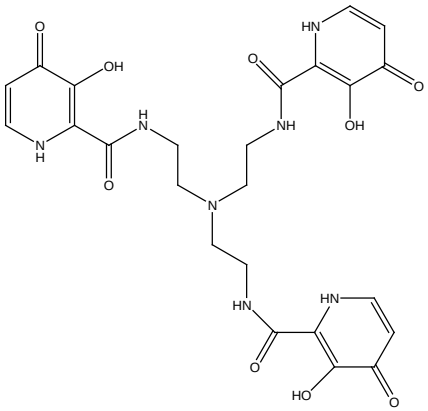

Tren(3,4-HP)$_3$

Figure 1.7. Bidentate and hexadentate hydroxypyridinones.

1.3.1.6. Hydroxypyrones

Hydroxypyrones differ from HPOs for the oxygen in the ring, which decreases the basicity of the –OH group. For instance, while DFP has a pK_a 9.8[24], kojic acid is characterized by a pK_a 7.7[33]. Hydroxypyrones chelate iron forming five-membered rings as their analogues HPOs do.

Kojic acid (KA) (Figure 1.8) is one of the most studied hydroxypyrones and it is a promising molecule for the development of more effective derivatives. An interesting iron chelator, 6-[5-hydroxy-2-hydroxymethyl-pyran-4-one]-5-hydroxy-2-hydroxymethyl-pyran-4-one (L1), demonstrated high efficacy for the *in vivo* mobilization of ferritin-bound iron[34]. Several similar ligands have been studied in these last years in our research group[33],[35],[36],[37] (See Figure 1.8). These ligands, constituted by two KA units joined by different linkers, form stable iron dinuclear complexes characterized by pFe values several orders of magnitude higher than that of the precursor. The main advantages and good perspectives are their easy and inexpensive synthesis, their relatively low molecular weight (340-450 Da), which makes them possible oral chelators; the chances of modulating their binding ability working on proper substituents in the KA units and in the linker[27].

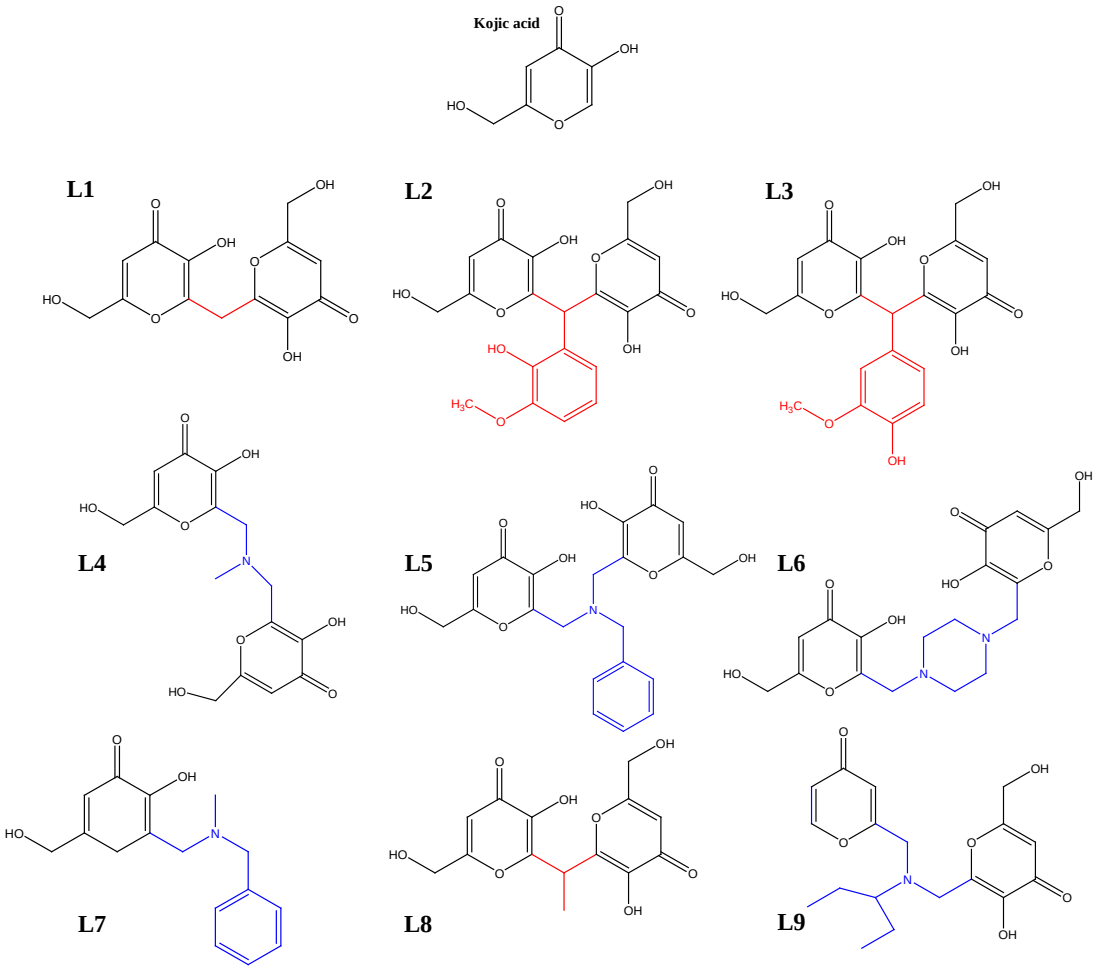

Figure 1.8. Hydroxypyrones kojic acid derivatives ligands synthesized in our research group.

1.4. Aluminium

Aluminium is the most abundant metallic element, and the third constituent of the earth's crust, after oxygen and silicon. Aluminium, due to its extremely low redox potential, occurs ubiquitously in the environment combined in salts and oxide forms. Because of its physical and chemical properties, aluminium metal and its compounds have a wide variety of uses: building, transportation, food packaging, beverage cans, cooking utensils, food additives, pharmaceutical preparations, surgery materials, cosmetics, water purification.

The chemistry of Al^{3+} is simpler than that of Fe^{3+}[38]. Aluminium is much more soluble than Fe^{3+}, and exhibits only one oxidation state in biological systems. Metallic Al is too reactive to be found free in nature, and the metal is won from its ores only with difficulty[39]. The effective ionic radius of hexa-coordinated Al^{3+} is 0.054 nm. By way of comparison other values are Ga^{3+} 0.062, Fe^{3+} 0.065, Mg^{2+} 0.072, Zn^{2+} 0.074, Fe^{2+} 0.078, and Ca^{2+} 0.100 nm. On the basis of the radii, though quite small, Al^{3+} is closest to

Fe^{3+} and Mg^{2+}. Ca^{2+} is much larger, and in its favoured eight-fold coordination exhibits a radius of 0.112 nm, yielding a volume nine times greater than Al^{3+}.

The fact that no physiological function in the course of evolution has been attributed to aluminium implies that its metabolism cannot benefit of any homeostatic regulatory process. In particular, its gastrointestinal absorption is not expected to be based on a specific active transport system, and it should therefore simply depend on the solution chemistry of the Al^{3+} ion in the gastrointestinal tract, i.e. the solubility of the ingested salts within the gastrointestinal pH interval and its complex formation with the anionic forms of these salts, which do not only induce Al^{3+} solubilisation but may also facilitate the absorption process[40].

Since 1970, aluminium has been recognized to cause serious diseases. Aluminium enters into the body from the environment and from diet and medications. Human exposure is mainly dietary, less than 5 per cent of oral intake is due to drinking water. Antiperspirants can also be a non-negligible source of aluminium absorption. Most exposed populations remain patients on dialysis, long-term antacid consumers and workers in the aluminium industry.

In biological systems Al^{3+} is chelated by the methylmalonate. The metal ion is chelated with two oxygen donors of two carboxylate amino acids aspartate and glutamate[41]. Despite of greater basicity of methylmalonate[42], it forms a weaker chelate (six-membered) with Al^{3+} than those with oxalate (five-membered)[43]. Lactate forms weak AlL^{2+}, AlL_2^{+}, and AlL_3 complexes in acidic solution where the hydroxyl group retains its proton[44]. The ligand that incorporates Al^{3+} into mammals is citrate. Ligand exists predominantly in the form of the tricarboxylate anion at pH > 6, and at the 0.1 mM concentration in the blood plasma is the predominant small Al^{3+} binder[39],[45],[46]. While citrate is the low molecular weight carrier of Al^{3+} in serum, transferrin is the high molecular weight carrier. The transferrin receptor is specific for transferrin and not for Fe^{3+}, and hence Al^{3+} may enter the central nervous system as does Fe^{3+}.

Toxic effects of aluminium chronic exposure are mainly neurological effects (encephalopathy, cognitive and motor disorders), bone disease (vitamin D resistant osteomalacia), and blood effects (microcytic anaemia). Aluminium also causes immune and allergic reactions. Other suspected effects are not confirmed, in particular the involvement of aluminium in a variety of neurodegenerative diseases (Alzheimer's disease, amyothrophic lateral sclerosis and Parkinson's disease)[10, 47].

1.4.1. Aluminium chelators

The awareness of aluminium toxicity has led several research groups to study new possibilities for chelating agents, some of them being already used for iron chelation. Both iron and aluminium, due to their short ionic radius and their high charge, are hard metals. As iron, aluminium prefers hard bases containing oxygen atoms, as hydroxamates, catecholates, bisphosphonates, salicylates, HPOs and hydroxypyrones[47]. The first aluminium chelator in clinical practice was DFO, for the

treatment of osteomalacia (Figure 1.7). Recently, some hydroxypyridinone derivatives have been studied as chelators for trivalent metal ions by the group of Santos[32] (Figure 1.9); the tetradentate iminodiacetic acid bis-(3,4-HP) and derivatives called IDAPr(3,4-HP)$_2$[48]; a ternary system composed by an arylpiperazine-containing bis-hydroxypyrydinone[49]; two hexadentate ligands, the tris-hydroxypyrydinone-based compounds KEMPPr(3,4-HP)$_3$ and KEMPBu(3,4-HP)$_3$, where the KEMP acid scaffold is attached to three 3,4-HP chelating moieties via different size spacers[31]; two new tris(3,4-HP) hexadentate chelators, NTA(BuHP)$_3$ ad NTP(PrHP)$_3$, in which the three HP units were connected by nitrilotriacetic acid (NTA) and nitrilopropionic acid (NTP)[50],[51]. High Fe^{3+} affinity was found for these last two chelators, being pFe = 27.9 for NTA(BuHP)$_3$ and pFe = 29.4 for NTP(PrHP)$_3$, and pAl = 22.0 and 22.4 respectively. Other ligands have been synthesized for tripositive metal ions with high pAl value, is the case of the tripodal O-TRENSOX and the similar triscatechol derivate TRENCAMS[52]. Bisphosphonates ligands showed high efficiency as Fe^{3+} and Al^{3+} chelators[53] (Figure 1.9). Hydroxypyrone ligands, studied in our group, based on two kojic acid units joined by different likers (Figure 1.8), and especially those designed by L1, L2 and L3, have a high affinity for Al^{3+} with pAl values of 12.8, 11.9 and 13.9 respectively[35].

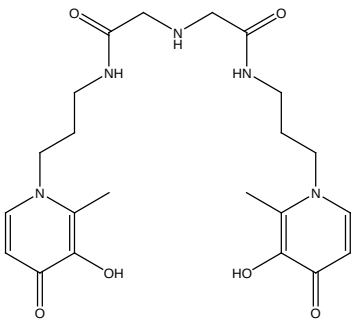

IDAPr(3,4-HP)$_2$

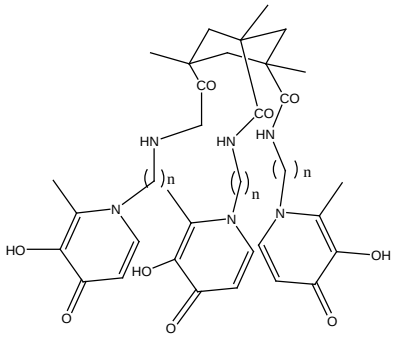

KEMPPr(3,4-HP)$_3$ n = 3

KEMPBu(3,4-HP)$_3$ n = 4

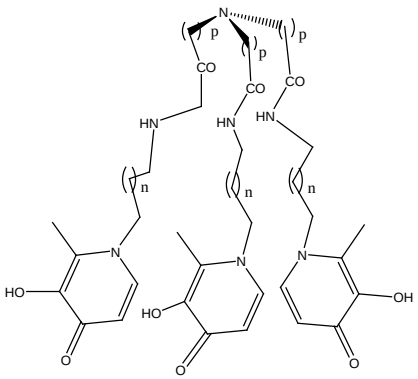

NTA(BuHP)$_3$ p = 1, n = 2

NTP(PrHP)$_3$ p = 2, n = 1

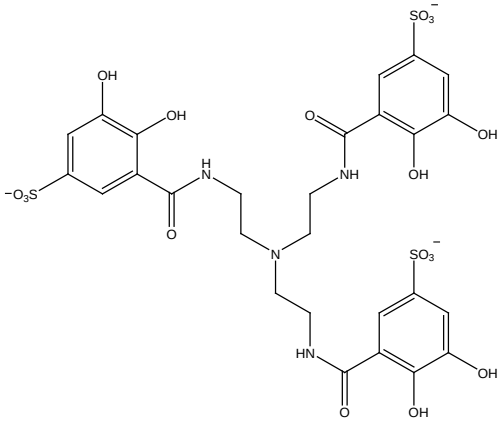

TRENCAMS

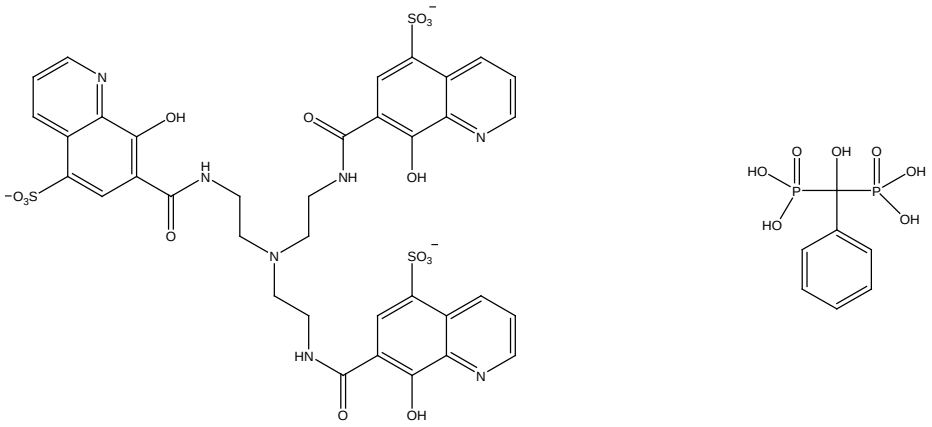

O-trensox Bisphosphonate (^{1}L)

Figure 1.9. Aluminium chelators.

1.5. Copper

Copper is present in different concentrations and chemical forms throughout the earth crust, surface, deep water and in the atmosphere (in trace amounts).

It is a micro-element essential for life. Copper is a redox-active metal that is responsible for the function of many cellular enzymes and proteins, so it is involved in important biological processes including respiration, angiogenesis and neuromodulation. Most of copper in human body is bound to biological macromolecules in both the oxidation states: Cu^{+} mainly present in the intracellular space (reducing environments) and Cu^{2+} in the extracellular space (oxidizing environments). Cu^{+} and Cu^{2+} have different chemical properties. Cu^{+} is not stable in aqueous solution where it is easily oxidized to Cu^{2+}. The standard reduction potential Cu^{2+}/ Cu^{+} is 0.153 V, thus reflecting the low likelihood that Cu^{2+} is reduced. Cu^{+} prefers to bind to soft ligands rather than intermediate ones as Cu^{2+} does. In proteins, while Cu^{2+} is usually anchored to His imidazole or N-terminal amino group, stable Cu^{+} sites are formed by sulfur thiolate or thioether from Cys and Met.

Copper behaves as catalytic cofactor of many human enzymes, like cytochrome-c oxidase (CcO), superoxide dismutase (SOD), ceruloplasmin, tyrosinase, peptidyl-α-monooxygenase and dopamine beta-monooxigenase[54]. The structural basis of the activity of copper enzymes and chaperones are becoming well elucidated[55]. Copper proteins are classified as either type 1, 2 or 3. Type 1 (blue copper sites) functions in single electron transfers[56]. In type 2 copper sites, copper acts as a catalytic centre and binds directly to substrates. Type 3 copper sites are binuclear and involved in the activation and transport of oxygen.

Copper can also play a key role in many diseases[57], including copper metabolism disorders, i.e. Menkes and Wilson diseases[58], neurodegenerative disorders like familial amyotrophic lateral sclerosis (FALS), Alzheimer's and prion diseases. Aβ plaques

found in Alzheimer's disease brains contain elevated levels of the metals ions copper, zinc and iron. Cu and Zn ions are thought to play an important role in binding to the Aβ protein and causing some of the aggregation, redox activity and downstream effects that lead to the symptoms of AD[59],[60],[61],[62],[63]. In diabetic animals and patients with diabetic cardiomyopathy high levels of systemic copper are found, with elevations in urinary copper, normal or elevated plasma copper and ceruloplasmin levels, and markedly elevated hepatic and renal copper levels[64],[65],[66],[67]. This impaired copper regulation has been implied in increased prooxidant stress, defective antioxidant defenses[68], and progressive damages to the blood vessels, heart, kidneys and nerves (the 'diabetic complications')[69].

Cu^{2+} becomes toxic when an excessive intracellular accumulation occurs. In Wilson's disease, the transport of copper into the secretory pathway for incorporation into ceruloplasmin for biliary excretion (the only mechanism for copper excretion from the body), is impaired[70]. Cu^{2+} can directly accelerate the production of ROS via the Fenton reaction and create a disturbance in the prooxidant-antioxidant balance, which can contribute to the development of cell damage and consecutive apoptosis[71]. Cells have therefore developed sophisticated machinery composed by a network of proteins to ensure tight control of copper in the cell during its acquisition and distribution within the biological system, avoiding circulation of "free" copper[72],[73]. "Free" copper ions can participate to the production of ROS, so it is necessary that copper adsorption, distribution, utilization and excretion is tightly regulated by those specific proteins. In addition to the generation of ROS, Cu^{2+} may manifest its toxicity by displacing other metal cofactors from their natural ligands.

1.5.1. Copper chelators

The treatment for copper overloading or intoxication is chelation therapy. Different molecules are already in clinical use and others in clinical trials. The three most important chelators used for the treatment of Wilson's disease are D-penicillamine (D-pen), triethylenetetramine ((N,N' –bis(2-aminoethyl)-1,2-ethanediamina, trientine, TETA, or Trien) and ammonium tetrathiomolibdate (TTM) (Figure 1.10). The first metal chelator used for copper overload in WD was BAL (Figure 1.10). This chelating agent contains two thiol groups that compete with body protein for copper binding and, once copper is chelated, the complex is excreted in the urine. BAL was originally developed as an antidote against lewisite during the World War II, and then used to treat metals intoxications[74]. D-penicillamine (D-pen), orally active and less toxic than BAL, was successively developed. More lipophilic D-pen derivatives have been synthesized to theoretically increase cell uptake of the chelator[75]. TETA was introduced in 1982 to be used in patients intolerant to D-pen[76]. Tetrathiomolibdate (TTM) can be administered to WD patients for initial therapy followed by zinc acetate for maintenance therapy with remarkable efficacy, and is thought to be a better choice than the traditional chelation by TETA[77].

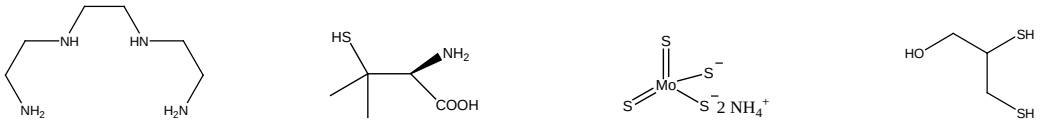

TETA, Trien **D-pen** **TTM** **BAL**

Figure 1.10. Main copper chelators for the treatment of Wilson's disease.

Examples of tripodal Cys-rich chelators to act as potential Cu^{+} chelators *in vivo* have been reported (H_nLx in Figure 1.11)[78],[79],[80]. Clioquinol ((5-chloro-7-iodo-8-hydroxyquinoline, CQ, in Figure 1.11) binds in a bidentate fashion with high affinity to a range of metal ions. CQ has been used in the past as an antibiotic[81], and recently, as antiproliferative agents against tumor cell lines, in the form of copper complexes[82],[83]. CQ was also found to reduce the formation of amyloid plaques[84], being able to partially disaggregate Cu-triggered Aβ aggregates by virtue of its high affinity for Cu^{2+}[85]. Two CQ analogues have been reported in the literature, consisting of two 8-hydroxyquinoline moieties linked through a spacer (C1, C2, Figure 1.11)[86],[87],[88]. These tetradentate ligands, C1 and C2, showed higher copper binding affinities and remarkable capacity to reduce the production of ROS.

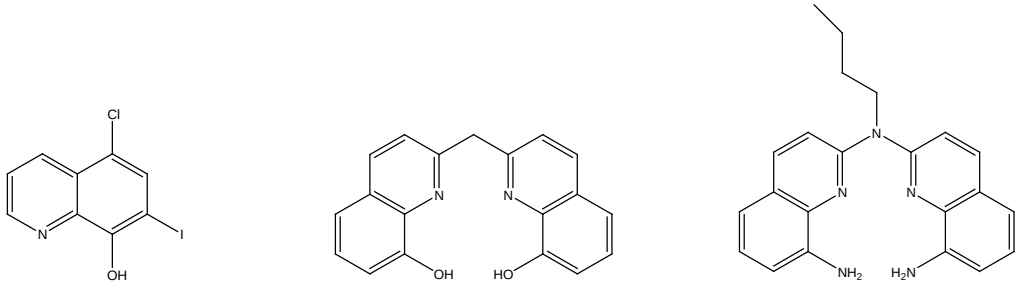

CQ **C^1** **C^2**

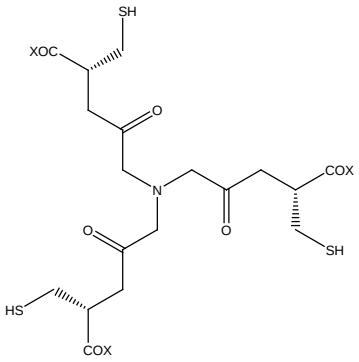

H_3L^1 : X = OEt

H_3L^2 : X = NH_2

H_3L^3 : X = OH

Figure 1.11. Copper chelators.

Recently, several bifunctional chelators (BFCs) have been synthesized. They are simply chelators with reactive bifunctional groups that can be covalently coupled (conjugated) to targeting vectors (e.g. peptides, nucleotides, antibodies, nanoparticles)[89]. The

general idea is that the introduction of a second function allows the chelator to work under specific conditions, in specific tissues or in the presence of specific biomolecules[90]. BFCs chelators for Alzheimer's disease (AD) have been synthesized taking advantage of the ability of some molecules to interact with Aβ. It is the case of K0 ligand in Figure 1.13, designed by merging the structural feature of CQ and the scaffold IMPY (Figure 1.12)[85],[91]. Also the ligand XH1 in Figure 1.13, where two molecules of Tht (Figure 1.12) are linked to DTPA[92]. Finally, in Cyc-KLVFF (Figure 1.13) a cyclen moiety is attached to a N-terminus of the KLVFF fragment (Figure 1.12) which is a β-sheet breaker that inhibits Aβ aggregation[93],[94],[95],[96],[97].

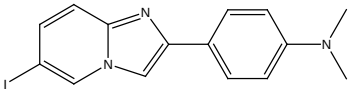

IMPY

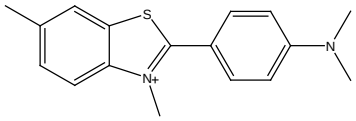

Tht

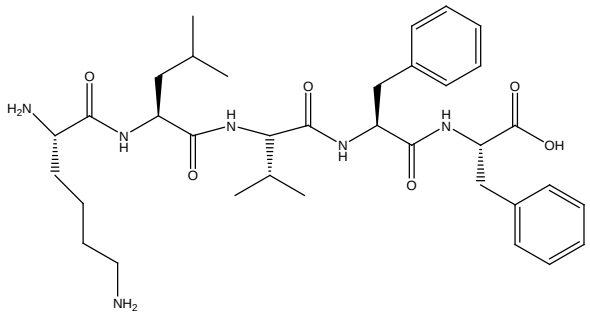

KLVFF

Figure 1.12. Molecules capable to interact with Aβ.

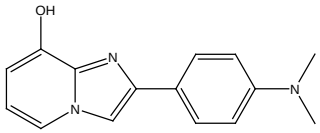

K0

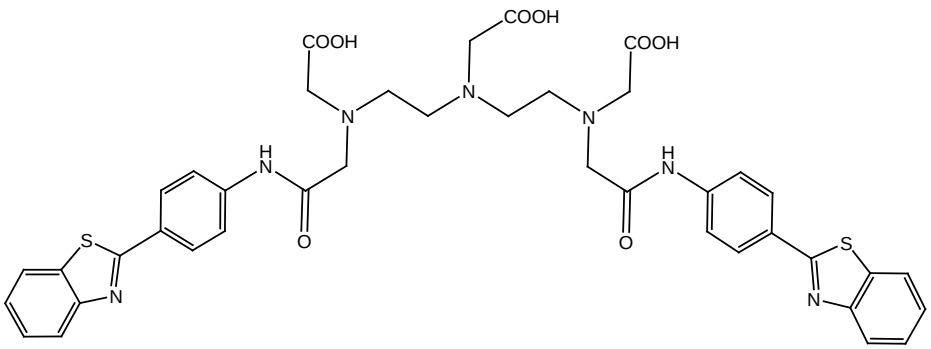

XH1

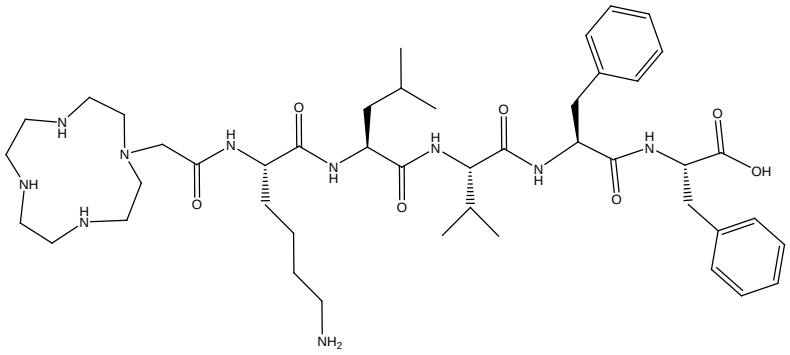

Cyc-KLVFF

Figure 1.13. Examples of copper bifunctional chelators.

Moreover, defective copper regulation is widespread in diabetes, where it has been linked to the causation of cardiovascular disease[67] and is now serving as a target for experimental therapeutic intervention by treatment with a Cu^{2+}-selective chelator[69],[98]. In this thesis the complex formation equilibria of two pharmaceutical agents to treat hypertension in diabetic patients with the essential metal ions Cu^{2+} and Zn^{2+} have been studied.

1.6. Zinc

Zinc (atomic weight 65.41 g/mol) is a soft, bluish-white metal (density 7.14 g/mL). It presents the oxidation states 0, +2. After iron is the most abundant trace element in the body and its higher concentrations are found in the brain and also in pancreatic cells. There are about 2.6 g of zinc in the body, and Zn^{2+} is involved in nearly all aspects of molecular and cell biology[99]. Zinc proteins account for about 10% of the human proteome, *ca* 3000 zinc proteins with physiological functions[100]. Zinc plays a role in the structure of proteins as well as in enzymatic catalysis. Its coordination chemistry within proteins has been widely studied[101]. The most common amino acids that supply ligands for Zn within the catalytic sites are Hys, Glu, Asp and Cys. In catalytic sites Zn usually forms complexes with water and any three nitrogen, oxygen and sulfur donors with His being the predominant chosen amino acid. Zinc, in its ionic form, can also exert important modulatory effects on neurotransmission and synaptic function, as well as regulate many signalling pathways[57]. In some cells relatively high concentrations of zinc can be reached in vesicles (milimolar, especially in synaptic vesicles in the brain) where it is stored and undergoes controlled release[102]. Zinc deficiency is therefore accompanied by dramatic consequences as erosion of the gastrointestinal tract, skin lesions, cardiac failure, malformations of brain and of male reproductive system[103]. However, zinc, and above all its “free” or loosely bound form, is very toxic to mammalian cells, and evidence of this is that zinc is a key factor in neuronal death associated with ischemia and seizures and in other neurological diseases states, as its implication as a trigger for neuronal loss in several neurological conditions. In fact,

deregulation of Zn^{2+} homeostasis is believed to be connected with mitochondrial dysfunction and oxidative stress, making the cation a possible contributor to the activation of pathophysiological pathways involved in brain aging and/or neurodegeneration. Thus, exposure to high Zn^{2+} concentrations both *in vitro* and *in vivo* promote neuronal death, and elevated Zn^{2+} levels are linked to the neuronal loss observed in epilepsy, ischemia and traumatic brain injury[104]. Metallothioneins (MTs) exert a crucial role in maintaining Zn^{2+} homeostasis. MTs are small proteins with a highly conserved sequence of 20 Cys residues yielding two domains for Zn^{2+} binding. Cellular oxidants may promote Zn^{2+} release from MTs and reducing agents may facilitate Zn^{2+} binding[105]. Therefore, the ability to release Zn^{2+} upon changes in the cellular redox state, renders MTs a reservoir of readily available Zn^{2+} under conditions of oxidative stress.

It is not only the right amount of zinc in the diet that maintains health. At least as important is the proper functioning of the dozens of proteins that control cellular zinc homeostasis, regulate intracellular traffic of zinc between the cytosol and vesicles/organelles, and determine the fluctuations of signalling Zn^{2+} ions. Cellular zinc deficiency or overload compromise the redox balance. Zinc supplementation may not readily remedy zinc deficiency if other factors limit the capability of a cell to control zinc. The role of zinc in human diseases requires a general understanding of the wide spectrum of functions of zinc, how zinc is controlled, how it interacts with the metabolism of other metal ions, in particular copper and iron, and how perturbation of specific zinc-dependent molecular processes causes disease and influences the progression of disease.

1.6.1. Zinc chelators

Although metal chelating agents represent a needed therapeutic strategy, they are accompanied by several undesirable side-effects. Long term use of not tissue-specific chelators, such as DFO, leads to affect the homeostasis of numerous biometals and disturbs the normal physiological functions of essential metal-dependent biomolecules such as metalloenzymes[106]. The ability to target specific tissues selectively, using bifunctional chelators may minimize the toxicity of metal chelators and enhance their effectiveness. Using the approach of synthesizing bifunctional chelators, a DTPA analog, XH1 (Figure 1.13) ligand, was developed to chelate excess of metals (especially Cu, Zn and Fe) and disturb aberrant metal-peptide interactions in AD.

Others ligands have been designed in order to act as metalloenzymes inhibitors[107]. They are a series of pyrone-based inhibitors of Zn^{2+}-dependent matrix metalloproteinases which could chelate the catalytic Zn^{2+} site and also anchor the compound via noncovalent interactions within the active site (Figure 1.14).

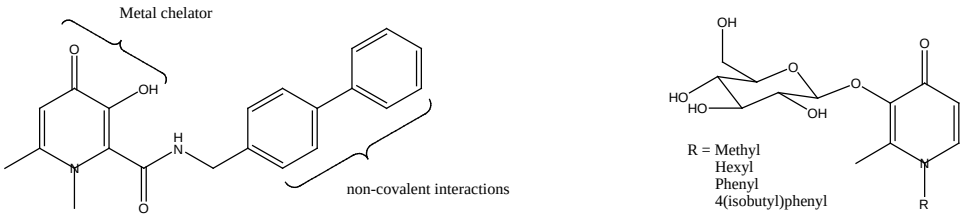

Figure 1.14. A pyrone matrix metalloproteinase inhibitor (left) and pyridinone glycosides (right) conjugate metal chelators.

A family of pyridinones glycosides have been synthesized by the group of Orvig[82] in order to passivate and/or remove excess of metal ions from the brain of AD patients using a multifunctional approach (Figure 1.14). This approach intend to functionalize the 3-hydroxy position of the 3,4-HP, to prevent premature systemic metal chelation prior to passage across the blood brain barrier (BBB). The use of glucose to protect the pyridinone allows glucose conjugates to gain access to the brain. Glycoconjugates have been used to deliver many drugs across the BBB[108],[109],[110],[111],[112].

Acute zinc intoxication, accidental or suicide is uncommon and limited cases are reported, and chelators as BAL and/or EDTA were used[113].

1.7. Gallium and its role in medicinal chemistry

Gallium occurs in nature as Ga^{3+} compounds, in trace amounts in zinc ores and in bauxite. Its stable oxidation state in solution is +3. Ionic radius (0.062 nm) and high charge dictate that Ga^{3+} is a hard acid in the HASAB theory, forming the strongest complexes with hard ligands such as hydroxide, fluoride, sulphate and phosphate, and weaker complexes with chloride and bisulfide ligands[6]. Ga^{3+} contains a full complement of 10 d-electrons in its valence shell, leading to high degree of covalent bonding in complexes compared to Al^{3+}[114]. Although gallium has no natural function in biology, gallium ions interact with processes in the body in a similar manner to Fe^{3+}. Indeed, in many pathological proliferating cells processes (which involve Fe^{3+} uptake), the presence of Ga^{3+} can induce an antiproliferative effect, particularly in cancer cells and some bacteria[115],[116] ,[117],[118]. Non-redox-active Ga^{3+} can inhibit (redox-active) Fe^{3+}-dependent pathways, including iron pathways in bacteria[119]. Moreover the possibility of using various ligands as metal carriers in chemotherapy has increased the need of a more exhaustive study of the aqueous coordination chemistry of gallium and its complexes[120] in order to design and modulate new and improved anti-tumour agents[121]. Gallium nitrate ($Ga(NO_3)_3$, Ganite) can suppress the growth of subcutaneously implanted tumours and it has completed a phase I clinical trial for treatment of children with brain tumours, neuroblastoma, rhabdomyosarcoma, non-Hodgkin's lymphoma and refractory solid tumours and phase II trials in patients with

relapsed or refractory non-Hodgkin's lymphoma. Gallium nitrate is also currently in phase I clinical trials for cystic fibrosis suffering patients[99],[119].

Gallium radioisotopes have been used for decades in diagnostic and medicinal chemistry[122] and nowadays their importance is ever increasing with the evolution of positron emission tomography (PET) in clinical use for imaging. Radiometal ions must be sequestered from aqueous solution by chelators to obviate transchelation and hydrolysis. The most typical ligands used to create radiopharmaceutical agents are bifunctional chelators (BFCs) (Figure 1.15)[89]. The chelator is tightly bound to the radiometal ion, thus, once is injected into a patient, the targeting molecule can selectively deliver the isotope without its loss from the radiopharmaceutical agent.

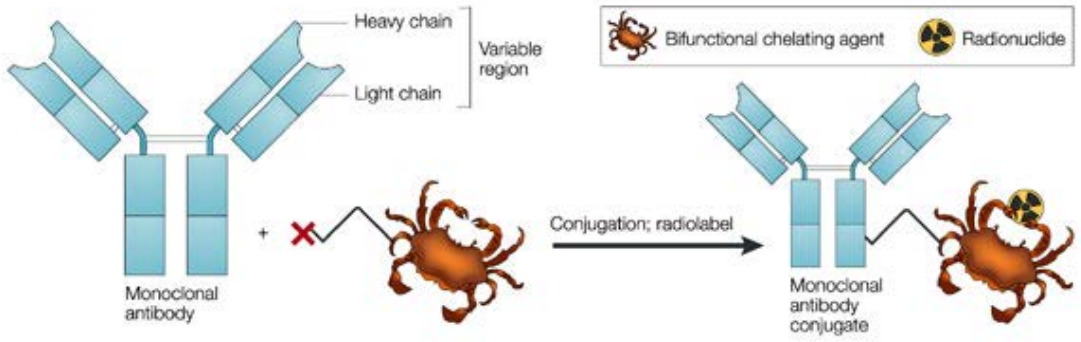

Figure 1.15. Illustration of a radiopharmaceutical agent containing a bifunctional chelator (BFCs) conjugated to a target molecule (e.g. antibody, peptide, nanoparticle).

Therefore radiopharmaceuticals supply a site-specific radioactive source *in vivo* for imaging or therapy. The radioisotope ^{67}Ga ($t_{1/2}$ = 3.25 days) has been increasingly used for single photon emission computed tomography (SPECT) imaging in chelator-based radiopharmaceuticals[122]. ^{68}Ga has suitable properties for high quality emission tomography (PET) imaging, including a short half-life ($t_{1/2}$ = 68 min), decay by 89% positron emission and a maximum positron energy of 1.899 keV, as well as the availability of a cost-effective generator system ^{68}Ge/^{68}Ga[123],[124]. ^{67}Ga is usually used as a model for ^{68}Ga in labelling studies experiments because of its longer half-life, which makes it more suitable for *in vitro* assays than ^{68}Ga. The success of a radiopharmaceutical is strongly dependent on its high thermodynamic stability and kinetic inertness to prevent hydrolytic demetallation and/or transmetallation by competitive endogenous molecules *in vivo*[125]. Specifically, the iron binding protein apo-transferrin has high affinity for Ga^{3+} because of the physical similarities with Fe^{3+}. Hence, it is important that the thermodynamic stabilities of the radiometal-chelate complexes be higher than those for any endogenous ligands.

The polydentate aminocarboxylates macrocycles NOTA and DOTA (Figure 1.16) have been radiolabelled by coordination with ^{68}Ga and extrafunctionalized with specific targeting molecules with promising results[124],[126]. Many attempts to find chelators with comparable kinetic inertness and thermodynamic stability have been involved the

synthesis of new chelators. A tripodal-based ligand with relevant feature for medical applications was synthesized by the group of Santos[125] ((NTP(PrHP)$_3$ Figure 1.9), the thermodynamic stability studies of the Ga^{3+}-complexes with the tris-hydroxypyrydinone ligand gave evidence of a higher stability compared with that of the Ga^{3+} complexes with the commercially available DOTA, EDTA, DFO, DTPA or even transferrin, preventing transmetallation and/or demetallation *in vivo*. A family of acyclic bifunctional chelating ligands were synthesized by the group of Orvig with optimal properties for the field of gallium radiopharmaceutical chemistry[127],[128],[129] (Figure 1.16). H_2dedpa ligand and its derivatives, although they are acyclic systems, form more stable complexes with Ga and radiolabel with Ga isotopes under mild-room temperature conditions and short reaction times, being comparable results with the macrocyclic chelate in use NOTA and exceeding the properties of DOTA, and other new Ga^{3+} ligands such as triazacyclononane-phosphinic acid chelators (TRAP) (Figure 1.16)[130],[131].

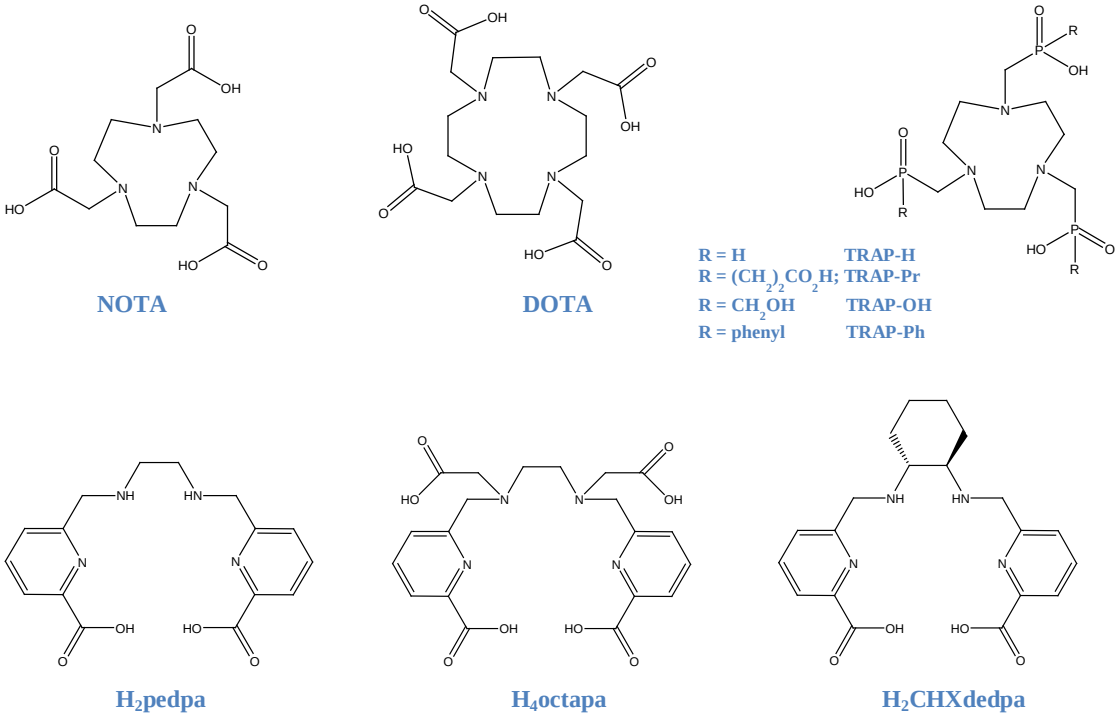

Figure 1.16. Aminocarboxylates macrocycles DOTA and NOTA, triazacyclononane-based bifunctional phosphinate ligand (TRAP) and the acyclic chelators, H_2pedpa, H_4octapa and H_2CHXdedpa.

1.8. Lanthanides and its applications in bone disorders

There is no known biochemical role of lanthanides in organisms, even though they interact with biological materials in specific ways which made them useful probes for therapeutic applications. The role of lanthanides in studies of Ca^{2+} biochemistry was first predicted by Williams and Birnbaum[132]. Ln^{3+} ions are isomorphic replacements of Ca^{2+} ions[133],[134], and rare earth metal ions may be used to probe calcium binding sites in proteins by evidences in changes in the absorption spectrum of a lanthanide upon binding to a protein (differently from the spectroscopically silent Ca^{2+} ions, lanthanide ions Ln^{3+} possess useful spectroscopic properties)[134]. The ability of Ln^{3+} in replacing Ca^{2+} ions resides on similarities in their chemistry. Thus, lanthanide ions form complexes primarily electrostatic in nature and analogous to those formed by the calcium ions. They have no crystal field stabilization energy (about 4.18 $kJ \cdot mol^{-1}$, while for transition metals is typically $\geq$ 418 $kJ \cdot mol^{-1}$) and negligible f-orbital-directing steric forces. The coordination number varies from 3 to 12. Although Ln^{3+} and Ca^{2+} have almost the same size, the trivalency in lanthanides confers them a much higher charge to volume ratio, so that they usually have much higher affinities than Ca^{2+} for given binding sites. Ca^{2+} and Ln^{3+} share almost the same coordination numbers in protein binding sites[132].

Lanthanides are considered bone-seekers as they have high affinity for bone due to the interaction with the inorganic phosphate in hydroxyapatite. Important and interesting properties of biological and synthetic hydroxyapatite ($Ca_5(PO_4)_3(OH)$, HAP), the main mineral component of bone and dental tissues, are that is a porous structure that is constantly being remodelled within the bone cycle, and can undergo substitution of both cations (Ca^{2+}) and anions (PO_4^{3-} and/or OH^-)[135],[136],[137],[138]. HAP ceramics are able to conduct new bone formation on their surface. In biological systems, the affinity of ^{153}Sm for Ca^{2+} in hydroxyapatite is used to treat pain associated with terminal bone cancer, whereas Gd^{3+} and Tb^{3+} are used as bone-targeting contrast agents. La_2CO_3 (Fosrenol) was approved in 2004 for treatment of hyperphosphatemia [139], an electrolyte imbalance that results in elevated serum phosphorous levels, and also inhibits osteoclast activity while stimulating osteoblast proliferation[140]. Fosrenol acts by binding phosphate and reducing its absorption by the formation of insoluble lanthanum phosphate complexes (K_{sp} = 4.0 x 10^{-23}) which can pass through the gastrointestinal tract unabsorbed[141]. *In vitro* experiments show that La^{3+} binds to phosphate in the pH range 3 – 7. However, the low oral bioavailability of Fosrenol related to its strong elimination through the GI tract, have stimulated research for new lanthanide compounds with an increased oral availability and decreased unwanted effects.

A series of 3-hydroxy-4-pyridinone ligands and a hexadentate phosphinate-EDTA derivative (Figure 1.17) were synthesized and coordinated to lanthanide ions by the group of Orvig[142],[143], in order to verify if ion exchange with hydroxyapatite was possible. Their complex formation equilibria with La^{3+} and Gd^{3+}, the extent of bioavailability and the cytotoxicity of the lanthanide complexes were studied. The introduction of the phosphinate group in the phosphinate-EDTA ligand was selected due

to the high affinity *in vivo* of phosphonate and phosphinate functional groups for bone. Low toxicity profiles were found in MG-63 cells (cells derived from a human osteosarcoma[144]). Lanthanide complex binding studies with HAP *in vitro* were made under physiological conditions and they show that lanthanide ions interact with HAP, but it is not clear if it is a surface interaction or if the Ln^{3+} is incorporated into the HAP crystal lattice[142].

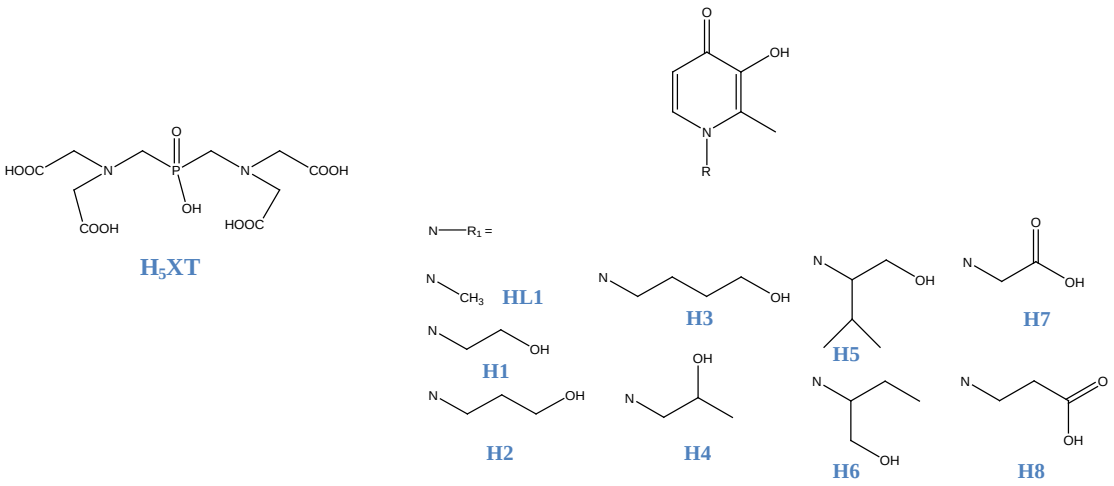

Figure 1.17. A summary of the ligands synthesized and studied with La^{3+} and Gd^{3+}, for their potential application for the treatment of osteoporosis.

1.9. Ligands

1.9.1. Bidentate ligand, (5-hydroxy-2-(hydroxymethyl)pyridin-4(1H)-one, P1)

As described in section 1.3.1.5, hydroxypyridinone ligands have been extensively studied as candidates for orally active iron chelators since the 1980s. Indeed, the European Union approved 3-hydroxy-1,2-dimethylpyridin-4(1H)-one (Deferiprone, DFP) as a clinical chelating agent for iron overload diseases in 2000. HPOs can be easily functionalized to improve their chelating properties, to change the lipophilicity and solubility and to gain additional properties such as fluorescence.

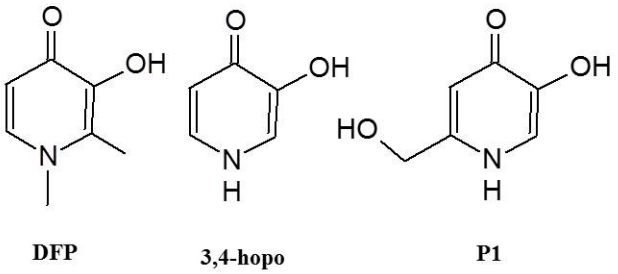

DFP **3,4-hopo** **P1**

Scheme 1. Chelating hydroxypyridinones and their abbreviations.

Only a few HPOs derivatives with hydrogen in position 1 are known, and 5-hydroxy-2-(hydroxymethyl)pyridin-4(1H)-one (P1) (Scheme 1 and 6), with its tautomeric forms, has only been considered in computational studies not accompanied by experimental studies[145]. Although different authors have debated about tautomeric equilibrium of the free DFP ligand and its derivatives, no tautomeric equilibrium in the corresponding metal complexes has been experimentally proven.

The tautomers are usually characterized by different hydrophobicity, pK and structure, and therefore different coordination ability. In this respect, the influence of medium polarity may be highly significant since a biological system involves either an aqueous medium (blood or plasma), or an essentially non-protic medium such as a cell membrane or even an enzymatic reaction center.[146] Based on these concerns, we considered that metal coordination may be improved in 3,4-hopo with N-H in position 1. Therefore, in this thesis for the first time a study of 5-hydroxy-2-(hydroxymethyl)pyridin-4(1H)-one (P1) is presented (a paper on the characterization of P1 and of its Fe^{3+}, Al^{3+}, Cu^{2+} and Zn^{2+} has been accepted for publication in Dalton Transactions)[147], by combining computational, chemical, and biological approaches. The use of complementary analytical techniques has allowed us to give evidence of the tautomeric changes of P1 as a function of pH, and to determine all of their possible forms and properties. We also present the coordination ability of P1 with the Fe^{3+} and Al^{3+} ions, as well as with the essential Cu^{2+} and Zn^{2+} ions, together with biodistribution studies on mice to evaluate *in vivo* its efficacy.

1.9.2. Tetradentate (L12-L15 and KβAK) ligands

1.9.2.1. L12-L15 ligands

Among the tetradentate kojic acid derivatives synthetized in our research group (Figure 1.8 in section 1.3.1.6), those characterized by the shorter linker present the highest values both of pAl and pFe (pM being the parameter generally used to evaluate the overall ability of a chelating agent toward a given metal ion, M[148]), i.e. the ligands L1, L2, L3 and L8 (Table 1.2).

Table 1.2. pFe and pAl values for L1-L9 ligands.

	KA	L1	L2	L3	L4	L5	L6	L8	L9
pFe	13.3	23.1	18.9	22.2	18.1	19.3	17.7	20.0	17.7
pAl	9.1	12.8	11.9	13.9	11.4	11.6	11.8	14.4	10.3

pM = $-\log_{10}(M_l)$ calculated at [M] = $1*10^{-6}$ M, [L] = $1*10^{-5}$ M and pH = 7.4.

Since L3, bearing a vanillin residue in the linker (Figure 1.8), presents an extremely good chelating ability, we synthesized a series of analogous molecules containing the different substituents in the linker shown in Scheme 2. These substitutions were intended to evaluate how the value of protonation constants can affect the pAl and pFe values, being a phenolic group characterized by a pK ~ 9 and a carboxylic group by a pK ~ 4.

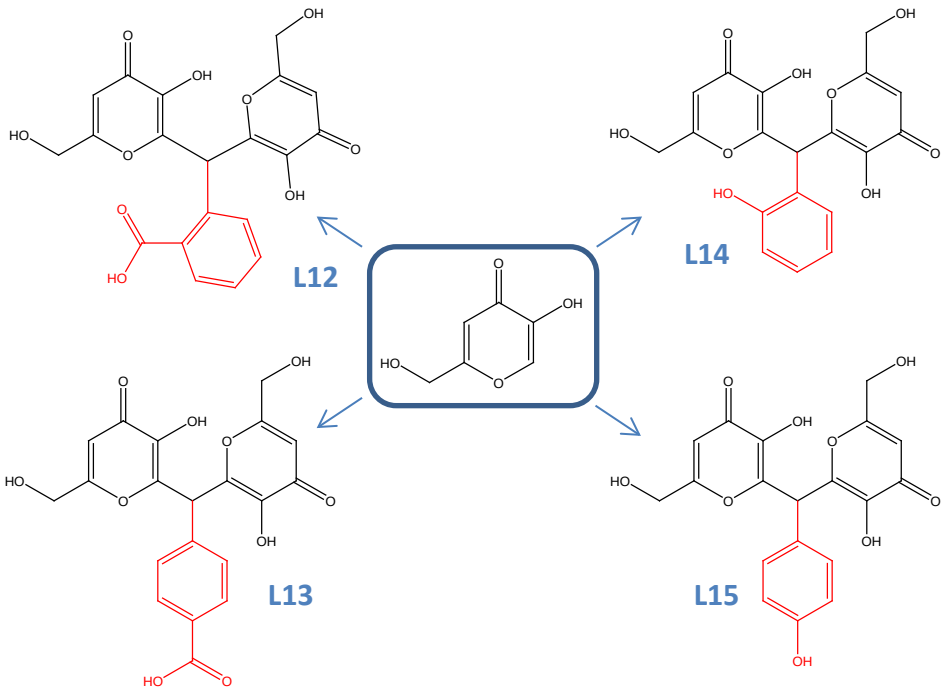

Scheme 2. Synthesized ligands L12, L13, L14 and L15.

1.9.2.2. KβAK ligand

Several previous reports have described kojic acid and its derivatives as inhibitors of melanin formation, both in vitro and in vivo[149],[150], speculating on a possible role for copper coordination mechanisms[151]. In 2011, Fishman et. al. determined a tyrosinase structure from Bacillus megaterium (TyrBm) with bound kojic acid, the first tyrosinase structure with a bound ligand. The kojic acid molecule occupies identical positions in both subunits of TyrBm and it is bound strongly by interactions with Phe, Pro, Asn and Arg residues. As opposed to the previously suggested modes for copper complex formation, the ligand was oriented with the hydroxymethyl towards the active site at the relatively far distance of 7 Å. Hence, the position and orientation of kojic acid causes an obstruction of the active site that could lead to inhibition of the tyrosinase enzyme.

In literature different kojic acid derivatives are reported as tyrosinase inhibitors. These studies mainly investigated the ability of the synthesized kojic acid derivatives to improve inhibitory properties by converting the methylene hydroxyl group into ester[152], hydroxylphenyl ester[153], glycoside[154] and amino acid derivatives[155],[156],[157],[158].

Kojic acid was reported as well as chelating agent for trivalent and bivalent metal ions[159],[160],[161],[162]. Encouraged by the promising results obtained in our previous reports of L1-L9 kojic acid derivatives (Figure 1.8) [33],[35],[163],[37],[36] , Kojic-βAla-Kojic ligand (Scheme 6) was synthesized. We studied Fe^{3+}, Al^{3+}, Zn^{2+} and Cu^{2+} complexes and compared the results with previously published data. Moreover, the tyrosinase inhibition efficacy of the new molecule was evaluated and compared with low effective inhibitors of melanin[27-30] in order to know whether two kojic acids were better than one and if the length and kind of linker could improve inhibitory activity.

1.9.3. Hexadentate ligand (SC)

A hexadentate hydroxypyrone ligand, 6,6',6''-(((nitrilotris(ethane-2,1-diyl))tris (azanediyl))tris(methylene))tris(3-hydroxy-4H-pyran-4-one) named SC, was synthesized to improve the coordination towards Fe^{3+} and other tripositive metal cations (Scheme 3). Complex formation equilibria are presented in section 3.3.5. with Fe^{3+} and Ga^{3+}.

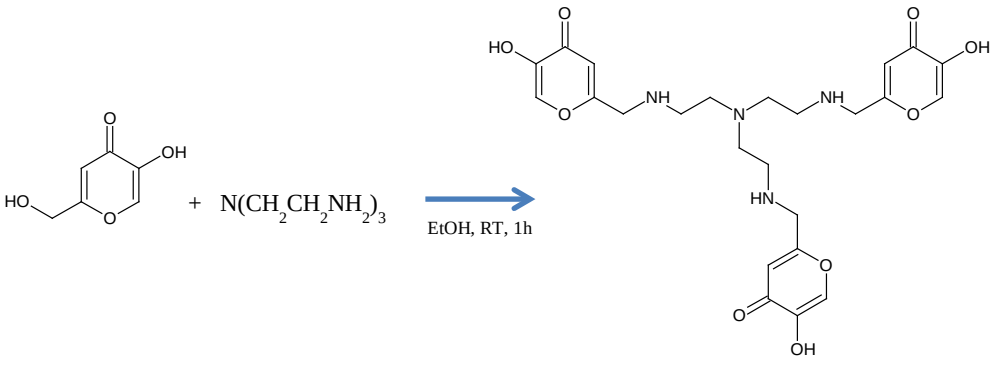

Scheme 3. Reaction scheme for the hexadentate ligand SC.

As mentioned in section 1.2, complex formation is entropically favoured by ligands in the order hexadentate > tetradentate > tridentate > bidentate. Moreover hexadentate ligands can adequately protect the metal ion from deleterious reactions, providing a shield of the surface of the metal and avoiding the exposition of the metal to the biological environment, with the consequent interactions with molecules that can led to the production of ROS. Stability constants and pM values provide a number for the direction and magnitude of the equilibrium in a metal-chelate coordination reaction under specific conditions, but they do not give any kinetic information such as dissociation rate[164],[165]. The rate of dissociation *in vivo* is a very important factor because determines the kinetic inertness of a metal-complex, regardless of thermodynamically stability. It is influenced by the highly dilution encountered *in vivo*, when a very tiny concentration of pharmaceutical agent is diluted into the blood pool for diagnosis or therapeutic purposes and it will encounter other endogenous ligands such as transferrin or ceruloplasmin that will compete for binding the metal and disturbing *in vivo* stability. Due to these kinetic reasons, hexadentate ligands can chelate metal ions at low metal concentrations more efficiently than bidentate or tetradentate ligands. In fact, considering the dissociation of bidentate (L_b), tetradentate (L_t) and hexadentate (L_h) ligands and the equations:

$M(L_b)_3 \leftrightharpoons M^{3+} + 3L_b \qquad k'_d = [M^{3+}]\,[L_b]^3/[M(L_b)_3]$

$M(L_t)_{3/2} \leftrightharpoons M^{3+} + 3/2L_t \qquad k''_d = [M^{3+}]\,[L_t]^{3/2}/[M(L_t)_{3/2}]$

$ML_h \leftrightharpoons M^{3+} + L_h \qquad k'''_d = [M^{3+}]\,[L_h]/[ML_h]$

where k'_d, k''_d, k'''_d are the dissociation equilibrium constants, since the degree of dissociation for bidentate ligands depends on $[ligand]^3$, for tetradentate on $[ligand]^{3/2}$ and for hexadentate on [ligand], the dilution dependence follows the order hexadentate < tetradentate < bidentate.

1.9.4. Losartan and Irbesartan

In section 1.5, the effects of Cu^{2+} disregulation in cardiovascular complications in diabetic patients were outlined, as well as the amelioration of these conditions by chelation therapy. In diabetic patients treated with sartans, an improvement of arterial complications was found (independently of lowering pressure), related with Cu^{2+} lowered levels[166], raising the possibility that sartans act in this case with a different mechanism. Since Losartan and Irbesartan (Scheme 4), registered in the USA and Europe for the treatment of cardiovascular disease in diabetic and non-diabetic patients, contain several nitrogen atoms at distances consistent with the existence of potential Cu^{2+}-binding sites[167], we hypothesized that sartan molecules could demonstrate Cu^{2+} binding properties. For these reasons complex formation equilibria with the essential metal ions Cu^{2+} and Zn^{2+} were studied, in collaboration with Prof. Garth Cooper from the University of Manchester.

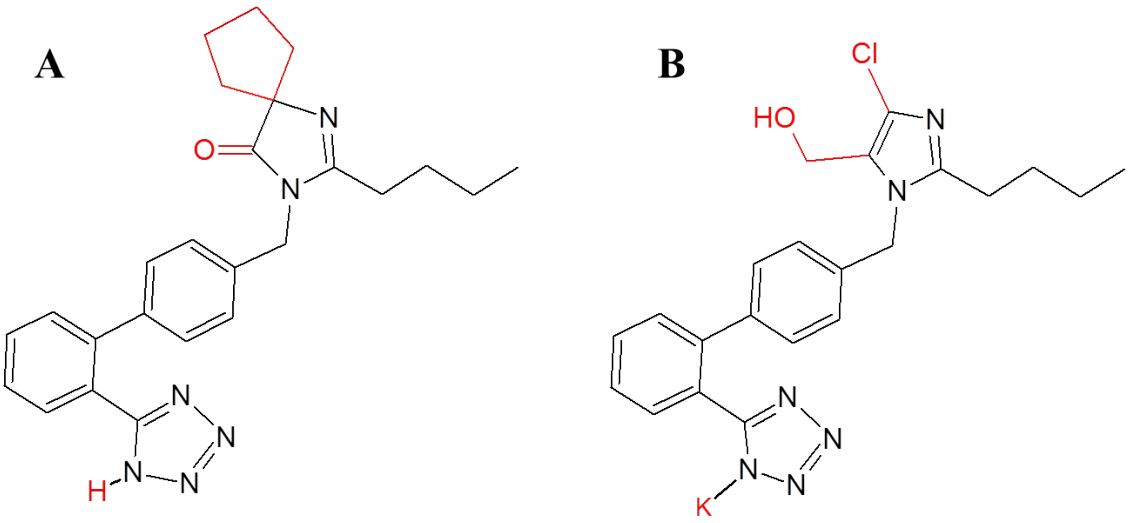

Scheme 4. Molecular structures of Irbesartan (A) and Losartan (B). The structural differences between molecules are marked in red.

1.9.5. Picolinic acid derivatives ligands (H_4pedpa, H_6dipedpa)

In the frame of the research by the group of Prof. Chris Orvig on lanthanide metal-based complexes for the treatment of bone disorders (section 1.8), during my three month period at the University of British Columbia a complete characterization of ligands H_4pedpa and H_6dipedpa (Scheme 5) and of their complexes with La^{3+} was made. Both ligands, bearing phosphonate groups, have high affinity towards bone and in particular to HAP. While a lanthanum complex with H_4pedpa could potentially be used to treat bone disorders such as osteoporosis, H_6dipedpa, like its analogous H_6phospa[168], could demonstrate interesting chelating ability towards the radioisotope ^{89}Zr. Thus it could be an alternative to DFO, the only chelator proven to be enough competent for the use with ^{89}Zr in positron emission tomography (PET) imaging.

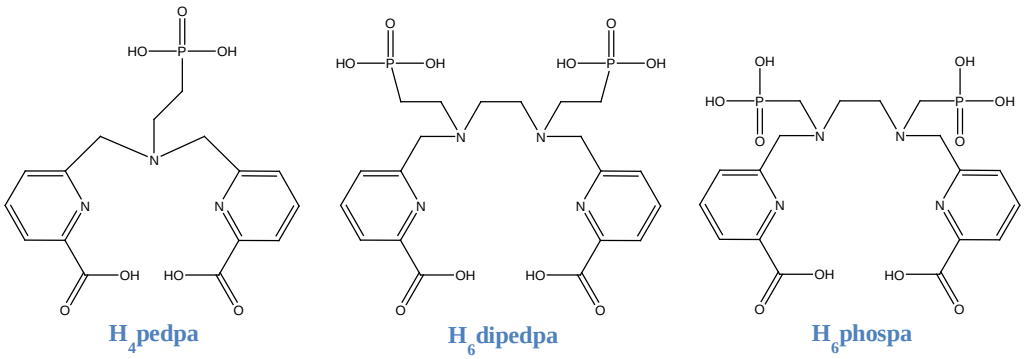

Scheme 5. Acyclic chelators H_4peda and H_6dipedpa and the recently published and promising H_6phospa

2. Experimental section

2.1. Materials and methods

HCl, NaCl, NaOH, ethanol, ethyl acetate, ammonia, benzyl chloride, D_2O, DCl, NaOD, $FeCl_3$, $AlCl_3$, $CuCl_2$, formaldehyde, 4-formylbenzoic acid, 2-formylbenzoic acid, 4-hydroxybenzaldehyde, 2-hydroxybenzaldehyde, tris(2-aminoethyl)amine (purity 99%, used without further purification) were Sigma Aldrich products, Desferal (DFO) was obtained from Biofutura Pharma products, 5-hydroxy-2-hydroxymethyl-pyran-4-one (kojic acid) was purchased from Fluka, Standard AAS solutions of Ga^{3+} and La^{3+} were purchased from Sigma Aldrich. Gallium Citrate ^{67}Ga for biodistribution studies was purchased by Mallinckrodt Medical B.V. Potassium Losartan and Irbesartan were purchased from TCI Europe. L1-L15, KβAK and SC ligands were synthesized in ours laboratories, while H_4pedpa and H_6dipedpa were synthesized by the PhD student David Weekes in the laboratories of Prof. Orvig.

Fe^{3+}, Al^{3+}, Cu^{2+} and Zn^{2+} metal ion standard solutions were prepared by dissolving the required amount of chloride salts in pure double distilled water and adding a stoichiometric amount of HCl to prevent hydrolysis. The spectrophotometric analysis of Fe^{3+}-Desferal complex was used to standardized Fe^{3+} solution, while EDTA titrations were used to standardized Al^{3+}, Cu^{2+} and Zn^{2+} solutions. Carbonate-free 0.1 M NaOH solution was prepared as reported in a previous papers[169].

2.1.1. Elemental analysis

Elemental data were obtained using a Fisons EA1108 CHNS/O. The melting points were measured on a Leica Galen III hot stage apparatus and are uncorrected.

2.1.2. NMR measurements

NMR measurements were performed at the Department of Chemistry and Pharmacy at the University of Sassari-Italy, on a Bruker Ascend™ 400 MHz spectrometer equipped with a 5 mm automated tuning and matching broad band probe (BBFO) with z-gradients, as previously described.[170],[171],[172] NMR experiments were carried out by using 5-7 mM concentration of the ligands in different solvents, D_2O, MeOD or DMSO at 25˚C in 5 mm NMR tubes. The pH of the solutions was adjusted with diluted DCl and NaOD on a pH meter Crison micro TT 2050 pH meter with an electrode Mettler Toledo InLab 422. The pD values measured in D_2O solutions were converted to the pH values by using the deuterium isotopic relation pH = pD–0.4. A stock acidic deuterated aqueous solution of $ZnCl_2$ salt was used in the metal-ligand titration analysis. The metal ion solution was added to Irbesartan and Losartan ligand solutions (80:20 MeOD:D_2O solution) and in the case of P1, L1-L8 in water, and the pH was then set to the right value just before the acquisition of the spectra. 2-D ^{1}H-^{13}C heteronuclear correlation spectra (HSQC) were acquired by using a phase-sensitive sequence employing Echo-

Antiecho-TPPI gradient selection with a heteronuclear coupling constant J_{XH} = 145 Hz, and shaped pulses for all 180° pulses on f2 channel with decoupling during acquisition. Sensitivity improvement and gradients in back-inept were also used. Relaxation delays of 2s and 90° pulses of about 10 μs were employed in all the experiments. Solvent suppression for 1D ^{1}H, 2D ^{1}H-^{1}H TOCSY (total correlation spectroscopy) experiments were carried out by using excitation sculpting with gradients. The spin-lock mixing time of TOCSY experiments was obtained with MLEV17. ^{1}H-^{1}H TOCSYs were performed by using mixing times of 60 ms. A combination of 1D, 2D TOCSY, HSQC experiments was used to assign the signals of both free and metal-bound ligands at different pH values. All NMR data were processed with TopSpin (Bruker Instruments) software and analyzed by Sparky 3.11 and MestRe Nova 6.0.2 (Mestrelab Research S.L.) programs.

2.1.3. Electrospray ionization-mass spectrometry (ESI-MS)

High-resolution mass spectra were performed in collaboration with the University of Wroclaw-Poland using a Bruker MicrO-TOF-Q spectrometer (Bruker Daltonik, Bremen, Germany), equipped with an Apollo II electrospray ionization source with an ion funnel. The spectra were recorded in the positive ion mode in the range 100 to 1500 *m/z*. The instrument parameters were: dry gas–nitrogen, temperature 200 °C, ion source voltage 4500 V, collision energy 10 eV. Analyte aqueous solutions (70 μl) were introduced at a flow rate of 3 μl/min. Stock solutions were prepared by using MeOH/H_2O mixture (50/50 v/v) as a solvent. The metal to ligand molar ratio was 1:1. The final pH of the solution was 4.0. The instrument was calibrated using the Tunemix mixture (BrukerDaltonik, Germany) in the quadratic regression mode. The overall charge of the analyzed ion was calculated on the base of distance between isotopic peaks. Data were processed by application of the Compass DataAnalysis 4.0 (Bruker Daltonik, Germany) program.

2.1.4. Calorimetry

Δ*H*° e Δ*S*° values were obtained with calorimetric titrations performed in collaboration with the University of Ferrara-Italy in the laboratories of Prof. Maurizio Remelli, on a Tronac 450 calorimeter equipped with a 25 mL Dewar titration vessel; the titrant solution was added using a 2 mL Hamilton syringe also in the thermostatic bath. A warming resistance (about 100 Ω) and a thermistor put into the solution allowed the instrument electric calibration and the detection of temperature variations respectively. The accuracy was daily checked by titrating a tris(hydroxy methyl)aminomethane solution partially neutralized with nitric acid. The thermostatic bath was at 25.00 ± 0.02 °C. The completely automated system was managed by a PC via Tronac 900 interface. The potential difference at thermistor ends was measured by a digital multimeter FLUKE 8840A. Home-made programs for the management of the calorimetric system and data acquisition and for gross heat correction from non-chemical factors[173] were all in BASIC language. The ionic strength was adjusted at 0.1 M with KCl. Δ*H*° values were computed from the calorimetric data by means of the least-squares computer

program HypDH[174], which minimizes the function: $U = \Sigma w_i(Q_i^o - Q_i^c)^2$, where w_i are statistical weights and Q_i^o, Q_i^c are the experimental and calculated heats, respectively, over n observations. A literature $\Delta H°_w$ value of 56.4 kJ mol^{-1}, was used in the calculations[175]. From experimental $\Delta H°$ values the corresponding $\Delta S°$ values were computed by means of the Gibbs-Helmholtz equation: $-\Delta G° = -\Delta H° + T\Delta S°$, where the free energy variation was calculated by the corresponding cumulative constants (β), given by potentiometry:

$-\Delta G° = 2.303\ RT \log \beta$.

2.1.5. X-ray diffraction (XRD) studies

Crystallographic studies were performed at the University of Granada-Spain in the laboratories of Dr. Duane Chosquesillo and Prof. Juan Niclós-Gutiérrez. Crystals of L1 ligand suitable for XRD were grown by slow evaporation of a solution of the compound (5 mg, in water:ethanol 70:30) placed in an opened vessel in air at room temperature. Single crystals of P1 were grown by slow evaporation of a methanol solution (30 mg in 3mL at 50 ºC). Crystals from L13 and L14 ligands were furthermore obtained, and their relative data analysis are being processed. The single crystal was protected at inert conditions in perfluoropolyether, mounted on MiTeGen Micromount and used for data collection on a Bruker D8 Venture diffractometer (100 K, MoKα). The data were processed with APEX2[176] and corrected for absorption using SADABS[177]. The structure was solved by direct methods[178], which revealed the position of all non-hydrogen atoms. These atoms were refined on F^2 by a full-matrix least-squares procedure using anisotropic displacement parameters. All hydrogen atoms were located in difference Fourier maps and included as fixed contributions riding on attached atoms with isotropic thermal displacement parameters 1.2 (C−H) or 1.5 (O−H) times those of the respective atom.

2.1.6. Potentiometry

The potentiometric studies of protonation and complex formation equilibria were performed with the use of thermostatted glass cell equipped with a magnetic stirrer, a Metrohm LL UNITRODE glass electrode, Metrohm 691 pH-meter, a Dosimat 665 Metrohm titrator, and under the flow of Argon. Titrations were performed at 25.0 °C using 0.1 M NaOH and 0.1 M NaCl as an ionic strength buffer. The electrode was calibrated daily for hydrogen ion concentration by HCl/NaOH titration in the above experimental conditions and the results were analyzed with Gran procedure[179]. Working ligand concentrations were: 1 mM (L7, L12-L15, SC, KβAK, H_4pedpa and H_6dipedpa), 0.4 mM (L1, L6), 0.5 mM (L2-L5) 0.8 mM (L8) and 0.5 mM (losartan and irbesartan) in 30:70 and 80:20 MeOH/H_2O mixtures, depending on ligand solubility in water. Potentiometric data were processed by Hyperquad2013 program[180].

2.1.7. Spectrophotometry UV-Vis

UV-Visible studies were carried out on a Varian Cary 50 UV/Vis Spectrophotometer. Ligand protonation equilibria were studied by titrating 20 mL of 0.5 mM ligand solutions[181] with 0.1 M NaOH at 0.1 M NaCl ionic strength using a joined potentiometric-spectrophotometric procedure. Spectra were recorded in the 200–400 nm spectral range with a 0.2 cm path length fiber optic. Fe^{3+} complex formation studies were made with the use of 0.5 mM ligand concentration and metal to ligand molar ratio 1:1. The Vis spectra were recorded in the 300-800 nm range using a 1 cm path length.

Because of the completely filled d shell of the Ga^{3+} ion, it was not possible to use spectrophotometric measurements in the visible region of the spectra, so were studied the variations in the ultraviolet spectra of the chelate and the free ligand *vs.* pH. The Al^{3+}, Cu^{2+} and Zn^{2+} complexes were studied with the use of only potentiometric method; 0.5mM ligand concentration and metal to ligand molar ratio 1:1. The obtained spectrophotometric data were processed by HypSpec program[182].

2.1.8. Spectrofluorimetry

Fluorescence spectra of losartan and irbesartan molecules were recorded on Varian Cary Fluorimeter. Ligand working concentrations were 0.032 mM in 30% and 80% methanol/water solutions. Batch measurements at variable pH were performed by adding proper amounts of HCl and NaOH. UV-Vis spectra at different pH revealed an isosbestic point at 280 nm, so this wavelength was chosen for excitation. Emission spectra were registered in the 290-490 nm spectral range.

2.1.9. EPR spectroscopy

EPR spectra were recorded in collaboration with the University of Wroclaw-Poland, at 77 K on a Bruker ELEXSYS E500 CW-EPR spectrometer equipped with an NMR teslameter (ER 036TM) and frequency counter (E 41 FC) at X-band frequency. The solutions for EPR measurements were prepared in water by adding ethylene glycol (30%) as a cryoprotectant. The experimental spectra were simulated by using WINEPR Simfonia 1.26 program and Spin (EPR OF S>1/2) program by Dr. Andrew Ozarowski, National High Field Magnetic Laboratory, University of Florida.

2.1.10. DFT calculation

Theoretical calculations for P1 ligand were performed under the supervision of Prof. Massimiliano Arca, at Density Functional Theory (DFT) level[183] with the Gaussian 09 package of programs (Rev. A.02)[184] on a E4 workstation equipped with four quad-core AMD Opteron 2.2 MHz processors and 16 Gb of RAM and running the 64 bit version of the Ubuntu 12.04 Linux operating system. Barone and Adamo's mPW1PW hybrid functional was adopted,[185] along with the Schäfer, Horn, and Ahlrichs double-ζ plus polarization all-electron basis sets[186] (BS) for all atomic species. The geometry of

the compounds was optimized with tight SCF convergence criterion and fine numerical "pruned" integration grids (75 radial shells and 302 angular points per shell). The nature of the minima of each optimized structure was verified by harmonic frequency calculations. NBO charges distributions[187] and Wiberg[188] bond indices were calculated at the optimized geometries. Solvation calculations were carried out in the gas phase and water, implicitly taken into account by means of the polarizable continuum model (PCM) in its integral equation formalism variant (IEF-PCM).[189] The programs Gaussview 5.0.8,[190] and Molden 5.2.4[191] were used to investigate the charge distributions and optimized geometries.

2.1.11. Partition coefficients

P1 and DFP octanol/water partition coefficients (log P) were calculated at 25 °C, as the logarithm of the ratio of their concentrations in n-octanol phase and in aqueous phase (Tris, pH = 7.4), using the well-established ''shake flask" method[31]. Each compound was added to a premixed suspension, containing 3 mL of n-octanol and 3 mL of the aqueous phase, and stirred for 4 h. The species concentration in the aqueous layer was evaluated by spectrophotometry with a Perkin Elmer Lambda 35 spectrophotometer, using a thermostated 1 cm path length cell, on the benzenoid bands of the compounds (λ = 280–290 nm). The measurements were done in triplicate and repeated three times.

2.1.12. Biodistribution studies

Biodistribution studies were performed by Prof. L. Gano at Campus Tecnológico e Nuclear, Instituto Superior Técnico, Universidade de Lisboa, Portugal. ^{67}Ga-citrate injection solution was prepared by dilution of commercial ^{67}Ga citrate solution with saline to obtain a final radioactive concentration of 5 -10 MBq/100 μL. Biodistribution studies were carried out in groups of 3 female Balb-C mice, weighing ca. 20-22 g (randomly bred, Charles River, from CRIFFA, France). Mice were intravenously injected with 100 μL (5 -10 MBq) of ^{67}Ga citrate via the tail vein immediately followed by intraperitoneal injection of 0.35 μmol of each ligand (P1 and DFP as a control) in 100 μL saline. Animals were maintained on normal diet ad libitum and were sacrificed by cervical dislocation at 1h and 24 h post-administration. The administered radioactive dose and the radioactivity in sacrificed animals were measured in a dose calibrator (Aloka, Curiemeter IGC-3, Aloka, Tokyo, Japan). The difference between the radioactivity in the injected and in sacrificed animal was assumed due to the whole body excretion. Tissue samples of main organs were then removed for counting in a gamma counter (Berthold LB2111, Berthold Technologies, Germany). Radioactivity remaining in the carcass was measured in the dose calibrator and expressed as percent of injected activity (%I.A.). Biodistribution results were expressed as percent of injected activity per gram of organ (%I.A./g) and presented as mean values ± SD.

2.1.13. Enzyme extraction, purification and tyrosinase activity

The mushroom tyrosinase (EC 1.14.18.1) from Agaricus bisporus was purified as previously described[192]. Tyrosinase inhibitory activity was determined by a spectrophotometric method. The compound solution was prepared in 10% DMSO solution. Each sample was diluted in a test tube with 0.05 M sodium phosphate buffer (pH 6.8). This was followed by the addition of 0.04-0.35 mL (S)-2-Amino-3-(3,4-dihydroxyphenyl)propanoic acid (L-DOPA, 10 mM) solution (in 10 mM acetic acid) and 0.034 mL mushroom tyrosinase (200 units/mL). The 2.000 mL solution was mixed, incubated for 10 min at 250C and the absorbance measured at 476 nm. The experiment was repeated with different inhibitor concentrations: 0.069, 0.139 and 0.279 mM. The absorbance of the same mixture without inhibitor was used as control with the addition of 10% DMSO water solution for its inhibitory effect. The percent inhibition of tyrosinase activity was calculated using the equation below:

$$\% \text{ inhibition} = (A-B)/A \times 100$$

where A represents the absorbance at 476 nm without the test sample, and B represents the absorbance at 476 nm with the test sample at the same substrate concentration.

In order to calculate IC50 values, 2 mM stock solutions of tyrosinase inhibitors (kojic acid and KβAK) were prepared in 10% ethanol/water mixture. IC50 values were determined after addition of various inhibitors amounts to enzyme assays to determine a range of inhibitors needed to encompass the IC50 value. Each 1 mL assay contained a fixed amount of enzyme, inhibitor, 3 mM L-DOPA (final concentration), and 100 mM phosphate buffer (final concentration) pH 6.5. The inhibition was also characterized in terms of an IC50 value by using GraFit Version 7.0.3 program (Erithacus Software Ltd., Horley, Surrey, UK) based on the following equation:

$$y = \frac{Range}{1+\left(\frac{x}{IC_{50}}\right)^{S}} + \text{Background}$$

where Range is the maximum y range, and s is a slope factor. The x axis represents the concentration of analyte. Data fitted to this equation are displayed with a logarithmically scaled x axis.

2.2. Synthesis of ligands

2.2.1. P1

Synthesis of 5-hydroxy-2-(hydroxymethyl)pyridin-4(1H)-one (P1)

5-hydroxy-2-(hydroxymethyl)pyridin-4(1H)-one was obtained from kojic acid (KA), following a standard synthetic procedure, previously described for the preparation of other pyridinones[31]. The first step involved the protection of the 5-hydroxyl group of KA with a benzyl group, by reaction with benzyl chloride and formation of 5-(benzyloxy)-2-(hydroxymethyl)-4H-pyran-4-one. This was converted in the corresponding pyridinone, 5-benzyloxy-2-(hydroxymethyl)-pyridin-4(1H)-one, by reaction with an ammonia aqueous solution under reflux (Michael addition, ring opening/closure, and dehydration). The benzyl protecting group was then removed by catalytic hydrogenolysis providing the final product P1.

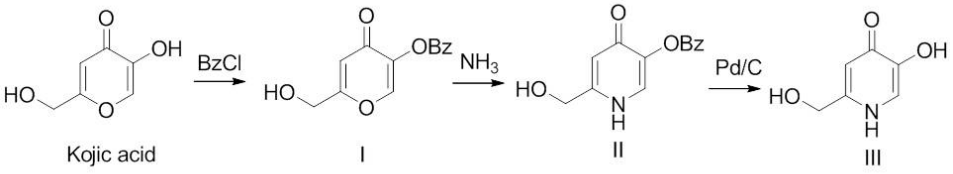

Scheme 6. Synthesis of P1.

5-Benzyloxy-2-(hydroxymethyl)-4H-pyran-4-one

Sodium hydroxide aqueous solution 11 M (10 mL) was added to 100 mL of a solution of KA (14.2 g, 100 mmol) in MeOH and the mixture was heated under reflux. Benzyl chloride (12.75 mL, 111 mmol) was added dropwise, and the reaction mixture was refluxed overnight. Once the reaction finished (checked by TLC; eluent: DCM/MeOH, 1:0.75), the mixture was cooled to room temperature. The precipitate was filtered and washed with an ethylic ether/petroleum ether mixture to obtain a light brown solid (18.016 g, 77% yield); M.p. 129 -131 °C (lit. value 129-130°C[193] and 132°C[194]). ^{1}H NMR (300 Hz, MeOD), δ (ppm): 8.01 (s, 1H, 6-HPy), 7.44–7.32 (m, 5H, HPh), 6.51 (s, 1H, 3-HPy), 5.02 (s, 2H, CH_2-Bz), 4.41 (s, 2H, CH_2-OH).

5-Benzyloxy-2-(hydroxymethyl)-pyridin-4(1H)-one

5-Benzyloxy-2-(hydroxymethyl)-4H-pyran-4-one (6.25 g, 26.91 mmol) was dissolved in methanol (25 mL) and then 25% ammonia aqueous solution (57.5 mL) was added. The mixture was refluxed in oil bath for 7 hours and the progress of the reaction was monitored by TLC (eluent: DMC/MeOH 6:0.75 solvent mixture). The reaction mixture was concentrated in a rotary evaporator to obtain a pale brown solid residue, which was recrystallized from ethanol/ethyl ether, leaving the pure target compound as beige product (5.659 g, 90% yield); M.p. 224 °C (lit. value 225-226 °C[193]). ^{1}H NMR (300

Hz, DMSO), δ (ppm): 11.3 (s, 1H, NH), 7.42 -7.30 (m, 5H, HPh), 6.11 (s, 1H, 6-HPy), 5.70 (s, 1H, 3-HPy), 5.00 (s, 2H, CH_2-Bz), 4.33 (s, 2H, CH_2-OH).

5-Hydroxy-2-(hydroxymethyl)pyridin-4(1H)-one (P1)

5-Benzyloxy-2-(hydroxymethyl)-pyridin-4(1H)-one (2.542 g, 10.99 mmol) was dissolved in methanol (200 mL) and 10% Pd/C (0.258 g) was added. The suspension was stirred for 4 h under H_2 atmosphere (2 bar). Afterwards the mixture was filtered and the solvent evaporated. Final recrystallization from EtOH/Et_2O afforded the pure product a pale brown color (1.065 g, 70% yield); M.p. 245-247 °C. ^{1}H NMR (300 Hz, MeOD), δ (ppm): 7.48 (s, 1H, 6-HPy), 6.44 (1s, 1H, 3-H-Py), 4.55 (s, 2H, CH_2-OH). ^{13}C NMR (400 Hz, D_2O), δ (ppm): 171.73 (C=O), 147.43 (C-OH), 145.65 (2-C-Py), 121.71 (6-C-Py), 111.09 (3-C-Py), 59.52 (CH_2OH). Elemental analysis (%) calculated for ($C_6H_7NO_3$ 0.1H_2O): C 50.40; H 5.08, N 9.80%; found: C 50.43, H 5.12, N 9.65%.

2.2.2. L12

2-{bis[3-hydroxy-6-(hydroxymethyl)-4-oxo-4*H*-pyran-2-yl]methyl} benzoic acid

0.3970 g (3.53 mmol) of dimethylamine and 0.5255 g (3.5 mmol) of 2-formylbenzoic acid were dissolved in 2 mL of EtOH and stirred at room temperature for 30 min. The solution was added dropwise into 20 ml ethanolic solution of kojic acid 1.0015 g (7.05 mmol). The reaction was carried out at room temperature for 24h; then the mixture was kept at -5C for 2h and the excess of substrate was filtered. The solvent was evaporated under reduced pressure. After extracting the sample using a saturated sodium carbonate solution, the water fraction was acidified with 2M HCl and above pH 3 a white precipitate appeared. The product was then filtered and washed with ethyl acetate and cold ethanol. Melting point 225ºC, Analytical data: 60.58 % yield, ESI–MS Found: 415.066 *m/z*; calculated 415.066 *m/z* for ($C_{20}H_{16}O_{10}$-H)$^-$, ^{1}H NMR (D_2O, 500 MHz) δ 4.31 (s, 4H, CH_2-OH), 6.49 (s, 2H), 6.71 (s, 2H), 7.28 (d, 1H), 7.41 (m, 2H), 7.67 (d, 1H).

2.2.3. L13

4-{bis[3-hydroxy-6-(hydroxymethyl)-4-oxo-4*H*-pyran-2-yl]methyl} benzoic acid

0.4045 g (3.27 mmol) of dimethylamine and 0.50315 g (3.35 mmol) of 2-formylbenzoic acid were dissolved in 2 mL of EtOH and stirred at room temperature for 30 min. The solution was added dropwise into 20 ml ethanolic solution of kojic acid 1.0004 g (7.04 mmol). The reaction was carried out at room temperature for 24h; then the mixture was kept at -5C for 2h and the excess of substrate was filtered. The solvent was evaporated under reduced pressure. After extracting the sample using a saturated sodium carbonate solution, the water fraction was acidified with 2M HCl. The reaction product was then filtered and washed with ethyl acetate and cold ethanol. Melting point 250ºC, Analytical data: 62.67 % yield, ESI–MS Found: 417.074 *m/z*; calculated 417.082 *m/z* for ($C_{20}H_{16}O_{10}$+H)$^+$, ^{1}H NMR (D_2O, 500 MHz) δ 4.34 (s, 2H), 6.21 (s, 1H), 6.49 (s, 2H), 7.40 (d, 2H), 7.87 (d, 2H).

2.2.4. L14

2,2'-[(2-hydroxyphenyl)methanediyl]bis[3-hydroxy-6-(hydroxymethyl)-4*H*-pyran-4-one]

0.4049 g (3.60 mmol) of dimethylamine and 0.4327 g (3.54 mmol) of 2-formylbenzoic acid were dissolved in 2 mL of EtOH and stirred at room temperature for 30 min. The solution was added dropwise into 20 ml ethanolic solution of kojic acid 1.0106 g (7.11 mmol). The reaction was carried out at room temperature for 24h; then the mixture was kept at -5C for 2h and the excess of substrate was filtered. The solvent was evaporated under reduced pressure. After extracting the sample using a saturated sodium carbonate solution, the water fraction was acidified with 2M HCl. The reaction product was then filtered and washed with ethyl acetate and cold ethanol. Melting point 255ºC, Analytical data: 69.38 % yield, ESI–MS Found: 389.076 *m/z*; calculated: 389.082 *m/z* for $(C_{19}H_{16}O_9+H)^+$, ^{1}H NMR (D_2O, 500 MHz) δ 4.33 (s, 4H), 6.29 (s, 1H), 6.50 (s, 2H), 6.89 (m, 2H), 7.11 (d, 1H), 7.22 (t, 1H).

2.2.5. L15

2,2'-[(4-hydroxyphenyl)methanediyl]bis[3-hydroxy-6-(hydroxymethyl)-4*H*-pyran-4-one]

0.4124 g (3.67 mmol) of dimethylamine and 0.4280 g (3.5 mmol) of 2-formylbenzoic acid were dissolved in 2 mL of EtOH and stirred at room temperature for 30 min. The solution was added dropwise into 20 ml ethanolic solution of kojic acid 1.0842 g (7.6 mmol). The reaction was carried out at room temperature for 24h; then the mixture was kept at -5C for 2h and the excess of substrate was filtered. The solvent was evaporated under reduced pressure. After extracting the sample using a saturated sodium carbonate solution, the water fraction was acidified with 2M HCl. The reaction product was then filtered and washed with ethyl acetate and cold ethanol. Melting point 285ºC, Analytical data: 71.81 % yield, ESI–MS Found: 389.078 *m/z*; calculated 389.078 *m/z* for $(C_{20}H_{16}O_{10}+H)^+$, ^{1}H NMR (D_2O, 500 MHz) δ 4.36 (s, 4H), 6.07 (s, 1H), 6.48 (s, 2H), 6.82 (d, 2H), 7.22 (d, 2H).

2.2.6. KβAK

The synthesis was performed according to a recently described method[195](Scheme 7).

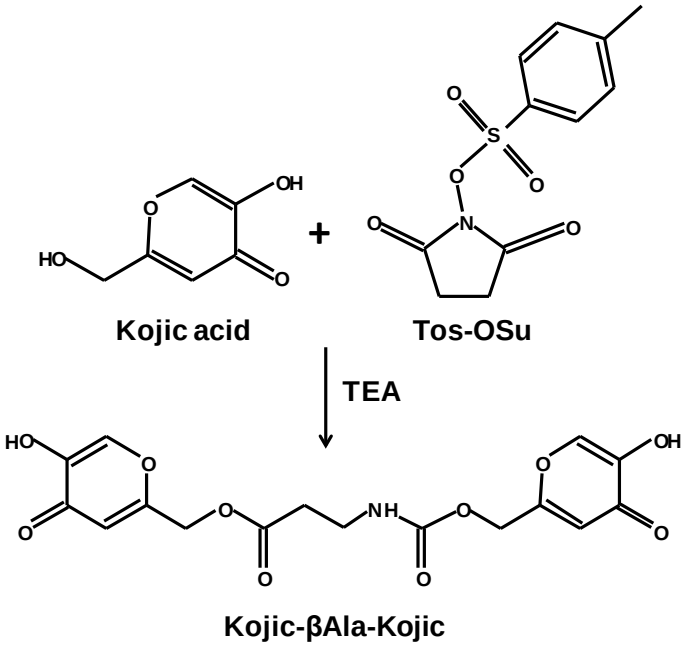

Scheme 7. Synthesis of (5-hydroxy-4-oxo-4H-pyran-2-yl)methyl 3-({[(5-hydroxy-4-oxo-4H-pyran-2 yl)methoxy]carbonyl}amino)propanoate (Kojic-βAla-Kojic, KβAK).

Synthesis of (5-hydroxy-4-oxo-4H-pyran-2-yl)methyl 3-({[(5-hydroxy-4-oxo-4H-pyran-2 yl)methoxy]carbonyl}amino)propanoate (Kojic-βAla-Kojic, KβAK)

Kojic acid (5.4 g, 38 mmol) and Tos-OSu (5.6 g, 21 mmol)[196],[197] were suspended in 40 mL of dioxane followed by dropwise addition of triethylamine (8 mL). After stirring the reaction mixture at 65ºC for 1 h, the solvent was evaporated under reduced pressure. After extracting the sample using a saturated sodium carbonate solution, the water fraction was acidified with HCl. The reaction product was extracted with ethyl acetate and dried over $MgSO_4$. The solvent was then evaporated and further purified by preparative HPLC according to the procedure described in below in this section. Sample identity and purity were confirmed by NMR, ESI-MS (Electrospray Ionization-Mass Spectrometry) and HPLC.

Analytical data: 92% yield, ESI–MS Found: 382.0810 m/z; calculated 382.0769 m/z for $(C_{16}H_{15}NO_{10})^+$, ^{1}H NMR (DMSO – d6, 500 MHz) δ 2.50 (t, 2H, J = 6.6Hz), 3.18 (q, 2H, J = 6.4Hz, J=12.72Hz), 4.78 (s, 1.8H), 4.87 (s, 2H), 6.30 (s, 1H), 6.39 (s, 1H), 7.50 (t, 0.8H, J = 5.5Hz), 7.99 (m, 2H). ^{13}C NMR (DMSO-d6, 500 MHz) δ 33.64, 36.41, 61.2, 61.3, 111.9, 112.5, 139.7, 139.8, 146.0, 155.1, 161.4, 162.5, 170.5, 173.6.

Synthesis of 1-{[(4-Methylphenyl)sulfonyl]oxy}pyrrolidine-2,5-dione (Tos-OSu)

The protocol used for the synthesis of Tos-OSu was similar to that previously described in the literature[196],[197]. Briefly, N-Hydroxyimide (93 mmol) and tosyl chloride (100 mmol) were dissolved in tetrahydrofuran (100 mL) and triethylamine (14.7 mL) was then added over 20 min. After 40 min, the solvent was removed in vacuo and 100 mL of 5% hydrochloric acid was added. The product was filtered off, washed twice with water and crystallized from ethyl acetate to give Tos-OSu. Analytical data: 92% yield, ESI–MS Found: 292.02 m/z; calculated 292.03 m/z for $(C_{11}H_{11}NO_5S + Na)^+$, ^1H NMR ($CDCl_3$, 500 MHz) δ 2.44 (s, 3H), 2.76 (s, 4H), 7.35 (d, 2H, J = 8.4 Hz), 7.87 (d, 2H, J = 8.4 Hz). ^{13}C NMR ($CDCl_3$, 500 MHz) δ 21.8, 25.4, 129.6, 130.3, 131.3, 147.3, 168.7.

Purification of Kojic-βAla-Kojic

Preparative reversed-phase HPLC was performed on a Tosoh TSKgel ODS-120T column (21.5 mm × 300 mm) (Tosoh, Tokyo, Japan) using the same solvent system, gradient 0.5% min-1 and a flow rate of 7 mL min-1. The crude product was analyzed by analytical HPLC using a Thermo separation HPLC system with UV detection (210 nm) on a Vydac Protein RP C18 column (250×4.6 mm, 5 mm) (Grace, Deerfield, IL, USA), with a gradient elution of 0-80% B in A (A = 0.1% TFA in water; B = 0.1% TFA in acetonitrile - H_2O, 4:1) for 45 min (flow rate 1 mL mL-1, rt).

2.2.7. SC

6,6',6''-(((nitrilotris(ethane-2,1-diyl))tris(azanediyl))tris(methylene))tris(3-hydroxy-4H-pyran-4-one)

Kojic acid (1.0 g, 7.04 mmol) was suspended in 20 mL ethanol followed by dropwise addition of tris(2-aminoethyl)amina (350 µL, 2.32 mmol) solved in $CHCl_3$ (2 mL). After stirring the reaction mixture at room temperature for 1 h, the precipitate was filtered and washed with ethyl acetate. Sample identity and purity were confirmed by NMR and elemental analysis. Analytical data: 98.5% yield, ^1H NMR (D_2O, 500 MHz) δ 2.83 (t, 6H, J = 2.81 Hz), 3.09 (t, 6H, J = 3.09 Hz), 4.49 (s, 6H), 6.49 (s, 3H), 7.82 (s, 3H). ^{13}C NMR (D_2O, 500 MHz) δ 39.84, 53.86, 62.92, 112.94, 145.16, 168.24, 184.01, 199.25. Elemental analysis (%) calculated for ($C_{24}H_{36}N_4O_{12}\cdot 3H_2O$): C 50.35; H 6.34, N 9.79 %; found: C 50.65, H 6.17, N 9.27 %.

3. Results and discussion

3.1. Structural studies

3.1.1. P1 Crystal structure[147]

The bond lengths and angles in the molecule P1 (Figure 3.1) have commonly encountered values (Table A5). The substituents at C4 and C5 are almost coplanar with the aromatic ring. In contrast, the torsion angle N1–C2–C7–O8 [-31.0(2)º] reveals a noticeable twisting for the C2 hydroxymethyl group towards the aromatic ring plane.

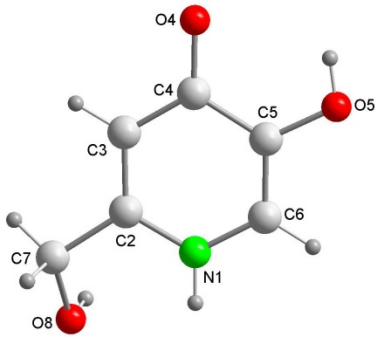

Figure 3.1. Ball and stick structure and atom labelling scheme of P1.

The crystal packing of P1 features infinite one-dimensional zig-zag chains along *c* axis, built up by classical hydrogen bonding interactions: N1-H1A···O4c and O5-H5A···O8a (operators for generating equivalent atoms: a, -x+1/2, -y+1, z-1/2; c, -x+1/2, -y+1, z+1/2, with with $R_2^2(10)$ hydrogen-bonding patterns (Figure 3.2a).

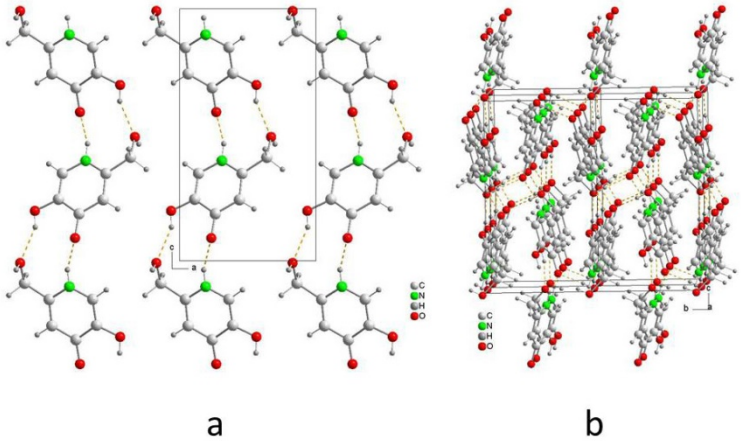

Figure 3.2. Crystal packing of P1 seen along the *a* (b) and *b* (a) directions.

Each molecule forms an additional hydrogen bond O8-H8A···O4^b (b, -x+1, y+1/2, -z+1/2) with a molecule of a neighbouring chain to give an infinite three-dimensional network (Figure 3.2b). Hence, the O4-carbonyl atom acts twice as H-acceptor whereas

the O8-H8A alcoholic moiety plays both H-donor and H-acceptor roles. The structural comparison of P1 with kojic acid,[198] shows that the O-heterocyclic atom of kojic acid does not act as H-acceptor in its crystal. In clear contrast, the isolobal N1-H1A group of P1 (replacing the O-heterocyclic donor of the kojic acid) acts as an H-donor for intermolecular interactions. In addition, the torsion angle O1–C2–C7–O8 [–167.8(2)˚] in KA shows that the hydroxymethyl substituent is oriented in the opposite direction respect to KA. These data will be of importance in the following considerations of tautomeric forms.

3.1.2. L1 Crystal structure[199]

The asymmetric unit of L1 ligand consists of one half-molecule. The molecule is completed by a two-fold symmetry element (Figure 3.3A) and exhibits two symmetry related intra-molecular H-bonds involving each OH phenol-like group as donor and the corresponding O keto–kojic group as acceptor (O5-H···O4 (2.750(3) Å, 112.00°). These interactions seem favoured by the almost coplanar array of each hydroxyl groups and its pyranone ring, forming a torsion angle O2-C3-C4-O3 of only 1.88°. The two pyranone rings of the kojic are planar and define a dihedral angle of 74.76(2)°. This molecular structure is close to that previously reported for L8[163] (Figure 3.3B, where the kojic moieties define a dihedral angle of 85.02º) but in the L1 molecule there is not the disorder reported for a hydroxymethyl group of L8. It is noteworthy that in the L1 ligand the KA units are turned in opposite direction, while in L8 the KA units are turned in the same direction.

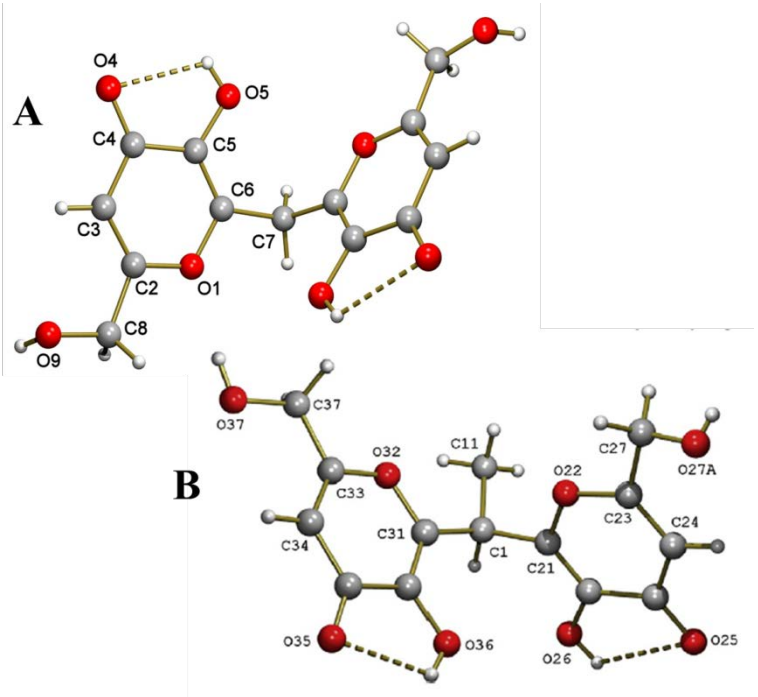

Figure 3.3. Asymmetric unit in the crystal of ligand L1 (A) and L8 (B). Intra-molecular H-bonding interactions are plotted as dash line.

In the crystal of L1, inter-molecular hydrogen bonds involving the keto-phenol moiety and the hydroxymethyl group (O(5)-H(5)···O(9), 2.687(3) Å, 153.2°; O(9)-H(9)···O(4) 2.653(3) Å, 170.3° (graph set $R^4_4(14)$, Figure 3.4A) associate adjacent molecules to generate a densely packed three-dimensional network (Figure 3.4B).

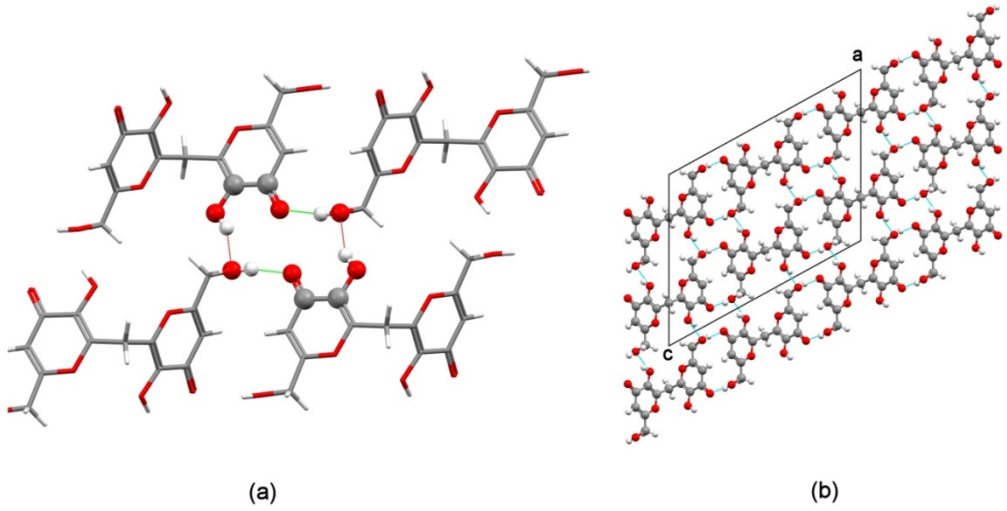

Figure 3.4. (A) Detail of the graph set $R^4_4(14)$ involving O-H···O contacts in L2. (B) View in the *ab* plane of the H-bonded 3D network of the crystal of L2.

3.1.3. L13 Ligand structure

In Figure A the structure of the L13 ligand is reported, which remarks that the intermolecular H bonds form a tridimensional network. These hydrogen bonds take place between the OH group of one KA unit and the carbonyl group of a second ligand, and between the OH group of the second KA unit and the CH_2OH group of a third ligand. A further point to be remarked is that the presence of a substituent on the linker moves the two kojic units in the same direction, as already observed in the L2, L3 and L8 ligand structures[35],[163].

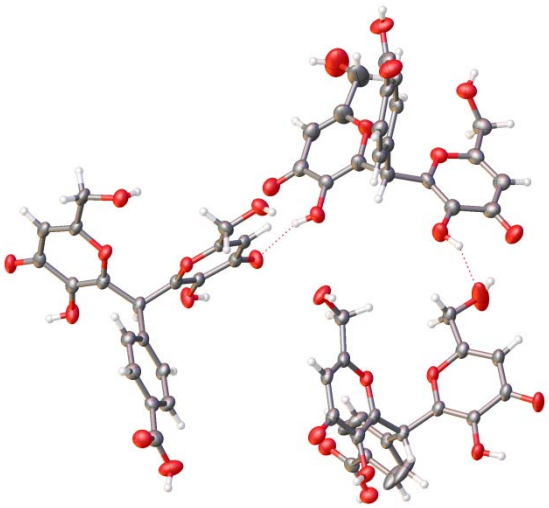

Figure A. Detail of the network structure showing the O-H···O contacts in L13.

3.2. Protonation equilibria studies

3.2.1. P1 Ligand[147]

The protonation equilibria of P1 have been examined with different techniques. Potentiometric-spectrophotometric measurements gave evidence of three different deprotonation steps according to the sequence (1).

$$H_3L^+ \leftrightharpoons H_2L \leftrightharpoons HL^- \leftrightharpoons L^{2-} \quad (1)$$

The loss of each proton markedly affects UV absorption spectra (Figure 3.5 and Figure A1), and three different pH regions (3 – 4.6, 7.3 – 10.5, and 10.6 – 13.2) relative to each single equilibrium can be identified, characterized by different bands and well defined isosbestic points. These features allowed the evaluation of the protonation constants (Table 3.1); the related speciation plot is presented in Figure 3.6A with superimposed the heights of UV bands, obtained by spectral decomposition. The trend of ^{1}H NMR signals of protons H3, H6 and H7 *vs* pH (Figure 3.6B, Figure A2 and Table A6) confirms the deprotonation sequence (1).

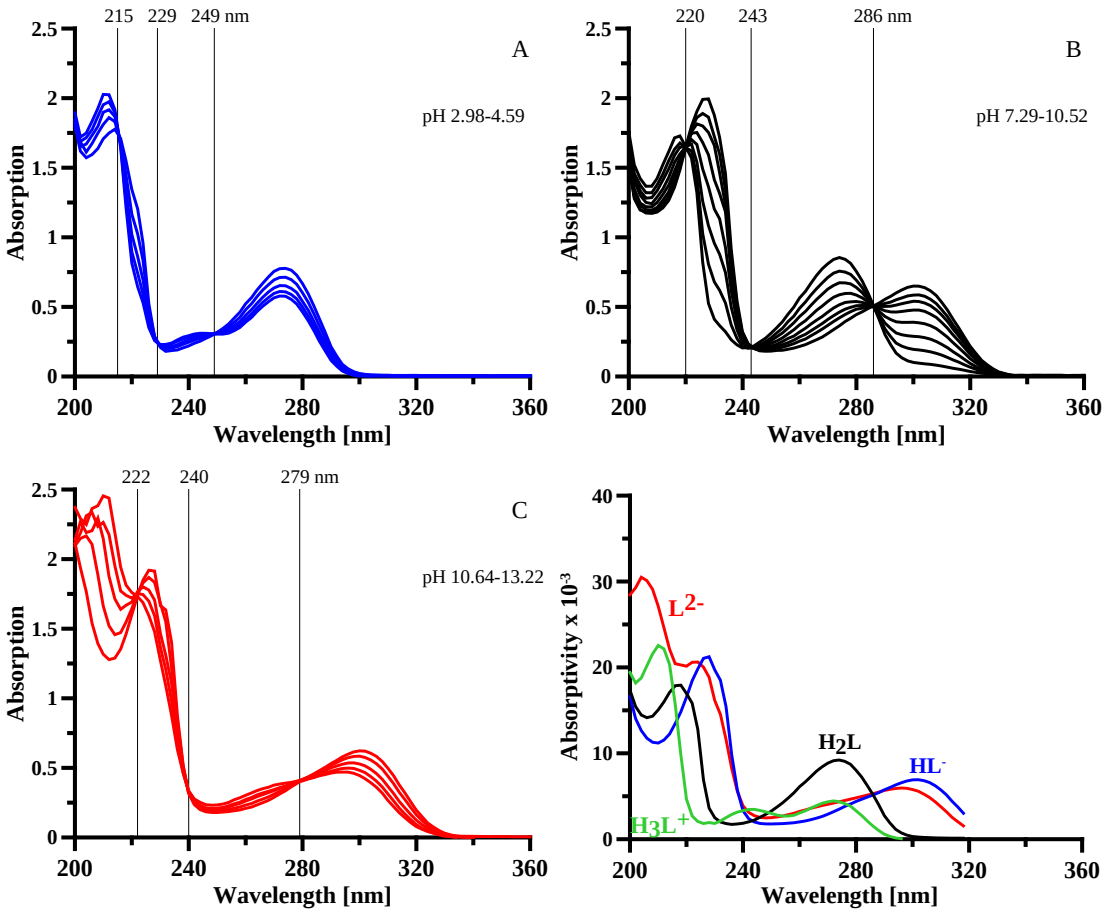

Figure 3.5. UV spectra collected during potentiometric titration of the ligand, C_L 4.95 x 10^{-4} M, using a 0.2 cm optical path length. A pH 2.98-4.59, B 7.29-10.52, C pH 10.64-13.22; D Absorptivity spectra of the ligand in the acidic and basic forms. 200-340 nm spectral range.

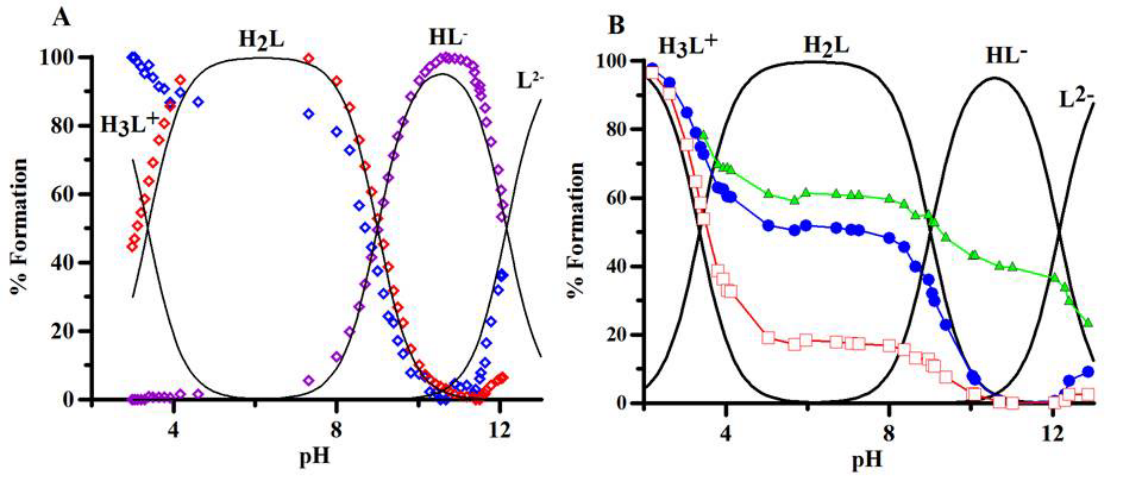

Figure 3.6. A) Normalized heights of the peaks at 248 nm(blue), 273nm (red) and 307 nm (violet), obtained by spectral decomposition, superimposed to the speciation plot of ligand. B) Normalize chemical shifts of H6 (●), H3 (■) and H7 (Δ) proton, superimposed to the speciation plot of ligand.

The first deprotonation (pH 2-5) mainly affects proton H3, suggesting that the proton is lost from the protonated oxygen in position 4. The signal of H6 reflects this effect though in a minor extent. The second step (pH 7.3 - 10.5), related to the deprotonation of the 5-hydroxy group, mainly reflects on H6 chemical shift. The last deprotonation (pH > 10.6) affects predominantly H7 signals of methylene group, which could be implied in a hydrogen bond between the OH group and the now deprotonated nitrogen atom. The high pK of this last dissociation suggests a keto-enol tautomer transition with dissociation from the hydroxyl group.

Table 3.1. Protonation constants for P1 at 25°C, 0.1 M KCl ionic strength, obtained using HyperQuad2013 program.[200] Standard deviations on the last figure in brackets. The literature values for DFP (Scheme 1, HL' in the neutral form) and 3,4-hopo are reported for comparison.

Species	P1 Log K	Species	DFP Log K[201]	3,4-hopo Log K[202]
H_3L^+	3.37(7)	$H_2L'^+$	3.66(1)	3.34(1)
H_2L	9.00(1)	HL'	9.82(2)	9.01(1)
HL^-	12.16(1)		-	-

The log *K* 9.00 and 3.37 are almost equal to those of 3,4-hopo[202], and somewhat lower than those of DFP (Table 3.1).[201] Conversely, the loss of a third proton is a new feature, which implies an equilibrium with a catechol-like molecule that loses its proton at basic pH values (log *K* 12.16). The deprotonation at the ring NH group of DL-α-amino-β-(6-oxo-1,6-dihydro-pyridin-6yl)propanoic acid (Stunzi et al.)[203] is characterized by a log *K* value of 11.8, similar to that of 2-hydroxypyridine (11.7).[204]

The ESI-MS measurements in D_2O give evidence of the exchange of four labile protons with deuterium. The spectrum of ligand in D_2O solution (Figure A3) shows five signals of different intensities. The most intense signals at 145.070 *m/z* and 146.076 *m/z* correspond to $[C_6H_5D_3O_3N]^+$ and $[C_6H_4D_4O_3N]^+$ deuterated on two or three oxygen

atoms and on a single nitrogen atom. The less intense signals at 142.050, 143.057 and 144.063 *m/z* match with the simulated spectra of $[C_6H_8O_3N]^+$, $[C_6H_7DO_3N]^+$ and $[C_6H_6D_2O_3N]^+$. The ESI-MS signals of free ligand at different pH values (1.68, 6.13, 11.5 and 13.7, Table A7) show that the molecular weight of the ligand does not change during the first (140.032 *m/z*) and third (139.032 *m/z*) deprotonation in negative mode spectrum, and does not present positively charged signals at basic pH. The presence of a peak at 139.032 *m/z*, a sticking peculiarity observed in aqueous solutions at pH >11.5, further confirms the last deprotonation process shown in Sequence 1.

The deprotonation sequence of P1 has been also investigated at DFT level by calculating the electronic energies of the possibly protonated forms of the ligand at their ground state optimized geometry. Based on the results recently published on related systems, DFT calculations were performed by using the mPW1PW hybrid functional[185] and Schäfer, Horn, and Ahlrichs double-ζ plus polarization all-electron basis sets (BS) for all of the atomic species.[186] In particular, the fully protonated cationic ligand H_3L^+, the three possible isomers of the neutral and monoanionic forms (H_2L and HL^-, respectively), and the completely deprotonated dianion L^{2-} were optimized, both in the gas phase and in water, implicitly taken into account by using the integral equation formalism of the polarizable continuous model (IEF-PCM) within the self-consistent reaction field (SCRF) approach (Scheme 8).[189]

Scheme 8. Lewis structures of the differently protonated forms of P1 optimized at the DFT level.

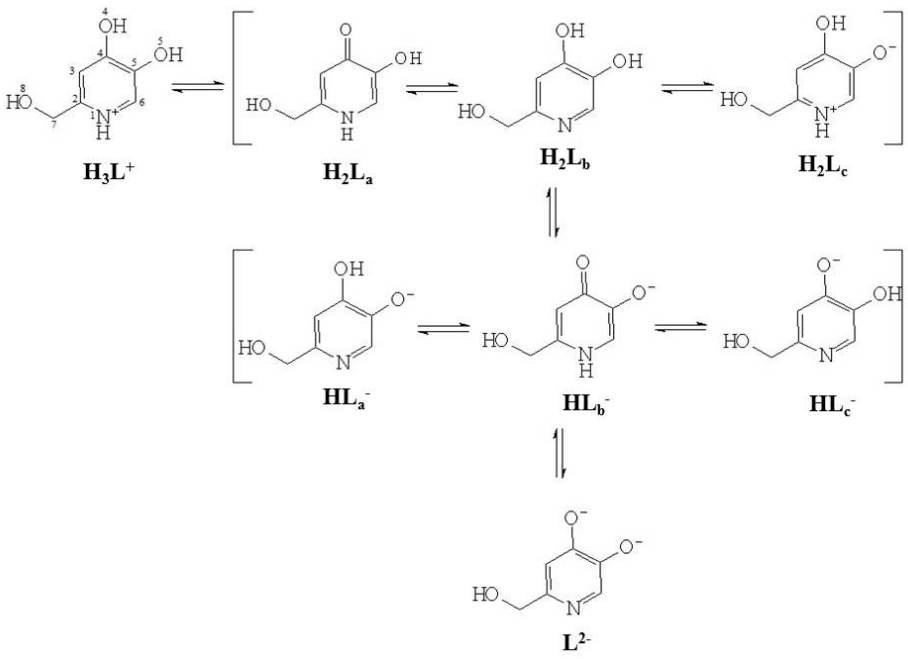

A comparison of the metric parameters optimized for the neutral isomer H_2L_a in the gas phase with the corresponding structural data (see section 3.1.1) shows very good agreement between the two sets of data, the principal bond distances being varied by less than 0.05 Å (Table A8). No significant changes in the optimized structural parameters were observed upon considering implicit solvation in the calculations, all the

bond lengths and angles differing by less than 0.01 Å and 2°, respectively for all of the eight forms of the ligand considered here. All of the compounds show a completely planar structure, except the hydroxymethyl substituent, whose orientation depends on the protonation pattern of the ligand. In particular, in the species where N1 is deprotonated (H_2L_b, HL_a^-, HL_c^-, and L^{2-}), the O8-H8 hydroxyl group is coplanar with the heterocyclic ring, and H8 is oriented towards N1 (C2-C7-O8-H8 dihedral angle ~ 0.0°), so that a hydrogen bond interaction can be observed between the two atoms (N1···H8 distance in the range 1.663-1.907 Å; Figure A4 for H_2L_b). A Second-Order Perturbation Theory Analysis (SOPTA) of Fock matrix in NBO basis allows for evaluation of the energy E_{SOPTA} of the interaction between the lone pair (LP) localized on N1 and the unfilled natural orbitals of the O8-H8 hydroxyl group in the range between 10.3 and 35.0 kcal/mol depending on the species. On the other hand, in the forms of the ligand showing N1 protonated (namely H_2L_a, H_2L_c, and HL_b^-), in agreement with what was found experimentally for H_2L_a, the O8-H8 moiety lies outside the plane described by the rest of the molecule, the N1-C2-C7-O8 and C2-C7-O8-H8 dihedral angles being in the ranges –23.0/–40.8 and –49.2/–78.8°, respectively (Table A8 and Figure A4 H_2La and H_2Lc). Finally, in H_3L^+, although the C7 hydroxyl group is coplanar with the heterocyclic ring, H8 is oriented opposite to N1 (C2-C7-O8-H8 dihedral angle ~180.0°). An analysis of the total electronic energies calculated for the three possible neutral tautomeric forms of the ligand suggests the tautomer H_2L_a to be the most stable (H_2L_b and H_2L_c being less stable by about 7 and 5 kcal/mol, respectively). This agrees with a first deprotonation of the ligand concerning H4, as hypothesized based on spectroscopic evidences, and with the X-ray diffraction analysis discussed above. In agreement with experimental data, H_2L_a is stabilized by a hydrogen bond (O4···H5 distance = 1.885 Å; Figure A4), the interactions between the LP localized on O4 and the unfilled natural orbitals of the O5-H5 hydroxyl group being calculated in E_{SOPTA} = 10.6 kcal/mol.

As far as the monoanionic forms of the ligand are concerned, the isomers HL_a^- and HL_c^- were calculated to be more stable than HL^-_b by 12 and 15 kcal/mol, respectively, thanks to the formation of two different hydrogen bonds, one involving the N1 atom and the hydroxymethyl pendant, and the other the C4–O4 and C5–O5 groups (O5···H4 distance in HL_a^- = 1.684 Å; O4···H5 distance in HL_c^- = 1.775 Å; E_{SOPTA} ~27 and 18 kcal/mol for HL_a^- and HL_c^-, respectively). This accounts for the mechanism suggested by experimental data for the second deprotonation of the ligand, which should involve the O5-H5 hydroxyl group, then followed by a rearrangement leading from the pyridinone HL_b^- to the catechol-like tautomer HL_a^-.

Each technique has given evidence of tautomeric forms, and together they provided a complete description of the deprotonation paths. As long as third deprotonation was not observed for 3,4-hopo, we believe that $–CH_2OH$ in the position 2 is important for the tautomer change of the molecule.

3.2.2. L12 Ligand

The protonation equilibria of L12 (Scheme 2) have been studied by potentiometry, UV-Vis spectrophotometry, ^{1}H-NMR spectroscopy and calorimetry. Protonation constants of L12 were determined by simultaneous potentiometric-spectrophotometric titrations[205]. Since L12 is constituted by two units of kojic acid joined by a methylene bridge substituted with a benzoic acid, three protonation equilibria were observed when a L12 solution 5.49×10^{-4} M was potentiometrically titrated with NaOH 0.1 M, at ionic strength 0.1 M NaCl and 25 °C (Figure 3.7). The log K values for the four examined ligands L12-L15 are reported in Table 3.2, together to the literature values for L2 and L3 ligands[35] in order to have a complete picture of the effects of the substituents. The thermodynamic parameters ΔG, ΔH and TΔS have been also reported in Table 3.2, evaluated from calorimetric measurements.

Table 3.2. Protonation constants values and thermodynamic parameters ΔG, ΔH and TΔS for L12-L15 ligands.

Ligand	log K	$-\Delta G^0$ (kJ mol^{-1})	$-\Delta H^0$ (kJ mol^{-1})	$T\Delta S^0$ (kJ mol^{-1})
L12	9.57 (3)	54.6 (1)	18.8 (6)	35.8 (6)
	7.44 (2)	42.4 (1)	12.1 (9)	30.3 (9)
	3.49 (1)	19.9 (1)	-1.3 (8)	21.2 (8)
L13	9.24 (2)	52.7 (1)	15.1 (6)	37.6 (6)
	7.04 (3)	40.2 (1)	11.3 (6)	28.9 (6)
	4.14 (1)	23.6 (1)	1.3 (4)	22.3 (4)
L14	10.10 (3)	57.6 (1)	25 (1)	33 (1)
	8.57 (1)	48.9 (1)	20 (1)	29 (1)
	6.91 (1)	39.4 (1)	13.8 (8)	25.6 (8)
L15	9.98 (2)	56.9 (1)	14.6 (6)	42.3 (6)
	8.47 (2)	48.3 (1)	16.7 (9)	31.6 (9)
	6.78 (1)	38.7 (1)	11.7 (8)	27.0 (8)
L2[35]	10.58 (3)	60.4 (2)	0 (1)	60 (1)
	8.92 (2)	50.9 (1)	14 (1)	37 (1)
	6.95 (1)	39.6 (1)	12 (2)	28 (2)
L3[35]	10.18 (2)	58.1 (3)	12 (1)	46 (1)
	8.84 (1)	50.4 (1)	16 (1)	34 (1)
	7.21 (1)	41.1 (1)	12 (1)	29 (1)

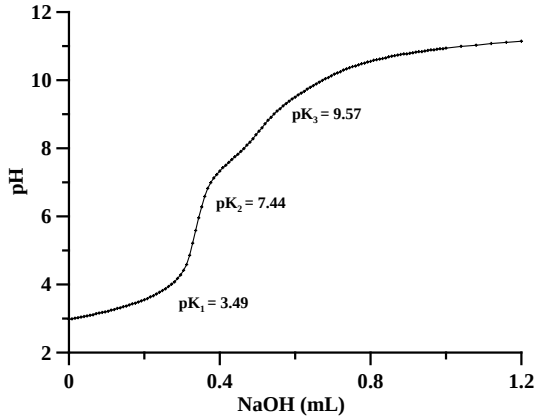

Figure 3.7. Potentiometric titration of L12 with NaOH 0.1M, NaCl 0.1M, 25°C.

The carboxylic group deprotonation in L12 takes place with $pK_1 = 3.49$, lower than that of the two OH groups in KA moieties, $pK_2 = 7.44$ and $pK_3 = 9.57$.

The UV-Vis spectra were registered during the simultaneous potentiometric-spectrophotometric titration (0.2 cm path length) at $4.86 \cdot 10^{-4}$ M ligand concentration. The four absorptivity spectra obtained by SPECFIT and HypSpec programs are presented in Figure 3.8. An easy attribution of the protonation steps that involves the OH group of KA moieties can be done on the basis of the characteristic spectra of KA[33], where the L^- and LH species are characterized by UV bands at 315 nm ($\varepsilon = 5900$ M^{-1} cm^{-1}) and 270 nm ($\varepsilon = 8700$ M^{-1} cm^{-1}), respectively, with a sharp isosbestic points at 242 nm and 290 nm (Figure A5).

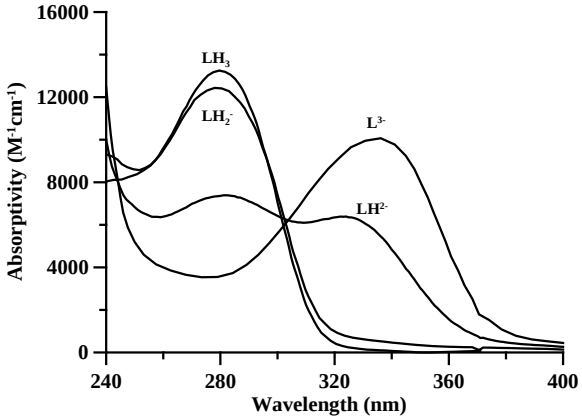

Figure 3.8. Absorptivity spectrum of L12 ligand.

LH_3 species of L12 has a maximum at 279 nm with $\varepsilon = 13330$ $mol^{-1} \cdot L \cdot cm^{-1}$, LH_2^- species has a maximum at 279 nm with $\varepsilon = 12500$ $mol^{-1} \cdot L \cdot cm^{-1}$, LH^{2-} species has two maxima at 281 nm $\varepsilon = 7390$ $mol^{-1} \cdot L \cdot cm^{-1}$ and 324 nm $\varepsilon = 6390$ $mol^{-1} \cdot L \cdot cm^{-1}$ and L^{3-} species has one maximum at 335 nm $\varepsilon = 10100$ $mol^{-1} \cdot L \cdot cm^{-1}$.

The trends of the peak heights after decomposition of the spectra in the Gaussian components[206], are in agreement with the speciation plots calculated by Hyss program with the pK values in Table 3.2 and (Figure 3.9).

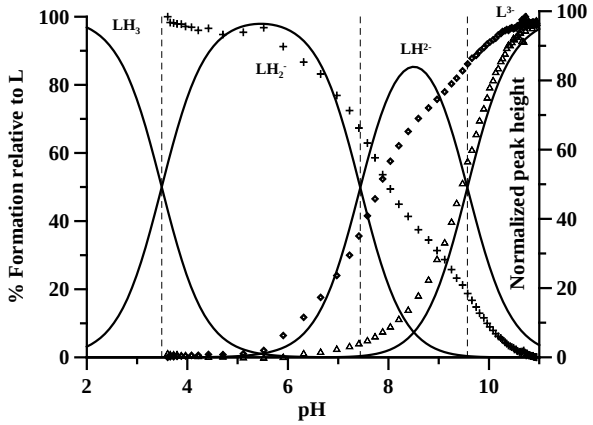

Figure 3.9. Speciation curves of ligand L12, with the overlapping trends of the heights of UV bands at 279 nm (+), 324 nm (◊) and 335 nm (Δ), obtained by spectral decomposition of the spectra in Figure 3.8 with the Specpeak program[206].

On the basis of the spectral changes observed during ligand spectrophotometric-potentiometric titration, the values $pK_2 = 7.44$ and $pK_3 = 9.57$, can be attributed to the two OH groups in KA moieties, while the first deprotonation, almost spectrophotometrically silent, is attributed to the carboxylic acid in the benzene ring.

Twenty two ^{1}H-NMR spectra in the pH range 1.4-13.05 were collected for L12 ligand (Figure A6). The variation of intrinsic chemical shifts (Table 3.3 and Figure 3.10) in the deprotonation steps allow to further define the deprotonation sequence obtained by UV-vis spectra, and to give evidence of some related structural rearrangements.

$$LH_3 \leftrightharpoons LH_2^- \leftrightharpoons LH^{2-} \leftrightharpoons L^{3-}$$

Table 3.3. Intrinsic chemical shifts of the different protons in L12 ligand in the different protonated species, calculated with HypNMR, and variations of the intrinsic chemical shifts connected to each deprotonation step.

Species	E	F	G	L	M	N	P
L^{3-}	6,50	6,33	4,20	6,94	7,24	7,23	7,28
LH^{2-}	6,27	6,42	4,38	7,27	7,29	7,29	7,35
LH_2^-	6,66	6,48	4,32	7,25	7,32	7,34	7,45
LH_3	6,76	6,49	4,29	7,29	7,52	7,45	7,88
Δδ	**E**	**F**	**G**	**L**	**M**	**N**	**P**
$LH^{2-} \rightarrow L^{3-}$	-0,23	0,10	0,17	0,33	0,04	0,06	0,07
$LH_2^- \rightarrow LH^{2-}$	0,39	0,05	-0,05	-0,02	0,04	0,05	0,11
$LH_3 \rightarrow LH_2^-$	0,10	0,01	-0,03	0,04	0,20	0,11	0,42

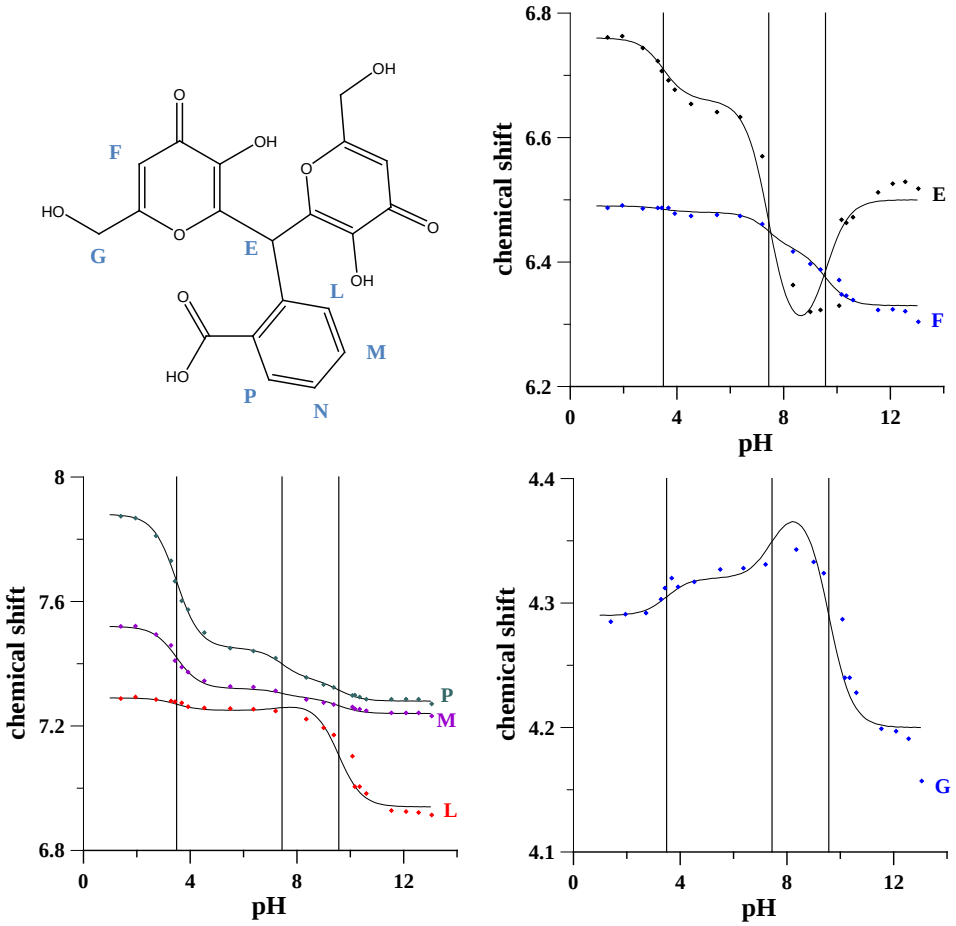

Figure 3.10. Chemical shifts of L12 ligand as a function of pH.

The first step due to the loss of a proton from the carboxylic group strongly affects P and M protons, and in a smaller amount N and E protons. The protons in ortho and para with respect to COOH are those mainly affected, and the formation of a hydrogen bond $COO^{-}\cdots HO$ requires a conformational change that affects the E proton on the linker (Figures 3.10 and 3.11). This is supported by the comparison of thermodynamic protonation data of Table 3.2 with the corresponding parameters reported in the literature for free benzoic acid under similar experimental conditions (pK = 3.99, $-\Delta H°$ = 0.87 $kJ\cdot mol^{-1}$, $T\Delta S°$ = 21.9 $kJ\cdot mol^{-1}$[207]): the protonation of the carboxylic group of L12 is characterized by less favorable $\Delta G°$ and $T\Delta S°$ values; the $\Delta H°$ value becomes endothermic, in agreement with the suggested break of the H-bond requested for carboxylate protonation.

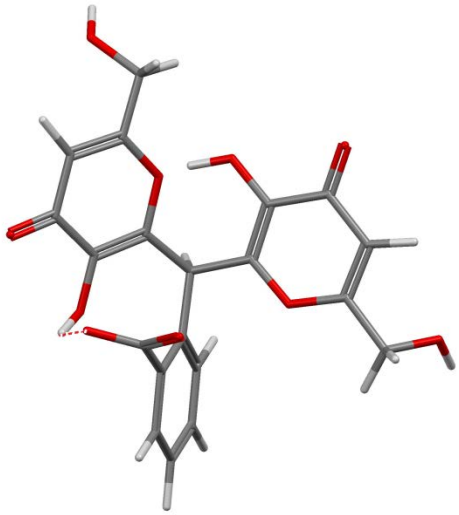

Figure 3.11. Hydrogen bond formation $COO^{-}\cdots HO$ after the first deprotonation of the carboxylic group.

The second step, the deprotonation of the OH group of one KA moiety, affects proton E, F and P. The proton F in the KA ring, in meta with respect to the OH group, is only slightly affected by its deprotonation. The remarkable change in the intrinsic chemical shift of E could derive from the breaking of $COO^{-}\cdots HO$ hydrogen bond and the formation of a new one $O^{-}\cdots HO$ between the two KA units. The breaking of the $COO^{-}\cdots HO$ hydrogen bond also affects the resonance of P, no more involved in hydrogen bonding (Figure 3.12).

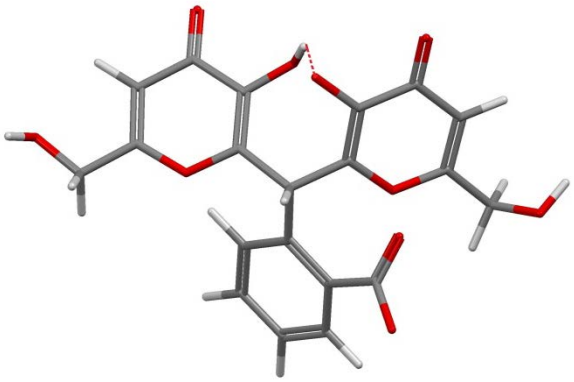

Figure 3.12. Hydrogen bond formation $O^{-}\cdots HO$ between the two KA units.

The third step involves the deprotonation of the OH group on the second KA unit. The $-O^{-}\cdots HO$ hydrogen bond is no more possible, and the molecule rearranges to form a new hydrogen bond involving the hydroxymethyl group. This reverses the chemical shift of E proton, and affects the resonances of G and L protons (Figure 3.13). The described pattern of H-bond formation and re-organization is the same already observed for bis-kojic acid derivatives containing a vanillin molecule in the linker[35] and the calorimetric data are in good agreement with those measured for the latter ligands.

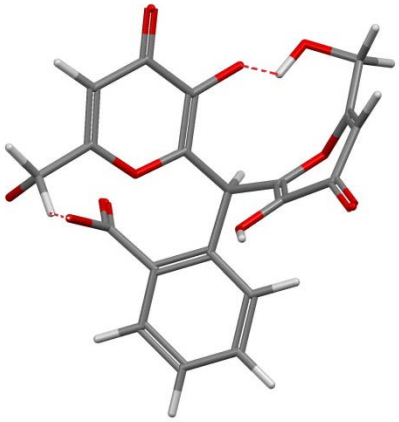

Figure 3.13. Hydrogen bond formation after the third deprotonation of L12.

3.2.3. L13 ligand

L13 differs from L12 ligand only for the position of the carboxylic group in the benzene ring (Scheme 2). Three protonation constants were evaluated from the potentiometric titration data relative to a L13 solution 5.01×10^{-4} M titrated with NaOH, at 0.1 M NaCl ionic strength and 25 ºC (Figure 3.14).

$$LH_3 \leftrightharpoons LH_2^- \leftrightharpoons LH^{2-} \leftrightharpoons L^{3-}$$

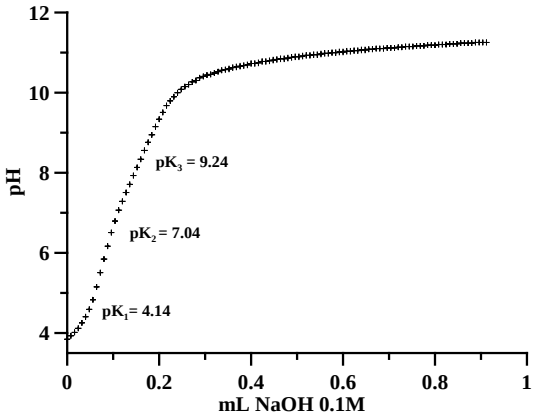

Figure 3.14. Potentiometric titration of L13 with .NaOH 0.1 M, NaCl 0.1 M, 25ºC.

UV-Vis spectra, collected during the simultaneous potentiometric-spectrophotometric titration (0.2 cm path length) of a $3.01 \cdot 10^{-4}$ M ligand solution allowed the evaluation by SPECFIT and HyperSpec programs of the four absorptivity spectra in Figure 3.15.

As in the case of L12, the attribution of the protonation steps involving the OH group of KA moieties, to the second ($pK_2 = 7.04$) and to the third deprotonations ($pK_3 = 9.24$) can be done. The first deprotonation spectrophotometrically silent takes place on the carboxylic group ($pK_1 = 4.14$).

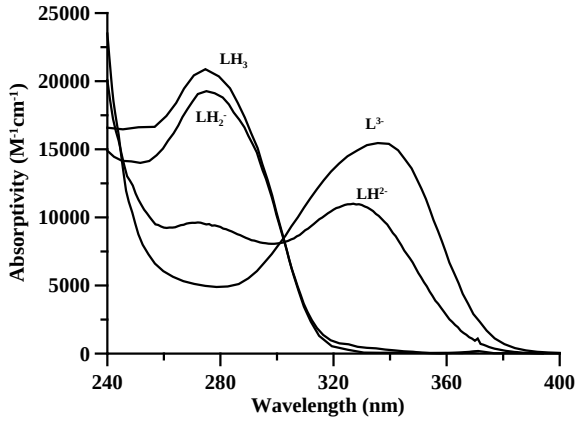

Figure 3.15. Absorptivity spectra of the four different protonated forms of L13 calculated on the whole spectra (pH 3.93-11.12)[180].

The trends of the peak heights, after decomposition of the spectra in the Gaussian components, overlap the speciation plots calculated by Hyss program with the log K values in Table 3.2 (Figure 3.16).

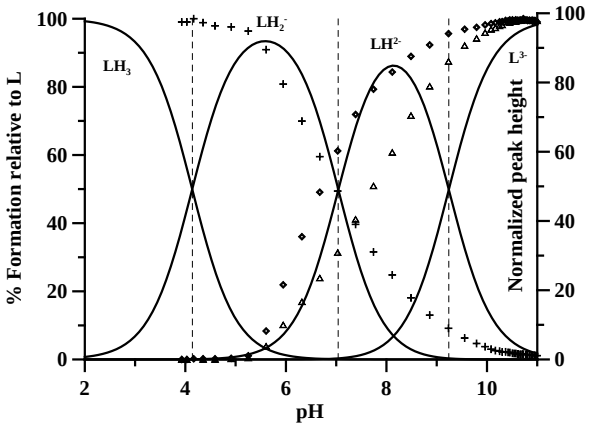

Figure 3.16. Speciation plots of L13ligand, with the overlapping trends of the heights of UV bands at 276 nm (+), 325 nm (◊) and 340 nm (Δ), obtained by spectral decomposition of the spectra in Figure 2.15 with the Specpeak program[206].

Table 3.4. Intrinsic chemical shifts of the different protons in L13 ligand in the different protonated species, calculated with HypNMR, and variations of the intrinsic chemical shifts connected to each deprotonation step.

Species	E	F	G	I	L
L^{3-}	6,43	6,34	4,28	7,72	7,21
LH^{2-}	6,07	6,42	4,36	7,75	7,31
LH_2^-	6,20	6,49	4,35	7,76	7,36
LH_3	6,22	6,49	4,34	7,93	7,43
Δδ	**E**	**F**	**G**	**I**	**L**
$LH^{2-} \rightarrow L^{3-}$	-0,36	0,08	0,07	0,03	0,10
$LH_2^- \rightarrow LH^{2-}$	0,13	0,07	-0,01	0,02	0,05
$LH_3 \rightarrow LH_2^-$	0,02	0,00	-0,01	0,17	0,07

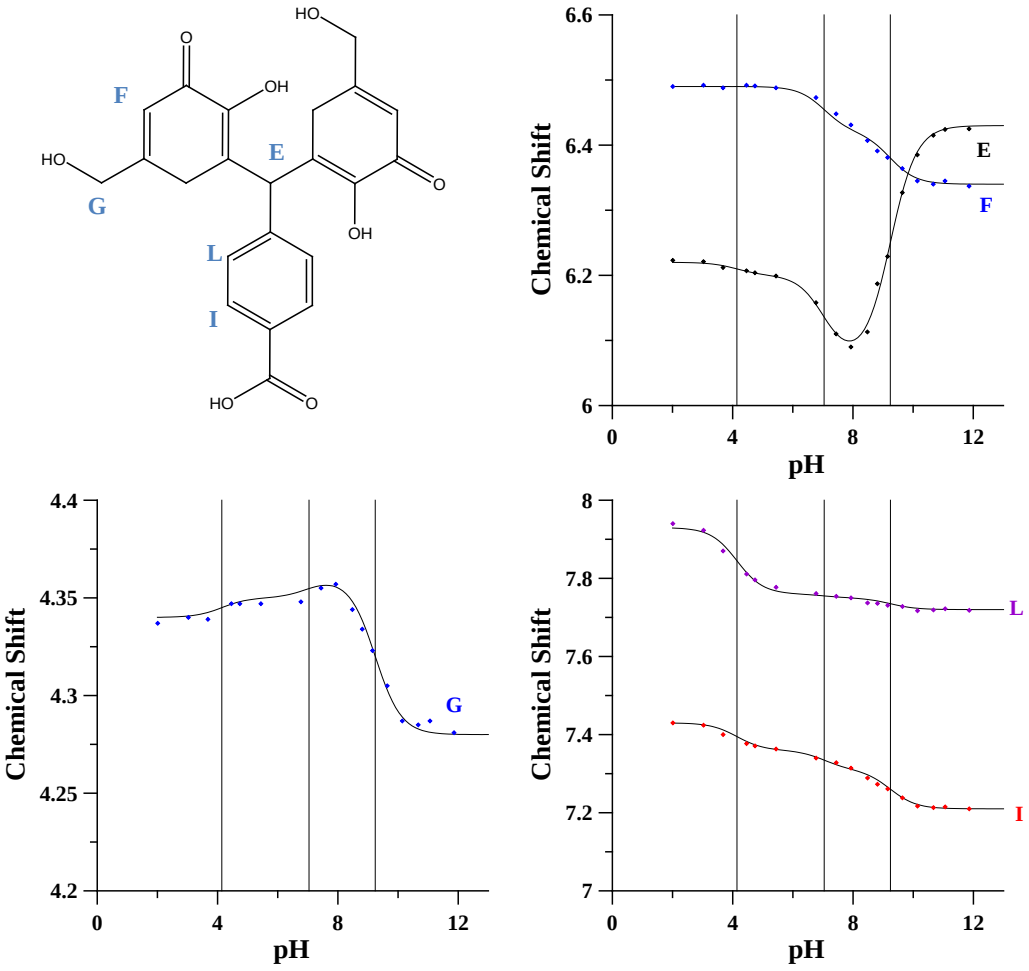

Figure 3.17. Chemical shifts of L13 ligand as a function of pH.

In the case of ^{1}H-NMR measurements, the first deprotonation step, due to the loss of a proton from the carboxylic group, strongly affects I and, in a smaller amount, L protons. The ortho and para protons with respect to COOH are those mainly affected, and no hydrogen bond $COO^{-}\cdots HO$- formation is observed (Figures 3.17 and 3.18 and Table 3.4). Contrarily to what discussed for L12, in the case of L13 all the thermodynamic parameters referring to carboxylate protonation are very similar to those reported for

free benzoic acid, in agreement to the observation that no H-bond is possible between the carboxylate group and the rest of the molecule.

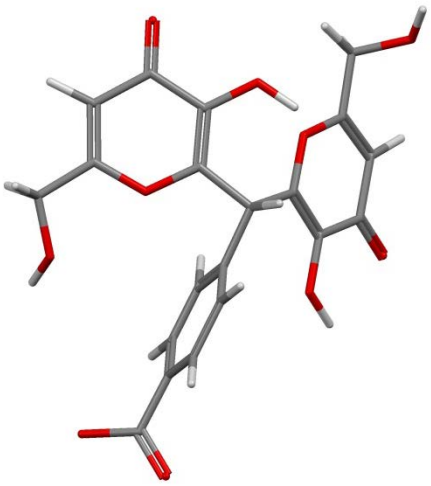

Figure 3.18. L13 ligand after the loss of the H on the carboxylic group.

In the second step E proton is the most affected, suggesting that the deprotonation of –OH group leads to the hydrogen bond OH---$^{-}$O between the two units of KA, which affects F and E protons (Figure 3.19).

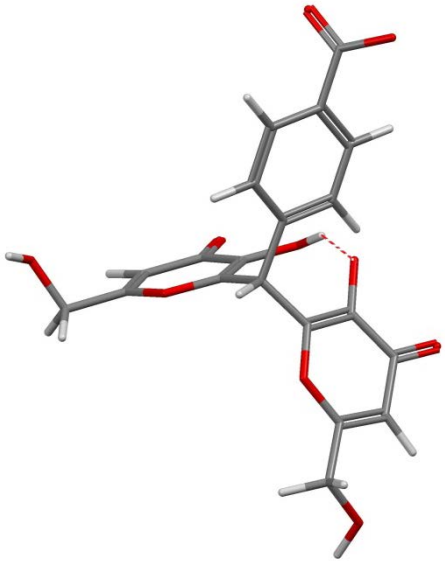

Figure 3.19. Hydrogen bond OH---$^{-}$O between the two units of KA after the second deprotonation of L13 ligand.

The hydrogen bond between the two KA moities breaks when the third deprotonation occurs. This last step involves the deprotonation of the second OH group. Two hydrogen bond are possible, between –COO^{-} and CH_2OH in one KA unit, and –O^{-} in the same unit with CH_2OH in the second unit. These imply a large torsion of the E protons , and the large $\Delta\delta$ of F, G and L protons (Figure 3.20). The similarity between the

thermodynamic parameters refferring to the second and the third proton dissociation from L13 and L12 justify the hypothesis that the behaviour of the two ligands, concerning the H-bonds formation, is also similar (Table 3.2).

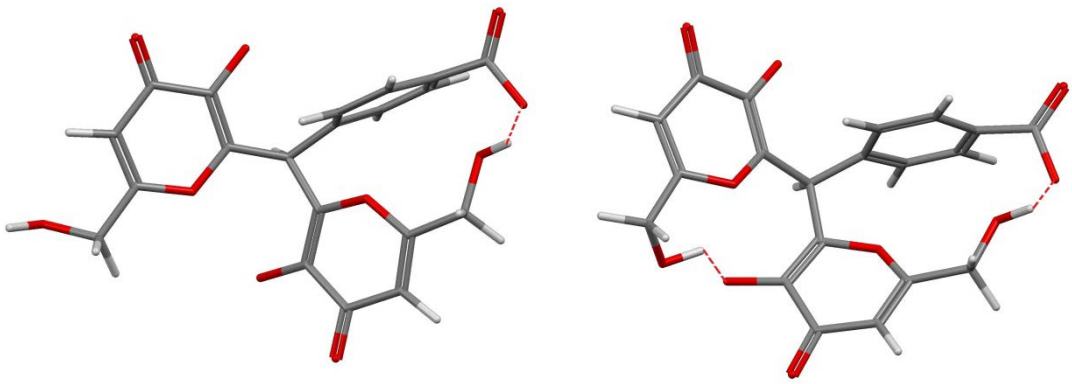

Figure 3.20. Hydrogen bond formation after the third deprotonation of L13 ligand.

3.2.4. L14 Ligand

The protonation equilibria of L14 were studied both by a potentiometric/UV-Vis spectrophotometric titration and by ^{1}H-NMR titration. L14 is characterized by two KA units joined by a linker bearing a benzene ring with a phenolic group in ortho position. Three protonation constants were estimated when a L14 solution 7.96×10^{-4} M was potentiometrically titrated with NaOH, at 0.1 M NaCl ionic strength and 25ºC (Table 3.2 and Figure 3.21).

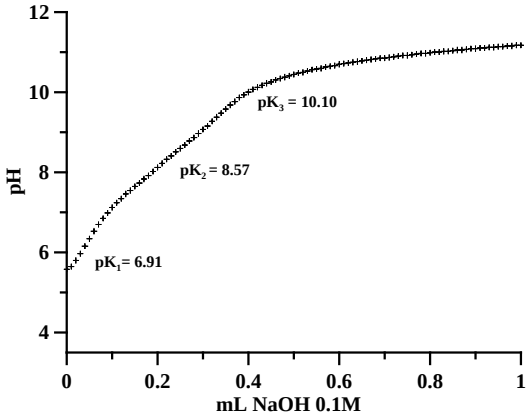

Figure 3.21. Potentiometric titration of L14 with NaOH 0.1M, NaCl 0.1M, 25ºC.

The absorptivity spectra collected during the simultaneous potentiometric-spectrophotometric titration (in 0.2 cm path length, at $3.65 \cdot 10^{-4}$ M ligand concentration) are presented in Figure 3.22. They show that the bands of the fully protonated species LH_3 are similar to those of the protonated LH species of KA, differing only in the

wavelength of the maximum, now shifted from 270 nm to 280 nm (ε = 18309 $M^{-1}\cdot cm^{-1}$). The intensity of this band decreases during the first deprotonation (red spectra), with the contemporary appearance of a new band at 326 nm (ε = 9129 $M^{-1}\cdot cm^{-1}$) with sharp isosbestic points at 242 nm and 302 nm. This permit to attribute the first deprotonation with pK_1 = 6.91to the OH group in one of the two KA moieties.

During the second deprotonation (blue curves) a further decrease on the band at 280 nm and an increase of that at 326 nm take place with pK_2 = 8.57, attributable to the second unit of kojic acid in the ligand.

Finally, when the deprotonation of the phenolic group takes place, (pK_3 = 10.10), the band at 326 is shifted to higher wavelengths where reach the maximum for the fully deprotonated species at 330 nm (ε = 14397 $M^{-1}\cdot cm^{-1}$).

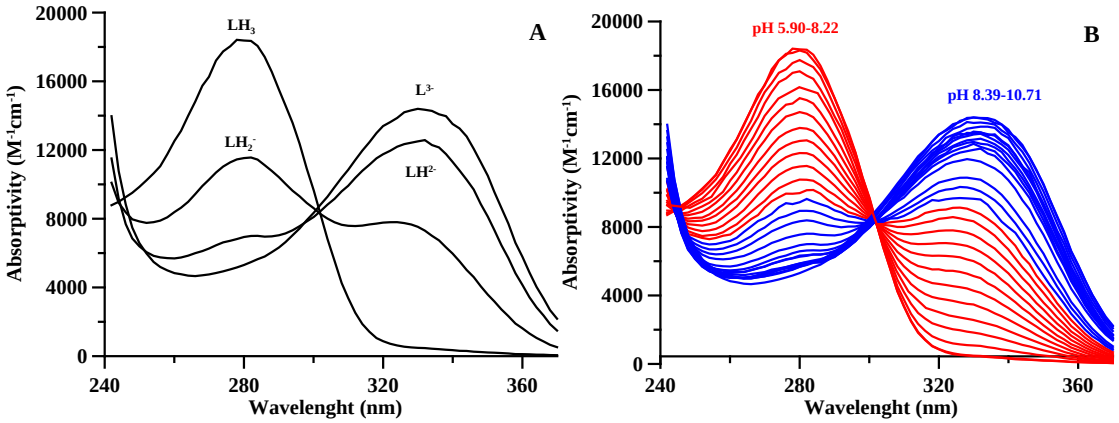

Figure 3.22. Absorptivity spectrum (A) collected during the spectrophotometric titration of L14 ($C_L = 3.65\cdot10^{-4}$ M, 0.2 cm optical path length), and selected absorptivity spectra (B) in the pH range 5.90-10.71.

The trends of the peak heights after decomposition of the spectra in the Gaussian components overlap the speciation plots in Figure 3.23.

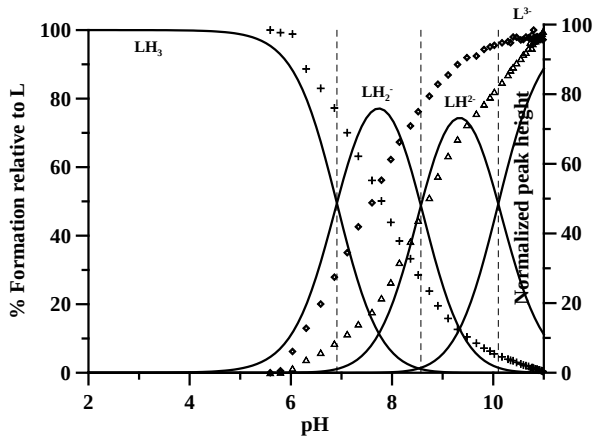

Figure 3.23. Speciation curves of ligand L14, with the overlapping trends of the heights of UV bands at 280 nm (+), 326 nm (◊) and 330 nm (Δ), obtained by spectral decomposition of the spectra in Figure 2.22 with the Specpeak program.

The variation of intrinsic chemical shifts (Table 3.5 and Figure 3.24) in the various deprotonation steps allow to better define the deprotonation sequence attributed by UV-Vis spectra, and to give evidence of some related structural rearrangements.

$$LH_3 \leftrightharpoons LH_2^- \leftrightharpoons LH^{2-} \leftrightharpoons L^{3-}$$

Table 3.5. Intrinsic chemical shifts of the different protons in L14 ligand in the different protonated species, calculated with HypNMR, and variations of the intrinsic chemical shifts connected to each deprotonation step.

Species	E	F	G	I	L	M	N
L^{3-}	6,32	6,34	4,29	6,99	6,53	7,05	6,64
LH^{2-}	6,20	6,37	4,38	7,32	6,88	7,17	6,87
LH_2^-	6,09	6,45	4,35	7,15	6,86	7,20	6,85
LH_3	6,30	6,50	4,33	7,12	6,89	7,23	6,91
Δδ	**E**	**F**	**G**	**I**	**L**	**M**	**N**
$LH^{2-} \rightarrow L^{3-}$	-0,11	0,03	0,09	0,34	0,34	0,12	0,23
$LH_2^- \rightarrow LH^{2-}$	-0,11	0,07	-0,04	-0,17	-0,02	0,02	-0,02
$LH_3 \rightarrow LH_2^-$	0,21	0,05	-0,02	-0,04	0,04	0,03	0,06

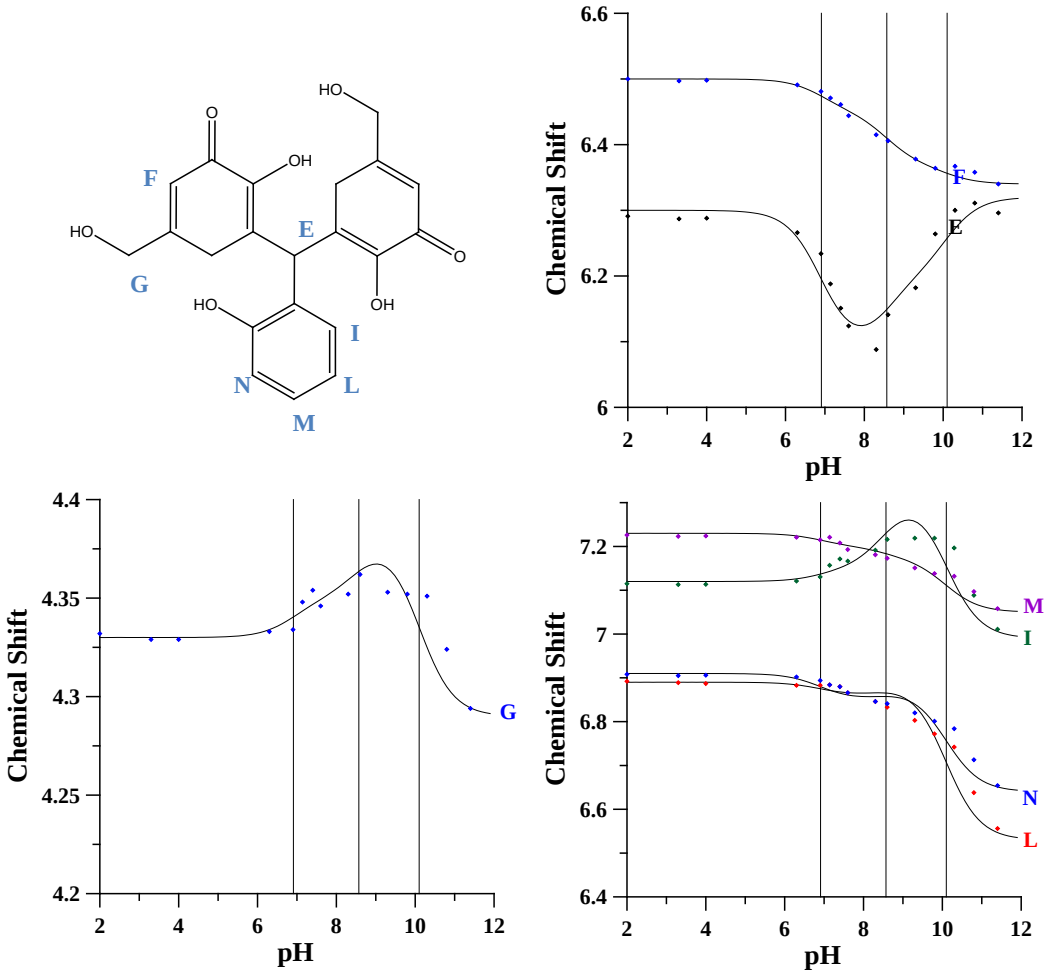

Figure 3.24. Chemical shifts of L14 ligand as a function of pH.

The first and the second deprotonation, as inferred from the UV-Vis spectra, take place from the OH groups of the KA units, also in agreement with the thermodynamics parameters of Table 3.2. The first deprotonated $–O^-$ can form hydrogen bonds either with the OH group of the phenol in the linker (Figure 3.25A), or with the OH group in the second KA unit (Figure 3.25B). The Δδ of N proton supports, the first hypothesis, also confirmed by the relevant Δδ of E proton, which in this case undergoes a strong rotation. Calorimetric data support the formation of a H-bond although they cannot give any hints on which one of the two hypotheses is the most likely.

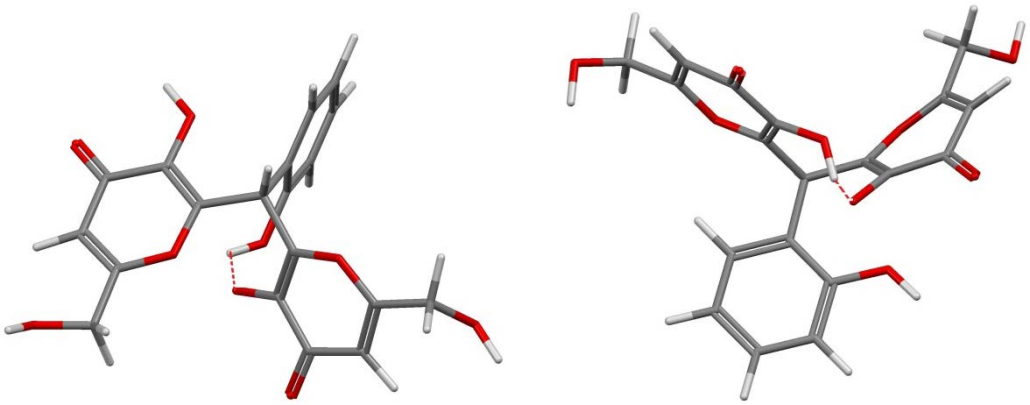

Figure 3.25.Two hypothesis of hydrogen bond formation after the first deprotonation of L14 ligand.

After the second deprotonation an opposite chemical shift takes place on E proton, presumably due to the formation of a hydrogen bond OH---$^-$O with the till protonated phenolic OH (or with the CH_2OH on the second KA unit), (Figure 3.26).

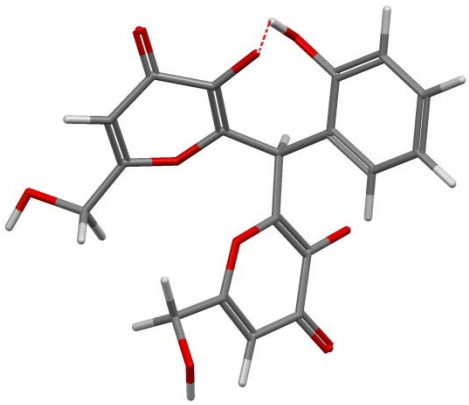

Figure 3.26. Second deprotonation of L14 ligand.

The third deprotonation affects the intrinsic chemical shifts of all the protons in the phenolic unit, and of the E proton. In theory the formation of hydrogen bond is possible between the phenolate group and one CH_2OH group of the kojic moiety (Figure 3.27);

however, the thermodynamic parameters do not support this suggestion. In fact, the formation of a H-bond which favors the –OH deprotonation would be reflected in lower pKa and -ΔH° values of L14 with respect to free phenol (pKa = 9.86, -ΔH° = 21.3 kJ mol^{-1}).[207]

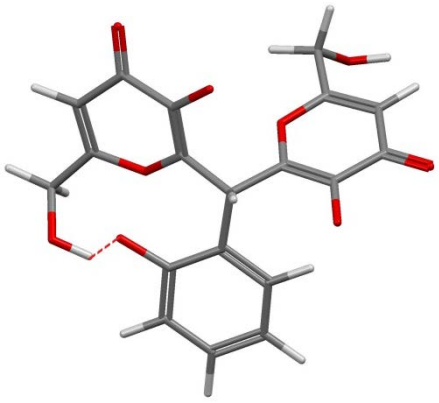

Figure 3.27. Hydrogen bond between $-O^-$ from the phenolic group and CH_2OH on one of the KA units after the third deprotonation of L14 ligand.

3.2.5. L15 Ligand

The protonation equilibria of L15 were studied by potentiometric titration, simultaneous potentiometric- spectrophotometric titration and ^{1}H-NMR spectra collected at different pH values and calorimetric titration. L15 differs from L14 for the phenolic group in para position.

Also in this case three protonation constants were calculated from potentiometric data obtained when a L15 solution $7.96 \cdot 10^{-4}$ M was titrated with NaOH, at 0.1 M NaCl ionic strength and 25 ºC (Table 3.2 and Figure 3.28).

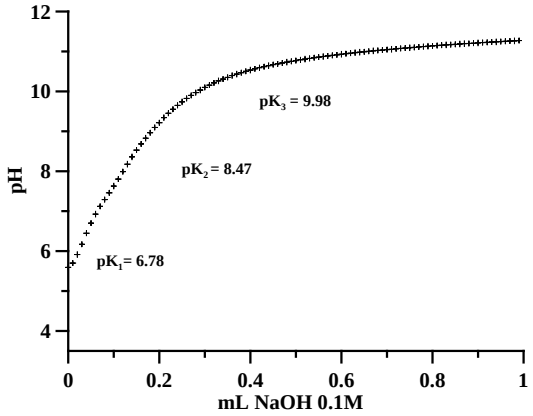

Figure 3.28. Potentiometric titration of L15 with NaOH 0.1 M, NaCl 0.1 M, 25ºC.

The absorptivity spectra calculated from the spectra collected during a titration (0.2 cm path length) of a $4.79 \cdot 10^{-4}$ M ligand solution are presented in Figure 3.29. The band of

the fully protonated species at 280 nm (ε = 19965 $M^{-1}\cdot cm^{-1}$) decreases during the first deprotonation (red spectra), with the contemporary appearance of a new band at 334 nm (ε = 4154 $M^{-1}\cdot cm^{-1}$), with sharp isosbestic points at 242 nm and 302 nm. This permit to attribute the first deprotonation with pK_1 = 6.78 to the OH group in one of the two KA moieties.

During the second deprotonation (blue curves) a further decrease on the band at 280 nm and an increase of that at 334 nm take place. This deprotonation with pK_2 = 8.47 is attributed to the second unit of KA unit.

The deprotonation of the phenolic group (pK_3 = 9.98) shifts the band at 334 to higher wavelengths, and the maximum for the fully deprotonated specie occurs at 340 nm (ε = 15762 $M^{-1}\cdot cm^{-1}$).

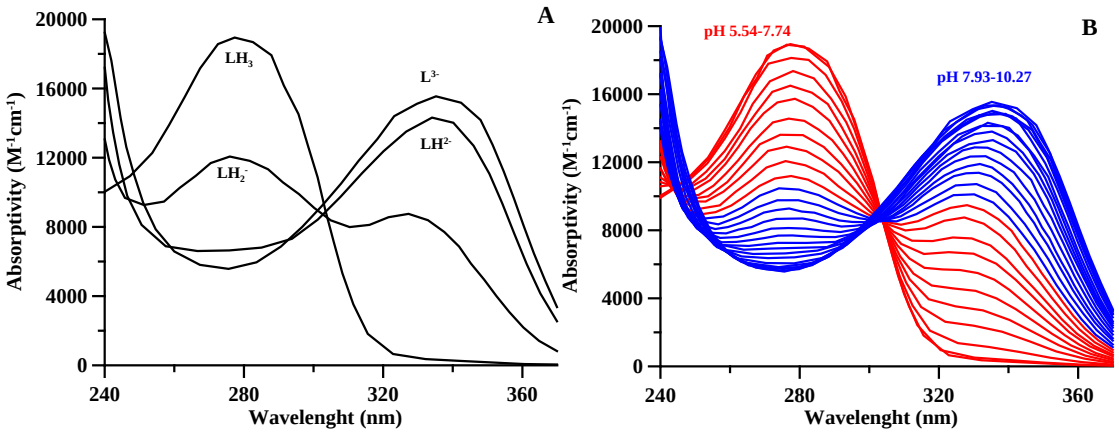

Figure 3.29. Absorptivity spectra (A) collected during the spectrophotometric titration of L15 ligand solution $C_L = 4.79\cdot10^{-4}$ M, 0.2 cm optical path length, and selected absorptivity spectra (B) in the pH range 5.54-10.27.

The trends of the peak heights, after decomposition of the spectra in the Gaussian components[206], follow the speciation plots in Figure 3.30.

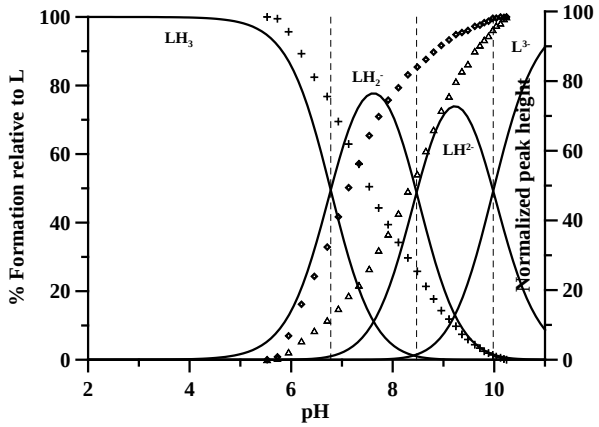

Figure 3.30. Speciation plots of ligand L15, with the overlapping trends of the heights of UV bands at 280 nm (+), 326 nm (◊) and 334 nm (Δ), obtained by spectral decomposition of the spectra in Figure 2.29 with the Specpeak program.

Table 3.6. Intrinsic chemical shifts of the different protons in L15 ligand in the different protonated species, calculated with HypNMR, and variations of the intrinsic chemical shifts connected to each deprotonation step.

Species	E	F	G	I	L
L^{3-}	6,26	6,32	4,31	6,91	6,50
LH^{2-}	6,17	6,37	4,33	7,11	6,78
LH_2^-	5,94	6,44	4,37	7,19	6,80
LH_3	6,07	6,48	4,35	7,21	6,82
Δδ	**E**	**F**	**G**	**I**	**L**
$LH^{2-} \rightarrow L^{3-}$	-0,09	0,04	0,03	0,20	0,28
$LH_2^- \rightarrow LH^{2-}$	-0,23	0,07	0,03	0,08	0,01
$LH_3 \rightarrow LH_2^-$	0,12	0,04	-0,01	0,03	0,02

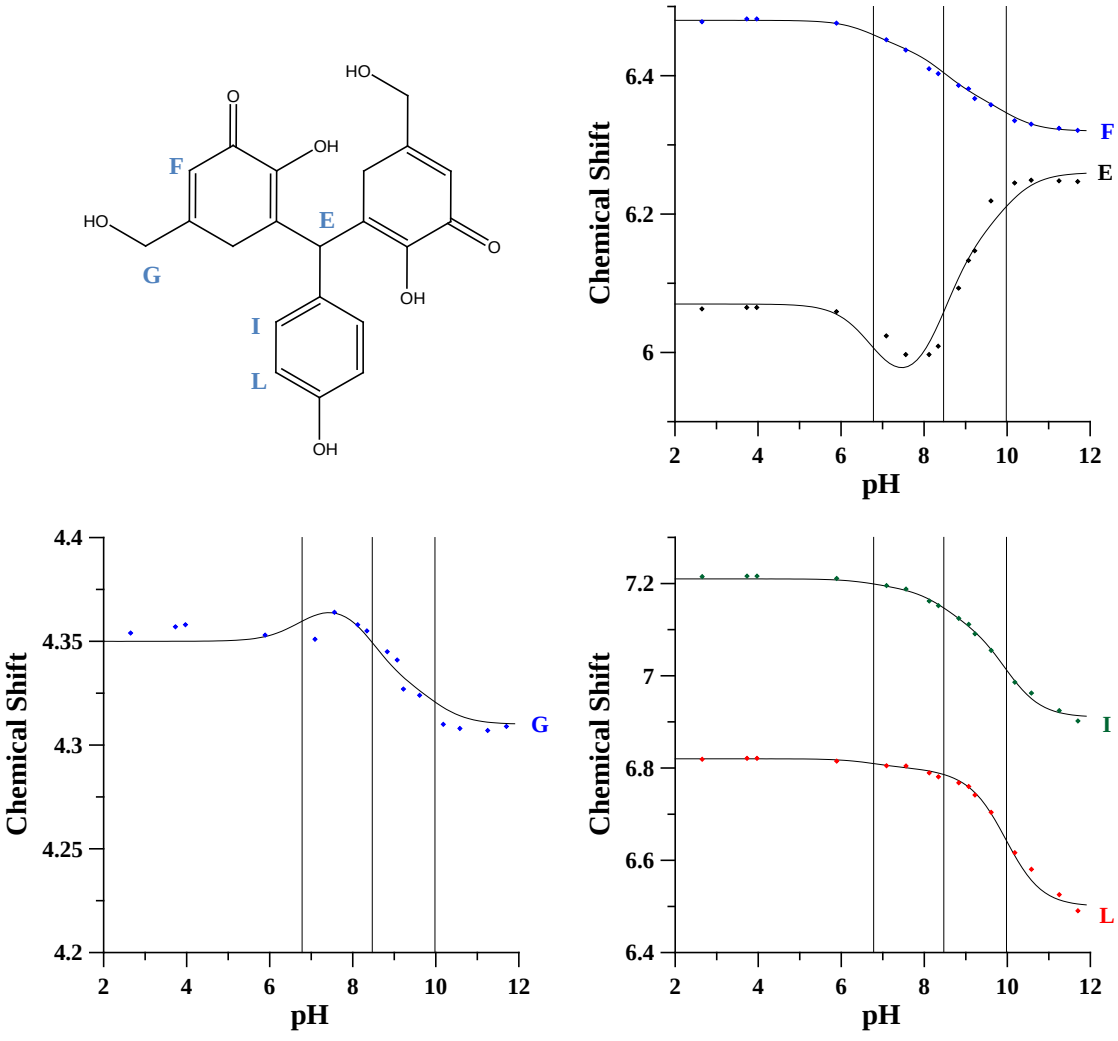

Figure 3.31. Chemical shifts of L15 ligand as a function of pH.

As far as regards NMR data, the first and the second deprotonations, as in the case of L14, take place from the OH groups of the KA units. The first deprotonated $-O^-$ can

form hydrogen bonds only with the OH group in the second KA unit (Table 3.6, Figures 3.31 and 3.32).

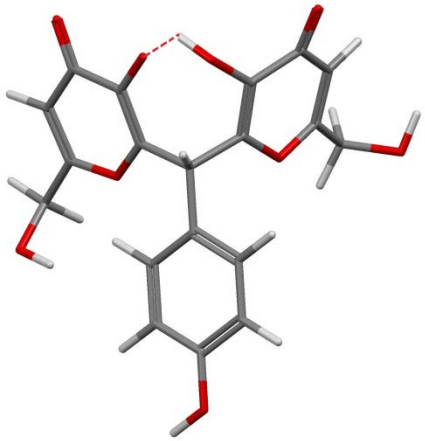

Figure 3.32. Hydrogen bond -OH---$^{-}$O between the two KA units of L15.

After the second deprotonation an opposite chemical shift takes place on E proton, due to the formation of a hydrogen bond OH---$^{-}$O with the CH_2OH on the second KA unit (Figures 3.31 and 3.33).

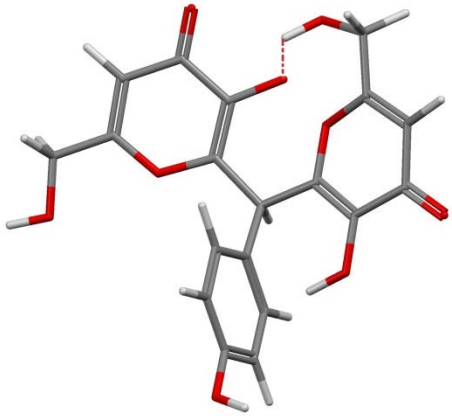

Figure 3.33. Hydrogen bond OH---$^{-}$O with the CH_2OH on the second KA unit after the second deprotonation of L15 ligand.

The third deprotonation affects the intrinsic chemical shifts of all the protons in the phenolic unit, and of the E proton. The only hydrogen bond possible is that of O^{-} group in the KA unit with one CH_2OH group (Figures 3.31 and 3.34). Calorimetric data support the above hypotheses on the protonation path of L14.

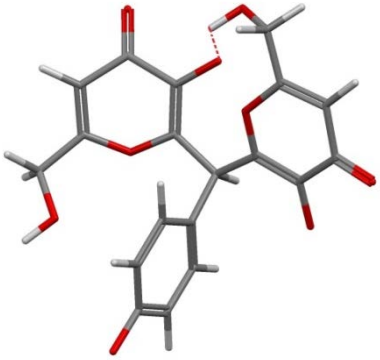

Figure 3.34. Hydrogen bond OH---$^{-}$O with the CH_2OH on the second KA unit after the third deprotonation of L15 ligand.

Different remarks can be done:

The carboxylic group deprotonation in L12 and L13 take place, as expected, at lower pH values than that of the phenolate group in each KA moiety, while those of the OH group in the aromatic ring in L14 and L15 take place with well distinct higher pK's values (about 1.5 units) than that of the more basic OH groups in KA units (Table 3.7).

Table 3.7. Ionization constants for L12-L15 ligands.

pK	L12	L13	L14	L15
pK_1	3,49 (3)	4,14 (2)	6,91 (3)	6,78 (2)
pK_2	7,44 (2)	7,04 (3)	8,57 (1)	8,47 (2)
pK_3	9,57 (1)	9,24 (1)	10,1 (1)	9,98 (1)

The negative charge assigned to the L12 molecule by the deprotonation of carboxylic group increases the basicity of phenolates leading to an increase on the first log K with respect to L14 of about 1 unit, and of about 0.5 units on the second. The analogous variation for the ligands L13 and L15 with the acidic group in *para* position in the aromatic ring are about 0.5 and 0.2 log K units. This difference can be explained by a further contribute, besides that of negative charge, related to the formation of a hydrogen bond between the *orto* COO^- and OH group that delays the loss of the involved proton. This is also substantiated by the lower log K value for the ortho carboxylic group whose deprotonation is favored by the hydrogen bond stabilization. An analogous trend was observed for the log K's of L2 and L3[35], even if the OCH_3 always in *orto* with respect to OH group made it more basic for its marked inductive effect.

More complex is the formation of hydrogen bonding in the case of an OH group in the aromatic ring. In fact, after the first deprotonation that now happens on OH group of KA unit, the hydrogen bond formation can occur either on the protonated OH in the aromatic ring (Figure 3.25A), and on the OH group in the second KA unit (Figure 3.25B). Presumably, they take place contemporary in different extent.

3.2.6. KβAK Ligand[1]

The KβAK ligand (Scheme 7) has three potential protonation sites and indeed was determined three protonation constants from combined potentiometric-UV titration data calculated by HypSpec software[180] (Table 3.8). In Figure 3.35, the four absorptivity spectra are reported, each representing a differently protonated form. The $[LH_3]^+$ band has the highest intensity at 268 nm (ε=10998 $M^{-1}cm^{-1}$). The first deprotonation at pH 2.9 can be attributed to nitrogen atom and does not significantly change the spectrum. The $[LH_2]$ band displays maximum intensity at 268 nm and does not differ in shape from the band of the fully protonated ligand. The two kojic acid units are separated by the hydrophobic linker and ligand is not symmetric; each kojic unit deprotonates at different pH levels: 7.15 and 8.44. The $[LH]^-$ and $[L]^{2-}$ bands are different: $[LH]^-$ band presents two maxima at 250 nm (ε=6400 $M^{-1}cm^{-1}$) and 317 nm (ε=5403 $M^{-1}cm^{-1}$); the $[L]^{-2}$ band has a maximum absorptivity at 317 nm (ε=8218 $M^{-1}cm^{-1}$). The charge of the molecule depends on the pH of the solution (Figure 2.36); negatively charged forms are in equilibrium at neutral pH.

Table 3.8. Protonation constants of the new ligand KβAK calculated with HyperQuad2013 program at 25°C and 0.1 M KCI ionic strength using the ligand concentration $5 \cdot 10^{-4}$ M. [a] Standard deviation values were calculated by the HyperQuad2013 program.

Specie	Log β	Log K
LH^-	8,44(4)[a]	8,44(4)
LH_2	15,59(4)[a]	7,15(4)
LH_3^+	18,5(1)[a]	2,9(1)

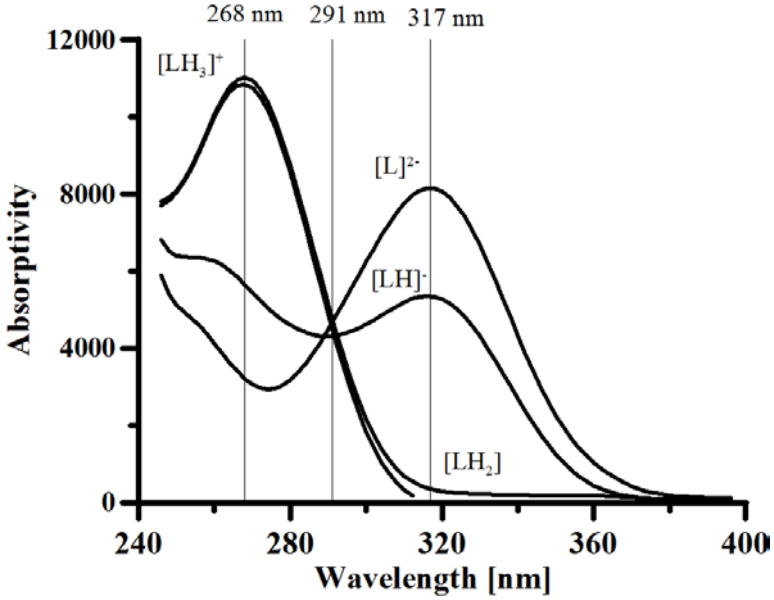

Figure 3.35. Absorptivity spectrum of the KβAK ligand using the HypSpec program, 0.2 cm path length and ligand concentration $5 \cdot 10^{-4}$ M.

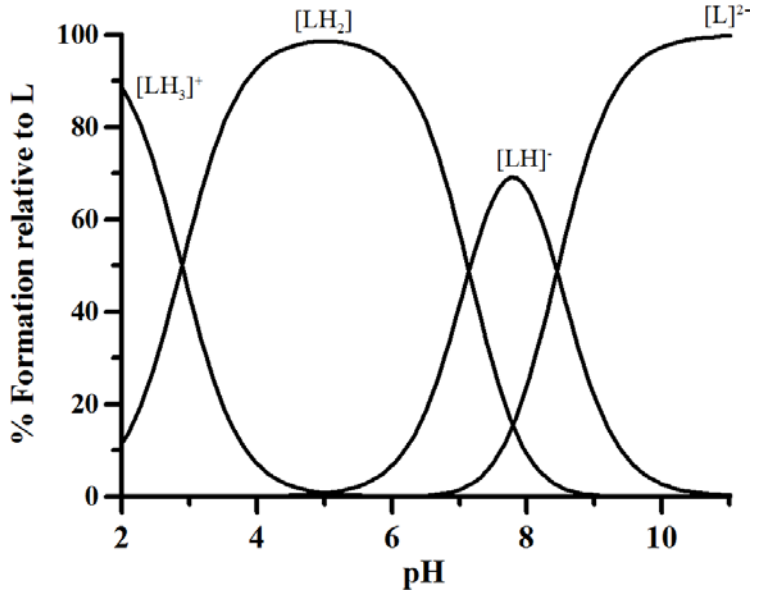

Figure 3.36. Speciation plots of the ligand calculated with the log β values shown in Table 3.8, using $5 \cdot 10^{-4}$ M ligand concentration.

The first and second protonations attributed to the kojic acid units differ significantly from the kojic acid protonation constant (7.70[33]). This is due to the formation of the intramolecular hydrogen bonds previously reported by our group for kojic acid derivatives[33],[35],[163],[37].

3.2.7. SC Ligand

Simultaneous potentiometric-spectrophotometric titrations[35] and ^{1}H-NMR spectra collected at different pH values gave evidence of six different protonation equilibria for SC ligand (Scheme 3).

The absorption spectra collected during the potentiometric-spectrophotometric titration (0.2 cm path length) on $2.47 \cdot 10^{-4}$ M ligand solution are presented in Figure 3.37A. From the UV spectra, an easy attribution of the protonation steps that involves the OH group of KA moieties can be done on the basis of the characteristic spectra of the KA[33] as outlined above for the tetradentate KA derivatives L12-L15. The absorption band of the fully protonated species LH_6^{3+} at 271 nm decreases during the first deprotonation, with the contemporary appearance of a new band at 315 nm, with sharp isosbestic points at 242 nm and 290 nm. This permit to attribute the first deprotonation with $pK_1 = 6.72$ to the OH group in one of the three KA moieties (Table 3.9). The second deprotonation takes place with $pK_2 = 7.7$, attributable to a second KA unit. When the third deprotonation occurs with $pK_3 = 8.11$, the trend of the heights of the peaks in Figure 3.37B, show that the characteristic band of the fully deprotonated kojic acid has not entirely reached its maximum at 320 nm. This suggests the presence of a micro-equilibrium between the loss of the proton from the last KA unit and the loss from a NH proton.

During the fourth deprotonation, the band at 320 nm reaches its maximum. The last two deprotonations (protons from NH groups) do not significantly change the spectra.

Table 3.9. Protonation constants of the new ligand SC calculated with HyperQuad2013 program at 25°C and 0.1 M KCI ionic strength using the ligand concentration $2.47 \cdot 10^{-4}$ M.

Species	LH^{2-}	LH_2^-	LH_3	LH_4^+	LH_5^{2+}	LH_6^{3+}
Log K	10.97	9.62	9.00	7.95	7.84	7.02

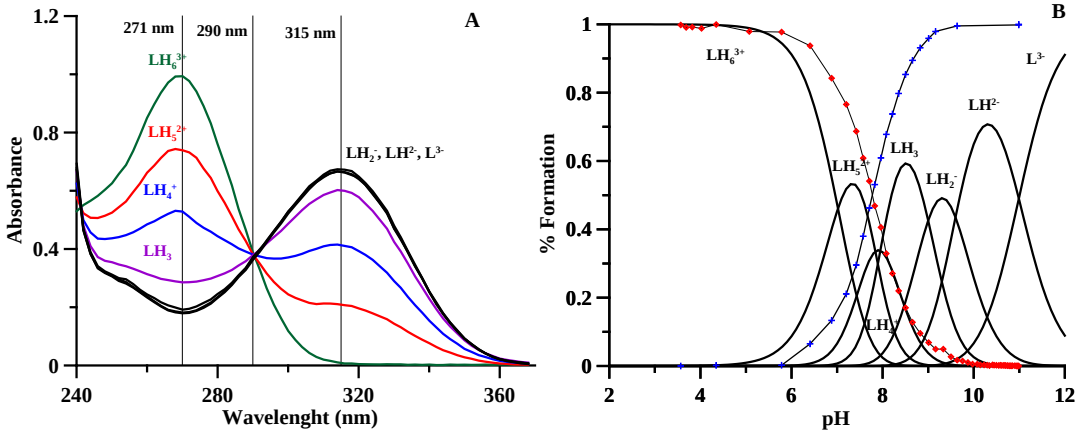

Figure 3.37. A) Absorbance spectrum of the new SC ligand using the HypSpec program, 0.2 cm path length and $2.47 \cdot 10^{-4}$ M ligand concentration; B) Speciation plots of SC ligand, with the overlapping trends of the heights of UV bands at 271 nm (■), 320 nm (+), obtained by spectral decomposition of the spectra with the Specpeak program.

The variation of intrinsic chemical shifts (Table 3.10) in the deprotonation steps allow to better define the deprotonation sequence attributed by UV-Vis spectra. The most affected nuclei for the first three deprotonations are Ha and Hb. In particular the variation of intrinsic chemical shift of Ha after the third deprotonation involves the equilibria between the loss of the proton from the OH group in the KA moiety and that from a NH group in the linker. Chemical shifts follow the trend of chemical shift simulated with potentiometric data (Figure 3.38).

Table 3.10. Intrinsic chemical shifts of the different protons in L15 ligand in the different protonated species, calculated with HypNMR program, and variations of the intrinsic chemical shifts connected to each deprotonation step.

Species	Ha	Hb	Hc	Hd	He
L^{3-}	7,64	6,34	4,36	2,61	2,45
LH^{2-}	7,65	6,35	4,36	2,72	2,52
LH_2^-	7,63	6,35	4,39	2,93	2,70
LH_3	7,71	6,37	4,33	2,94	2,67
LH_4^+	7,78	6,42	4,49	3,13	2,88
LH_5^{2+}	7,95	6,48	4,36	2,99	2,73
LH_6^{3+}	8,01	6,51	4,43	3,08	2,81

Δδ	Ha	Hb	Hc	Hd	He
$LH^{2-} \rightarrow L^{3-}$	0,01	0,01	0,00	0,10	0,07
$LH_2^{-} \rightarrow LH^{2-}$	-0,01	0,00	0,03	0,21	0,18
$LH_3 \rightarrow LH_2^{-}$	0,07	0,02	-0,06	0,01	-0,03
$LH_4^{+} \rightarrow LH_3$	0,07	0,04	0,16	0,19	0,21
$LH_5^{2+} \rightarrow LH_4^{+}$	0,17	0,06	-0,13	-0,14	-0,15
$LH_6^{3+} \rightarrow LH_5^{2+}$	0,07	0,03	0,07	0,09	0,08

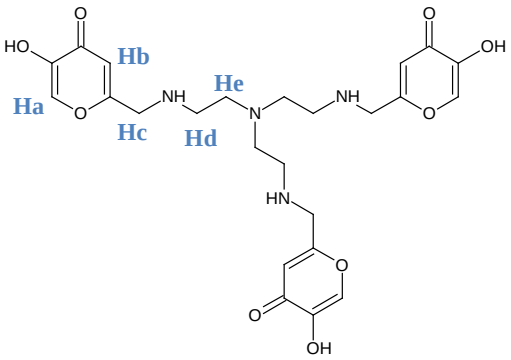

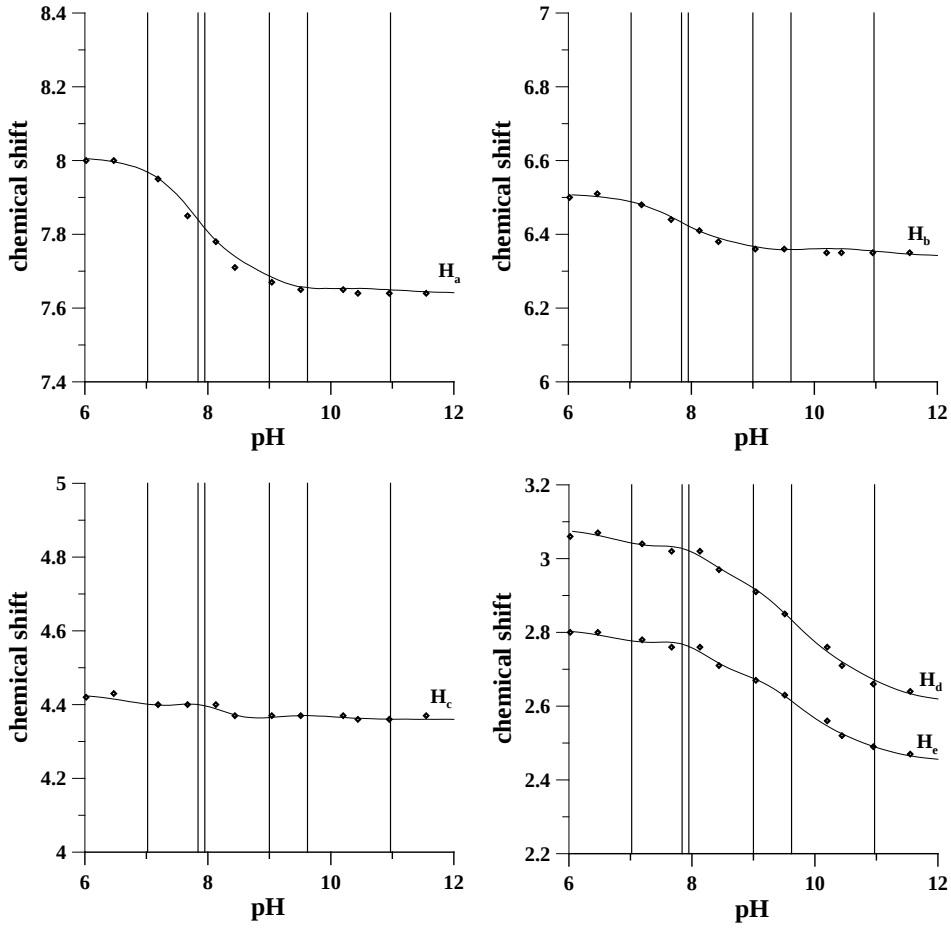

Figure 3.38. Chemical shifts of SC ligand as a function of pH.

3.2.8. Losartan and Irbesartan ligands

The study of the acid–base behavior is of great relevance in pharmacology. This is particularly true in the case of antihypertensive drugs, in which the examination of acid-base properties helps in the understanding of physiological mechanisms in which their receptor antagonists is implied.[208] Regularly assumed cardiovascular drugs are more and more formulated into controlled-release forms, where the knowledge of dissociation constants is of great importance.[209] Moreover Losartan and Irbesartan solubility is related to the protonation state of the molecules. The water solubility is drasticaly lowered in acidic pH. The highest water solubility of Losartan determined spectrophotometrically at 280 nm at pH 3 was $5.72 \cdot 10^{-5}$ M, while that of Irbesartan $4.64 \cdot 10^{-4}$ M. Irbesartan is more water soluble than Losartan at the acidic pH of stomach and this could be the reason why the overall bioavailability of Irbesartan (60-80%[210]) is higher than that of Losartan (33%[211]).

Losartan and Irbesartan contain both acidic and basic centers, the first on the tetrazole ring, the second on the imidazole in Losartan, and on the 5-oxo-imidazole in Irbesartan. A number of protonation constants are reported in literature, without any mention neither to the experimental conditions in which they were determined, nor to the used techniques (Losartan 2.36 and 5.55[212], 4.9[213], 5.6[214] and Irbesartan 4.5[215]).

Reliable data are presented by Tosco et al.,[216] who evaluated potentiometrically in co-solvent mixtures of variable composition the pK_a values of both groups. These values plotted against the mixture composition allow to extrapolate the values in water and to compare them with those of some tetrazole ligands reported in literature (tetrazole 4.89,[217] methyltetrazole 5.50,[218] and 5-phenyl-1H tetrazole 4.38[219]). Their results demonstrate that the acidity of the tetrazole moiety increases with aromatic 5-substitution, reflecting a larger delocalization of the negative charge on the aromatic moiety, together with the influence of the electron withdrawing substituent. Consequently, the first dissociation can be attributed to the imidazole ring and the second to the tetrazole ring.[216]

Potentiometry and spectrophotometry are the most adequate and versatile techniques for the study of equilibrium constants in homogeneous phase.[220],[221] The low drug solubility in water at acidic pH prevented potentiometric studies in aqueous solution. The ligand protonation studies were thus performed in 30:70 and 80:20 MeOH/H_2O mixtures, being methanol effects on pKa values extensively studied.[222]

Irbesartan and Losartan are biprotic ligands and deprotonate in the same manner. In the 30:70 MeOH/H_2O mixtures (Table 3.11) Irbesartan loose imidazole proton with pK_{a1} 3.59, while Losartan with pK_{a1} 2.95. After the first deprotonation, ligands exist in the zwitterionic form because of the negative charge on the tetrazole nitrogen. The tetrazole ring of Irbesartan deprotonates with pK_{a2} 5.03, while that of Losartan with pK_{a2} 4.5. According to the plot of p_sK_a vs. weight-% of MeOH[216], the higher %MeOH the lower pK_{a1} and the higher pK_{a2}. Indeed, in 80:20 MeOH/H_2O (Table 3.11), pK_{a1} of Losartan is

2.56, while pKa_2 5.07. In the case of Irbesartan, pK_{a1} became lower (3.25), while pK_{a2} remains almost unchanged (4.98). At physiological pH ligands exist in anionic form.

Irbesartan and Losartan contain a complicated molecular structure and two protonation equilibria can be monitored spectrophotometrically with close dissociation constants. Both molecules exhibit quite similar absorption bands, and the spectral range from 240 to 310 nm, with an isosbestic point at ~280 nm, was selected as the most convenient for an estimation of protonation constants.

Table 3.11. Dissociation constants determined potentiometrically at 25^0C and 0.1 M NaCl ionic strength.

	Irbesartan		Losartan	
	30:70 MeOH/H_2O	80:20 MeOH/H_2O	30:70 MeOH/H_2O	80:20 MeOH/H_2O
pK_{a1}	3.6(1)	3.25(1)	3.06(7)	2.56(1)
pK_{a2}	5.0(1)	4.98(1)	4.38(4)	5.07(1)

The pK_a values calculated with HypSpec[182] program slightly differ, and are much less reliable than those potentiometrically determined in Table 3.11. Their low reliability depends on the slight variation with pH presented by the absorptivity spectra of Irbesartan and Losartan shown in Figure 3.39.

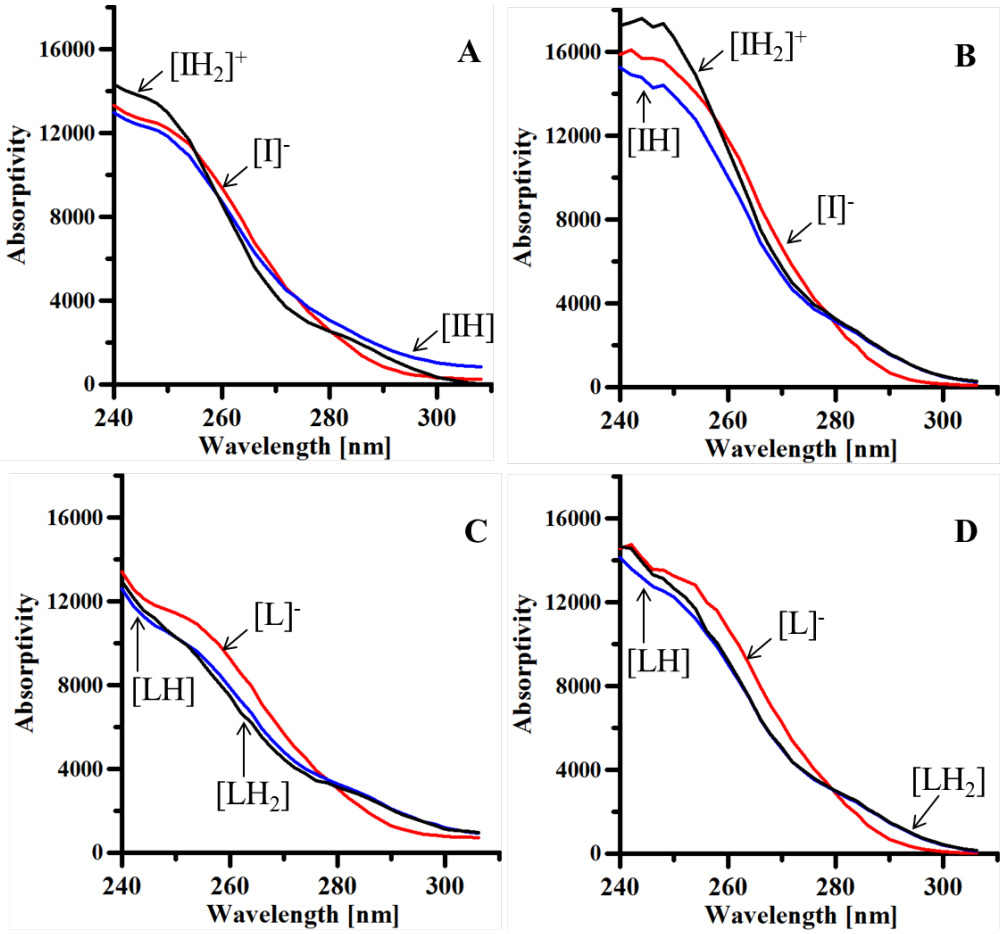

Figure 3.39. Absorptivity spectrum of the irbesartan (A 30% and B 80% methanol/water solution) and losartan (C 30% and D 80% methanol/water solution) using the HypSpec program, 0.2 cm path length and ligand concentration 0.5mM.

The presence of different fluorescent groups (fluorophores) as biphenyl[223] and imidazole[224] allowed the study of the emission properties of both Irbesartan and Losartan from pH 1 to pH 7. In the pH range 1-2 the maximum of fluorescence peak shifts towards higher energy both in 30:70 (Figure 3.40A and 3.41A) and 80:20 MeOH/H_2O (Figure 3.40D and 3.41C) solutions. In the pH range 2-7, upon excitation at 280 nm in 30:70 MeOH/H_2O solution both drugs show an emission band centered at 376 nm (Figure 3.40B and Figure 3.41B), that in 80:20 MeOH/H_2O is shifted to 370 nm (Figure 3.40E and Figure 3.41D) due to the polarity decrease of the solvent.

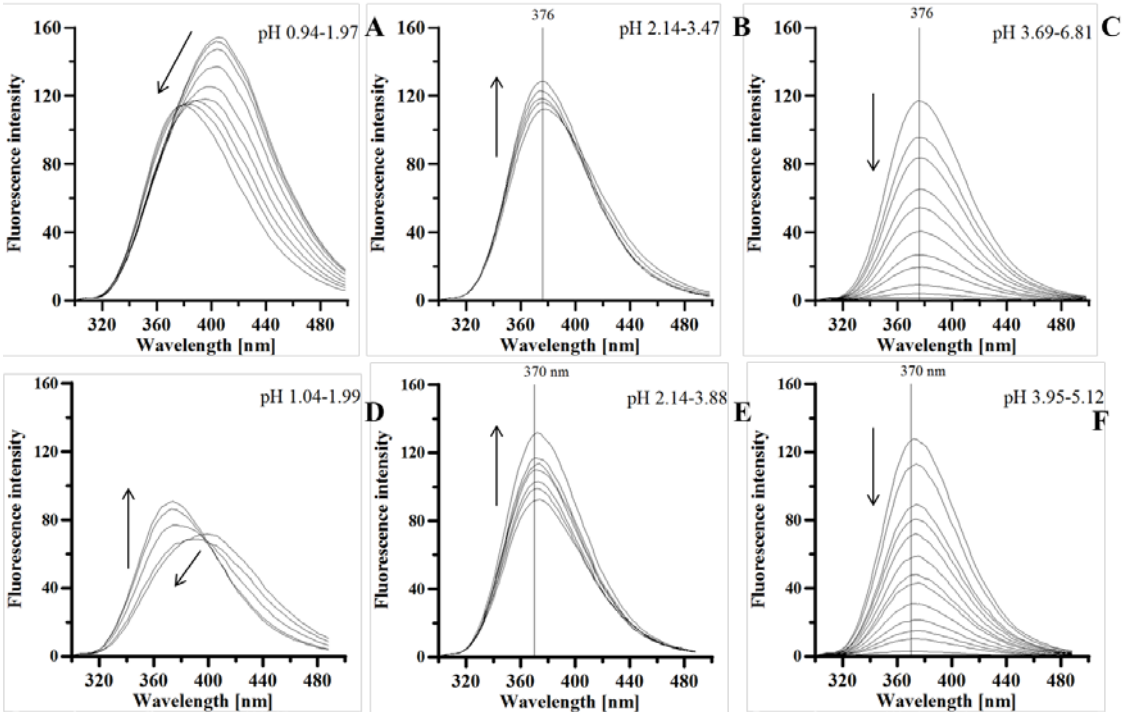

Figure 3.40. Fluorescence spectra of Irbesartan in 30% methanol/water (A-C) and 80%methanol/water (D-F) solution in pH dependent titration.

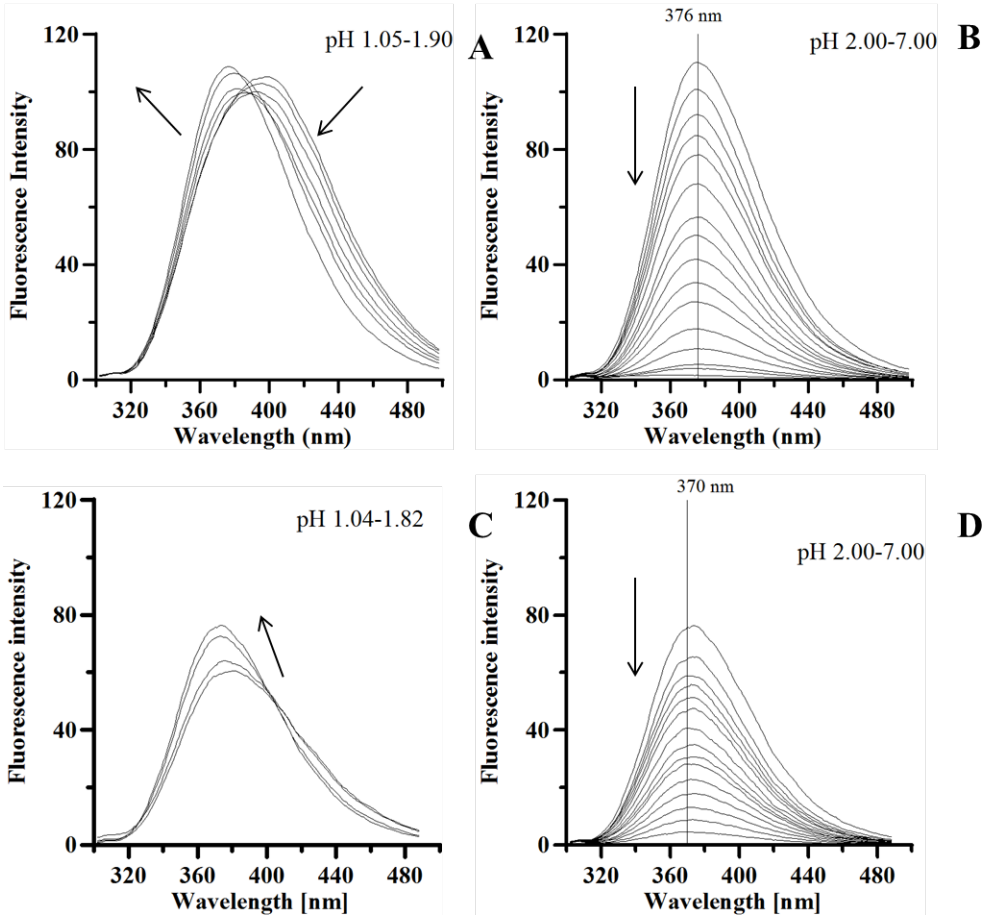

Figure 3.41. Fluorescence spectra of Losartan in 30% methanol/water (A,B) and 80%methanol/water (C,D) solution in pH dependent titration.

The plot of the fluorescence intensity at fixed wavelength (from pH 2 to pH 7) superimposed to the speciation plot obtained from the potentiometric results (Figure 3.42) shows that the fluorescence emission is always related to the imidazole deprotonation. The deprotonation imidazole has a quenching effect in Losartan and a slight increasing effect in Irbesartan. The anionic form of both drugs is not fluorescent and its presence lowers the fluorescence intensity, mainly in the case of Losartan. The fluorescence intensity of Irbesartan is increasing in the pH range 2-3.6 (Figure 3.42, A ~15% of intensity in 30:70 MeOH/H_2O and Figure 3.42, B ~40% of intensity in 80:20 MeOH/H_2O solutions) and decreases in the pH range 3.8-7, while the fluorescence intensity of Losartan gradually decreases in the pH range 2-7 both in 30:70 MeOH/H_2O (Figure 3.42, C) and 80:20 MeOH/H_2O solutions (Figure 3.42, D).

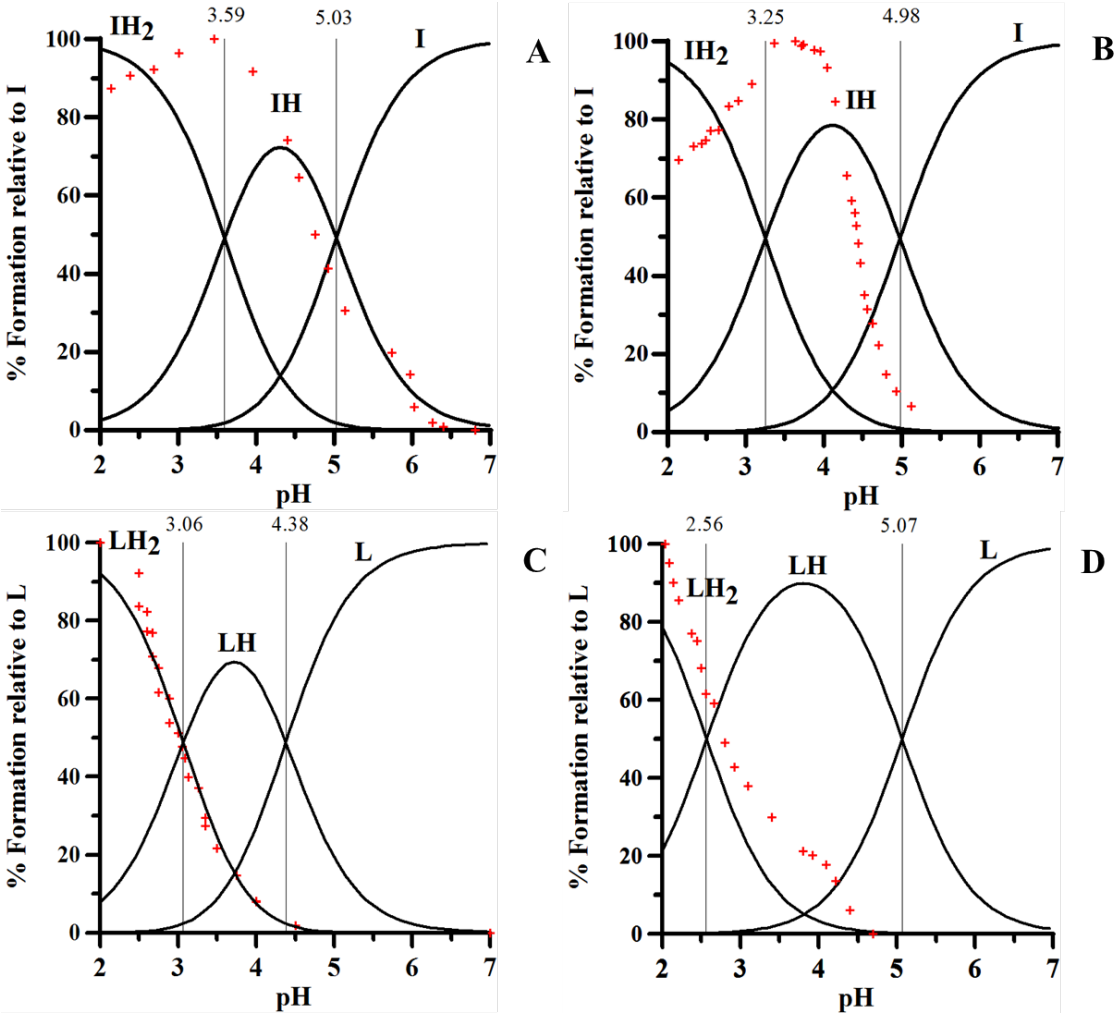

Figure 3.42. The fluorescence intensity at 376 nm (A,C) and 370 nm (B,D), normalized to the scale 0–100% (+), and species concentration as a fraction of the total acid concentration (solid lines) for Irbesartan (A,B) and Losartan (C,D). The charges are omitted for the simplicity.

In the previous studies of Jiménez et al.[208] spectrofluorimetry was wrongly used for the pK_a determination. Their studies made in 5% methanol revealed only one pK_a value for each molecule and attributed pK_a values of Losartan 3.15±0.07 and Irbesartan 4.70±0.06 to the tetrazole group.

3.2.9. Picolinic acid derivatives

Potentiometric titrations of ligands H_4pedpa and H_6dipedpa were carried out using $1 \cdot 10^{-3}$ M ligand solutions at 0.16 M NaCl ionic strength and 25 ºC. In order to calculate the more acidic protonation constants from the phosphonate groups, which may not be calculated on the bases of potentiometric titration[53], ^{1}H-NMR and ^{31}P-NMR titrations were performed.

H_4pedpa ligand, gave evidence of five different deprotonation steps according to the sequence:

$$H_5L^+ \leftrightharpoons H_4L \leftrightharpoons H_3L^- \leftrightharpoons H_2L^{2-} \leftrightharpoons HL^{3-} \leftrightharpoons L^{4-}$$

The more acidic logK_a at 1.7 was calculated on the basis of ^{1}H NMR and ^{31}P H NMR titrations, and the remaining constants were calculated by fitting the potentiometric data using HyperQuad2013 program. These constants are presented in Table 3.12, and the speciation plot calculated with the fitted protonation constants is shown in Figure 3.43.

Table 3.12. Protonation constants for H_4pedpa at 25°C, 0.16 M NaCl ionic strength, obtained using HyperQuad2013 program.[200] Standard deviations on the last figure in brackets.

Species	log β	log K
LH^{3-}	8.43 (2)	8.43
LH_2^{2-}	14.71 (3)	6.28
LH_3^-	18.21 (4)	3.5
LH_4	20.72 (7)	2.51
LH_5^+	22.46	1.7

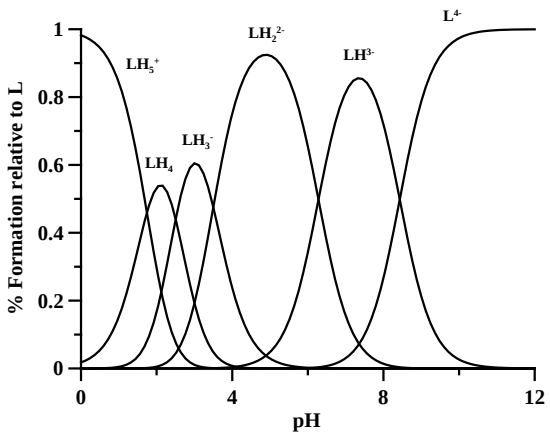

Figure 3.43. Speciation plots of the ligand calculated with the log β values shown in Table 3.12, using $1 \cdot 10^{-3}$ M ligand concentration.

Considering that simple phosphonate moieties, e.g. methylphosphonic acid, possess two protonation sites, with log K_{HL} ~ 7.5 and log K_{H2L} ~ 2.2[225], and that in α-aminophosphonates and β-derivatives log Ks vary in the range 5.0-6.5 and 0.5-1.5 for the first and second protonation, respectively, the protonation constants calculated for H_4pedpa (log K = 1.7 and log K = 6.28), can be attributed to the phosphonate moiety. Thus, the introduction of the amino group leads to the decrease of log K's of phosphonate group, being log K values for the amino function in α- and β-aminophosphonates in the range 9.5-10.5 and 10.0-11.0 respectively.

Moreover, ^{1}H NMR and ^{31}P NMR titrations gave evidence of the deprotonation steps (Table 3.13 and Figure 3.44). The nuclei H_4, H_5 and P are the most affected at pH between 8 and 9, so the potentiometrically calculated log K = 8.43 is attributable to the deprotonation of the amino function. An easy attribution can be made on the basis of the Δδ values for each deprotonation step (Table 3.13 red values). Thereby, the first deprotonation with pK = 1.7, is attributable to the more acidic phosphonate proton and the second and third deprotonations to the carboxylic groups on the pyridine ring with pK = 2.51 and 3.5.

In Figure 3.44 the chemical shifts follow the trend of calculated chemical shifts.

Table 3.13. Intrinsic chemical shifts of the different protons in H_4pedpa ligand in the different protonated species, calculated with HypNMR program, and variations of the intrinsic chemical shifts connected to each deprotonation step.

Species	H1	H2	H3	H4	H5	H6
L^{4-}	7,55	7,55	7,22	3,92	3,03	1,78
LH^{3-}	7,61	7,61	7,27	4,62	3,65	2,07
LH_2^{2-}	7,68	7,68	7,31	4,59	3,61	2,23
LH_3^{-}	7,84	7,83	7,49	4,69	3,68	2,22
LH_4	7,92	7,86	7,51	4,68	3,72	2,14
LH_5^{+}	7,88	7,82	7,50	4,68	3,70	2,38

Δδ (ppm)	H1	H2	H3	H4	H5	H6
$LH^{3-} \rightarrow L^{4-}$	-0,06	-0,06	-0,05	-0,69	-0,62	-0,29
$LH_2^{2-} \rightarrow LH^{3-}$	-0,07	-0,07	-0,04	0,02	0,05	-0,16
$LH_3^{-} \rightarrow LH_2^{2-}$	-0,16	-0,15	-0,18	-0,10	-0,07	0,00
$LH_4 \rightarrow LH_3^{-}$	-0,08	-0,03	-0,02	0,02	-0,04	0,09
$LH_5^{+} \rightarrow LH_4$	0,04	0,04	0,01	0,00	0,02	-0,24

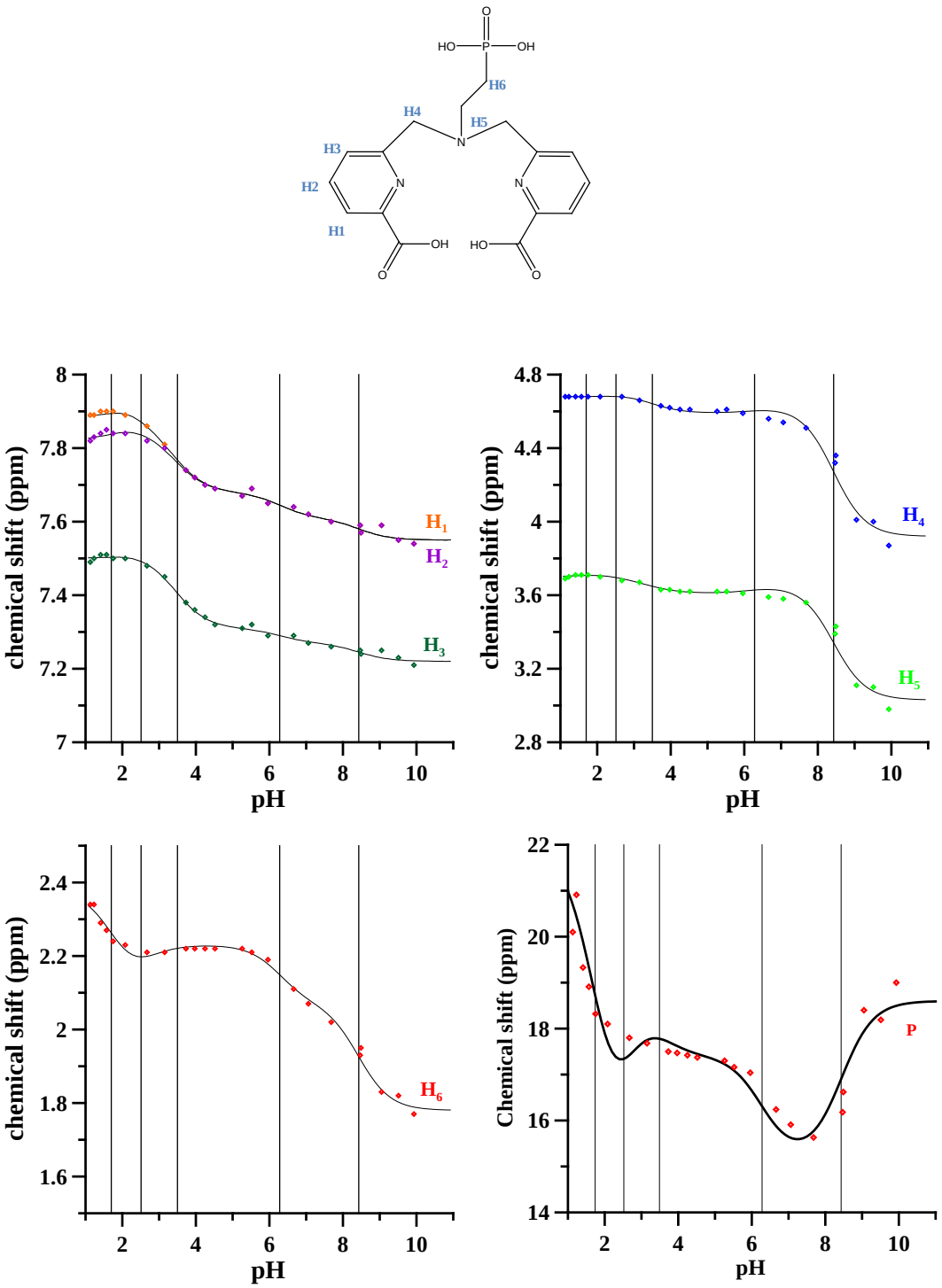

Figure 3.44. Chemical shifts of H_4pedpa ligand as a function of pH.

Potentiometric and ^{1}H-NMR and ^{31}P-NMR titrations of H_6dipedpa ligand were carried out and gave evidence of the eight different deprotonation steps according to the sequence:

$$H_8L^{2+} \leftrightharpoons H_7L^{+} \leftrightharpoons H_6L \leftrightharpoons H_5L^{-} \leftrightharpoons H_4L^{2-} \leftrightharpoons H_3L^{3-} \leftrightharpoons H_2L^{4-} \leftrightharpoons HL^{5-} \leftrightharpoons L^{6-}$$

In this case the two more acidic log K's from the phosphonate groups were calculated from ^{1}H NMR titrations and the others were calculated by fitting the potentiometric data, were the LH_8^{2+} and LH_7^{+} species were considered as strong acids. The calculated protonation constants are reported in Table 3.14 and the speciation plots are presented in Figure 3.45.

Table 3.14. Protonation constants for H_6dipedpa at 25°C, 0.16 M NaCl ionic strength, obtained using HyperQuad2013 program.[200] Standard deviations on the last figure in brackets.

Species	log β	log K
LH^{5-}	10.95 (3)	10.95
LH_2^{4-}	20.07 (3)	9.12
LH_3^{3-}	27.31 (3)	7.24
LH_4^{2-}	33.22 (3)	5.91
LH_5^{-}	37.24 (4)	4.02
LH_6	39.45 (1)	2.21
LH_7^{+}	41.25 (5)	1.8
LH_8^{2+}	41.95 (7)	0.7

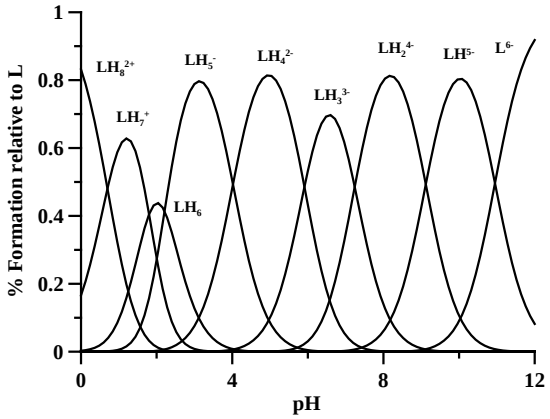

Figure 3.45. Speciation plots of the H_6dipedpa ligand calculated with the log β values shown in Table 3.14, using $1 \cdot 10^{-3}$ M ligand concentration.

In this case it was difficult to attribute the deprotonation sites on the basis of the Δδ values, as nuclei may be affected not only by the deprotonations but also by their structural rearrangements due to hydrogen bonding. Nonetheless the first two deprotonations are attributed to the most acidic protons on phosphonate groups (pK 0.7 and 1.8), the last two deprotonations are attributed to the amino functions (pK 9.12 and 10.95). Carboxylic groups on the pyridine ring deprotonate at pK 2.21 and 4.02

respectively while the more basic protons on phosphonate moieties are lost at pK 5.91 and 7.24. In Figure 3.46 the chemical shifts follow the trend of chemical shift simulated with potentiometric data.

Table 3.15. Intrinsic chemical shifts of the different protons in H_6dipedpa ligand in the different protonated species, calculated with HypNMR program, and variations of the intrinsic chemical shifts connected to each deprotonation step.

Species	H1	H2	H3	H4	H5	H6	H7
L^{6-}	7,66	7,66	7,24	3,47	2,25	2,59	1,57
LH^{5-}	7,68	7,68	7,26	3,80	2,73	2,92	1,62
LH_2^{4-}	7,70	7,70	7,29	4,06	3,08	3,13	1,73
LH_3^{3-}	7,70	7,70	7,31	3,98	3,05	3,08	1,84
LH_4^{2-}	7,87	7,77	7,44	4,40	3,51	3,33	1,97
LH_5^{-}	7,99	7,91	7,57	4,57	3,68	3,44	2,01
LH_6	8,13	8,29	7,80	4,83	3,92	3,67	2,20
LH_7^{+}	8,03	7,90	7,64	4,60	3,86	3,58	2,03
LH_8^{2+}	7,82	8,13	7,43	4,89	3,59	3,44	2,59
Δδ (ppm)	**H1**	**H2**	**H3**	**H4**	**H5**	**H6**	**H7**
$LH^{5-} \rightarrow L^{6-}$	-0,02	-0,02	-0,02	-0,33	-0,48	-0,33	-0,05
$LH_2^{4-} \rightarrow LH^{5-}$	-0,02	-0,02	-0,04	-0,26	-0,36	-0,21	-0,11
$LH_3^{3-} \rightarrow LH_2^{4-}$	0,01	0,01	-0,01	0,08	0,03	0,06	-0,10
$LH_4^{2-} \rightarrow LH_3^{3-}$	-0,17	-0,08	-0,13	-0,42	-0,46	-0,26	-0,13
$LH_5^{-} \rightarrow LH_4^{2-}$	-0,12	-0,14	-0,13	-0,18	-0,17	-0,11	-0,04
$LH_6 \rightarrow LH_5^{-}$	-0,15	-0,37	-0,23	-0,26	-0,24	-0,22	-0,18
$LH_7^{+} \rightarrow LH_6$	0,10	0,39	0,16	0,23	0,06	0,09	0,16
$LH_8^{2+} \rightarrow LH_7^{+}$	0,21	-0,23	0,21	-0,29	0,27	0,14	-0,56

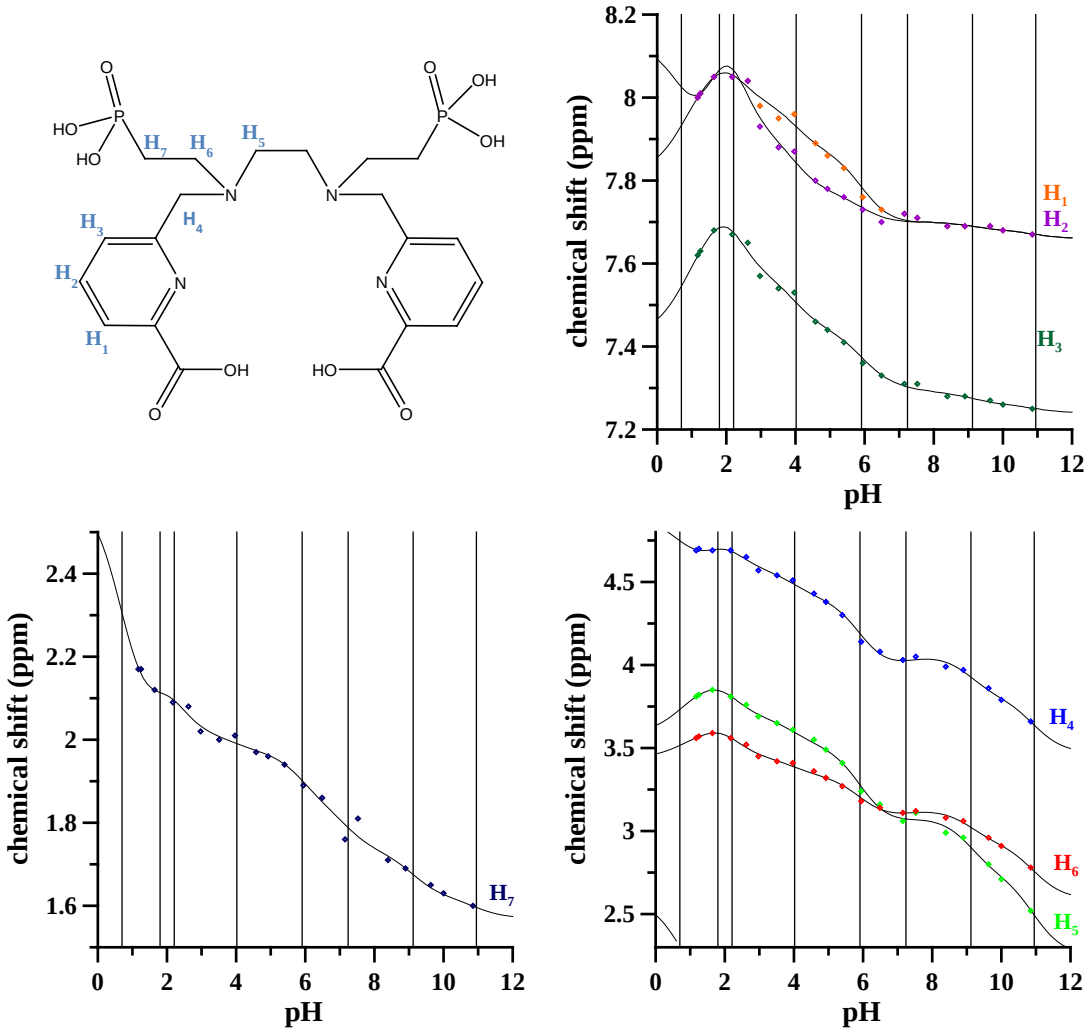

Figure 3.46. Chemical shifts of H_6dipedpa ligand as a function of pH.

3.3. Complex-formation equilibria studies

3.3.1. Complex formation equilibria of P1 ligand[147]

3.3.1.1. Complex formation equilibria with Fe^{3+}

The iron complex formation was studied by potentiometric-spectrophotometric combined titrations, ESI-MS and NMR. Some spectra collected during a Fe^{3+}-P1 titration are presented in Figure 3.47, representative of the transformations that occur with pH. Up to pH 2 a new band centred at 550 nm increases in intensity (Figure 3.47A), due to the formation of a $[FeLH]^{2+}$ complex from the colourless hexaaquo-iron species. In the pH range 2-3 (Figure 3.47B) a new band appears at 500 nm with a clear isosbestic point at 585 nm, related to the formation of a $[FeL_2H_2]^{+}$ complex. By increasing the pH a new band forms at 460 nm related to the neutral $[FeL_3H_3]$ complex, with an isosbestic point at 488 nm. The behaviour up to pH 5 is similar to that of deferiprone that presents in sequence similar bands due to the formation of 1:1, 1:2 and 1:3 complexes[201].

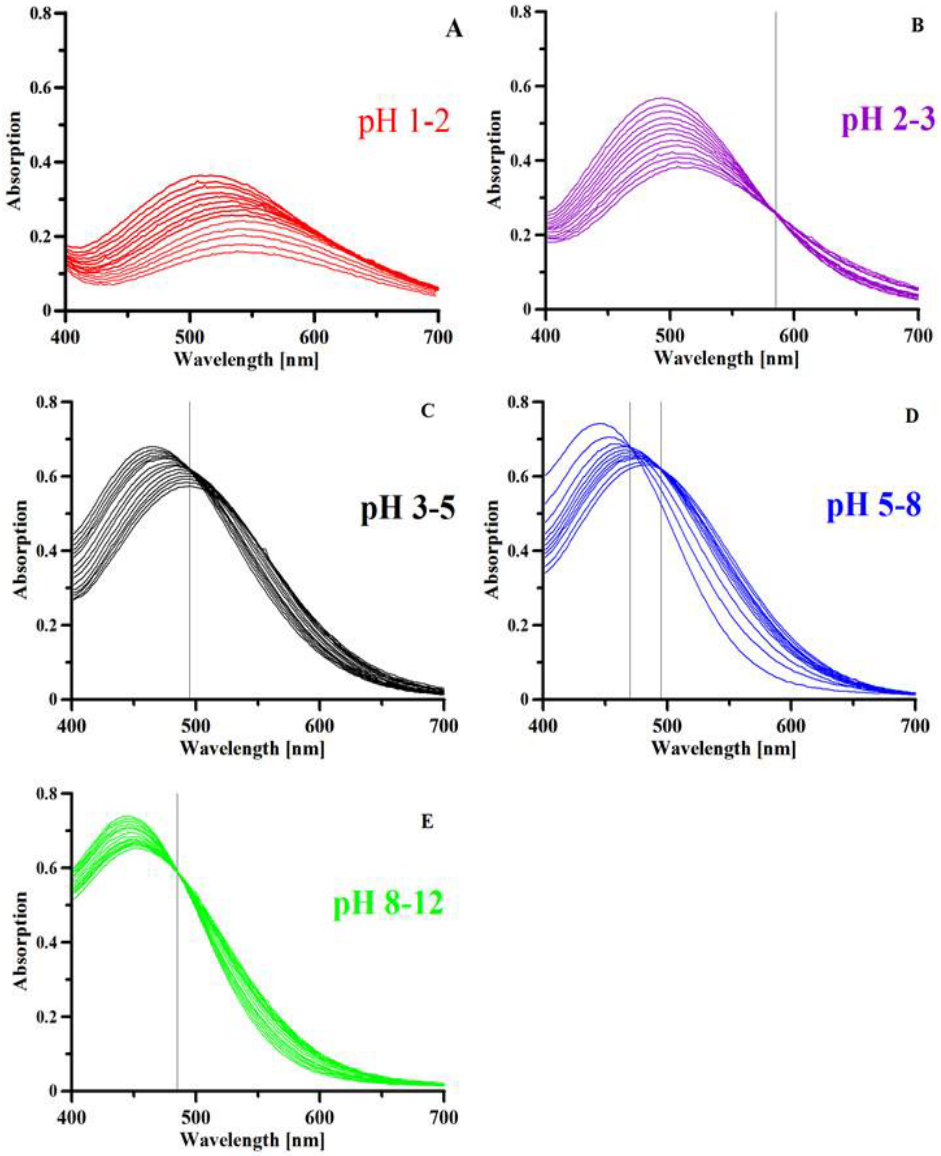

Figure 3.47. Spectra obtained by increasing pH values of Fe^{3+}-P1 system (25°C, 0.1 M KCl ionic strength, P1 concentration 4.9×10^{-4} M, 1:3 Fe/L molar ratio, optical path length 1 cm). These spectra were divided in different pH ranges to remark the transformations there occurring.

A different behaviour is featured by P1 at pH > 5: first a new band appears at 445 nm with a clear isosbestic point at 464 nm, that at pH > 9 further transforms into a new band at slightly higher wavelength, with an isosbestic point at 485 nm. These last transformations, taking into account the potentiometric results, are related to the loss of a proton from the neutral species modelled as FeL_3H_3 (possibly corresponding to $Fe(HL)_3$) giving a negatively charged complex modelled as $[FeL_3H_2]^-$, and then of two further protons to give the $[FeL_3]^{3-}$ complex. Such changes were observed above pH 7 by Scarrow et al. for 3,2-hopo, but not for 3,4-hopo[202]. The first isosbestic point of tris(3,2-hopo) iron complex at 494 nm was attributed by the authors to the mono-deprotonation with pK value of 9.04. A second deprotonation occurred around pH 11. It has to be remarked that, while DFP and P1 iron complexes are well soluble in the pH

range 2-11, the neutral tris(hydroxypyridinonato) iron complexes with the three hopo ligands studied by Scarrow et al.[202] are quite insoluble. The negative charge in the complexes of P1 with general model $[FeL_3H_{3-n}]^{n-}$ further contributes to increase their solubility. The stability constants of the Fe^{3+}-P1 complexes obtained by the spectrophotometric-potentiometric results are reported in Table 3.16, and the related speciation plot in Figure 3.48.

Table 3.16. Metal-ligand complex formation constants at 25°C, 0.1 M KCl ionic strength, obtained using HyperQuad2013 program.[200] Standard deviations on the last figure in brackets.

Model	Fe^{3+}		Al^{3+}	
	Logβ	p*K*	Logβ	p*K*
$[MLH]^{2+}$	25.92(9)		23.32(9)	
$[ML_2H_2]^{+}$	49.12(1)		45.18(6)	
ML_3H_3	71.43(6)		65.25(7)	
$[ML_3H_2]^{-}$	65.33(3)	6.1	58.30(4)	6.95
$[ML_3]^{3-}$	46.03(5)	9.65	38.41(5)	9.95
pM	22.0		15.1	
Model	Cu^{2+}		Zn^{2+}	
	Logβ	p*K*	Logβ	p*K*
$[MLH]^{+}$	21.78(7)		18.79(6)	
ML_2H_2	41.42(7)		36.70(4)	
$[ML_2H]^{-}$	34.21(5)	7.21	26.02(9)	10.68
$[ML_2]^{2-}$	24.68(5)	9.53	----	
pM	10.1		6.3	

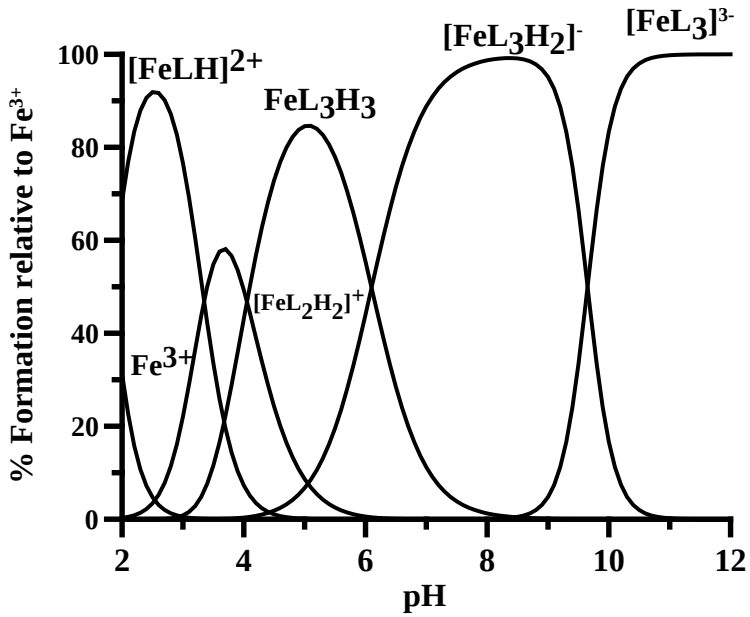

Figure 3.48. Speciation plots of P1 complexes with Fe^{3+} at 1 µM metal ion concentration and 10 µM ligand concentration (log β in Table 3.16).

The pFe^{3+} value 22.0 of P1-iron complexes is noticeable higher than that of deferiprone (20.6)[201], 3,4-hopo (20.6)[202] and 3,2-hopo (16.3)[202]. This is due on one side to the loss of the nitrogen proton from the complex with model FeL_3H_3, with corresponding

tautomeric change to the catechol form, and on the other to the protonation constant of the OH group lower in P1 than in deferiprone.

The ESI-MS data confirm the potentiometric-spectrophotometric results. Positively charged complexes form at acidic pH: $[FeL_2H_2]^+$ (336.004 m/z), $[FeL_2H_2+Cl^-+K^+]^+$ (409.940 m/z) and $[FeL_3H_3+K^+]^+$ (515.002 m/z), while at neutral and basic pH $[FeL_2H_2]^+$ (336.004 m/z), $[FeL_3H_3+Na^+]^+$ (499.029 m/z) and $[FeL_3H_3+K^+]^+$ (515.002 m/z), complexes are present. At basic pH also, the formation of negatively charged complex $[FeL_2]^-$ (333.998 m/z) is observed (Figure A7 and Table A9).

The interaction of P1 with Fe^{3+} ions has been followed by NMR at two different pH values. In Figure 3.49 the aromatic region of ^1H NMR spectra of P1 is reported. The spectra were obtained by using sub-stoichiometric amounts of Fe^{3+} ions, from 0:1 till to 0.2:1 metal to ligand molar ratio at pH 7 and 11.5. Both aromatic protons, H3 and H6, are affected by the interaction with Fe^{3+} ions.

In the aromatic region of ^1H NMR spectra, at pH 7, a selective broadening of signals was evidenced and both aromatic protons, H3 and H6, were affected by the interaction with Fe^{3+} ions. In particular, the H6 proton is the most affected suggesting the involvement in the coordination of the deprotonated oxygen in the position 5 to give a FeL_3H_3 species.

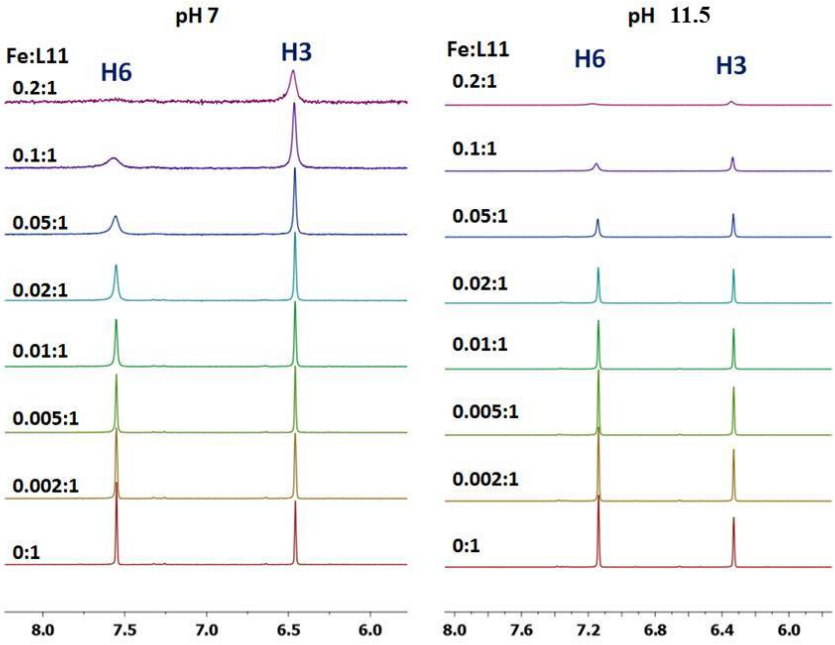

Figure 3.49. Stacked aromatic region of 1D ^1H NMR spectra of P1 by increasing sub-stoichiometric amounts of Fe^{3+}, at pH 7 (left) and pH 11.5 (right) at 25 °C.

Ga^{3+} ions have been used as a diamagnetic probe for the paramagnetic Fe^{3+} ions, in order to prevent the NMR paramagnetic line broadening. The aromatic region of ^1H NMR spectra obtained by adding incremental amounts of Ga^{3+} ions to P1 solution at neutral pH shows that, similarly to Fe^{3+}, H6 and H3 were the most affected protons by

metal coordination, giving however in this case an upfield and a downfield shift, respectively (Figure A8).

The spectra obtained at pH 11.5 (Figure 3.49) confirm that the deprotonation of the pyridine nitrogen protons affects, after Fe^{3+} coordination, in the same way H3 as well as H6, suggesting the deprotonation of both oxygen atoms at pH > 11 without any hydrolysis of the complex. These features are in agreement with the proposed scheme of tautomerism. For Ga^{3+}-P1 system, the signals H3 and H6 were affected, also at high pH, in a similar way to that of Fe^{3+}-P1 (Figure A9).

DFT calculations were recently used by our group to investigate the relative stabilities of Al^{3+} and Fe^{3+} complexes featuring the 2,2'-[(2-hydroxy-3-methoxyphenyl)methanediyl]bis [3-hydroxy-6-(hydroxymethyl)-4H-pyran-4-one] and 2,2'-[(4-hydroxy-3-methoxyphenyl)methanediyl]bis[3-hydroxy-6-hydroxymethyl)-4H-pyran-4-one] ligands[35]. Encouraged by these results, we optimized the structures of the complexes $Fe(HL)_3$ and $[FeL_3]^{3-}$ at the same level of theory as free ligand. In both cases, the $3d^5$ Fe^{3+} metal ion has been considered to assume a high-spin configuration (spin sextet state). In the neutral complex, the metal ion is chelated by the three HL^- ligands in an only slightly distorted octahedral fashion (O4-Fe-O13 angle = 96.15°; Figure 3.50). The three ligand units show corresponding bond lengths and angles, with barely distinguishable Fe–O ("hydroxy") and Fe–O ("keto") lengths in the complex (Fe-O4 and Fe-O5 distances = 2.082 and 1.994 Å, respectively, in the gas phase). A comparison of the metric parameters optimized for $Fe(HL)_3$ in the gas phase (Figure 3.50 and Table A10) with the corresponding ones determined by X-ray diffraction for the neutral complexes $Fe(P2)_3$, isolated in $Fe(P2)_3 \cdot 3H_2O$[226], and $Fe(P3)_3$[227] show a very good agreement between the experimental and calculated sets of data [P2 = 3-hydroxy-6-hydroxymethyl-1-methylpyrid-4-onato; P3 = 1,2-dimethyl-3-hydroxypyrid-4-onato; average structural Fe–O distances: 2.007 and 2.018 Å; C–O: 1.314 and 1.320 Å; O–Fe–O, 81.27° and 80.91 for $Fe(P2)_3$ and $Fe(P3)_3$, respectively; average calculated Fe–O distances: 2.039 Å; C–O: 1.275 Å; O–Fe–O, 79.29° for $Fe(HL)_3$.

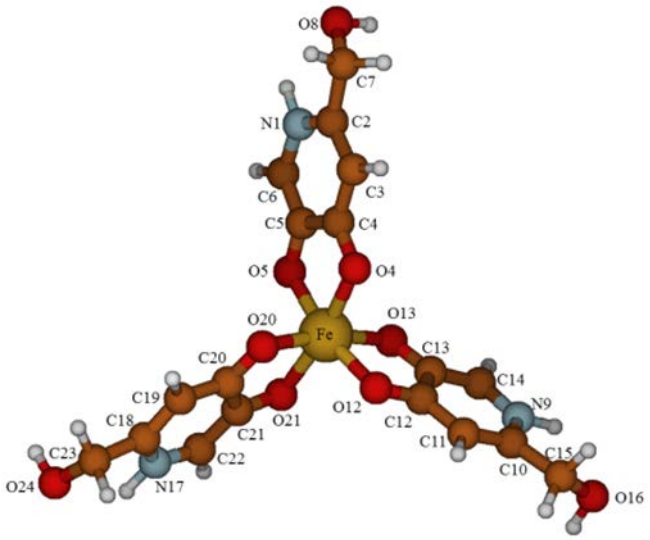

Figure 3.50. Ball and stick drawing of the DFT-optimized molecular structure of the neutral complex $Fe(HL)_3$ (purple = Fe; red = O; grey = C; blue = N; white = H).

By complete deprotonation of the complex $Fe(HL)_3$, the anionic species $[FeL_3]^{3-}$ is ideally obtained. As expected, the coordination environment at the high-spin central metal ion is not changed as compared to the corresponding neutral complex, with only a marginal elongation of the Fe–O and C–O distances [average optimised Fe–O distances: 2.056 Å; C–O: 1.287 Å; O–Fe–O, 78.77°; corresponding average structural metric parameters for trianionic tris-catecholate Fe^{3+} complexes: Fe–O, 2.01(3) Å; C–O, 1.33(2) Å; O–Fe–O, 80(1)°], reflecting an unchanged pattern of bond orders at the iron centre [average Wiberg[188] bond index: 0.332 and 0.331 for FeL_3H_3 and $[Fe(L)_3]^{3-}$, respectively]. As observed for the free ligand, the deprotonation of the N-heterocycles results in the formation of hydrogen bonds between the nitrogen atoms and the hydroxymethyl pendants (distance N···H(O) = 1.724 Å). The SOPTA allows evaluating the energy of the non-bonding hydrogen interaction in 13.1 kcal/mol for each ligand in the gas phase. This stabilization, amounting to about 40 kcal/mol, might be at the origin of the stability of such trianionic complex.

3.3.1.2. Complex formation equilibria with Al^{3+}

Aluminium with P1 forms $[AlLH]^{2+}$, $[AlL_2H_2]^{+}$ and AlL_3H_3 complexes. Analogous but weaker to those with iron. The first deprotonation of AlL_3H_3 complex occurs with pK 6.95 and other two protons are lost together with pK 9.9 (Table 3.16, Figure 3.51). The pAl^{3+} of the formed aluminium complexes is similar to that of DFP (Table A11).

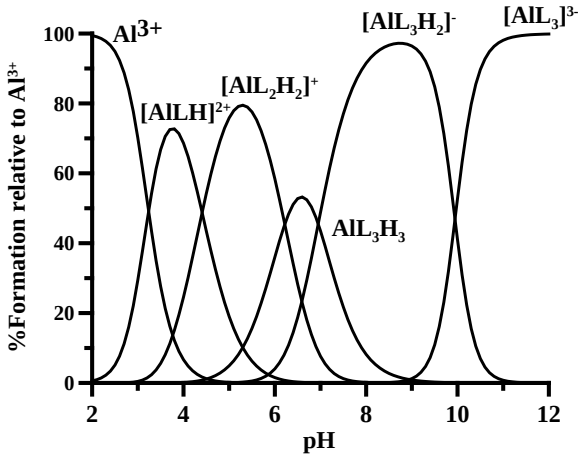

Figure 3.51. Speciation plots of P1 complexes with Al^{3+} at 25 ^{0}C, 0.1 M KCl ionic strength, 0.5 mM ligand concentration and 1:3 Al^{3+}/ligand molar ratio.

The ESI-MS spectra both at neutral and basic pHs show the signals of $[AlL_2]^-$ (305.030 m/z), $[AlL_2H_2]^+$ (307.056 m/z), $[AlL_3H_3+H]^+$ (448.101 m/z), $[AlL_3H_3+Na]^+$ (470.074 m/z) and $[AlL_3H_3+K]^+$ (486.049 m/z) complexes (Figure A10 and Table A12).

The interaction of Al^{3+} ions with P1 has been studied in the pH range 2.2 -10.7 by NMR. The stacked aromatic region of 1D ^{1}H NMR spectra of P1:Al^{3+} system at 3:1

molar ratio is reported in Figure 3.52. At pH 2.2, new signals from two species labeled as A and B besides the free ligand signals are shown in Figure 3.52. The specie A can be attributed the 1:1 complex and is not present at pH 3.6. The species B has maximum at pH 4.4 and exists till pH 6.9; this species, in agreement with the potentiometric results, can be identified as $[AlL_2H_2]^+$ species. The third species (species C), present in 3.6-10.7 pH range, can be identified as AlL_3 in all the different protonation states. The different degree of the protonation for all of the complex species does not influence the coordination mode of the ligand towards Al^{3+} ions.

At lower pH (2.2 -5.4) the signals in 12.4-12.1 ppm range are observed. The position of chemical shift for these protons strongly suggest that they are located on nitrogen atoms.

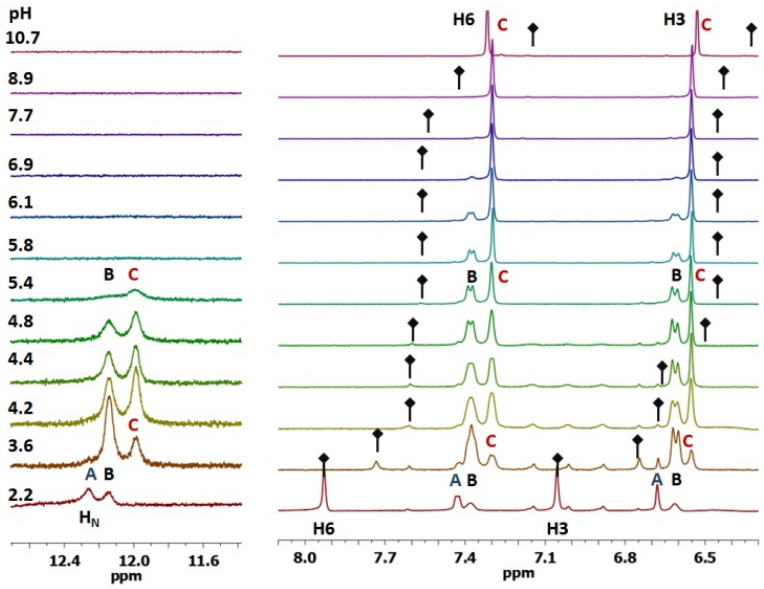

Figure 3.52. Stacked aromatic region of 1D ^{1}H NMR spectra of P1:Al^{3+} system, 3:1 molar ratio, with changing the pH. Arrows indicate the position of H6 and H3 proton signals in the free status of the ligand.

3.3.1.3. Copper complexes

P1 ligand forms with copper ions a $[CuLH]^+$ complex from pH 2, replaced by CuL_2H_2 at pH 5. CuL_2H_2 loses a proton forming the $[CuL_2H]^-$ complex with pK 7.21. A second deprotonation takes place with pK 9.53 (Table 3.16 and Figure 3.53). The pCu^{2+} value of the formed copper complexes is similar to that of DFP and 3,4-hopo (Table A11).

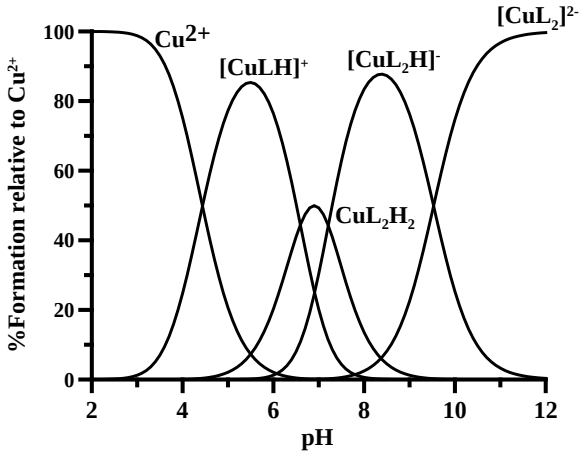

Figure 3.53. Speciation plots of P1 complexes with Cu(II) at 25 ^{0}C, 0.1 M KCl ionic strength, 0.5 mM ligand concentration and 1:2 Cu(II)/ligand molar ratio.

In the ESI-MS spectra at neutral and basic pH the signals of $[CuL_2H]^-$ (341.989 m/z), $[CuL_2H_2+H]^+$ (344.002 m/z), $[CuL_2H_2+Na]^+$ (365.985 m/z) and $[CuL_2H_2+K]^+$ (381.963 m/z) are observed (Table A13 and Figure A11).

3.3.1.4. Zinc complexes

P1 forms similar Zn^{2+} complexes to those with Cu^{2+}, though the zinc complexes are weaker. $[ZnLH]^+$ species forms from pH 4, reaching its maximum at pH ~ 6 while the species $[ZnL_2H_2]$ appears and becomes predominant at pH 9. This last complex deprotonates at pH > 10 (Table 3.16 and Figure 3.54), similarly to Zn-DFP complexes, suggesting the formation of a hydroxo complex $[ZnL_2OH]^-$ (pK 11.25[228]). The pZn^{2+} value of the formed complexes is similar to that of 3,4-hopo (Table A11).

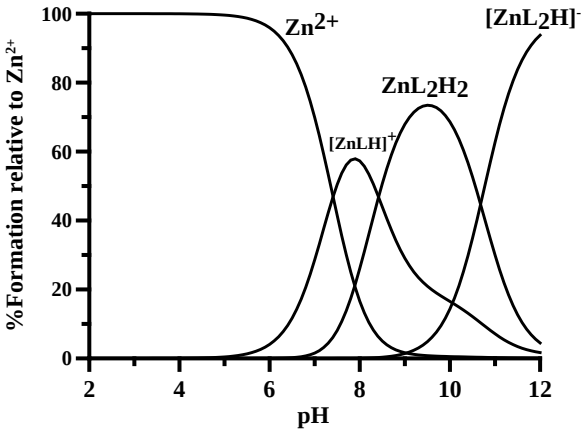

Figure 3.54. Speciation plots of P1 complexes with Zn^{2+} at 25 ^{0}C, 0.1 M KCl ionic strength, 0.5 mM ligand concentration and 1:2 Zn^{2+}/ligand molar ratio.

The ESI-MS spectra at neutral pH show only one signal attributed to $[ZnL_2H_2+K]^+$ (382.970 m/z) (Figure A12).

The complexation ability of the ligand towards Zn^{2+} ions can be followed by ^{1}H NMR spectroscopy.[185],[189] The stacked aromatic region of 1D ^{1}H NMR spectra for P1:Zn^{2+} system at 2:1 molar ratio as a function of pH (from 2.8 to 11.5) is reported in Figure 3.55. The H6 and H3 chemical shifts can be observed compared to those of the free ligand. No zinc interaction with the ligand is observed until pH 4, as expected from potentiometric results. At higher pH values, changes in the chemical shift values, $\Delta\delta = \delta_{Zn} - \delta_{free}$, have been determined. A dynamic equilibrium between $[ZnLH]^{+}$ and ZnL_2H_2 species has been detected, forming faster than the NMR timescale. This results in an average signal for H6 and H3, deriving from both complexes. $[ZnLH]^{+}$ is present in the pH range 4-9, with a maximum at pH ~ 6.5, in agreement with potentiometric data, even though its signals overlap those of the ZnL_2H_2 species. Both species are present until pH 9, where ZnL_2H_2 complex becomes predominant. By increasing the pH from 9.8 to 11.5, no changes in the chemical shifts of H6 and H3 protons for $[ZnL_2H]^{-}$ species have been detected, except for a slight broadening of the signals, confirming the presence of Zn complexes together with Zn hydroxides.

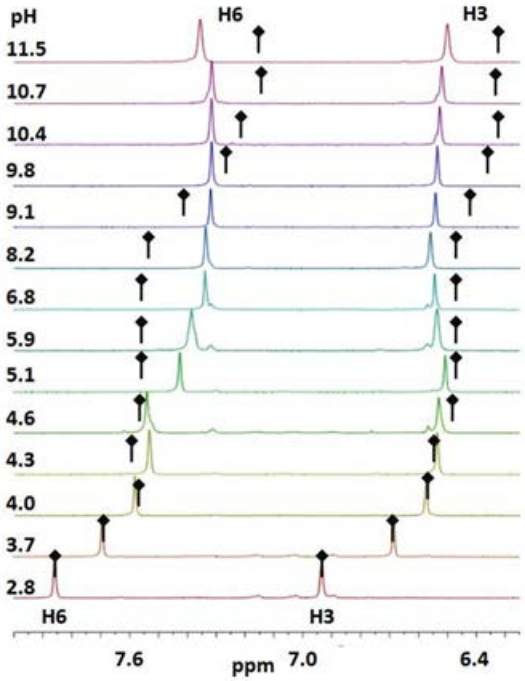

Figure 3.55. Stacked aromatic region of 1D ^{1}H NMR spectra for P1:Zn^{2+} system, 2:1 molar ratio, as a function of pH. Arrows indicate the position of H6 and H3 proton signals in the free status of the ligand.

It has to be remarked that the pAl^{3+}, pCu^{2+}, pZn^{2+} calculated for P1 complexes are almost equal to those for deferiprone and 3,4-hopo (see Table A11), in contrast with the net increase relative to iron complexes. This behaviour drives us to define P1 as an iron chelator more selective than deferiprone.

3.3.2. Complex formation equilibria of L12-L15 ligands

3.3.2.1. Complex formation equilibria with Fe^{3+}

The complex formation equilibria were studied using constant ligand concentration and 1:1, 1:2 and 1:3 Fe^{3+}/ligand molar ratios. The strong visible bands of Fe^{3+} complexes allow the study of complex formation equilibria by simultaneous potentiometric-spectrophotometric measurements. The spectra were recorded in the 300–700 nm range, after addition of known volumes of NaOH solution to the ligand/iron solution (0.5 cm path length, concentrations of L12-L15 ligands between $1.12 \cdot 10^{-4}$ M to $4.29 \cdot 10^{-4}$ M), at 25 ºC and 0.1M NaCl ionic strength. Basic titrations of all ligands gave precipitation, and in the case of L12 and L13 ligands, precipitation occurred even at pH > 1.3 and 3.0 respectively, with complete dissolution of precipitate at higher pH values. Since complex formation was almost complete when Fe^{3+} and ligands were mixed, additional spectra were collected in the range 0-2 by adding hydrochloric acid until the disappearance of the band of complexes. Some of the collected spectra are reported on Figure 3.56. These spectra collected at acidic pH values look similar (wavelength of maxima and absorptivity) to those measured for the 1:2 Fe^{3+} complex with kojic acid[33], so we hypothesized the formation of $Fe_2L_2H_2$ complex. The heights of the peak at around 500 nm was calculated by spectral decomposition, and its trend with pH allowed to estimate the stability constant of the complex formed in the pH range 0-2, successively refined with HypSpec program (Table 3.17).

The potentiometric data were then elaborated with HyperQuad2013 program, taking the value of the stability constant of the $Fe_2L_2H_2$ complex constant. This treatment allowed to determine the existence of the complexes reported in Table 3.17, and the related formation constants. The calculated speciation plots are shown in Figure 3.57.

Table 3.17. Stability constants of metal complexes calculated with HyperQuad program at 25°C and 0.1 M NaCI ionic strength using the ligand concentration $1.12 \cdot 10^{-4}$ to $4.29 \cdot 10^{-4}$ M and metal to ligand molar ratio 1:1. Charges are omitted for simplicity. Protonation constants of the ligands and overall stability constants (log βpqr) of the metal complexes were calculated by using eqs: pM + qH + rL = MpHqLr, βpqr =([MpHqLr])/([M]p[H]q[L]r).

Model	log β L2	pK L2	log β L3	pK L3	log β L12	pK L12	log β L13	pK L13	log β L14	pK L14	log β L15	pK L15
Fe_2L	26.86	---	---	---	---	---	---	---	---	---	---	---
$Fe_2L_2H_2$	---	---	---	---	47.72 (3)	---	47.42 (4)	---	59.78 (5)	---	57.39 (2)	---
Fe_2L_2H	49.57	---	---	---	44.23 (6)	3.49	--	3.09	55.42 (6)	4.36	53.15 (6)	4.24
Fe_2L_2	47.43	2.14	48.82	---	40.09 (3)	4.14	41.60 (5)		50.61 (5)	4.81	48.41 (5)	4.74
$Fe_2L_2H_{-1}$	43.91	3.52	45.97	2.85	34.31 (4)	5.78	36.28 (5)	5.21	44.95 (4)	5.66	41.13 (4)	7.28
$Fe_2L_2H_{-2}$	---	---	42.29	3.68	28.13 (3)	6.18	30.06 (4)	6.25	37.14 (3)	7.81	---	---
$Fe_2L_2H_{-3}$	---	---	---	---	---	---	22.42 (4)	7.66	---	---	---	---
$Fe_2L_2H_{-4}$	---	---	---	---	---	---	12.35 (6)	10.07	---	---	---	---
pFe	18.9		22.2		17.1		18.7		20.4		18.7	

All complexes are dimers of general formula $[Fe_2L_2H_r]$; when r is negative, the species are actually hydroxo complexes.

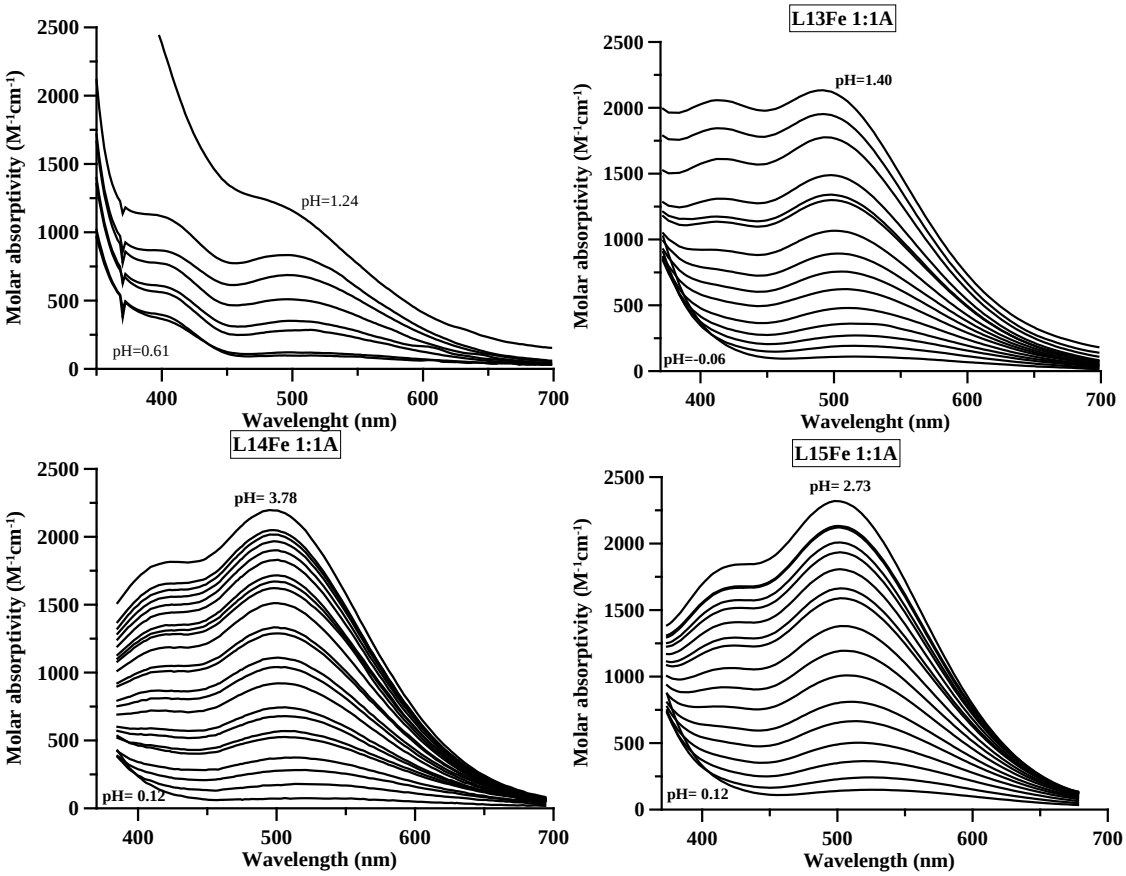

Figure 3.56. Some spectra of the titration of: a) Fe^{3+}:L12 1:1 Me/L molar ratio [L12] = $2.83 \cdot 10^{-4}$ M, b) Fe^{3+}:L13 1:1 Me/L molar ratio [L13] = $3.96 \cdot 10^{-4}$ M, c) Fe^{3+}:L14 1:1 Me/L molar ratio [L14] = $1.12 \cdot 10^{-4}$ M, c) Fe^{3+}:L15 1:1 Me/L molar ratio [L15] = $4.29 \cdot 10^{-4}$ M.

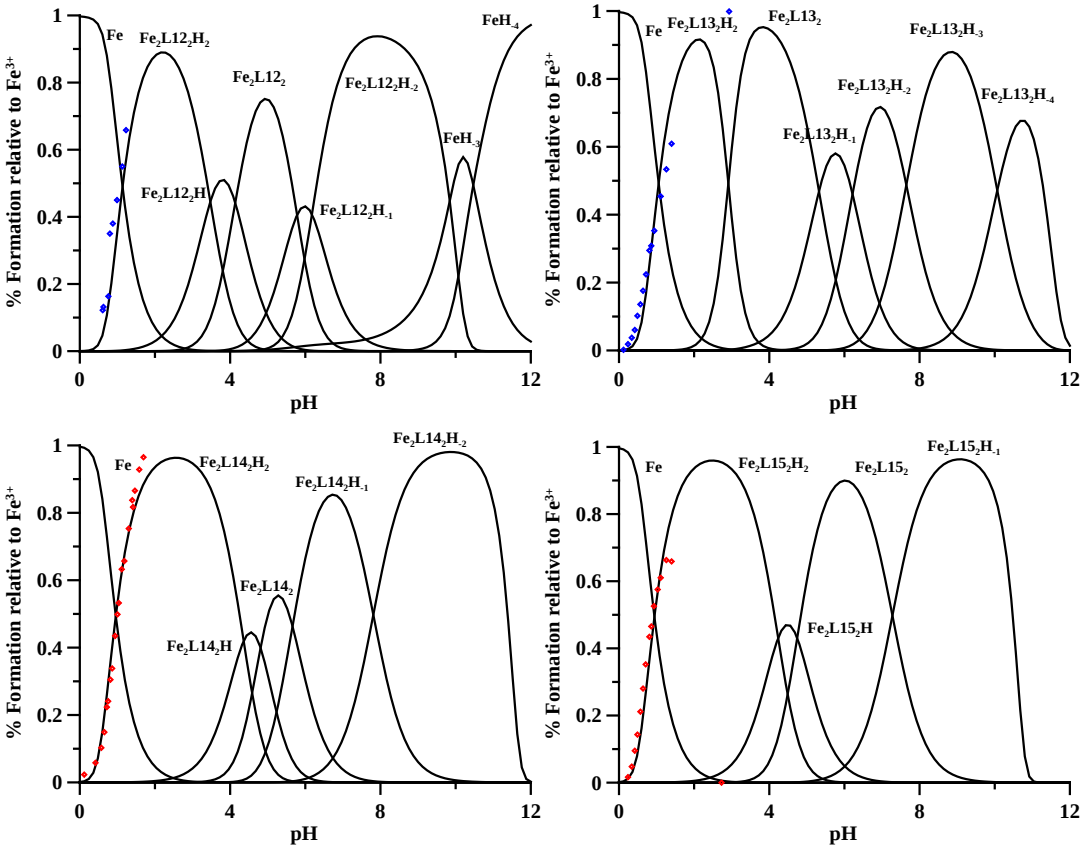

Figure 3.57. Speciation plots of L12-L15 complexes calculated on the basis of stability constants reported in Table 3.17, using ligand concentrations between $1.12 \cdot 10^{-4}$ M to $4.29 \cdot 10^{-4}$ M and metal to ligand molar ratio 1:1, overlapping the heights of the peaks calculated by spectral decomposition using Specpeak program[206]. Charges are omitted for simplicity.

The calculated speciation plots shown in Figure 3.57 and the pK sequence for the loss of the protons from the $Fe_2L_2H_2$ complex (Table 3.17) permit some considerations.

Starting from L12, the initial $[Fe_2L_2H_2]^{2+}$ complex can be hypothesized as a dinuclear complex in which each Fe^{3+} ion is coordinated by two KA units from two different ligands through the two oxygen atoms (carbonyl and deprotonated OH group) as shown in Scheme 9A. Each iron atom is presumably hexacoordinated, with the coordination completed by two water molecules. This complex loose the protons from the two carboxylic groups with pK 3.49 and 4.14, the first equal to the pK of the free ligand and the second slightly higher, even if the positive charge of the entire molecule should have lowered these values. The complete formation of the neutral complex Fe_2L_2 between pH 4 and 5 determines its precipitation. At higher pH values two of the coordinated water molecules loose one proton with very similar pK values 5.78 and 6.18, leading to the re-dissolution of the precipitate. The complex $[Fe_2L_2H_{-2}]^{2-}$ is the prevailing species at physiological pH, and the corresponding pFe^{3+} value was estimated 17.1.

The coordination scheme of L13 with Fe^{3+} is similar to that of L12, but the two carboxylic protons are lost together with pK 3.09, which is lower than the corresponding values for L12. This is in line with what expected from the positive charge of the entire molecule that favours the deprotonation of the carboxylic groups.

Furthermore the neutral complex Fe_2L_2 with L13 loses up to four protons from the coordinated water molecules, the first two with pK 5.21 and 6.25 and the second two with pK 7.66 and 10.07. The prevailing species at pH 7.4 is always $[Fe_2L_2H_{-2}]^{2-}$ (Figure 3.57), but accompanied by a non-negligible amount of the $[Fe_2L_2H_{-3}]^{3-}$ species, and this determines the higher pFe^{3+} value 18.7 (Table 3.17).

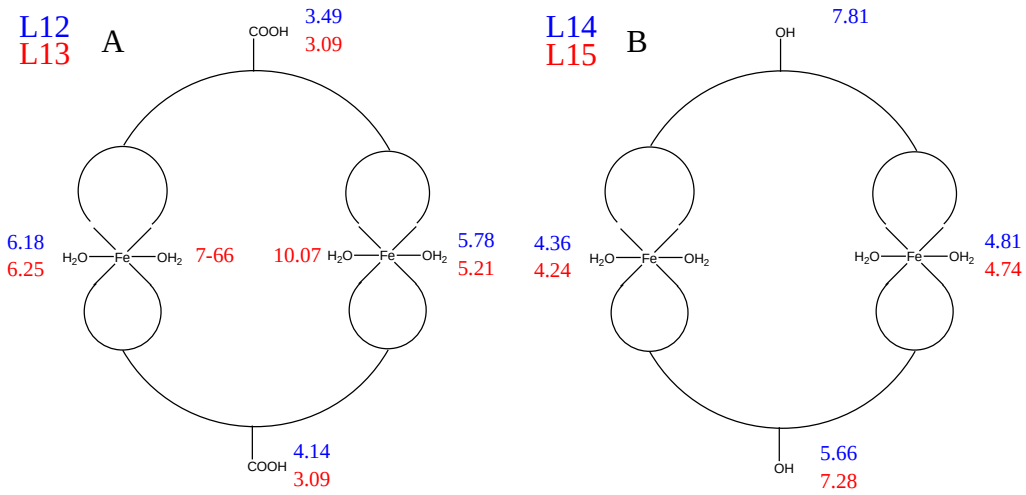

Scheme 9. Hypothesized coordination scheme of L12-L15 ligands with Fe^{3+}.

The behaviour of L14 and L15 is only apparently similar to that of L12 and L13 (Scheme 9B). The deprotonation of the coordinated water molecules takes place with lower pK values (4.26 and 4.81 for L14, and 4.24 and 4.74 for L15), since the starting molecule is now positively charged. The following pKs (two for L14 and one for L15) are difficult to be attributed, being equally possible that the proton is lost from further coordinated water molecules or from the phenolic group on the linker. We trust in the quantum chemical calculations in progress to clarify this point. The prevailing species at pH 7.4 is the negative $[Fe_2L_2H_{-1}]^{-}$ species in the case of L14 (Figure 3.57), which determines a very interesting pFe^{3+} value 20.4 (Table 3.17). In the case of L15 the neutral species Fe_2L_2 is that prevailing at physiological pH for the higher pK value, and this determines a lower pFe^{3+} value 18.7.

The ESI-MS measurements support the previous statements. In fact for the $FeCl_3$/L12 system (Figure A46), the presence of dinuclear iron complexes with positive charges is confirmed by the signals at *m/z* 466.973, 475.976, 484.991 and 493.980 assigned to $[Fe_2(L12_{ox})H_2]^{2+}$, $[Fe_2(L12_{ox})H_2+H_2O]^{2+}$, $[Fe_2(L12_{ox})H_2+2H_2O]^{2+}$ and $[Fe_2(L12_{ox})H_2+3H_2O]^{2+}$ Figure A46A) respectively. The same system in negative mode ESI-MS (Figure A47) shows the presence of dinuclear $[Fe_2(L12_{ox})_2H_2+3Cl]^{-}$ complex (m/z 1040.870). The reaction between $FeCl_3$ and L13 is characterized by the presence of signal deriving from the complexes with 2:2 stoichiometry (Figure A48): $[Fe_2(L13)_2H_2]^{2+}$ (*m/z* 469.995), $[Fe_2(L13)_2H_2+H_2O]^{2+}$ (*m/z* 478.998) and $[Fe_2(L13)_2H_2+2H_2O]^{2+}$ (*m/z* 488.004). The ESI-MS spectrum of Fe/L15 solution (Figure A49) confirms the formation of iron dinuclear complexes. The signals at m/z 441.991,

450.998 and 460.004 can be assigned to $[Fe_2(L15)_2H_2]^{2+}$, $[Fe_2(L15)_2H_2+H_2O]^{2+}$ and $[Fe_2(L15)_2H_2+2H_2O]^{2+}$ respectively (Figure A49A).

3.3.2.2. Complex formation equilibria with Al^{3+}

The ligands L12-L15 form with aluminium ion complexes similar to those observed with iron, but of lower stability. This implicates that the complexation happens at higher pH values than with iron, so with L12 at low pH a mononuclear complex $[AlL_2H_2]^-$ is initially formed in which one Al^{3+} ion is coordinated by two KA units of two different ligands, being the two COOH already deprotonated and the two remaining OH groups on the non-coordinating KA moieties till protonated (Scheme 10A). This molecule binds at pH 5 a second aluminium ion giving the neutral binuclear complex Al_2L_2 (Figure 3.58). In the case of L13 the first formed complex is $[Al_2L_2H]^+$ till protonated on a carboxylic group. All the binuclear complexes at increasing pH form hydroxo-complexes in a similar fashion as that observed with iron ions (Scheme 10B). The prevailing species at physiological pH are $[Al_2L_2H_{-1}]^-$ and $[Al_2L_2H_{-2}]^{2-}$ in different ratios and the pAl^{3+} values are 12.7 and 12.2 for L12 and L13 respectively (Table 3.18).

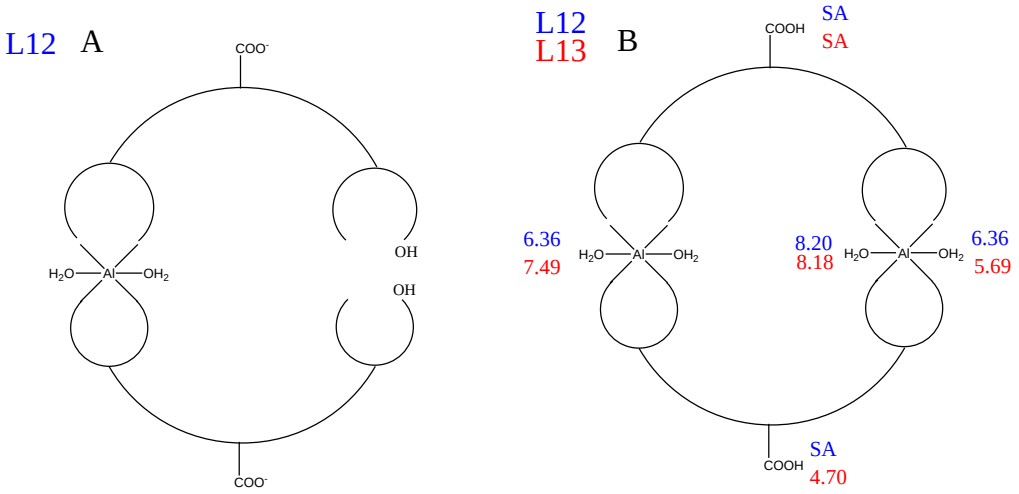

Scheme 10. Hypothesized coordination scheme of L12-L13 ligands with Al^{3+}.

A behavior analogous to that observed with iron is presented by L14 and L15 (Scheme 11). The prevailing species at pH 7.4 are also in this case $[Al_2L_2H_{-1}]^-$ and $[Al_2L_2H_{-2}]^{2-}$ in different ratios and the pAl^{3+} values are 13.2 and 13.3 for L14 and L15 respectively, higher than the corresponding values with L12 and L13, as with iron.

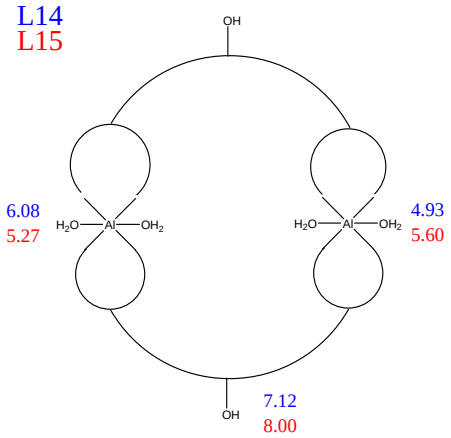

Scheme 11. Hypothesized coordination scheme of L14-L15 ligands with Al^{3+}.

Table 3.18. Logβ complex formation constants of Al^{3+} with L12-L15 ligands.

Model	log β L12	log β L13	log β L14	log β L15
$Al_2L_2H_2$	---	---	48.58 (6)	48.6 (1)
Al_2L_2H	---	34.96 (6)	43.65 (6)	43.0 (2)
Al_2L_2	30.81 (4)	30.26 (6)	37.57 (7)	37.73 (8)
$Al_2L_2H_{-1}$	---	24.57 (5)	30.45 (5)	29.7 (1)
$Al_2L_2H_{-2}$	18.09 (4)	17.08 (7)	---	---
$Al_2L_2H_{-3}$	9.89 (5)	8.90 (6)	---	---
AlL_2H_2	35.95 (5)	---	---	---
pAl	**12.7**	**12.2**	**13.2**	**13.3**

H_{-n} are referred to hydroxo complexes.

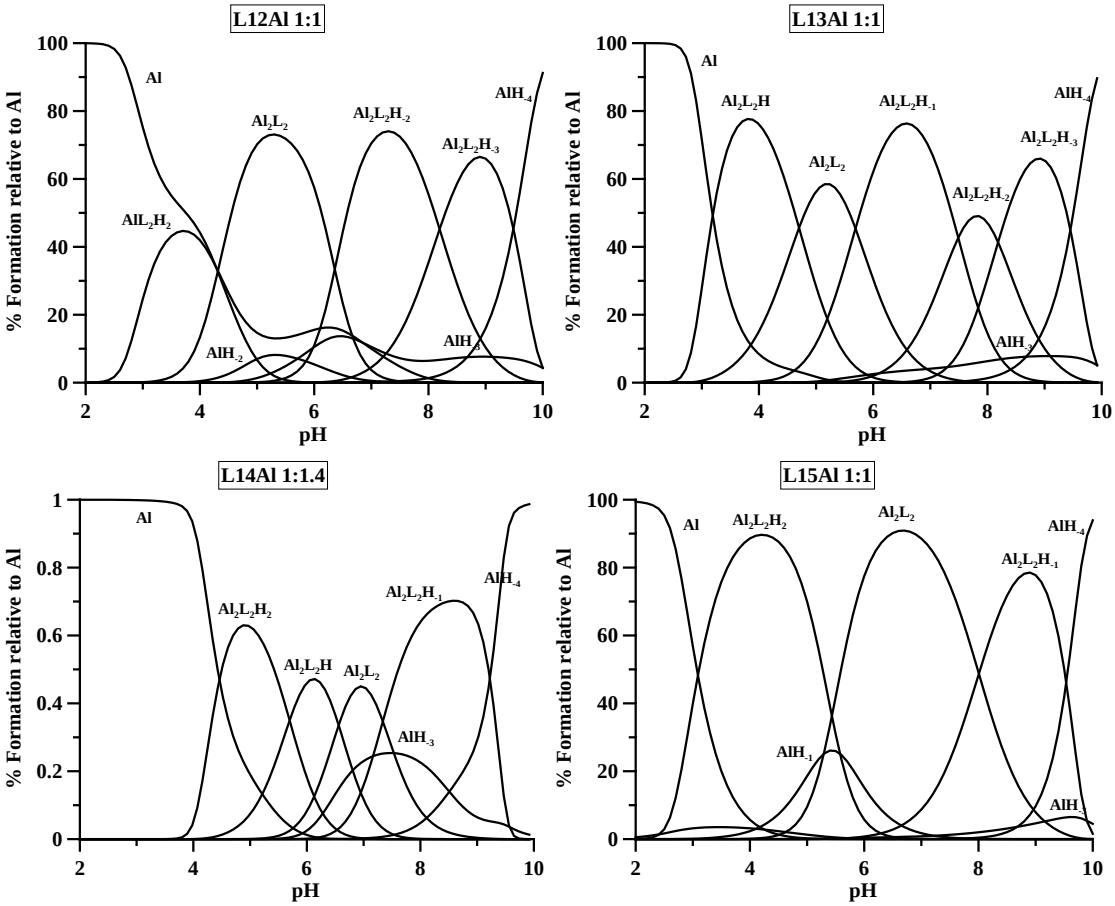

Figure 3.58. Speciation plots of L12-L15 complexes calculated on the basis of stability constants reported in Table 3.18, using a ligand concentration 5 × 10^{-4} M and metal to ligand molar ratio 1:1 . Charges are omitted for simplicity.

These findings are substantiated by ESI-MS results. In ESI-MS spectrum of L12 ligand with Al^{3+} ions (Figure A50) in positive mode, we can observe an intense signal at 441.035 *m/z* corresponding to $[Al_2(L12)_2H_2]^{2+}$ complex (Figure A50A) and a lower intensity signal at 440.027 *m/z* corresponding to $[Al_2(L12_{ox})_2H_2]^{2+}$ complex (Figure A50B). Each of the dinuclear complexes is present in mono- and bis-hydrated form represented by the signals at 450.041 *m/z* (attributed to $[Al_2(L12)_2H_2+H_2O]^{2+}$ complex), 459.045 (attributed to $[Al_2(L12)_2H_2+2H_2O]^{2+}$ complex), 449.033 *m/z* (attributed to $[Al_2(L12_{ox})_2H_2+H_2O]^{2+}$ complex) and 458.038 *m/z* (attributed to $[Al_2(L12_{ox})_2H_2+2H_2O]^{2+}$ complex). The dinuclear aluminium complexes can be observed as well in negative mode ESI-MS spectrum (Figure A51). The signals at 474.999, 915.036, 933.022 and 951.009 *m/z* can be attributed to $[Al_2(L12)_2+2Cl]^{2-}$ (Figure A51A), $[Al_4(L12)_4+2Cl]^{2-}$, $[Al_4(L12)_4+2Cl+2H_2O]^{2-}$ and $[Al_4(L12)_4+2Cl+4H_2O]^{2-}$ (Figure A51B) respectively.

The ESI-MS spectra of the reaction mixture of $AlCl_3$/L13 is characterized by the presence of two major peaks (Figure A52) at *m/z* 441.029 and 459.040, attributed to the dinuclear $[Al_2(L13)_2H_2]^{2+}$ and $[Al_2(L13)_2H_2+2H_2O]^{2+}$ complexes respectively (Figure A52A). Electrospray ionization with tandem mass spectrometry (MS/MS) spectrum of the $[Al_2(L13)_2H_2]^{2+}$ complex shows that the dinuclear complex is degraded into mononuclear $[Al(L13)H]^{+}$ (*m/z* 459.040) complex (Figure A53A).

The ESI-MS spectrum of Al^{3+} complexes with L14 ligand shows four different species (Figure A54). The major signals, at *m/z* 413.038, 422.044 and 431.049 came from the dinuclear complex with stoichiometry $[Al_2(L14)_2H_2]^{2+}$ and its adducts with water, $[Al_2(L14)_2H_2+H_2O]^{2+}$ and $[Al_2(L14)_2H_2+2H_2O]^{2+}$ (Figure A54A). The charged hydrates are stable in vacuum when using relatively in-source collision energy (10 eV). The low intensity signal at *m/z* 607.077 can be attributed to $[Al_2(L14)_3H_5]^{2+}$ complex (Figure A54B). The electrospray ionization with tandem mass spectrometry (MS/M) spectrum of $[Al_2(L14)_2H_2]^{2+}$ (Figure A55) shows the presence of stable hydrated dinuclear complexes $[Al_2(L14)_2H_2+H_2O]^{2+}$ and $[Al_2(L14)_2H_2+2H_2O]^{2+}$ with the signals at *m/z* 422.049 and 431.056 respectively.

3.3.2.3. Complex formation equilibria with Cu^{2+}

In the acidic pH range 2-3 copper forms with L12 and L13 ligands $[Cu_2LH]^{2+}$ binuclear complexes, in which a ligand molecule binds two copper ions, one with each KA moiety. This complex transforms in a $[Cu_2L_2H]^{-}$ and then in a $[Cu_2L_2]^{2-}$ complex with pK's 5.31 and 5.95. These values appear too high (~2 units higher than in the free ligand) to be attributed to the deprotonation of a carboxylic group, even also taking into account the negative charge of the entire molecule. A further possibility is that in $[Cu_2L_2H]^{-}$ one copper ion is coordinated by two KA units and the second by one, being the remaining till protonated on the OH group (Scheme 12B). This complex transforms with pK 5.31 and 5.55 for L12 and L13 respectively in the $[Cu_2L_2]^{2-}$. This complex loses two further protons from the coordinated water molecules with pK 6.31 and 9.31 for L12, and one proton at 6.19 for L13 (Scheme 12C). The prevailing species at pH 7.4 is the $[Cu_2L_2H_{-1}]^{3-}$ complex that determines pCu^{2+} values 11.1 and 9.9 for L12 and L13 respectively (Figure 3.59 and Table 3.19).

Table 3.19. Logβ complex formation constants of Cu^{2+} with L12-L15 ligands.

Cu	log β L12	log β L13	log β L14	log β L15
$CuLH_2$	---	---	25.34 (5)	24.9 (1)
CuLH	---	---	---	---
Cu_2LH	22.62 (4)	20,89 (4)	---	---
$Cu_2L_2H_2$	---	---	44.84 (2)	45.14 (6)
Cu_2L_2H	35,10 (2)	32,31 (3)	38.68 (3)	---
Cu_2L_2	29,79 (1)	26,36 (5)	31.89 (5)	33.14 (7)
$Cu_2L_2H_{-1}$	23,48 (3)	20,17 (3)	21.3 (1)	23.8 (2)
$Cu_2L_2H_{-2}$	14,17 (2)	---	---	---
pCu	**11.1**	**9.9**	**10.2**	**10.9**

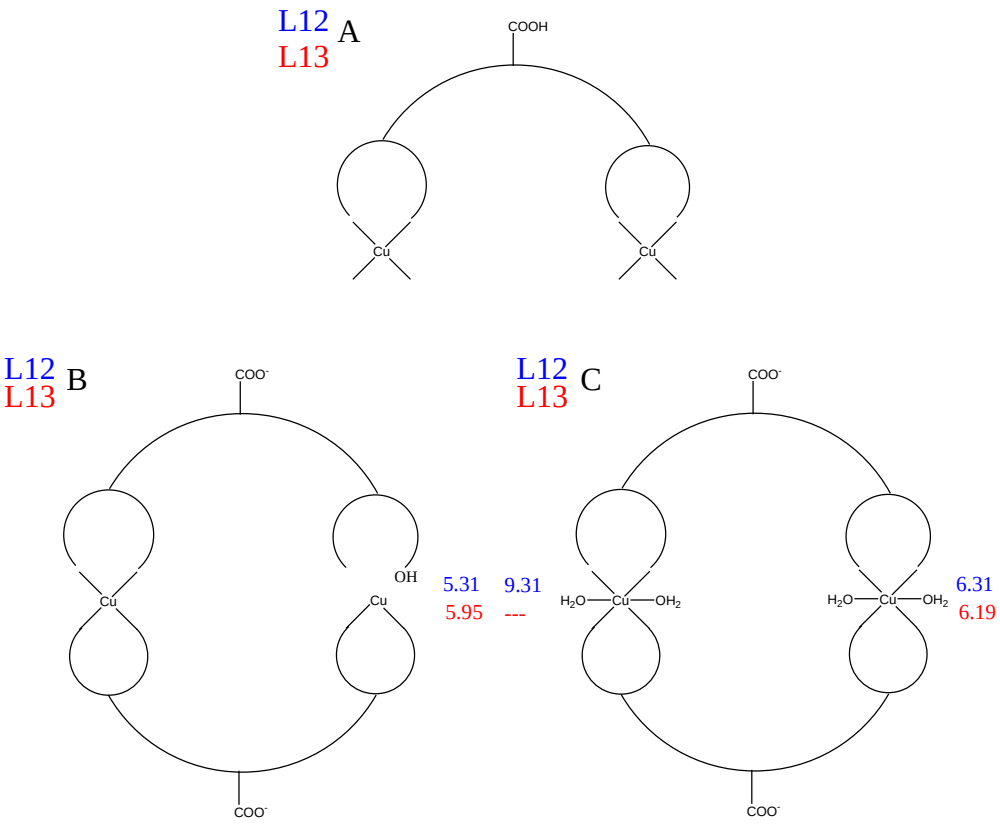

Scheme 12. Hypothesized coordination scheme of L12-L13 ligands with Cu^{2+}.

The L14 and L15 ligands form with copper the $[CuLH_2]^+$ complex in which Cu^{2+} is coordinated by one KA unit being protonated the second KA unit and the phenolic group on the linker. This transforms in the $Cu_2L_2H_2$ neutral complex that loses a proton from the coordinated water molecule with pK 6.16 and 6.00 for L14 and L15 respectively, then from the phenolic groups with pK 6.79 and 6.00 the first, and 9.34 and 10.6 the second, always for L14 and L15 respectively (Scheme 13). The prevailing species at pH 7.4 are $[Cu_2L_2H]^-$ and $[Cu_2L_2]^{2-}$ for L15, determining the pCu^{2+} values 12.2 and 10.9 respectively, always higher for the ortho substituent as in L12 and L13 Figure 3.59 and Table 3.19). The phenolic ligands in this case are better ligands than the carboxylic ones.

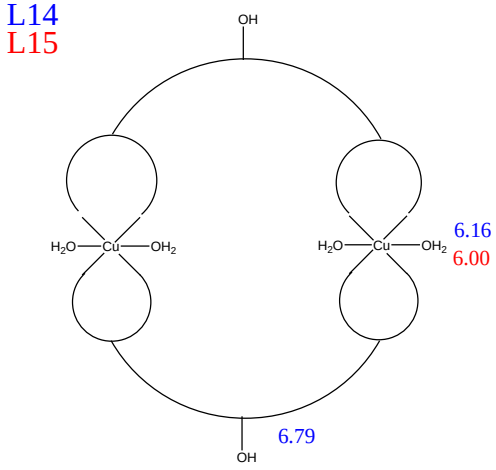

Scheme 13. Hypothesized coordination scheme of L14-L15 ligands with Cu^{2+}.

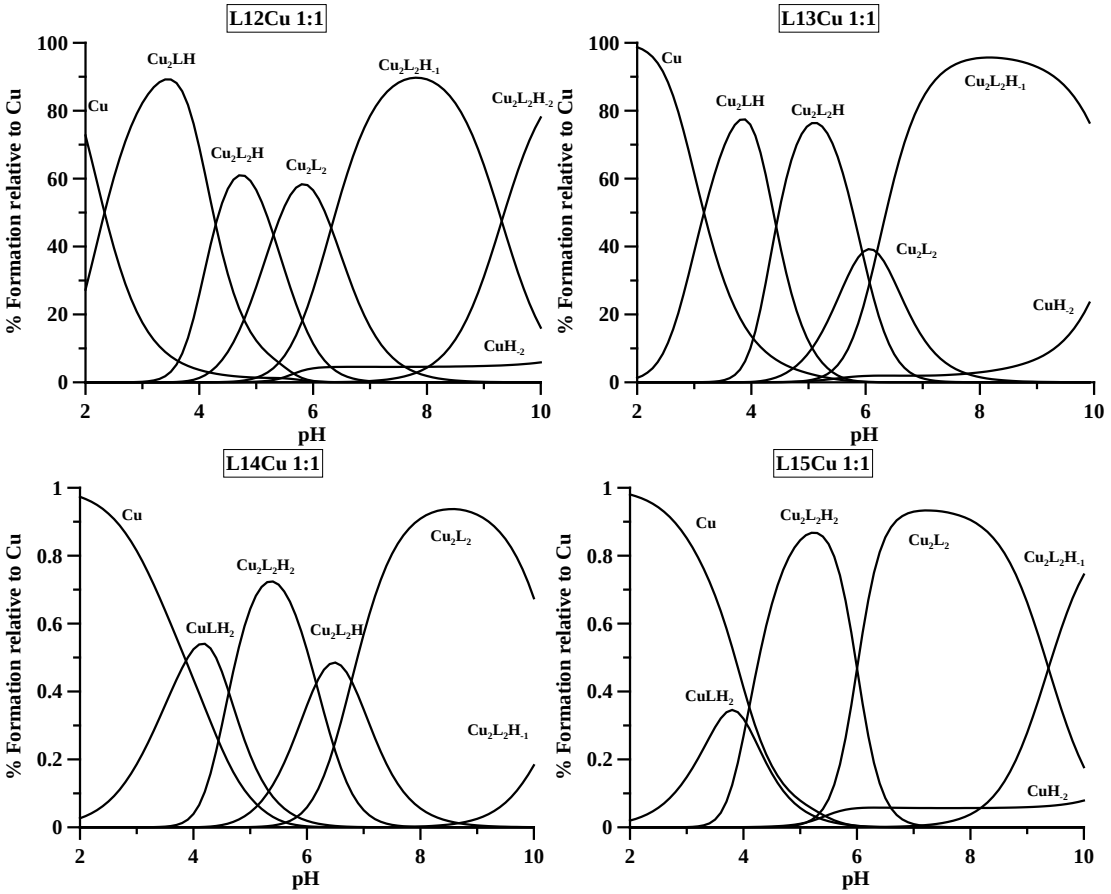

Figure 3.59. Speciation plots of L12-L15 complexes calculated on the basis of stability constants reported in Table 3.19, using a ligand concentration $5 \cdot 10^{-4}$ M and metal to ligand molar ratio 1:1. Charges are omitted for simplicity.

The ESI-MS spectra of the reaction mixture of $CuCl_2$/L12 (Figure A56) is characterized by the presence of few peaks: 475.974 *m/z* attributed to overlapping signals of $[Cu(L12_{ox})H_2]^+$ and $[Cu_2(L12_{ox})_2H_4]^{2+}$ and 493.990 *m/z* attributed to $[Cu(L12_{ox})H_2+H_2O]^+$ complex.

The presence of mononuclear and dinuclear copper/L13 complexes is confirmed by the signals at *m/z* 477.986 and 954.960 (Figure A57). The overlapping signals at *m/z* 477.986 are assigned to $[Cu(L13)H_2]^+$ and $[Cu_2(L13)_2H_4]^{2+}$ complexes respectively (Figure A57A). The signal at *m/z* 954.960 corresponds to the $[Cu_2(L13)_2H]^+$ specie (Figure A57B).

The ESI-MS spectrum of Cu^{2+} complexes with L14 ligand shows high intensity signal of free ligand at *m/z* 389.076 and lower intensity signals of the Cu/L14 complexes (Figure A58). As long as the sample preparation and ESI-MS measurements conditions were the same for of metal/L14 solution, it can be concluded that the affinity of ligand toward copper ions is lower than that toward aluminum ions. The signal at *m/z* 449.991 can be attributed to two overlapping species $[Cu(L14)H_2]^+$ and $[Cu_2(L14)_2H_4]^{2+}$ (Figure A58A). The low intensity signals at m/z 838.061 and 898.972 show the presence of $[Cu(L14)_2H_5]^+$ (Figure A58B) and $[Cu_2(L14)_2H_3]^+$ (Figure A58C) complexes respectively.

The ESI-MS spectrum of Cu^{2+} complexes with ligand L15 (Figure A59) is similar to that of Cu^{2+} complexes with ligand 14, which indicates the formation of similar complexes. However, the intensity of the peak corresponding to $[(L15)H_3+H]^+$ at *m/z* 389.078 is lower, indicating that ligand 15 has a higher tendency to form copper complexes. The presence of $[Cu(L15)H_2]^+$ and $[Cu_2(L15)_2H_3]^{2+}$ is marked by the overlapping signals at *m/z* 449.995 (Figure A59A) . The low intensity signals at *m/z* 898.983 and 920.976 are attributed to $[Cu_2(L15)_2H_3]^+$ ($C_{38}H_{29}Cu_2O_{18}$) and $[Cu_2(L15)_2H_2+Na]^+$ complexes (Figure A59B).

3.3.2.4. Complex formation equilibria with Zn^{2+}

The first complex formed with Zn^{2+} with L12 and L13 is the dinuclear complex $[Zn_2LH]^{2+}$ in which each metal ion is coordinated by one KA unit on the same molecule, being the carboxylic group till protonated (Scheme 19A). This complex transforms with L12 in a $[Zn_2L_2]^{2-}$ species coordinated by two KA units being the carboxylic groups deprotonated (Scheme 14B). In L13 instead it transforms in a $[Zn_2L_2H]^-$ complex, and then in a $[Zn_2L_2]^{2-}$ form with pK 6.1. This value is too high to be attributable to a carboxylic group, even taking into account the negative charge on the molecule. So a form as that reported in Scheme 14C can be hypothesized, in which both carboxylic groups are deprotonated and one Zn^{2+} ion is coordinated by two KA moieties, and the second by only one KA unit, being the second not implied in bonding and till protonated. The pK 6.1 thus corresponds to the loss of this proton, with the bonding of zinc by the second KA unit.

Table 3.20. Logβ complex formation constants of Zn^{2+} with L12-L15 ligands.

Model	log β L12	log β L13	log β L14	log β L15
Zn_2LH	19.3 (2)	18.61 (9)	---	---
$Zn_2L_2H_2$	---	---	40.0 (1)	38.3 (1)
Zn_2L_2H	---	27.2 (1)	---	30.8 (1)
Zn_2L_2	23.5 (1)	21.13 (8)	27.1 (2)	---
$Zn_2L_2H_{-1}$	16.0 (1)	12.2 (1)	---	---
pZn*	**7.5**	**6.8**	**7.7**	**6.4**

H_{-n} are referred to hydroxo complexes.

A final deprotonation occur both in L12 and L13 giving the hydroxo-complex $[Zn_2L_2H_{-1}]^{3-}$ with pK 7.5 and 8.9 for L12 and L13 respectively.

The prevailing species at pH 7.4 are with L12 $[Zn_2L_2]^{2-}$ and $[Zn_2L_2H_{-1}]^{3-}$ in similar amounts, giving a pZn^{2+} 7.5, and $[Zn_2L_2]^{2-}$ with L13 giving a lower pZn^{2+} 6.8 (Figure 3.60 and Table 3.20).

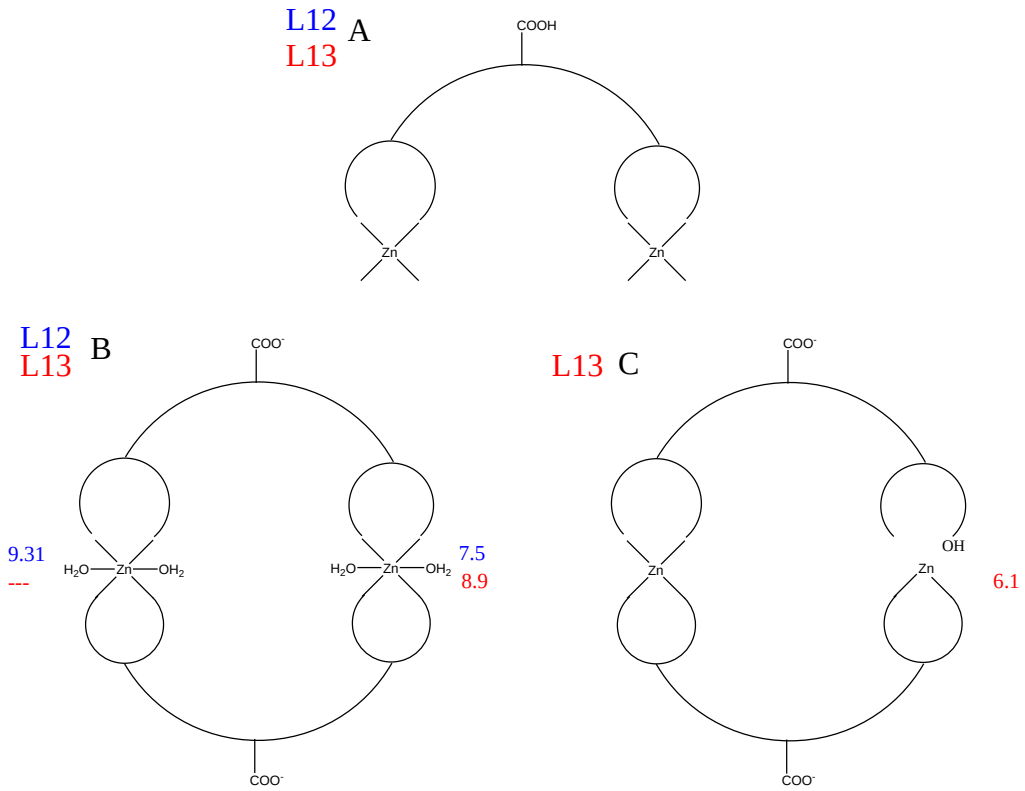

Scheme 14. Hypothesized coordination scheme of L12-L13 ligands with Zn^{2+}.

The first formed complex with the ligands L14 and L15 is the neutral complex $[Zn_2L_2H_2]$ that in the case of L14 loses two protons from the coordinated water molecules with pK 6.5 (Scheme 15), 0.4 units lower than in the free ligand, and in L15 only one proton with pK 7.5. Deprotonation of phenolic protons were not observed at high pH values. At pH 7.4 the species $[Zn_2L_2]^{2-}$ exists in L14, and $[Zn_2L_2H_2]$ and $[Zn_2L_2H]^{-}$ in L15, giving respectively the low pZn^{2+} values 7.7 and 6.4 (Figure 3.60 and Table 3.20).

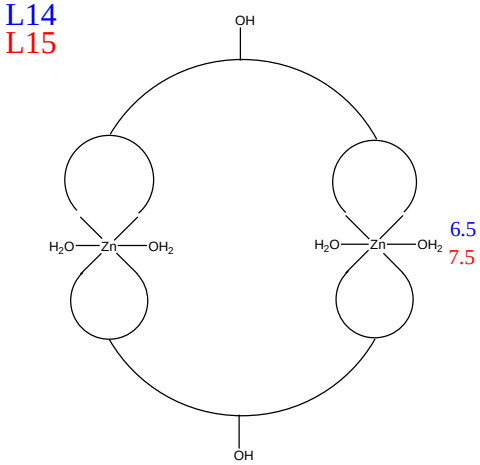

Scheme 15. Hypothesized coordination scheme of L14-L15 ligands with Zn^{2+}.

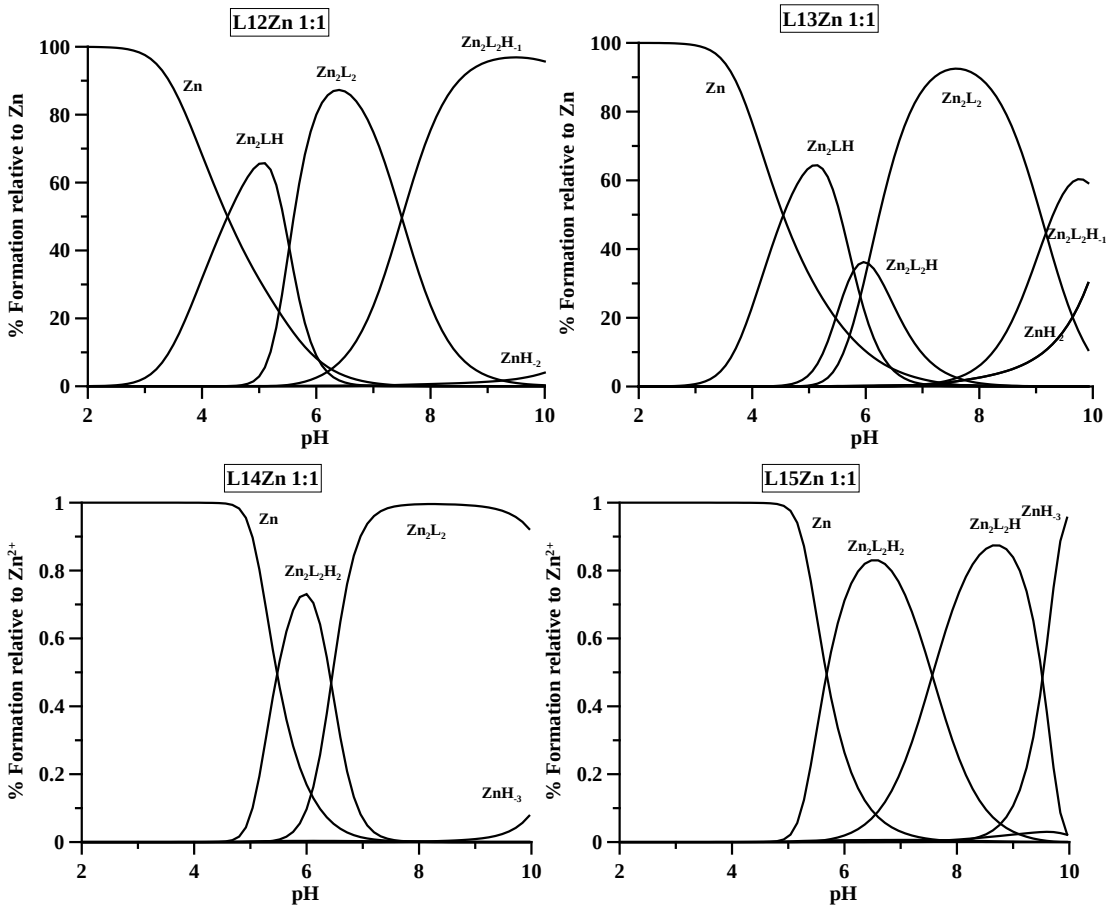

Figure 3.60. Speciation plots of L12-L15 complexes calculated on the basis of stability constants reported in Table 3.20, using a ligand concentration 5 × 10^{-4} M and metal to ligand molar ratio 1:1 . Charges are omitted for simplicity.

For the reaction between $ZnCl_2$ and L12 (Figure A60 and Figure A61), ESI-MS spectra are characterized by the presence of signal deriving from the positively and negatively charged mononuclear complexes: $[Zn(L12_{ox})H_2]^+$ (m/z = 476.972, Figure A60A), $[Zn(L12)H_2]^+$ (m/z = 478.979, Figure A60A) and $[Zn(L12)]^-$ (m/z = 477.096, Figure A61A), $[Zn(L12)H+Cl]^-$ (m/z = 512.952, Figure A61B), $[Zn(L12)H_2+2Cl]^-$ (m/z = 548.920).

The ESI-MS spectra of $ZnCl_2$/L13 system confirm the formation of mononuclear and dinuclear zinc complexes (Figure A62). The signal at *m/z* 478.988 is attributed to overlapping mono e dinuclear $[Zn_2(L13)_2H_4]^{2+}$, $[Zn(L13)H_2]^+$ complexes (Figure A62A). The signals at *m/z* 496.998 and 514.977 are assigned to $[Zn(L13)H_2+H_2O]^+$ and $[Zn(L13)H_2+2H_2O]^+$ complexes respectively (Figure A62B). The signals at *m/z* 496.998 and 514.977 corresponds to $[Zn(L13)H_2+H_2O]^+$ and $[Zn(L13)H_2+2H_2O]^+$ complexes (Figure A62C).

The ESI-MS spectrum of Zn^{2+} complexes with ligand 14 (Figure A63), shows intense signal of free ligand at *m/z* 389.075 and low intensity signal at *m/z* 450.990. This signal is assigned to overlapping complexes with the stoichiometry $[Zn_2(L14)_2H_4]^{2+}$ and $[Zn(L14)H_2]^+$ respectively (Figure A63A).

Electrospray ionization with tandem mass spectrometry (MS/MS) spectrum of the $[Zn_2(L14)_2H_4]^{2+}$ complex shows the formation of hydrated mononuclear complex $[Zn(L14)H_2+H_2O]^+$ with the signal at *m/z* 469.004.

The spectrum of L15 with Zn^{2+} solution (Figure A64) shows the presence of free ligand intensive signal at m/z 389.079 and low intensity signals of the mono e dinuclear complexes. The signal at m/z 450.995 can be attributed to two overlapping $Zn(L15)H_2]^+$ and $[Zn_2(L15)_2H_4]^{2+}$ complexes (Figure A64A), while the signals at m/z 469.006 and 486.977 can be assigned to $[Zn(L15)H_2+H_2O]^+$ and $[Zn(L15)H_2+2H_2O]^+$ (Figure A64) respectively. The *m*/*z* values of the molecular ions are in excellent agreement with the calculated masses.

3.3.3. Complex formation equilibria of L1-L8 ligands[199]

Here is presented the complete characterization of the complex formation equilibria of copper and zinc with the ligands L1-L8 (Scheme 9, previously studied in our research group with Al^{3+} and Fe^{3+} metal ions[33]), together with a speciation study, showing the degree at which the studied ligands interfere on the homeostatic equilibria of these two essential metal ions.

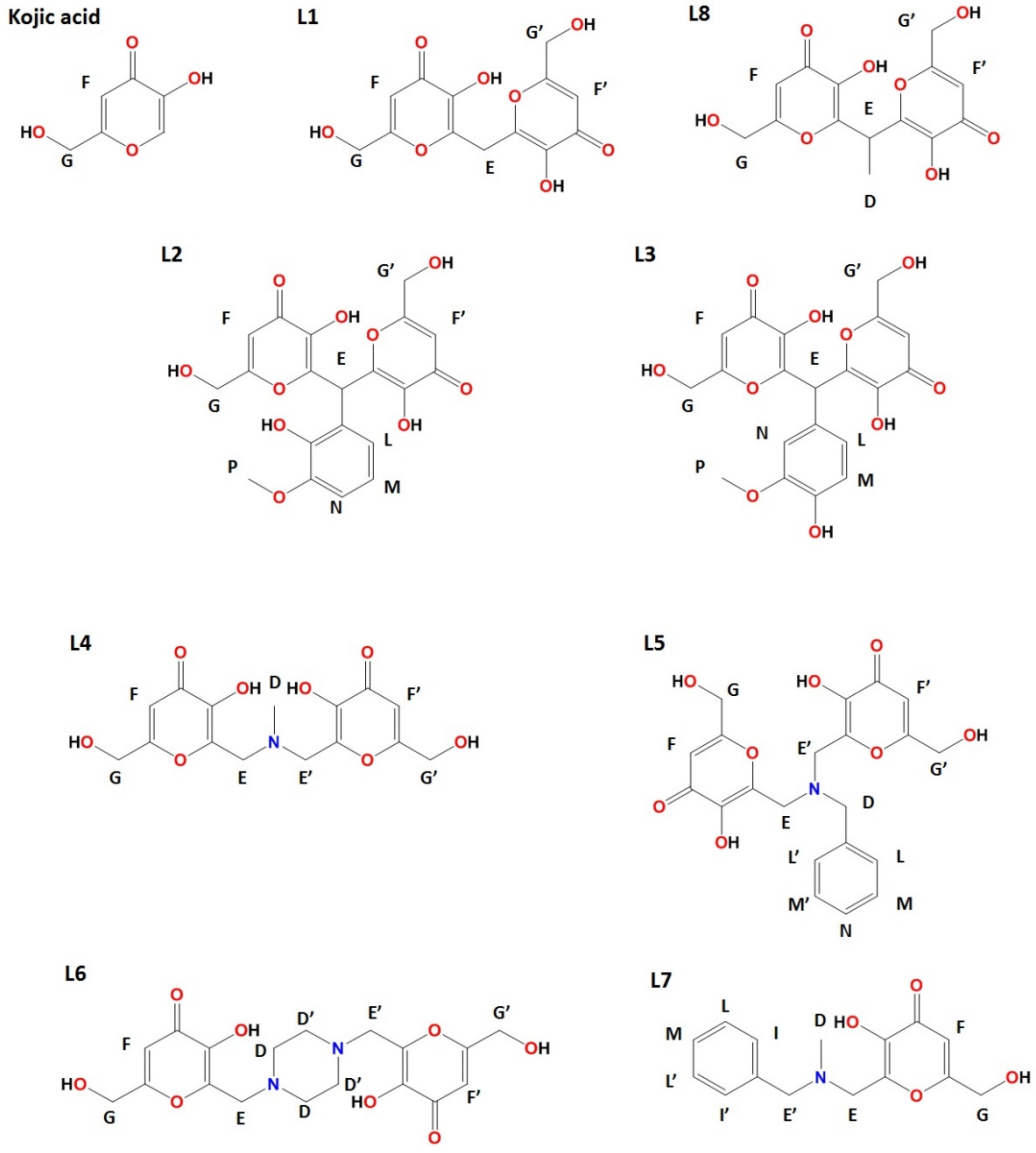

Scheme 16. Molecular structures of L1-L8 ligands.

Ligand protonation constants were previously studied and the logβ and logK values are summarized in Table 3.21.[33],[35],[163],[37],[36]

Table 3.21. Protonation constants of kojic acid (KA) and L1-L8 ligands. [33]

	KA	L1	L2	L3	L4	L5	L6	L7	L8
$logK_1$	7.70	9.48*	10.58	10.18	9.19*	9.01*	8.52*	8.49*	9.49*
$logK_2$		6.59*	8.92*	8.84*	7.51*	7.61*	7.81*	6.02	6.69*
$logK_3$			6.95*	7.21*	4.38	3.35	5.49		
$logK_4$							1.97		
$log\beta_1$	7.70	9.48	10.58	10.18	9.19	9.01	8.52	8.49	9.49
$log\beta_2$		16.07	19.50	19.02	16.70	16.62	16.33	14.51	16.18
$log\beta_3$			26.45	26.23	21.08	19.97	21.82		
$log\beta_4$							23.79		

*logK attributed to the protonation of –OH groups of kojic acid units on the base of spectrophotometric evidence.

The biskojic acid derivatives are symmetric molecules, nevertheless two KA units do not lose their protons contemporary and pKs are different than those of free KA. As remarked in the previous works the pK's for the deprotonations of the two kojic units present an opposite trend: the first one takes place at a lower and the second at higher pK values with respect to that of KA (Figure 3.61).

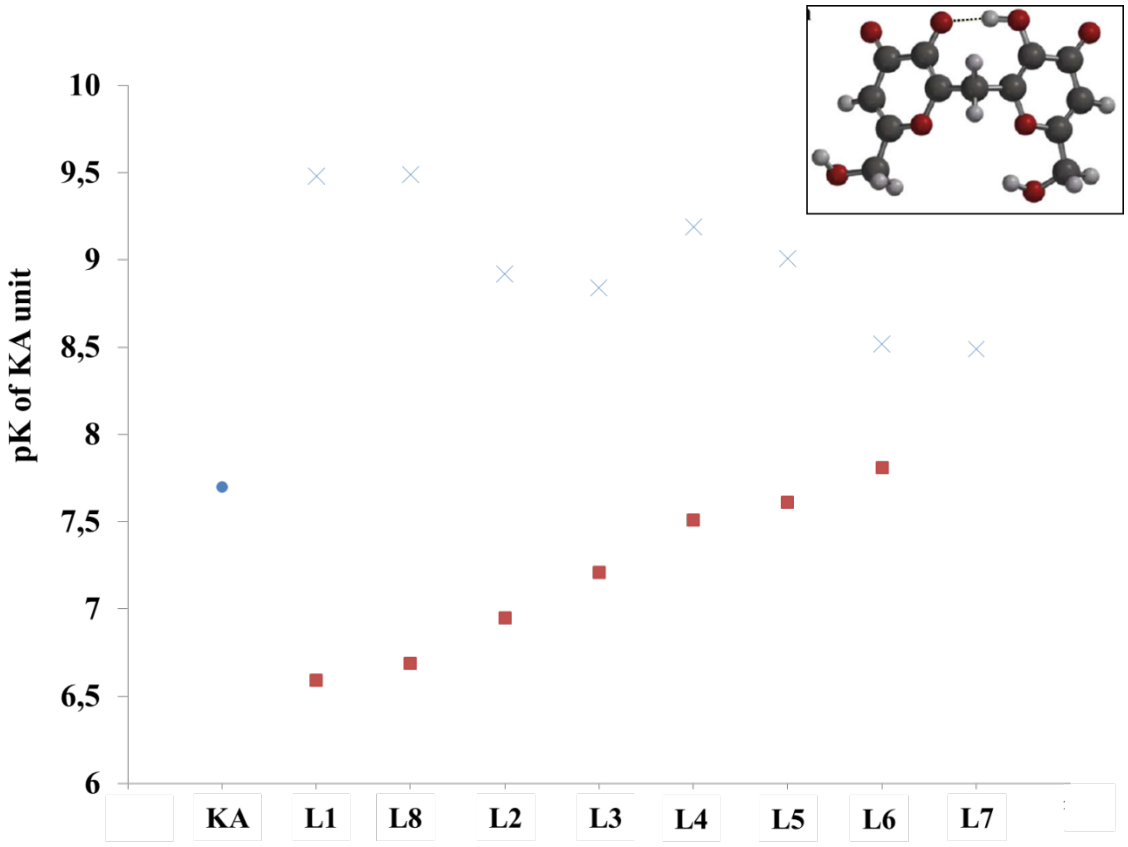

Figure 3.61. Comparison of pK values of kojic acid units of L1-L8 ligands. (●) pK of kojic acid, (X) basic pK, (■) acidic pK.

The presence of two kojic units with two -OH groups leads to a stabilization of the first deprotonation through hydrogen bond, in which the proton is shared between the two $-O^-$ groups. The formation of this hydrogen bond favours the lowering of the first pK and proportionally the increase of the second one (Figure 3.61).

L1 and L8 ligands are two similar kojic acid derivatives, differing by the presence of a methyl group in the linker that determines the different crystal structures of protonated forms described in section 3.1.2. This difference between L1 and L8 in the solid state exists also in solution, as remarked by different NMR trend of the $-CH_2-$ and $-CH_3$ signals in L1 and L8 as a function of pH. The first[33] changes noticeably during the first deprotonation due to the bond rotation to allow the hydrogen bond formation, while $-CH_3$ signal in L8 is practically unaffected by this deprotonation.

Previously studied iron complex formation constants are summarized in Table 3.22. The ligands L1-L3 and L8, with a single carbon in the linker between two KA units, form the most stable iron complexes of 2:2 stoichiometry ($pFe^{3+} \geq 20$). The ligands L4-L6, with longer linker containing nitrogen, form 2:3 complexes of lower stability.

Table 3.22. logβ complex formation constants of Fe^{III} with KA and L1-L8 ligands. [199]

Model	KA	L1	L2	L3	L4	L5	L6	L7	L8
Fe_2L			26.86						
$FeLH_3$							25.25		
$FeLH_2$					22.21	21.9			
FeLH		18.1							18.4
FeL	8.5								
$Fe_2L_2H_4$									
Fe_2L_2H			49.57						
Fe_2L_2		38.14	47.43	48.82					41.11
$Fe_2L_2H_{-1}$		35.05	43.91	45.97					38.97
$Fe_2L_2H_{-2}$		30.37		42.29					
$Fe_2L_3H_4$					69.1		70.3		
$Fe_2L_3H_3$					66.10	67.2	66.2		
$Fe_2L_3H_2$					61.6	64.1	61.2		
Fe_2L_3H					56.19	59.9			
Fe_2L_3					49.75	53.5	49.4		55.08
FeL_2H_2								33.0	
FeL_2H								28.2	
FeL_2	17.04	31.66						22.6	
FeL_2H_{-1}		22.83						15.7	
FeL_2H_{-2}		13.94							
FeL_3	24.15							27.1	
pFe*	13.3	23.1	18.9	22.2	18.1	19.3	17.7	16.7	20.0

***** Negative logarithm of the concentration of the free Fe^{III} in solution, calculated for total [ligand] = 10^{-5}M and total [iron] = 10^{-6}M at pH 7.4.

H_{-n} are referred to hydroxo complexes.

3.3.3.1. Complex formation equilibria with Cu^{2+} and Zn^{2+}

The protonation constants pKs of L1 and L8 are similar[33], nevertheless their complexes with copper ions are different (Figure 3.62A and 3.62B, Table 3.23). L1 forms a mononuclear complex $[Cu(L1)H]^+$ from pH 2, followed by dinuclear complexes $[Cu_2(L1)_2H]^+$, $[Cu_2(L1)_2]$ and $[Cu_2(L1)_2H_{-1}]^-$ starting from pH 3. The hydroxyl group of one of the ligand molecules deprotonates at pH 5.97. As shown in Figure 3.62, $[Cu_2(L1)_2H]^+$, $[Cu_2(L1)_2]$ and $[Cu_2(L1)_2H_{-1}]^-$ species are in equilibrium around pH 6. The $[Cu_2(L1)_2H_{-1}]^-$ and $[Cu(L1)H_{-1}]^{2-}$ complexes are the products of the hydrolysis of $[Cu_2(L1)_2]$ complex above pH 6. With regard to L8, it forms from pH 3 only a dinuclear complex stable even at basic pH, in which both ligand molecules are completely deprotonated. The orientation of two KA in the same direction in the L8 ligand leads to the direct formation of dinuclear complexes. It is likely, that the presence of hydrophobic methyl group in the linker leads to different coordination geometries of dinuclear complex and lowers the access of water in the coordination core preventing the hydrolysis of the $[Cu_2(L8)_2]$ complex. L8 forms dinuclear complexes more stable than corresponding L1 complexes, as previously observed for iron complexes (Table 3.62).

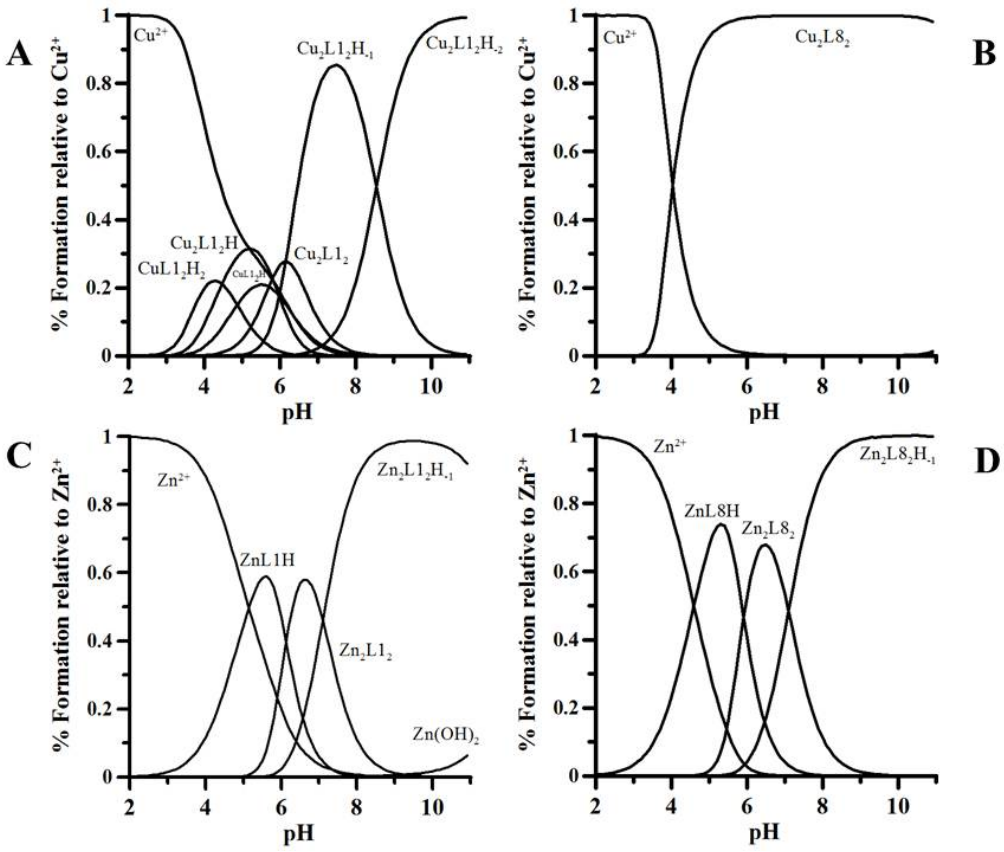

Figure 3.62. Speciation plots of L1 (A and C) and L8 (B and D) complexes calculated on the basis of stability constants reported in Table 3.23 (copper) and Table 3.24 (zinc), using a ligand concentration $4 \cdot 10^{-4}$ M (L1), $8 \cdot 10^{-4}$ M and metal to ligand molar ratio 1:1. Charges are omitted for simplicity.

Table 3.23. Logβ complex formation constants of Cu^{2+} with KA and L1-L8 ligands.

Model	KA	L1	L2	L3	L4	L5	L6	L7	L8
Cu_2L							16.04(2)		
$CuLH_2$									
CuLH		15.4(1)			16.78(4)	16.0(1)		13.50(4)	
CuL	6.6								
$CuLH_{-1}$		3.22(7)			1.79(4)	2.49(7)		-0.91(5)	
$CuLH_{-2}$								-12.10(2)	
$Cu_2L_2H_3$				52.0(7)					
$Cu_2L_2H_2$			47.34(9)	47.4(4)					
Cu_2L_2H		30.57(9)	41.0(2)	41.1(3)	32.3(2)	32.1(1)			
Cu_2L_2		24.6(1)	32.6(2)	32.5(5)	27.81(7)	27.7(1)	23.63(8)		26.9(1)
$Cu_2L_2H_{-1}$		18.1(1)				20.1(1)			
CuL_2H_2								26.43(4)	
CuL_2H								20.33(4)	
CuL_2	11.8							13.43(1)	
pCu*	7.3	9.4	10.2	10.5	10.4	10.0	8.5	7.2	8.8

***** Negative logarithm of the concentration of the free Cu^{2+} in solution, calculated for total [ligand] = 10^{-5}M and total [iron] = 10^{-6}M at pH 7.4.

H_{-n} are referred to hydroxo complexes.

Although L1 and L8 coordinate Zn^{2+} ions in the same mode (Figure 3.62C and 3.62D, Table 3.24), the stability of the L8 complexes is higher (Table 3.24). $[ZnLH]^+$ complexes form with both ligands, from pH 3. They transform in $[Zn_2L_2]$ complexes, from pH 5. The zinc dinuclear complexes are weaker than copper dinuclear complexes and hydrolyze at pH higher than 6. It is likely that the higher stability of L8 complexes with respect to those of L1 depends on the contribution both of inductive and conformational effects of methyl group in the linker.

Table 3.24. Logβ complex formation constants of Zn^{2+} with KA and L1-L8 ligands.

Model	KA[229]*	L1	L2	L3	L4	L5	L6	L7	L8
$ZnLH_2$			24.63(6)						
ZnLH		14.60(8)	18.80(7)	18.7(1)	16.49(6)		15.12(7)	12.3(1)	14.77(5)
ZnL	4.9						8.68(5)		
$ZnLH_{-1}$							-0.74(6)		
$ZnLH_{-2}$								-12.86	
Zn_2L_2H			34.99(8)	33.0(3)					
Zn_2L_2		20.4(2)	27.5(2)	22.9(2)	25.1(1)	20.6(9)			21.1(1)
$Zn_2L_2H_{-1}$		13.3(1)			15.7(2)	15.6(9)			14.0(2)
ZnL_2H								17.5(1)	
ZnL_2	9.1							9.92(6)	
pZn**	6.1	6.6	7.6	7.9	8.8	7.1	7.8	6.1	6.8

***** Studies made at 21^0C degrees.

****** Negative logarithm of the concentration of the free Zn^{2+} in solution, calculated for total [ligand] = 10^{-5}M and total [iron] = 10^{-6}M at pH 7.4.

H_{-n} are referred to hydroxo complexes.

Similarly to L8, other two biskojic derivatives, L2 and L3, form directly dinuclear complexes from pH 3 (Figure 3.63A and 3.63B, Table 3.23). In $[Cu_2L_2H_2]$ complexes, Cu^{2+} ions are coordinated to kojic units, being orto-vanillin and vanillin on the linker still protonated. These groups do not contribute to metal ion coordination and deprotonate at pH 6.3 and 8.4 in the case of orto-vanillin, and at pH 6.3 and 8.6 in the case of vanillin. The difference of Cu^{2+} coordination between these two ligands is that L3 forms $[Cu_2(L3)_2H_3]^+$ complex where one of the hydroxyl group of kojic acid remain protonated until pH 4.6. It is due to the pK_1 of L3 (7.21) higher than that of L2 (6.95). In the consequence pCu^{2+} of L3 (10.5) results slightly higher than that of L2 (10.2) (Table 3.23).

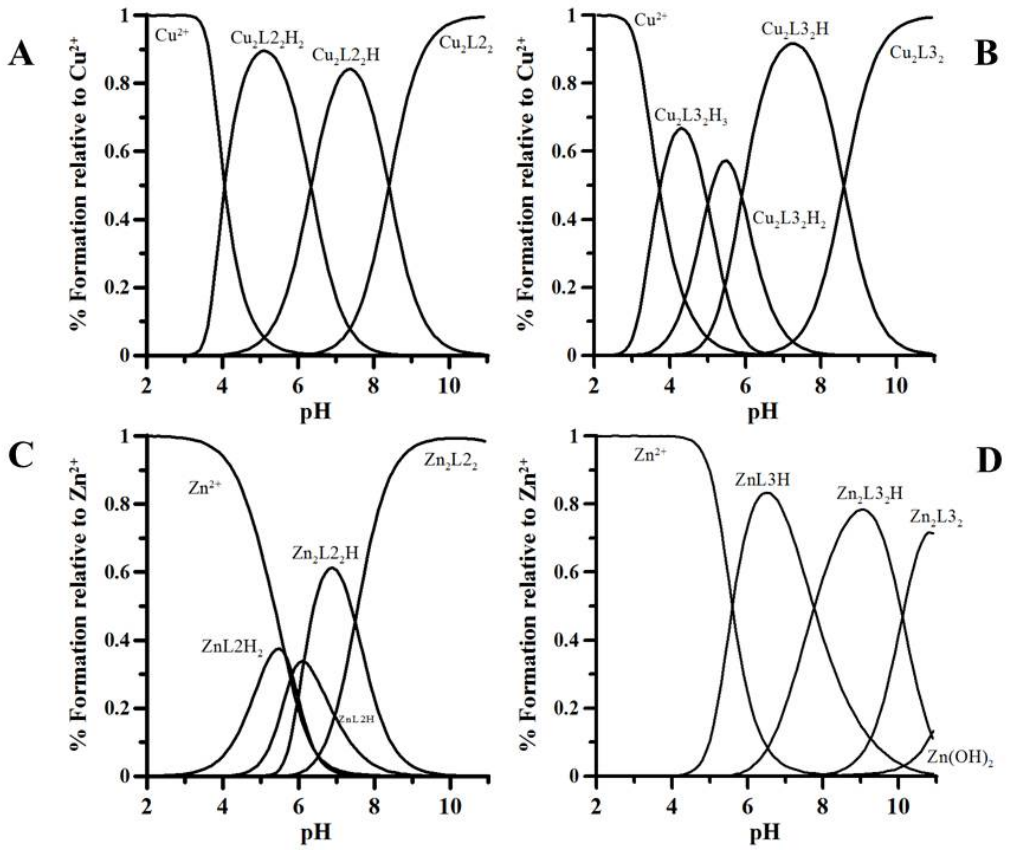

Figure 3.63. Speciation plots of L2 (A and C) and L3 (B and D) complexes calculated on the basis of stability constants reported in Table 3.23 (copper) and Table 3.24 (zinc), using a ligand concentration 5×10^{-4} M and metal to ligand molar ratio 1:1 . Charges are omitted for simplicity.

Zinc coordination by L2 and L3 is weaker than that of copper (Figure 3.63C and 3.63D, Table 3.24). From pH 3 mononuclear complexes $[Zn(L2)H_2]^+$ and [Zn(L2)H] are forming, while formation of [Zn(L3)H] species appears from pH 4. The zinc(II) ion is bound in $[Zn(L2)H_2]^+$ complex only to one KA unit, while the second KA unit remains protonated until pH 5.83 when [Zn(L2)H] is forming. $[Zn_2(L2)_2H]^-$ is a dominant species at pH 7. Although the hydroxyl group of o-vanilin in the linker do not participate the metal coordination it deprotonates at pH 7.49 thus lower than pK_3 of free ligand. The possible explanation may the formation of hydrogen bond between deprotonated hydroxyl group of the linker and $–CH_2OH$ of kojic acid. $[Zn_2(L2)_2]^{2-}$ complex does not hydrolyze even at pH 10. L3 forms directly [Zn(L3)H] from pH 4. Such complexes are replaced by dinuclear complexes $[Zn_2(L3)_2H]^-$ from pH 5. The hydroxyl group of vanillin in the linker do not participate the metal coordination and deprotonate at pH 10.1 (pK_3 10.18). The lack of hydrolysis of dinuclear complexes of L2 and L3 may be explain by the limited access of water molecule into the coordination core, due to the hydrophobic linker between two KA units.

Similarly to L1, L4 and L5 ligands forms from pH 3 [CuLH] complexes, but the remaining proton is bound to the nitrogen (Figure 3.64A and 3.64B, Table 3.23). From pH 3.5 the dinuclear $[Cu_2L_2H]^+$ complexes are formed. The proton of $[Cu_2L_2H]^+$ complexes is bound to the nitrogen, which do not coordinate metal ion, and dissociate at pH ~4. At basic pH occurs the hydrolysis of the dinuclear complexes, that leads to the

decomposition of the complexes. The $[Cu_2(L5)_2]$ complexes are weaker than $[Cu_2(L4)_2]$ and hydrolyze at lower pH. Such an important difference in the complex stability might be explained by the opposite inductive effects of methyl group in L4, and of benzyl group in L5.

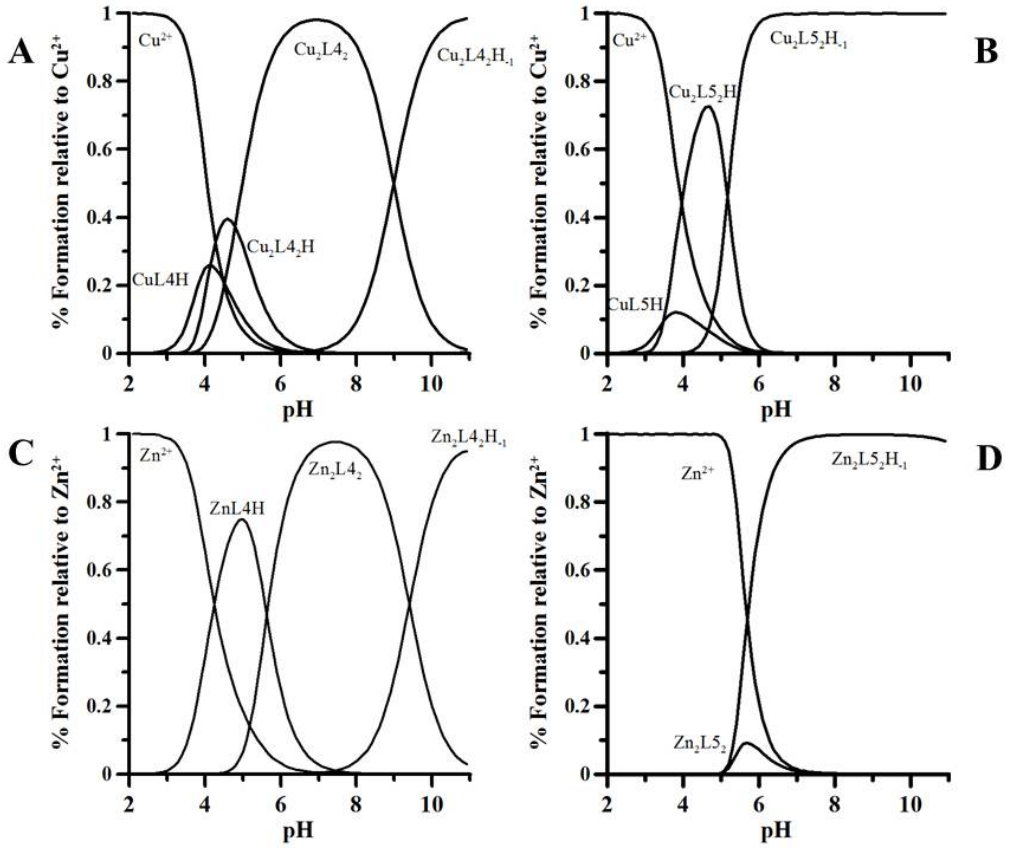

Figure 3.64. Speciation plots of L4 (A and C) and L5 (B and D) complexes calculated on the basis of stability constants reported in Table 3.23 (copper) and Table 3.24 (zinc), using a ligand concentration $5 \cdot 10^{-4}$M and metal to ligand molar ratio 1:1. Charges are omitted for simplicity.

Regarding zinc(II) complexes only L4 forms mononuclear [ZnLH] species (Figure 3.64C, Table 3.24). The dinuclear complex of L4 is stronger than that of L5 and hydrolyze at basic pH, while $[Zn_2(L5)_2]$ complex hydrolyze at pH 6 (Figure 3.64D).

L6 ligand contains two piperazine nitrogen atoms in the linker, which is the longest linker among ligands presented here (Scheme 8). One ligand molecule coordinates two metal ions in the acidic pH (Figure 3.65A). From pH 5 the dinuclear species $[Cu_2(L6)_2]$ forms and is stable even at pH 10. The formation of dinuclear complex $[Zn_2(L6)_2]$ was not observed (Figure 3.65B). L6 forms only mononuclear species $[Zn(L6)H]^+$ from pH 4 that deprotonates at pH 6.4, while at pH 9.4 the hydrolysis of the complex starts.

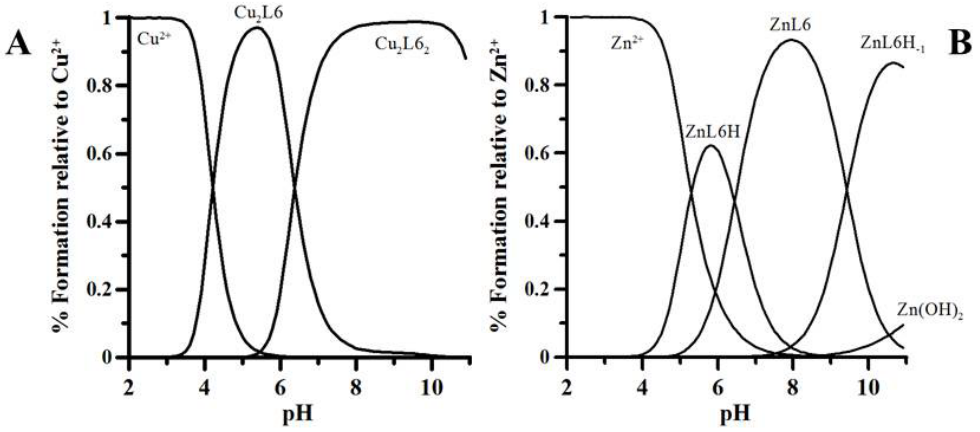

Figure 3.65. Speciation plots of L6 complexes with copper (A) and zinc (B) calculated on the basis of stability constants reported in Table 3 and 4, using a ligand concentration $4 \cdot 10^{-4}$ M and metal to ligand molar ratio 1:1. Charges are omitted for simplicity.

L7 ligand, a step-product in the synthesis of L5, contains only one kojic acid unit and has one nitrogen atom in the linker (Scheme 8). As L5, it forms mononuclear $[Cu(L7)H]^{2+}$ complexes with copper ions from pH 3 (Figure 3.66A), but weaker than that of L5. The explanation is the pK=9.49 of KA unit, which is higher than that of KA unit of L5 (7.61). From pH 5, two L7 ligands coordinate one copper ion in the $[Cu(L7)_2H_2]^{2+}$ complexes. The nitrogen atoms do not coordinate metal and deprotonate at pH 6.1 and 6.9. The $[Cu(L7)_2]$ complex hydrolyze at basic pH.

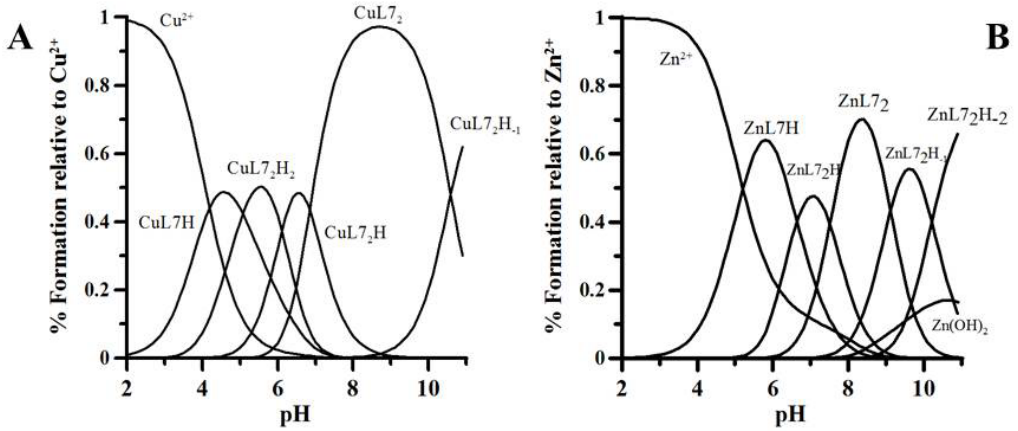

Figure 3.66. Speciation plots of L7 complexes with copper (A) and zinc (B) calculated on the basis of stability constants reported in Table 3.23 and 3.24, using a ligand concentration 1×10^{-3} M and metal concentration 5×10^{-4} M. Charges are omitted for simplicity.

L7 ligand forms from pH 3 weak $[Zn(L7)H]^{2+}$ complexes, which transforms into $[Zn(L7)_2H]^{+}$ complex at pH 5. Similar to copper complexes, nitrogen atom does not coordinate zinc ion and deprotonates at pH 7.51. The stability constants of 1:1 and 1:2 (metal to ligand molar ratio) L7 complexes and higher than that of KA acid [229] (Table 3.24).

The biskojic ligands: L8, L2 and L3 do not have nitrogen in the linker and form directly dinuclear complexes with Cu^{2+} ions at pH 3. L1, in contrary to L4 and L5, does not have

nitrogen in the linker but forms, as they do, first mononuclear 1:1 and then 2:2 complexes. It is likely that the stoichiometry of the formed complexes depends on the orientation of the kojic acid units. The ligands with the limited torsion angles due to short and hydrophobic linker have KA units in the same direction (L2, L3 and L8) and form directly 2:2 complexes with both KA units deprotonated. The ligands with lower steric effects form first 1:1 and then 2:2 complexes.

3.3.3.2. UV-Vis studies

The Cu^{2+} complex formation was studied by UV-Vis spectrophotometry. The UV spectrum from 230 to 370 nm of KA [33] and L7 [163] in the pH range 2-10 were previously reported and there is no absorption of the free ligands above 370 nm. The formation of $[Cu(KA)]^{+}$ in acidic pH is marked on the absorptivity spectrum by a maximum at 780 nm. The band at ~400 nm, assigned as the charge transfer O(phenol)→Cu^{2+} transition [230], confirm the metal coordination to the pair of O-donor atoms, the carbonyl and the vicinal hydroxyl groups of KA (Figure 3.67A). Above pH 5 the $[Cu(KA)_2]$ complex precipitates.

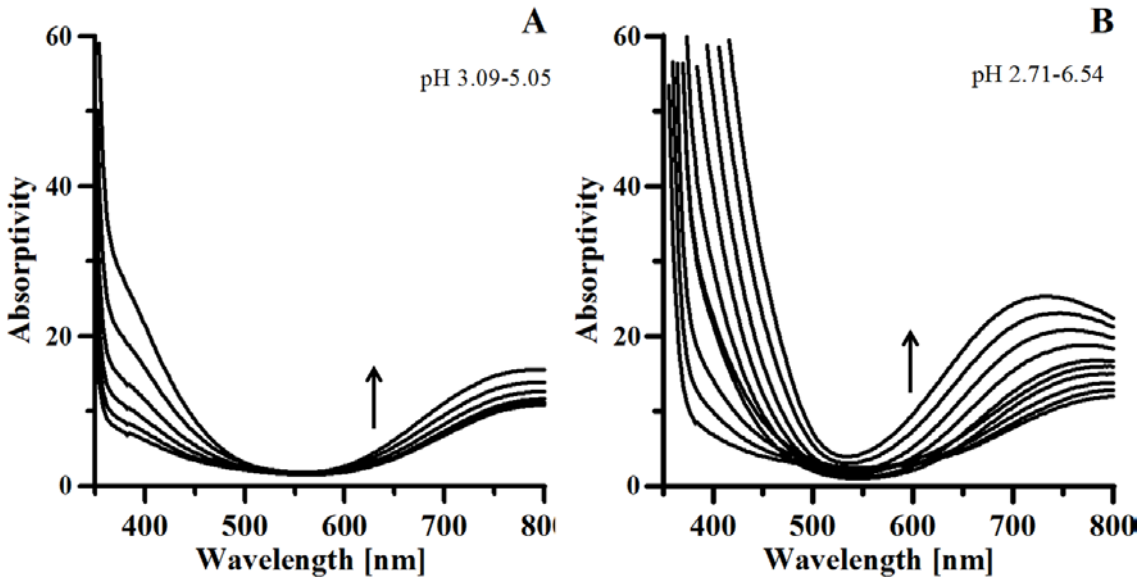

Figure 3.67. UV-Vis spectra of Cu/kojic acid (A) system (1:2 metal/ligand molar ratio) and Cu/L7 (B) system (1:2 metal/ligand molar ratio).

The spectra of copper(II)/L7 system at low pH are the same as spectra of $[CuKA]^{+}$ (Figure 3.67B). It confirms the formation of $[Cu(L7)H]^{2+}$ complex and the metal coordination only by KA unit. The formation of $[Cu(L7)_2H_2]^{2+}$ and $[Cu(L7)_2H]^{+}$ complexes is marked by the hypsochromic shift of the absorptivity maximum from 780 to 750 nm. The absorptivity of $[Cu(L7)_2H_2]^{2+}$ complex is twice of that of $[Cu(L7)H]^{+}$.

3.3.3.3. EPR studies

Due to solubility reasons, only L4, L5 and L7 Cu^{2+} complexes have been studied in water solution by EPR spectroscopy. L4 and L5 ligands show similar behavior towards Cu^{2+} ions. The EPR parameters of the complex with ligand L4, observed in the frozen solution at pH ~3, correspond to mononuclear (S=1/2) species with Cu^{2+} ions, i.e. $[CuLH]^+$ (Table 3.25), ($g_{||}$ = 2.366, $A_{||}$ = 134.65 G) which are in agreement with an axial local symmetry of the Cu^{2+} center. By increasing the pH above 4, a new EPR spectrum of distinctly different form appears. It exhibits the lines corresponding to triplet transitions between S=1 levels splitted in Zero Magnetic Field (ZFS) (Figure 3.68), due to anisotropy of spin-spin interaction in the formed dinuclear complexes.

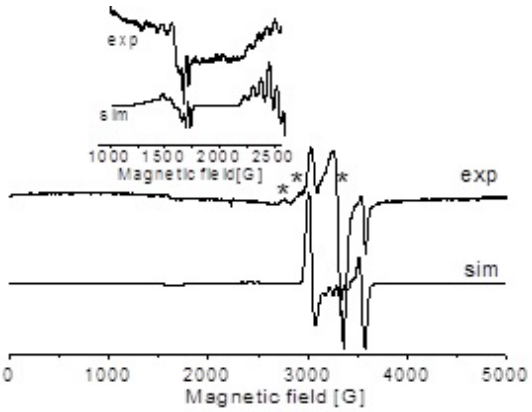

Figure 3.68. The frozen solution EPR spectra (exp) of Cu^{2+}/L4 system and simulated (sim) using the spin Hamiltonian parameters given in the text. In the inset a multiplied magnified fragment portion of the spectrum is shown; (pH 4.32, 77 K; $[Cu^{2+}] = 3 \cdot 10^{-3}$ M, metal to ligand ratio of 1:2). The stars indicate the signals due to S=1/2 mononuclear species.

The formation of dimeric species, predicted by potentiometric data analysis, is also evidenced by the hyperfine splitting (hs) due to the interaction of the unpaired electron with two Cu^{2+} nuclei ($\sum I = 2 \times 3/2$) that leads to seven hs lines, $A_{||}$ = 73 G, which appears about half of $A_{||}$ value for S = 1/2 Cu^{2+} species. The characteristic hyperfine splitting is seen for the two different resonance transitions: the "forbidden" ($\Delta Ms = 2$, at ~1500 G) and the "allowed" ($\Delta Ms = 1$, ~2400 G). The calculated theoretical spectrum (sim) gave the best fit to the experimental spectrum using the S=1 spin Hamiltonian parameters, $g_x = g_y = g_\perp = 2.07$, $g_z = g_{||} = 2.38$, $A_{||}$ = 73 G and $|D| = 0.049 cm^{-1}$. The g tensor components suggest similar coordination sphere to that proposed in the mononuclear complex. A relatively small D value allows to assume that ZFS originates mainly from magnetic dipole-dipole interactions dominating strongly the exchange coupling anisotropy and $D = D_{dip}$. Hence using the point-dipole model it is possible to calculate an approximate value of Cu-Cu distance in the dinuclear species of about 4 Å[231],[232],[233]. The g and A tensors parameters, $g_{||}$ = 2.38 , $g_\perp$ = 2.087 and $A_{||}$ = 135-140 G are very similar to those assigned to the species observed at low pH.

Table 3.25. Spectroscopic characteristic of Cu^{2+} complexes.

Ligand	Species	EPR		
		$A_{\|\|}$	$g_{\|\|}$	$g_{\perp}$
L4	$[CuLH]^{+}$	134.65	2.37	2.09
	$[Cu_2L_2H]^{+}$	73	2.38	2.07
	$[Cu_2L_2]$	73	2.38	2.07
	$[CuLH_{-1}]^{-}$	160.10	2.29	2.09
L5	$[CuLH]^{+}$	133.50	2.37	2.09
	$[Cu_2L_2H]^{+}$	75	2.38	2.07
	$[Cu_2L_2H_{-1}]^{-}$	75	2.38	2.07
L7	$[CuLH]^{2+}$	133.50	2.37	2.09
	$[CuL_2H_2]^{2+}$	151.80	2.32	2.09
	$[CuL_2H]^{+}$	151.80	2.32	2.09
	$[CuL_2]$	151.80	2.32	2.09

$[Cu^{2+}] = 3 \cdot 10^{-3}$ M, Cu^{2+} to ligand ratio of 1:2; for Cu2+aq $A_{||} = 119.4$, $g_{||} = 2.42$.

No dinuclear complexes were observed for L7 ligand. The presence of $[Cu(L7)H]^{2+}$ and $[Cu(L7)_2H_x]^{n+}$ forms was confirmed by EPR spectra, indicating tetragonal coordination around Cu^{2+} ion (Figure 3.69, Table 3.25).

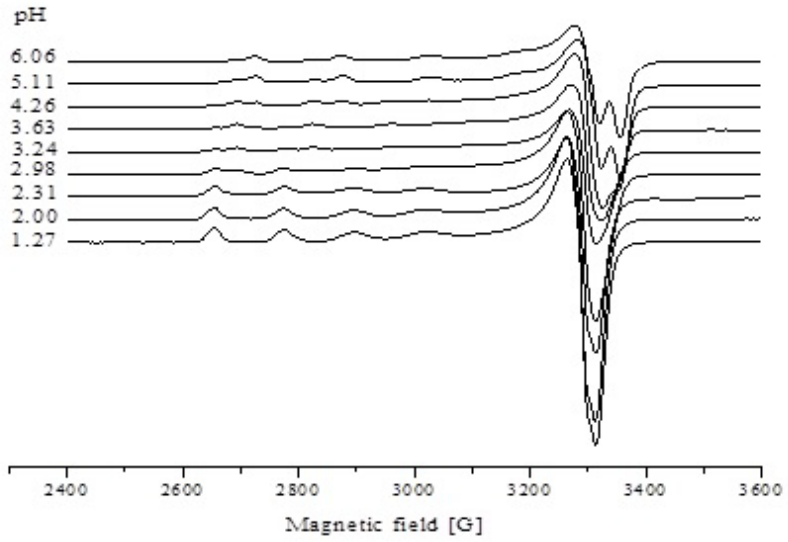

Figure 3.69. EPR spectra of Cu^{2+}/L7 species depending on pH at 77 K; $[Cu^{2+}] = 3 \cdot 10^{-3}$ M, metal to ligand ratio of 1:2.

3.3.3.4. ESI-MS studies

In order to confirm speciation studies, mass spectrometry was used as a complementary technique. It is a powerful tool providing qualitative information on metal complexes formed in solution. This method can be successfully applied to determine the metal-to-ligand stoichiometry directly from the *m/z* values. ESI-MS spectra of copper complexes of L4, L5 and L7 confirm formation of complexes of various stoichiometries. The ESI-MS spectra of the reaction mixture of $Cu(ClO_4)_2$/L4 (Figure A13) is characterized by the presence of few major peaks, attributed to the mononuclear $[Cu(L4)H]^+$ (*m/z* 401.03) and $[Cu(L4)+2Na^+ + Cl^-]^+$ (*m/z* 480.97) species, and dimeric $[Cu_2(L4)_2H]^+$ (*m/z* 803.03) and $[Cu_2(L4)_2+Na]^+$ (m/z 825.01) complexes. The signal at *m/z* 432.49 corresponds to $[Cu_3(L4)_2]^{2+}$ species, and the peak at *m/z* 762.10 indicates the formation of $[Cu(L4)_2H_2+Na^+]^+$ complex. None of these species was detected by potentiometric studies. A comparison between experimental and simulated signals showed an excellent agreement.

For the $Cu(ClO_4)_2$/L5 system (Figure A14), the presence of mononuclear and dinuclear copper complexes is confirmed by the signals at *m/z* 477.05, and 955.07 assigned to $[Cu(L5)H]^+$ and $[Cu_2(L5)_2H]^+$, respectively. The signals at *m/z* 508.51, 892.16 correspond to the $[Cu_3(L5)_2]^{2+}$ and $[Cu(L5)_2H_3]^+$ species.

For the reaction between $Cu(ClO_4)_2$ and L7 (Figure A15), ESI-MS spectrum is characterized by the presence of signal deriving from the complexes with 1:1, $[Cu(L7)]^+$ (*m/z* 337.04) and $[Cu(L7)H+ClO_4^-]^+$ (*m/z* 437.00), and 1:2 $[Cu(L7)_2H]^+$ (*m/z* 612.17) stoichiometry.

The ESI-MS spectra of the reaction mixture of $Zn(ClO_4)_2$/L1 is characterized by the presence of few major peaks (Figure A16), attributed to the mononuclear $[Zn(L1)H]^+$ (*m/z* 340.97), $[Zn(L1)_2H_3]^+$ (*m/z* 655.04) and $[Zn(L1)_2H_2+Na^+]^+$ (*m/z* 677.02), and

dinuclear $[Zn_2(L1)_2H]^+$ (*m/z* 718.95), $[Zn_2(L1)_2+Na^+]^+$ (m/z 740.93), $[Zn_2(L1)_2H_2+ClO_4^-]^+$ (*m/z* 820.90) and $[Zn_2(L1)_3H_3]^+$ (*m/z* 1015.00) complexes. The signal at *m/z* 391.94 corresponds to $[Zn_3(L1)_2]^{2+}$ species, the peak at *m/z* 1078.91 indicates the formation of $[Zn_3(L1)_3H]^+$ complex.

The presence of mononuclear and dinuclear zinc/L2 complexes is confirmed by the signals at *m/z* 481.02, 899.10 and 921.09 assigned to $[Zn(L2)H]^+$, $[Zn(L2)_2H_3]^+$ and $[Zn(L2)_2H_2 + Na^+]^+$ respectively (Figure A17). The signals at *m/z* 513.98 and 963.02 correspond to the $[Zn_3(L2)_2]^{2+}$ and $[Zn_2(L2)_2H]^+$ species.

For the reaction between $Zn(ClO_4)_2$ and L3, ESI-MS spectrum (Figure A18) is characterized by the presence of signal deriving from the complexes with 1:1, $[Zn(L3)H]^+$ (*m/z* 481.02) and 1:2 $[Zn(L3)_2H_3]^+$ (*m/z* 899.10) stoichiometry.

The ESI-MS spectra of $Zn(ClO_4)_2$/L4 system, confirm the formation of mononuclear and dinuclear zinc complexes. The signals at *m/z* 402.02, 741.12 and 805.03 are assigned to $[Zn(L4)H]^+$, $[Zn(L4)_2H_3]^+$ and $[Zn_2(L4)_2H]^+$ respectively (Figure A19). The signal at *m/z* 434.98 corresponds to $[Zn_3(L4)_2]^{2+}$ species, the peak at *m/z* 636.48 indicates the formation of $[Zn_4(L4)_3]^{2+}$ complex.

Also L5 forms the mononuclear and dinuclear species with zinc(II) ions. The signals on the ESI-MS spectrum were attributed to $[Zn(L5)H]^+$ (*m/z* 478.06), $[Zn(L5)H_2 + ClO_4^-]^+$ (*m/z* 578.01), $[Zn(L5)_2H_3]^+$ (*m/z* 893.18) and $[Zn_2(L5)_2H]^+$ (*m/z* 959.09) (Figure A20).

The ESI-MS spectrum of L6 and $Zn(ClO_4)_2$ solution is characterized by the presence of signal deriving from the 1:1 complex $[Zn(L6)H]^+$ (*m/z* 459.06) stoichiometry (Figure A21).

The ESI-MS spectra of the reaction mixture of $Zn(ClO_4)_2$/L8 (Figure A22) is characterized by the presence of few major peaks, attributed to the mononuclear and dinuclear species. The signals at *m/z* 373.00 and 683.06 corresponds to $[Zn(L8)H]^+$ and $[Zn(L8)_2H_3]^+$ species respectively. The formation of dinuclear complexes is confirmed by the signals at m/z 746.97 and 848.93 assigned to $[Zn_2(L8)_2H]^+$ and $[Zn_2(L8)_2H_2 + ClO_4^-]^+$ respectively.

The L1-L8 zinc complexes with stoichiometry 1:2, 3:2 and 4:3 (metal/ligand) molar ratio were not observed in potentiometric studies and may be the products formed only in the ESI-MS conditions.

The ESI-MS spectrum of the $Zn(ClO_4)_2$/L7 system, shows the presence of mononuclear zinc complexes at *m/z* 338.03 and 613.14 assigned to $[Zn(L7)]^+$ and $[Zn(L7)_2H]^+$ respectively (Figure A23).

3.3.3.5. NMR studies

NMR measurements have been used to study the coordination behavior of the ligands in aqueous solution towards the diamagnetic Zn^{2+} ions.

For easiness, all the ligands from L1 to L8 can be gathered into two groups: A) including L1, L2, L3 and L8, and B) including L4, L5, L6 and L7 ligands. The ligands in group A, bear two kojic rings bound together by a methylene bridge as in L1, plus a methyl side chain as in L8, or an o-vanillin or vanillin substituent as in L2 and L3, respectively. The ligands in group B, except L7, are characterized by the presence of nitrogen atoms in the linker between the two kojic acids residues: in particular, an ethylazanediyl bridge in L4 and L5, and a piperazine in L6. In L7 an ethylazanediyl connects one kojic unit to a phenyl ring.

The different structures of the ligands are reflected in the different proton and carbon NMR signals. In Table 3.26 the assignment of ^{1}H and ^{13}C NMR chemical shifts of the free ligands from L1 to L8 in aqueous solution, at physiological pH 7.4 and at 298 K, are reported.

Table 3.26. Assignments of ^{1}H and ^{13}C NMR chemical shifts of free L1-L2-L3-L8 and L4-L5-L6-L7 ligands in aqueous solution at physiological pH 7.4 and 298 K.

$^{1}H\delta$ ppm

Ligand							
L1	**F-F'** 6.422	**G-G'** 4.396	**E** 4.110				
	F-F'	**G-G'**	**E**		**L**	**M**	**N**	**P**
L2	6.495	4.333	6.308		6.745	6.862	6.993	3.785
	F-F'	**G-G'**	**E**		**L**	**M**	**N**	**P**
L3	6.497	4.372	6.073		6.849	6.847	6.987	3.750
	F-F'	**G-G'**	**E**	**D**				
L8	6.422	4.430	4.833	1.560				

$^{13}C\delta$ ppm

Ligand							
L1	**F** 110.050	**G** 60.012	**E** 29.362				
	F-F'	**G-G'**	**E**		**L**	**M**	**N**	**P**
L2	109.840	59.842	38.269		120.986	120.500	112.310	56.298
	F-F'	**G-G'**	**E**		**L**	**M**	**N**	**P**
L3	109.834	59.916	42.386		121.697	115.872	112.993	56.042
	F-F'	**G-G'**	**E**	**D**				
L8	109.891	60.020	NA	11.981				

$^{1}H\delta$ ppm

Ligand							
L4	**F-F'** 6.392	**G-G'** 4.386	**E-E'** 3.766	**D** 2.440			
	F-F'	**G-G'**	**E-E'**	**D**	**L-L'**	**M-M'**	**N**
L5	6.242	4.325	3.868	3.805	7.286	7.255	7.207
	F-F'	**G-G'**	**E-E'**	**D-D'**			
L6	6.469-6.458	4.432	3.725-3.710	3.197-2.797			
	F	**G**	**E-E'**	**D**	**L-L'**	**M-M'**	**N**
L7	6.321	4.377	3.919-3.886	2.488	7.314	7.323	7.314

$^{13}C\delta$ ppm

Ligand							
L4	**F-F'** 109.597	**G-G'** 59.890	**E-E'** 53.005	**D** 43.189			
	F-F'	**G-G'**	**E-E'**	**D**	**L-L'**	**M-M'**	**N**
L5	109.400	59.991	51.728	59.645	129.580	128.360	128.060
	F-F'	**G-G'**	**E-E'**	**D-D'**			

L6	NA	NA	NA	NA			
	F	**G**	**E-E'**	**D**	**L-L'**	**M-M'**	**N**
L7	109.577	60.032	53.015-60.886	41.685	128.714	130.053	128.714

It is possible to see that carbon and proton signals from the two kojic aromatic rings are overlapped, showing that they appear equivalent on the NMR time scale due to their relative rapid reorientation. Actually, a free rotation around all the bonds is also suggested by the diffuse degeneration of the δ values of the groups bearing geminal protons that show no resolution of H–H coupling constants. This behavior occurs in all the solvents used in the NMR analysis (H_2O, DMSO and MeOD), as shown in Figure 3.70 for L2 ligand, by way of example.

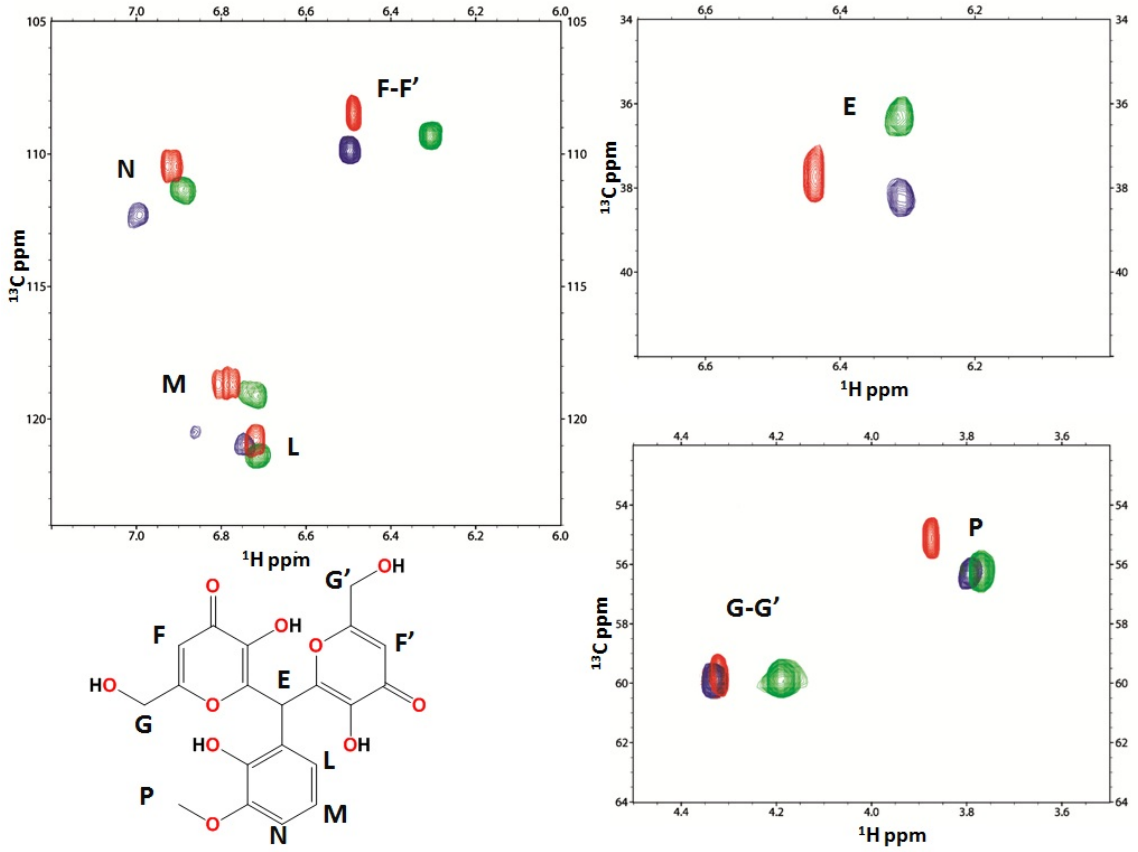

Figure 3.70. Comparison of 2D ^{1}H - ^{13}C HSQC spectra of the free L2 ligand in different solvents: H_2O-D_2O (blue), MeOD (red) and DMSO (green) at 298 K.

Zinc complexes with the ligands included in group A showed in water solution several species in equilibrium among them in the NMR time scale, as already reported in the literature for similar systems[172],[234],[235],[36]. The complexity of the NMR spectra stems from the coexistence of some species with different stoichiometry, as evidenced from the potentiometric study, and probably from isomers with the same stoichiometry but different spatial conformation. An example of this phenomenon is shown in Figure A24 (appendix) for L3:Zn system. A comparable behavior is found for all the ligand in A group including L1, L2, L3 and L8.

The poor water solubility of L5 and L6 ligands gave rise to precipitation in presence of zinc ions and prevented an accurate analysis of the ligand-Zn system in aqueous environment. It was possible to give evidence of the L4 coordination ability toward Zn^{2+} ions, even though the coexistence of several species in equilibrium in the NMR time scale (Figure 3.71). These species are probably in equilibrium also among structural isomers, as confirmed by potentiometric study through which mononuclear and dinuclear species were detected at pH 6.

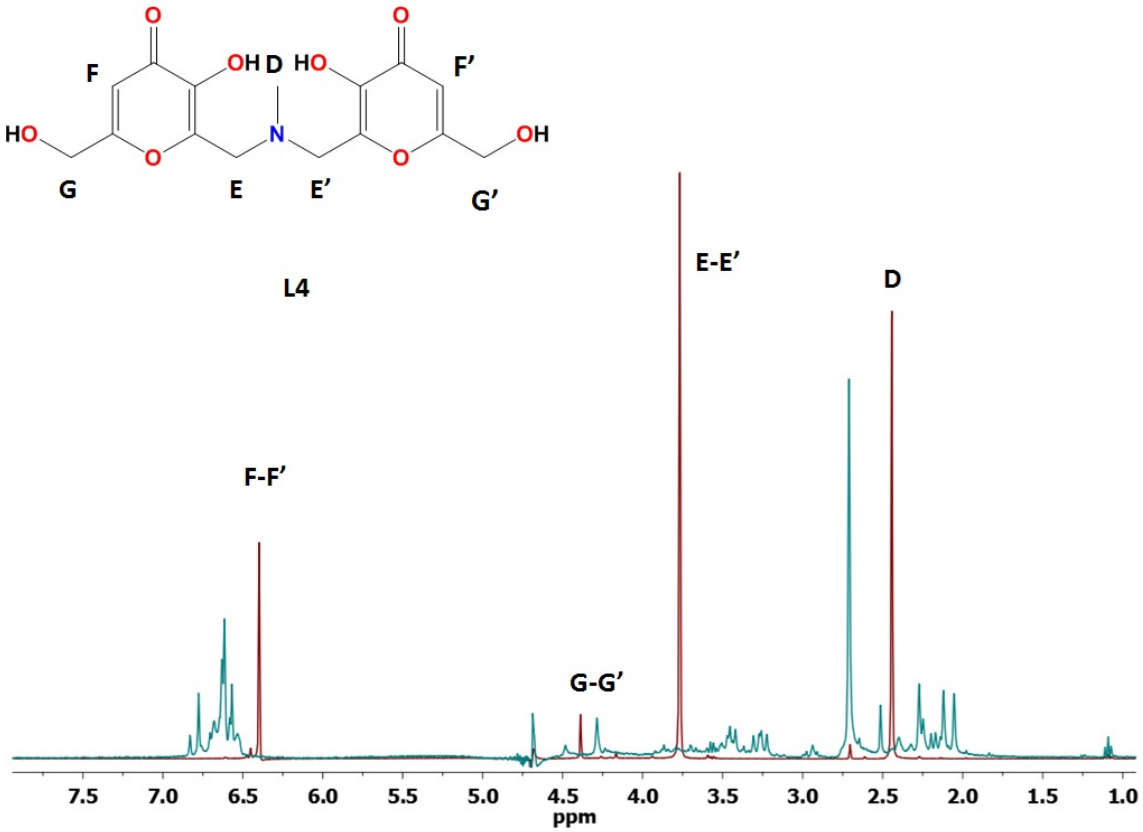

Figure 3.71. Comparison of ^{1}H 1D spectra of L4 free (red) and L4-Zn^{II} system, 1:0.5 molar ratio (blue), at pH 6.

Despite the presence of several species, the general trend of the Δδ changes makes possible to highlight a plausible mode of coordination involving the oxygen atoms from phenolate and carbonylic groups of the kojic ring.

The coordination ability of L7 ligand was analyzed in water solution at pH 4 and 7.2. At acidic pH only $[ZnL7H]^{+}$ complex is formed and mainly affects chemical shift of F proton, and in a lesser extend Δδ of E proton (Figure A25). The 2D 1H-12C spectrum of L7 ligand with Zn^{2+} ions at pH 7.2 (Figure 3.72) shows a new predominant species after Zn^{2+} interaction. The analysis of Δδ variations upon Zn^{2+} addition to the ligand solution resulted in a deshielded environment for G, E and F protons, consistent with a decrease in the electron density in the ring due the metal coordination to O-phenolate and O-carbonylic. The downfield shifts of D and E' protons and carbon nuclei frequency could

be explained by the torsion of metal coordination sphere respect to the rest of the molecule.

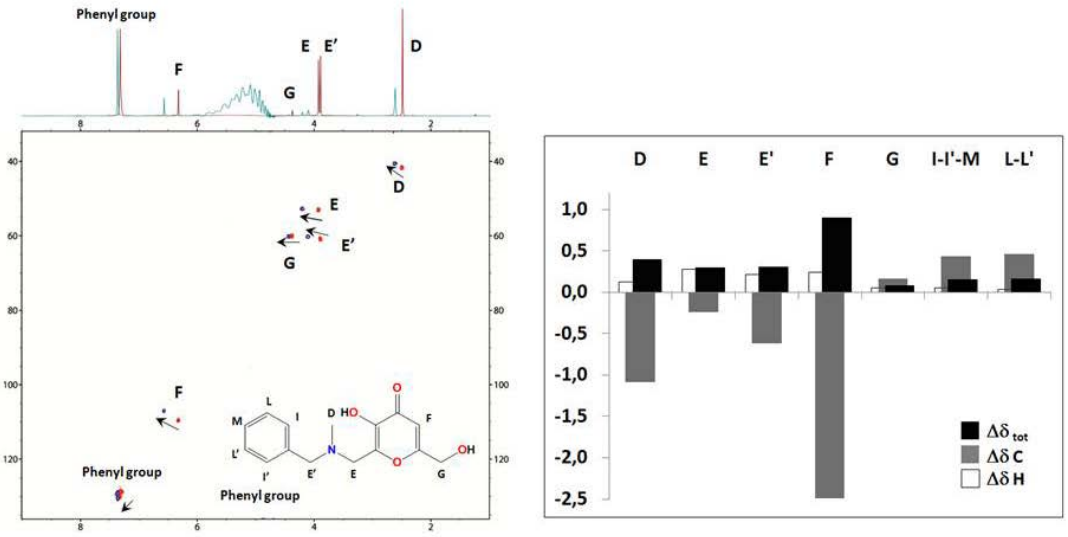

Figure 3.72. Selected aliphatic region of 2D ^{1}H-^{13}C spectrum for the free L7 ligand (red), and L-Zn2+ system, 2:1 molar ratio (blue), in H_2O-D_2O, at pH 7.2. The new resonances of L7 upon Zn^{II} interaction are indicated by arrows and the chemical shifts differences $\Delta\delta = \delta_{bound} - \delta_{free}$ and the combined $\Delta\delta_{tot} = [(\Delta\delta_H)^2+(0.341\cdot\Delta\delta_C)^2]^{1/2}$ are showed in the histogram.

3.3.4. Complex formation equilibria of KβAK ligand[1]

3.3.4.1. Complex formation equilibria with Cu^{2+} and Zn^{2+}

KβAK forms mononuclear complexes with copper ions at pH 2, which become dinuclear complexes at pH 3. The presence of one proton in the $[CuLH]^+$ complex can be attributed to one kojic acid unit, and discards the possibility of ring-closed mononuclear coordination. At pH 6.23, the $[Cu_2L_2]$ complex is formed, while at pH 7.28, 8.83 we observe displacement of protons of the water molecules in the coordination sphere (Figure 3.73). The ESI-MS studies of the copper complexes at neutral pH (Figure A26, S27) confirm the formation of $[CuLH]^+$ and $[Cu_2L_2H]^+$ complexes.

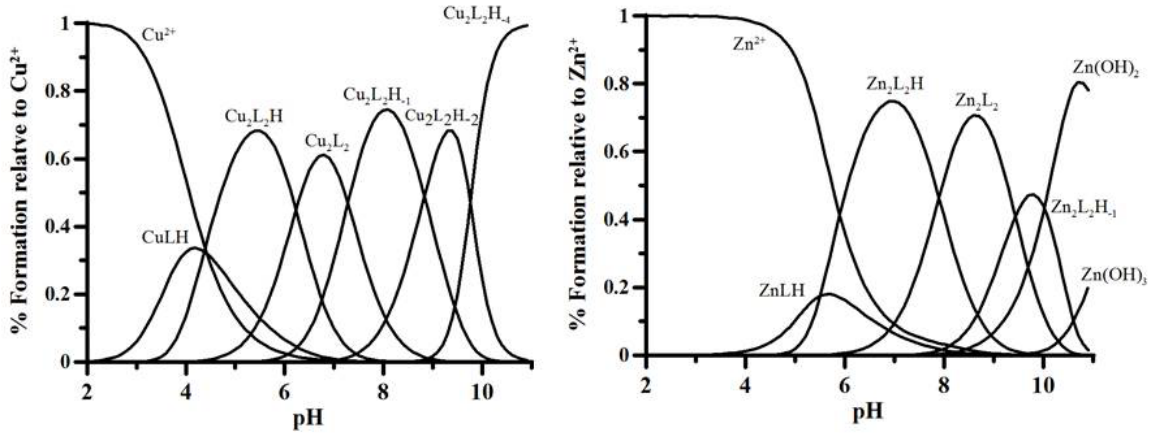

Figure 3.73. Speciation plots of ligands complexes with Cu^{2+} (left) and Zn^{2+} (right) calculated on the basis of stability constants reported in table 2 using $5 \cdot 10^{-4}$M ligand concentration and 1:1 metal to ligand molar ratio. Charges are omitted for simplicity.

The interesting results arising from the ms/ms experiment (Figure A28) with mononuclear complex (442.994 m/z) make it possible to locate the metal ion in the unsymmetrical complex. Figure 3.74 shows the possible fragments that can be obtained from the two different complexes reported as A and Z, respectively. In Table 3.27 and Figure 3.74, with the exception of the A5-Z5 and A6-Z6 pairs, we can see that A1 fragment of the complex is equal to Z1, A2 to Z2 and so forth. A6, Z6 and A5 fragments are not present in the spectrum, while Z5 yields an intensive signal. The presence of Z5 suggests that metal coordination by kojic acid (B) occurs closer to the nitrogen atom. The simulated spectra are in perfect agreement with the observed signals (Figure A27-29, Table A14).

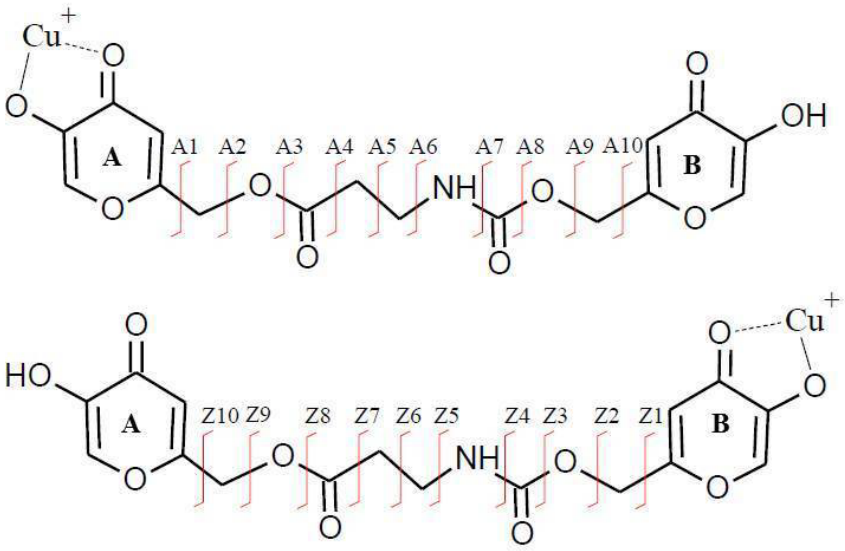

Figure 3.74. Theoretical ms/ms fragments of the CuLH complex (442.997 m/z).

Table 3.27. Signals (m/z values) obtained for the fragments of the $[CuLH]^+$ complex, using a ligand concentration 1·10-4 M and metal to ligand molar ratio 1:1 in H_2O:CH_3OH (50:50) solution, pH 7. * Fragments not present in the spectrum.

Type	*m/z*	Type	*m/z*
A1	172.93*	**Z1**	172.93*
A2	186.94	**Z2**	186.94
A3	202.94	**Z3**	202.94
A4	230.93	**Z4**	230.93
A5	244.95*	**Z5**	245.95
A6	258.97*	**Z6**	259.96*
A7	273.98	**Z7**	273.98
A8	301.97	**Z8**	301.97
A9	317.97	**Z9**	317.97
A10	331.98*	**Z10**	331.98*

The stoichiometry of the zinc complexes is not different from that of copper complexes (Figure 3.73), although the zinc complexes are weaker (Table 3.28). The pZn (6.1) value is much lower than pCu (8.3). $[ZnLH]^+$ complexes start to form at pH 4, whereas $[Zn_2L_2H]^+$ complexes start to form at pH 5. At pH 7.9, the $[Zn_2L_2]$ complex is formed and at pH 9.44 water molecules in the coordination sphere are deprotonated. The mono- and dinuclear complexes were confirmed by the ESI-MS experiments (Figure A30). The ms/ms experiment (Figure A31) with $[ZnLH]^+$ complex (443.99 m/z) shows the coordination of zinc ions by the B kojic acid unit (Table A15, Figures S32,S33).

Table 3.28. Stability constants of metal complexes calculated with HyperQuad program at 25°C and 0.1 M KCI ionic strength using the ligand concentration 5·10−4 M and metal to ligand molar ratio 1:1. Charges are omitted for simplicity. Protonation constants of the ligands and overall stability constants (log βpqr) of the metal complexes were calculated by using eqs: pM + qH + rL = MpHqLr, βpqr =([MpHqLr])/([M]p[H]q[L]r).

Model	Fe^{3+}	Al^{3+}	Cu^{2+}	Zn^{2+}
MLH	18.7(1)[a]	15.75(2)[a]	15.03(7)[a]	13.07(5)[a]
M_2L_2H	-	30.32(8)[a]	29.23(4)[a]	24.45(2)[a]
M_2L_2	35.3(1)[a]	26.09(3)[a]	23.00(4)[a]	16.55(3)[a]
$M_2L_2H_{-1}$	32.12(9)[a]	20.4(2)[a]	15.72(4)[a]	7.11(4)[a]
$M_2L_2H_{-2}$	28.06(5)[a]	16.01(2)[a]	6.89(4)[a]	-
$M_2L_2H_{-3}$	21.00(4)[a]	8.87(3)[a]	-	-
$M_2L_2H_{-4}$	12.35(4)[a]	0.73(3)[a]	-12.63(6)[a]	-
$M_2L_2H_{-6}$	-7.51(5)[a]	-18.3(2)[a]		
pM*	**18.5**	**12.7**	**8.3**	**6.1**

H_{-n} are referred to hydroxo complexes. [a] Standard deviation values were calculated by the HyperQuad2013 program.

* Negative logarithm of the concentration of the free metal in solution, calculated for total [ligand] = 10^{-5}M and total [metal] = 10^{-6}M at pH 7.4.

3.3.4.2. Iron and aluminium complexes

The ligand starts forming monomeric complexes with iron ions at pH lower than 1. Their presence is indicated by the spectra within the range of 400-700 nm (Figure 3.75). The values for absorptivity with maximum absorption at 500 nm correspond to those of kojic acid complexes, confirming the formation of mononuclear complex. At pH 2, dinuclear complexes form with water molecules in the coordination sphere. In ESI-MS spectrum (Figure A34) we can observe an intensive signal at 434.995 m/z corresponding to $[Fe_2L_2]^{2+}$ complex (Figure A34, Panel A) and a low intensity signal at 453.005 m/z corresponding to $[FeL(H_2O)]^{+}$ complex (Figure A34, Panel B). The signal indicating $[FeL(H_2O)]^{+}$ could refer to a breakdown product of the $[Fe_2L_2(H_2O)_2]^{2+}$ complex (Figure A34 Panel D) that we observe deprotonated at neutral pH.

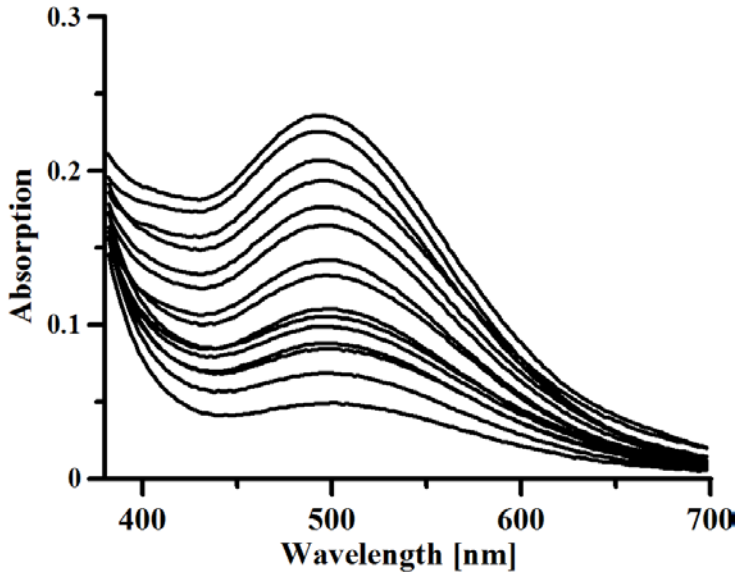

Figure 3.75. Spectra of the $[FeLH]^{2+}$ complex in a pH range of 0.80-2.10 obtained using $5 \cdot 10^{-4}$M ligand concentration and 1:1 metal to ligand molar ratio and 1 cm path length.

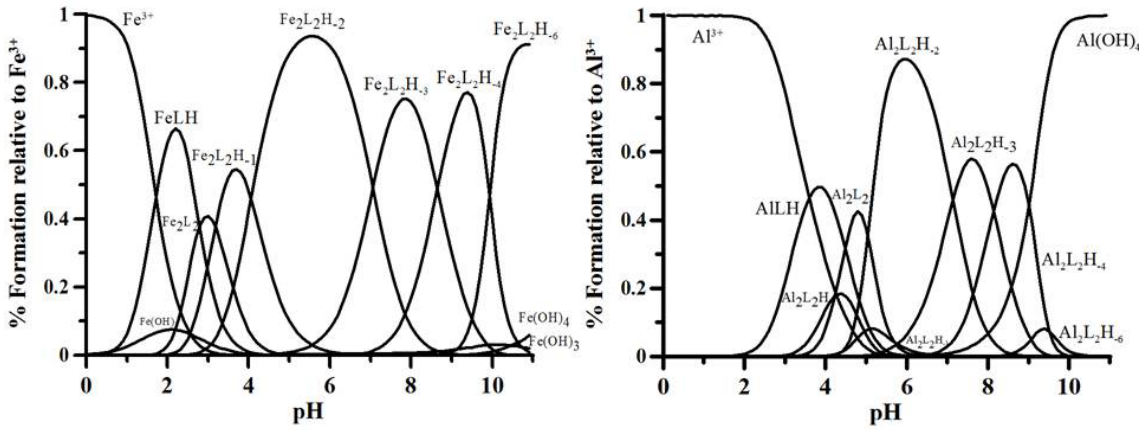

Figure 3.76. Speciation plots of ligand complexes with iron(III) (left) and Al3+ (right) calculated on the basis of stability constants reported in Table 3 using $5 \cdot 10^{-4}$M ligand concentration and 1:1 metal to ligand molar ratio. Charges are omitted for simplicity.

The stoichiometry of aluminium complexes is the same as that of iron complexes, although the pAl value (12.7) is lower than the pFe value (18.5) (Table 3.28). The mononuclear complex $[AlLH]^+$ exists from pH 2 to pH 6 (Figure 3.76). The dinuclear complex $[Al_2L_2H]$ starts to form at pH 3 and at pH 4.3 loses its last proton. The presence of mono (single charged) and dinuclear (double charged) complexes is confirmed by two overlapping signals at 406.039 m/z in the ESI-MS spectrum (Figure A35, panel A). Two of the coordination water molecules in the coordination sphere are forming most likely bridges between two aluminium ions. In the ESI-MS spectrum (Figure A35) we observe a signal at 424.050 m/z for $[AlL(H_2O)]^+$, which confirms the importance of water in the complex structure. The signal corresponding to $[AlL(H_2O)]^+$ could indicate a breakdown product of the $[Al_2L_2(H_2O)_2]^{2+}$ complex that we observe deprotonated at neutral pH.

3.3.5. Complex formation equilibria of SC ligand

3.3.5.1. Complex formation equilibria with Fe^{3+}

The complex formation equilibria were studied by simultaneous spectrophotometric-potentiometric measurements, both on a set of solutions at different concentrations of HCl from pH 0.4 to pH 2.6, and from basic titrations starting from pH 2.7. Some spectra collected during these titrations are presented in Figure 3.77. When pH increases from 0.4 to 2 (red curves), a wide band appears at ~500 nm attributable to the complex $[Fe(SC)H_5]^{5+}$ on the basis of its similarity with the spectra of 1:1 iron complex with kojic acid[33]. When pH increases from 2 to 3.2, a new band appears at 479 nm, attributed to the formation of $[Fe(SC)H_4]^{4+}$, where two units of KA coordinate one Fe^{3+} ion, for the similarity in wavelength of maximum and absorptivity with the spectra of the 1:2 Fe:KA complex[33]. After pH 3.2 (blue curves) a new band at 395 nm increases with an isosbestic point at 485 nm. This band corresponds to the formation of the complex $[Fe(SC)H_3]^{3+}$ and Fe^{3+} is coordinated by all the three KA units, for similarity in wavelength of maximum and absorptivity with the spectra of the 1:3 Fe:KA complex[33]. At pH 7.3 (green curves) the complex deprotonates and at pH > 8.5 precipitations of the neutral Fe(SC) complex occurs.

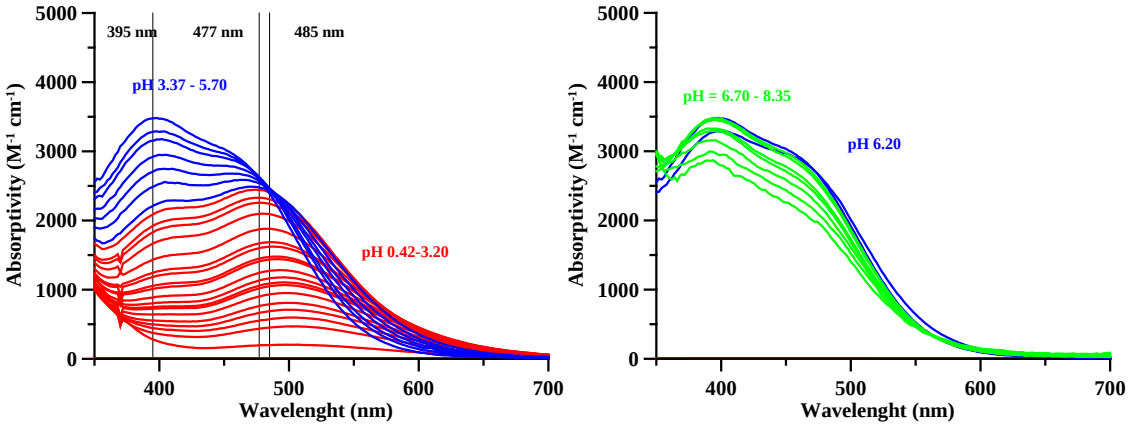

Figure 3.77. Some spectra of the titration of Fe3+:SC 1:1 Me/L molar ratio [SC] = $2.36 \cdot 10^{-4}$ M, at 0.1 M NaCl ionic strength and 25 °C, 1cm optical path length. Red curves, pH 0.42-3.20; Blue curves, pH 3.37-6.20; Green curves, pH 6.70-8.35.

By simultaneous fitting of the potentiometric and spectrophotometric data the stability constants in Table 3.29 were obtained. The first deprotonation of the $[Fe(SC)H_3]^{3+}$ complex occurs with pK 7.50 and the second and the third deprotonations occur simultaneously with pK 8.63. These values are lower than those of the free ligand (9.00, 9.62 and 10.97) for the different charges of complex and free ligand (3+ and 0 respectively). In Figure 3.78 the related speciation plot is reported.

Table 3.29. Stability constants of metal complexes calculated with HyperQuad program at 25°C and 0.1 M NaCI ionic strength using the ligand concentration [SC] = $2.36 \cdot 10^{-4}$ M and metal to ligand molar ratio 1:1.

Species	Logβ	pK
$[Fe(SC)H_5]^{5+}$	53.5 (6)	-
$[Fe(SC)H_4]^{4+}$	52.12 (7)	1.38
$[Fe(SC)H_3]^{3+}$	48.12 (4)	4.00
$[Fe(SC)H_2]^{2+}$	40.62 (4)	7.50
Fe(SC)	23.37 (5)	8.63
pFe^{3+}	**18.4**	

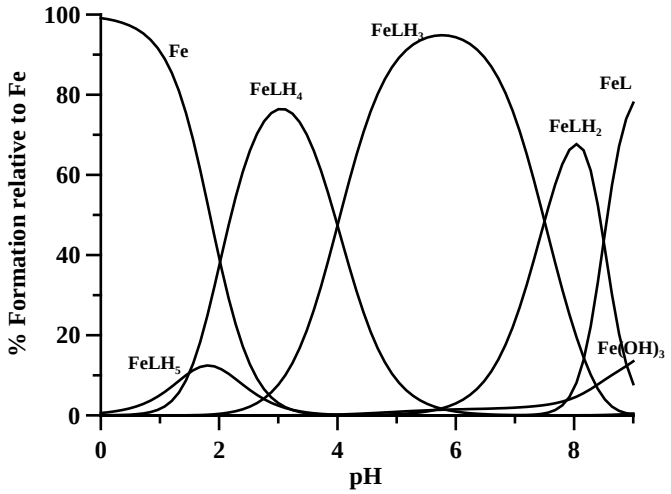

Figure 3.78. Speciation plots of SC complexes with Fe^{3+} calculated on the basis of stability constants reported in Table 3.29 using $2.36 \cdot 10^{-4}$ M ligand concentration and 1:1 metal to ligand molar ratio. Charges are omitted for simplicity.

3.3.5.2. Complex formation equilibria with Ga^{3+}

The study of formation of Ga^{3+} complexes with SC by use of direct potentiometry was hindered by the complete formation of complexes at the starting of the titration, so the study of the Ga^{3+}:SC system required spectrophotometric measurements. Thus, the overall stability constants of the Ga^{3+} complexes with SC were studied by spectrophotometric measurements on a set of solutions from pH 0.11 until pH 12, and by potentiometric titrations. Some of the collected spectra are presented in Figure 3.79.

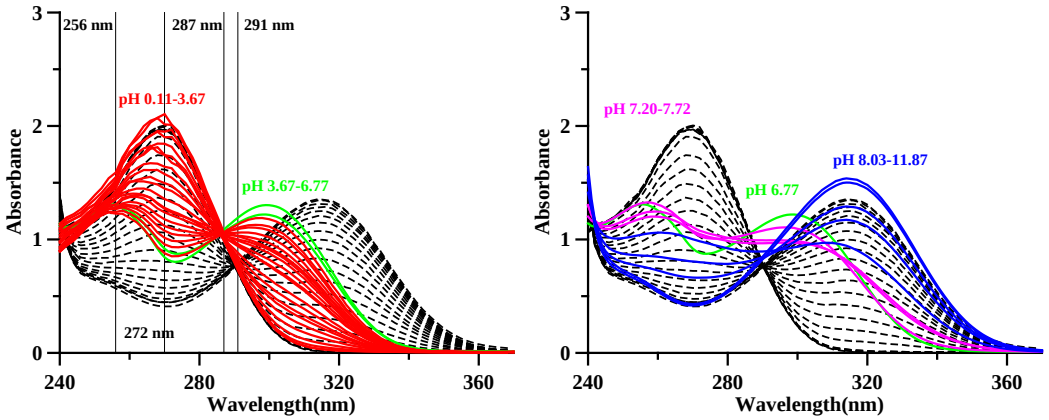

Figure 3.79. Some absorbance spectra of the titration of Ga^{3+}:SC 1:1 Me/L molar ratio [SC] = $9.86 \cdot 10^{-5}$ M, at 0.1 M NaCl ionic strength and 25 °C, 1 cm optical path length (red, green, violet and blue curves), overlapping to the normalized free ligand SC spectra collected during a simultaneous potentiometric-spectrophotometric titration.

Because of the completely filled d shell of the Ga^{3+} ion, it was not possible to perform spectrophotometric measurements in the visible region of the spectra. However, it was possible to take advantage of the spectral changes in the ultraviolet region, were the ligand absorbs.

Figure 3.79 shows some spectra of the Ga^{3+}-SC complex (1:1 molar ratio, [SC] = $9.86 \cdot 10^{-5}$ M) collected during the spectrophotometric titrations, overlapping to the spectra of free SC collected as discussed in section 3.2.7. Starting from very acidic pH, various differently protonated 1:1 complex are formed. Starting from pH 0.11, the band at 272 nm, corresponding to the fully protonated ligand starts to decrease and in the meantime two new bands, at 305 nm and at 256 nm, appear with the shift of the characteristic isosbestic of SC ligand from 291 nm to 287 nm. This trend can be observed until pH 7.5. Some sort of dissociation of the metal ion from the chelating groups takes place above pH 7.5. At pH > 8.03 the spectra of the chelate become similar to those of the free ligand (with a maximum at 315 nm), as shown in Figure 3.79, not accompanied by precipitation phenomena. This spectral behaviour, together with the potentiometric results, indicate the possible dissociation of some chelating KA moieties from Ga^{3+} and the formation of complex hydroxo-species avoiding the precipitation of the metal hydroxides. The calculated complex formation constants (the first three from the spectral results and the following from the titration data) are reported in Table 3.30 together with the corresponding pK's.

Surely the pK 4.98 correspond to the formation of a hydroxo-compound, and presumably the last three (8.67 for two protons and 9.80) are relative to the deprotonation of the charged nitrogen atoms. The remaining pK's are difficult to be attributed because they depend both on the formation of hydroxo-compounds and on the deprotonation of the OH group of the KA units, no more bounded to Ga^{3+}.

Table 3.30. Stability constants of metal complexes calculated with HyperQuad program at 25°C and 0.1 M NaCI ionic strength using the ligand concentration [SC] = $4.88 \cdot 10^{-4}$ M and metal to ligand molar ratio 1:1.

Species	Logβ	pK
$[Ga(SC)H_5]^{5+}$	53.0	
$[Ga(SC)H_4]^{4+}$	50.5	2.5
$[Ga(SC)H_3]^{3+}$	47.46 (4)	3.04
$[Ga(SC)H_2]^{2+}$	42.48 (3)	4.98
$[Ga(SC)H]^{+}$	34.88 (3)	7.60
$[Ga(SC)H_{-1}]^{-}$	18.67 (3)	8.105
$[Ga(SC)H_{-3}]^{2-}$	1.33 (3)	8.67
$[Ga(SC)H_{-4}]^{3-}$	-8.47 (4)	9.8
pGa^{3+}	20.2	

The decomposition of the spectra collected during the spectrophotometric Ga^{3+}-SC titration in the Gaussian components (Figure 3.80) shows that from acidic pH the $[Ga(SC)H_5]^{5+}$ species is formed and one kojic acid unit is coordinating Ga^{3+} ion, while at pH 3.5 the third proton from KA units is lost, and from pH 7.6 the complex start to hydrolyze and the band of the totally deprotonated kojic acid reaches its maximum confirming that at least one or two KA units are no more involved in Ga^{3+} coordination. Figure 3.80 shows the speciation plots of the Ga^{3+}-SC system calculated by the stability constants in Table 3.30.

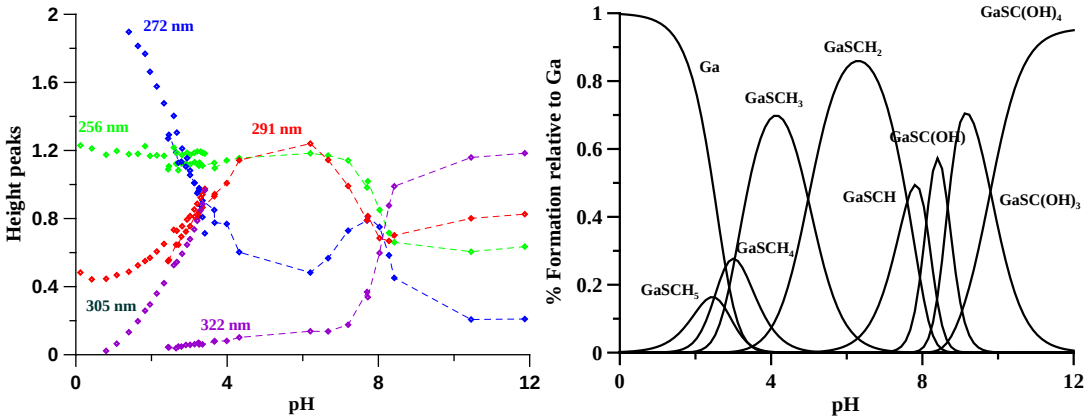

Figure 3.80. A) Peak heights obtained by spectral decomposition *vs.* pH using Specpeak program[206]. B) Speciation plots of SC complexes with Ga^{3+} calculated on the basis of stability constants reported in Table 3.30 using $9.86 \cdot 10^{-5}$M ligand concentration and 1:1 metal to ligand molar ratio. Charges are omitted for simplicity.

3.3.6. Complex formation equilibria of Losartan and Irbesartan ligands

3.3.6.1. Cu^{2+} and Zn^{2+} complexes formation equilibria

The complex formation equilibria with Cu^{2+} and Zn^{2+} were studied potentiometrically in a 80:20 MeOH/H_2O solution due to the low solubility of the formed complexes both in water and 30:70 MeOH/H_2O solution. The studies were carried out at 0.5 mM ligand concentration in 1:2 and 1:4 metal/ligand molar ratios. At 1mM ligand concentration complex precipitation occurrs. The results are reported in Table 3.31.

Table 3.31. Complex formation constants, logβ_{pqr} and pM values at 25.0 °C and 0.1 M NaCl ionic strength in 80:20 MeOH:H_2O solution. The charges are omitted for the simplicity.

Specie	Irbesartan	Losartan
LH	4.98(1)	5.07(1)
LH_2	3.25(1)	2.56(1)
CuL	-	4.12(7)
CuL_2	6.89(3)	7.1(3)
CuL_2H_{-1}	-	2.40(9)
CuL_2H_{-2}	-4.03(1)	-3.6(4)
pCu^{2+}	6.7	7.4
ZnL	-	3.7(1)
ZnL_2	-	6.2(1)
ZnL_2H_{-1}	0.42(8)	0.4(2)
ZnL_2H_{-2}	-6.51(4)	-6,69(8)
pZn^{2+}	6.0	6.0

In the following we indicate with I and L the completely deprotonated forms of Irbesartan and Losartan. A weak [CuI_2] complex is formed between Irbesartan and copper ions from pH 4, replaced by a [CuI_2H_{-2}] complex from pH 5 (Figure 3.81A). Zinc forms with Irbesartan weaker complexes than copper with the same stoichiometry (Figure 3.81B, Table 3.31).

The Cu^{2+}/Losartan complexes are slightly stronger than those with Irbesartan (Table 3.31). A 1:1 Cu/Losartan complex is already formed from pH 2.5, replaced by 1:2 differently protonated complexes (Figure 3.81C). Also in this case, zinc complexes weaker than those of copper, with the same stoichiometry, are formed from pH 3 (Figure 3.81D).

Precipitation of copper complexes in 80:20 MeOH/H_2O solution starts at pH~5, while zinc complexes precipitate above pH 7.5. The low solubility of copper complexes can

be attributed to the formation of the dimeric $[Cu(Ligand)_2(H_2O)_3]_2$ complex synthesized and characterized by Etcheverry et al.[236] Their FTIR and Raman studies demonstrated that copper ion in $[Cu(Ligand)_2(H_2O)_3]_2$ complex is coordinated to the ligand through the nitrogen atoms of the tetrazol moieties. The formation of a dimeric complex was revealed by EPR measurements at room temperature. The metal centers are in a tetragonal distorted environment. Minor amounts of a monomeric complex are also present.

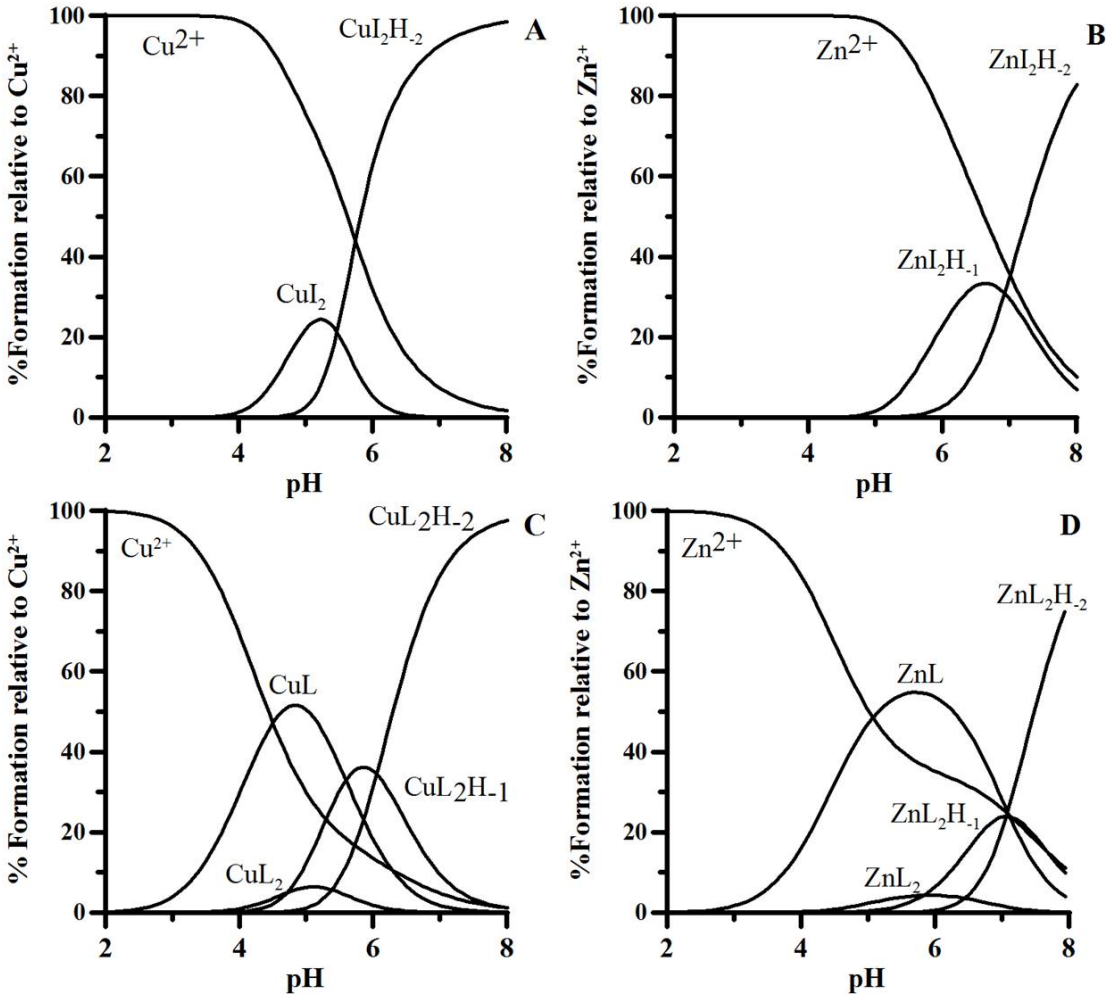

Figure 3.81. Speciation plots relative of copper and zinc complexes calculated using the stability constants in Table 3.31. Ligand concentration was 0.5 mM and a 1:2 metal to ligand ratio was used. The charges are omitted for the simplicity.

Isothermal titration calorimetry by Denadai et al.[237] shows that complexation in water is a stepwise process, driven by enthalpy and entropy. 1:1 Cu^{2+}/Losartan species are formed at low molar ratio, while a 1:2 Cu^{2+}/Losartan species is formed at molar ratio greater than 1.[237] The 1:2 stoichiometry complex is enthalpically favored, due to the strong metal-ligand bond, improved by Ligand Field Stabilization Energy (LFSE). The entropic contribution has been attributed to the loss of water molecules occurring in complexation and to the loosening of complex molecular structure due to tetragonal distortion. The formation of copper-active Van der Waals interactions between the aliphatic chain of Losartan in the solid state stabilizes the Cu^{2+}/Losartan complexes.

3.3.6.2. *ESI-MS characterization of Cu^{2+} and Zn^{2+} complexes*

ESI-MS spectroscopy applied to Irbesartan and Losartan complexes with Cu^{2+} and Zn^{2+} confirms Denadai et al. [237] findings. In fact already the pure sartans' ESI-MS spectra confirm that Van der Waals interactions between sartan aliphatic chains lead to the formation of dimers in solution: $[2I+H]^+$ (857.472 *m/z*, $C_{50}H_{57}N_{12}O_2$), $[2I+Na]^+$ (879.454 *m/z*, $C_{50}H_{56}N_{12}O_2Na$), $[2I+2Na]^+$ (901.436 *m/z*, $C_{50}H_{55}N_{12}O_2Na$), $[2L+K+H]^+$ (883.285 *m/z*, $C_{44}H_{46}Cl_2KN_{12}O_2$), $[2L+2K]^+$ (921.241 *m/z*, $C_{44}H_{45}Cl_2K_2N_{12}O_2$), $[2L+3K]^+$ (959.199 *m/z*, $C_{44}H_{44}Cl_2K_3N_{12}O_2$) and $[2L+3K+Na]^+$ (982.189 *m/z*, $C_{44}H_{45}Cl_2K_3N_{12}O_2$) (Figure A36D-F and Figure A37C-F).

The ESI-MS signals of Irbesartan with Cu^{2+} ion can be attributed to $[CuI+H]^+$ (491.162*m/z*, $C_{25}H_{28}N_6OCu$, Figure A38A) and $[CuI_2+2H]^+$ (919.394 *m/z*, $C_{50}H_{56}N_{12}O_2Cu$, Figure A38B). The charge and empirical formula of the complexes suggest some redox reactions. Electrospray ionization with tandem mass spectrometry (MS/MS) of the $[CuI+H]^+$ complex show four signals: 463.16 *m/z*, 448.14 *m/z*, 352.09 *m/z* and 296.03 *m/z*, whose isotopic patterns perfectly fit (Figure A39A-D) to the complexes presented in Figure 3.82. The lowest *m/z* signal suggests copper ion coordination by tetrazol ring.

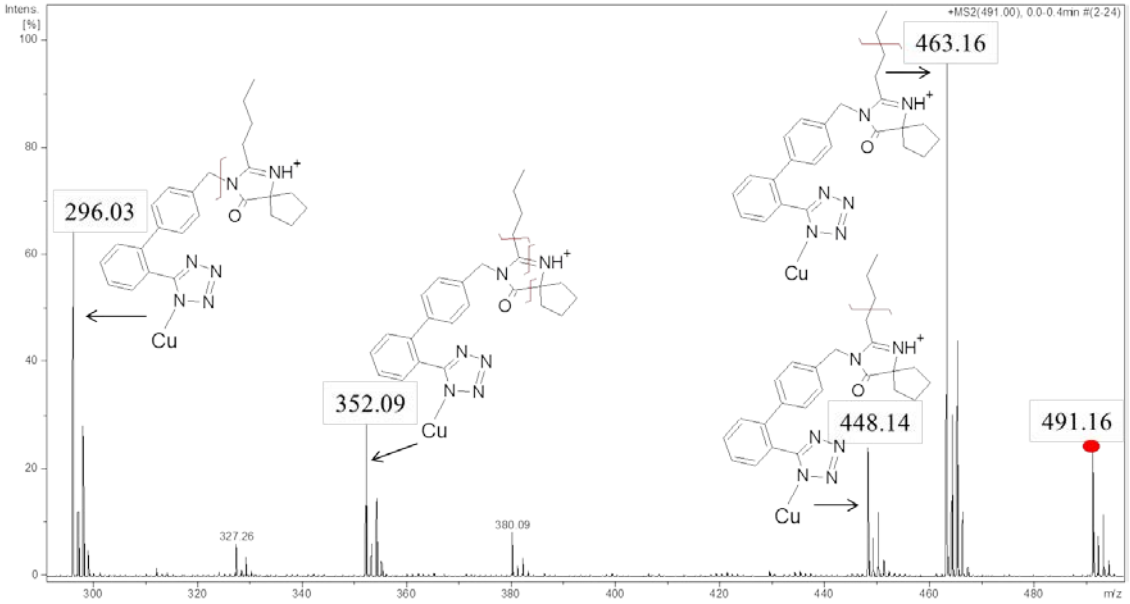

Figure 3.82. Electrospray ionization with tandem mass spectrometry (MS/MS) spectrum of the $[CuI+H]^+$ complex. The precursor ion selected for fragmentation in the MS/MS experiment is indicated by a dot.

The ESI-MS spectrum of Irbesartan with zinc(II) confirms the formation of $[ZnI]^+$ complex ($C_{25}H_{27}N_6OZn$ 491.155 *m/z*, Figure A40A*)* and of its mono- and bis-hydrated forms: $[ZnI+H_2O]^+$ and $[ZnI+2H_2O]^+$ ($C_{25}H_{29}N_6O_2Zn$ 509.160 *m/z*, $C_{25}H_{31}N_6O_3Zn$ 527.131 m/z, Figure A40B and A40C, respectively). The signal at 919.395 *m/z* is attributed to the $[ZnI_2+H]^+$ complex ($C_{50}H_{55}N_{12}O_2Zn$, Figure A40D). MS/MS spectrum of the $[ZnI]^+$ complex, even at low collision energy (15 eV), leads to the decomposition

of the complex. The MS/MS spectrum of the $[ZnI_2+H]^+$ complex shows three signals at 491.16, 449.16 and 429.25 *m/z*, attributed to the $[ZnI]^+$ complex, to the $[C_{22}H_{20}N_6OZn]^+$ fragment and to $[I+H]^+$ (Figure A41).

The ESI-MS spectra of free Losartan solution, and with Cu^{2+} and Zn^{2+} ions are reported in Figure 3.83.

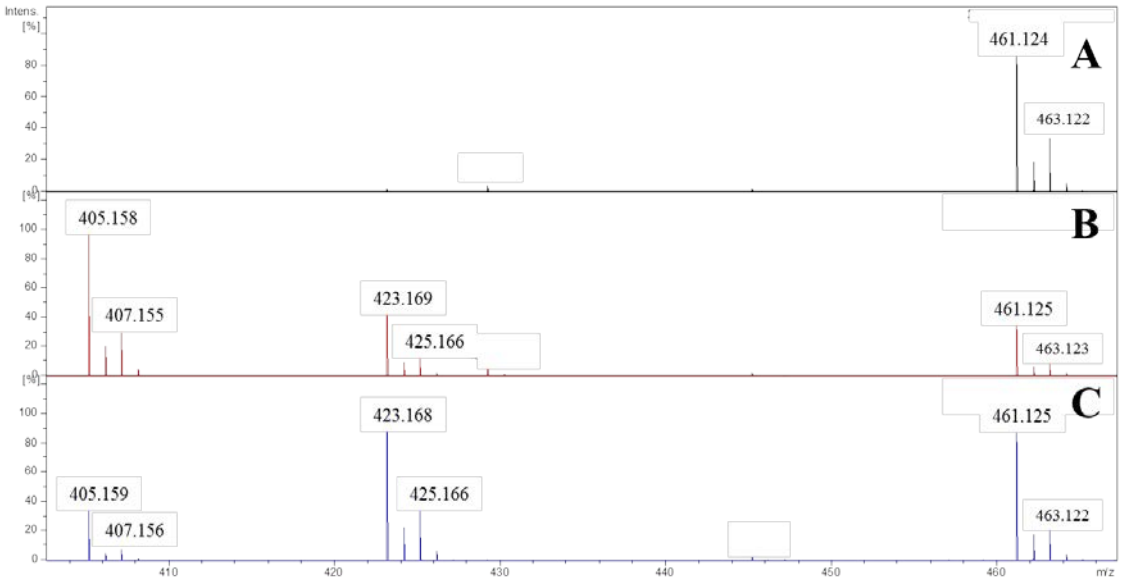

Figure 3.83.ESI-MS spectra of Losartan A) pure, B) with copper at 1:1 molar ratio, and C) with zinc at 2:1 molar ratio in the 400-470 *m/z* range.

The signal at 461.124 *m/z* corresponds to Losartan $[L+K+H]^+$ ($C_{22}H_{23}ClKN_6O$). In the presence of metal ions two additional signals at 423.169 and 405.158 *m/z* are present attributable to $[L+2H]^+$ ($C_{22}H_{24}ClN_6O$) and $[L-H_2O]^+$ ($C_{22}H_{22}ClN_6$) respectively. One of the possible explanations of this phenomenon is that in the presence of these metal ions the reaction in Scheme 17 occurs.

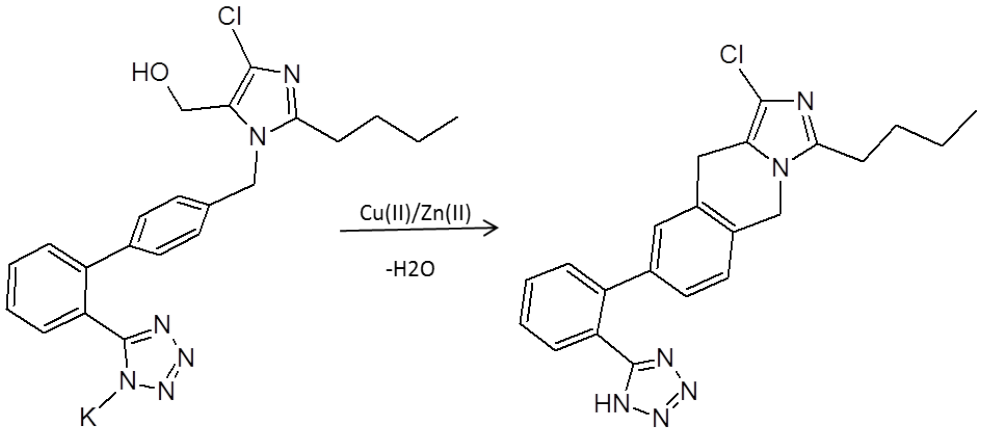

Losartan **3-butyl-1-chloro-8-[2-(1*H*-tetrazol-5-yl)phenyl]-5,10-dihydroimidazo[1,5-*b*]isoquinoline**

Scheme 17. Suggested formation of 3-butyl-1-chloro-8-[2-(1H-tetrazol-5-yl)phenyl]-5,10-dihydroimidazo[1,5-b]isoquinoline by rearrangement of Losartan in presence of metal ions.

ESI-MS spectrum of Losartan with copper (molar ratio 1:1) shows low intensity signals attributed to $[CuL+H]+$ ($C_{22}H_{23}ClN_6OCu$ 485.092 m/z, Figure A42A), $[CuL_2+2H]+$ ($C_{44}H_{46}Cl_2N_{12}O_2Cu$ 907.252 m/z, Figure A42C), $[Cu_3L_4]^{2+}$ ($C_{88}H_{88}Cl_4N_{24}O_4Cu_3$ 936.701 m/z, Figure A9D), $[CuL_2+H+K]+$ ($C_{44}H_{45}Cl_2N_{12}O_2CuK$ 945.209 m/z, Figure A42E) and $[Cu_3L_2]^+$ ($C_{44}H_{44}Cl_2N_{12}O_2Cu_3$ 1031.098 m/z, Figure A42F). Charge and empirical formulae of $[CuL+H]^+$, $[CuL_2+2H]^+$ and $[CuL_2+H+K]^+$ complexes suggest a redox reactions analogously to those observed with Irbesartan. MS/MS of the $[CuL+H]^+$ complex, even at low collision energy (10 eV), leads to its decomposition. MS/MS spectrum of the $[CuL_2+2H]^+$ complex shows one signal at 461.134 m/z, which can be attributed to $[L+K]^+$ (Figure A41).

ESI-MS spectrum of Losartan with Zn^{2+} ion at 1:2 metal to ligand molar ratio shows three signals at 485.083, 907.245 and 937.701 *m/z*, which can be attributed to $[ZnL]^+$ ($C_{22}H_{22}ClN_6OZn$), $[ZnL_2+H]^+$ ($C_{44}H_{44}Cl_2N_{12}O_2Zn$) and $[Zn_3L_4]^{2+}$ ($C_{88}H_{88}Cl_4N_{24}O_4Zn_3$), respectively.

The redox activity of Cu^{2+}/Losartan complexes was previously observed by Etcheverry et al.[236] Their studies showed weak Superoxido Dismutase activity of $[Cu(Ligand)_2(H_2O)_3]_2$ complex at pH 10.2.

3.3.6.3. NMR characterization of Zn^{2+} complexes

Free Losartan ligand has been studied by NMR techniques in different solvents and ^1H 1D NMR spectra in D_2O at pH 7.0, in MeOD-d_4 and DMSO-d_6 are shown in Figure A43. In Table A16 ^1H and ^{13}C chemical shift assignments of signals of the free ligand are reported in the different solvents. The low solubility of the ligand in aqueous solution and the precipitation by adding Zn^{2+} ions at a 5-7 mM concentration of Losartan and 1:0.5 and 1:1 ligand/metal molar ratio prevented the NMR study in water.

For this reason the interaction of Losartan with Zn^{2+} ions has been followed in MeOD and DMSO. In Figure 3.84 the comparison of ^{1}H 1D NMR spectra of Losartan:Zn^{2+} system in MeOD solvent at molar ratios of 1:0, 1:0.5 and 1:1 is shown, respectively.

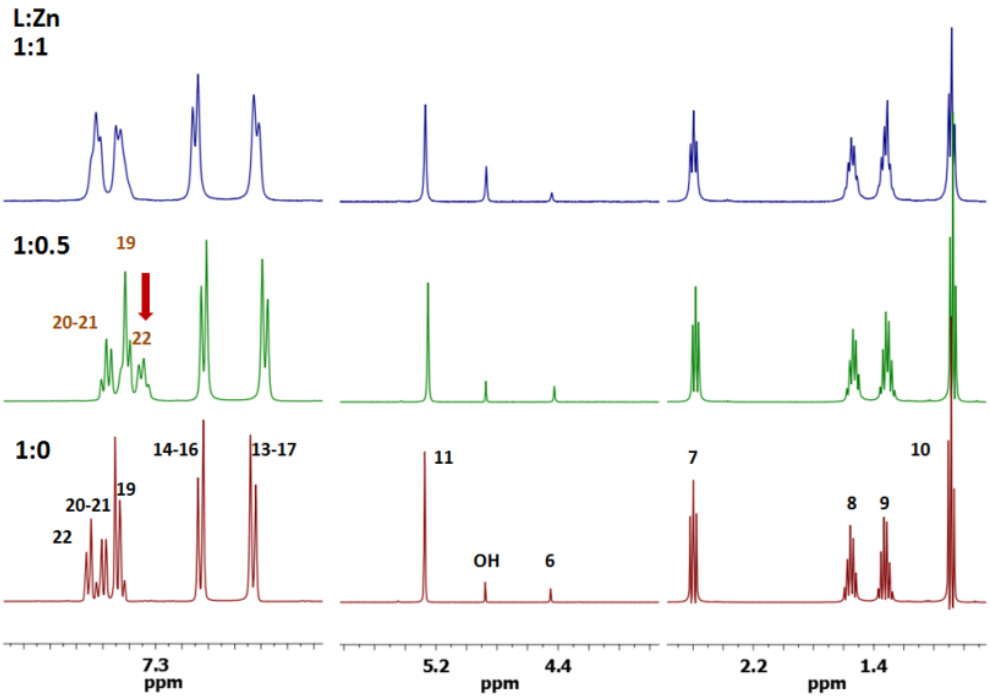

Figure 3.84. ^{1}H 1D NMR spectra of Losartan:Zn^{2+} system in MeOD-d4 solvent in the molar ratio of 1:0, 1:0.5 and 1:1 at 25°C and pH 7.

Perturbations were clearly observed in the aromatic region of the spectra starting at 1:0.5 L:Zn^{2+} molar ratio. Indeed, changes in chemical shifts were detectable for H-22, the closest proton to tetrazolate moiety, together with H-19 and to a lesser extent for H-13, -17, -14 and -16 from biphenyl, that are further away from the tetrazolate moiety. No overt changes were observed for the other protons of the molecule, except for a slight broadening of the signals. Based on these findings, tetrazole appears to be the anchoring site for Zn^{2+} ion, in agreement with the potentiometric and spectroscopic results.

The more evident broadening of the signals at molar ratio 1:1 can be ascribed to the presence of chemical exchange in an intermediate regime with respect to the NMR timescale. The same behaviour of Losartan with Zn^{2+} ions was observed in DMSO-d_6 solution. Comparison of ^{1}H 1D NMR spectra of free Losartan and Losartan:Zn^{2+} system at a molar ratio 1:1 is reported in Figure 3.85, and aromatic region within 2D ^{1}H-^{13}C HSQC spectra in Figure 3.86. In fact, H-22, H-20, H-19 and H-21 were the protons most affected after adding Zn^{2+} ions to the ligand solution, suggesting that the same coordination as in MeOD is retained also in DMSO-d_6 solvent.

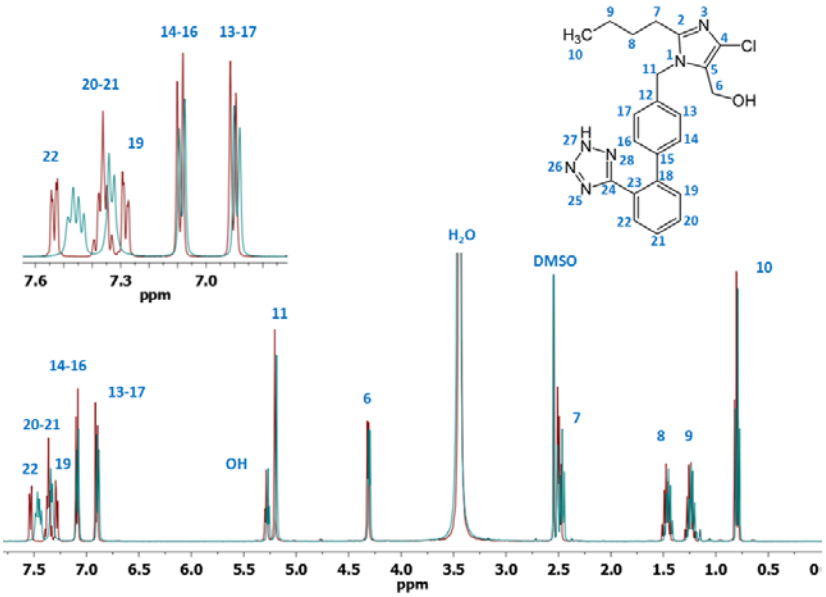

Figure 3.85. Comparison 1H 1D NMR spectra of free Losartan (red) and Losartan:Zn^{2+} system at a molar ratio of 1:1 (blue), in DMSO-d6 solvent, at 25°C and pH 7.

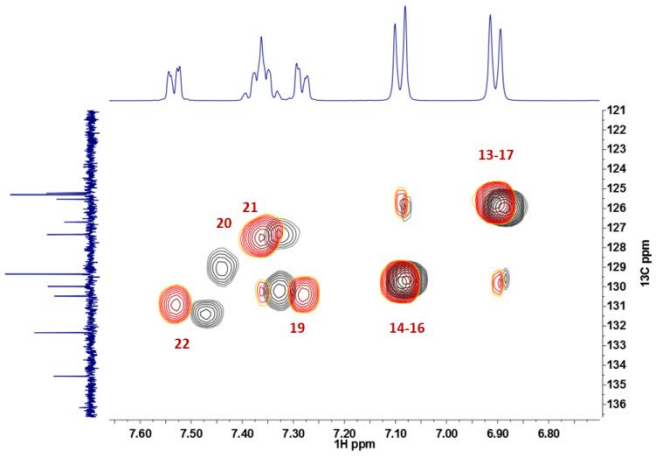

Figure 3.86. Comparison of 2D ^{1}H-^{13}C HSQC NMR spectra of free Losartan (red) and Losartan:Zn^{2+} system at a molar ratio of 1:1 (blue), in DMSO-d6 solvent, at 25°C and pH 7.

Also in the case of Irbesartan the spectra were obtained in MeOD solution where the ligand is soluble at the concentration used for NMR experiment. In Figure A44 the ^{1}H 1D NMR spectrum obtained in this solvent is shown, while in Figure A45 the ^{1}H 2D COSY NMR spectra of aliphatic region in the same MeOD solution are shown. When adding Zn^{2+} ions to Irbesartan methanolic solution, perturbation in NMR spectra were detected. In Figure 3.87 a comparison of ^{1}H 1D NMR spectra of Irbesartan:Zn^{2+} system at a molar ratio of 1:0, 1:0.5 and 1:1 is shown.

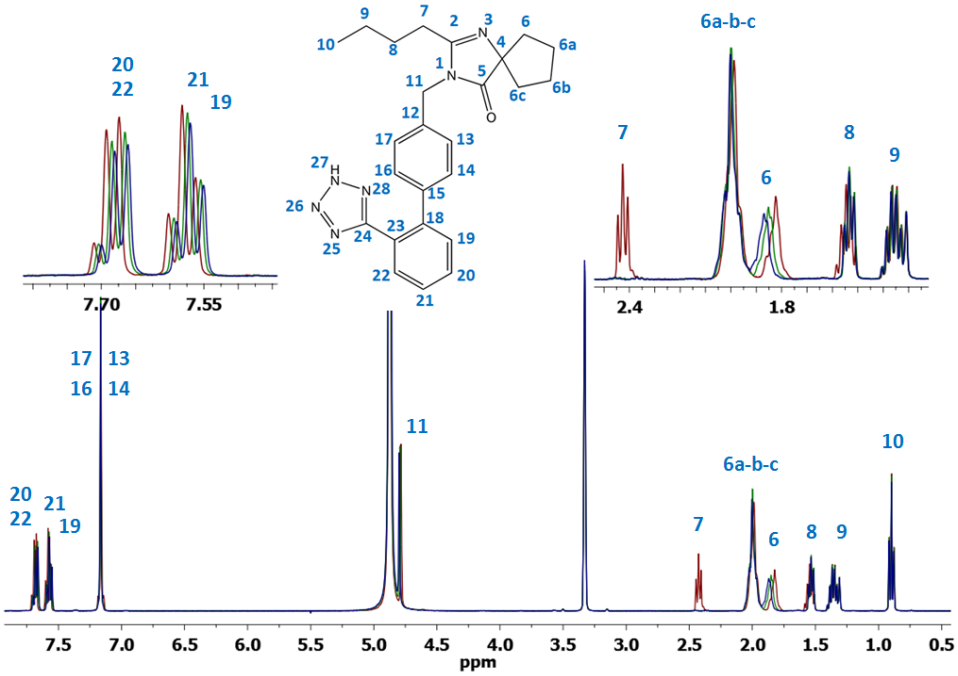

Figure 3.87. ^{1}H 1D NMR spectra of Irbesartan:Zn^{2+} system in MeOD-d4 solvent at a molar ratio of 1:0 (red), 1:0.5 (green) and 1:1(blue) at 25°C and pH 7.

The most apparent feature emerging from ^{1}H 1D spectra is related to the complete disappearance of the signal of the protons in the 7th position on the aliphatic chain, followed by a change in the multiplicity of the signal of the two protons in the 8th position, as expected and highlighted in the inset. This feature can be explained by the presence of a possible tautomerism induced by Zn^{2+} ions, as reported in the Scheme 18:

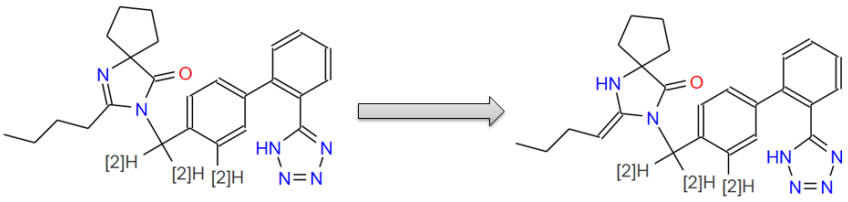

Scheme 18. Possible tautomerism induced by Zn^{2+} ions.

The signal of methylene proton on the 7th position can then shift towards lower field, under the water signal, as expected. Taking into account that protons and carbons of tetrazole and biphenyl moieties show only minor changes in their chemical shifts upon Zn^{2+} addition, we can suggest that the coordination site of Zn^{2+} ions can be mostly located on the imidazolic ring of Irbesartan ligand in our NMR conditions.

3.3.7. Complex formation equilibria of H_4pedpa and H_6dipedpa ligands

3.3.7.1. Complex formation equilibria with La^{3+}

The complex formation equilibria of La^{3+} with H_4pedpa and H_6dipedpa ligands have been studied by potentiometric titrations and in the case of H_4pedpa ligand by ^{1}H NMR titrations. The potentiometric results, analyzed with HyperQuad2013 program, gave the complexation schemes and complex formation constants reported in Tables 3.32 and 3.33 which allowed to obtain the related speciation plots in Figures 3.88 and 3.90.

H_4pedpa forms from pH 2 a 1:1 neutral LaLH complex, in which presumably La^{3+} is bound through the three nitrogen atoms and two oxygen atoms of carboxylate groups, being the phosphonate group till protonated. This last proton is lost with pK 4.45, lower than that in the free ligand. This should imply the involvement of phosphonate in La^{3+} coordination. The complex loses a further proton from a coordinated water molecule with pK 10.08 giving a hydroxo-complex.

Table 3.32. Stability constants of metal complexes calculated with HyperQuad program at 0.16 M NaCI ionic strength and 25°C using [H_4pedpa] = $6.52 \cdot 10^{-4}$ M ligand concentration and 1:1 metal to ligand molar ratio.

Species	log β	log K
LaLH	17.03 (3)	
$[LaL]^-$	12.58 (2)	4.45
$[LaLH_{-1}]^{2-}$	2.50 (4)	10.08
pLa^{3+}	**12.4**	

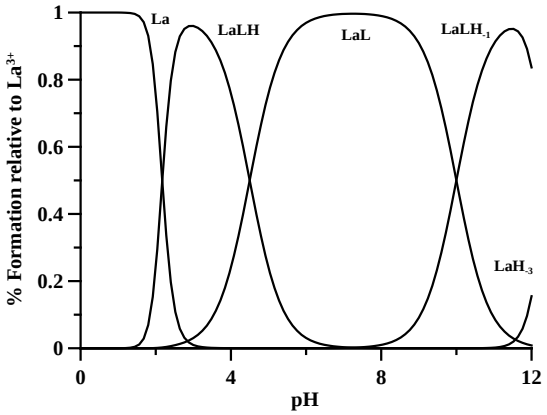

Figure 3.88. Speciation plots of H_4pedpa complexes with La^{3+} calculated on the basis of stability constants reported in Table 3.32 using $3.26 \cdot 10^{-3}$ M ligand concentration and 1:1.5 metal to ligand molar ratio. Charges are omitted for simplicity.

From ^{1}H NMR titrations of the H_4pedpa ligand and of the mixture La^{3+}: H_4pedpa 1:1.5 metal to ligand molar ratio, the implication of the phosphonate group in La^{3+} coordination is clear (Figure 3.89). Already in the spectrum of the free ligand, the resonances due to the H5 and H6 methylene groups show a fine structure (apparent

doublet of doublets) indicating the inequivalence of each proton within the same methylene, which is typical for a slow rotating methylene moiety. The frequency difference among the two protons of both H5 and H6 become even more pronounced upon complex formation, due to a further reduction of the methylene rotation about the C-C bonds.

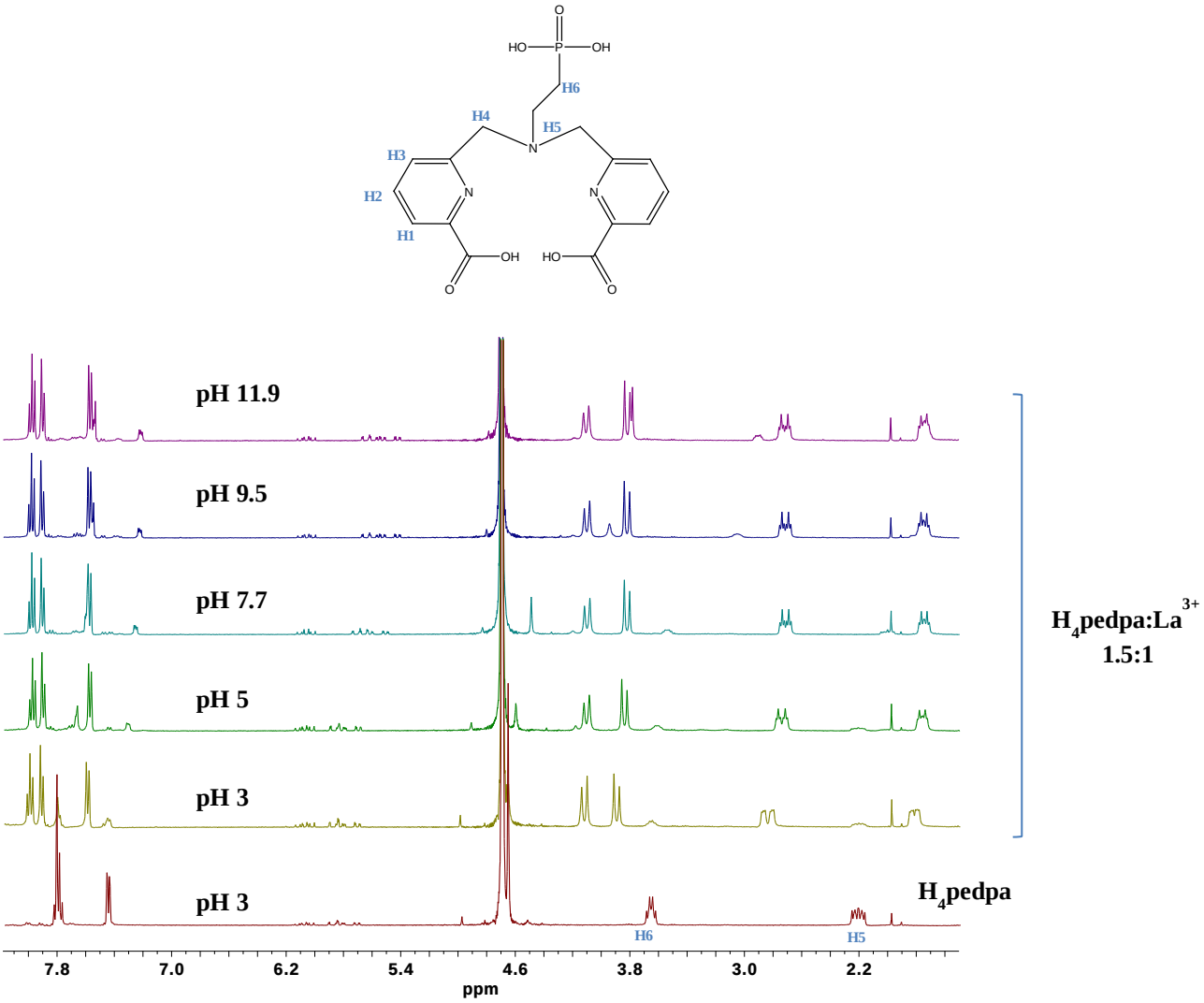

Figure 3.89. ^{1}H NMR spectra of H_4pedpa:La^{3+} system in D_2O solvent at a molar ratio of 1.5:1 at 25°C and pH range 3-11.9. ^{1}H NMR spectra of H_4pedpa ligand at pH 3 (red spectra).

A similar complexation scheme is shown by H_6dipedpa. From the potentiometric data, presumably the second phosphonate group is not involved in coordination. ^{1}H NMR titrations are at the moment in progress, which will aid in attributing coordination schemes to the variously protonated complexes pointed out by potentiometry. The pLa^{3+} values for the two ligands are practically equal (Tables 3.32 and 3.33).

Table 3.33. Stability constants of metal complexes calculated with HyperQuad program at 0.16 M NaCI ionic strength and 25°C using [H_6dipedpa] = 6.43·10^{-4} M ligand concentration and 1:1 metal to ligand molar ratio.

Species	log β	log K
$La(LH_3)$	34.25 (3)	
$[La(LH_2)]^-$	30.95 (1)	3.3
$[La(LH)]^{2-}$	24.60 (1)	6.35
$[LaL]^{3-}$	14.26 (2)	10.34
pLa^{3+}	**12.7**	

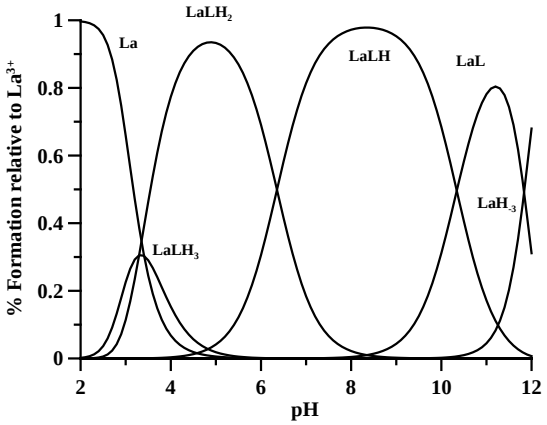

Figure 3.90. Speciation plots of H_6dipedpa complexes with La^{3+} calculated on the basis of stability constants reported in Table 3.33 using 6.43·10^{-4} M ligand concentration and 1:1 metal to ligand molar ratio. Charges are omitted for simplicity.

3.4. Lipophilicity, drug-like descriptors and Biodistribution studies of P1 ligand[147]

3.4.1. Lipophilicity and drug-like descriptors

Lipophilicity greatly influences the pharmacokinetic and pharmacodynamic profile of a drug, and the partition coefficient between water and *n*-octanol (log P) is the parameter in use for its evaluation. Log P of P1, and of DFP for comparison, were measured with the "shake-flask" method. The obtained values (Table 3.34) are quite similar, though that of P1 (-0.90) is slightly less than that of DFP (-0.82). The same lipophilicity order was obtained from *in silico* calculations, using QikProp program.[238] This program provides also a number of indicators of the pharmacokinetic profile of a drug, as the ability to cross the blood-brain barrier (log BB), the ability to be absorbed through the intestinal tract to the bloodstream (Caco-2 cell permeability) and the verification of *Lipinski's rule of five* [9] (Table 3.34).

Although P1 does not present any violation of the restricted Lipinski´s rule, it presents some limitations to barrier-crossing ability compared to DFP. In particular, P1 presents lower permeability through the Caco-2 membranes (higher than 500 nm/sec is considered good)[238], as well as through the blood-brain barrier (log BB < -1.0, poorly distributed to the brain) and thus lower bioavailability into the central nervous system. Interestingly the tautomeric diphenolic form H_2L_b is characterized by slightly better pharmacokinetic descriptors than H_2L_a, namely in terms of membrane permeability, due to the increased aromaticity of the molecule that involves a lipophilicity enhancement.

Table 3.34. Experimental values of octanol/water coefficient log P for P1 (in the neutral forms H_2L_a and H_2L_b) and DFP, and calculated values for clog P, ability to cross the blood-brain barrier (log BB), ability to be absorbed through the intestinal track to the blood (Caco-2 cell permeability), bioavailability into the central nervous system and the verification of Lipinski's rule of five.[9]

Name	DFP	H_2L_a	H_2L_b
MW	138	141	141
logP[a]	-0.82	-0.90	-
clogP[b]	0.915	-0.795	0.520
log BB[b,c]	-0.254	-1.021	0.978
Caco-2 Permeability (nm/s)[b]	1141	192	256
CNS[b]	+/-	--	-
Violations of Lipinsky rules[b]	0	0	0

[a]octanol/water partition coefficients, values measured in the present work

[b]Predicted values using program QikProp v.2.5[55]

[c]blood/brain partition coefficient

3.4.2. Biodistribution studies of P1 ligand

To evaluate the efficacy of the new ligand P1 as a chelating agent for mobilization of metal ions, we studied the biodistribution profile of the well-established radiotracer ^{67}Ga-citrate in female mice with simultaneous intraperitoneal administration of the ligand solution. The effect of this chelator on the ^{67}Ga uptake and clearance on the major organs and on the excretion can be viewed in comparison with the drug DFP (Figure 3.91).

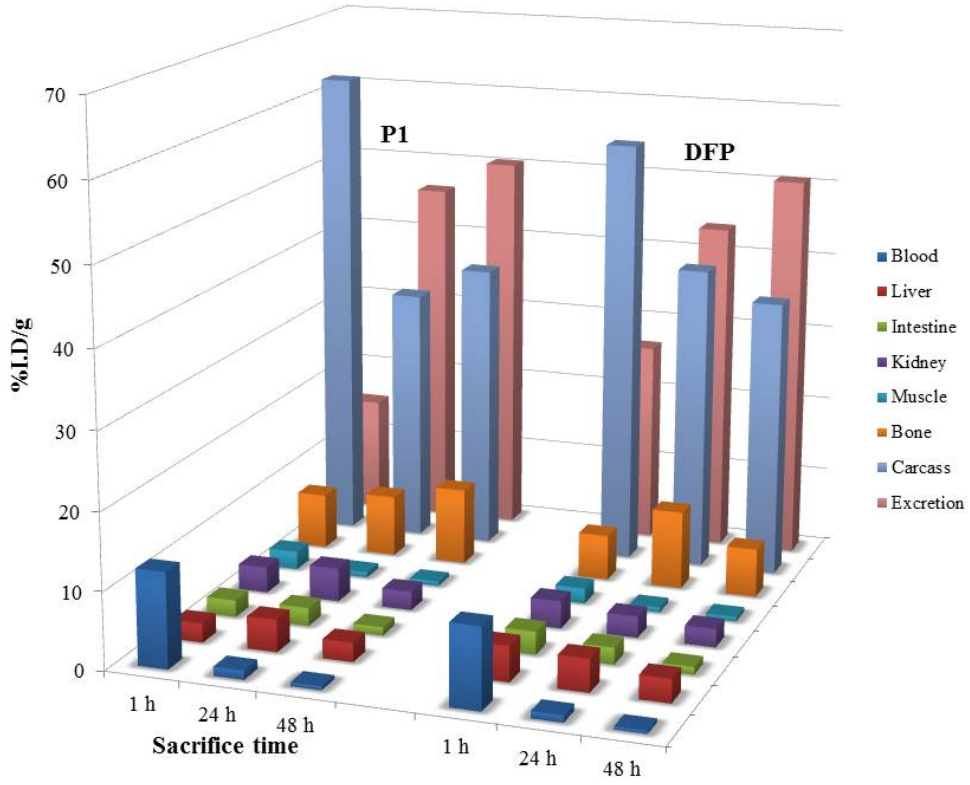

Figure 3.91. Biodistribution data in the most relevant organs, expressed as % I. A./g for ^{67}Ga-citrate with simultaneous intraperitoneal injection of P1 or deferiprone, at 1, 24 and 48 h after administration in female Balb-C mice (n = 3).

Although the effect of DFP on the biodistribution of radiotracer in metal-overload mice has been previously reported, those studies involved a different animal model (CD1)[51],[37]and so it was necessary to reevaluate it herein for Balb-C mice.

The co-administration of the ligand P1 enhanced the overall excretion rate of radioactivity from whole animal body as efficiently as DFP, 24 and 48 h after administration. No significant differences in the radioactivity remaining in the carcass and in the rate of radioactivity elimination were found, except at 1 h.

The main differences in the distribution profile are related with the blood clearance and the hepatic uptake at 1 h. P1 induces slower clearance from blood as well as lower liver uptake than DFP at 1 h after administration, which may be attributed to a highest level of plasmatic protein binding, eventually due to the 2-hydroxymethyl group and to some minor decrease on the lipophilicity.

Overall, this biodistribution profile, similar to that of DFP, shows an increase of the radiotracer elimination rate and attests the ability of the ligand to chelate the radiometal *in vivo*.

Generally, ligands containing an identical chelating group possess similar pFe^{3+} values: for instance, 3-hydroxypyridin-2-one ligands possess pFe^{3+} values of 16, whereas the pFe^{3+} values for 3-hydroxypyridin-4-ones are around 20. However the introduction of adjacent functions can have a dramatic effect on pFe^{3+} values. It was previously established that the introduction of an amide function on the position 4 of 3-hydroxypyridin-2-ones reduces the pK values increasing the pFe^{3+} values, due to the formation of a stable intramolecular hydrogen bond between the amide proton and the adjacent oxygen donor atom.[239]

Catechol, with very large iron and proton binding constants, binds iron best in slightly basic solutions. It appears that the ligands with the best iron-binding potential have aromatic characters and form planar five-membered chelate rings with a high-spin ferric ion. There is a substantial amount of delocalization in the bonding of the catecholate anion to Fe^{3+}, which contributes to the great stability of these complexes.[240] This is also possible for the iron hydroxypyridinone complexes.

Among the hydroxypyridinones, the stepwise formation constants increase as the oxygen-binding groups move away from the ring nitrogen. This is evidence for the importance of the catechol-like resonance form of the iron-bound hydroxypyridinone, since in this aromatic resonance form the nitrogen has a positive charge and will be more stable further from the iron center.

3.5. Enzymatic inhibition studies of KβAK[1]

Over the past 5 years we have synthesized several different kojic acid derivatives (Scheme 9 and Figure 1.8) with the aim of individuating effective iron and aluminium chelating agents. One of the requisites of a ligand used in chelation therapy is that it must not interfere with proper enzymatic activity. This issue was carefully considered when evaluating our molecules for tyrosinase inhibitory activity. In the present study, the results obtained on the tyrosinase inhibitory activity of seven biskojic derivatives and a mono kojic derivative L7 are compared.

In Figure 3.92, the percentage inhibition of kojic acid (84%) is compared with that of its analogues. The results show that KβAK has the highest inhibition efficiency (91%), ligands L1-L5 have low inhibition efficiency (24-36%), while L6 and L7 have no influence whatsoever on tyrosinase activity.

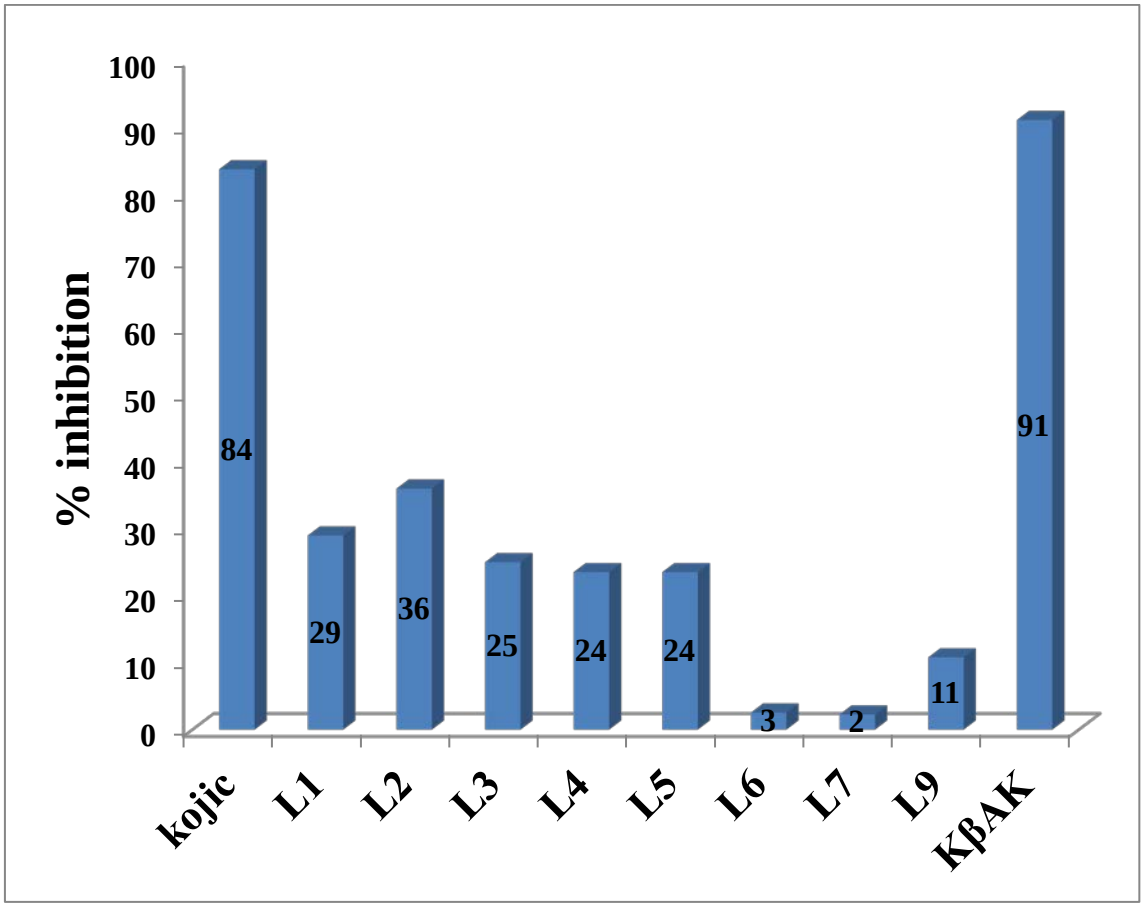

Figure 3.92. Diagram of tyrosinase inhibition. The percent inhibition of tyrosinase activity calculated as: % inhibition = (A-B)/A · 100; A represents the absorbance at 476 nm without the test sample, and B represents the absorbance at 476 nm whit the test sample at the same substrate concentration. The experiment was repeated with different inhibitors concentrations: 0.069, 0.139 and 0.279 mM.

Based on these preliminary results, we decided to investigate the inhibitory activity of the most promising ligand KβAK and compare with KA. Figure 3.93 shows the activity of the enzymes (Ctrl 1 and Ctrl 2) acting on the substrate L-tyrosine after 30 (A) and 90 min (B), respectively. At increasing concentrations of KA, the tyrosinase-mediated

formation of the pigment dopachrome was delayed after 30 min (Figure 3.93A). In the presence of KβAK at the same concentration, the inhibitory activity became much stronger, as demonstrated by the complete lack of melanin formation even after 90 min of incubation (Figure 3.93B).

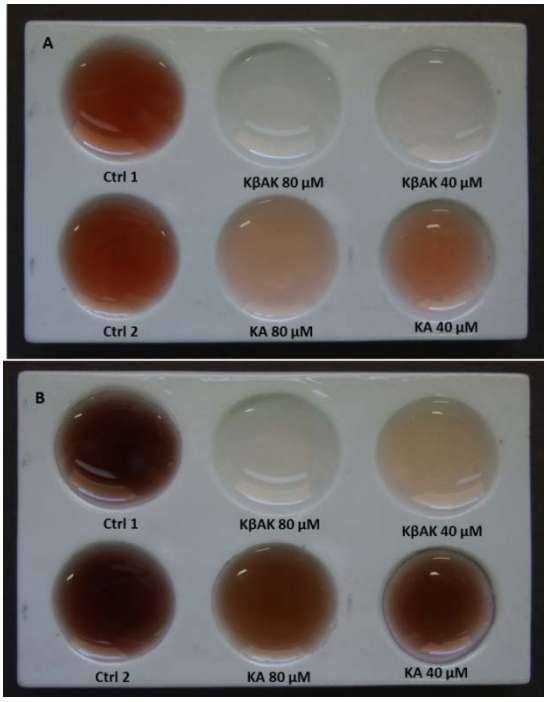

Figure 3.93. Inhibitory effect of KA and KβAK on catalitic activity of mushroom tyrosinase after 30 min (A) and 90 min (B) of incubation. Two different concentrations (40 and 80 µM) were tested.

IC50 values for tyrosinase inhibitors can vary for a number of reasons, including choice of assay conditions, rate determinations, solvent considerations, and also the purity of the tyrosinase.[241]For instance, reported IC50 values for kojic acid vary from 10 to 300 µM.[241]Under our experimental conditions the IC50 value for KβAK was equal to 6.8±0.9 µM, whereas that of kojic acid was amounting to 35.4±4.3 µM. Although our findings cannot explain the mechanism of KβAK inhibition, we can notice that the IC50 of the new inhibitor is approximately 1/5 that of kojic acid. This result is lower than that of most effective Kojic-Phenylalanine-Kojic (1/382) reported in the literature[152].

Our tyrosinase inhibition studies were performed and compared with the data of Kobayashi et al. prepared under the same experimental conditions[152].Nevertheless, the extracted mushroom enzymes had low homology with the more complex mammalian ones (22-24% sequence identity with 48-49% sequence coverage)[242]. Recent[242] reports suggest that inhibition studies with human tyrosinase could be more informative.

The two-step synthesis of KβAK is time and cost-saving in comparison with the multi-step synthesis of other kojic acid derivatives as tyrosinase inhibitors [152],[158]. In the catalytic activity test, KβAK proved to be a better inhibitor than kojic acid, and above all, was far more effective after 30 and 60 min (Figure 3.93). This strong inhibitory effect cannot be explained by the contemporary presence of two kojic acid units, since the L1-L6 and L9 ligands possess two kojic acid units and are less effective than KβAK and even kojic acid alone. Neither is L7 an antagonist of tyrosinase activity. Initially,

we hypothesized that the presence of an aromatic ring in the ligand structure (L2, L3, L5, and L7) could facilitate docking into the active site of tyrosinase, similarly to kojic acid conjugates with phenylanine[152]. According to this hypothesis, Phe90 residue could form π-π stacking interactions between the aromatic rings of the linker. However, the results of our laboratory tests showed exactly the contrary. Neither the hydrophilic chain between the two kojic units of L9, nor the shorter and more hydrophobic chains of L1 and L4 resulted to be capable of increasing inhibitory activity, the latter two yielding slightly better results.

4. Conclusions

4.1. P1

P1 combines the hydroxypyridinone and catechol features: at low pH it coordinates efficiently metal ions as 5-hydroxy-2-(hydroxymethyl)pyridin-4(1*H*)-one, while at basic pH as 2-(hydroxymethyl)pyridine-3,4-diol. The presence of hydroxymethyl group favours the tautomeric equilibrium in the free ligand, due to the formation of the hydrogen bond N1···H8. The tautomeric transformation in the presence of metal ions occurs at lower pH than in the free ligand. On the basis of pFe^{3+} values, P1 should be considered a more efficient iron chelator (pFe^{3+} 22.0) than the clinically-used DFP (20.67)[201], its 3,4-hopo analogues (20.77) and far more effective than catechol (pFe 14.7).[243] The high pFe^{3+} value of P1 depends on two different factors, namely (i) the high stability of the iron complexes, mainly attributed to the tautomeric rearrangement of pyridinone ligand into the catechol-like ligand; and (ii) the log K 9.00 of P1, lower than that determined for deferiprone by 0.82 units. The chelating ability of P1 toward aluminium, copper and zinc ions is not higher than that of the corresponding DFP and 3,4-hopo, and this renders P1 a more selective iron chelator.

The bio-distribution studies on mice showed that P1 is as effective as clinically-used DFP, notwithstanding the negative charge on the complex existing at physiological pH (where the species modelled as $[FeL_3H_2]^-$ is prevalent) could hinder in some extent the crossing of membranes, and thus iron excretion. The bioavailability parameters presented in Table 3.34 characterize P1 as a less effective compound than DFP, even if the difference between the parameters of H_2L_a and H_2L_b should mitigate this limit. The study of metabolism of P1 in living organisms could be of paramount importance, since it has been reported that 1'-hydroxyalkyl substituents prevent glucuronidation *in vivo* in hydroxypyridinones.

These overall promising results urge further studies to verify *in vivo* if the toxicity, bioavailability and pharmacokinetic properties of P1 can open a new way to future clinical trials.

4.2. L12-L15

The detailed potentiometric, spectrophotometric, ^{1}H NMR and calorimetric study of the protonation equilibria of L12-L15 ligands has allowed not only to obtain the protonation constants of each ligand and attribute each protonation steps to the basic groups of the ligands, but also to give evidence of the H-bonding intramolecular interactions that characterize the differently protonation species.

The complex formation equilibria of these ligands have been characterized not only with the toxic metal ions Fe^{3+} and Al^{3+}, but also with the two essential metal ions Cu^{2+} and Zn^{2+}. The main formed complexes with all the studied metal ions are binuclear 2:2

metal/ligand complexes with various protonation degrees. The relative stability constants and the pM values were calculated, and the relative speciation plots were presented. The pFe^{3+} values 20.4 obtained with the L14 ligand is of particular interest, being comparable with that of Deferiprone, one of the chelators in use in the treatment of iron overload diseases. The overall results have furthermore allowed to propose detailed coordination schemes for the formed complexes.

4.3. L1-L18

The examined ligands are characterized, with the exception of L7 alone, by the presence of two kojic units joined by different linkers. They all form with Cu^{2+} dinuclear complexes with different degree of protonation, and L1, L4 and L5 form also 1:1 complexes. Only L7 ligand forms mononuclear 1:1 and 1:2 complexes. In the case of Zn^{2+}, mononuclear 1:1 and binuclear 2:2 complexes, are formed.

On the base of our results we propose the coordination mode shown in the Scheme 19. We observe the same stoichiometry and coordination geometry for L1-L6 and L8 ligands, whether or not a nitrogen atom is present in the linker.

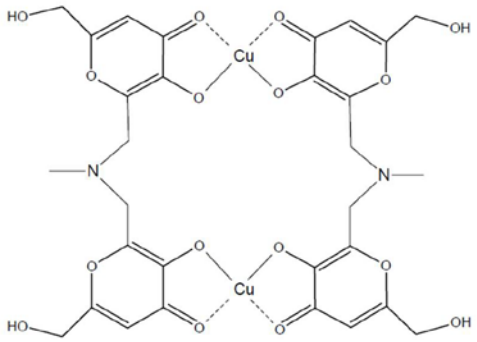

Scheme 19. Proposed coordination model for the dinuclear complex $[Cu_2(L4)_2]$.

Besides the similarity of complexation model of all ligands, also the stability of the formed complexes is comparable, as evaluated from pM values (Tables 3.23 and 3.24). In particular, we have observed that the mean pCu^{2+} is about ten units lower than the corresponding pFe^{3+} value (Table 3.22), and pZn^{2+} is two-three units lower than pCu^{2+}. On the basis of these results, the ligands L1-L8 are totally selective toward iron, i.e. also a presence of the essential metal ions Cu^{2+} and Zn^{2+} in large excess (> 100 times) does not perturb iron chelation. On the contrary, when the chelating agent exceeds the amount required to completely coordinate the present iron, copper is quantitatively bound by the available ligand even at micromolar concentration. Furthermore, the ligand still available after copper complexation will bind zinc, largely available in the organism, despite its very low stability. These considerations have been substantiated by speciation calculations, using Hyss program [180], the copper and zinc stability constants

reported in Tables 3.23 and 3.24 and the iron stability constants (Table 3.22), neglecting all the essential metal ion interactions with endogenous molecules. This speciation study gives evidence of a potential drawback of iron chelation therapy, i.e. the depletion of essential metal ions. This fact is amply reported in literature, above all for zinc because of its large amount in organism and because it is less strongly bound to endogenous macromolecules than copper[244],[245], [246], [247].

The evaluation of complex formation equilibria between any ligand proposed for toxic metal ion removal and the essential metal ions is a task of paramount importance.

4.4. KβAK

The neutral form of KβAK at physiological pH together with its low molecular weight suggests high bioavailability. The chemical properties are in agreement with Lipinski's rules[9] for orally active drug (no more than 5 hydrogen bonds; no more than 10 hydrogen bond acceptors; a molecular mass less than 500 Daltons) and candidate it for pharmaceutical applications.

KβAK form with Fe^{3+}, Al^{3+}, Cu^{2+} and Zn^{2+} metals mono- and dinuclear complexes. The molecule is selective for trivalent ions with pFe and pAl higher than pCu and pZn values. The strength of iron and aluminium complexes with KβAK is similar to those formed with L2 and L4 (Table 4.1). Among previously synthesized bis-kojic acid derivatives, KβAK is the weakest copper and zinc chelator.

Table 4.1. Comparison of pM values for KA, L1-L9 and KβAK ligands. [[33], [35], [37], [163], [36],[199]]

pM*	KA	L1	L2	L3	L4	L5	L6	L7	L9	KβAK
pFe	13.3[33]	23.1[33]	18.9[35]	22.2[35]	18.1[163]	19.3[163]	17.7[163]	16.7[163]	17.7[36]	18.5
pAl	9.1[33]	12.8[33]	11.9[35]	13.9[35]	11.2[37]	11.6[37]	11.8[37]	9.9[37]	10.3[36]	12.7
pCu	7.3	8.8[199]	10.2[199]	10.5[199]	10.3[199]	10.8[199]	8.5[199]	7.2[199]	9.7[36]	8.3
pZn	6.1	6.6[199]	7.6[199]	7.9[199]	8.8[199]	7.1[199]	7.8[199]	6.1[199]	7.6[36]	6.1

[a] Negative logarithm of the concentration of the free metal in solution, calculated for total [ligand] = 10^{-5} M and total [metal] = 10^{-6} M at pH 7.4.

L1-L6 and L9 ligands form [CuL] and [Cu_2L_2] complexes, while KA and L7 ligands form [CuL_2] complexes. The strength of the complexes, evaluated by pCu values (the higher the pCu the stronger the coordination), does not influence the inhibitory properties. In fact, the most effective inhibitory ligands (kojic acid and KβAK) had the lowest pCu values (Table 4.1).

The mechanisms underlying kojic acid inhibition are not yet fully understood and although our findings offer some insight, further research is warranted to explore this topic.

In conclusion, the key to success of the KβAK as a tyrosinase inhibitor could rely on the peculiarities of the chain between the two kojic acid units. Indeed, its hydrophobic properties are sufficient to allow for a perfect fit into the active site of the enzyme, without creating any unconformity with Phe90. However, this hypothesis is based solely on results obtained in the laboratory and needs to be confirmed by computational studies of docking and crystallographic data.

4.5. SC

SC ligand is the first hexadentate ligand derived from KA synthesized by our group, with the aim of obtaining a strong iron chelator forming a single 1:1 complex. It is formed by three KA units connected by a tris aminoethylamina. SC in the fully protonated form behaves as an hexaprotic acid (3 –OH groups on the KA units and three protonated nitrogen atoms in the connecting amine), and its protonation steps have been fully characterized by potentiometric, spectrophotometric and NMR techniques.

The complex formation equilibria with Fe^{3+}, the target metal ion, and with Ga^{3+} for possible medical applications have been studied. As expected only 1:1 differently protonated complexes are formed, in which Fe^{3+} is first coordinated by a single KA unit at very acidic pH, then by two and finally at pH 6 by all the three KA units. The formed pFe^{3+} value 18.4 is not high as expected, not better than those with the corresponding tetradentate chelators.

It shows better coordinating properties toward Ga^{3+} with pGa^{3+} 20.2 about two units higher than that with Fe^{3+}. We hope that a detailed quantum mechanical study will permit to clarify the reasons of the different chelating capacity toward the two metal ions, but also will give the necessary information to a correct design of improved hexadentate KA ligands.

4.6. Losartan and Irbesartan

The use of different complementary techniques has allowed both to give the protonation and complex formation constants of Irbesartan and Losartan with Cu^{2+} and Zn^{2+}, and to attribute the protonation sequence and the coordination sites. The fluorescence behavior of both drugs was also explained in terms of presence of protonated/deprotonated species.

In particular clear evidence of the binding of both metal ions through the tetrazole moiety is obtained, except for the Zn^{2+}/Irbesartan system. In this case NMR measurements gave evidence of a possible tautomerism involving the imidazole ring

and the connected aliphatic chain. ESI-MS spectra remarked that in the 1:1 Zn^{2+}/Irbesartan complex one or two water molecules are present.

4.7. Picolinic acid derivatives

The preliminary results of La^{3+} complexes with the two new ligands synthesized by the group of Prof. Orvig show that both ligands form differently protonated 1:1 complexes. Further NMR, quantum chemical and X-ray diffraction studies are necessary to attribute a coordination scheme to the found complexes.

Bibliography

[1] J. I. Lachowicz, V. M. Nurchi, G. Crisponi, M. G. Jaraquemada-Pelaez, A. Rescigno, P. Stefanowicz, M. Cal and Z. Szewczuk, *Journal of Inorganic Biochemistry* 2015, *151*, 36-43.

[2] W. Kaim, B. Schwederski and A. Klein, *Bioinorganic Chemistry: Inorganic Elements in the Chemistry of Life. An Introduction and Guide.*, John Wiley & Sons, 2013.

[3] V. M. Nurchi, G. Crisponi, *Metal Ion Toxicity* in Ecyclopedia of Inorganic and Bioinorganic Chemistry, John Wiley & Sons, 2015. (DOI: 10.1002/97811 19951438.eibc0126.pub2)

[4] L. Ronconi and P. J. Sadler, *Coordination Chemistry Reviews* 2007, *251*, 1633-1648.

[5] O. Andersen, *Mini Reviews in Medicinal Chemistry* 2004, *4*, 11-21.

[6] R. G. Pearson, *Journal of the American Chemical Society* 1963, *85*, 3533-3539.

[7] R. C. Hider, Z. D. Liu and S. Piyamongkol, *Transfusion Science* 2000, *23*, 201-209.

[8] Z. D. Liu and R. C. Hider, *Coordination Chemistry Reviews* 2002, *232*, 151-171.

[9] C. A. Lipinski, F. Lombardo, B. W. Dominy and P. J. Feeney, *Advanced Drug Delivery Reviews* 2012, *64*, 4-17.

[10] L. E. Scott and C. Orvig, *Chemical Reviews* 2009, *109*, 4885-4910.

[11] V. A. Levin, *Journal of Medicinal Chemistry* 1980, *23*, 682-684.

[12] W. H. Oldendorf, *Experimental Biology and Medicine* 1974, *147*, 813-816.

[13] R. R. Crichton, *Biological Inorganic Chemistry: An Introduction.*, Elsevier, 2007.

[14] J. B. Neilands, *Annual Review of Biochemistry* 1981, *50*, 715-731.

[15] Z. J. Bulaj, R. S. Ajioka, J. D. Phillips, B. A. LaSalle, L. B. Jorde, L. M. Griffen, C. Q. Edwards and J. P. Kushner, *New England Journal of Medicine* 2000, *343*, 1529-1535.

[16] V. Gordeuk, J. Mukiibi, S. J. Hasstedt, W. Samowitz, C. Q. Edwards, G. West, S. Ndambire, J. Emmanual, N. Nkanza and Z. Chapanduka, *New England Journal of Medicine* 1992, *326*, 95-100.

[17] G. M. Brittenham, *Hematology: basic principles and practice* 2000, *3*, 397-428.

[18] E. A. Dertz, A. Stintzi and K. N. Raymond, *Journal of Biological Inorganic Chemistry* 2006, *11*, 1087-1097.

[19] R. C. Hider, A. R. Mohd-Nor, J. Silver, I. E. Morrison and L. V. Rees, *Dalton Transactions* 1981, 609-622.

[20] R. Hider and A. Hall, *Progress in Medicinal Chemistry* 1990, *28*, 41-173.

[21] D. S. Kalinowski and D. R. Richardson, *Pharmacological Reviews* 2005, *57*, 547-583.

[22] H. Keberle, *Annals of the New York Academy of Sciences* 1964, *119*, 758-768.

[23] P. M. Ihnat, J. L. Vennerstrom and D. H. Robinson, *Journal of Pharmaceutical Sciences* 2000, *89*, 1525-1536.

[24] G. Crisponi and M. Remelli, *Coordination Chemistry Reviews* 2008, *252*, 1225-1240.

[25] J. Meiwes, H.-P. Fiedler, H. Haag, H. Zähner, S. Konetschny-Rapp and G. Jung, *FEMS Microbiology Letters* 1990, *67*, 201-205.

[26] R. J. Bergeron, M. Xin, R. E. Smith, M. Wollenweber, J. S. McManis, C. Ludin and K. A. Abboud, *Tetrahedron* 1997, *53*, 427-434.

[27] G. Crisponi, V. M. Nurchi and M. A. Zoroddu, *Thalassemia Reports* 2014, *4*.

[28] R. J. Motekaitis and A. E. Martell, *Inorganica Chimica Acta* 1991, *183*, 71-80.

[29] R. A. Yokel, A. M. Fredenburg, P. W. Durbin, J. Xu, M. K. Rayens and K. N. Raymond, *Journal of Pharmaceutical Sciences* 2000, *89*, 545-555.

[30] M. A. Santos, S. M. Marques and S. Chaves, *Coordination Chemistry Reviews* 2012, *256*, 240-259.

[31] R. Grazina, L. Gano, J. Šebestík and M. A. Santos, *Journal of Inorganic Biochemistry* 2009, *103*, 262-273.

[32] S. Gama, M. Gil, L. Gano, E. Farkas and M. A. Santos, *Journal of Inorganic Biochemistry* 2009, *103*, 288-298.

[33] V. M. Nurchi, G. Crisponi, J. I. Lachowicz, S. Murgia, T. Pivetta, M. Remelli, A. Rescigno, J. Niclós-Gutíerrez, J. M. González-Pérez, A. Domínguez-Martín, A. Castiñeiras and Z. Szewczuk, *Journal of Inorganic Biochemistry* 2010, *104*, 560-569.

[34] R. C. Fox and P. D. Taylor, *Bioorganic & Medicinal Chemistry Letters* 1998, *8*, 443-446.

[35] V. M. Nurchi, J. I. Lachowicz, G. Crisponi, S. Murgia, M. Arca, A. Pintus, P. Gans, J. Niclos-Gutierrez, A. Domínguez-Martín and A. Castineiras, *Dalton Transactions* 2011, *40*, 5984-5998.

[36] V. M. Nurchi, G. Crisponi, M. Arca, M. Crespo-Alonso, J. I. Lachowicz, D. Mansoori, L. Toso, G. Pichiri, M. Amelia Santos, S. M. Marques, J. Niclós-Gutiérrez, J. M. González-Pérez, A. Domínguez-Martín, D. Choquesillo-Lazarte, Z. Szewczuk, M. Antonietta Zoroddu and M. Peana, *Journal of Inorganic Biochemistry* 2014, *141*, 132-143.

[37] L. Toso, G. Crisponi, V. M. Nurchi, M. Crespo-Alonso, J. I. Lachowicz, D. Mansoori, M. Arca, M. A. Santos, S. M. Marques, L. Gano, J. Niclós-Gutíerrez, J. M. González-Pérez, A. Domínguez-Martín, D. Choquesillo-Lazarte and Z. Szewczuk, *Journal of Inorganic Biochemistry* 2014, *130*, 112-121.

[38] P. Zatta, M. Nicolini and B. Corain, *Aluminum in Chemistry, Biology and Medicine.* 1991, 97-12.

[39] R. B. Martin in *Bioinorganic Chemistry, Vol.* Wiley-VCH Verlag GmbH & Co. KGaA, 2006.

[40] G. Berthon, *Coordination Chemistry Reviews* 2002, *228*, 319-341.

[41] S. Daydé, D. Champmartin, P. Rubini and G. Berthon, *Inorganica Chimica Acta* 2002, *339*, 513-524.

[42] E. Marklund and L.-O. Ohman, *Acta Chemica Scandinavica* 1990, *44*, 353-4357.

[43] S. Sjöberg and L.-O. Öhman, *Dalton Transactions* 1985, 2665-2669.

[44] E. Marklund, S. Sioberg and L.-O. Ohman, *Acta Chemica Scandinavica* 1986, *40*, 367-373.

[45] K. Berend, G. B. van der Voet and F. A. de Wolff in *Acute aluminum intoxication, Vol.* Springer, 2002, pp. 1-58.

[46] L.-O. Ohman, *Inorganic Chemistry* 1988, *27*, 2565-2570.

[47] G. Crisponi, V. M. Nurchi, M. Crespo-Alonso and L. Toso, *Current Medicinal Chemistry* 2012, *19*, 2794-2815.

[48] S. Chaves, P. I. Dron, F. A. Danalache, D. Sacoto, L. Gano and M. A. Santos, *Journal of Inorganic Biochemistry* 2009, *103*, 1521-1529.

[49] S. Gama, P. Dron, S. Chaves, E. Farkas and M. A. Santos, *Dalton Transactions* 2009, 6141-6150.

[50] S. Chaves, S. M. Marques, A. M. Matos, A. Nunes, L. Gano, T. Tuccinardi, A. Martinelli and M. A. Santos, *Chemistry A European Journal* 2010, *16*, 10535-10545.

[51] S. Chaves, A. Capelo, L. Areias, S. M. Marques, L. Gano, M. A. Esteves and M. A. Santos, *Dalton Transactions* 2013, *42*, 6033-6045.

[52] F. Biaso, P. Baret, J.-L. Pierre and G. Serratrice, *Journal of Inorganic Biochemistry* 2002, *89*, 123-130.

[53] E. Gumienna-Kontecka, R. Silvagni, R. Lipinski, M. Lecouvey, F. C. Marincola, G. Crisponi, V. M. Nurchi, Y. Leroux and H. Kozlowski, *Inorganica Chimica Acta* 2002, *339*, 111-118.

[54] M. Tegoni, D. Valensin, L. Toso and M. Remelli, *Current Medicinal Chemistry* 2014, *21*, 3785-3818.

[55] Y. Zhang, V. L. Dawson and T. M. Dawson, *Neurobiology of Disease* 2000, *7*, 240-250.

[56] B. S. Berlett and E. R. Stadtman, *Journal of Biological Chemistry* 1997, *272*, 20313-20316.

[57] H. Kozlowski, A. Janicka-Klos, J. Brasun, E. Gaggelli, D. Valensin and G. Valensin, *Coordination Chemistry Reviews* 2009, *253*, 2665-2685.

[58] M. Mori, A. Hattori, M. Sawaki, N. Tsuzuki, N. Sawada, M. Oyamada, N. Sugawara and K. Enomoto, *The American Journal of Pathology* 1994, *144*, 200.

[59] M. Lovell, J. Robertson, W. Teesdale, J. Campbell and W. Markesbery, *Journal of the Neurological Sciences* 1998, *158*, 47-52.

[60] M. A. Smith, P. L. Harris, L. M. Sayre and G. Perry, *Proceedings of the National Academy of Sciences* 1997, *94*, 9866-9868.

[61] A. I. Bush, *Trends in Neurosciences* 2003, *26*, 207-214.

[62] A. I. Bush and R. E. Tanzi, *Neurotherapeutics* 2008, *5*, 421-432.

[63] P. A. Adlard, R. A. Cherny, D. I. Finkelstein, E. Gautier, E. Robb, M. Cortes, I. Volitakis, X. Liu, J. P. Smith and K. Perez, *Neuron* 2008, *59*, 43-55.

[64] D. Gong, J. Lu, X. Chen, S. Reddy, D. Crossman, S. Glyn-Jones, Y.-S. Choong, J. Kennedy, B. Barry and S. Zhang, *Diabetologia* 2008, *51*, 1741-1751.

[65] G. J Cooper, *Current Medicinal Chemistry* 2012, *19*, 2828-2860.

[66] G. J. Cooper, Y.-K. Chan, A. M. Dissanayake, F. E. Leahy, G. F. Keogh, C. M. Frampton, G. D. Gamble, D. H. Brunton, J. R. Baker and S. D. Poppitt, *Diabetes* 2005, *54*, 1468-1476.

[67] G. J. Cooper, A. R. Phillips, S. Y. Choong, B. L. Leonard, D. J. Crossman, D. H. Brunton, E. L. Saafi, A. M. Dissanayake, B. R. Cowan and A. A. Young, *Diabetes* 2004, *53*, 2501-2508.

[68] J. Lu, D. Gong, S. Choong, H. Xu, Y. Chan, X. Chen, S. Fitzpatrick, S. Glyn-Jones, S. Zhang and T. Nakamura, *Diabetologia* 2010, *53*, 1217-1226.

[69] G. JS Cooper, *Current Medicinal Chemistry* 2012, *19*, 2828-2860.

[70] A. Ala, A. P. Walker, K. Ashkan, J. S. Dooley and M. L. Schilsky, *The Lancet* 2007, *369*, 397-408.

[71] V. Medici, A. Santon, G. Sturniolo, R. D'inca, S. Giannetto, V. Albergoni and P. Irato, *Archives of Toxicology* 2002, *76*, 509-516.

[72] L. Banci, I. Bertini, F. Cantini and S. Ciofi-Baffoni, *Cellular and Molecular Life Sciences* 2010, *67*, 2563-2589.

[73] N. J. Robinson and D. R. Winge, *Annual Review of Biochemistry* 2010, *79*, 537.

[74] D. Denny-Brown and H. Porter, *New England Journal of Medicine* 1951, *245*, 917-925.

[75] M. Chvapil, F. Kielar, F. Liska, A. Silhankova and K. Brendel, *Connective Tissue Research* 2005, *46*, 242-250.

[76] J. Walshe, *The Lancet* 1982, *319*, 643-647.

[77] G. J. Brewer, F. Askari, M. T. Lorincz, M. Carlson, M. Schilsky, K. J. Kluin, P. Hedera, P. Moretti, J. K. Fink and R. Tankanow, *Archives of Neurology* 2006, *63*, 521-527.

[78] A. M. Pujol, C. Gateau, C. Lebrun and P. Delangle, *Journal of the American Chemical Society* 2009, *131*, 6928-6929.

[79] A. M. Pujol, M. Cuillel, A. S. Jullien, C. Lebrun, D. Cassio, E. Mintz, C. Gateau and P. Delangle, *Angewandte Chemie* 2012, *124*, 7563-7566.

[80] A. M. Pujol, C. Gateau, C. Lebrun and P. Delangle, *Chemistry-A European Journal* 2011, *17*, 4418-4428.

[81] A. Khalifa, *Journal of Chemotherapy* 2007, *19*, 620-631.

[82] D. E. Green, M. L. Bowen, L. E. Scott, T. Storr, M. Merkel, K. Böhmerle, K. H. Thompson, B. O. Patrick, H. J. Schugar and C. Orvig, *Dalton Transactions* 2010, *39*, 1604-1615.

[83] A. Barilli, C. Atzeri, I. Bassanetti, F. Ingoglia, V. Dall'Asta, O. Bussolati, M. Maffini, C. Mucchino and L. Marchiò, *Molecular Pharmaceutics* 2014, *11*, 1151-1163.

[84] R. A. Cherny, C. S. Atwood, M. E. Xilinas, D. N. Gray, W. D. Jones, C. A. McLean, K. J. Barnham, I. Volitakis, F. W. Fraser and Y.-S. Kim, *Neuron* 2001, *30*, 665-676.

[85] A. M. Mancino, S. S. Hindo, A. Kochi and M. H. Lim, *Inorganic Chemistry* 2009, *48*, 9596-9598.

[86] C. Deraeve, M. Pitié, H. Mazarguil and B. Meunier, *New Journal of Chemistry* 2007, *31*, 193-195.

[87] C. Deraeve, A. Maraval, L. Vendier, V. Faugeroux, M. Pitié and B. Meunier, *European Journal of Inorganic Chemistry* 2008, *2008*, 5622-5631.

[88] C. Deraeve, C. Boldron, A. Maraval, H. Mazarguil, H. Gornitzka, L. Vendier, M. Pitie and B. Meunier, *Chemistry-A European Journal* 2008, *14*, 682-696.

[89] E. W. Price and C. Orvig, *Chemical Society Reviews* 2014, *43*, 260-290.

[90] C. Rodríguez-Rodríguez, M. Telpoukhovskaia and C. Orvig, *Coordination Chemistry Reviews* 2012, *256*, 2308-2332.

[91] J. J. Braymer, A. S. DeToma, J.-S. Choi, K. S. Ko and M. H. Lim, *International Journal of Alzheimer's Disease* 2010, *2011*.

[92] A. Dedeoglu, K. Cormier, S. Payton, K. A. Tseitlin, J. N. Kremsky, L. Lai, X. Li, R. D. Moir, R. E. Tanzi and A. I. Bush, *Experimental Gerontology* 2004, *39*, 1641-1649.

[93] W.-h. Wu, P. Lei, Q. Liu, J. Hu, A. P. Gunn, M.-s. Chen, Y.-f. Rui, X.-y. Su, Z.-p. Xie and Y.-F. Zhao, *Journal of Biological Chemistry* 2008, *283*, 31657-31664.

[94] C. Hilbich, B. Kisters-Woike, J. Reed, C. L. Masters and K. Beyreuther, *Journal of Molecular Biology* 1992, *228*, 460-473.

[95] W. P. Esler, E. R. Stimson, J. R. Ghilardi, Y.-A. Lu, A. M. Felix, H. V. Vinters, P. W. Mantyh, J. P. Lee and J. E. Maggio, *Biochemistry* 1996, *35*, 13914-13921.

[96] L. O. Tjernberg, J. Näslund, F. Lindqvist, J. Johansson, A. R. Karlström, J. Thyberg, L. Terenius and C. Nordstedt, *Journal of Biological Chemistry* 1996, *271*, 8545-8548.

[97] J. Bieschke, S. J. Siegel, Y. Fu and J. W. Kelly, *Biochemistry* 2008, *47*, 50-59.

[98] G. Cooper, A. Young, G. Gamble, C. Occleshaw, A. Dissanayake, B. Cowan, D. Brunton, J. Baker, A. Phillips and C. Frampton, *Diabetologia* 2009, *52*, 715-722.

[99] P. Chellan and P. J. Sadler, *Philosophical Transactions of the Royal Society of London A: Mathematical, Physical and Engineering Sciences* 2015, *373*, 20140182.

[100] C. Andreini, L. Banci, I. Bertini and A. Rosato, *Journal of Proteome Research* 2006, *5*, 196-201.

[101] D. S. Auld in *Zinc coordination sphere in biochemical zinc sites, Vol.* Springer, 2001, pp. 85-127.

[102] A. Sigel, H. Sigel and R. K. Sigel, *Interrelations between essential metal ions and human diseases*, Springer, 2013, p.

[103] W. Maret and H. H. Sandstead, *Journal of Trace Elements in Medicine and Biology* 2006, *20*, 3-18.

[104] P. W. Mantyh, J. R. Ghilardi, S. Rogers, E. DeMaster, C. J. Allen, E. R. Stimson and J. E. Maggio, *Journal of Neurochemistry* 1993, *61*, 1171-1174.

[105] V. Frazzini, E. Rockabrand, E. Mocchegiani and S. Sensi, *Biogerontology* 2006, *7*, 307-314.

[106] G. Crisponi, V. M. Nurchi, M. Crespo-Alonso, G. Sanna, M. A. Zoroddu, G. Alberti and R. Biesuz, *PloS one* 2015, *10*, e0133050.

[107] D. T. Puerta, J. Mongan, B. L. Tran, J. A. McCammon and S. M. Cohen, *Journal of the American Chemical Society* 2005, *127*, 14148-14149.

[108] G. Battaglia, M. La Russa, V. Bruno, L. Arenare, R. Ippolito, A. Copani, F. Bonina and F. Nicoletti, *Brain Research* 2000, *860*, 149-156.

[109] E. J. Bilsky, R. D. Egleton, S. A. Mitchell, M. M. Palian, P. Davis, J. D. Huber, H. Jones, H. I. Yamamura, J. Janders and T. P. Davis, *Journal of Medicinal Chemistry* 2000, *43*, 2586-2590.

[110] F. Bonina, C. Puglia, M. G. Rimoli, D. Melisi, G. Boatto, M. Nieddu, A. Calignano, G. L. Rana and P. d. Caprariis, *Journal of Drug Targeting* 2003, *11*, 25-36.

[111] M. Zhang, Z. Zhang, D. Blessington, H. Li, T. M. Busch, V. Madrak, J. Miles, B. Chance, J. D. Glickson and G. Zheng, *Bioconjugate Chemistry* 2003, *14*, 709-714.

[112] M. Rouquayrol, B. Gaucher, J. Greiner, A.-M. Aubertin, P. Vierling and R. Guedj, *Carbohydrate Research* 2001, *336*, 161-180.

[113] O. Andersen, *Chemical Reviews* 1999, *99*, 2683-2710.

[114] S. A. Wood and I. M. Samson, *Ore Geology Reviews* 2006, *28*, 57-102.

[115] C. R. Chitambar, *International Journal of Environmental Research and Public Health* 2010, *7*, 2337-2361.

[116] S. Ohtake, V. Truong-Le, D. Lechuga-Ballesteros, L. Yee, B. V. Pham, R. Martin and A. Saxena in *Gallium formulation for the treatment and prevention of infectious diseases, Vol.* Google Patents, 2014.

[117] M. M. Hart and R. H. Adamson, *Proceedings of the National Academy of Sciences* 1971, *68*, 1623-1626.

[118] M. M. Hart, C. F. Smith, S. T. Yancey and R. H. Adamson, *Journal of the National Cancer Institute* 1971, *47*, 1121-1128.

[119] L. R. Hoffman and B. W. Ramsey, *CHEST Journal* 2013, *143*, 207-213.

[120] W. R. Harris and A. E. Martell, *Inorganic Chemistry* 1976, *15*, 713-720.

[121] T. Storr, K. H. Thompson and C. Orvig, *Chemical Society Reviews* 2006, *35*, 534-544.

[122] C. J. Anderson and M. J. Welch, *Chemical Reviews* 1999, *99*, 2219-2234.

[123] D. Shetty, Y.-S. Lee and J. M. Jeong, *Nuclear Medicine and Molecular Imaging* 2010, *44*, 233-240.

[124] H. R. Maecke, M. Hofmann and U. Haberkorn, *Journal of Nuclear Medicine* 2005, *46*, 172S-178S.

[125] S. Chaves, A. C. Mendonça, S. M. Marques, M. I. Prata, A. C. Santos, A. F. Martins, C. F. Geraldes and M. A. Santos, *Journal of Inorganic Biochemistry* 2011, *105*, 31-38.

[126] D. Putzer, M. Gabriel, B. Henninger, D. Kendler, C. Uprimny, G. Dobrozemsky, C. Decristoforo, R. J. Bale, W. Jaschke and I. J. Virgolini, *Journal of Nuclear Medicine* 2009, *50*, 1214-1221.

[127] E. Boros, C. L. Ferreira, J. F. Cawthray, E. W. Price, B. O. Patrick, D. W. Wester, M. J. Adam and C. Orvig, *Journal of the American Chemical Society* 2010, *132*, 15726-15733.

[128] E. Boros, C. L. Ferreira, B. O. Patrick, M. J. Adam and C. Orvig, *Nuclear Medicine and Biology* 2011, *38*, 1165-1174.

[129] C. F. Ramogida, J. Pan, C. L. Ferreira, B. O. Patrick, K. Rebullar, D. T. Yapp, K.-S. Lin, M. J. Adam and C. Orvig, *Inorganic Chemistry* 2015.

[130] J. Notni, J. Šimeček, P. Hermann and H. J. Wester, *Chemistry-A European Journal* 2011, *17*, 14718-14722.

[131] J. Notni, P. Hermann, J. Havlíčková, J. Kotek, V. Kubíček, J. Plutnar, N. Loktionova, P. J. Riss, F. Rösch and I. Lukeš, *Chemistry-A European Journal* 2010, *16*, 7174-7185.

[132] E. R. Birnbaum, J. E. Gomez and D. W. Darnall, *Journal of the American Chemical Society* 1970, *92*, 5287-5288.

[133] S. P. Fricker, *Chemical Society Reviews* 2006, *35*, 524-533.

[134] C. Evans, *Trends in Biochemical Sciences* 1983, *8*, 445-449.

[135] J. S. Cho, D. S. Yoo, Y. C. Chung and S. H. Rhee, *Journal of Biomedical Materials Research Part A* 2014, *102*, 455-469.

[136] A. Bigi, E. Boanini, C. Capuccini and M. Gazzano, *Inorganica Chimica Acta* 2007, *360*, 1009-1016.

[137] L. Rintoul, E. Wentrup-Byrne, S. Suzuki and L. Grøndahl, *Journal of Materials Science: Materials in Medicine* 2007, *18*, 1701-1709.

[138] A. Serret, M. Cabanas and M. Vallet-Regi, *Chemistry of Materials* 2000, *12*, 3836-3841.

[139] J. Xu, Y.-X. Zhang, X.-Q. Yu, Z.-H. Liu, L.-N. Wang, J.-H. Chen, Y.-P. Fan, Z.-H. Ni, M. Wang and F.-H. Yuan, *BMC Nephrology* 2013, *14*, 29.

[140] N. D. Atherton, J. W. Totten and M. D. Gaitonde in *Treatment of bone diseases, Vol.* Google Patents, 2006.

[141] T. B. Drüeke, *Seminars in Dialysis* 2007, pp. 329-332.

[142] Y. Mawani, J. F. Cawthray, S. Chang, K. Sachs-Barrable, D. M. Weekes, K. M. Wasan and C. Orvig, *Dalton Transactions* 2013, *42*, 5999-6011.

[143] J. Cawthray, D. Weekes, O. Sivak, A. Creagh, F. Ibrahim, M. Iafrate, C. Haynes, K. Wasan and C. Orvig, *Chemical Science* 2015, *6*, 6439-6447.

[144] Z. Xue, M. Lin, J. Zhu, J. Zhang, Y. Li and Z. Guo, *Chemical Communications* 2010, *46*, 1212-1214.

[145] I. Rogachevskii, V. Plakhova and T. Shelykh, *Russian Journal of General Chemistry* 2009, *79*, 104-116.

[146] A. R. Katritzky, C. D. Hall, B. El-Gendy and B. Draghici, *Journal of Computer-aided Molecular Design* 2010, *24*, 475-484.

[147] N. V. M. Lachowicz J. I. , G. Crisponi, M. G. Jaraquemada-Pelaez, M. Arca, A. Pintus, M. A. Santos, C. Quintanova, L. Gano, Z. Szewczuk, M. A. Zoroddu, M. Peana, A. Domínguez-Martín, and D. Choquesillo-Lazarte,, *Dalton Transactions* 2016, *accepted 16-02-2016*.

[148] W. R. Harris, K. N. Raymond and F. L. Weitl, *Journal of the American Chemical Society* 1981, *103*, 2667-2675.

[149] V. Kahn, N. Ben-Shalom and V. Zakin, *Journal of Agricultural and Food Chemistry* 1997, *45*, 4460-4465.

[150] Y. Mishima, S. Hatta, Y. Ohyama and M. Inazu, *Pigment Cell Research* 1988, *1*, 367-374.

[151] M. Sendovski, M. Kanteev, V. S. Ben-Yosef, N. Adir and A. Fishman, *Journal of Molecular Biology* 2011, *405*, 227-237.

[152] Y. Kobayashi, H. Kayahara, K. Tadasa and H. Tanaka, *Bioorganic & Medicinal Chemistry Letters* 1996, *6*, 1303-1308.

[153] J. Kadokawa, T. Nishikura, R. Muraoka, H. Tagaya and N. Fukuoka, *Synthetic Communications* 2003, *33*, 1081-1086.

[154] T. Nishimura, T. Kometani, H. Takii, Y. Terada and S. Okada, *Journal of Fermentation and Bioengineering* 1994, *78*, 37-41.

[155] G. O'Brien, J. Patterson and J. Meadow, *The Journal of Organic Chemistry* 1962, *27*, 1711-1714.

[156] Y. Kobayashi, H. Kayahara, K. Tadasa, T. Nakamura and H. Tanaka, *Bioscience, biotechnology, and biochemistry* 1995, *59*, 1745-1746.

[157] H. Kim, J. Choi, J. K. Cho, S. Y. Kim and Y.-S. Lee, *Bioorganic & Medicinal Chemistry Letters* 2004, *14*, 2843-2846.

[158] S. Y. K. J.M. Noh, D.H. Kim, Y.S. Lee, *Peptide Science* 2007, *88*, 300-307.

[159] B. E. Bryant and C. Fernelius, *Journal of the American Chemical Society* 1954, *76*, 5351-5352.

[160] W. McBryde and G. Atkinson, *Canadian Journal of Chemistry* 1961, *39*, 510-525.

[161] T. Hediund and L.-O. Ghman, *Acta Chemica Scandinavia A* 1988, *42*, 702-709.

[162] M. M. Finnegan, T. G. Lutz, W. O. Nelson, A. Smith and C. Orvig, *Inorganic Chemistry* 1987, *26*, 2171-2176.

[163] L. Toso, G. Crisponi, V. M. Nurchi, M. Crespo-Alonso, J. I. Lachowicz, M. A. Santos, S. M. Marques, J. Niclós-Gutiérrez, J. M. González-Pérez and A. Domínguez-Martín, *Journal of Inorganic Biochemistry* 2013, *127*, 220-231.

[164] A. E. Martell and R. M. Smith, *Other organic ligands*, Springer, 1977, p.

[165] R. M. Smith and A. E. Martell, *Science of the Total Environment* 1987, *64*, 125-147.

[166] J. Karalliedde, A. Smith, L. DeAngelis, V. Mirenda, A. Kandra, J. Botha, P. Ferber and G. Viberti, *Hypertension* 2008, *51*, 1617-1623.

[167] J. F. Da Silva and R. J. P. Williams, *The biological chemistry of the elements: the inorganic chemistry of life*, Oxford University Press, 2001, p.

[168] E. W. Price, B. M. Zeglis, J. S. Lewis, M. J. Adam and C. Orvig, *Dalton Transactions* 2014, *43*, 119-131.

[169] H. Mauser, *Zeitschrift für Elektrochemie, Berichte der Bunsengesellschaft für Physikalische Chemie* 1962, *66*, 882-882.

[170] M. Peana, S. Medici, V. M. Nurchi, G. Crisponi and M. A. Zoroddu, *Coordination Chemistry Reviews* 2013, *257*, 2737-2751.

[171] M. A. Zoroddu, M. Peana and S. Medici, *Dalton Transactions* 2007, 379-384.

[172] M. A. Zoroddu, S. Medici, M. Peana and R. Anedda, *Dalton Transactions* 2010, *39*, 1282-1294.

[173] L. Hansen, T. Jensen, S. Mayne, D. Eatough, R. Izatt and J. Christensen, *The Journal of Chemical Thermodynamics* 1975, *7*, 919-926.

[174] P. Gans, A. Sabatini and A. Vacca, *Journal of Solution Chemistry* 2008, *37*, 467-476.

[175] A. Vacca, A. Sabatini and L. Bologni, *Journal of the Chemical Society, Dalton Transactions* 1981, 1246-1250.

[176] V. B. A. APEX2 Software, 2014.

[177] V. B. A. SADABS, 2012.

[178] G. M. Sheldrick, *Acta Crystallographica Section A: Foundations of Crystallography* 2008, *64*, 112-122.

[179] G. Gran, *Analyst* 1952, *77*, 661-671.

[180] P. Gans, A. Sabatini and A. Vacca, *Talanta* 1996, *43*, 1739-1753.

[181] V. M. Nurchi, J. I. Lachowicz, G. Crisponi, S. Murgia, M. Arca, A. Pintus, P. Gans, J. Niclos-Gutierrez, A. Domínguez-Martín, A. Castineiras, M. Remelli, Z. Szewczuk and T. Lis, *Dalton Transactions* 2011, *40*, 5984-5998.

[182] P. Gans, A. Sabatini and A. Vacca, *Annali di Chimica* 1999, *89*, 45-49.

[183] W. Koch and M. C. Holthausen, *A chemist's guide to density functional theory*, Wiley-Vch Weinheim, 2001.

[184] M. Frisch, G. Trucks, H. B. Schlegel, G. Scuseria, M. Robb, J. Cheeseman, G. Scalmani, V. Barone, B. Mennucci and G. Petersson, *Wallingford, CT* 2009, *19*, 227-238.

[185] C. Adamo and V. Barone, *The Journal of Chemical Physics* 1998, *108*, 664-675.

[186] A. Schäfer, H. Horn and R. Ahlrichs, *The Journal of Chemical Physics* 1992, *97*, 2571-2577.

[187] A. E. Reed, R. B. Weinstock and F. Weinhold, *The Journal of Chemical Physics* 1985, *83*, 735-746.

[188] K. B. Wiberg, *Tetrahedron* 1968, *24*, 1083-1096.

[189] J. Tomasi, B. Mennucci and R. Cammi, *Chemical Reviews* 2005, *105*, 2999-3094.

[190] A. Frisch, H. Hratchian and R. Dennington II, *Inc., Wallingford CT* 2009.

[191] G. Schaftenaar and J. H. Noordik, *Journal of Computer-aided Molecular Design* 2000, *14*, 123-134.

[192] B. Marongiu, A. Piras, S. Porcedda, E. Tuveri, E. Sanjust, M. Meli, F. Sollai, P. Zucca and A. Rescigno, *Journal of Agricultural and Food Chemistry* 2007, *55*, 10022-10027.

[193] L. Saghaie, M. Pourfarzam, A. Fassihi and B. Sartippour, *Research in Pharmaceutical Sciences* 2013, *8*, 233.

[194] S. Fakih, M. Podinovskaia, X. Kong, H. L. Collins, U. E. Schaible and R. C. Hider, *Journal of Medicinal Chemistry* 2008, *51*, 4539-4552.

[195] M. Cal, M. Jaremko, Ł. Jaremko and P. Stefanowicz, *Amino acids* 2013, *44*, 1085-1091.

[196] P. Stefanowicz, Ł. Jaremko, M. Jaremko and T. Lis, *New Journal of Chemistry* 2006, *30*, 258-265.

[197] M. C. Sheikh, S. Takagi, A. Ogasawara, M. Ohira, R. Miyatake, H. Abe, T. Yoshimura and H. Morita, *Tetrahedron* 2010, *66*, 2132-2140.

[198] J. Lokaj, J. Kožíšek, B. Koreň, M. Uher and V. Vrabel, *Acta Crystallographica Section C: Crystal Structure Communications* 1991, *47*, 193-194.

[199] J. I. Lachowicz, V. M. Nurchi, G. Crisponi, M. d. G. Jaraquemada-Pelaez, M. Ostrowska, J. Jezierska, E. Gumienna-Kontecka, M. Peana, M. A. Zoroddu, D. Choquesillo-Lazarte, J. Niclós-Gutiérrez and J. M. González-Pérez, *Journal of Inorganic Biochemistry* 2015, *151*, 94-106.

[200] http://www.hyperquad.co.uk/HQ2013.htm.

[201] V. M. Nurchi, G. Crisponi, T. Pivetta, M. Donatoni and M. Remelli, *Journal of Inorganic Biochemistry* 2008, *102*, 684-692.

[202] R. C. Scarrow, P. E. Riley, K. Abu-Dari, D. L. White and K. N. Raymond, *Inorganic Chemistry* 1985, *24*, 954-967.

[203] H. Stunzi, L. Harris, D. Perrin and T. Teitei, *Australian Journal of Chemistry* 1980, *33*, 2207-2220.

[204] E. Spinner and J. White, *Journal of the Chemical Society B* 1966, 991-995.

[205] G. Crisponi, M. Casu, V. M. Nurchi, F. Cesare-Marincola, T. Pivetta and R. Silvagni, *Talanta* 2002, *56*, 441-449.

[206] M. A. M.C. Aragoni, G. Crisponi, V.M. Nurchi, *Analitica Chimica Acta* 1995, *316*, 195-204.

[207] L. D. Pettit and K. Powell, *Chemistry International* 2006.

[208] E. Cagigal, L. Gonzalez, R. Alonso and R. Jimenez, *Journal of Pharmaceutical and Biomedical Analysis* 2001, *26*, 477-486.

[209] M. Meloun, T. Syrový and A. Vrána, *Analytica Chimica Acta* 2005, *533*, 97-110.

[210] J. C. Gillis and A. Markham, *Drugs* 1997, *54*, 885-902.

[211] K. L. Goa and A. J. Wagstaff, *Drugs* 1996, *51*, 820-845.

[212] K. E. McCarthy, Q. Wang, E. W. Tsai, R. E. Gilbert, D. P. Ip and M. A. Brooks, *Journal of Pharmaceutical and Biomedical Analysis* 1998, *17*, 671-677.

[213] R. Williams, M. Alasandro, V. Fasone, R. Boucher and J. Edwards, *Journal of Pharmaceutical and Biomedical Analysis* 1996, *14*, 1539-1546.

[214] C. I. Furtek and M.-W. Lo, *Journal of Chromatography B: Biomedical Sciences and Applications* 1992, *573*, 295-301.

[215] S.-Y. Chang, D. B. Whigan, N. N. Vachharajani and R. Patel, *Journal of Chromatography B: Biomedical Sciences and Applications* 1997, *702*, 149-155.

[216] P. Tosco, B. Rolando, R. Fruttero, Y. Henchoz, S. Martel, P. A. Carrupt and A. Gasco, *Helvetica Chimica Acta* 2008, *91*, 468-482.

[217] T. Eicher and S. Hauptmann, *Thieme, New York* 1995.

[218] V. Ostrovskii, G. Koldobskii, N. Shirokova and V. Poplavskii, *Chemistry of Heterocyclic Compounds* 1981, *17*, 412-416.

[219] L. Haussen, E. Baca and P. Scheiner, *Journal of Heterocyclic Chemistry* 1970, *7*, 991.

[220] M. C. Aragoni, M. Arca, G. Crisponi, F. Cristiani, F. Isaia and V. M. Nurchi, *Talanta* 1996, *43*, 1357-1366.

[221] G. Crisponi, *Reactive and Functional Polymers* 1997, *34*, 121-126.

[222] A. Avdeef, J. E. Comer and S. J. Thomson, *Analytical Chemistry* 1993, *65*, 42-49.

[223] J. Bridges, P. Creaven and R. Williams, *Biochemistry J* 1965, *96*, 872-878.

[224] J. Jayabharathi, V. Thanikachalam, N. Srinivasan and M. V. Perumal, *Spectrochimica Acta Part A: Molecular and Biomolecular Spectroscopy* 2012, *90*, 125-130.

[225] K. Popov, H. Rönkkömäki and L. H. Lajunen, *Pure and Applied Chemistry* 2001, *73*, 1641-1677.

[226] J. J. Molenda, M. A. Basinger, T. P. Hanusa and M. M. Jones, *Journal of Inorganic Biochemistry* 1994, *55*, 131-146.

[227] J. Charalambous, A. Dodd, M. McPartlin, S. O. Matondo, N. D. Pathirana and H. R. Powell, *Polyhedron* 1988, *7*, 2235-2237.

[228] T. Jakusch, K. Gajda-Schrantz, Y. Adachi, H. Sakurai, T. Kiss and L. Horváth, *Journal of Inorganic Biochemistry* 2006, *100*, 1521-1526.

[229] A. Okac and Z. Kolarik, *Collect. Czech. Chem. Commun* 1959, *24*, 266-272.

[230] E. W. Ainscough, A. G. Bingham, A. M. Brodie, J. M. Husbands and J. E. Plowman, *Dalton Transactions* 1981, 1701-1707.

[231] B. B. A. Abragam, *Clarendon Press, Oxford University Press* 1970, *25*, 846-847.

[232] M. Cabras and M. Zoroddu, *Inorganica Chimica Acta* 1987, *135*, L19-L20.

[233] L. P. Battaglia, A. C. Bonamartini, S. Ianelli, M. A. Zoroddu and G. Sanna, *Journal of the Chemical Society, Faraday Transactions* 1991, *87*, 3863-3867.

[234] S. Medici, M. Peana, L. G. Delogu and M. A. Zoroddu, *Dalton Transactions* 2012, *41*, 4378-4388.

[235] M. Peana, S. Medici, V. M. Nurchi, J. I. Lachowicz, G. Crisponi, M. Crespo-Alonso, M. A. Santos and M. A. Zoroddu, *Journal of Inorganic Biochemistry* 2015, *148*, 69-77.

[236] S. B. Etcheverry, E. G. Ferrer, L. Naso, D. A. Barrio, L. Lezama, T. Rojo and P. A. M. Williams, *Bioorganic & Medicinal Chemistry* 2007, *15*, 6418-6424.

[237] Â. M. Denadai, J. G. Da Silva, P. P. Guimarães, L. B. S. Gomes, A. S. Mangrich, E. I. de Rezende, I. M. Daniel, H. Beraldo and R. D. Sinisterra, *Materials Science and Engineering: C* 2013, *33*, 3916-3922.

[238] QikProp, *Version 2.5, LCC, New York, NY* 2005.

[239] J. Xu, B. Kullgren, P. W. Durbin and K. N. Raymond, *Journal of Medicinal Chemistry* 1995, *38*, 2606-2614.

[240] D. J. Gordon and R. F. Fenske, *Inorganic Chemistry* 1982, *21*, 2916-2923.

[241] E. Neeley, G. Fritch, A. Fuller, J. Wolfe, J. Wright and W. Flurkey, *International Journal of Molecular Sciences* 2009, *10*, 3811-3823.

[242] M. C. S. Fogal, L. Giaretta, F. Lanciai, L. Nogara, L. Bubacco, E. Bergantino, *Molecular Biotechcnology* 2015, 1-13.

[243] V. M. Nurchi, T. Pivetta, J. I. Lachowicz and G. Crisponi, *Journal of Inorganic Biochemistry* 2009, *103*, 227-236.

[244] K. H. Maclean, J. L. Cleveland and J. B. Porter, *Blood* 2001, *98*, 3831-3839.

[245] R. Galanello, *Therapeutics and Clinical Risk Management* 2007, *3*, 795.

[246] E. Erdoğan, D. Canatan, A. R. Örmeci, H. Vural and F. Aylak, *Journal of Trace Elements in Medicine and Biology* 2013, *27*, 109-111.

[247] R. C. Hider, *American Journal of Kidney Diseases* 2010, *55*, 614-615.

Appendix

Supplementary Figures and Tables

Appendix

List of Figures

List of Tables

TableA1. Crystal data and structure refinement for L1.

Empirical formula	C_{13} H_{12} O_8
Formula weight	296.23
Temperature	100.0 K
Wavelength	0.71073 Å
Crystal system, space group	Monoclinic, C2/c
Unit cell dimensions	a = 20.527(3) Å, □ =90°
	b = 4.2812(5) Å, □
	c = 16.072(2) Å, □ = 90°
Volume	1238.1(3) $Å^3$
Z, calculated density	4, 1.589 Mg/m3
Absorption coefficient	0.135 mm^{-1}
F(000)	616
Crystal size	0.10 x 0.08 x 0.06 mm^3
Theta range for data collection	2.680 - 25.138°
Limiting indices	-22<=h<=24, -5<=k<=4, -19<=l<=19
Reflections collected/unique	5677/1104 [R(int) = 0.1183]
Completeness to theta = 25.138°	99.5 %
Absorption correction	Semi-empirical from equivalents
Max. and min. transmission	0.7452 and 0.6469
Refinement method	Full-matrix least-squares on F^2
Data / restraints / parameters	1104 / 0 / 98
Goodness-of-fit on F^2	1.023
Final R indices [I>2sigma(I)]	R1 = 0.0474, wR2 = 0.0818
R indices (all data)	R1 = 0.1076, wR2 = 0.0988
Largest diff. peak and hole	0.202 and -0.237 e.$Å^{-3}$

TableA2. Crystal data and structure refinement for P1.

Identification code	15jnac842
Empirical formula	$C_6H_7NO_3$
Formula weight	141.13
Temperature	100(2) K
Wavelength	0.71073 Å
Crystal system, space group	Orthorhombic, $P2_12_12_1$
Unit cell dimensions	a = 6.8410(4) Å α = 90°
	b = 7.0291(3) Å β = 90°
	c = 12.6402(4) Å γ = 90°
Volume	607.82(5) $Å^3$
Z, Calculated density	4, 1.542 Mg/m^3
Absorption coefficient	0.125 mm^{-1}
F(000)	296
Crystal size	0.100 x 0.100 x 0.100 mm
Theta range for data collection	3.223° to 27.492°
Limiting indices	-8<=h<=8, -9<=k<=9, -14<=l<=16
Reflections collec./unique	8040/1390 [R(int) = 0.0245]
Completeness to theta = 25.242	99.9 %
Refinement method	Full-matrix least-squares on F^2
Data / restraints / parameters	1390 / 0 / 91
Goodness-of-fit on F^2	1.094
Final R indices [I>2sigma(I)]	R1 = 0.0264, wR2 = 0.0666
R indices (all data)	R1 = 0.0278, wR2 = 0.0675
Absolute structure parameter	-0.5(4)
Extinction coefficient	n/a
Largest diff. peak and hole	0.251 and -0.186 $e.Å^{-3}$

TableA3. Bond lengths [A] and angles [deg] for P1.

O(4)-C(4)	1.2887(19)
O(5)-C(5)	1.3555(19)
O(5)-H(5A)	0.8400
O(8)-C(7)	1.4200(19)
O(8)-H(8A)	0.8400
N(1)-C(2)	1.347(2)
N(1)-C(6)	1.363(2)
N(1)-H(1A)	0.8801
C(2)-C(3)	1.372(2)
C(2)-C(7)	1.510(2)
C(3)-C(4)	1.416(2)
C(3)-H(3)	0.9500
C(4)-C(5)	1.435(2)
C(5)-C(6)	1.363(2)
C(6)-H(6)	0.9500
C(7)-H(7A)	0.9900
C(7)-H(7B)	0.9900

C(5)-O(5)-H(5A)	109.5
C(7)-O(8)-H(8A)	109.5
C(2)-N(1)-C(6)	121.93(14)
C(2)-N(1)-H(1A)	119.0
C(6)-N(1)-H(1A)	119.0
N(1)-C(2)-C(3)	119.81(15)
N(1)-C(2)-C(7)	116.69(14)
C(3)-C(2)-C(7)	123.50(15)
C(2)-C(3)-C(4)	121.22(15)
C(2)-C(3)-H(3)	119.4
C(4)-C(3)-H(3)	119.4
O(4)-C(4)-C(3)	123.79(15)
O(4)-C(4)-C(5)	119.91(15)
C(3)-C(4)-C(5)	116.29(14)
O(5)-C(5)-C(6)	118.62(14)
O(5)-C(5)-C(4)	121.21(14)
C(6)-C(5)-C(4)	120.17(14)
N(1)-C(6)-C(5)	120.46(15)
N(1)-C(6)-H(6)	119.8
C(5)-C(6)-H(6)	119.8
O(8)-C(7)-C(2)	112.54(13)
O(8)-C(7)-H(7A)	109.1
C(2)-C(7)-H(7A)	109.1
O(8)-C(7)-H(7B)	109.1
C(2)-C(7)-H(7B)	109.1
H(7A)-C(7)-H(7B)	107.8

Symmetry transformations used to generate equivalent atoms:

Figure A1. UV spectra collected during potentiometric titration of the ligand, C_L 4.95 x 10^{-4} M, using a 0.2 cm optical path length. A pH 2.98-4.59, B 7.29-10.52, C pH 10.64-13.22. 240-340 nm spectral range.

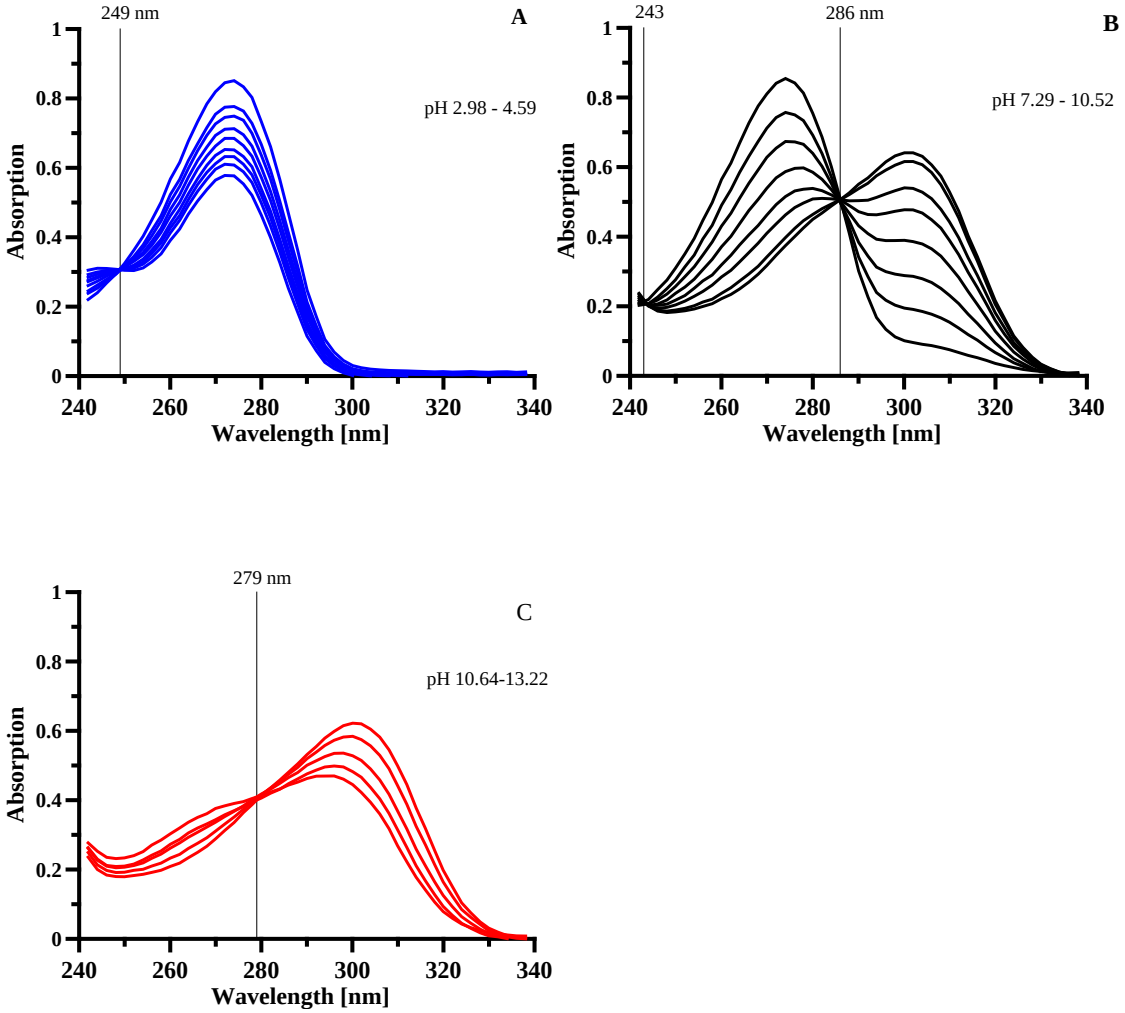

Figure A2. Stacked 1D ^{1}H NMR spectra in the aromatic region for P1 ligand by changing the pH from 0.65 to 13.30, at 298 K.

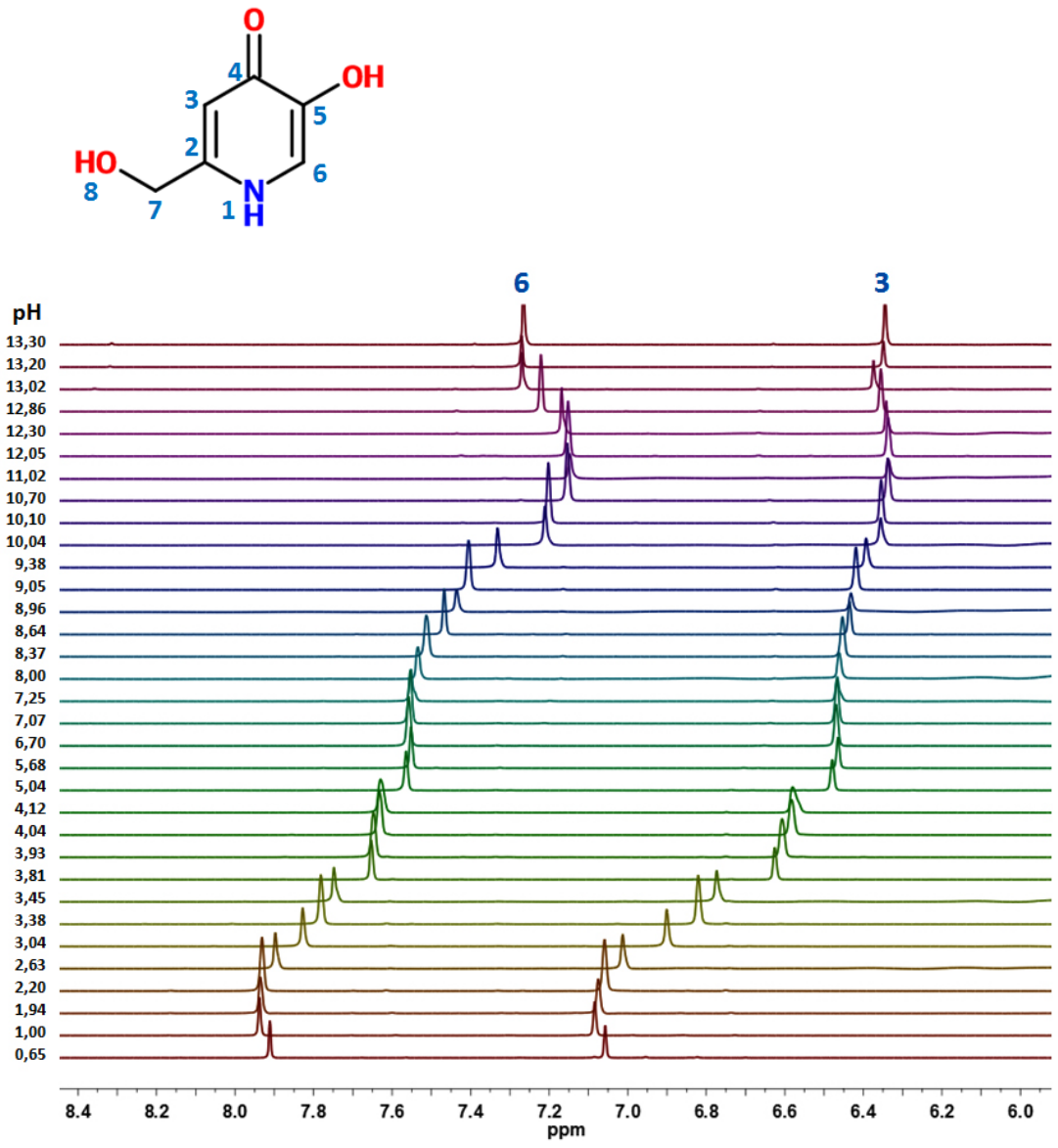

TableA4. Chemical shifts assignment for ^1H of P1 by changing the pH from 0.65 to 13.30, in aqueous solution (90%-10% H_2O-D_2O), at 298 K.

pH	H6	H3	H7
0.65	7.911	7.032	NA
1.00	7.938	7.084	NA
1.67	7.949	7.082	4.723
1.94	7.935	7.075	NA
2.20	7.931	7.059	NA
2.63	7.898	7.013	NA
3.04	7.828	6.901	NA
3.26	7.781	6.820	NA
3.45	7.731	6.738	4.624
3.38	7.748	6.774	NA
3.81	7.653	6.626	4.585
3.93	7.648	6.607	4.580
4.04	7.632	6.583	4.580
4.12	7.630	6.580	4.577
5.04	7.564	6.479	4.545
5.68	7.552	6.465	4.537
5.96	7.563	6.474	4.547
6.70	7.558	6.469	4.545
7.07	7.554	6.467	4.544
7.25	7.552	6.466	4.544
8.00	7.534	6.462	4.539
8.37	7.513	6.453	4.532
8.64	7.467	6.435	4.517
8.96	7.436	6.432	4.518
9.05	7.405	6.419	4.508
9.10	7.386	6.416	4.507
9.38	7.331	6.393	4.488
10.04	7.211	6.356	4.463
10.10	7.202	6.355	4.464
10.70	7.154	6.338	4.450
11.02	7.147	6.336	4.448
12.05	7.152	6.337	4.434
12.30	7.168	6.342	4.421
12.40	7.200	6.355	4.403
12.86	7.221	6.355	4.374
13.02	7.270	6.374	4.346
13.20	7.270	6.349	4.273
13.30	7.265	6.345	4.268

Figure A3. Experimental data for peaks of the P1 ligand at pD 7 in D_2O solution are shown at the top of the panel and compared with the data calculated for the $[C_6H_8O_3N]^+$ (142.061 m/z, Panel A) $[C_6H_7DO_3N]^+$ (143.057 m/z, Panel B), $[C_6H_6D_2O_3N]^+$ (144.063 *m/z*, Panel C), $[C_6H_5D_3O_3N]^+$ (145.070 *m/z*, Panel D) and $[C_6H_4D_4O_3N]^+$ (146.076 *m/z* Panel E).

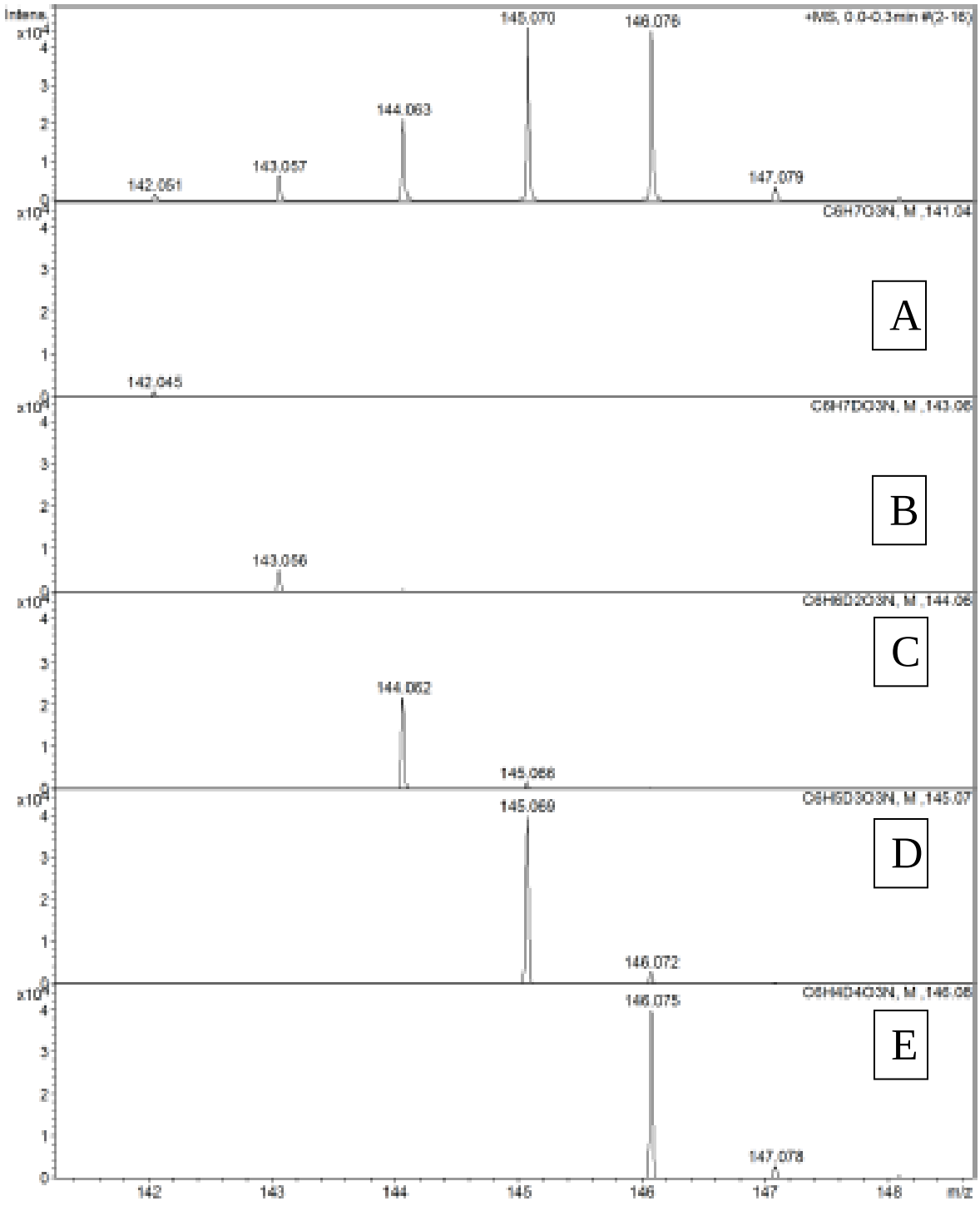

TableA5. ESI-MS *m/z* data of P1 in aqueous solution at different pH.

pH	Negative	Intensity	Positive	Intensity
1.68	140.032	10000	142.054	15000
6.13	140.034	8000	142.054	8000
11.5	139.032	2500	-	-
13.7	139.033	4000	-	-

TableA6. Selected optimized bond lengths (Å) and angles (°) for the differently protonated forms of P1[a] in the gas phase and in water (IEF-PCM SCRF model, in parenthesis).[b] [a] The neutral form of P1 corresponds to H_2L. [b]Atom numbering scheme as in Figure 1. Molecular schemes as in Scheme 6.

	H_3L^+	H_2L_a	H_2L_b	H_2L_c	HL_a^-	HL_b^-	HL_c^-	L^{2-}
N1-H1	1.025 (1.023)	1.014 (1.017)	/	1.018 (1.021)	/	1.011 (1.015)	/	/
N1-C2	1.337 (1.336)	1.349 (1.344)	1.325 (1.327)	1.336 (1.332)	1.321 (1.322)	1.345 (1.337)	1.327 (1.328)	1.322 (1.322)
C2-C3	1.389 (1.388)	1.373 (1.378)	1.400 (1.399)	1.397 (1.397)	1.411 (1.410)	1.383 (1.384)	1.398 (1.398)	1.404 (1.404)
C3-C4	1.392 (1.391)	1.435 (1.428)	1.386 (1.388)	1.385 (1.383)	1.379 (1.379)	1.448 (1.347)	1.417 (1.416)	1.433 (1.425)
C4-O4	1.325 (1.324)	1.237 (1.294)	1.351 (1.342)	1.310 (1.319)	1.335 (1.337)	1.235 (1.248)	1.265 (1.269)	1.258 (1.266)
O4-H4	0.966 (0.967)	/	0.963 (0.965)	1.010 (1.005)	1.014 (1.004)	/	/	/
C4-C5	1.425 (1.423)	1.470 (1.463)	1.408 (1.412)	1.467 (1.459)	1.452 (1.448)	1.523 (1.509)	1.455 (1.451)	1.519 (1.502)
C5-O5	1.322 (1.331)	1.328 (1.336)	1.345 (1.345)	1.253 (1.266)	1.276 (1.280)	1.245 (1.262)	1.348 (1.349)	1.265 (1.275)
O5-H5	0.968 (0.969)	0.987 (0.987)	0.966 (0.968)	/	/	/	0.998 (0.992)	/
C5-C6	1.380 (1.377)	1.361 (1.362)	1.389 (1.387)	1.405 (1.406)	1.408 (1.407)	1.418 (1.407)	1.372 (1.373)	1.424 (1.415)
N1-C6	1.349 (1.348)	1.374 (1.368)	1.334 (1.337)	1.362 (1.361)	1.348 (1.349)	1.382 (1.377)	1.356 (1.355)	1.365 (1.363)
C2-C7	1.504 (1.501)	1.510 (1.512)	1.515 (1.515)	1.507 (1.510)	1.520 (1.518)	1.499 (1.508)	1.524 (1.521)	1.526 (1.522)
C7-O8	1.393 (1.395)	1.405 (1.402)	1.384 (1.393)	1.405 (1.402)	1.391 (1.396)	1.419 (1.408)	1.391 (1.395)	1.396 (1.398)
O8-H8	0.962 (0.962)	0.963 (0.965)	0.976 (0.979)	0.963 (0.964)	0.989 (0.985)	0.964 (0.964)	0.990 (0.986)	1.015 (0.995)
N1-C2-C3	118.70 (118.88)	120.74 (120.46)	122.05 (122.43)	118.96 (118.93)	122.50 (122.45)	118.96 (119.02)	124.46 (124.17)	123.00 (122.70)
C2-C3-C4	119.36 (119.25)	120.59 (120.53)	118.47 (118.40)	119.32 (118.16)	117.40 (117.35)	123.70 (123.01)	119.62 (119.63)	122.74 (122.36)
C3-C4-C5	120.06 (119.98)	115.39 (115.56)	119.33 (119.07)	122.64 (122.74)	121.69 (121.81)	116.05 (116.52)	114.35 (114.57)	114.67 (115.19)
C4-C5-C6	117.89 (118.14)	121.34 (121.39)	117.61 (117.92)	114.80 (114.93)	114.65 (114.69)	115.05 (115.48)	121.39 (121.37)	115.06 (115.44)
C5-C6-N1	119.60 (119.47)	119.06 (118.86)	122.75 (122.64)	119.79 (119.79)	123.11 (123.10)	123.66 (123.07)	122.07 (121.92)	126.90 (126.47)
C6-N1-C2	124.38 (124.28)	122.88 (123.19)	119.79 (119.53)	125.48 (125.45)	120.65 (120.89)	122.57 (122.87)	118.10 (118.34)	117.63 (117.82)
C2-N1-H1	114.54 (115.21)	116.31 (116.17)	/	114.86 (114.78)	/	117.52 (116.85)	/	/
C5-C4-O4	114.15 (114.39)	116.86 (116.78)	115.27 (116.18)	111.46 (111.77)	111.27 (111.95)	121.35 (120.32)	116.25 (116.57)	121.65 (120.90)
C4-O4-H4	113.71 (113.05)	/	110.80 (111.66)	99.48 (99.56)	96.88 (98.30)	/	/	/
C6-C5-O5	120.46 (120.81)	124.97 (124.76)	121.37 (121.21)	129.75 (129.40)	130.16 (129.53)	123.88 (124.24)	126.32 (125.61)	123.59 (123.72)
C5-O5-H5	110.47 (109.27)	101.60 (101.14)	108.06 (108.31)	/	/	/	98.03 (99.32)	/
N1-C2-C7	116.05 (116.40)	114.92 (115.32)	115.12 (114.74)	116.08 (116.34)	114.05 (114.41)	116.43 (116.37)	112.88 (113.35)	112.11 (113.35)
C2-C7-O8	106.79 (107.45)	112.33 (112.32)	111.38 (110.67)	112.03 (111.87)	109.99 (109.85)	112.85 (112.77)	110.28 (110.09)	109.06 (109.19)
C7-O8-H8	110.39 (110.07)	108.44 (108.65)	104.35 (103.39)	108.48 (108.76)	100.86 (101.58)	105.87 (108.12)	100.67 (101.42)	97.38 (99.70)

Figure A4. DFT optimized geometries of the three possible neutral forms of ligand P1 in the gas phase, showing the different types of hydrogen bond-type interactions.

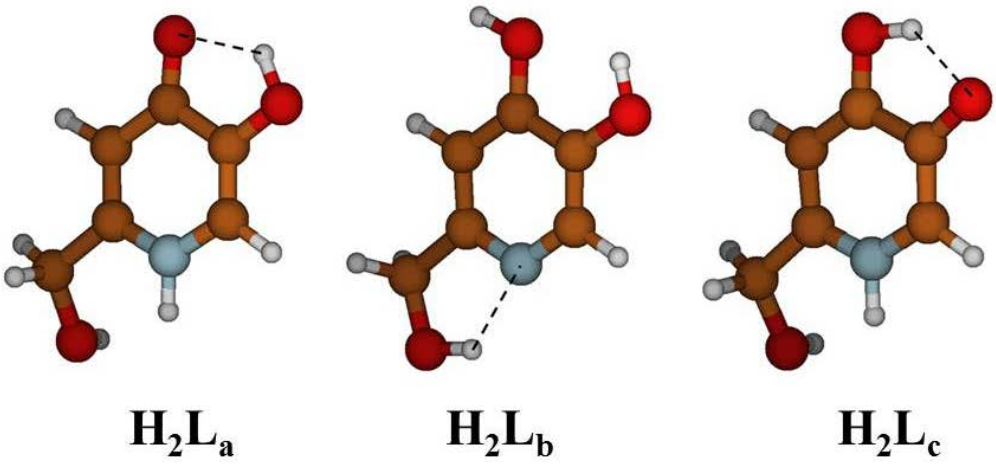

Figure A5. Absorptivity spectra at 0.1 M KCl ionic strength, 25 °C of basic (a) and acidic titrations (b) of Kojic acid.

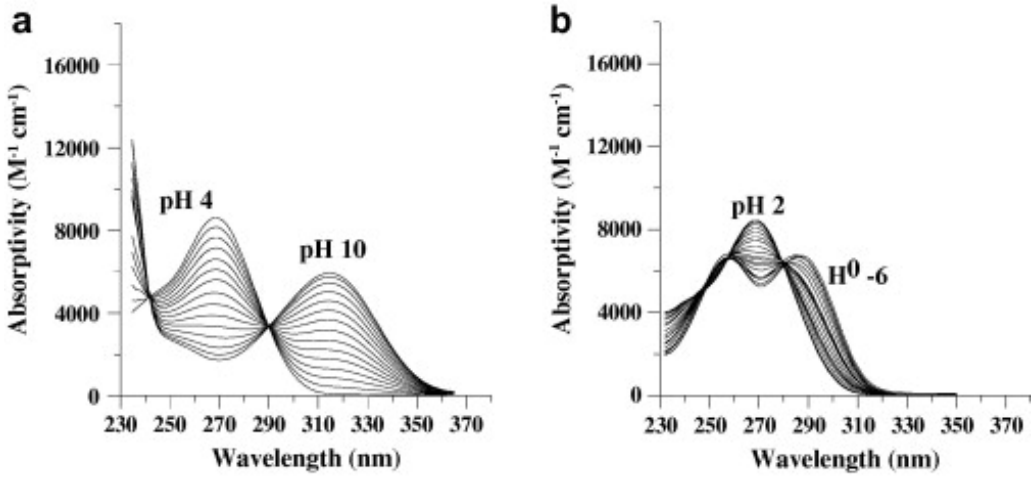

Figure A6. ^{1}H NMR spectra for L12 ligand by changing the pH from 1.4 to 13.05, at 298 K.

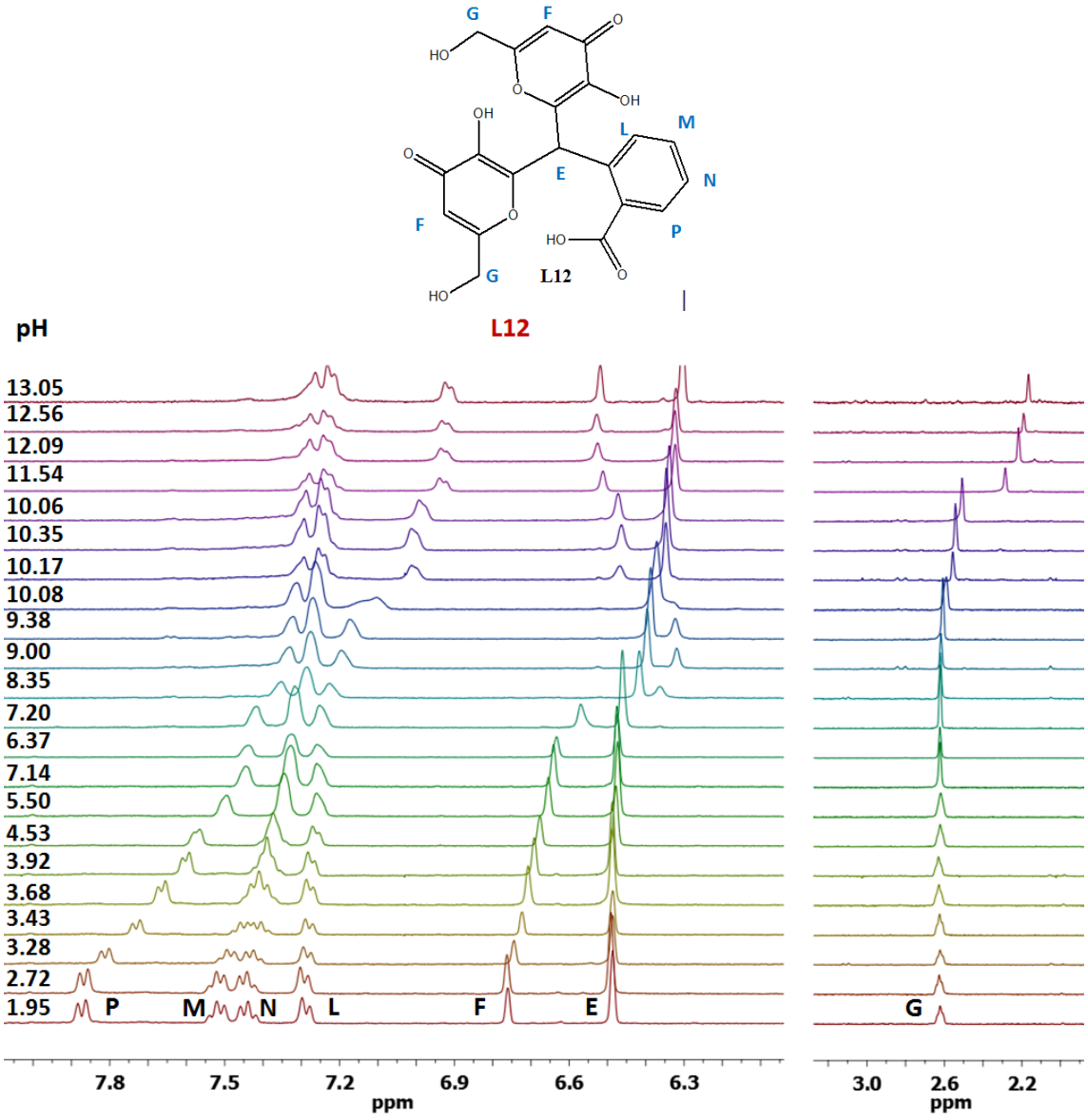

Figure A7. Fe^{3+}–P1 complexes. Experimental data for peak *m/z* = 333.998 (Panel A), 336.004 (Panel B), 409.940 (Panel C), 499.029 (Panel D) and 515.010 (Panel E) are shown at the top of the panel and compared with the data calculated for the Fe^{3+} complex (lower panel).

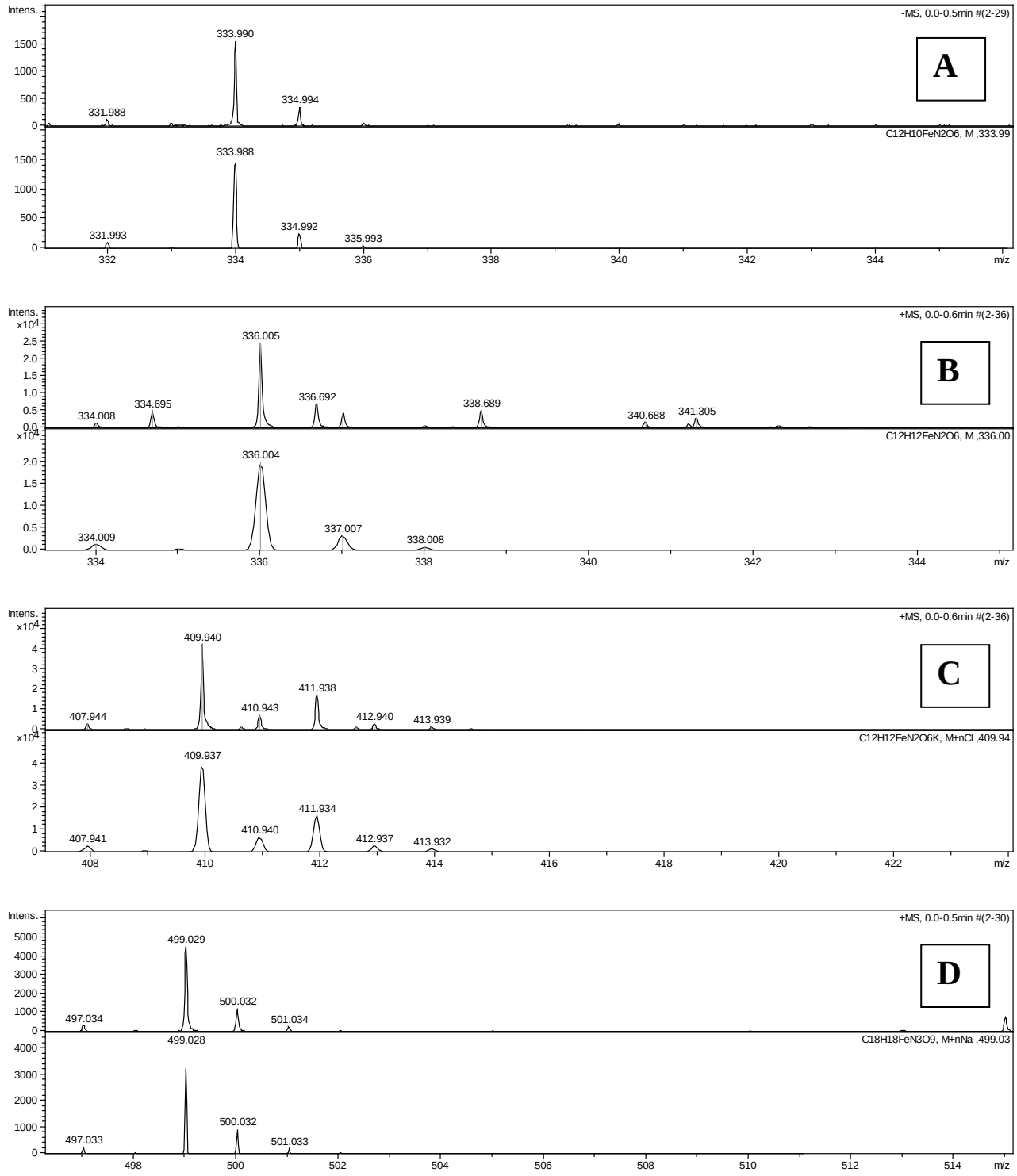

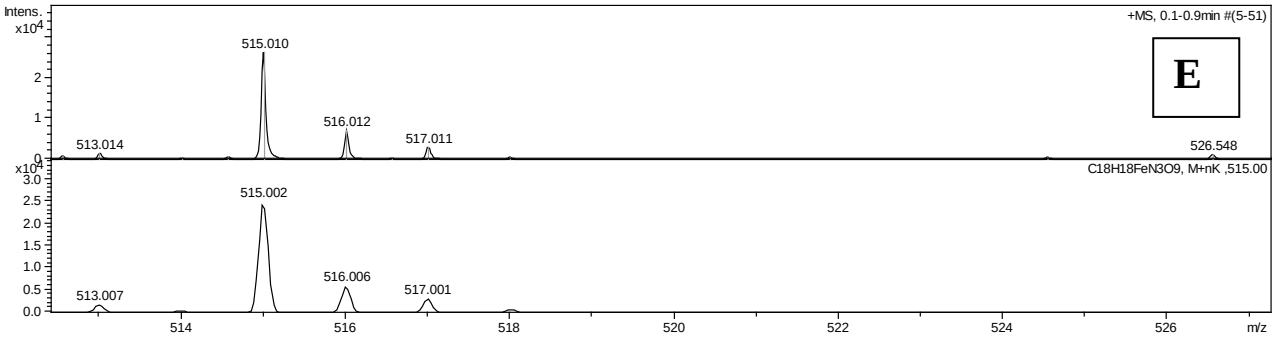

TableA7. ESI-MS *m/z* data of Fe^{3+}–P1 aqueous solution in different pH.

pH	Negative	Intensity	Positive	Intensity	Species
			336.004	15000	$[FeL_2H_2]^+$
2.16	-	-	409.944	25000	$[FeL_2H_2+Cl+K]^+$
			515.002	800	$[FeL_3H_3+K]^+$
			336.005	20000	$[FeL_2H_2]^+$
3.25	-	-	409.940	40000	$[FeL_2H_2+Cl+K]^+$
			515.006	2500	$[FeL_3H_3+K]^+$
6.78	-	-	515.015	25000	$[FeL_3H_3+K]^+$
9.52	-	-	515.005	15000	$[FeL_3H_3+K]^+$
11.10	-	-	515.008	12000	$[FeL_3H_3+K]^+$
	333.998	1500	-	-	$[FeL_2]^-$
	-	-	336.001	5000	$[FeL_2H_2]^+$
>11	-	-	499.029	4000	$[FeL_3H_3+Na]^+$
	-	-	515.002	800	$[FeL_3H_3+K]^+$

Figure A8. Stacked 1D ^{1}H NMR spectra of P1 ligand by increasing amount of Ga^{3+}, as a diamagnetic probe of Fe^{3+}, in phosphate buffer solution at 298 K.

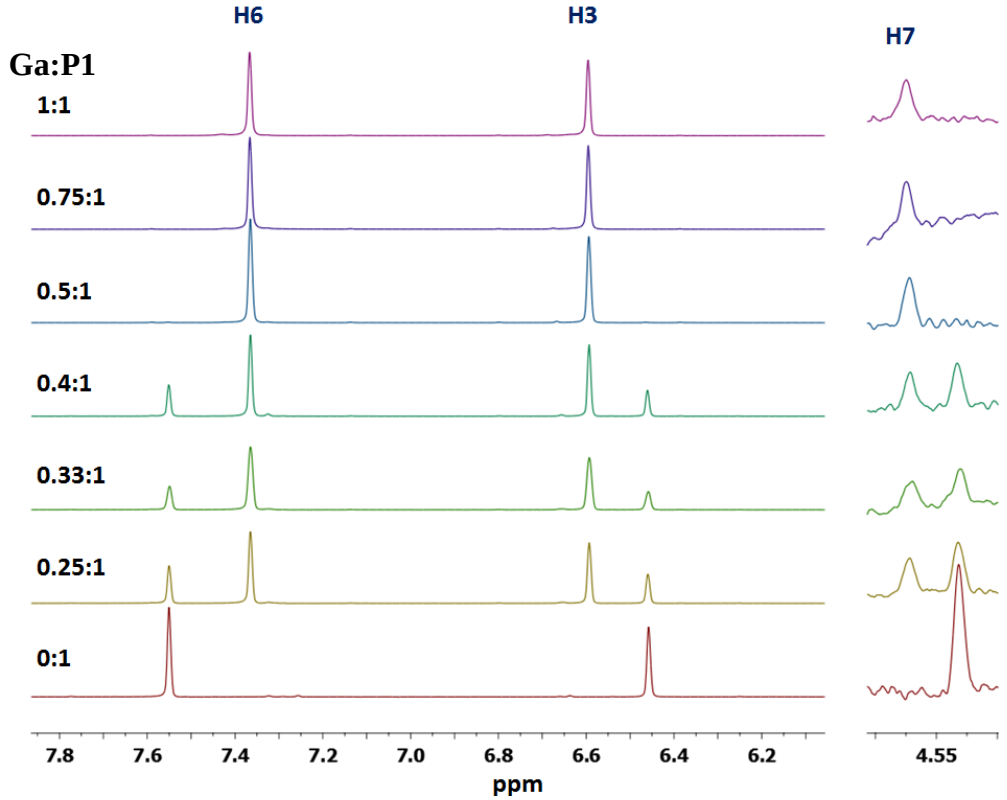

Figure A9. The comparison of the relative ratio of H3/H6 in term of peak integral and peak high ratio between pH 7 (black square) and pH 11.5 (orange rhombus).

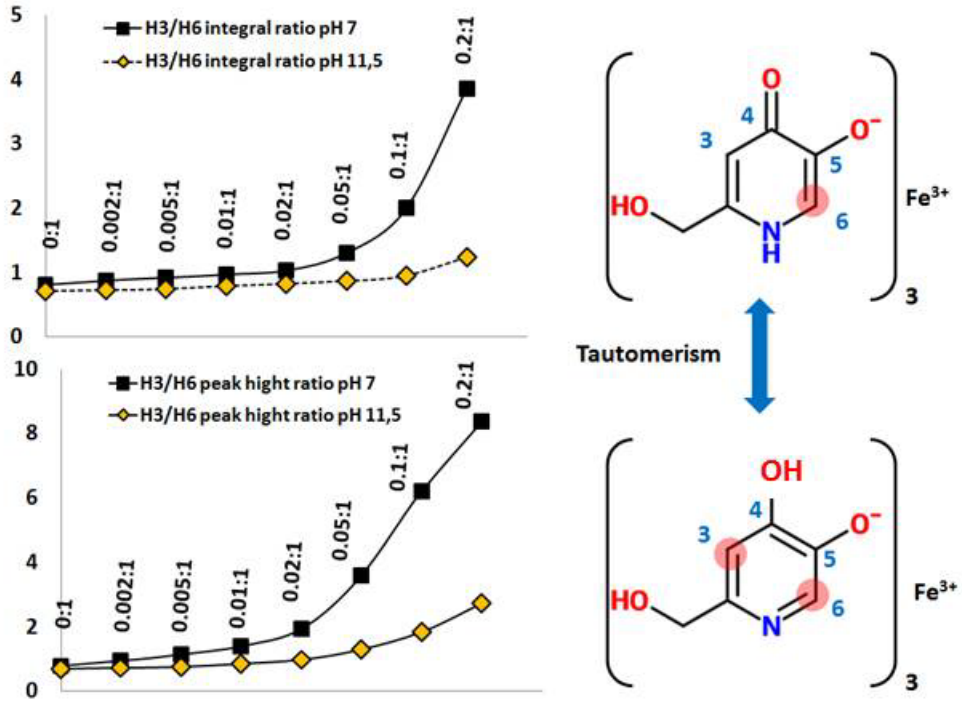

Table A8. Selected optimized bond lengths (Å) and angles (°) for Fe^{3+}–P1[a] complexes in the gas phase.[b]

	$Fe(HL)_3$	$[Fe(L)_3]^{3-}$		$Fe(HL)_3$	$[FeL_3]^{3-}$
Fe-O4	2.082	2.082	O5-Fe-O20	96.43	98.15
Fe-O5	1.994	2.030	O4-C4-C5	116.58	116.71
Fe-O12	2.082	2.081	O5-C5-C4	116.35	114.78
Fe-O13	1.995	2.030	C2-N1-H1	116.02	/
Fe-O20	2.081	2.081	C3-C2-C7	124.64	123.79
Fe-O21	1.995	2.030	C2-C7-O8	112.30	109.61
C4-O4	1.263	1.280	C7-O8-H8	108.22	99.08
C5-05	1.287	1.295	O12-C12-C13	116.56	116.71
C12-O12	1.263	1.280	O13-C13-C12	116.34	116.36
C13-O13	1.287	1.295	C10-N9-H9	115.97	/
C20-O20	1.263	1.280	C11-C10-C15	124.60	123.82
C21-O21	1.287	1.295	C10-C15-O16	112.33	109.60
N1-C2	1.343	1.324	C15-O16-H16	108.26	99.08
N1-C6	1.368	1.356	O20-C20-C21	116.58	116.72
N1-H1	1.015	/	O21-C21-C20	116.34	116.35
C4-C5	1.466	1.459	C18-N17-H17	116.02	/
C2-C7	1.508	1.525	C19-C18-C23	124.60	123.79
C7-O8	1.406	1.394	C18-C23-O24	112.33	109.60
O8-H8	0.963	1.000	C23-O24-H24	108.25	99.08
N9-C10	1.343	1.324	Fe-O4-C4-C3	-178.62	-179.71
N9-C14	1.368	1.356	Fe-O5-C5-C6	177.91	179.45
N9-H9	1.015	/	Fe-O12-C12-C11	-179.17	-179.57
C12-C13	1.466	1.459	Fe-O13-C13-C14	178.55	179.27
C10-C15	1.508	1.525	Fe-O20-C20-C19	-178.87	-179.67
C15-O16	1.406	1.394	Fe-O21-C21-C22	178.19	179.35
O16-H16	0.963	1.000	O4-Fe-O13-C13	88.74	91.93
N17-C18	1.343	1.324	O12-Fe-O21-C21	89.12	92.08
N17-C22	1.368	1.356	O20-Fe-O5-C5	89.47	91.86
N17-H17	1.015	/	O4-C4-C5-O5	0.39	0.02
C21-C20	1.466	1.459	C3-C2-N1-H1	-178.09	/
C18-C23	1.508	1.525	C6-N1-C2-C7	-177.55	-179.95
C23-O23	1.406	1.394	N1-C2-C7-O8	-26.57	0.19
O23-H23	0.963	1.000	C2-C7-O8-H8	-74.65	-0.01
Fe-O5-C5	114.96	114.78	O12-C12-C13-O13	0.35	0.28
Fe-O4-C4	112.80	113.37	C11-C10-N9-H9	-178.22	/
O4-Fe-O5	79.29	78.77	C14-N9-C10-C15	-177.46	-179.95
O4-Fe-O13	96.15	98.15	N9-C10-C15-O16	-26.15	0.02
Fe-O12-C12	112.84	113.38	C10-C15-O16-H16	-75.07	0.00
Fe-O13-C13	114.96	114.75	O20-C20-C21-O21	0.38	0.30
O12-Fe-O13	79.29	78.77	C19-C18-N17-H17	-178.14	/
O12-Fe-O21	96.48	98.16	C22-N17-C18-C23	-177.52	-179.99
Fe-O20-C20	112.83	113.39	N17-C18-C23-O24	-26.37	-0.05
Fe-O21-C21	114.94	114.76	C18-C23-O24-H24	-74.83	0.08
O20-Fe-O21	79.30	78.78			

TableA9. Complex formation constants (log β) of P1 with Fe^{3+}, Al^{3+}, Cu^{2+} and Zn^{2+} ions, and literature complex formation constants of DFP and 3,4-hopo. The charges are omitted for simplicity.

	P1					**DFP**				**3,4-hopo**			
Model	**Fe^{3+}**	**Al^{3+}**	**Cu^{2+}**	**Zn^{2+}**	**Model**	**Fe^{3+}** [1]	**Al^{3+}** [2]	**Cu^{2+}** [1]	**Zn^{2+}** [3]	**Fe^{3+}** [4]	**Al^{3+}**	**Cu^{2+}** [5]	**Zn^{2+}** [5]
ML	25.92(9)	23.32(9)	21.78(7)	18.79(6)	ML	15.01(1)	11.91	10.42	7.24	14.26(3)	----	9.49	6.81
ML_2H_2	49.12(1)	45.18(6)	41.42(7)	36.70(4)	ML_2H	----	----	21.98		----	----	----	----
ML_2H	----	----	34.21(5)	26.02(9)	ML_2	27.03(1)	22.83	19.09	13.55	25.73(1)	----	17.13	12.54
ML_2	----	----	24.68(5)	----	ML_2H_{-1}	----	----	8.49	2.30	----	----	----	----
ML_3H_3	71.43(6)	65.25(7)	----	----	ML_3	37.43(1)	32.25	----	15.2	34.91(1)	----	----	----
ML_3H_2	65.33(3)	58.30(4)	----	----									
ML_3H	55.62(9)	47.48(5)	----	----									
ML_3	44.63(5)	38.41(5)	----	----									
pM^{n+}	22.0	15.1	10.1	6.3	pM^{n+}	20.7	15.4	10.1	6.2	20.6	NF	9.7	6.4

[1] V. M. Nurchi, G. Crisponi, T. Pivetta, M. Donatoni and M. Remelli, *Journal of Inorganic Biochemistry*, 2008, **102**, 684-692.

[2] D. J. Clevette, W. O. Nelson, A. Nordin, C. Orvig and S. Sjoeberg, *Inorganic Chemistry*, 1989, **28**, 2079-2081.

[3] T. Jakusch, K. Gaida-Schrantz, Y. Adachi, H. Sakurai, T. Kiss, L. Horvath, *J. Inorg. Biochem.*, (2006), 100:1521-1526.

[4] R. C. Scarrow, P. E. Riley, K. Abu-Dari, D. L. White and K. N. Raymond, *Inorganic Chemistry*, 1985, **24**, 954-967.

[5] H. Stunzi, L. Harris, D. Perrin and T. Teitei, *Australian Journal of Chemistry*, 1980, **33**, 2207-2220.

TableA10. ESI-MS *m/z* data of Al^{3+}–P1 aqueous solution at different pH.

pH	Negative	Intensity	Positive	Intensity	Species
4.06	305.032	3000	-	-	$[AlL_2]^-$
6.21	305.032	5000	-	-	$[AlL_2]^-$
	-	-	486.049	25000	$[AlL_3H_3+K]^+$
7.00	305.032	300	-	-	$[AlL_2]^-$
	-	-	307.051	15000	$[AlL_2H_2]^+$
	-	-	448.101	300	$[AlL_3H_3+H]^+$
7.70	-	-	486.049	20000	$[AlL_3H_3+K]^+$
10.83	305.032	10000	-	-	$[AlL_2]^-$
	-	-	486.049	25000	$[AlL_3H_3+K]^+$
>11	305.043	300	-	-	$[AlL_2]^-$
	-	-	307.049	1500	$[AlL_2H_2]^+$
	-	-	470.074	1250	$[AlL_3H_3+Na]^+$

Figure A10. Al^{3+}–P1 complexes. Experimental data for peak *m/z* = 305.030 (Panel A), 307.056 (Panel B), 448.101 (Panel C), 470.074 (Panel D) and 486.048 (Panel E) are shown at the top of the panel and compared with the data calculated for the Al^{3+} complex (lower panel).

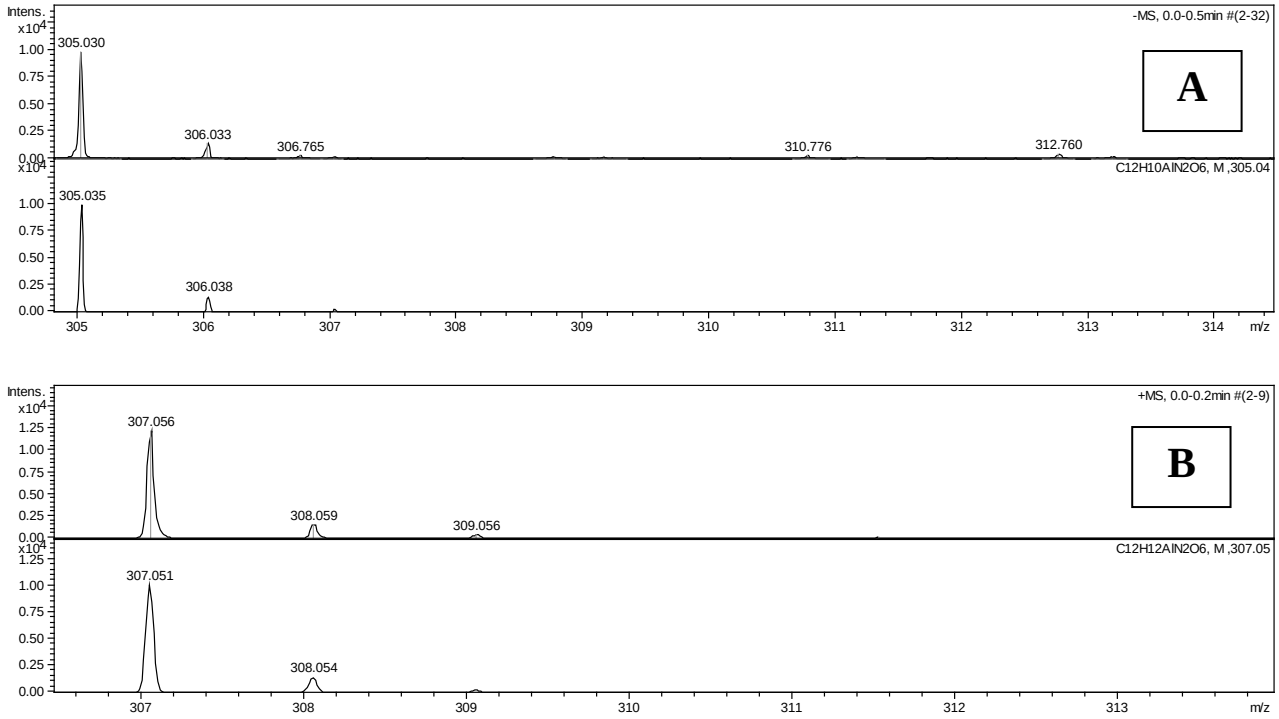

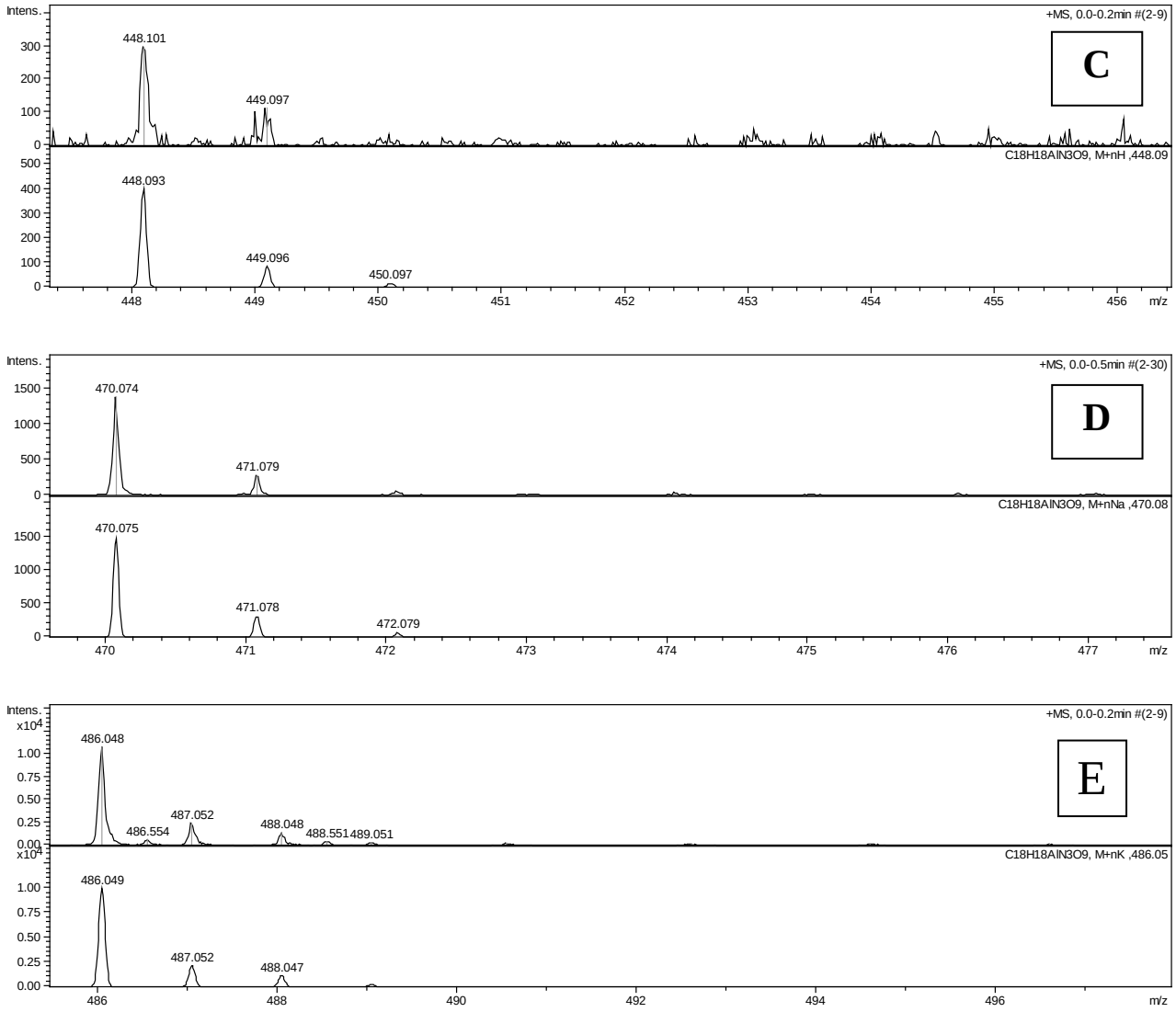

Figure A11. Cu^{2+}–P1 complexes. Experimental data for peak *m/z* = 236.924 (Panel A), 341.989 (Panel B), 344.009 (Panel C), 365.985 (Panel D) and 381.963 (Panel E) are shown at the top of the panel and compared with the data calculated for the Cu^{2+} complex (lower panel).

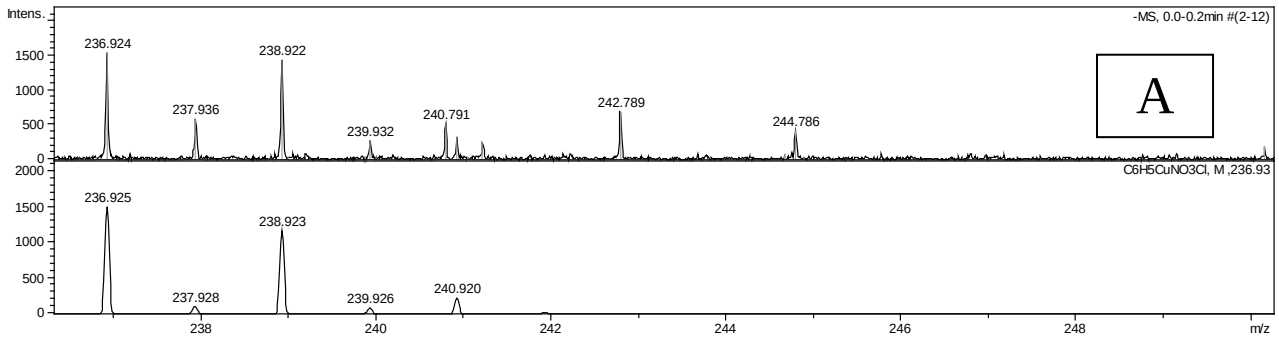

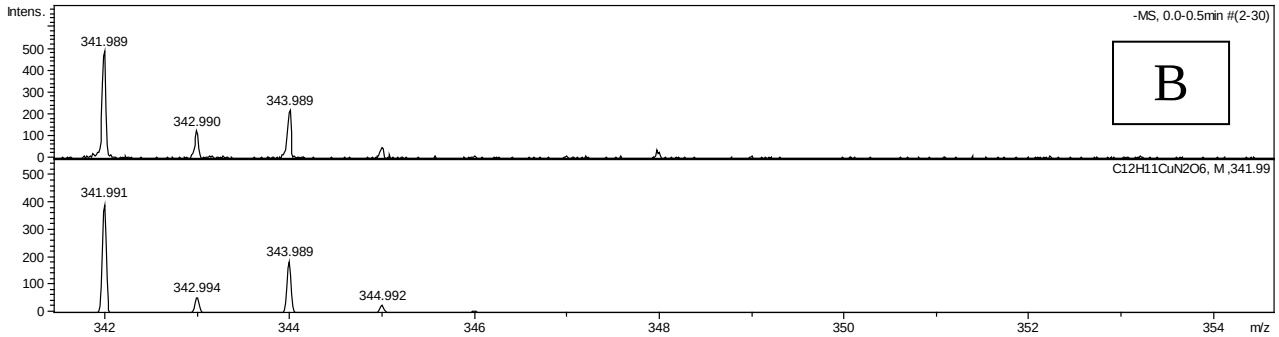
Intens.
-MS, 0.0-0.5min #(2-30)
B
341.989
342.990
343.989
C12H11CuN2O6, M ,341.99
341.991
343.989
342.994
344.992
m/z

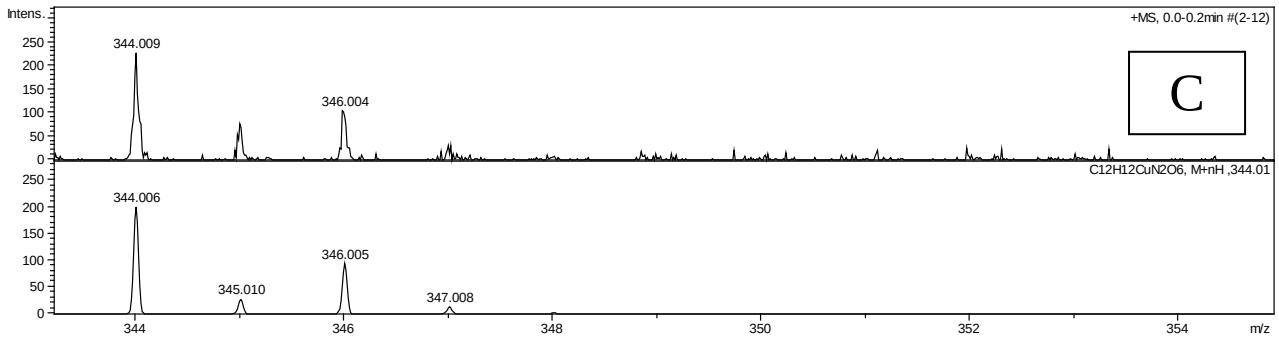
Intens.
+MS, 0.0-0.2min #(2-12)
C
344.009
346.004
C12H12CuN2O6, M+nH ,344.01
344.006
346.005
345.010
347.008
m/z

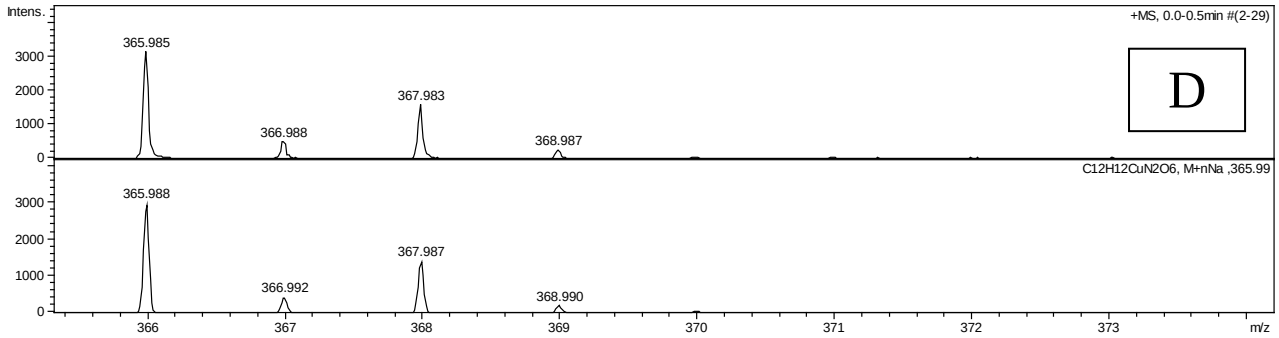
Intens.
+MS, 0.0-0.5min #(2-29)
D
365.985
367.983
366.988
368.987
C12H12CuN2O6, M+nNa ,365.99
365.988
367.987
366.992
368.990
m/z

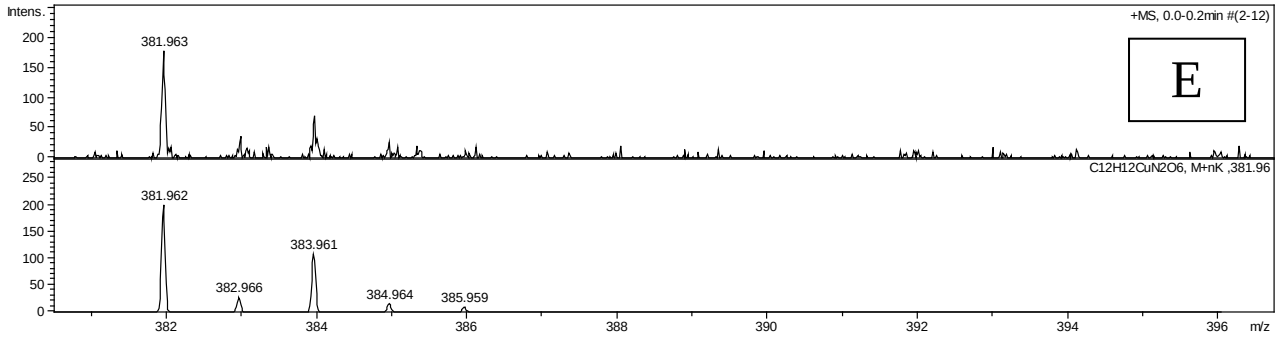
Intens.
+MS, 0.0-0.2min #(2-12)
E
381.963
C12H12CuN2O6, M+nK ,381.96
381.962
383.961
382.966
384.964
385.959
m/z

TableA11. ESI-MS *m/z* data of Cu^{2+}–P1 aqueous solution at different pH.

pH	Negative	Intensity	Positive	Intensity	Species
3.90	236.924	1500	-	-	$[CuL+Cl]^-$
7.00	-	-	344.009	200	$[CuL_2H_2+H]^+$
	-	-	381.963	200	$[CuL_2H_2+K]^+$
>11	341.989	500	-	-	$[CuL_2H]^-$
	-	-	344.002	2000	$[CuL_2H_2+H]^+$
	-	-	365.985	2000	$[CuL_2H_2+Na]^+$

Figure A12. Zn^{2+}–P1 complexes. Experimental data (pH 7.0) for peak *m/z* = 382.970 are shown at the top of the panel and compared with the data calculated for the zinc(II) complex (lower panel).

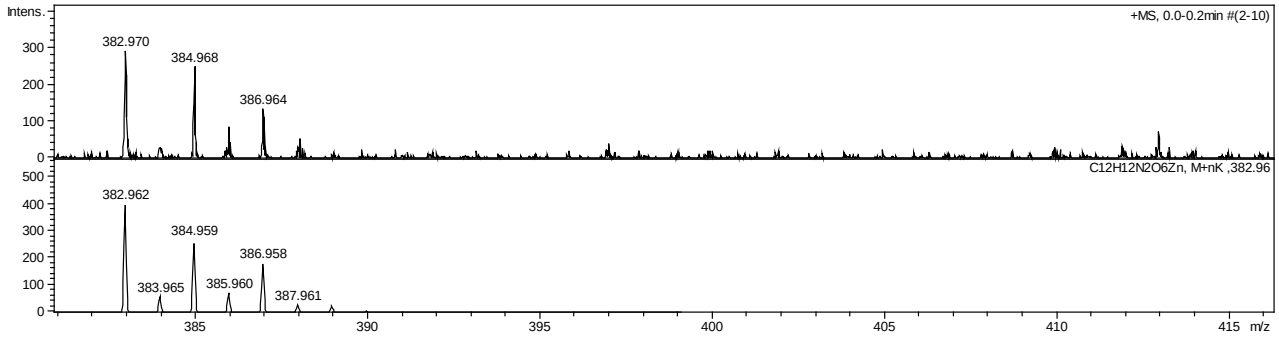

Figure A13. ESI-MS spectra of the $Cu(ClO_4)_2$/L4 system in a ratio 1:1 at pH 7.

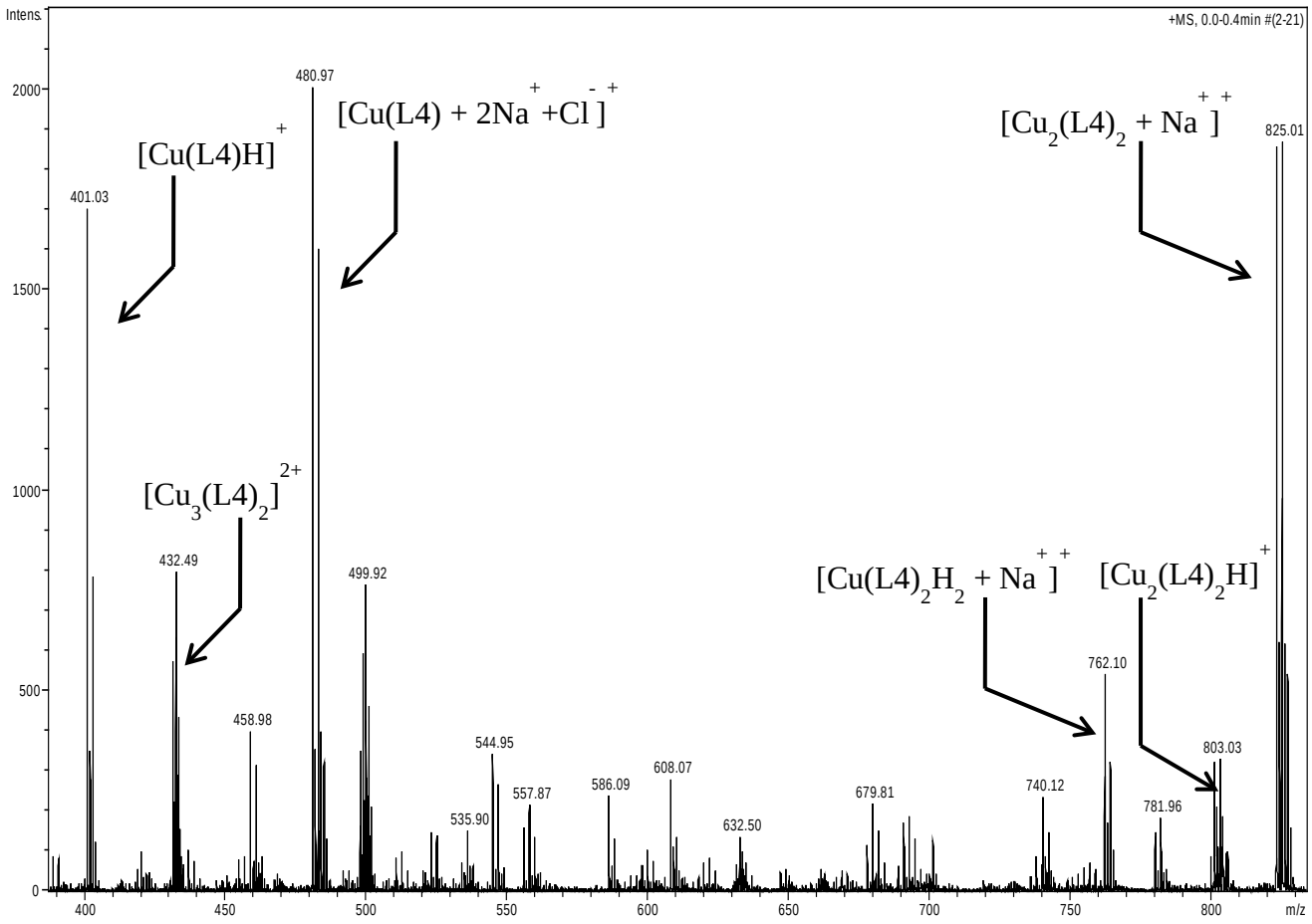

Figure A14 . ESI-MS spectra of the $Cu(ClO_4)_2$/L5 system in a ratio 1:1 at pH 7.

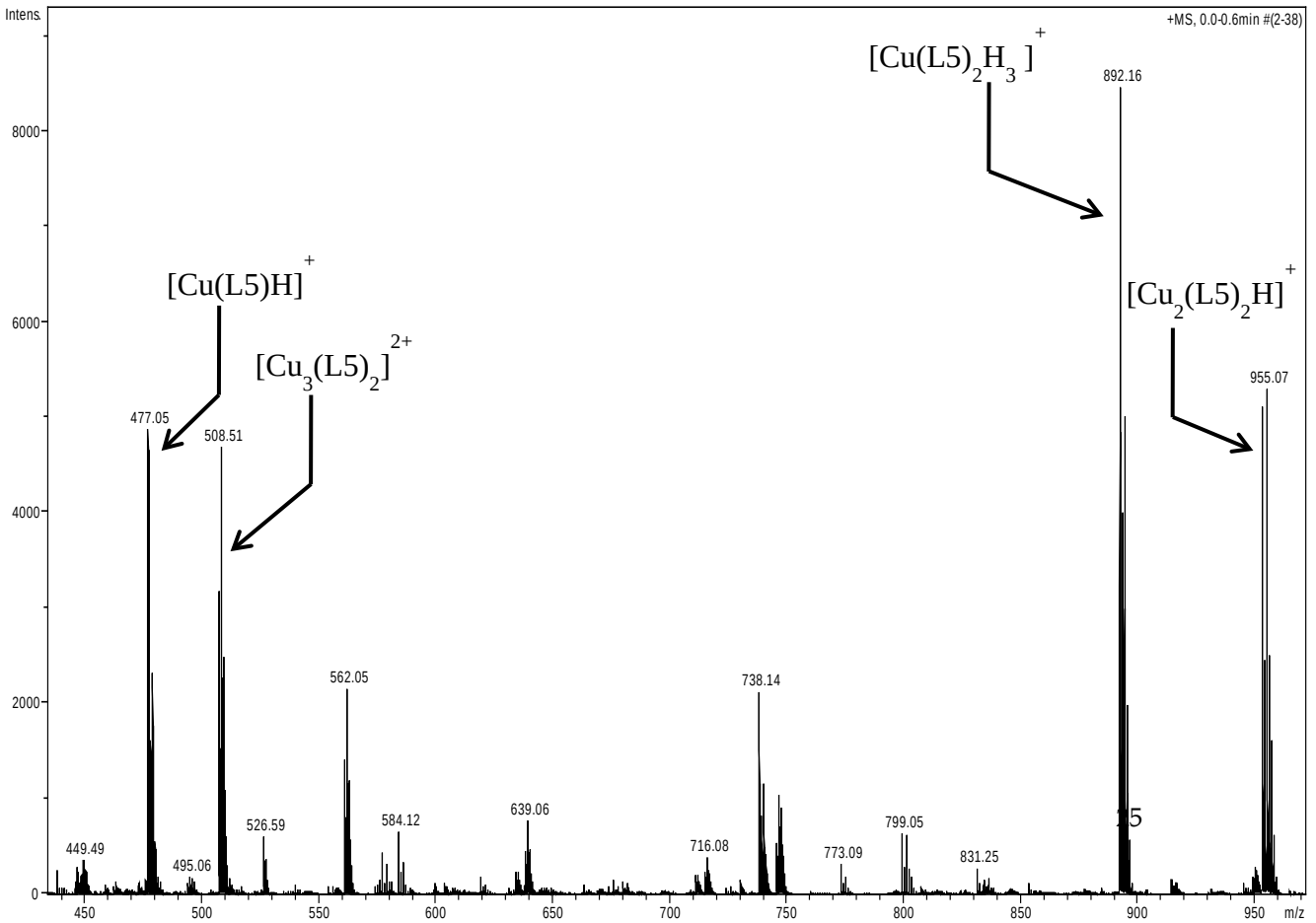

Figure A15. ESI-MS spectra of the $Cu(ClO_4)_2$/L7 system in a ratio 1:1 at pH 7.

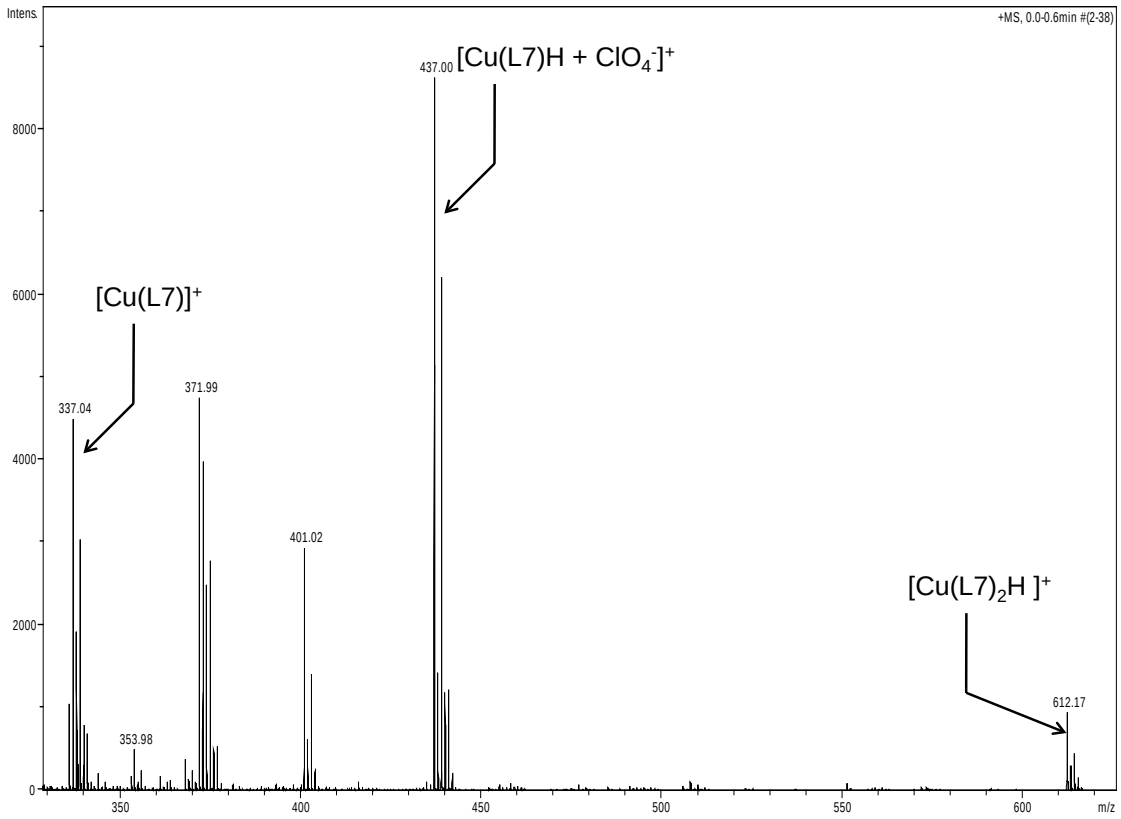

Figure A16. ESI-MS spectra of the $Zn(ClO_4)_2$/L1 system in a ratio 1:1 at pH 7.

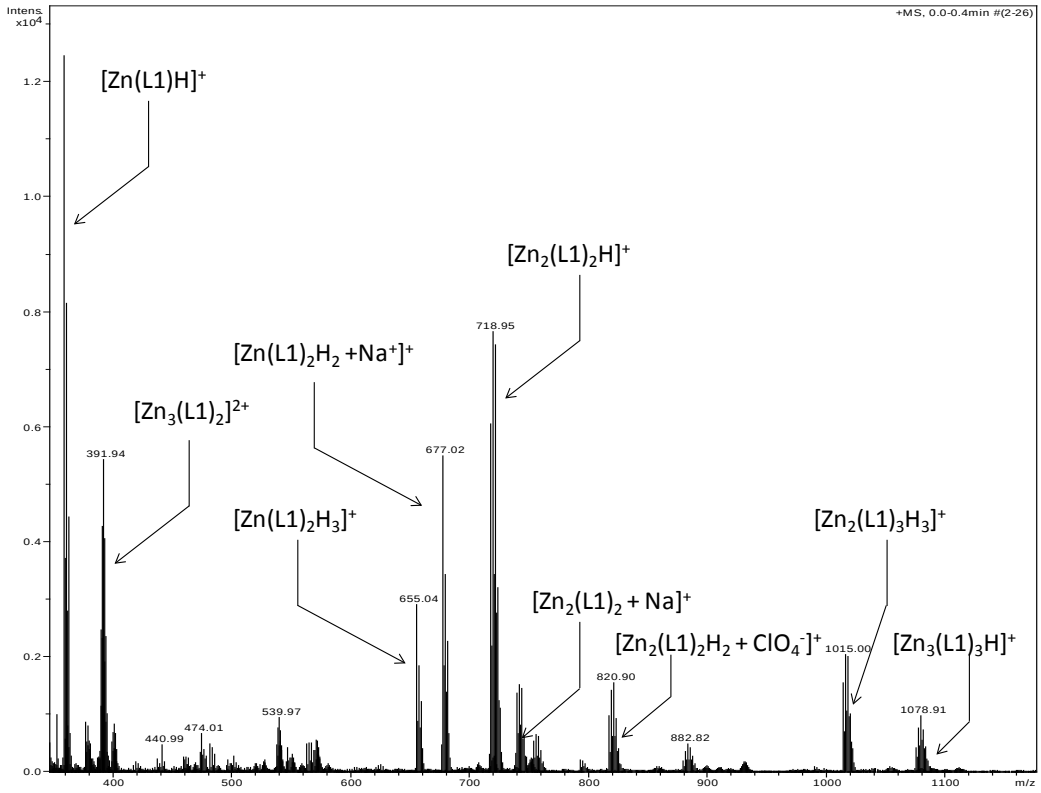

Figure A17. ESI-MS spectra of the $Zn(ClO_4)_2$/L2 system in a ratio 1:1 at pH 7.

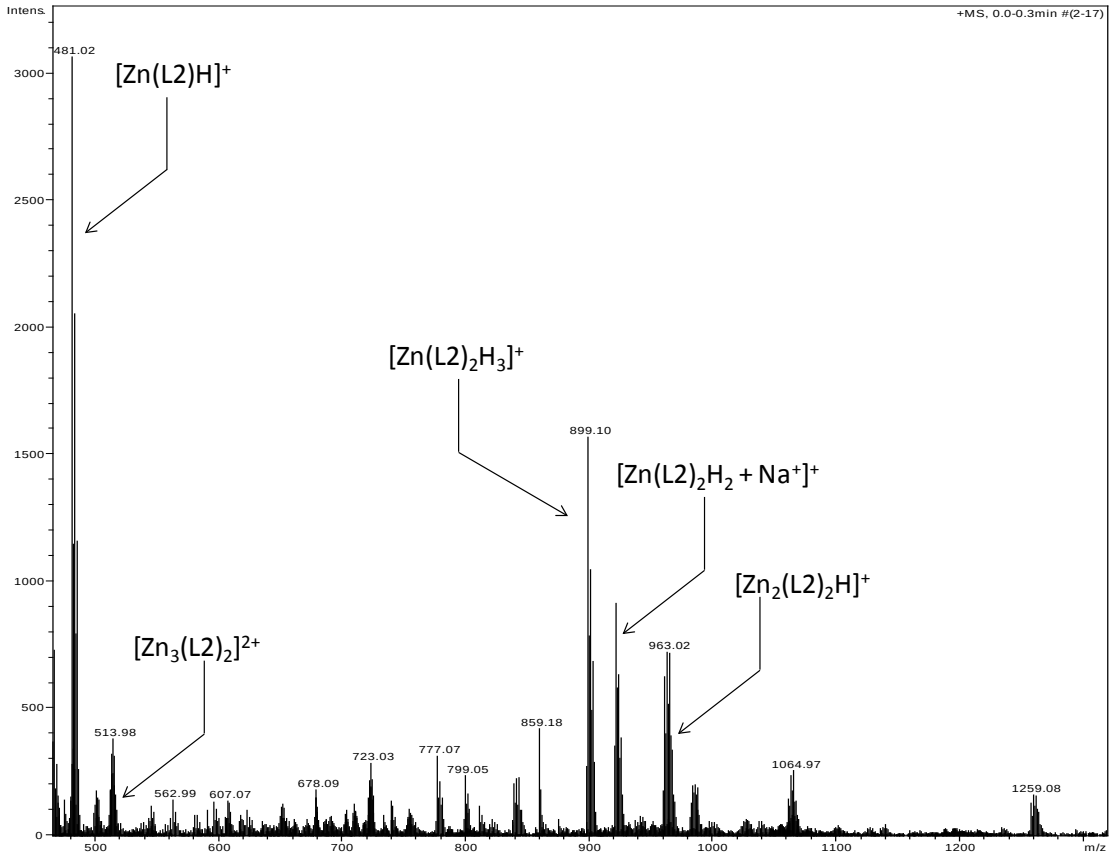

Figure A18. ESI-MS spectra of the $Zn(ClO_4)_2$/L3 system in a ratio 1:1 at pH 7.

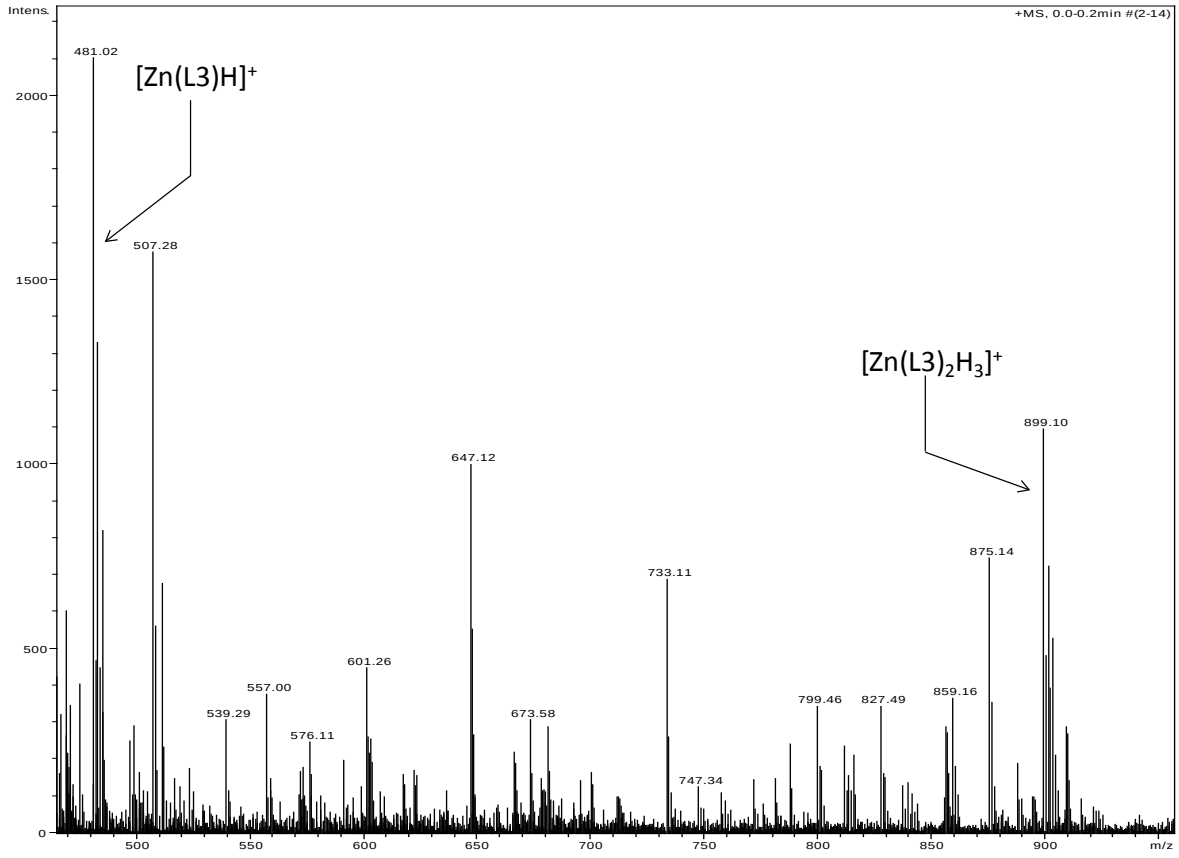

Figure A19. ESI-MS spectra of the $Zn(ClO_4)_2$/L4 system in a ratio 1:1 at pH 7.

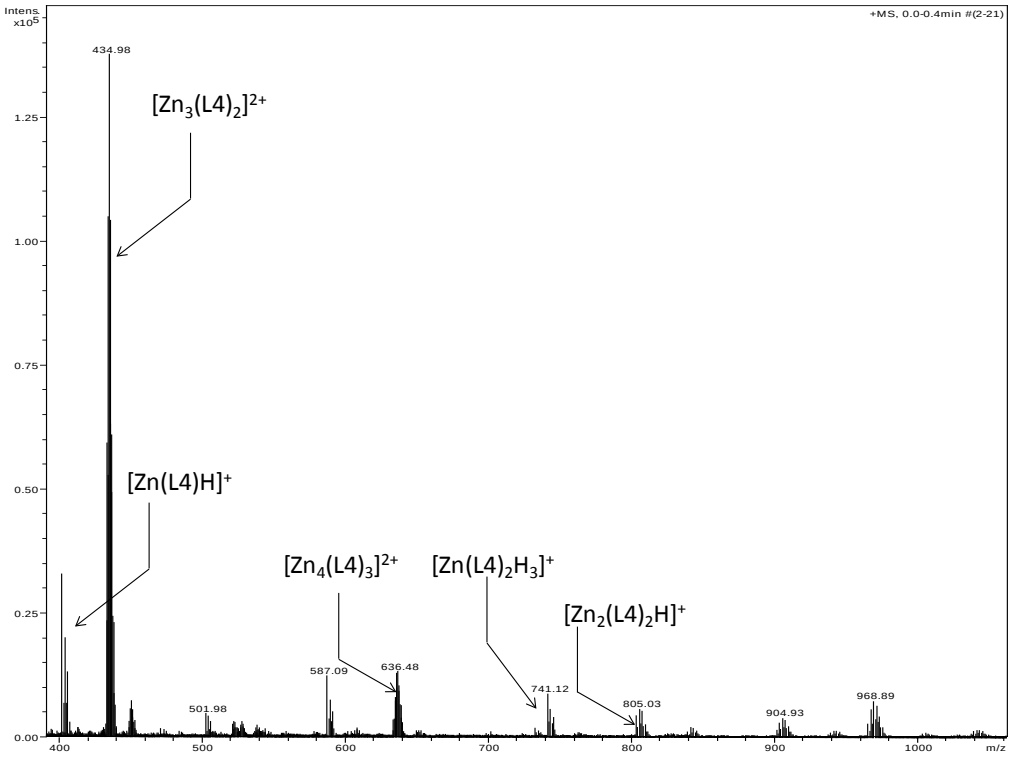

Figure A20. ESI-MS spectra of the $Zn(ClO_4)_2$/L5 system in a ratio 1:1 at pH 7.

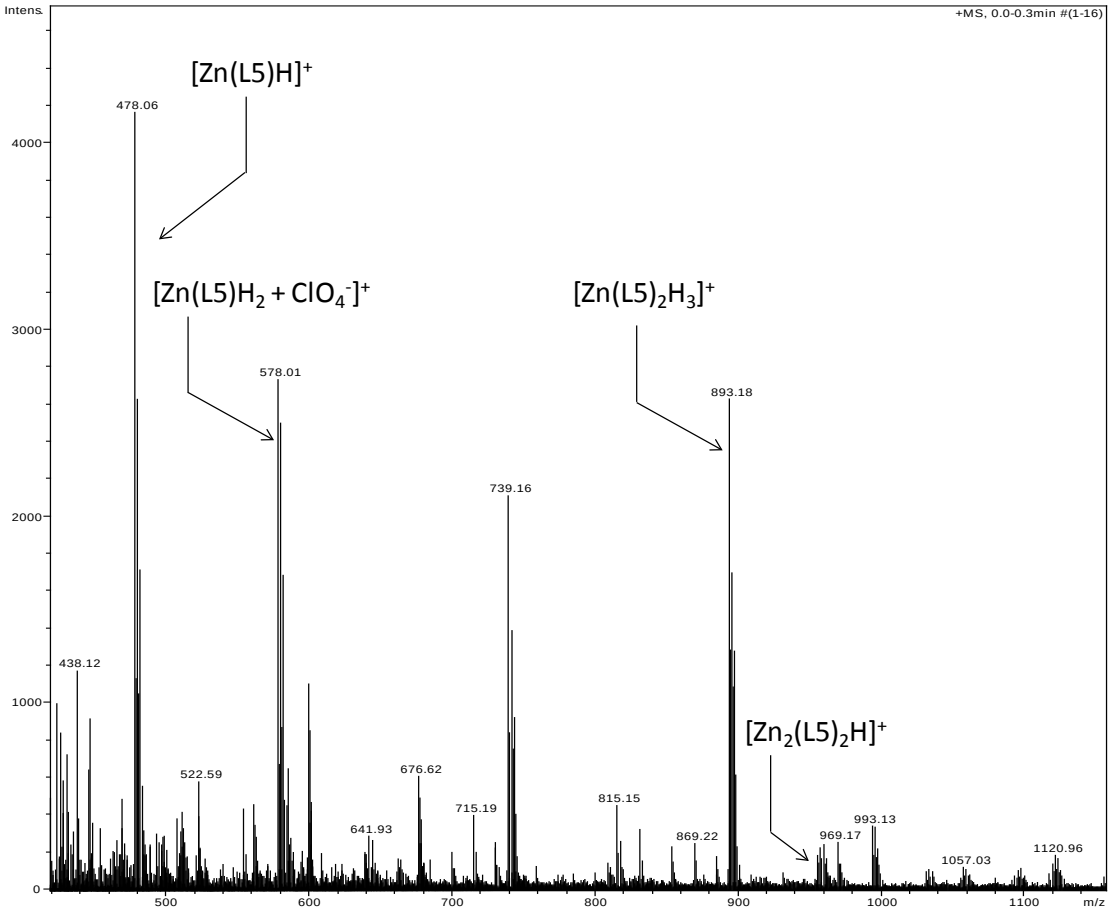

Figure A21. ESI-MS spectra of the $Zn(ClO_4)_2$/L6 system in a ratio 1:1 at pH 7.

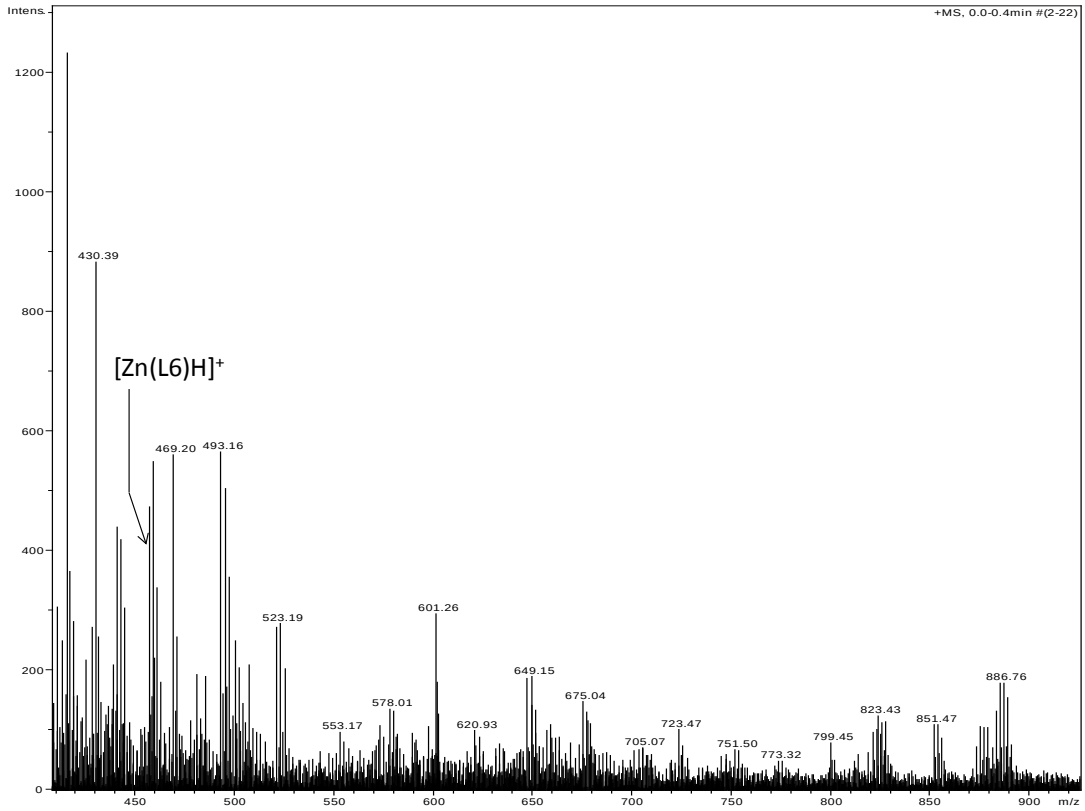

Figure A22. ESI-MS spectra of the $Zn(ClO_4)_2$/L8 system in a ratio 1:1 at pH 7.

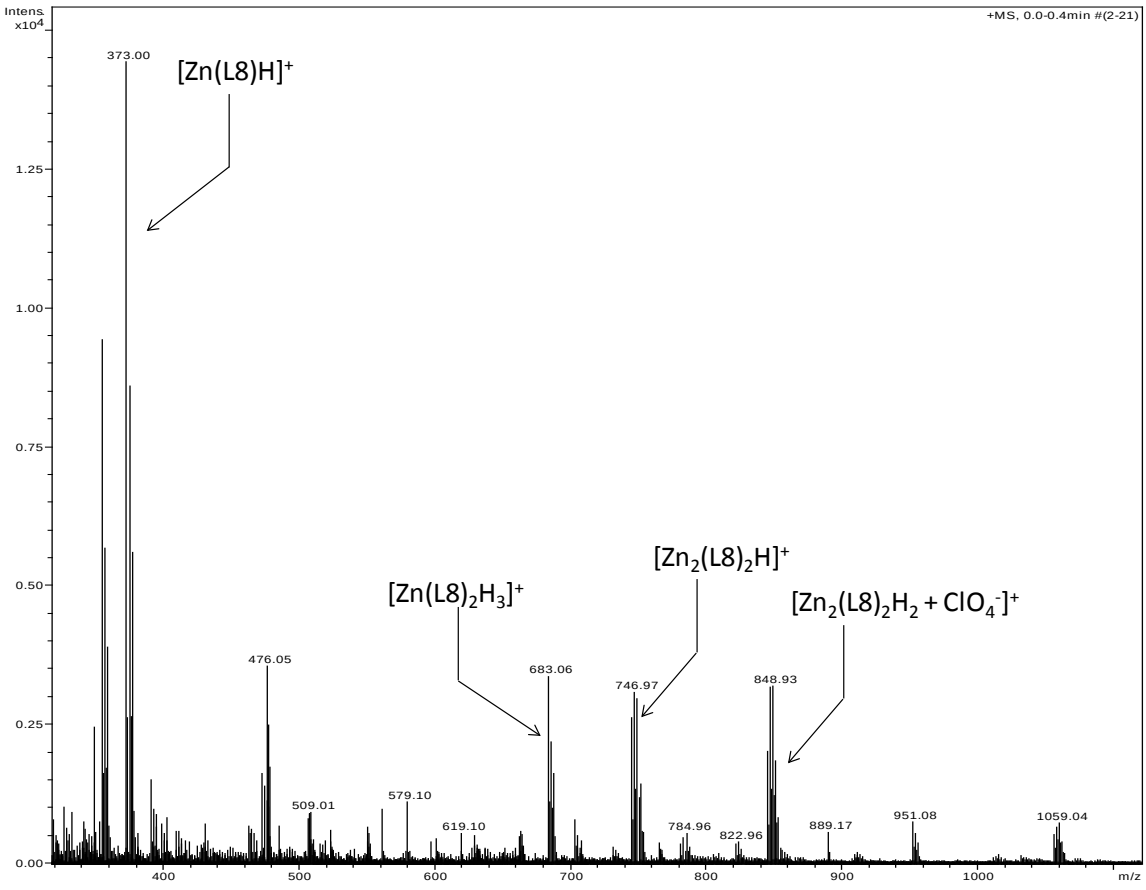

Figure A23. ESI-MS spectra of the $Zn(ClO_4)_2$/L7 system in a ratio 1:1 at pH 7.

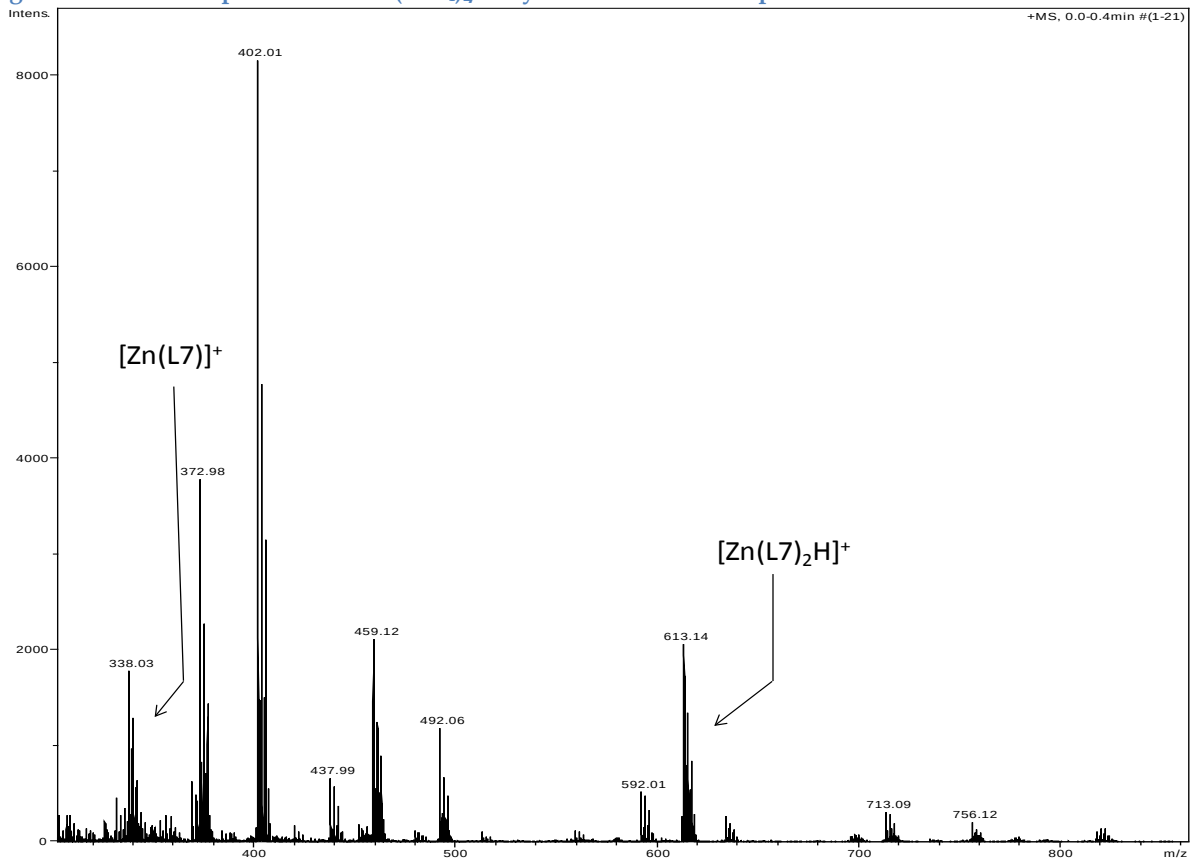

Figure A24. Comparison of ^1H 1D spectra of L3 free (red) and L3-Zn^{II} system, 1:0.5 molar ratio (blue), at pH 8.4.

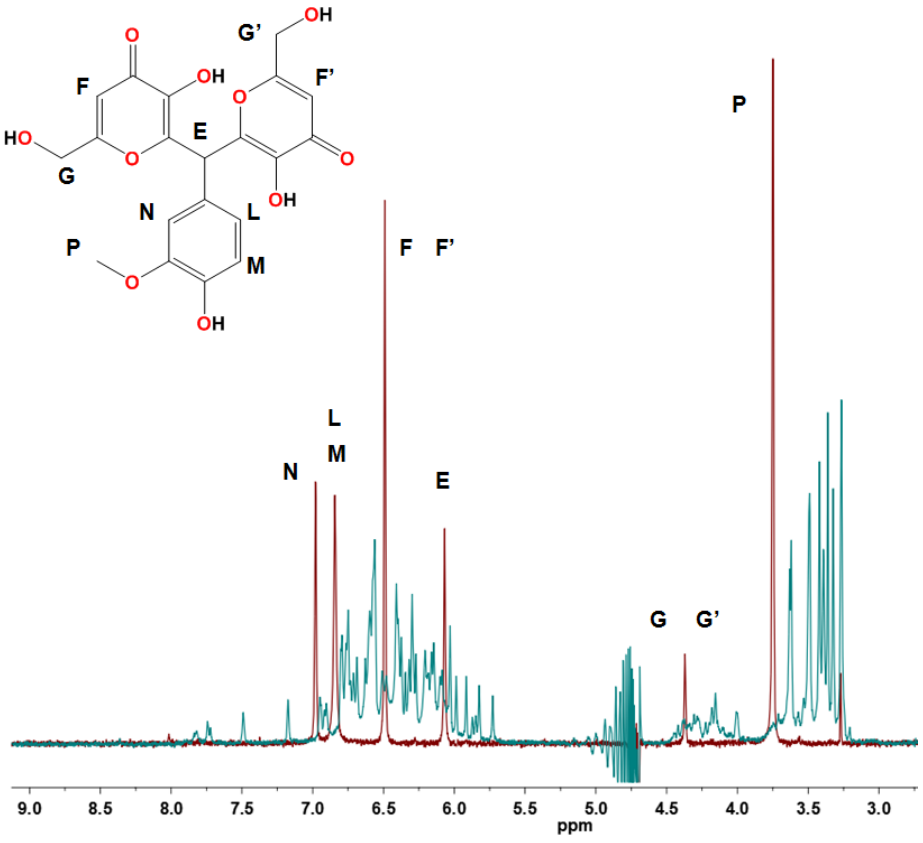

Figure A25. 2D ^{1}H-^{13}C spectrum for the free L7 ligand (red), and L-Zn(II) system, 1:1 molar ratio (black), in H_2O-D_2O, at pH 4.0. The new resonances of L7 upon Zn^{II} interaction are indicated by arrows and the chemical shifts differences $\Delta\delta = \delta_{bound} - \delta_{free}$ and the combined $\Delta\delta_{tot} = [(\Delta\delta_H)^2+(0.341 \cdot \Delta\delta_C)^2]^{1/2}$ are showed in the histogram.

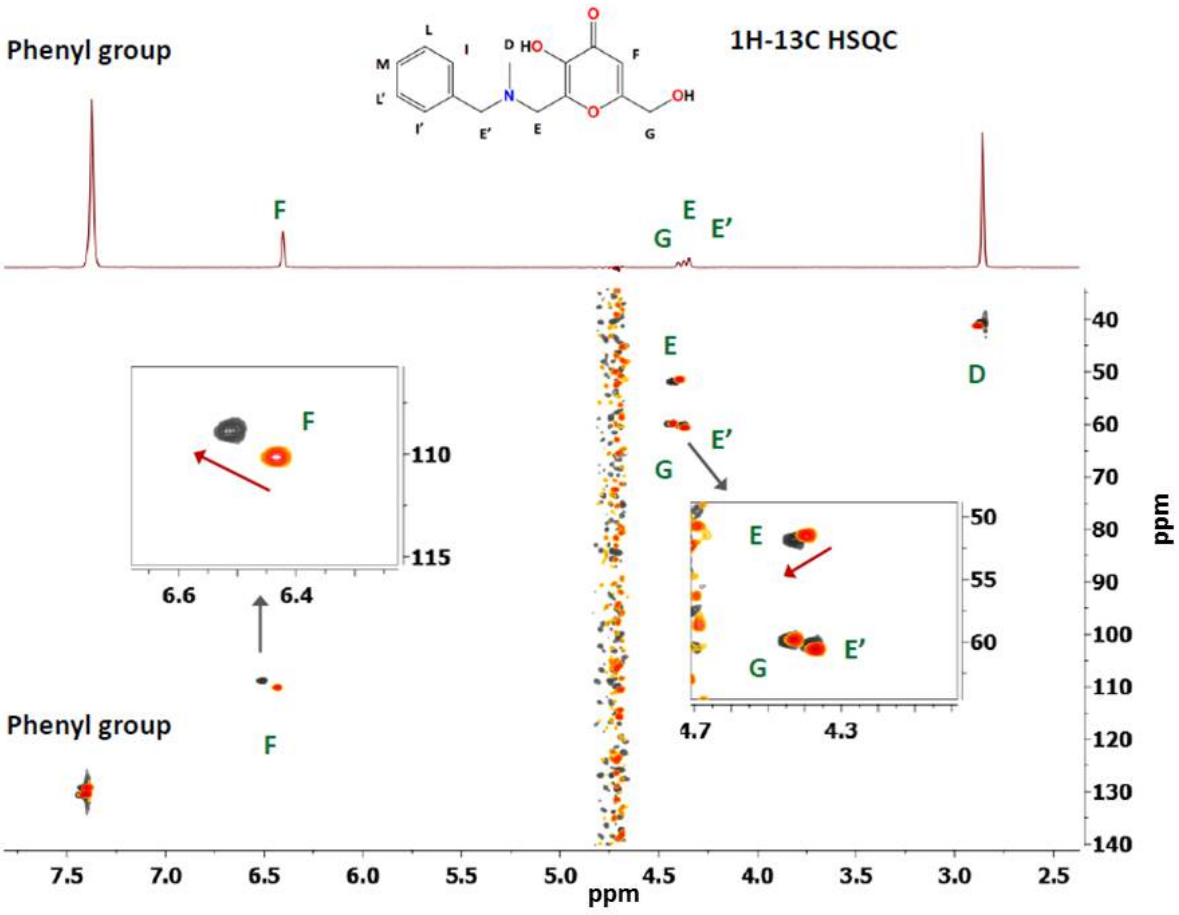

Figure A26. The full spectrum of KβAK with Cu^{2+} solution in the molar ratio 1:1. Panel A) Experimental data for peak m/z = 442.9947 are shown at the top of the panel and compared with the data calculated for the $[CuLH]^+$ ($C_{16}H_{14}NO_{10}Cu$) complex (lower panels). Panel B) Experimental data for peak m/z = 461.0058 are shown and compared with the data calculated for the $[CuLH(H_2O)]^+$ ($C_{16}H_{16}NO_{11}Cu$) complex (lower panel).

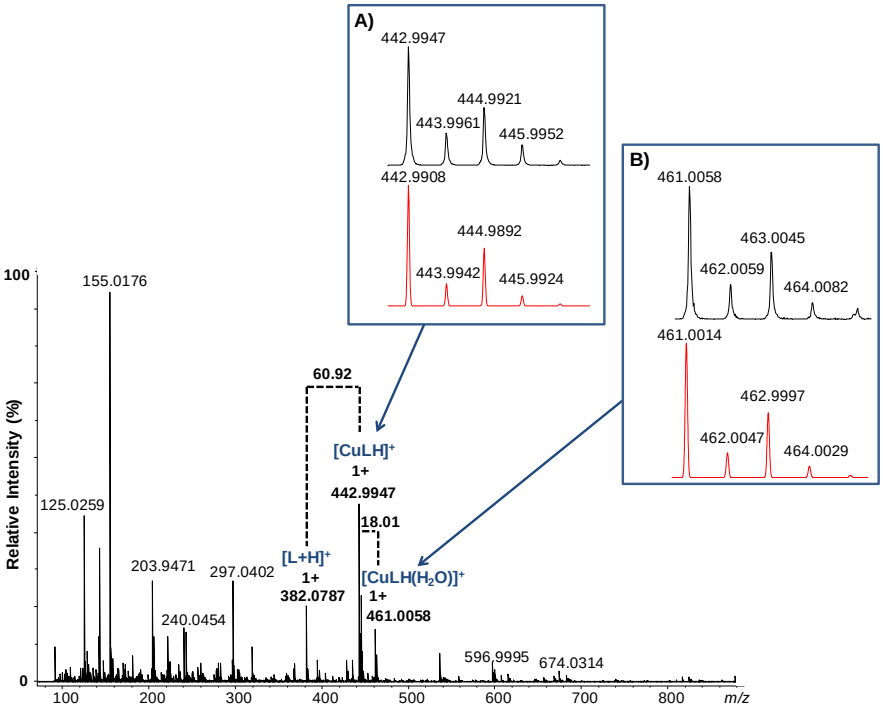

Figure A27. Expanded range of the product-ion spectrum of 810-910 m/z (from the spectrum in Fig S26). Panel A) Experimental data for peak m/z = 824.0589 are shown at the top of the panel and compared with the data calculated for the $[CuL_2H_3]^+$ ($C_{32}H_{29}N_2O_{20}Cu$) complex (lower panels). Panel B) Experimental data for peak m/z = 884.9732 are shown and compared with the data calculated for the $[Cu_2L_2H]^+$ ($C_{32}H_{27}N_2O_{20}Cu_2$) complex (lower panel).

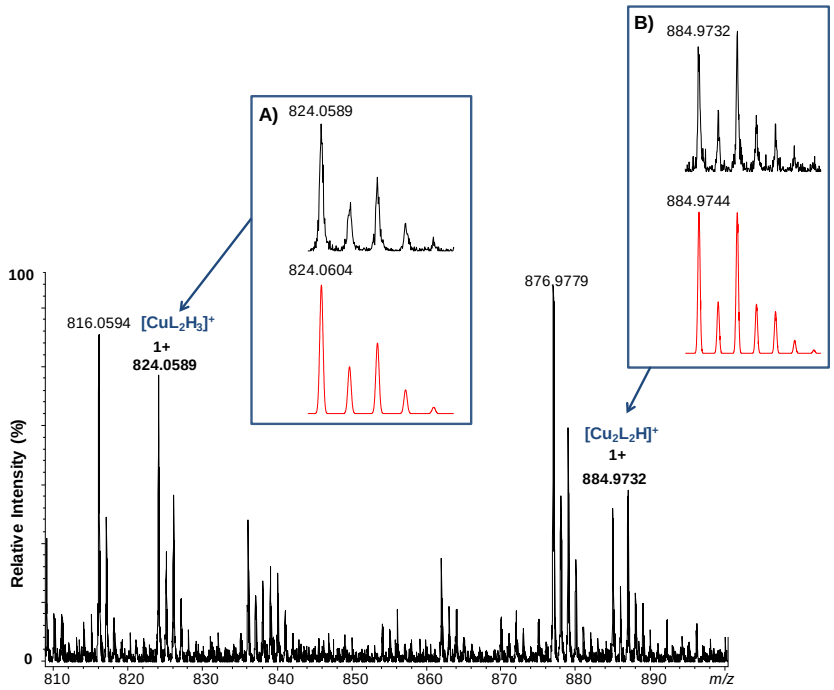

Figure A28. Electrospray ionization with tandem mass spectrometry (MS/MS) spectrum of the $[CuLH]^+$ complex. The peak selected for fragmentation in the MS/MS experiment is indicated by a diamond.

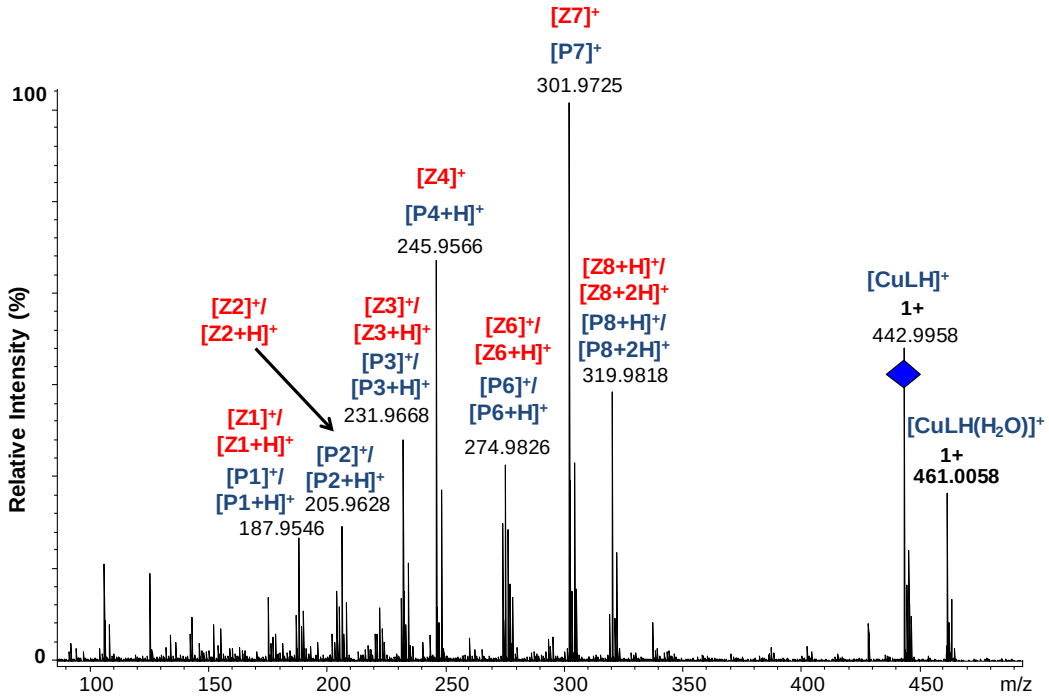

Figure A29. Electrospray ionization with tandem mass spectrometry (MS/MS) spectrum of the $[CuLH]^+$ complex. Comparisons between experimental and isotopic patterns of ions found in MS/MS experiments are presented in panels A-G.

Panel A)

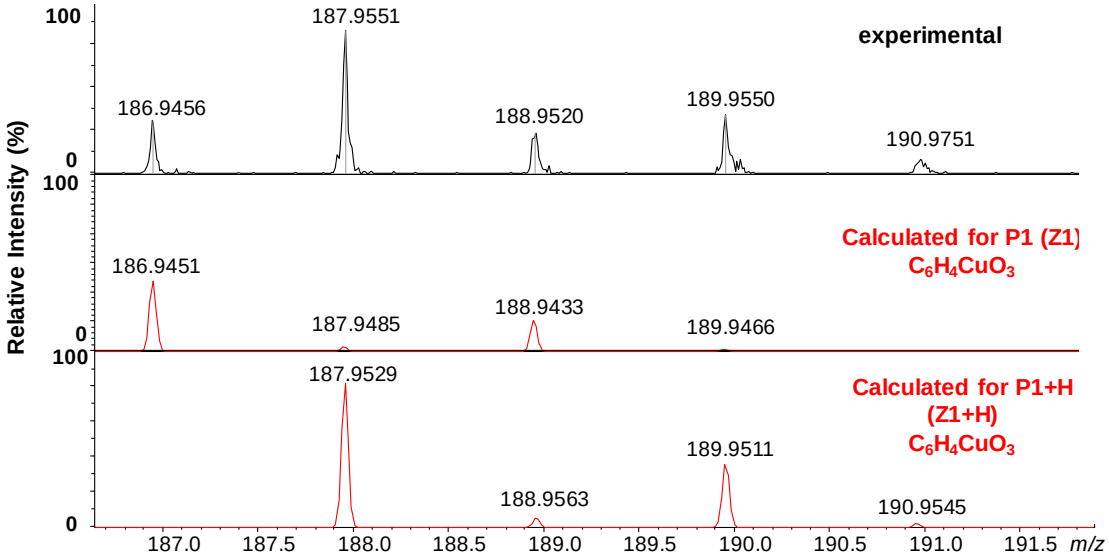

Panel B)

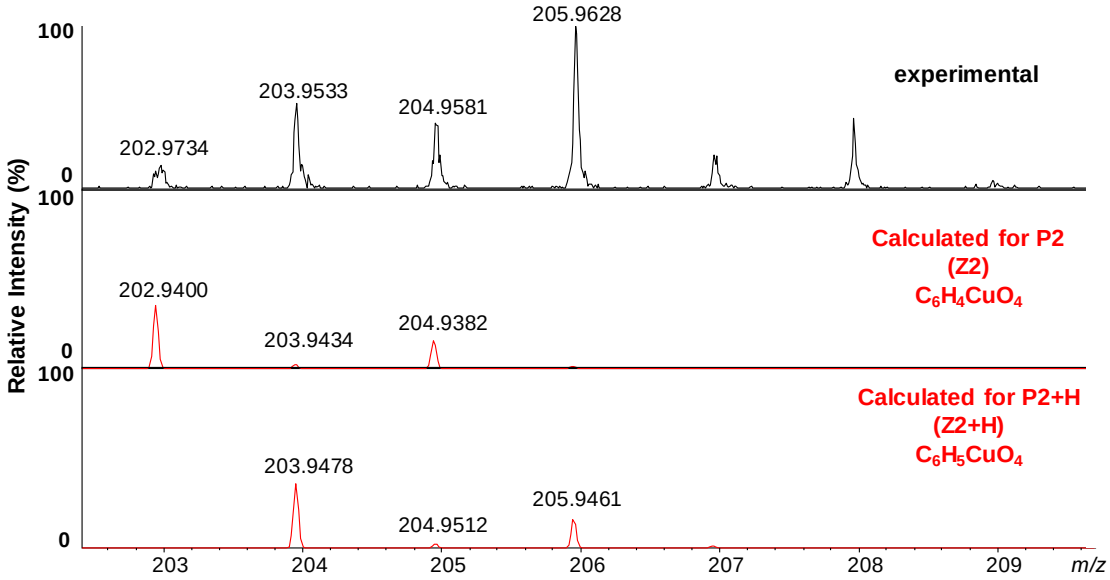

Panel C)

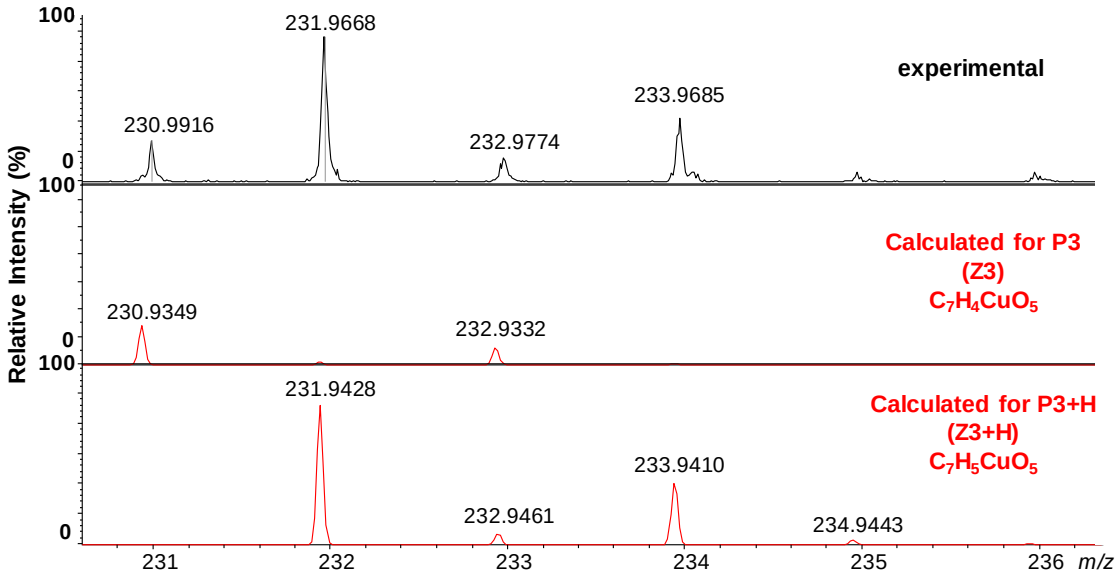

Panel D)

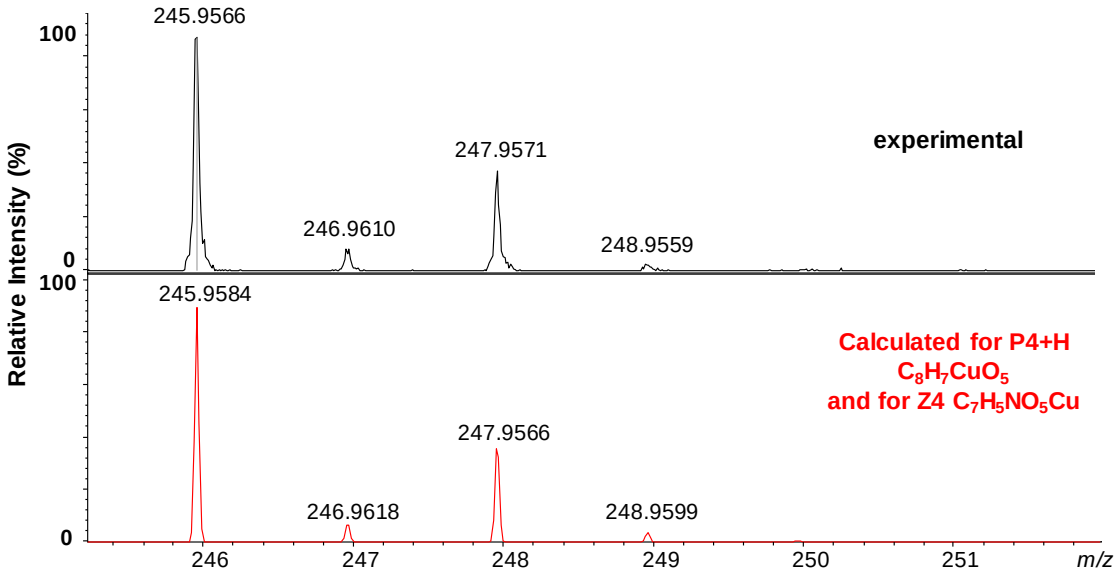

Panel E)

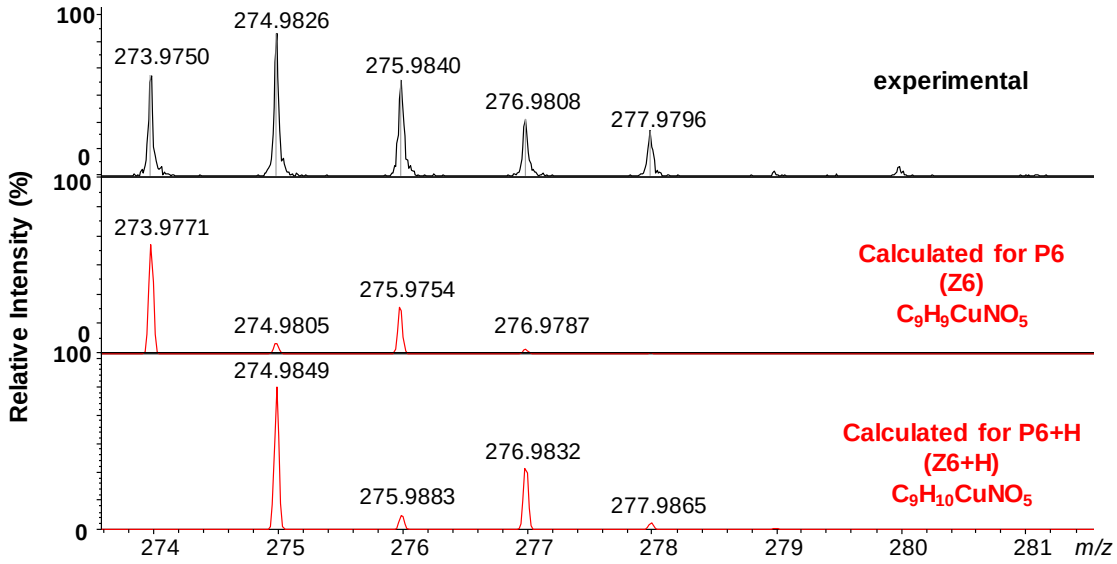

Panel F)

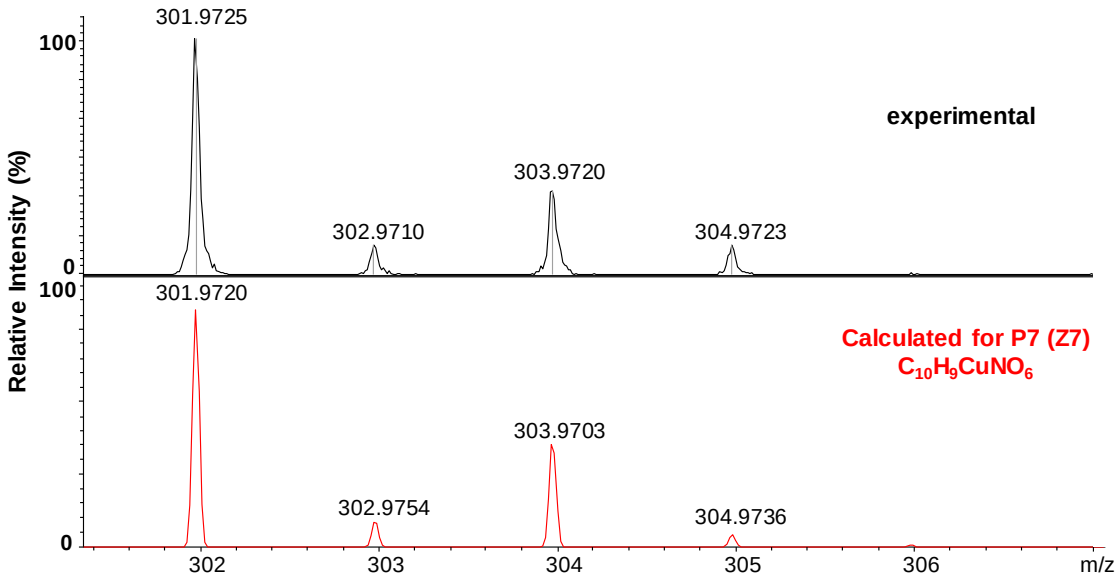

Panel G)

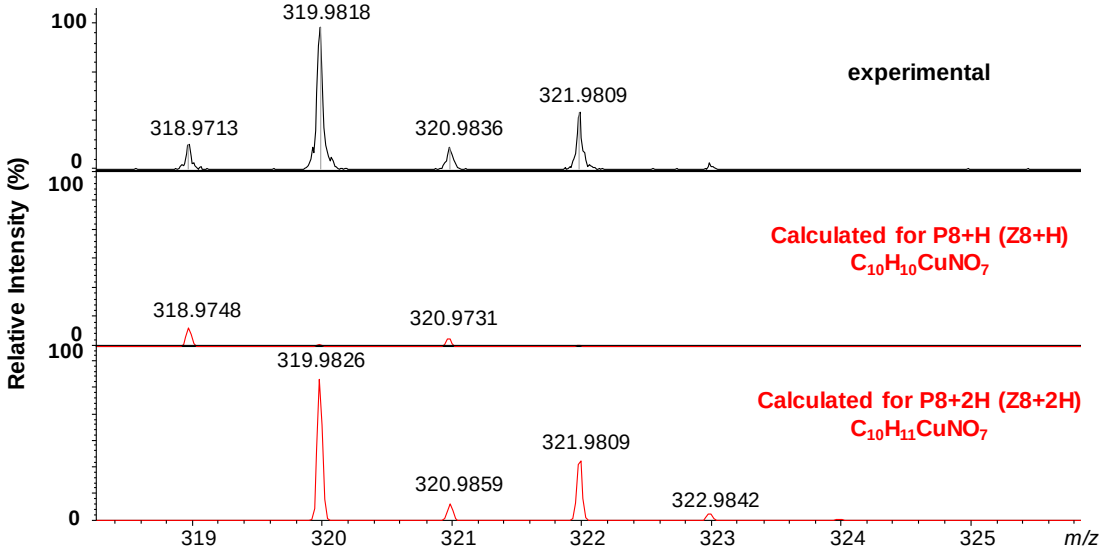

TableA12. Comparison of m/z values (experimental and calculated) for the most abundant isotopic peaks of the $[CuLH]^+$ complex.

compound	calculated *m/z* value	experimental *m/z* value	elemental formula of complex	compound	calculated *m/z* value	experimental *m/z* value	elemental formula of complex
P1	186.9451	186.9399	C6H4O3Cu	Z1	186.9451	186.9399	C6H4O3Cu
P1+H	187.9485	187.9551	C6H5O3Cu	Z1+H	187.9485	187.9551	C6H5O3Cu
P2	202.9400	202.9734	C6HO4Cu	Z2	202.9400	202.9734	C6HO4Cu
P2+H	203.9478	203.9533	C6H5O4Cu	Z2+H	203.9478	203.9533	C6H5O4Cu
P3	230.0949	230.9946	C7H4O5Cu	Z3	230.0949	230.9946	C7H4O5Cu
P3+H	231.9428	231.9668	C7H5O5Cu	Z3+H	231.9428	231.9668	C7H5O5Cu
P4	--------	---------	C8H6O5Cu	Z4	245.9566	245.9458	C7H5NO5Cu
P4+H	245.9584	245.9566	C8H7O5Cu	Z4+H	--------	--------	C7H6NO5Cu
P6	273.9771	273.9750	C9H9NO5Cu	Z6	273.9771	273.9750	C9H9NO5Cu
P6+H	274.9849	274.9826	C9H10NO5Cu	Z6+H	274.9849	274.9826	C9H10NO5Cu
P7	301.9720	301.9725	C10H9NO6Cu	Z7	301.9720	301.9725	C10H9NO6Cu
P8+H	318.9748	318.9713	C10H10NO7Cu	P8+H	318.9748	318.9713	C10H10NO7Cu
P8+2H	319.9826	319.9818	C10H11NO7Cu	P8+2H	319.9826	319.9818	C10H11NO7Cu

Figure A30. **Fig. S 1.** The full spectrum of KβAK with Zn^{2+} solution in the molar ratio 1:1. The upper panel shows the isotopic patterns obtained for experimental data m/z = 443.9945 and m/z 462.0015 compared to those calculated for $[ZnLH]^+$ ($C_{16}H_{14}NO_{10}Zn$) and the $[ZnLH(H_2O)]^+$ ($C_{16}H_{16}NO_{11}Zn$).

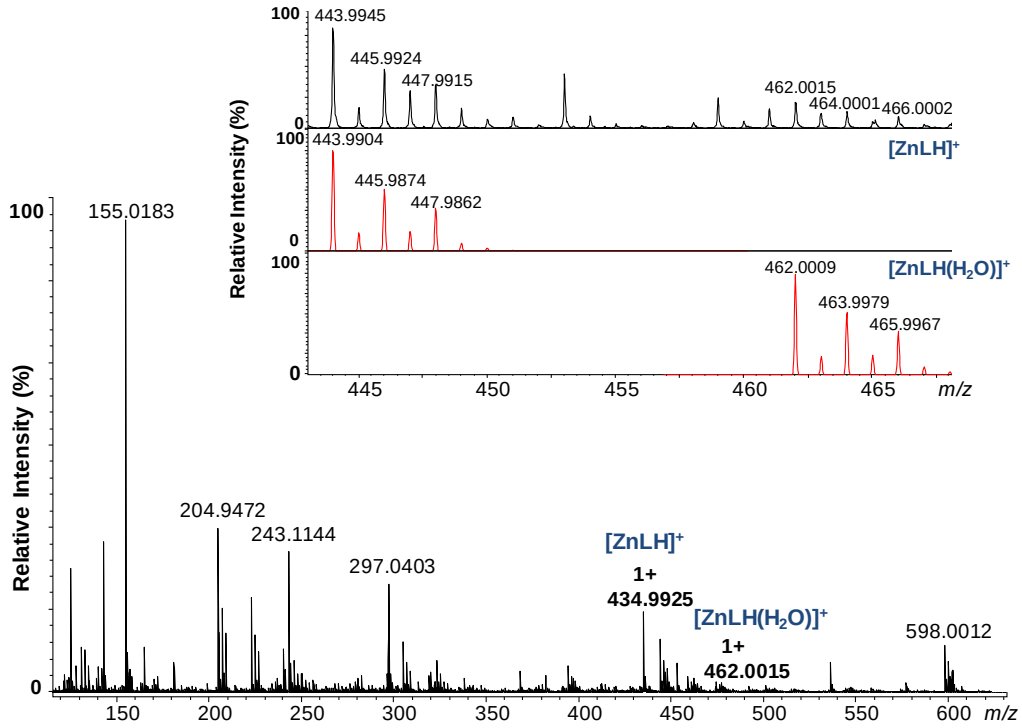

Figure A31. Schematic presentation of the collision-induce dissociation fragmentation of $[ZnLH]^+$.

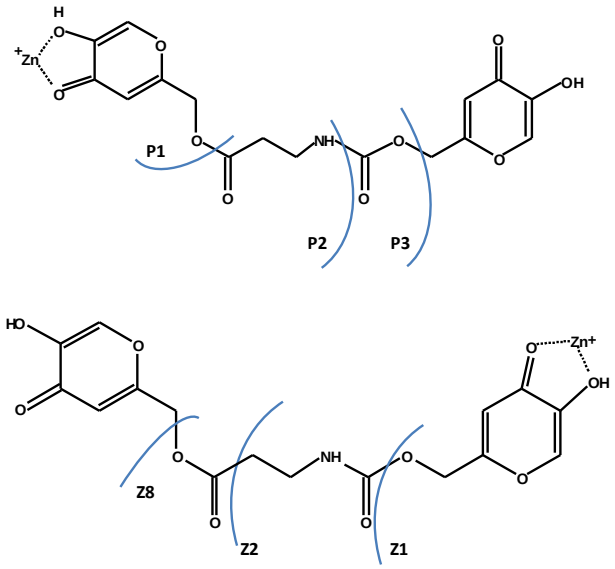

TableA13. Comparison of m/z values (experimental and calculated) for the most abundant isotopic peaks of the $[ZnLH]^+$ complex.

compound	calculated *m/z* value	experimental *m/z* value	elemental formula of complex	compound	calculated *m/z* value	experimental *m/z* value	elemental formula of complex
P1	203.9396	203.9646	C6H4O4Zn	Z1	203.9396	203.9646	C6H4O4Zn
P1+H	204.9474	204.9512	C6H5O4Zn	Z1+H	204.9474	204.9512	C6H5O4Zn
P2+H	275.9845	275.9833	C9H10NO5Zn	Z2+H	275.9845	275.9833	C9H10NO5Zn
P3+H	319.9743	319.9724	C10H10NO7Zn	Z3+H	319.9743	319.9724	C10H10NO7Zn

Figure A32. Electrospray ionization with tandem mass spectrometry (MS/MS) spectrum of the $[ZnLH]^+$ complex. The peak selected for fragmentation in the MS/MS experiment is indicated by a diamond.

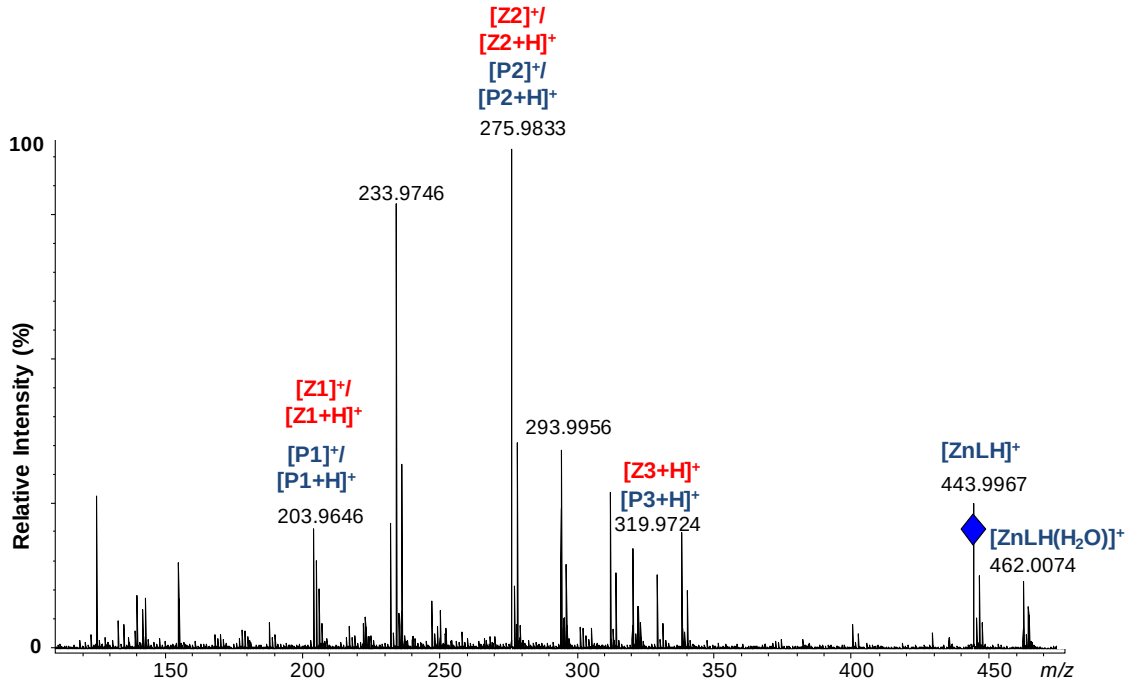

Figure A33. Electrospray ionization with tandem mass spectrometry (MS/MS) spectrum of the $[ZnLH]^+$ complex. Comparisons between experimental and isotopic patterns of ions found in MS/MS experiments are presented in panels A-C.

Panel A)

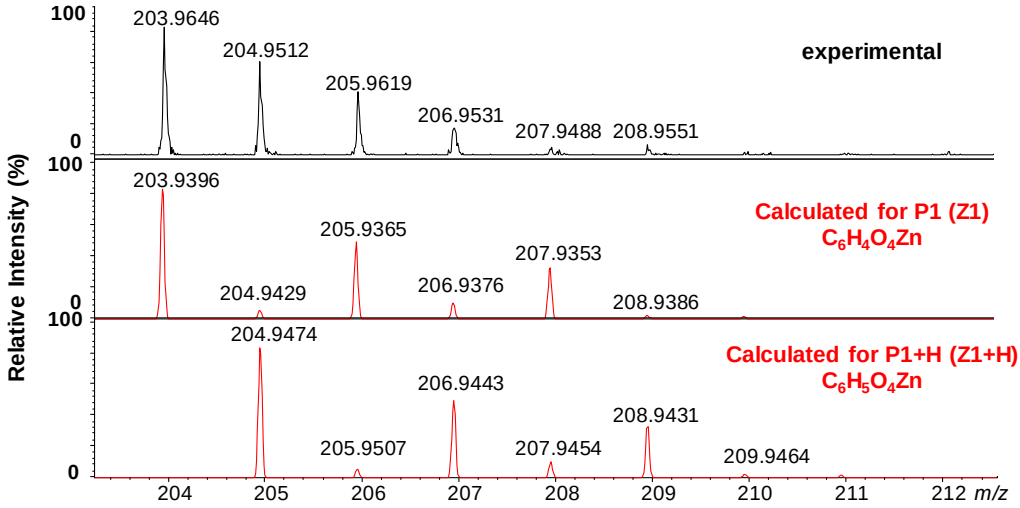

Panel B)

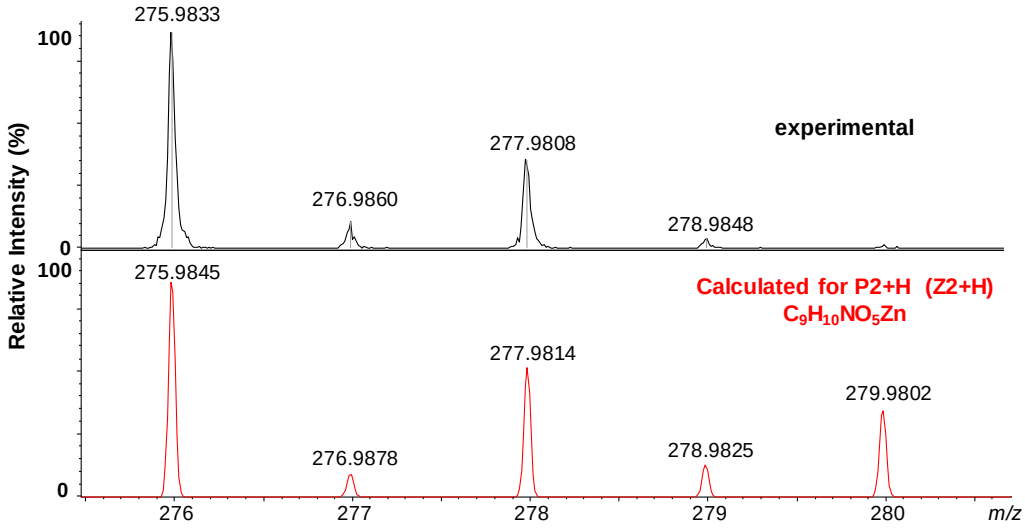

Panel C)

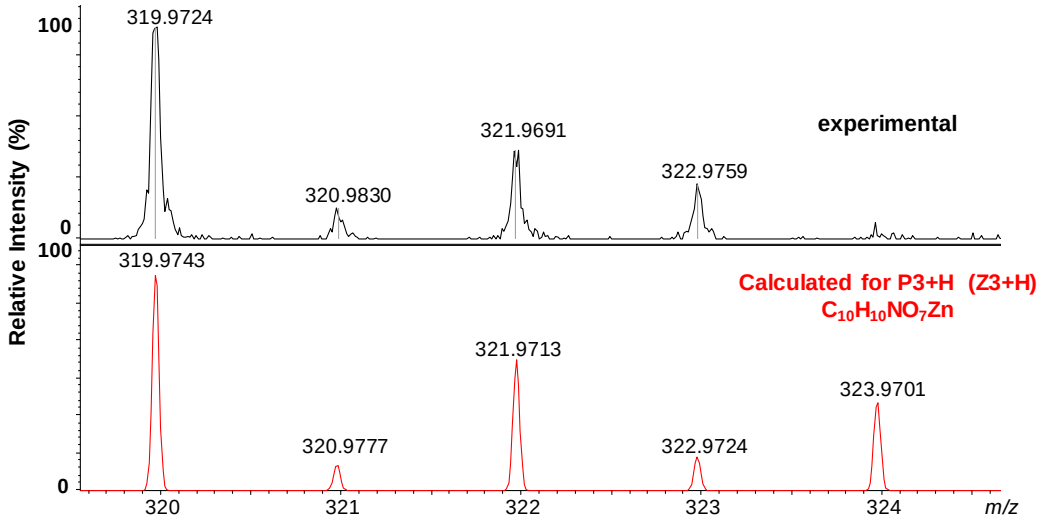

Figure A34. The full spectrum of KβAK with Fe^{3+} solution in the molar ratio 1:1. Panel A) Experimental data for peak m/z = 434.9948 are shown at the top of the panel and compared with the data calculated for the $[Fe_2L_2]^{2+}$ ($C_{32}H_{26}N_2O_{20}Fe_2$) complex (lower panels). Panel B) Experimental data for peak m/z = 453.0046 are shown and compared with the data calculated for the $[FeL(H_2O)]^+$ ($C_{16}H_{15}NO_{11}Fe$) complex (lower panel). Panel C)Experimental data for peak m/z = 889.9407 are shown and compared with the data calculated for the $[Fe_2L_2\ H(H_2O)]^+$ ($C_{32}H_{30}N_2O_{21}Fe_2$) complex (lower panel). Panel D) Experimental data for peak m/z = 904.9491 are shown at the top of the panel and compared with the data calculated for the $[Fe_2L_2H(H_2O)_2]^+$ ($C_{32}H_{29}N_2O_{21}Fe_2$) complex (lower panel).

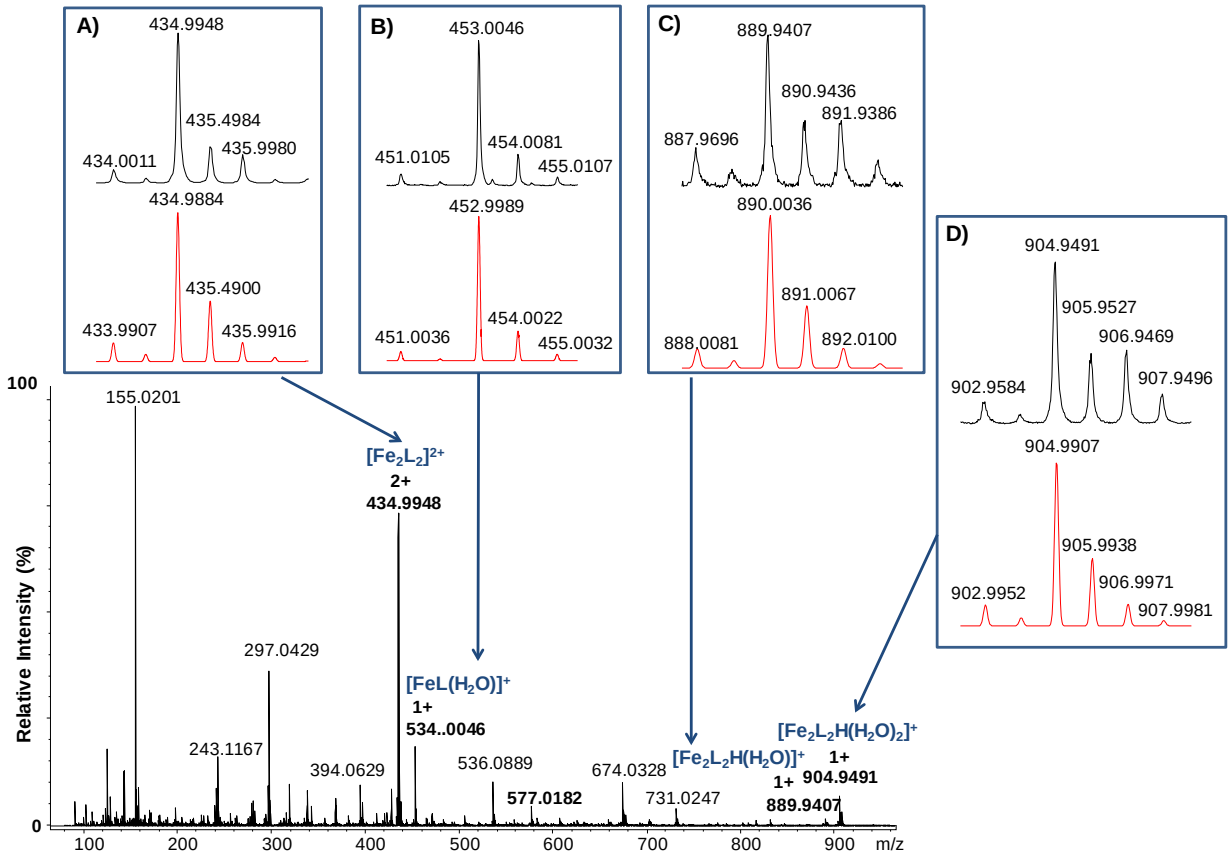

Figure A35. The full spectrum of Kojic-βAla-Kojic with aluminium solution in the molar ratio 1:1. Panel A) Experimental data for peak m/z = 406.0391 are shown at the top of the panel and compared with the data calculated for the $[Al_2L_2]^{2+}$ ($C_{32}H_{26}N_2O_{20}Al_2$) and $[AlLH]^+$ ($C_{16}H_{13}NO_{10}Al$) complexes, respectively (lower panels). Panel B) Experimental data for peak m/z = 424.0526 are shown at the top of the panel and compared with the data calculated for the $AlLH(H_2O)^+$ complex (lower panel).

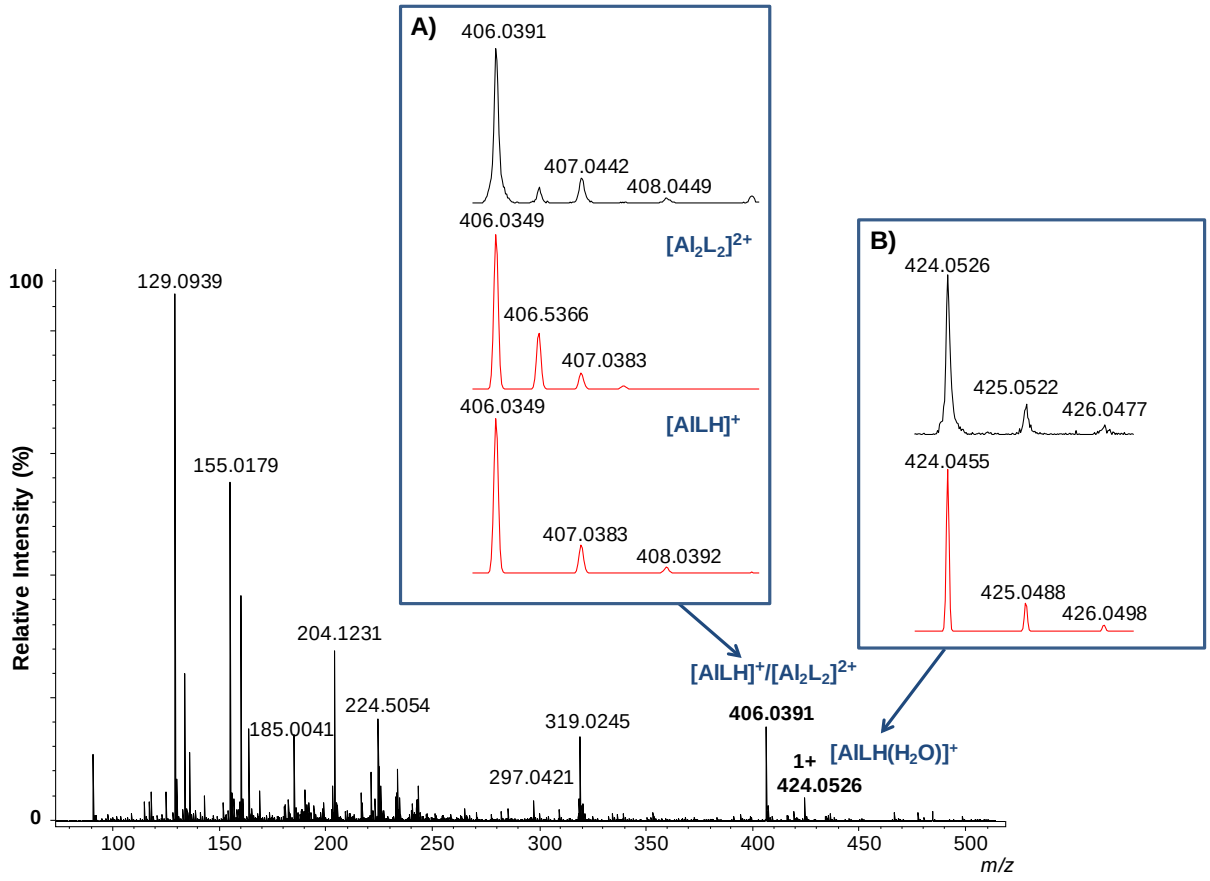

Figure A36. The full ESI-MS spectrum of Irbesartan solution.

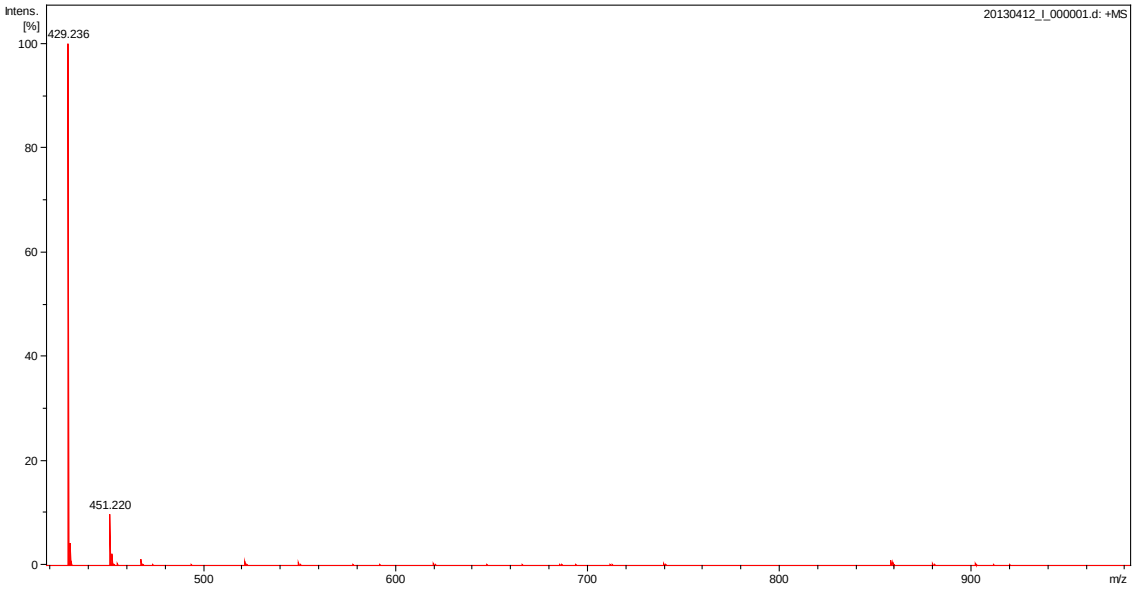

A) Experimental data for peak m/z = 429.236 are shown at the top of the panel and compared with the data calculated for the $[I+H]^+$ ($C_{25}H_{29}N_6O$) (lower panel).

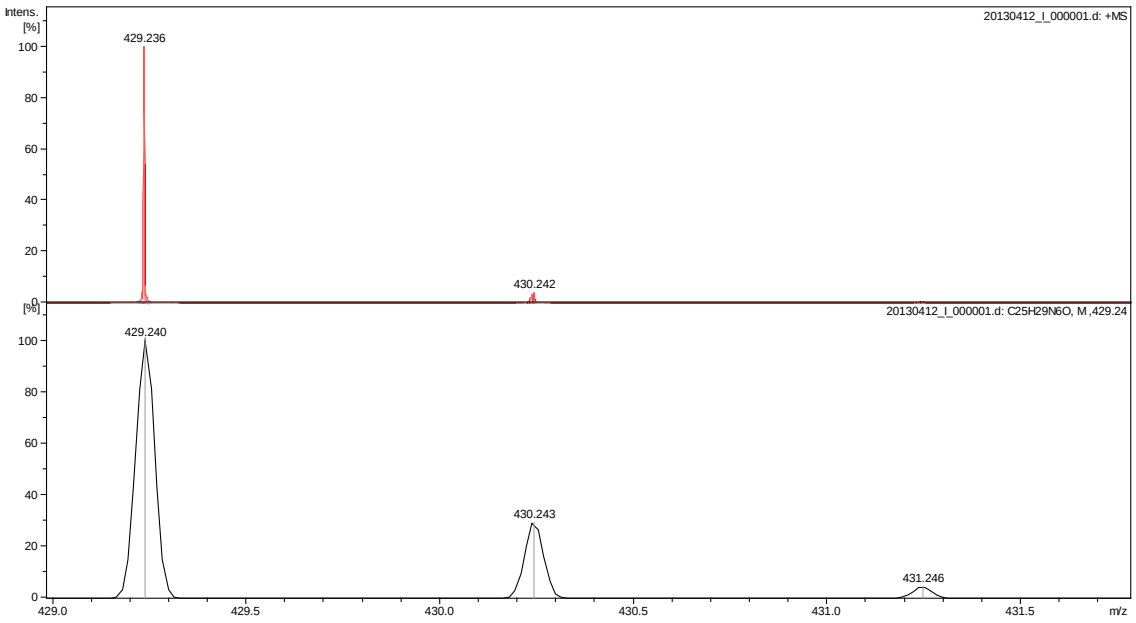

B) Experimental data for peak m/z = 451.220 are shown at the top of the panel and compared with the data calculated for the $[I+Na]^+$ ($C_{25}H_{28}N_6O$+Na) (lower panel).

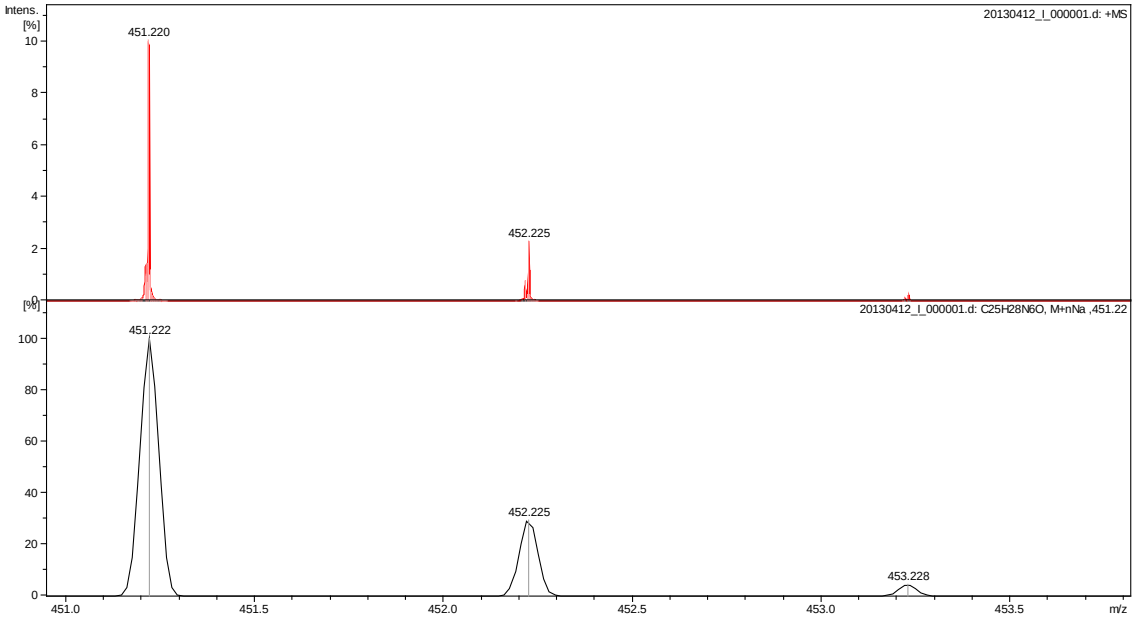

C) Experimental data for peak m/z = 467.196 are shown at the top of the panel and compared with the data calculated for the $[I+K]^+$ ($C_{25}H_{28}N_6O+K$) (lower panel).

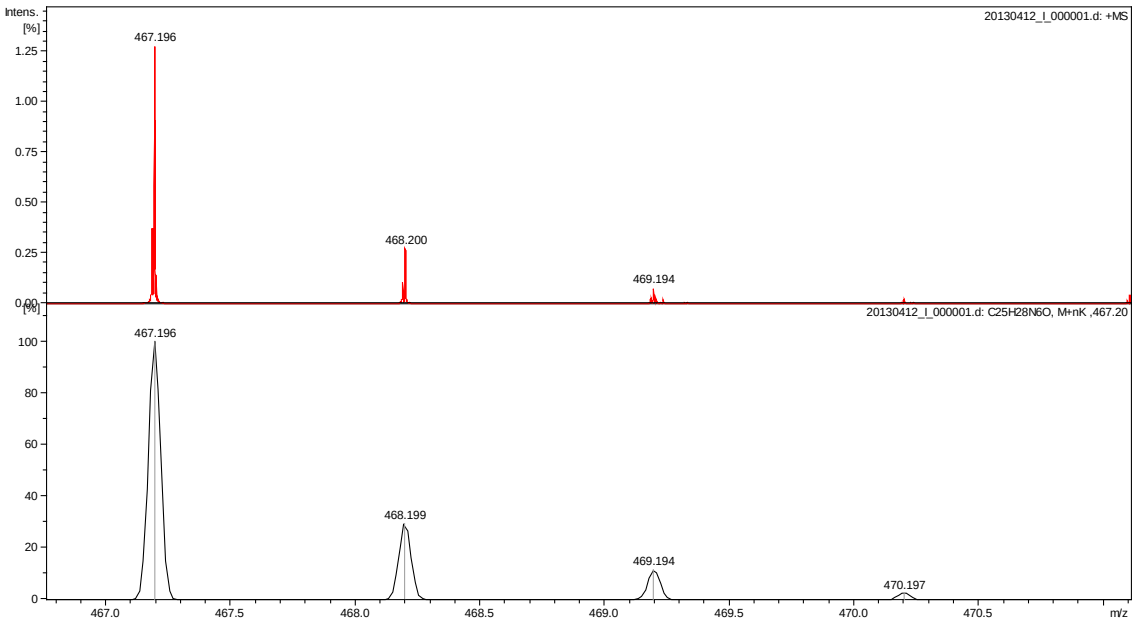

D) Experimental data for peak m/z = 857.472 are shown at the top of the panel and compared with the data calculated for the $[2I+H]^+$ ($C_{50}H_{57}N_{12}O_2$) (lower panel).

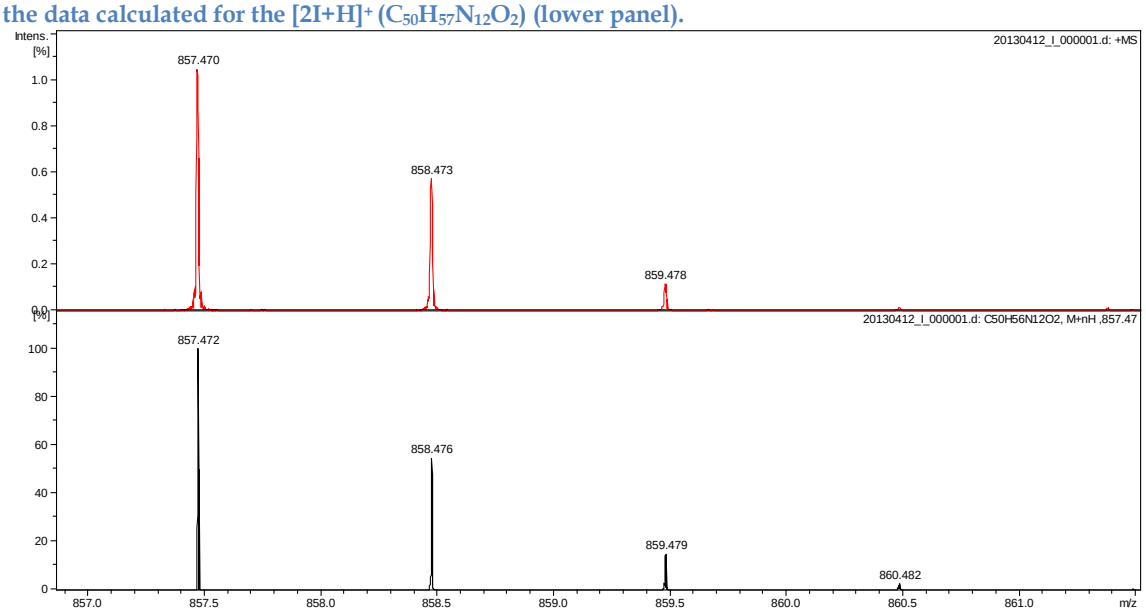

E) Experimental data for peak m/z = 879.454 are shown at the top of the panel and compared with the data calculated for the $[2I+Na]^+$ ($C_{50}H_{56}N_{12}O_2Na$) (lower panel).

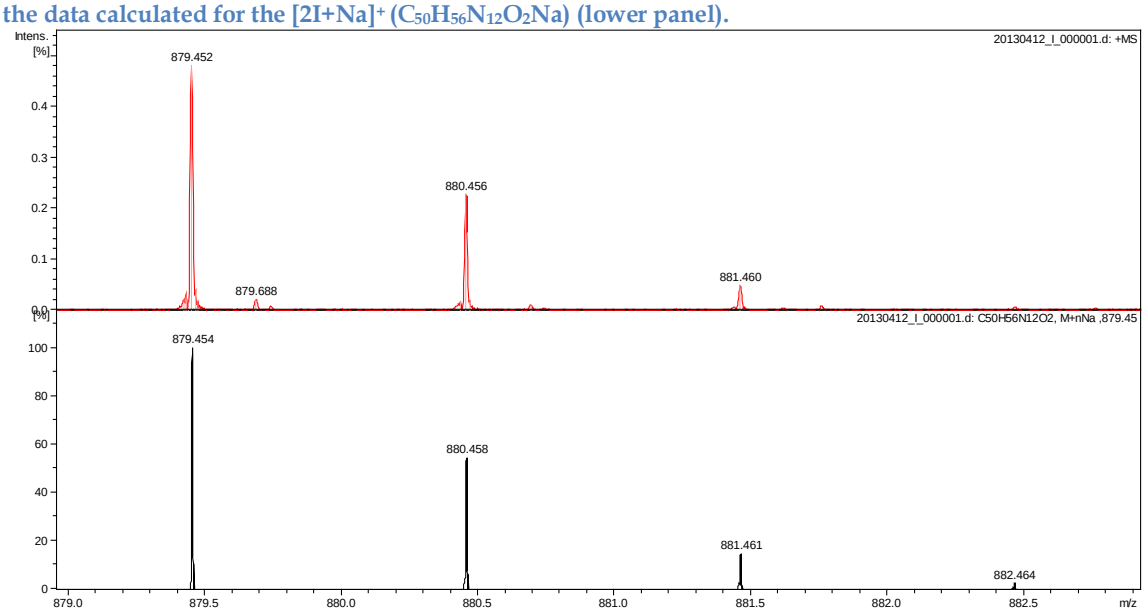

F) Experimental data for peak m/z = 901.436 are shown at the top of the panel and compared with the data calculated for the $[2I+2Na]^+$ ($C_{50}H_{55}N_{12}O_2Na_2$) (lower panel).

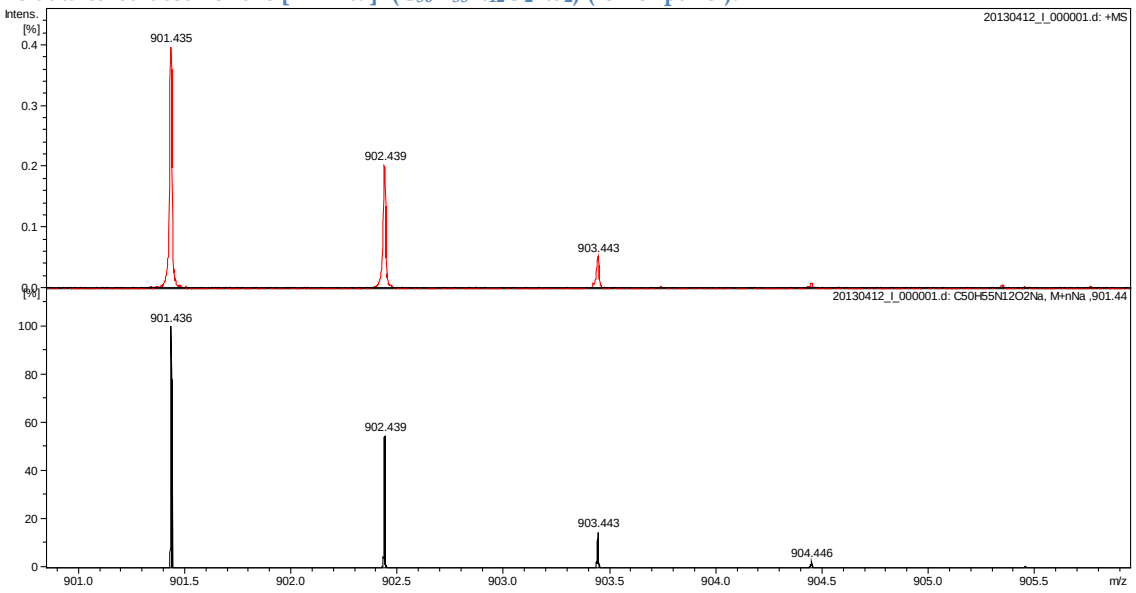

Figure 37. The full ESI-MS spectrum of Losartan solution.

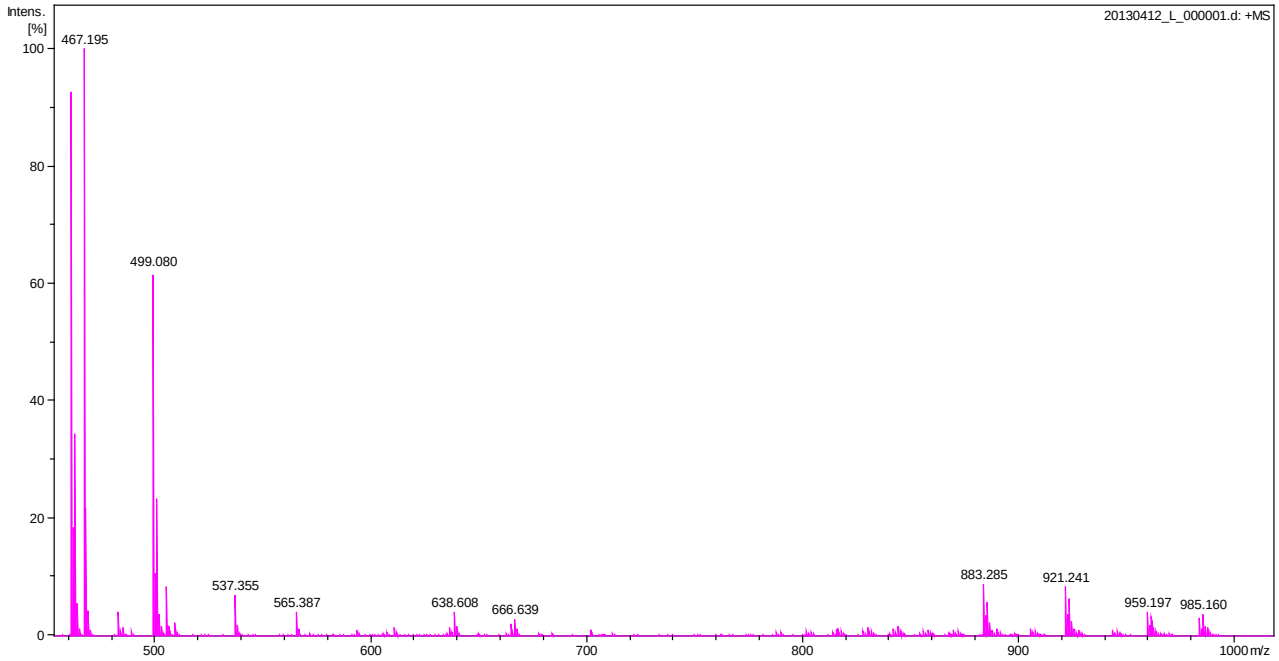

A) Experimental data for peak m/z = 461.125 are shown at the top of the panel and compared with the data calculated for $[L+K]^+$ ($C_{22}H_{23}N_6OKCl$) (lower panel).

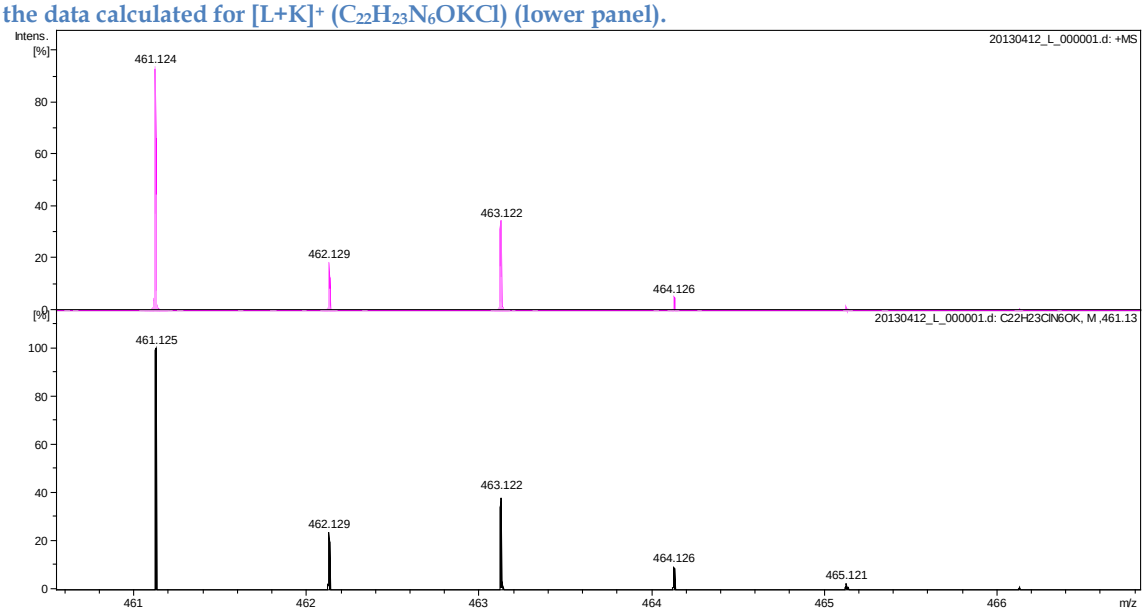

B) Experimental data for peak m/z = 483.108 are shown at the top of the panel and compared with the data calculated for $[L+K+Na]^+$ ($C_{22}H_{22}N_6OKClNa$) (lower panel).

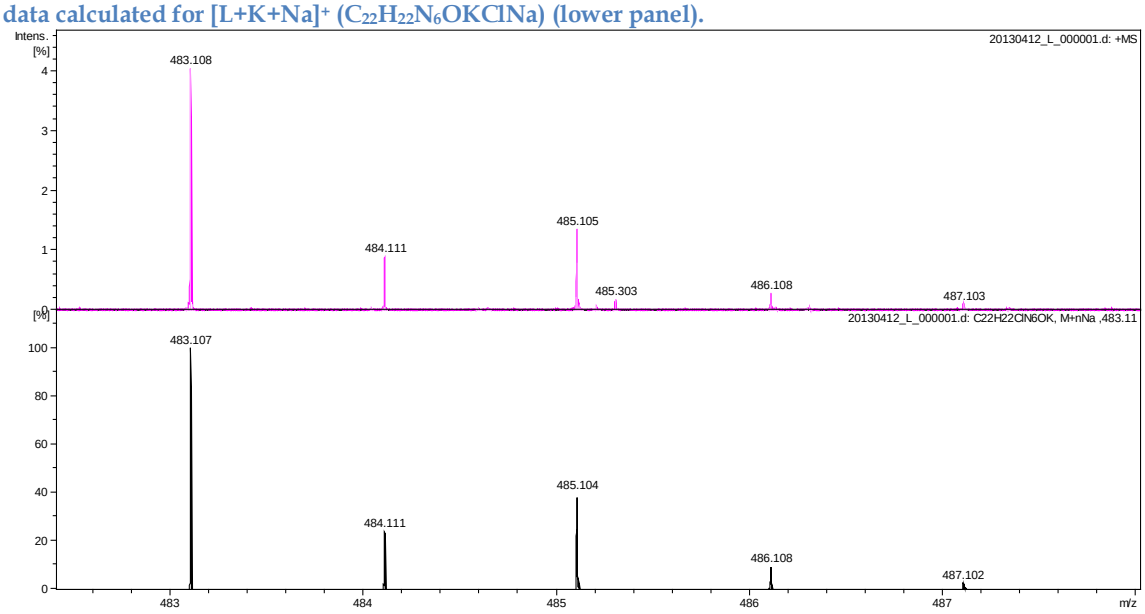

C) Experimental data for peak m/z = 883.285 are shown at the top of the panel and compared with the data calculated for $[2L+K+H]^+$ ($C_{44}H_{46}N_{12}O_2KCl_2$) (lower panel).

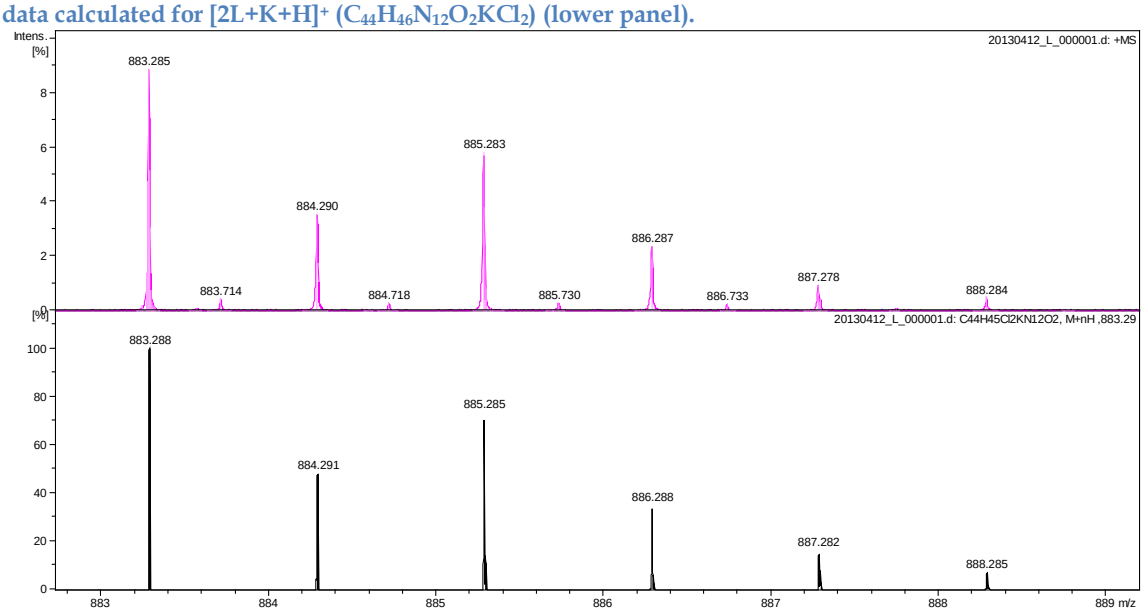

D) Experimental data for peak m/z = 921.241 are shown at the top of the panel and compared with the data calculated for $[2L+2K]^+$ ($C_{44}H_{45}N_{12}O_2K_2Cl_2$) (lower panel).

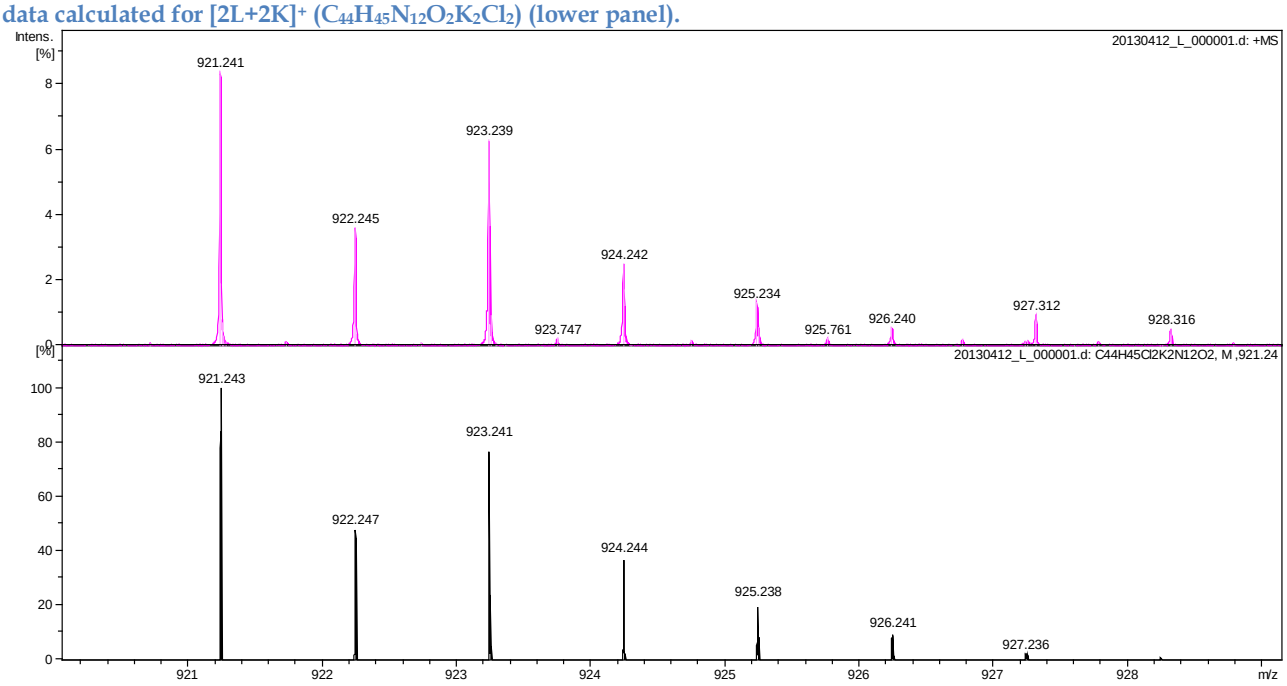

E) Experimental data for peak m/z = 959.199 are shown at the top of the panel and compared with the data calculated for $[2L+3K]^+$ ($C_{44}H_{44}N_{12}O_2K_3Cl_2$) (lower panel).

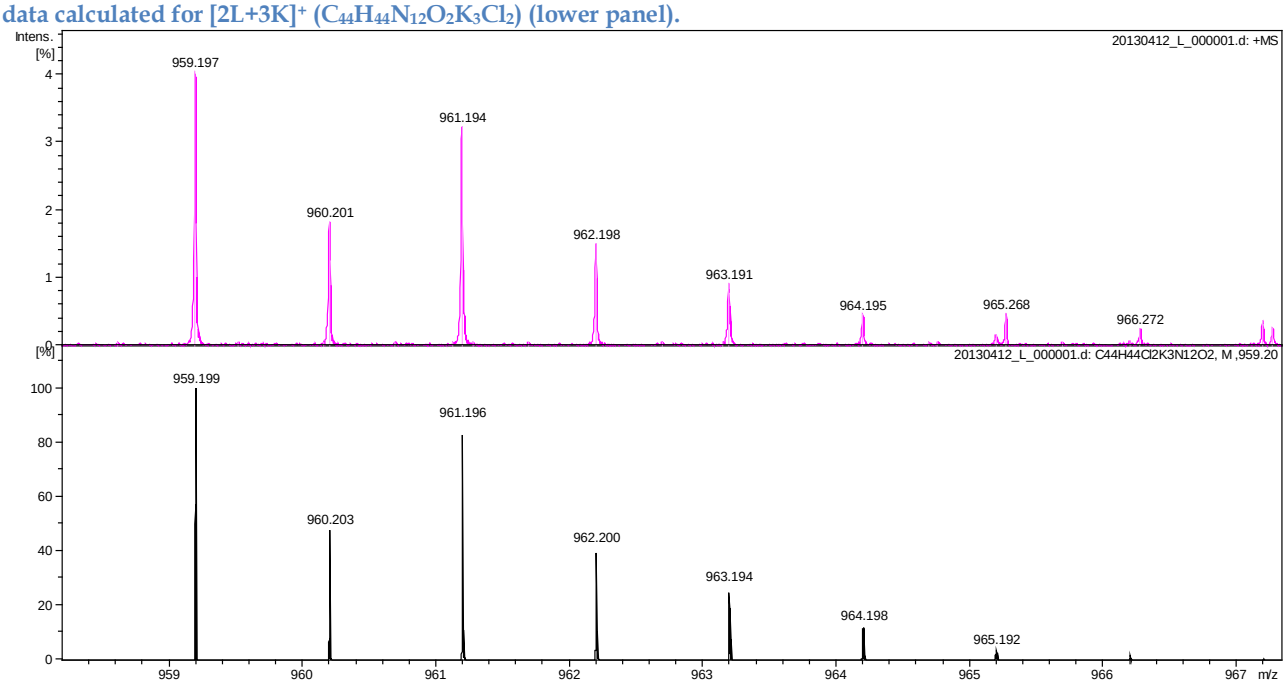

F) Experimental data for peak m/z = 982.189 are shown at the top of the panel and compared with the data calculated for $[2L+3K+Na]^+$ ($C_{44}H_{44}N_{12}O_2K_3Cl_2Na$) (lower panel).

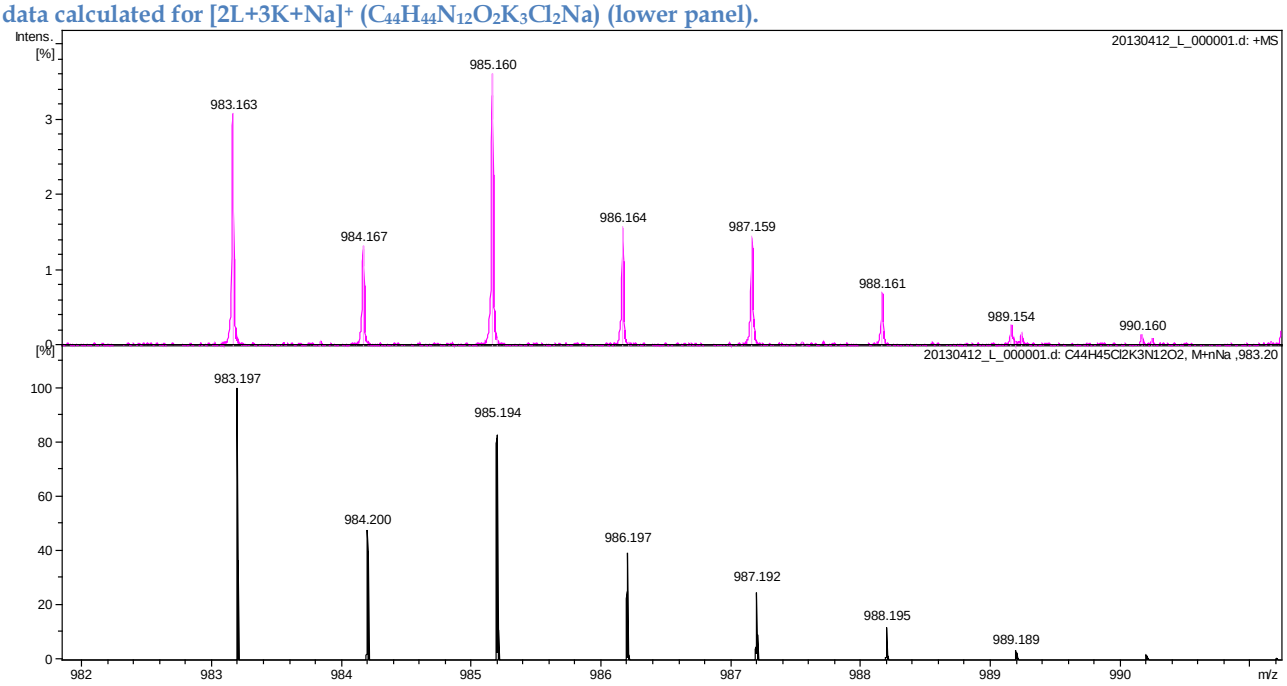

Figure A38. The full spectrum of Irbesartan with copper solution in the molar ratio 1:2 (metal:ligand)

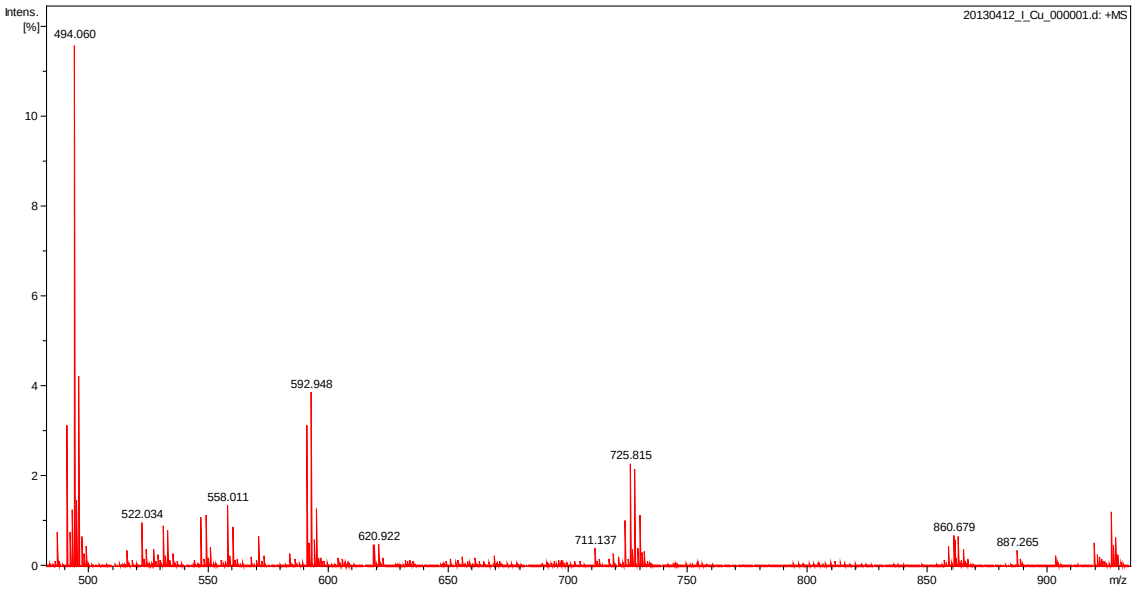

A) Experimental data for peak m/z = 491.162 are shown at the top of the panel and compared with the data calculated for the $[CuI+H]^+$ ($C_{25}H_{28}N_6OCu$) (lower panel).

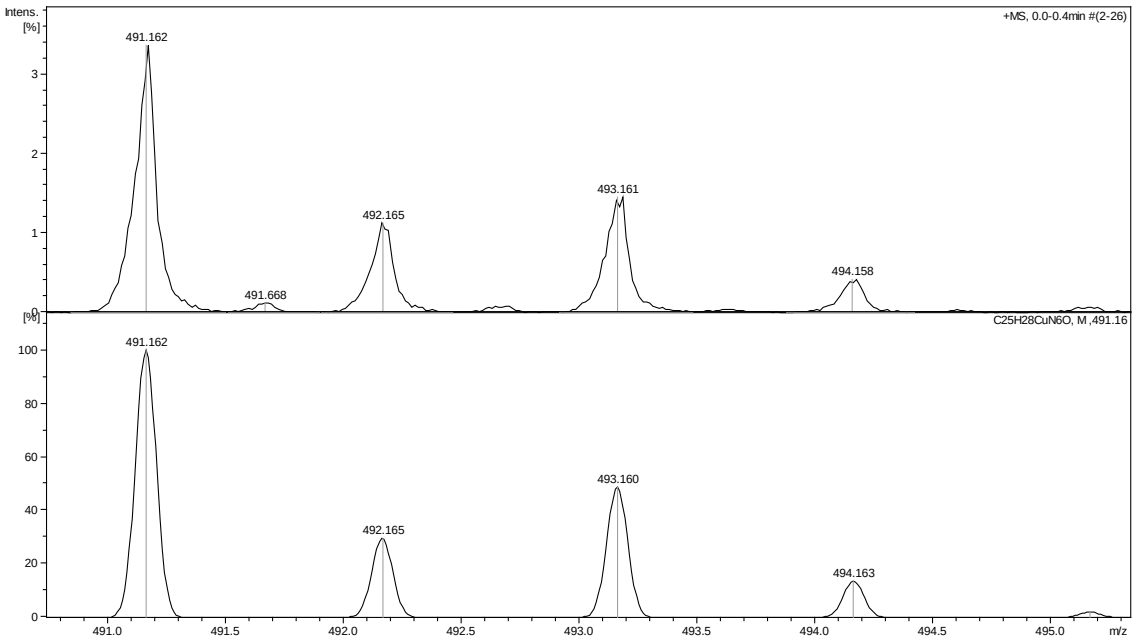

B) Experimental data for peak m/z = 919.394 are shown at the top of the panel and compared with the data calculated for the $[CuI_2+2H]^+$ ($C_{50}H_{56}N_{12}O_2Cu$) (lower panel).

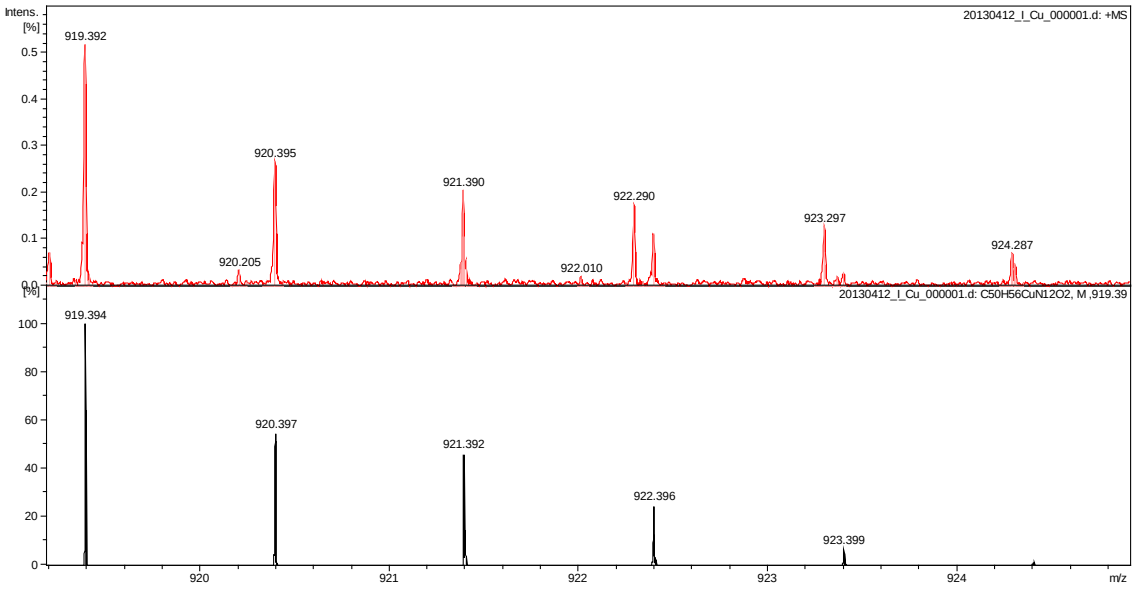

Figure A39. Electrospray ionization with tandem mass spectrometry (MS/MS) spectrum of the $[CuIH]^+$ complex. The peak selected for fragmentation in the MS/MS experiment is indicated by a diamond.

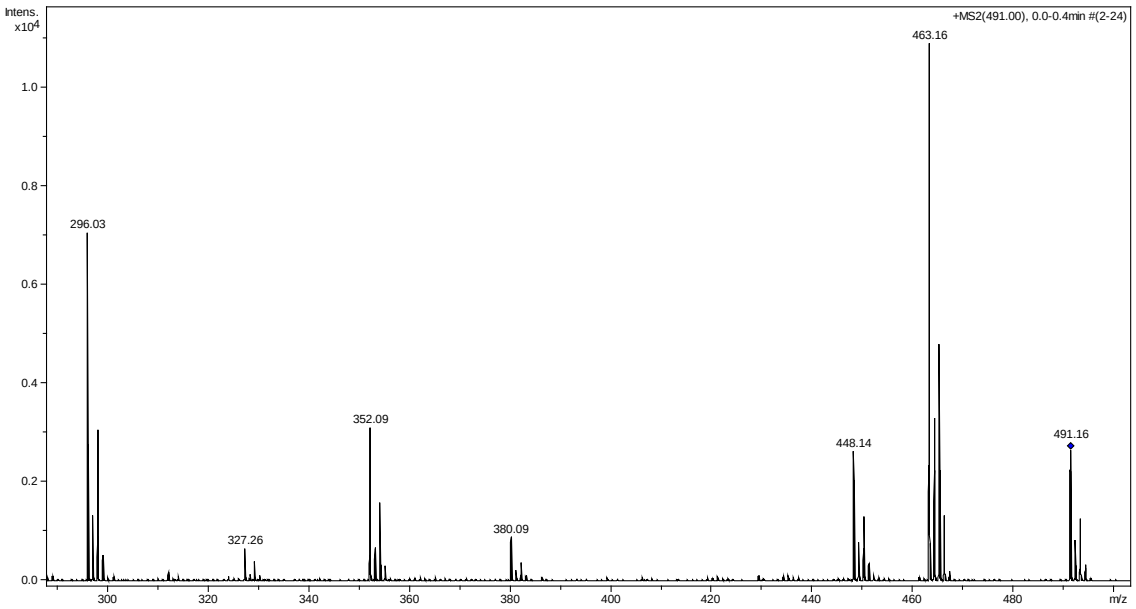

A) Experimental data for peak m/z = 296.03 are shown at the top of the panel and compared with the data calculated for the $C_{14}H_9N_4Cu$ fragment (lower panel).

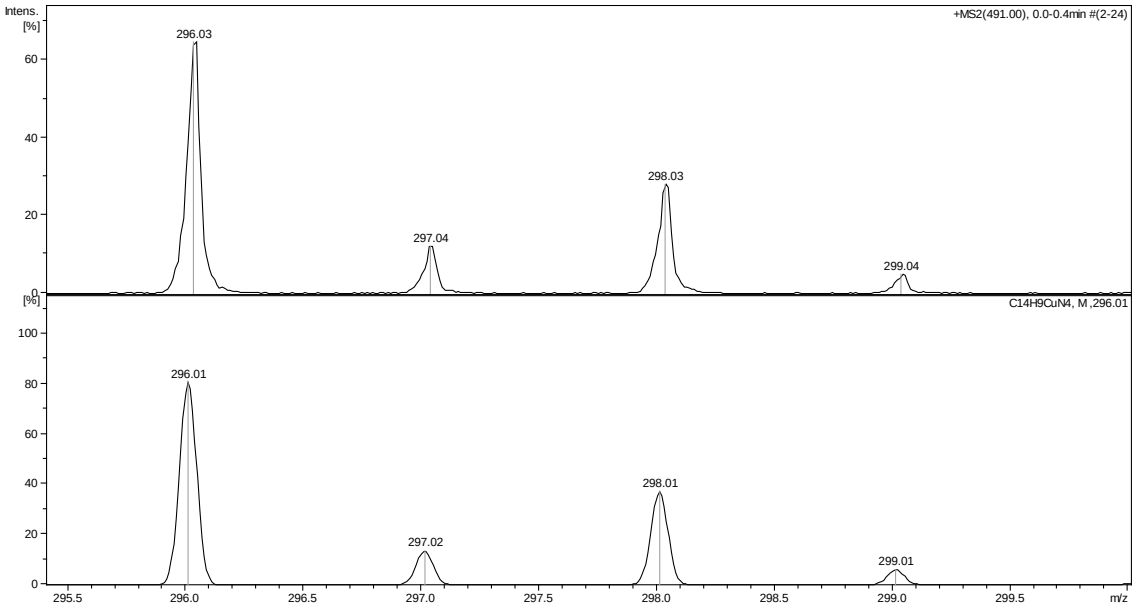

B) Experimental data for peak m/z = 352.09 are shown at the top of the panel and compared with the data calculated for the $C_{16}H_{11}N_5Cu$ fragment (lower panel).

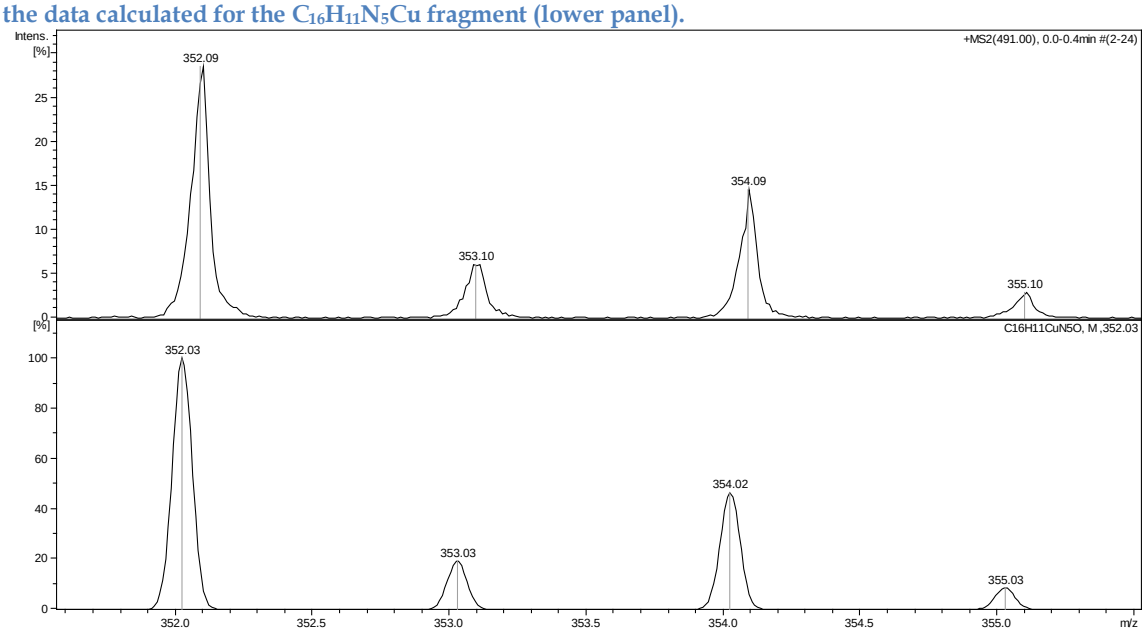

C) Experimental data for peak m/z = 448.14 are shown at the top of the panel and compared with the data calculated for the $C_{22}H_{21}N_6OCu$ fragment (lower panel).

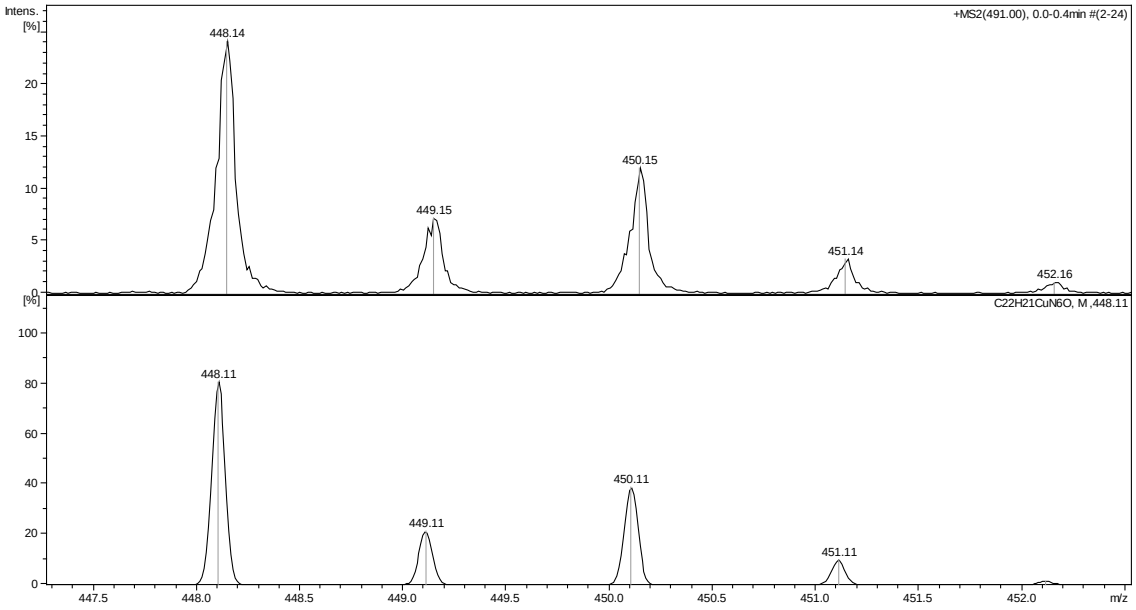

D) Experimental data for peak m/z = 463.16 are shown at the top of the panel and compared with the data calculated for the $C_{23}H_{24}N_6OCu$ fragment (lower panel).

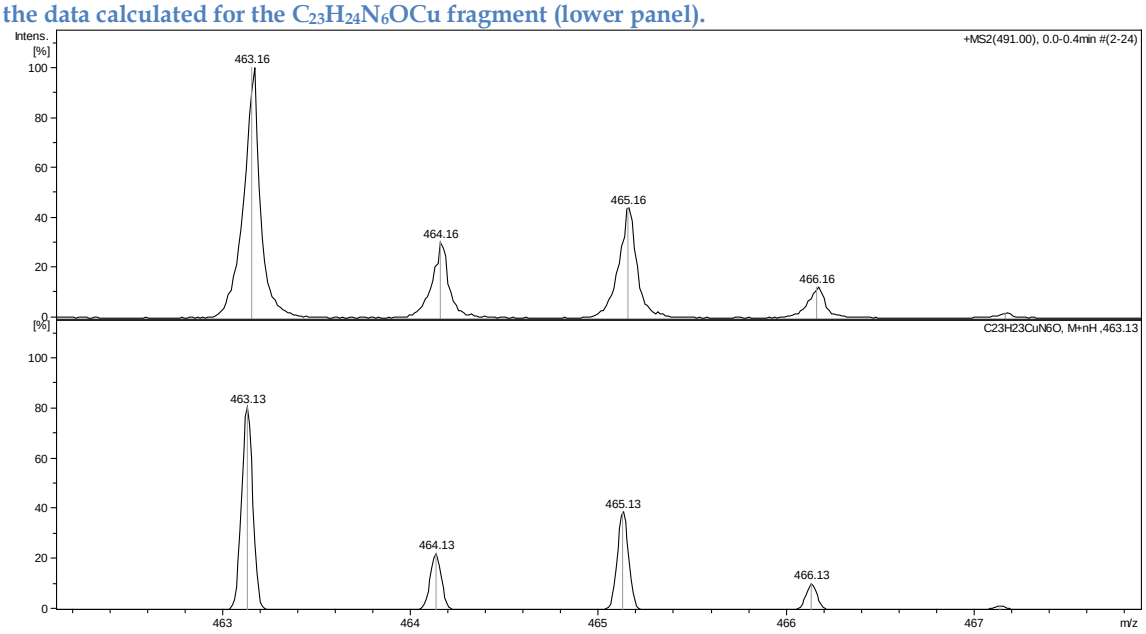

Figure A40. The full spectrum of Irbesartan with zinc solution in the molar ratio 1:2 (metal:ligand).

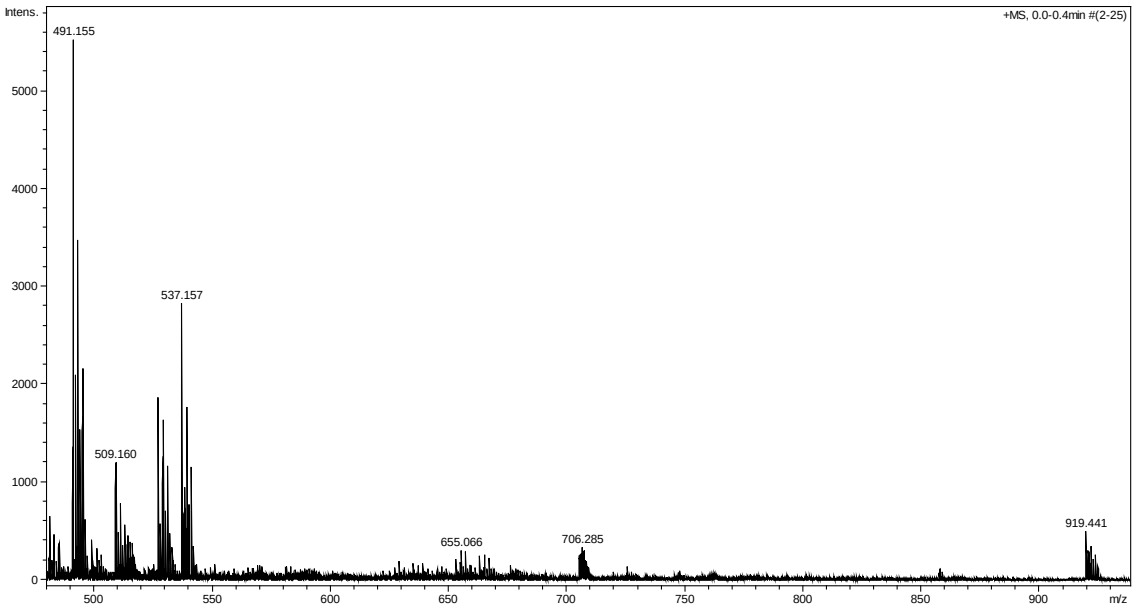

A) Experimental data for peak m/z = 491.162 are shown at the top of the panel and compared with the data calculated for the $[ZnI+H]^+$ ($C_{25}H_{27}N_6OZn$) complex (lower panel).

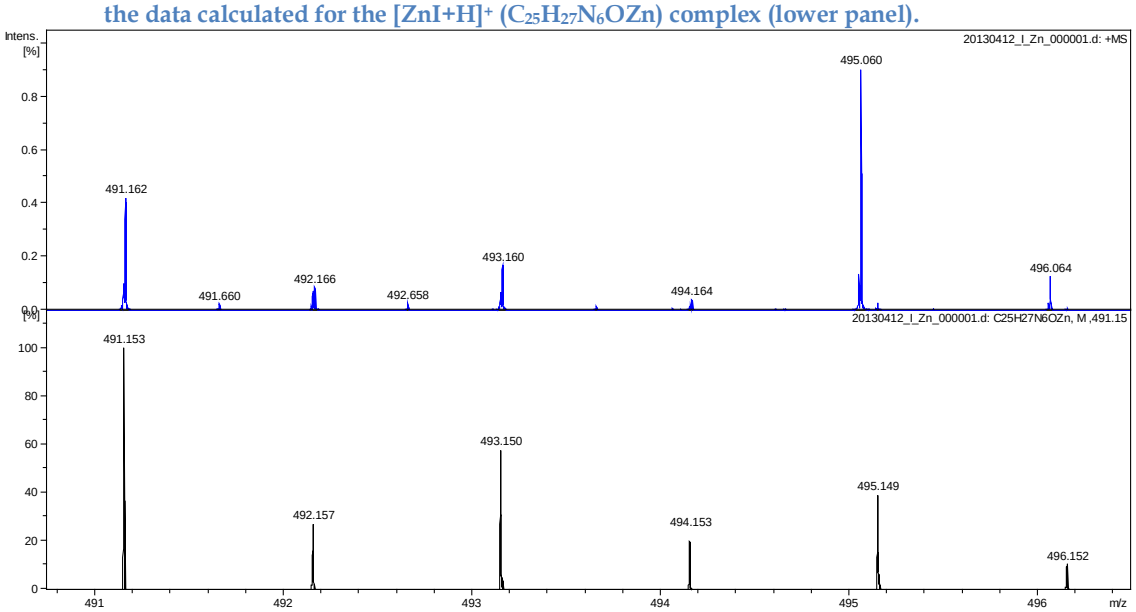

B) Experimental data for peak m/z = 509.160 are shown at the top of the panel and compared with the data calculated for the $[ZnI+H+H_2O]^+$ ($C_{25}H_{29}N_6O_2Zn$) complex (lower panel).

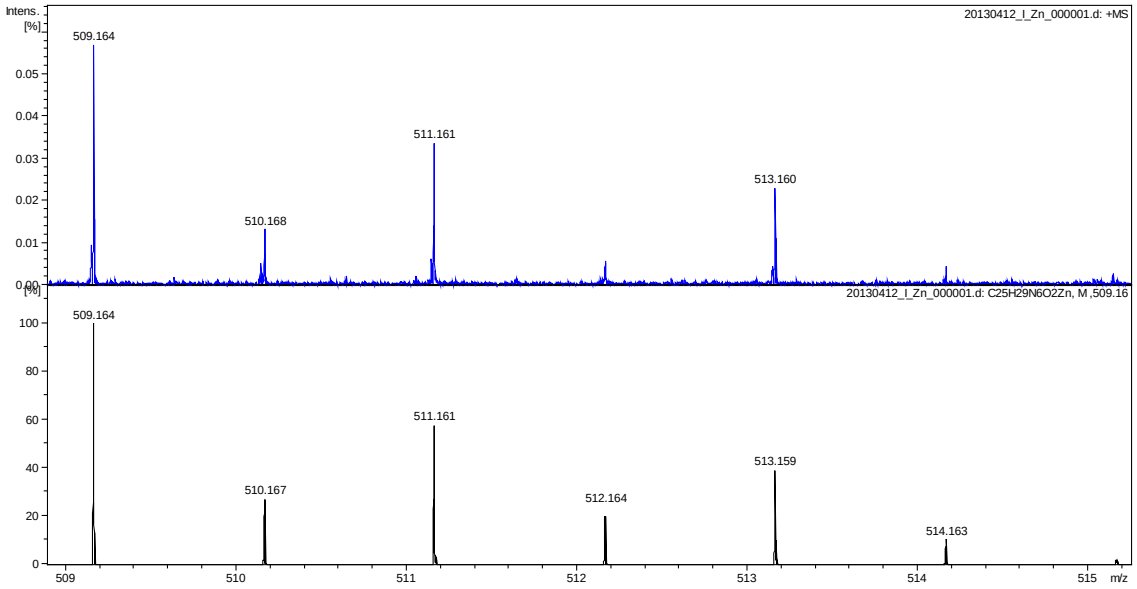

C) Experimental data for peak m/z = 527.131 are shown at the top of the panel and compared with the data calculated for the $[ZnI+H+2H_2O]^+$ ($C_{25}H_{31}N_6O_3Zn$) complex (lower panel).

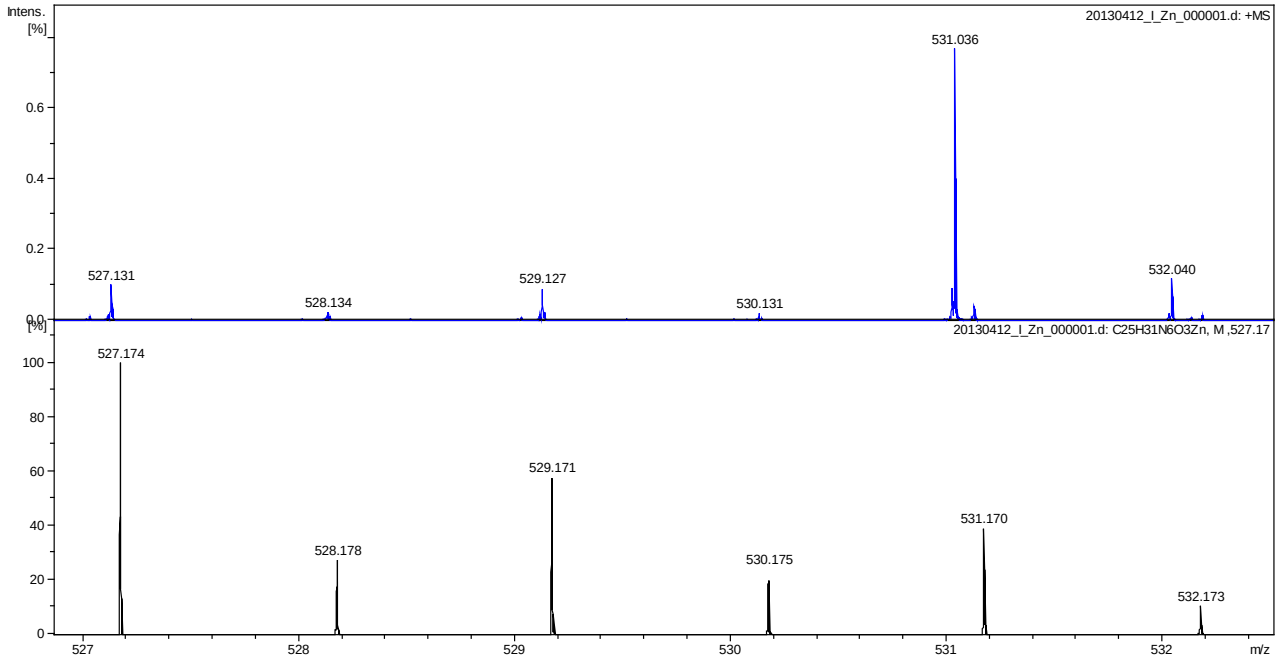

D) Experimental data for peak m/z = 919.395 are shown at the top of the panel and compared with the data calculated for the $[ZnI_2+H]^+$ ($C_{50}H_{55}N_{12}O_2Zn$) complex (lower panel).

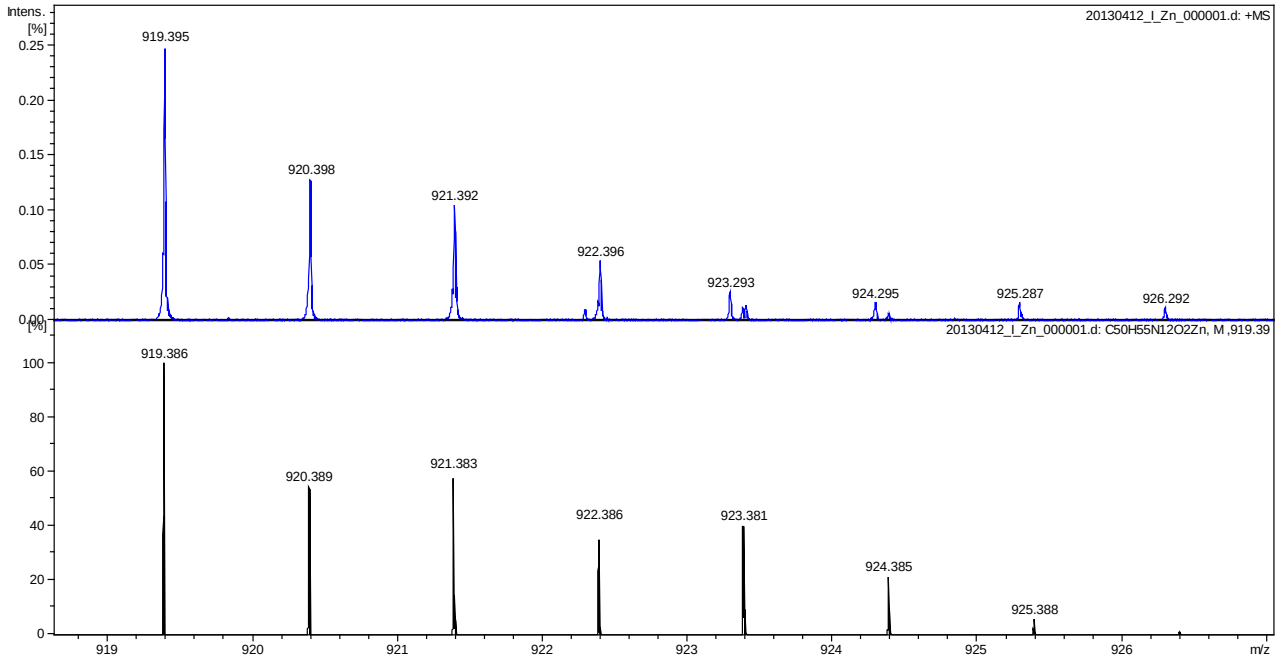

Figure A41. Electrospray ionization with tandem mass spectrometry (MS/MS) spectrum of the $[ZnI_2+H]^+$ complex. The peak selected for fragmentation in the MS/MS experiment is indicated by a diamond. The collision energy was set at 10 eV.

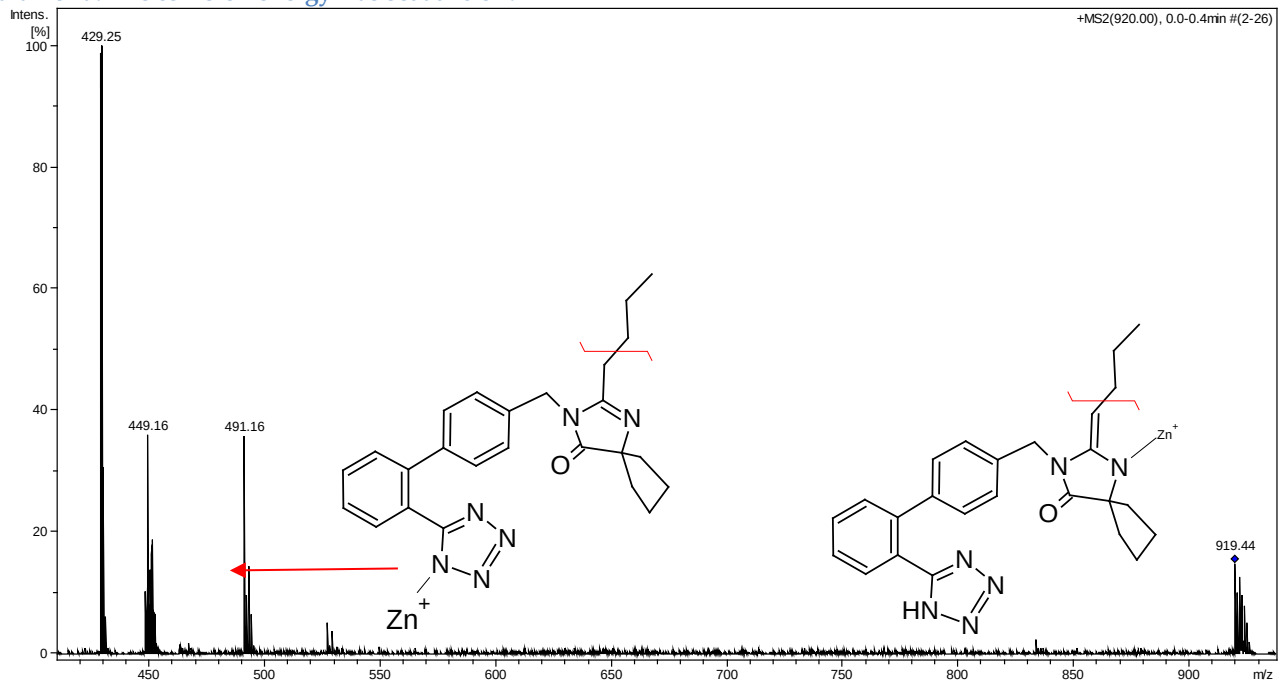

A) Experimental data for peak m/z = 449.16 are shown at the top of the panel and compared with the data calculated for the ($C_{22}H_{20}N_6OZn$) fragment (lower panel).

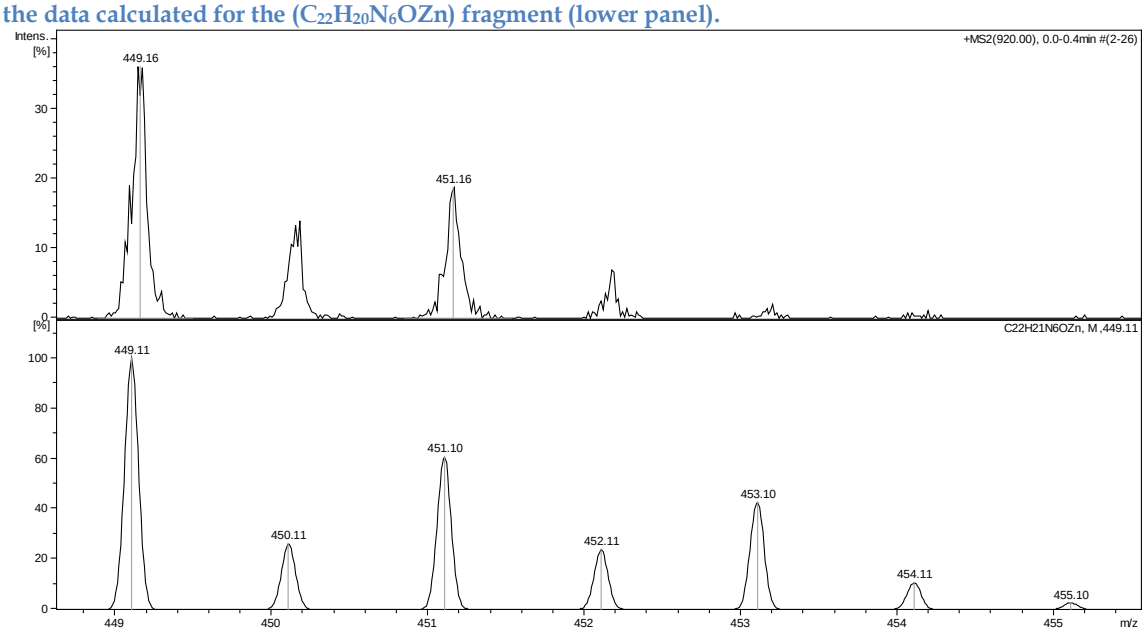

Figure A42. ESI-MS spectrum of losartan with copper solution in 1:1 molar ratio; 480-1040 m/z range.

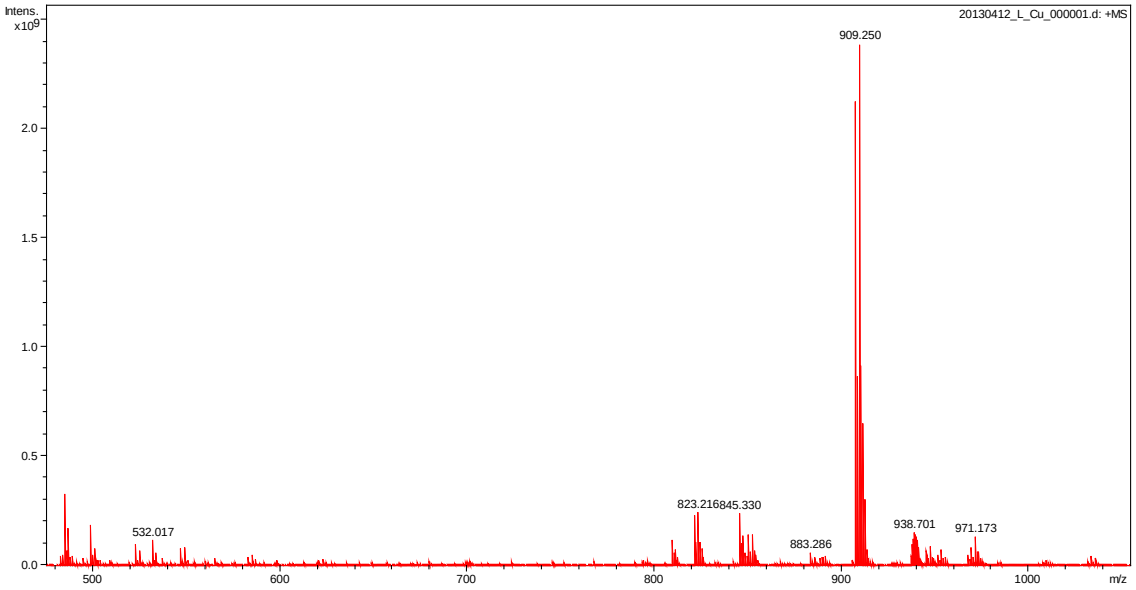

A) **Experimental data for peak m/z = 485.092 are shown at the top of the panel and compared with the data calculated for $[CuL+H]^+$ ($C_{22}H_{23}ClN_6OCu$) (lower panel).**

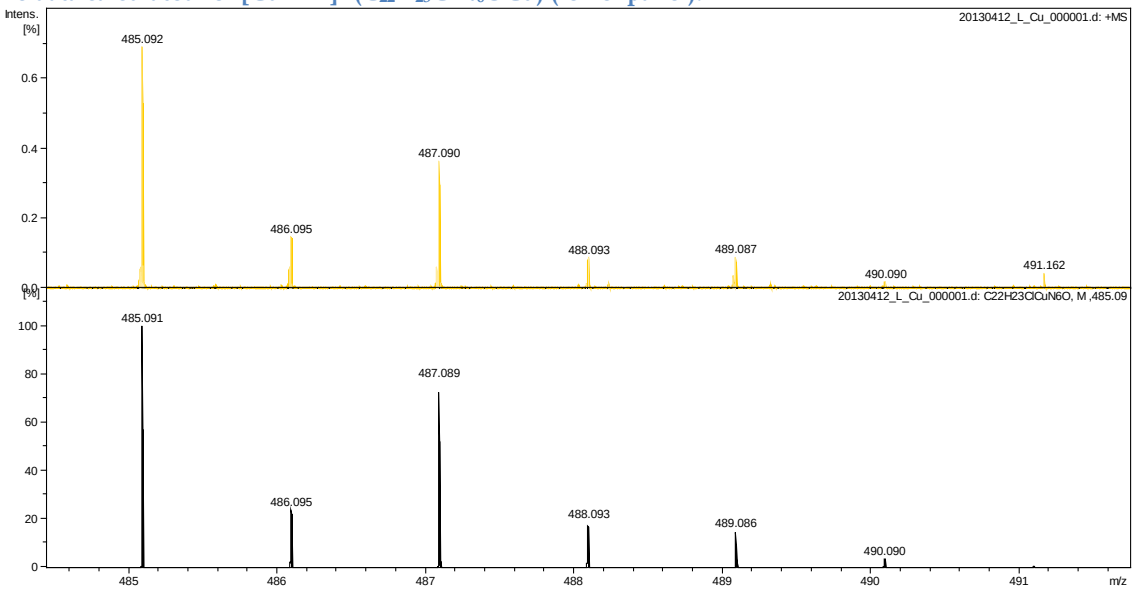

B) Experimental data for peak m/z = 499.081 are shown at the top of the panel and compared with the data calculated for $[L+2K]^+$ ($C_{22}H_{22}ClK_2N_6O$) (lower panel).

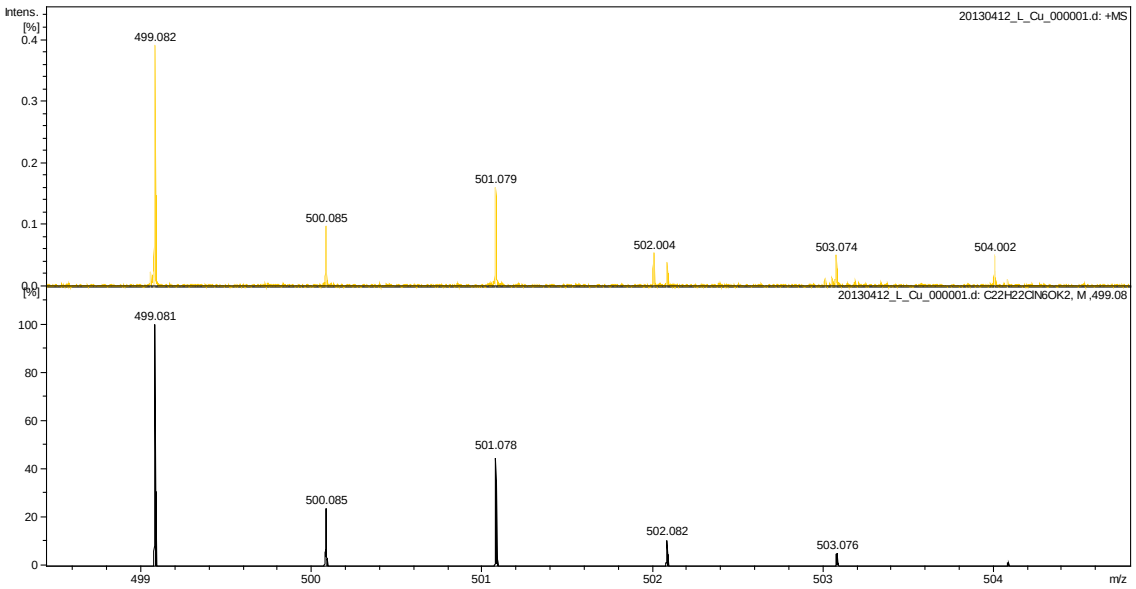

C) Experimental data for peak m/z = 907.252 are shown at the top of the panel and compared with the data calculated for $[CuL_2+2H]^+$ ($C_{44}H_{46}Cl_2N_{12}O_2Cu$) (lower panel).

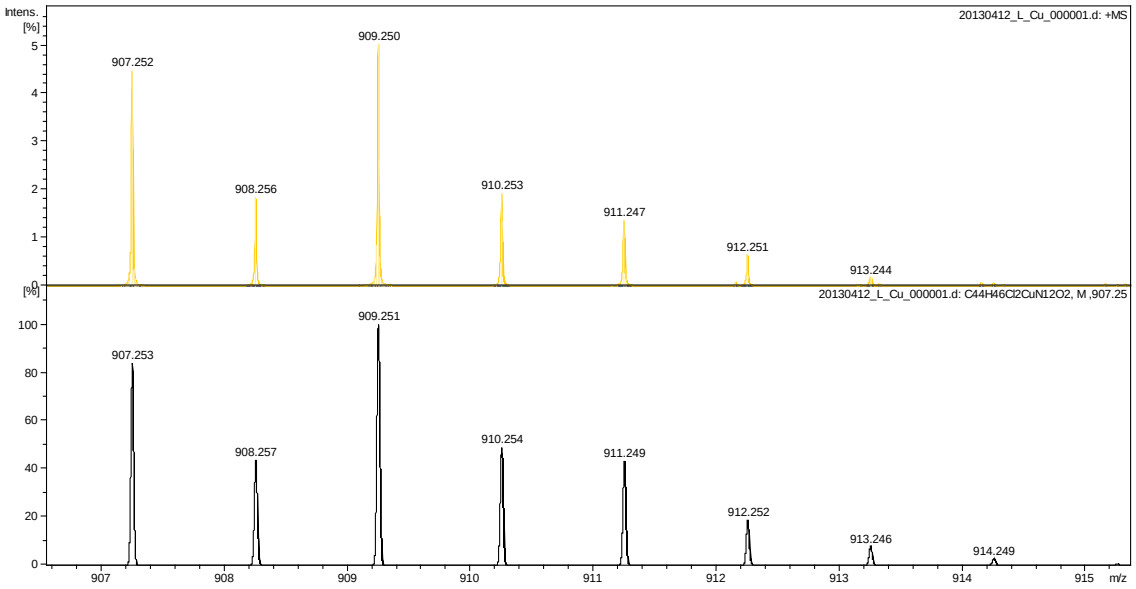

D) Experimental data for peak m/z = 936.701 are shown at the top of the panel and compared with the data calculated for $[Cu_3L_4]^{2+}$ ($C_{88}H_{88}Cl_4N_{24}O_4Cu_3$) (lower panel).

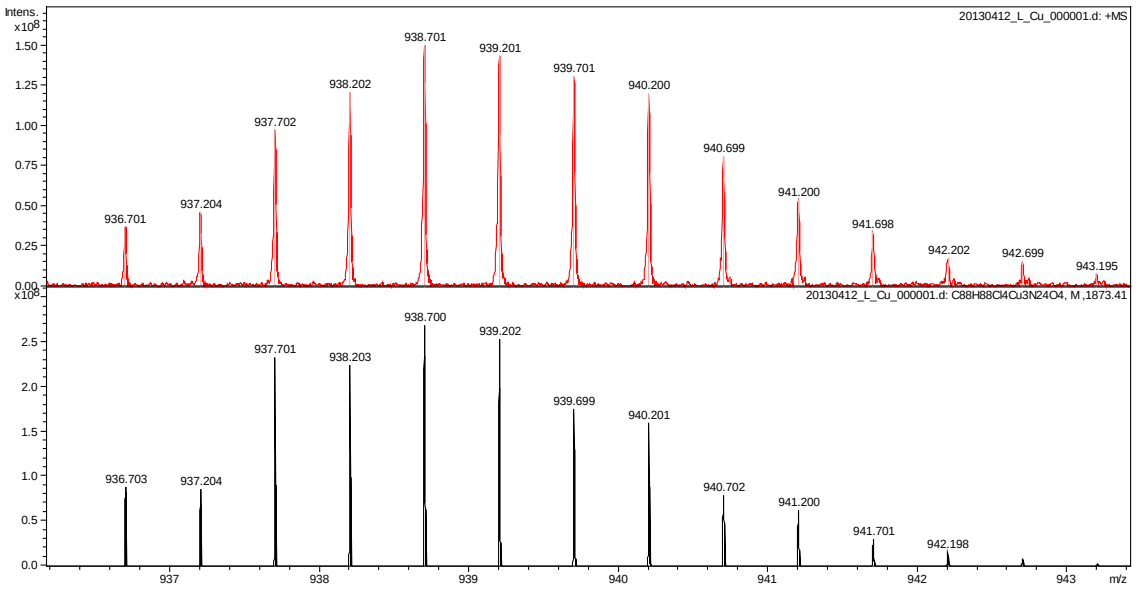

E) Experimental data for peak m/z = 945.209 are shown at the top of the panel and compared with the data calculated for $[CuL_2+K+H]^+$ ($C_{44}H_{45}Cl_2N_{12}O_2CuK$) (lower panel).

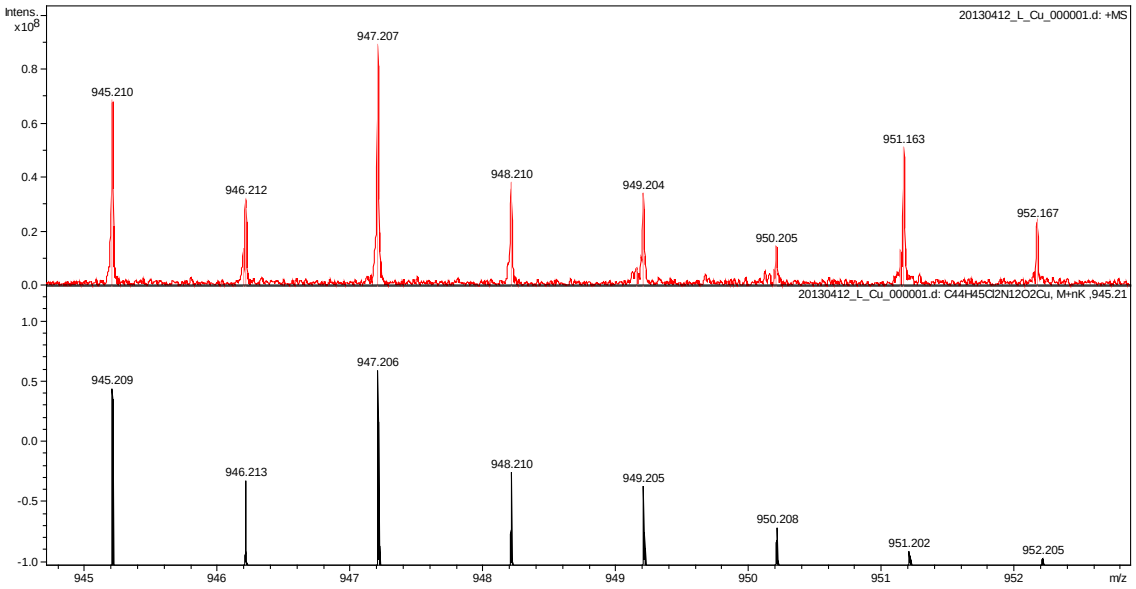

F) Experimental data for peak m/z = 1031.098 are shown at the top of the panel and compared with the data calculated for $[Cu_3L_2]^+$ ($C_{44}H_{44}Cl_2N_{12}O_2Cu_3$) (lower panel).

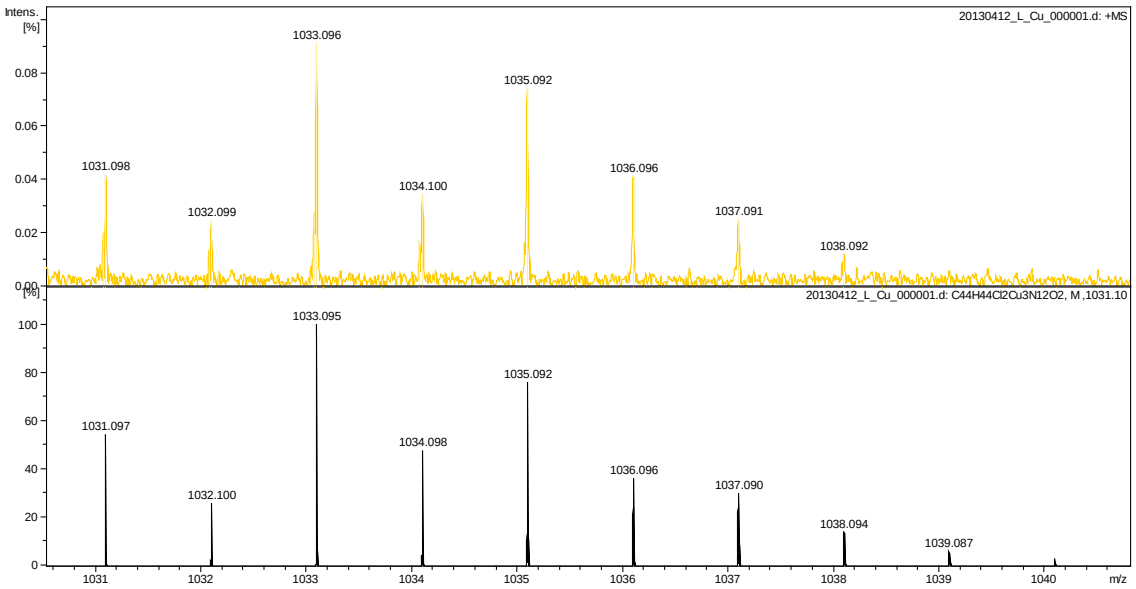

Figure A43. ^{1}H 1D NMR spectra of free Losartan in D_2O at pH 7.0, MeOD-d4 and DMSO-d6 at T = 298.

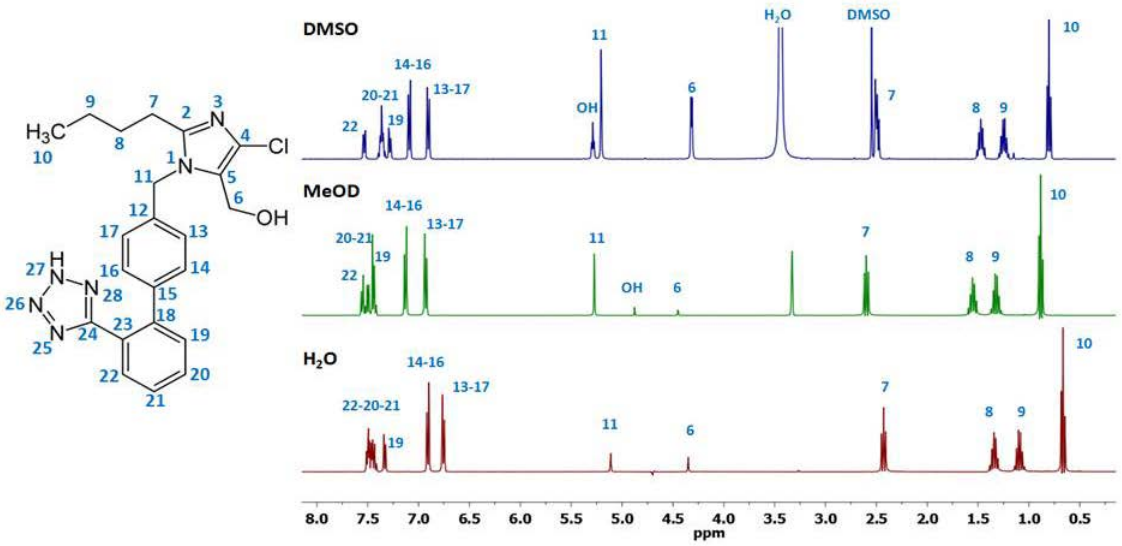

TableA14. ^{1}H and ^{13}C chemical shift assignment of free Losartan in D_2O at pH 7.0, MeOD-d4 and DMSO-d6 at T = 298.

proton	H_2O	DMSO-d6	MeOd-d4	shape	Coupling Constant	integration	carbon	H_2O	DMSO-d6	MeOd-d4
n°	δ ppm	δ ppm	δ ppm	multiplicity	J Hz	intensity	n°	δ ppm	δ ppm	δ ppm
6	4,349	4,317*	4,449	singlet	*doublet J=4,85 Hz (DMSO-d6)	2H	**6**	51,244	51,656	51,691
7	2,429	2,492	2,599	triplet	J = 7,9 Hz; 7,6 Hz; 7,9 Hz	2H	**7**	25,591	26,109	25,868
8	1,345	1,474	1,556	quintuplet		2H	**8**	28,656	29,397	29,438
9	1,093	1,247	1,322	sextet		2H	**9**	21,331	21,892	21,696
10	0,665	0,803	0,884	triplet	J=7.6 Hz; 7.32 Hz; 7.6 Hz	3H	**10**	12,706	13,714	12,456
11	5,112	5,205	5,273	singlet		2H	**11**	46,737	46,787	44,731
13	6,756	6,904	6,930	doublet	J = 8.1 Hz, 8.0 Hz; 8,1 Hz	1H	**13**	125,56	125,725	125,268
14	6,908	7,091	7,129	doublet	J = 8.1 Hz, 8.0 Hz; 8,1 Hz	1H	**14**	129,275	129,792	129,788
16	6,908	7,091	7,129	doublet	J = 8.1 Hz, 8.0 Hz; 8,1 Hz	1H	**16**	129,275	129,792	129,788
17	6,756	6,904	6,930	doublet	J = 8.1 Hz, 8.0 Hz; 8,1 Hz	1H	**17**	125,56	125,725	125,268
19	7,332	7,283	7,435	multiplet		1H	**19**	130,048	130,373	128,657
20	7,440	7,363	7,458	multiplet		1H	**20**	130,07	127,463	129,788
21	7,440	7,363	7,458	multiplet		1H	**21**	130,07	127,463	129,788
22	7,494	7,533	7,546	multiplet		1H	**22**	127,683	131,016	130,397
OH	NA	5,287§	4,877	singlet	§ triplet J = 5 Hz (DMSO-d6)	1H				

Figure A44. ^{1}H 1D NMR spectra of free Irbesartan in MeOD-d4 at T = 298.

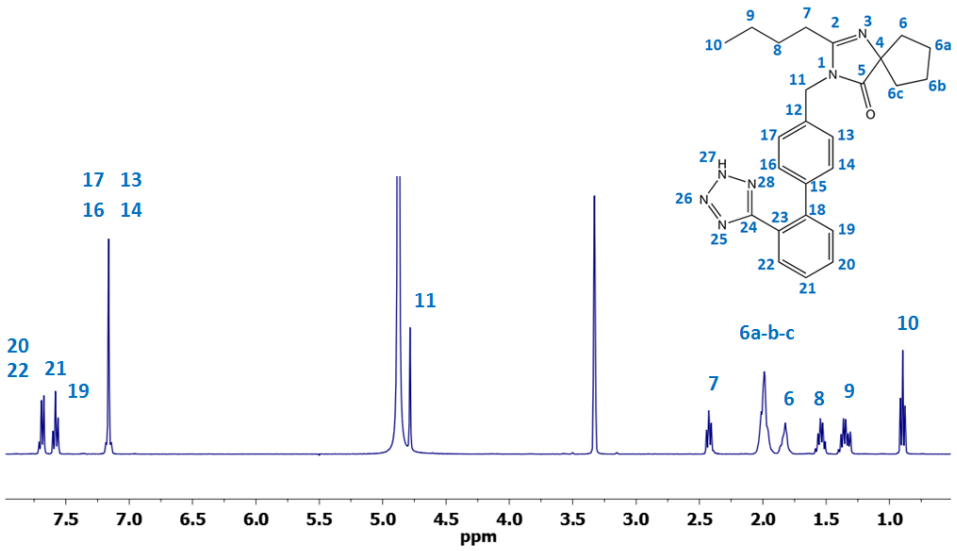

Figure A45. Aliphatic region of ^{1}H 2D COSY NMR spectra of free Irbesartan in MeOD-d4 at T = 298.

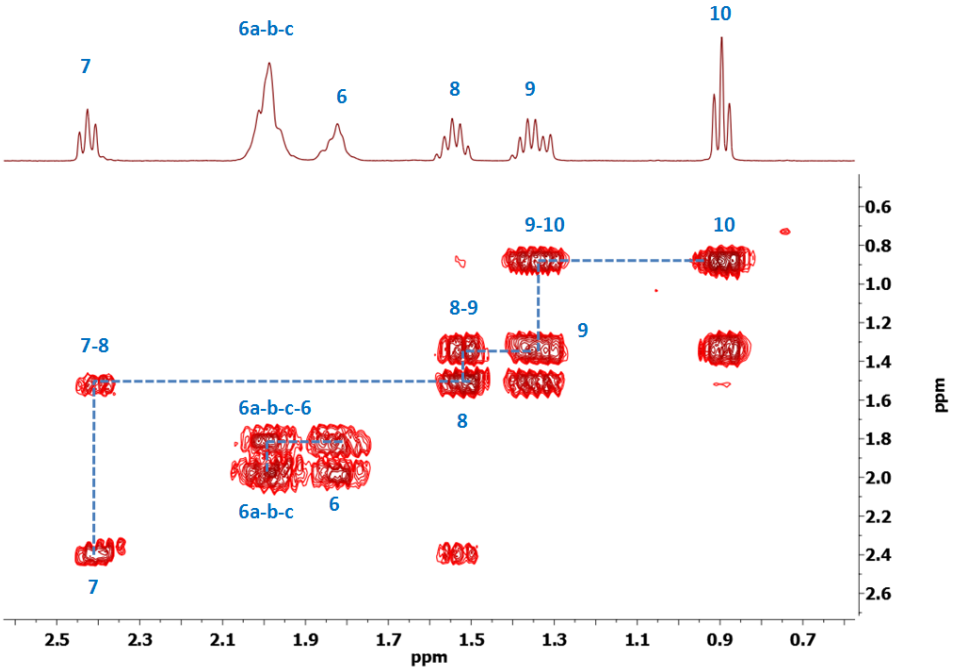

Figure A46. The full spectrum of L12 with Fe^{3+} solution in the molar ratio 1:1 in positive mode.

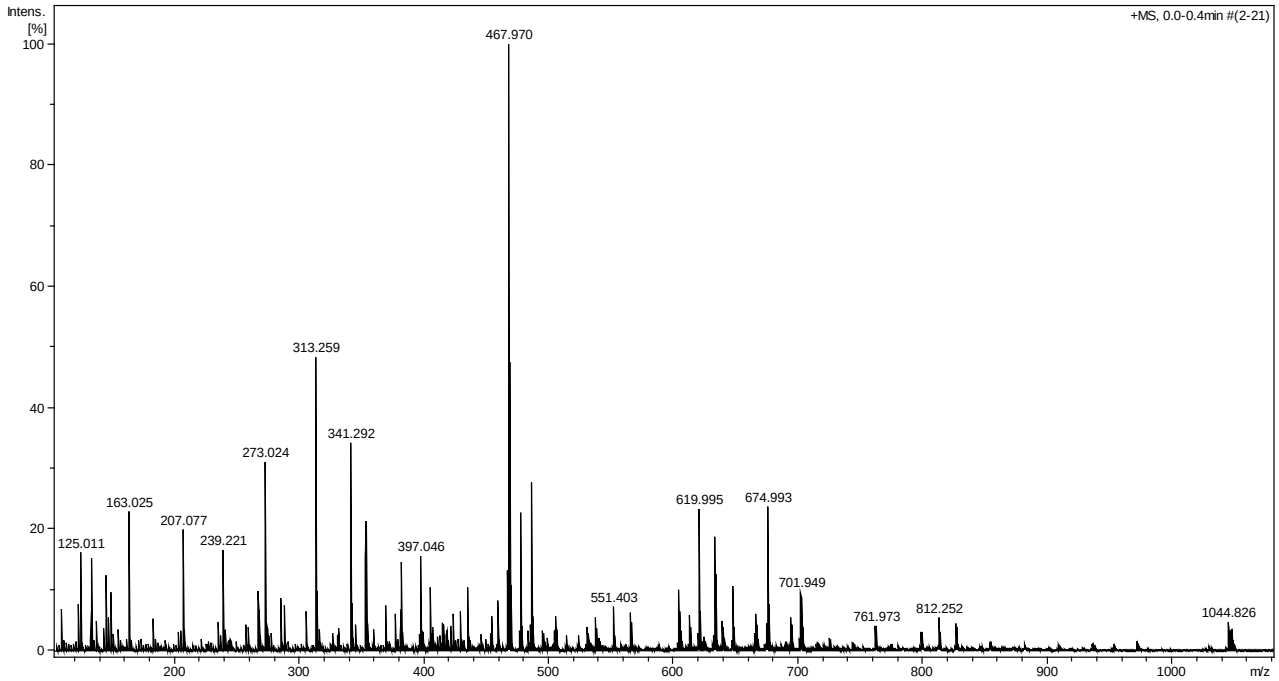

A) Experimental data for peak m/z = 466.973, 475.976, 484.991 and 493.980 are shown at the top of the panel and compared with the data calculated for the $[Fe_2(L12_{ox})H_2]^{2+}$ ($C_{40}H_{24}Fe_2O_{20}$), $[Fe_2(L12_{ox})H_2+H_2O]^{2+}$ ($C_{40}H_{26}Fe_2O_{21}$), $[Fe_2(L12_{ox})H_2+2H_2O]^{2+}$ ($C_{40}H_{28}Fe_2O_{22}$) and $[Fe_2(L12_{ox})H_2+3H_2O]^{2+}$ ($C_{40}H_{30}Fe_2O_{23}$) complexes (lower panels).

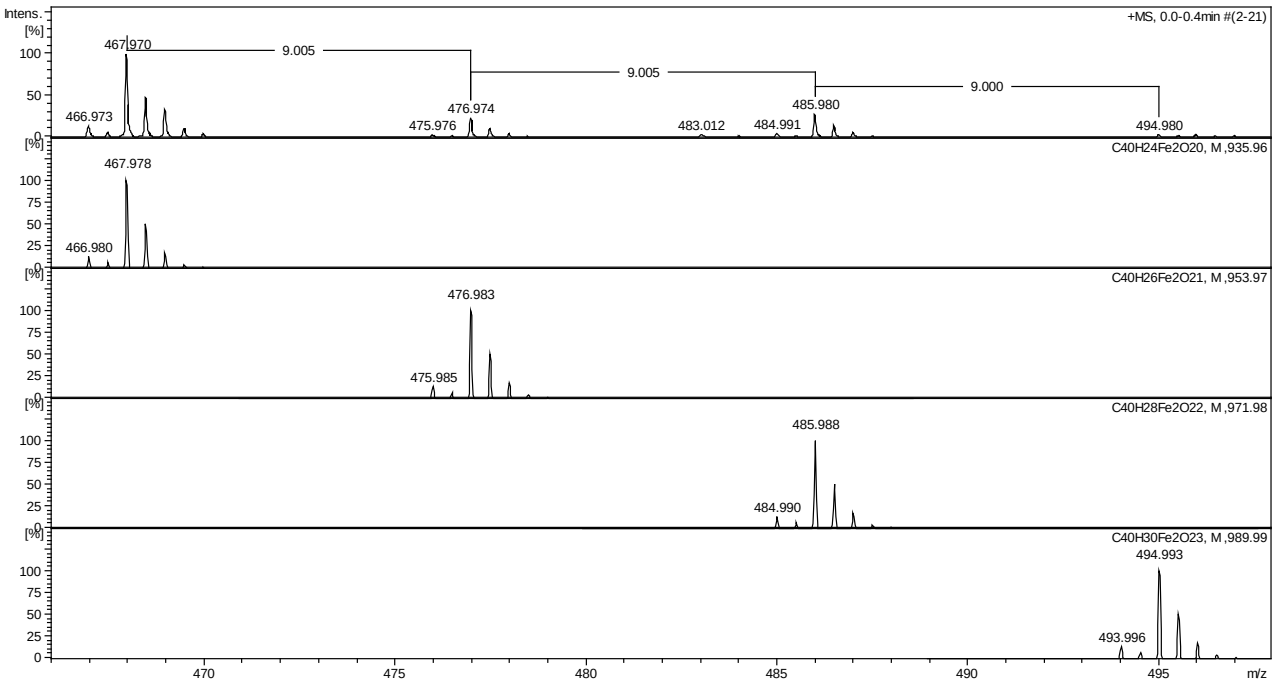

FigureS 47. The full spectrum of L12 with Fe^{3+} solution in the molar ratio 1:1 in negative mode.

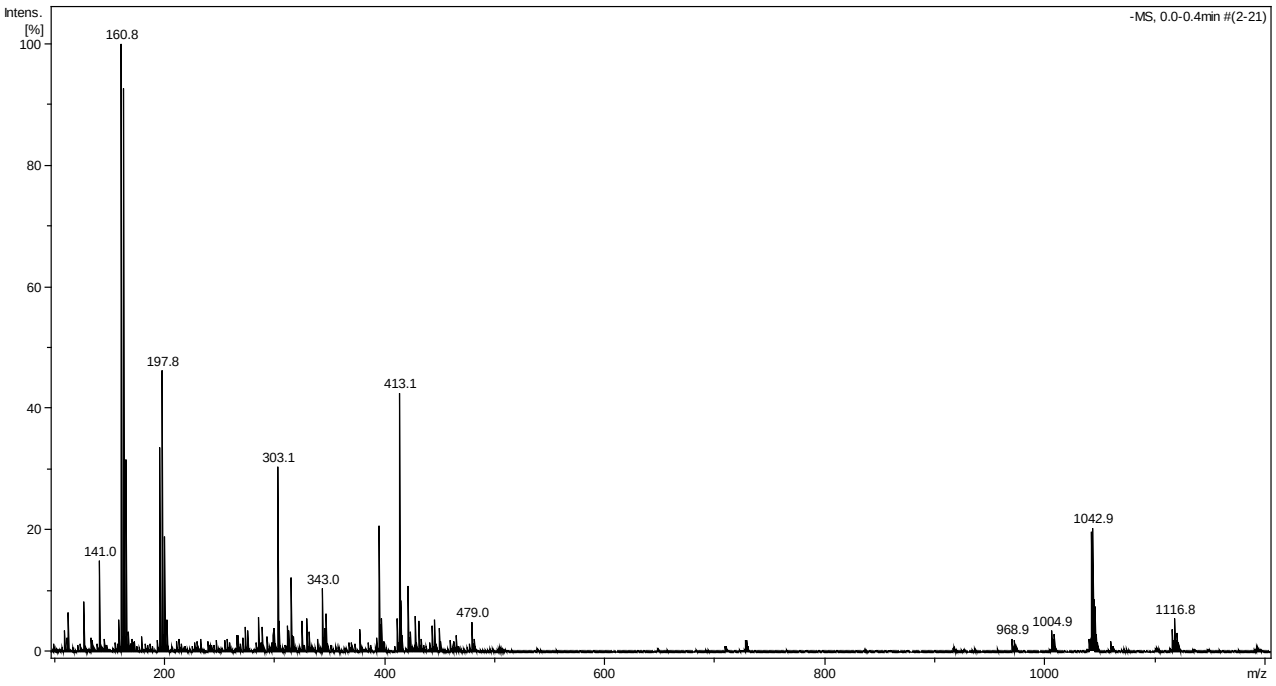

A) Experimental data for peak m/z = 1040.870 are shown at the top of the panel and compared with the data calculated for the $[Fe_2(L12_{ox})_2H_2+3Cl]^-$ ($C_{40}H_{24}Cl_3Fe_2O_{20}$) complex (lower panel).

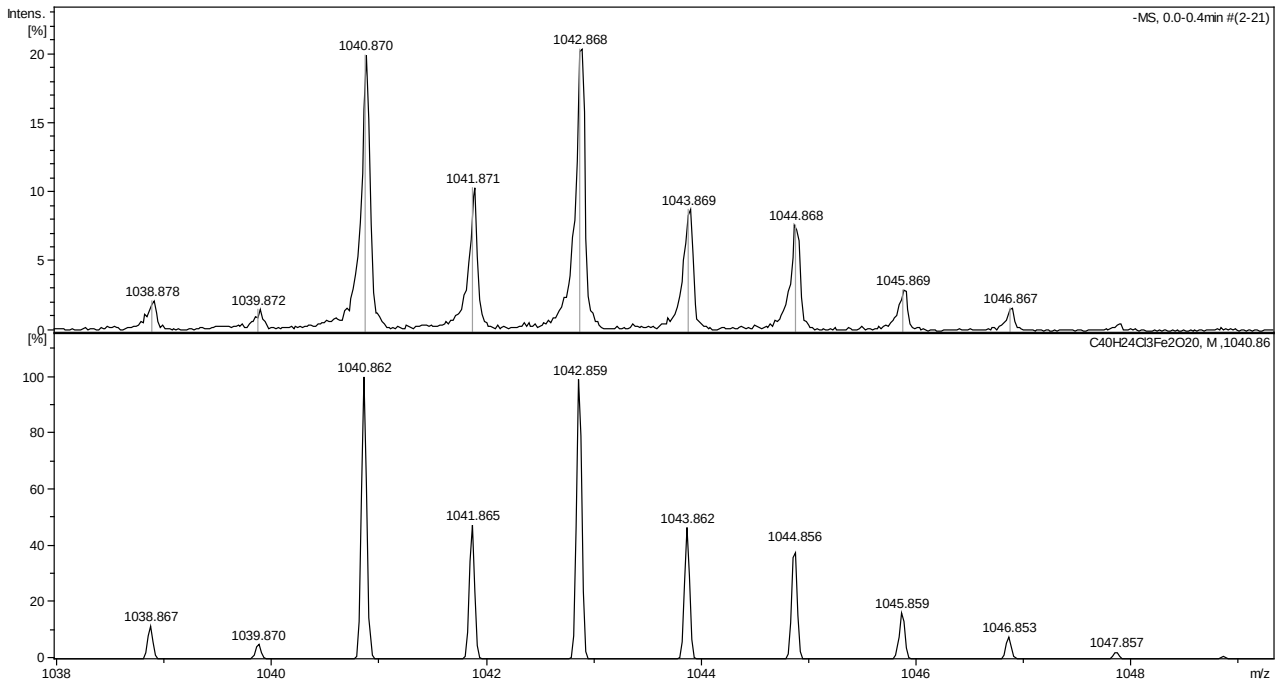

Figure A48. The full spectrum of L13 with Fe^{3+} solution in the molar ratio 1:1 in positive mode.

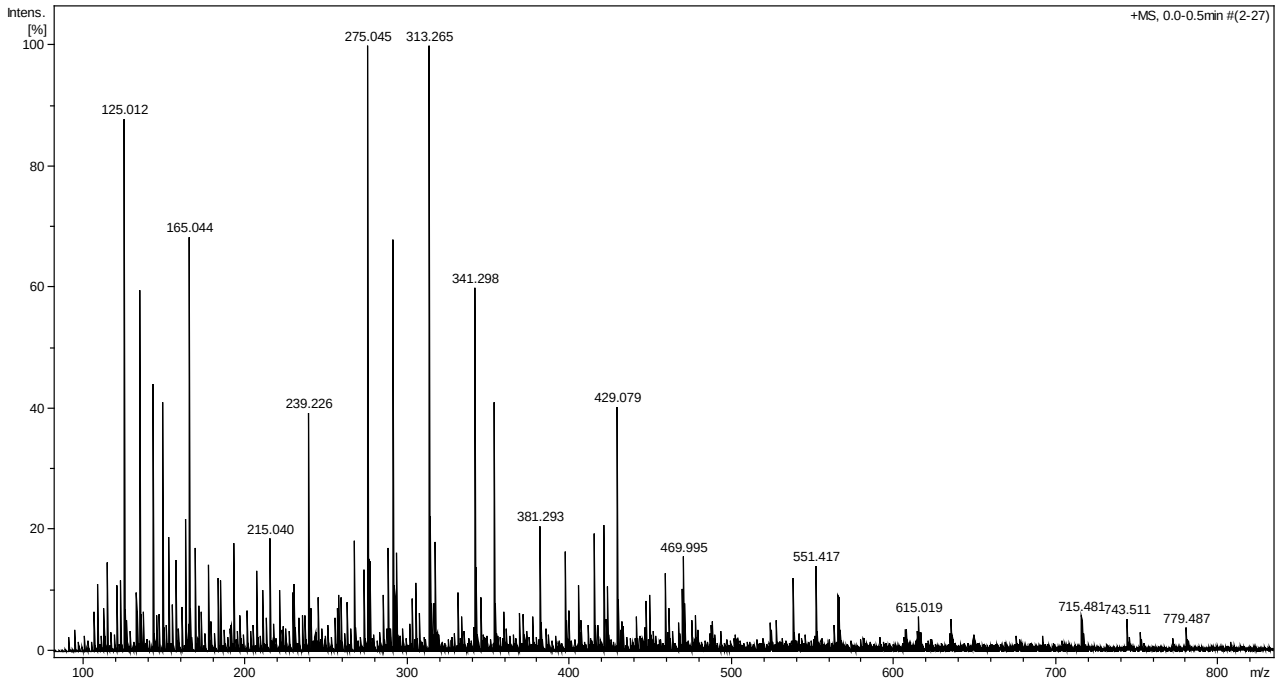

A) Experimental data for peak m/z = 469.995, 478.998 and 488.004 are shown at the top of the panel and compared with the data calculated for the $[Fe_2(L13)_2H_2]^{2+}$ ($C_{40}H_{28}Fe_2O_{20}$), $[Fe_2(L13)_2H_2+H_2O]^{2+}$ ($C_{40}H_{30}Fe_2O_{21}$) and $[Fe_2(L13)_2H_2+2H_2O]^{2+}$ ($C_{40}H_{32}Fe_2O_{22}$) complexes (lower panels).

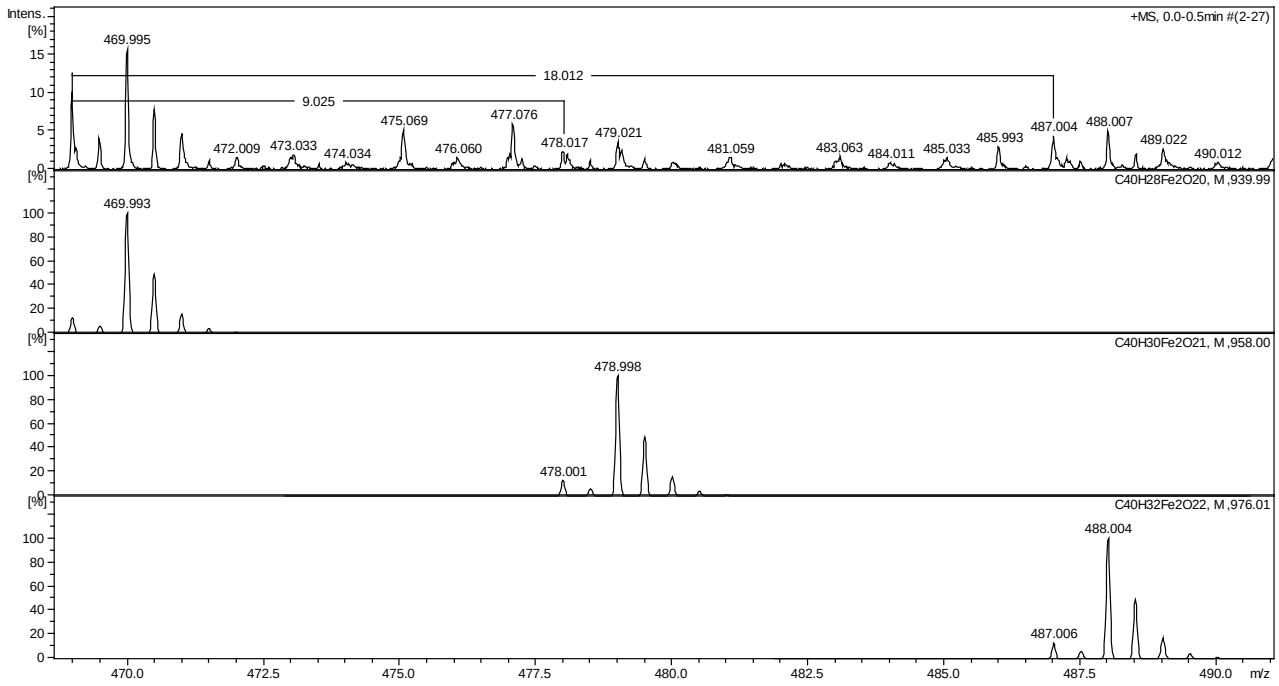

Figure A49. The full spectrum of L15 with Fe^{3+} solution in the molar ratio 1:1 in positive mode.

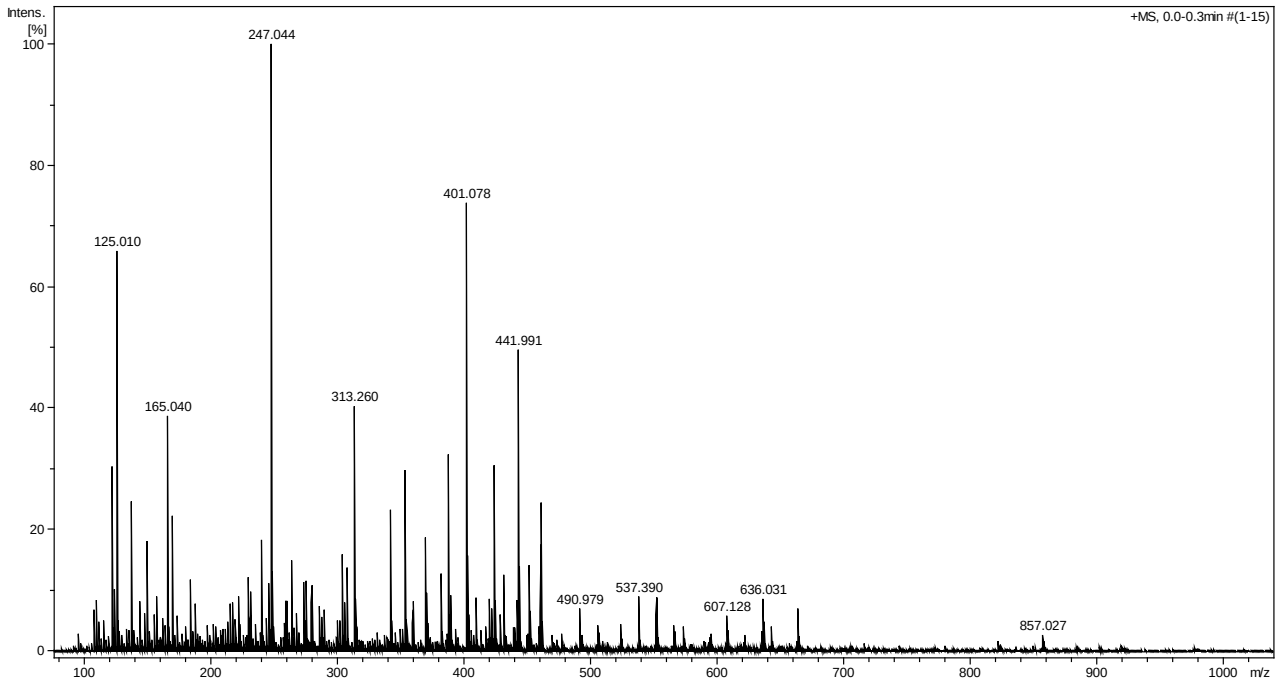

A) Experimental data for peak m/z = 441.991, 450.998 and 460.004 are shown at the top of the panel and compared with the data calculated for the $[Fe_2(L15)_2H_2]^{2+}$ ($C_{38}H_{28}Fe_2O_{18}$), $[Fe_2(L15)_2H_2+H_2O]^{2+}$ ($C_{38}H_{30}Fe_2O_{19}$) and $[Fe_2(L15)_2H_2+2H_2O]^{2+}$ ($C_{38}H_{32}Fe_2O_{20}$) (lower panels).

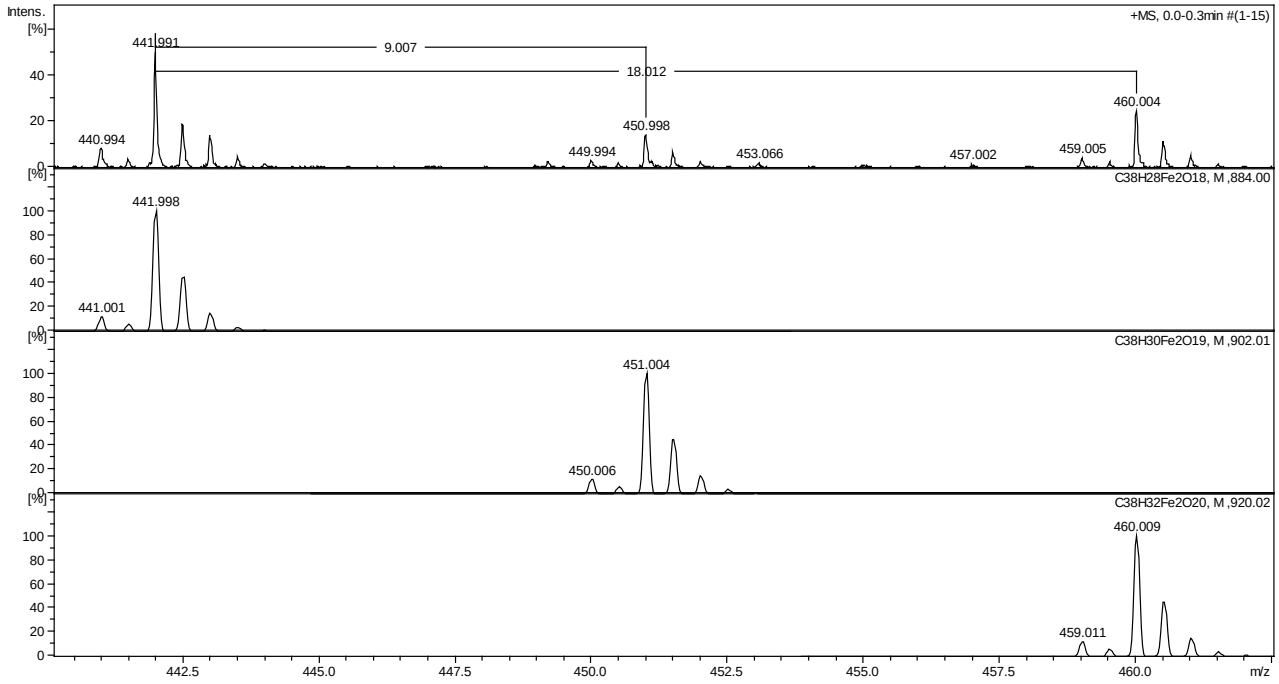

Figure A50. The full spectrum of L12 with Al^{3+} solution in the molar ratio 1:1 in positive mode.

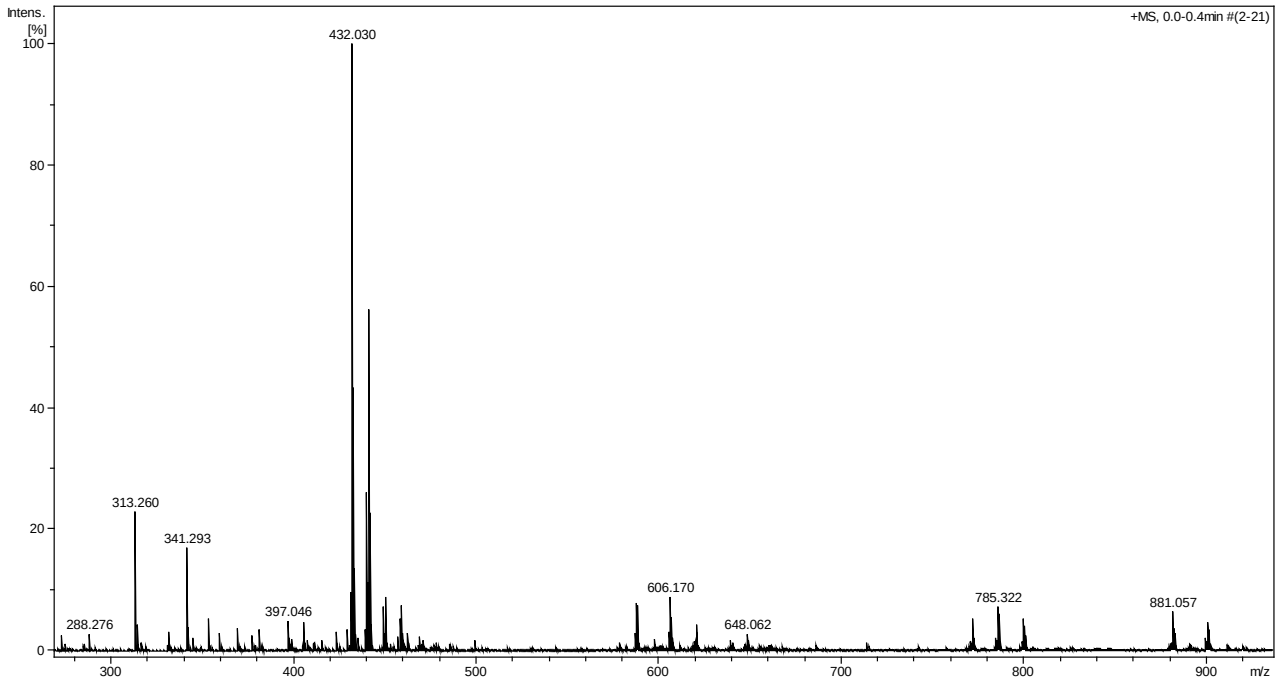

A) Experimental data for peak m/z = 441.035, 450.041 and 459.045 are shown at the top of the panel and compared with the data calculated for the $[Al_2(L12)_2H_2]^{2+}$ ($C_{40}H_{28}Al_2O_{20}$), $[Al_2(L12)_2H_2+H_2O]^{2+}$ ($C_{40}H_{30}Al_2O_{21}$) and $[Al_2(L12)_2H_2+2H_2O]^{2+}$ ($C_{40}H_{32}Al_2O_{22}$) complexes (lower panels).

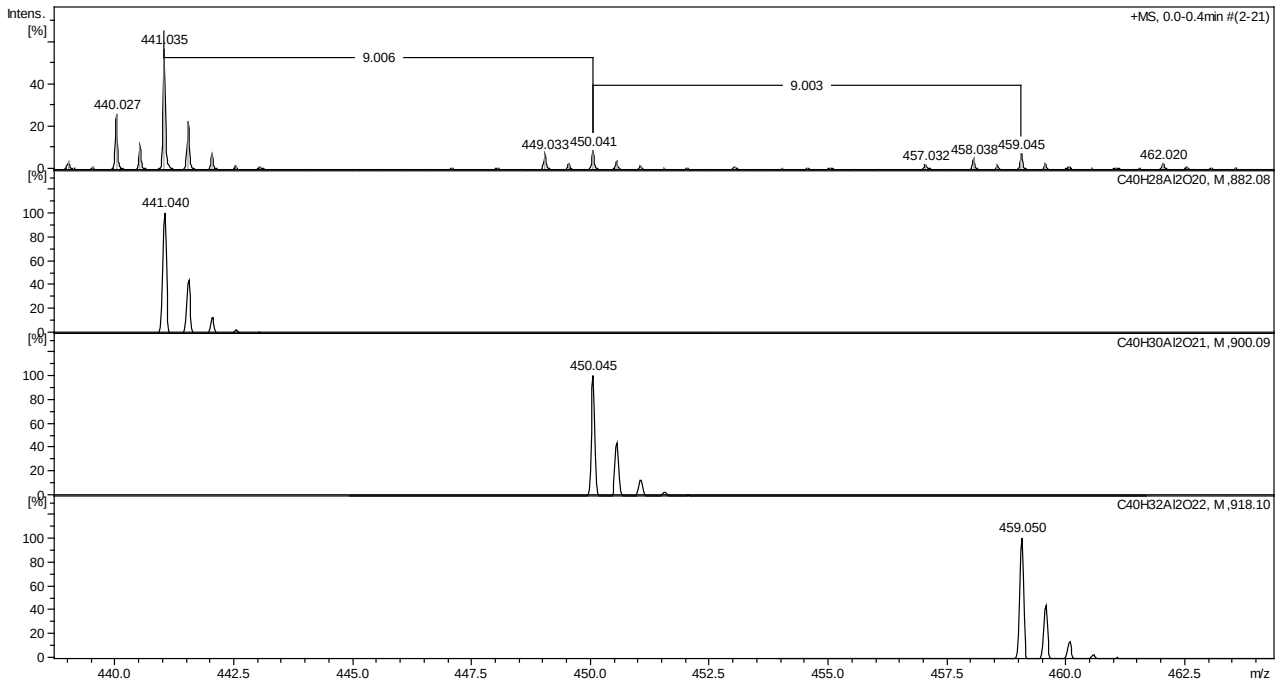

B) Experimental data for peak m/z = 440.027, 449.033 and 458.038 are shown at the top of the panel and compared with the data calculated for the $[Al_2(L12_{ox})_2H_2]^{2+}$ ($C_{40}H_{26}Al_2O_{20}$), $[Al_2(L12_{ox})_2H_2+H_2O]^{2+}$ ($C_{40}H_{28}Al_2O_{21}$) and $[Al_2(L12_{ox})_2H_2+2H_2O]^{2+}$ ($C_{40}H_{30}Al_2O_{22}$) complexes (lower panels).

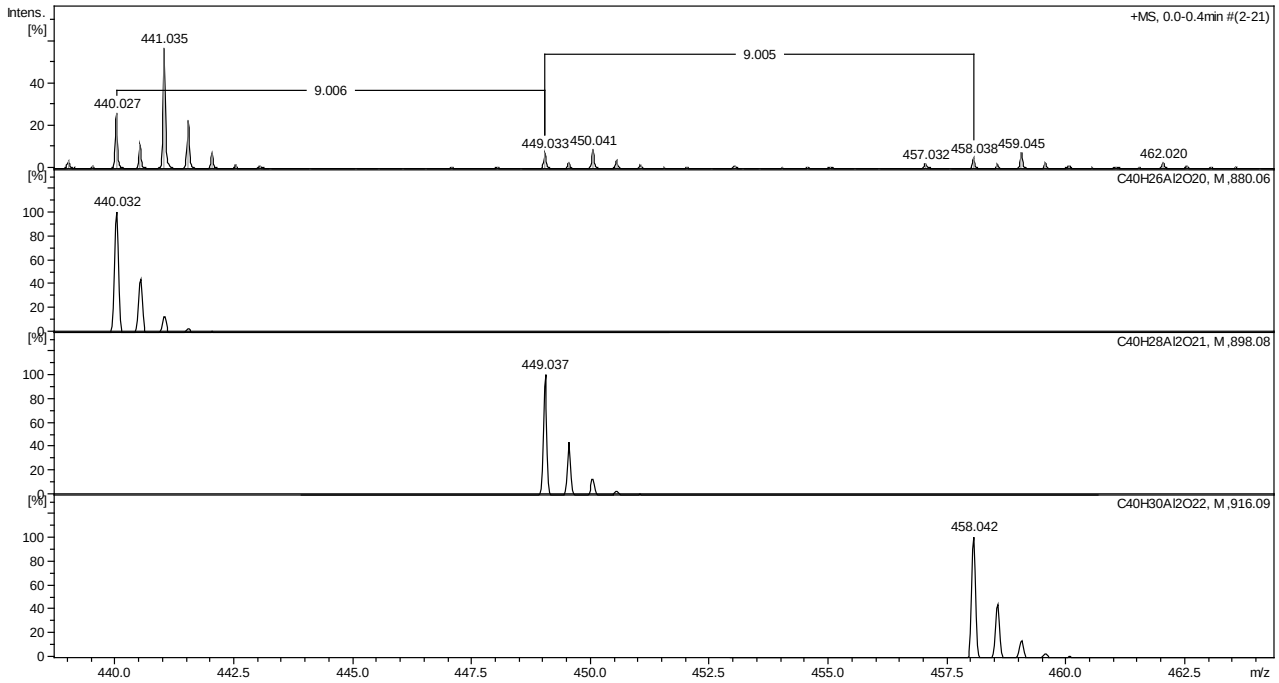

Figure A51. The full spectrum of L12 with Al^{3+} solution in the molar ratio 1:1 in negative mode.

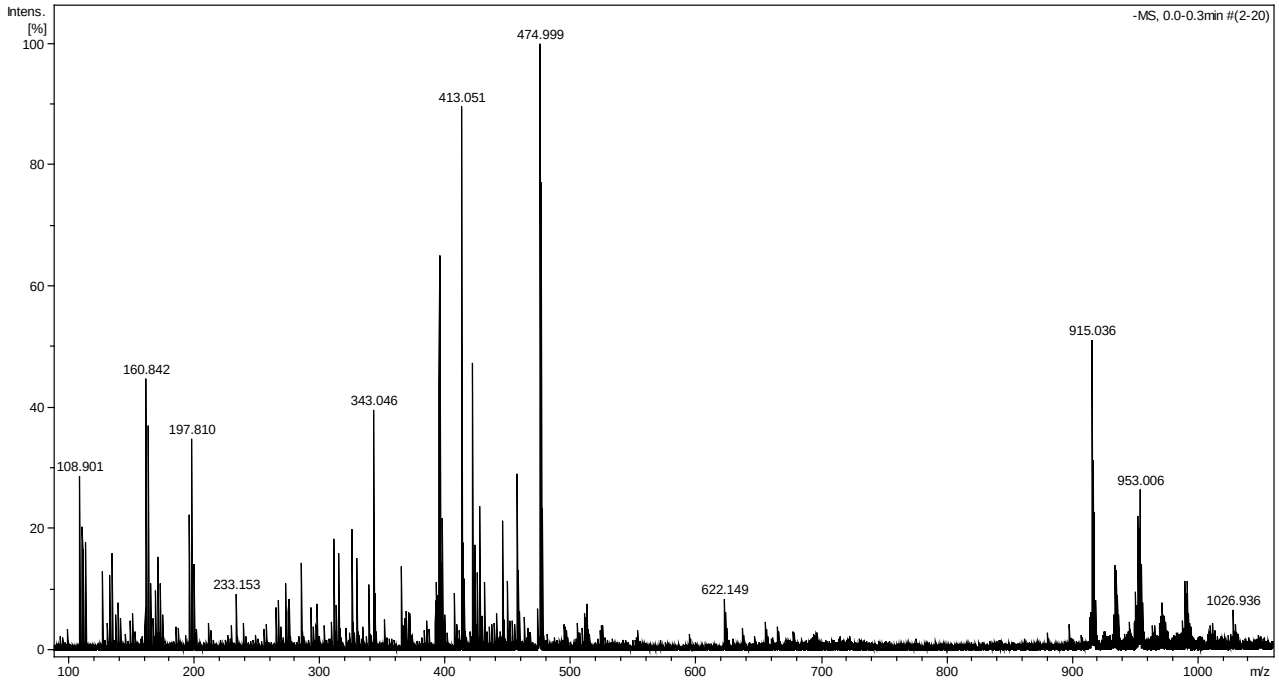

A) **Experimental data for peak m/z = 474.999 are shown at the top of the panel and compared with the data calculated for the $[Al_2(L12)_2+2Cl]^{2-}$ ($C_{40}H_{26}Al_2Cl_2O_{20}$) complex (lower panel).**

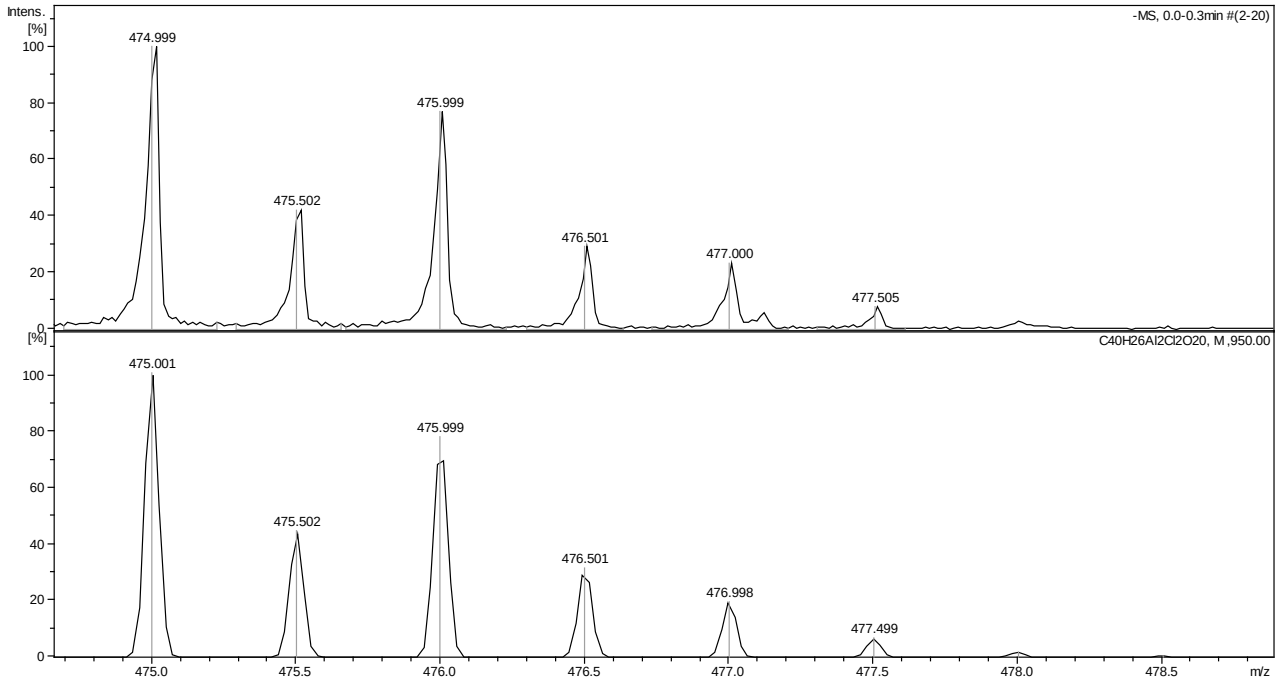

B) Experimental data for peak m/z = 915.036, 933.022 and 951.009 are shown at the top of the panel and compared with the data calculated for the $[Al_4(L12)_4+2Cl]^{2-}$($C_{80}H_{52}Al_4Cl_2O_{40}$), $[Al_4(L12)_4+2Cl+2H_2O]^{2-}$ ($C_{80}H_{56}Al_4Cl_2O_{42}$) and $[Al_4(L12)_4+2Cl+4H_2O]^{2-}$ ($C_{80}H_{60}Al_4Cl_2O_{44}$) complexes.

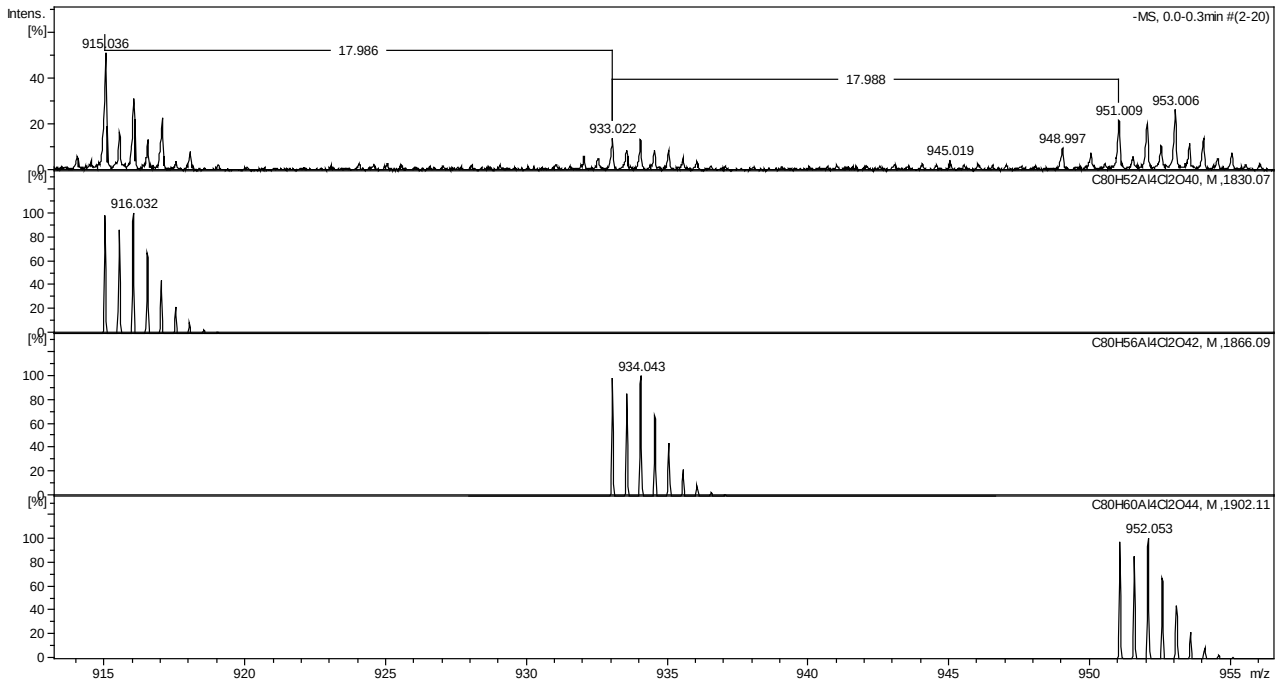

Figure A52. The full spectrum of L13 with Al^{3+} solution in the molar ratio 1:1 in positive mode.

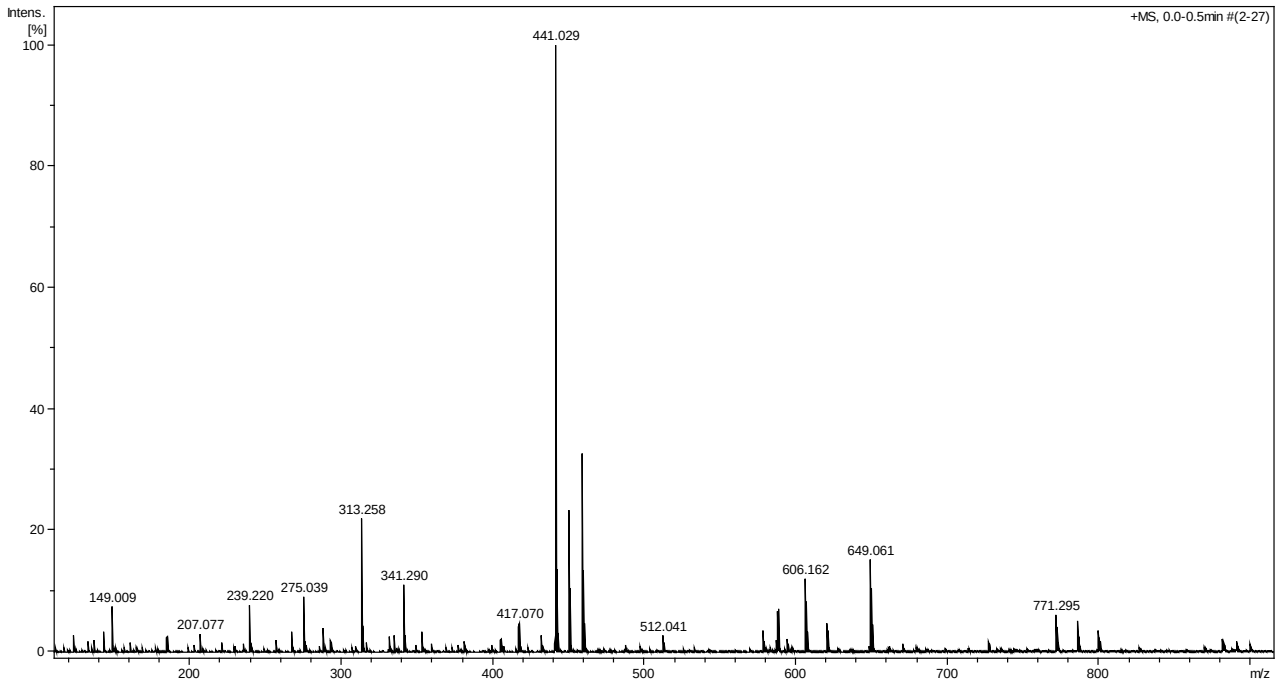

A) Experimental data for peak m/z = 441.029 and 459.040 are shown at the top of the panel and compared with the data calculated for the $[Al_2(L13)_2H_2]^{2+}$ ($C_{40}H_{28}Al_2O_{20}$) and $[Al_2(L13)_2H_2+2H_2O]^{2+}$ ($C_{40}H_{32}Al_2O_{22}$) complexes (lower panels).

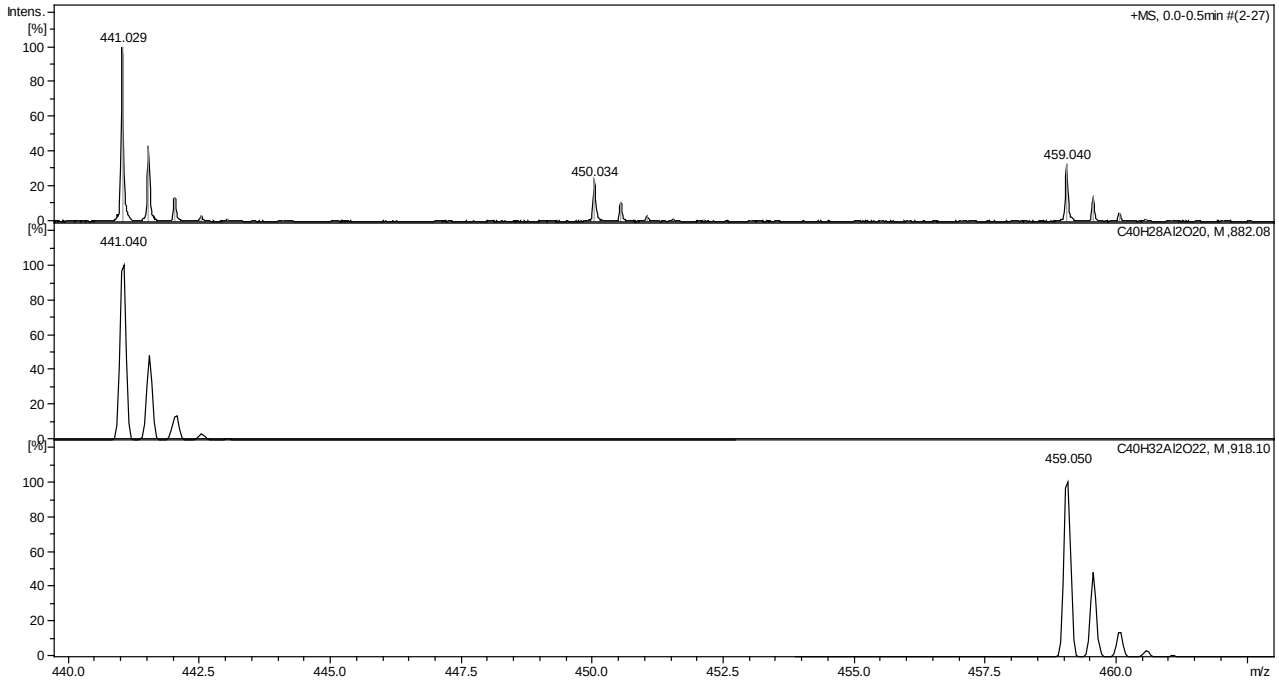

Figure A53. Electrospray ionization with tandem mass spectrometry (MS/MS) spectrum of the $[Al_2(L13)_2H_2]^{2+}$ complex. The peak selected for fragmentation in the MS/MS experiment is indicated by a diamond.

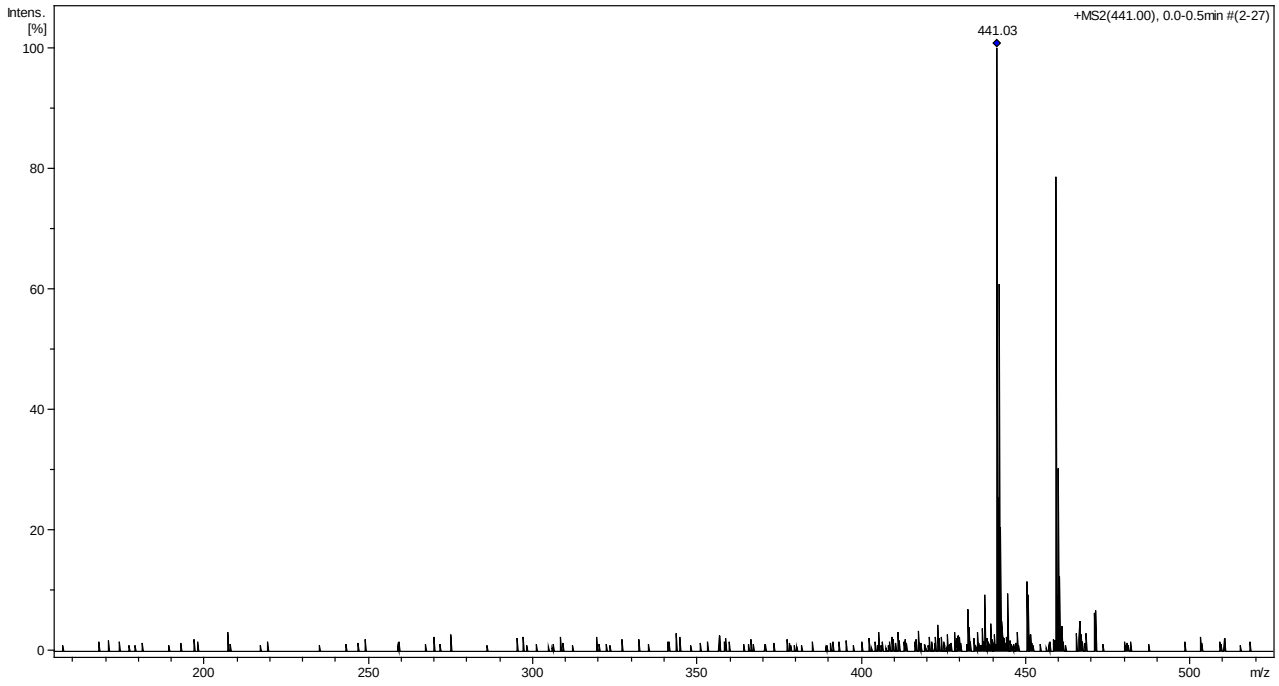

A) Experimental data for peak m/z = 459.040 are shown at the top of the panel and compared with the data calculated for the $[Al(L13)H]^+$ ($C_{40}H_{28}Al_2O_{20}$) complex (lower panel).

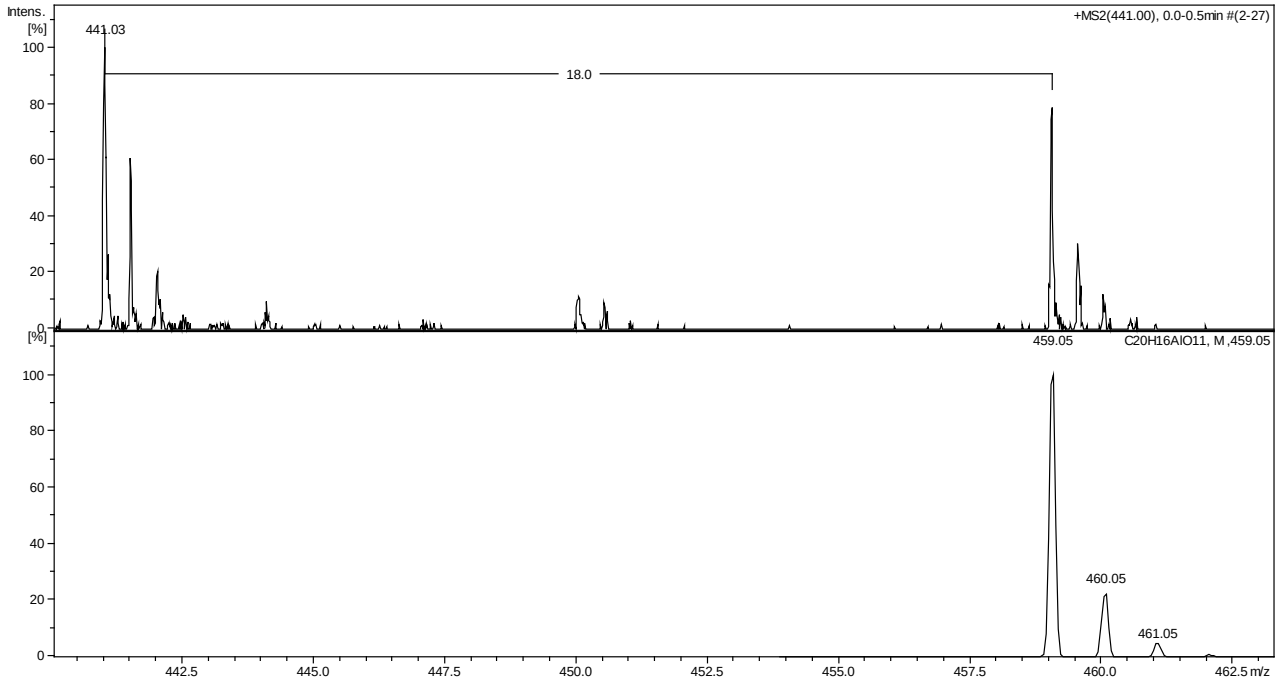

Figure A54. The full spectrum of L14 with Al^{3+} solution in the molar ratio 1:1 in positive mode.

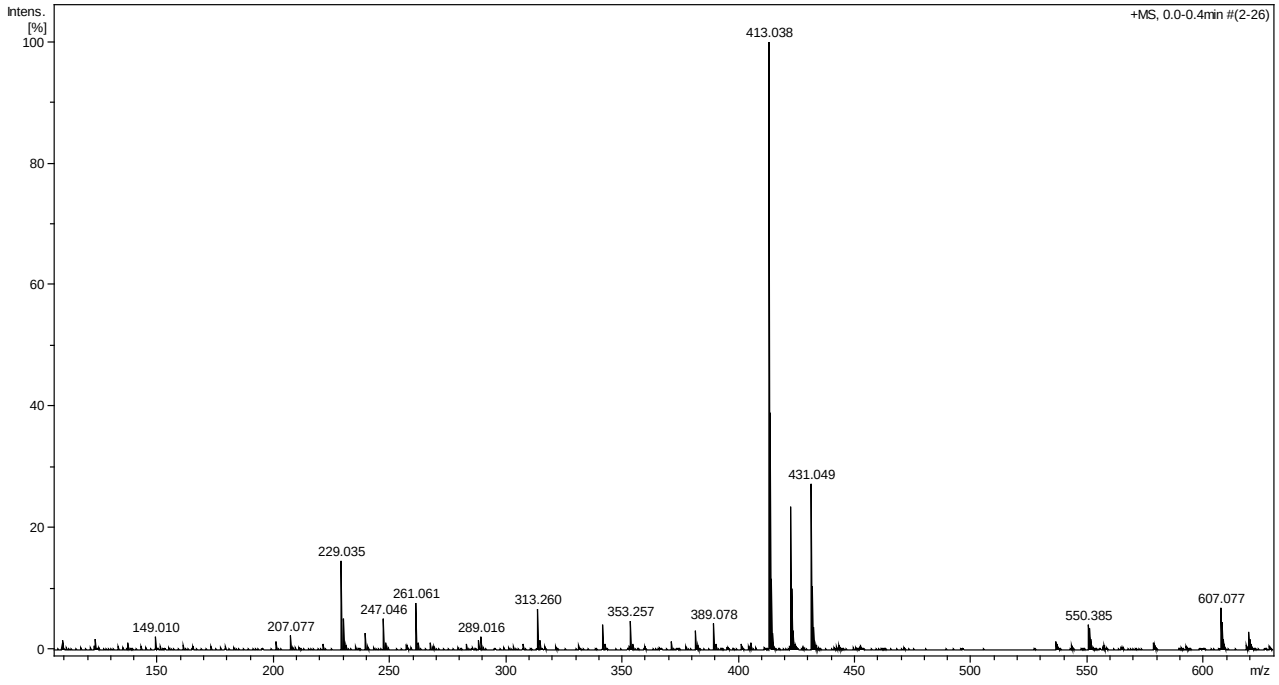

A) Experimental data for peak m/z = 413.038, 422.044 and 431.049 are shown at the top of the panel and compared with the data calculated for the $[Al_2(L14)_2H_2]^{2+}$ ($C_{38}H_{28}Al_2O_{18}$), $[Al_2(L14)_2H_2+H_2O]^{2+}$ ($C_{38}H_{30}Al_2O_{19}$) and $[Al_2(L14)_2H_2+2H_2O]^{2+}$ ($C_{38}H_{32}Al_2O_{20}$) complexes (lower panels).

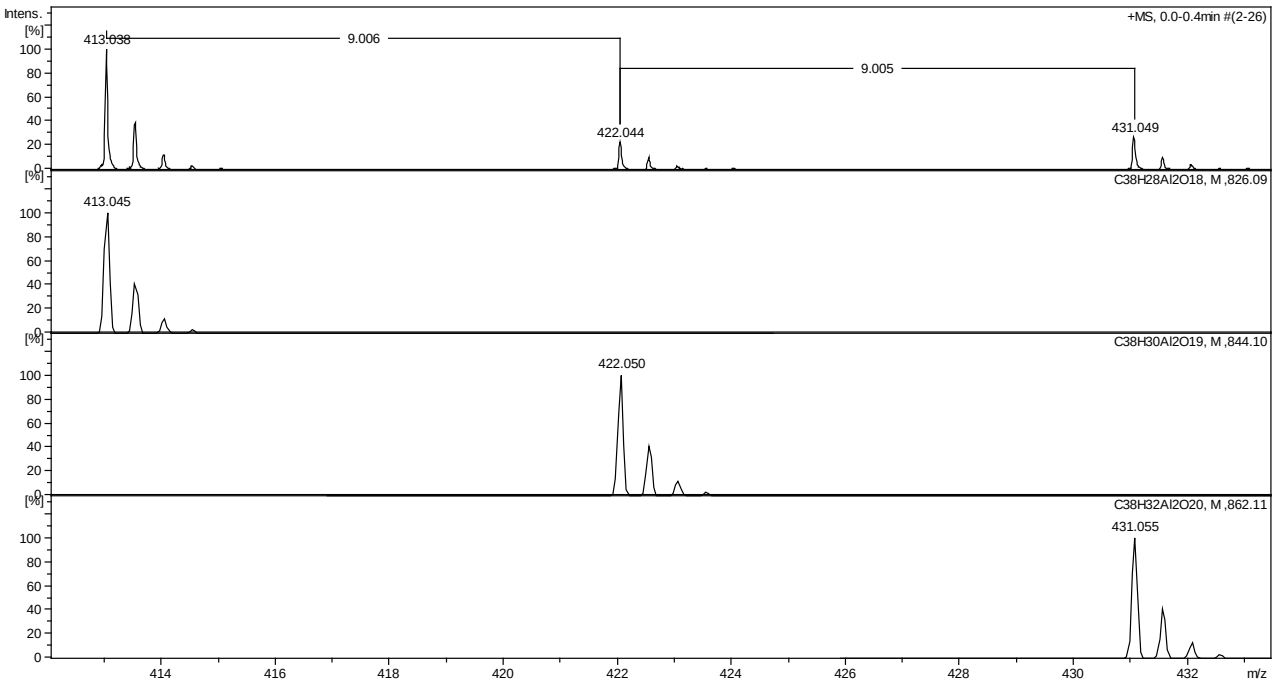

B) Experimental data for peak m/z = 607.077 are shown at the top of the panel and compared with the data calculated for the $[Al_2(L14)_3H_5]^{2+}$ ($C_{57}H_{44}Al_2O_7$) complex (lower panel).

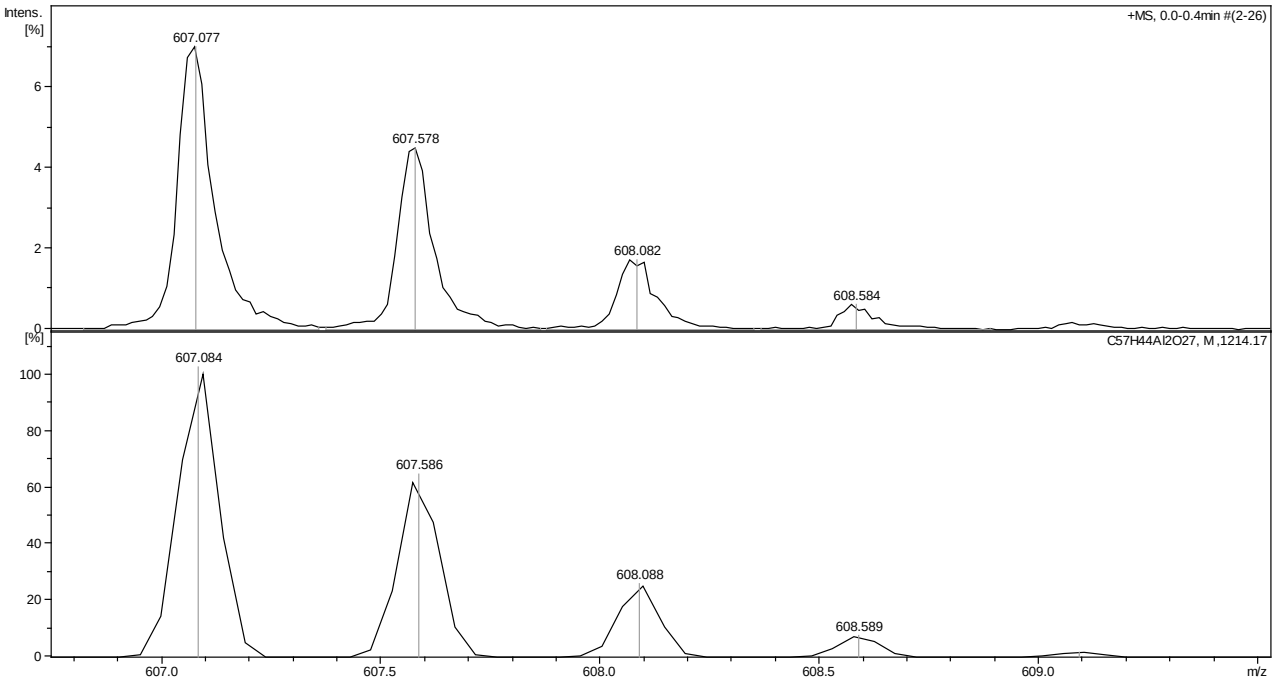

Figure A55. Electrospray ionization with tandem mass spectrometry (MS/MS) spectrum of the $[Al_2(L14)_2H_2]^{2+}$ complex. The peak selected for fragmentation in the MS/MS experiment is indicated by a diamond.

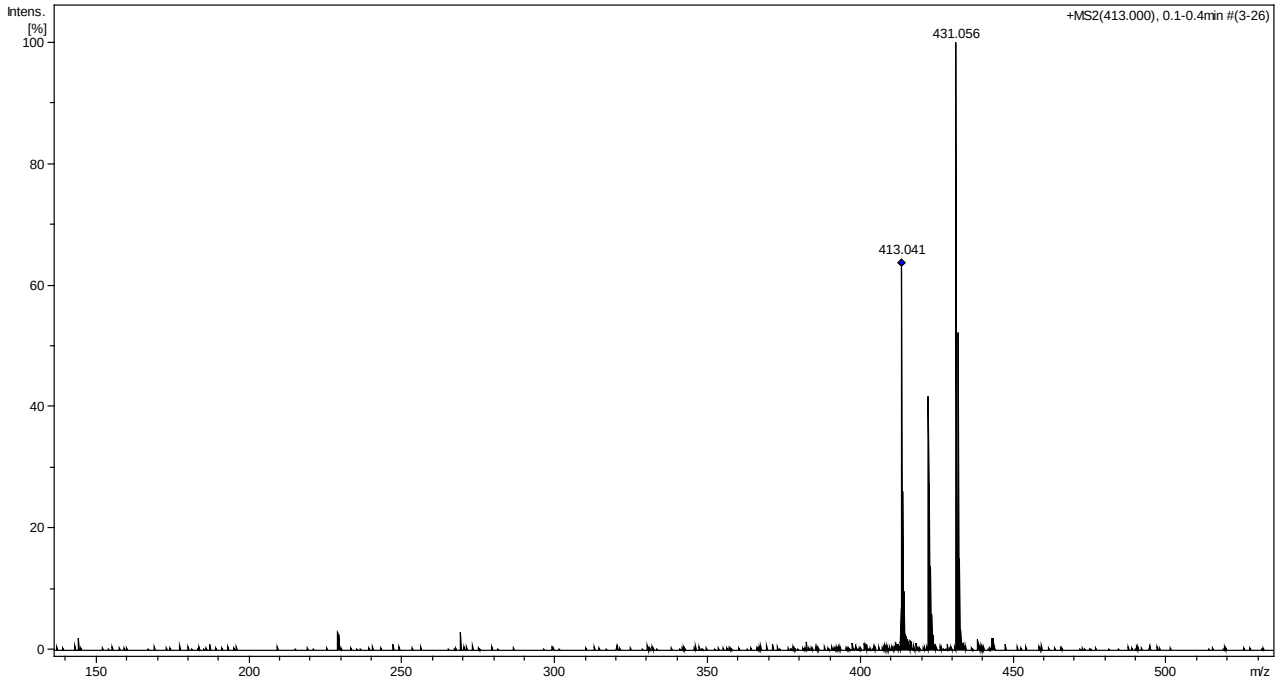

A) **Experimental data for peak m/z = 413.041, 422.049 and 431.056 are shown at the top of the panel and compared with the data calculated for the $[Al_2(L14)_2H_2]^{2+}$ ($C_{38}H_{28}Al_2O_{18}$), $[Al_2(L14)_2H_2+H_2O]^{2+}$ ($C_{38}H_{30}Al_2O_{19}$) and $[Al_2(L14)_2H_2+2H_2O]^{2+}$ ($C_{38}H_{32}Al_2O_{20}$) complexes (lower panels).**

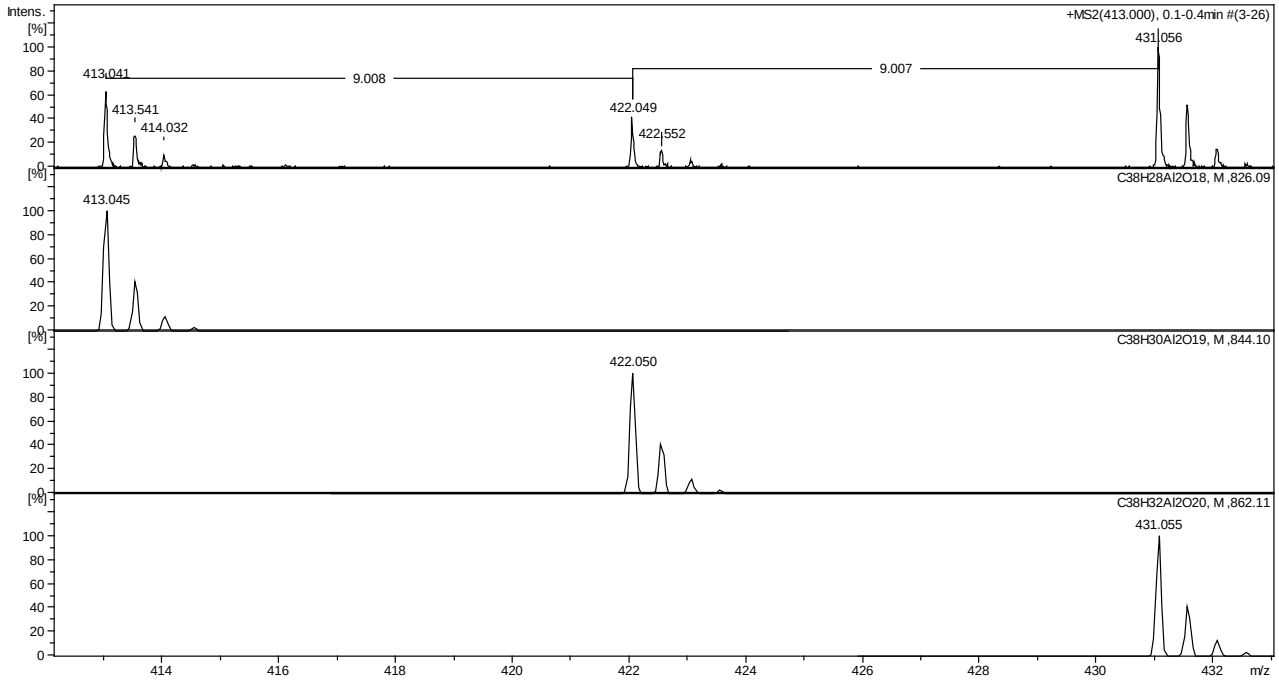

Figure A56. The full spectrum of L12 with Cu^{2+} solution in the molar ratio 1:1 in positive mode.

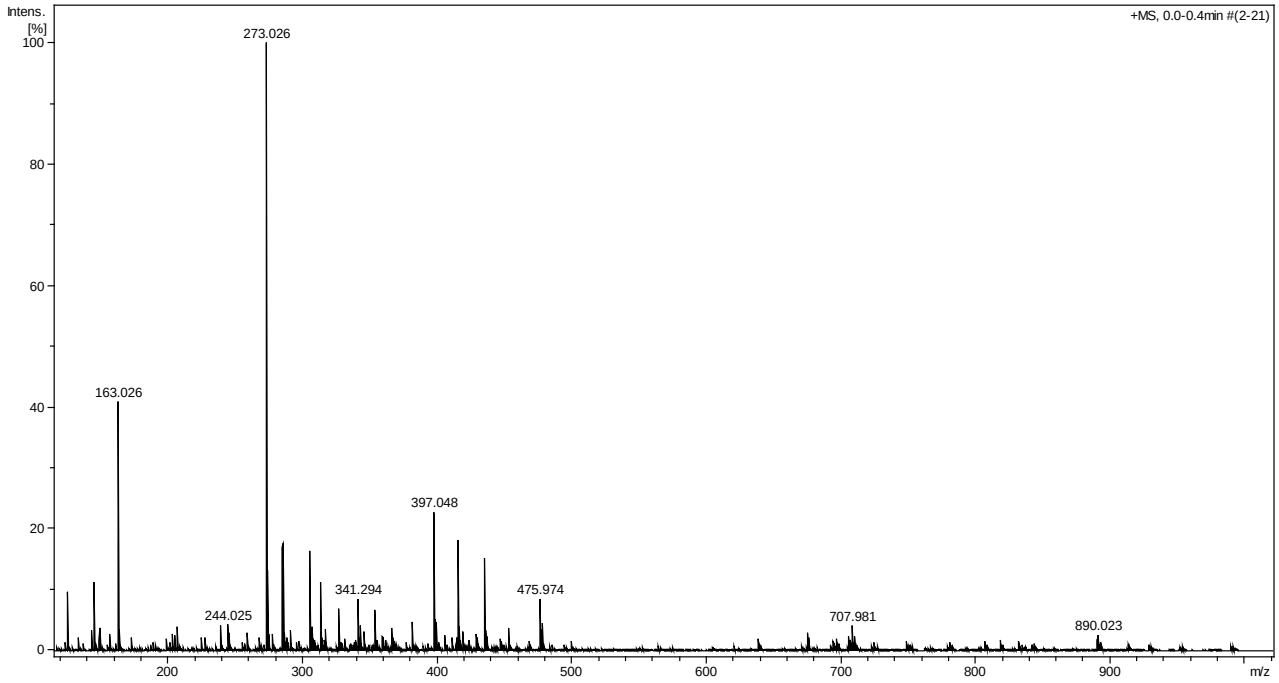

A) Experimental data for peak m/z = 475.974 and 493.980 are shown at the top of the panel and compared with the data calculated for the $[Cu(L12_{ox})H_2]^+$ ($C_{20}H_{13}CuO_{10}$), $[Cu_2(L12_{ox})_2H_4]^{2+}$ ($C_{40}H_{26}Cu_2O_{20}$) and $[Cu(L12_{ox})H_2+H_2O]^+$ ($C_{20}H_{15}CuO_{11}$) complexes (lower panels).

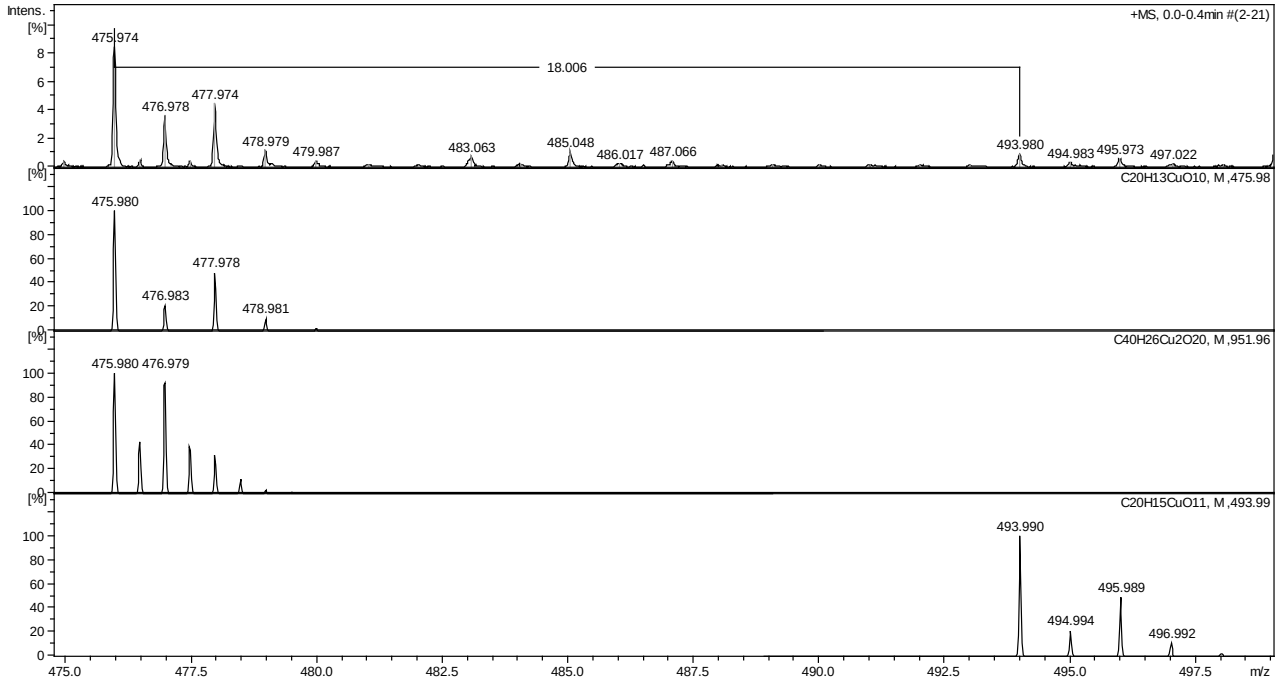

Figure A57. The full spectrum of L13 with Cu^{2+} solution in the molar ratio 1:1 in positive mode.

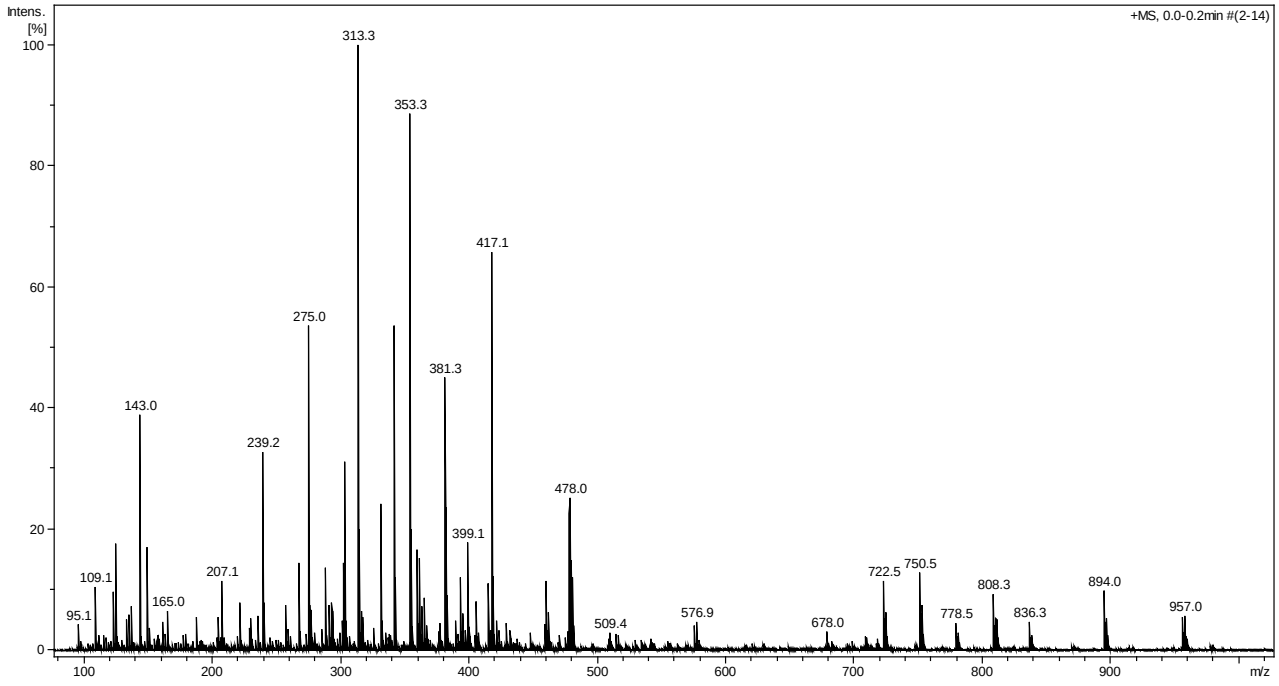

A) Experimental data for peak m/z = 477.986 are shown at the top of the panel and compared with the data calculated for the $[Cu(L13)H_2]^+$ ($C_{20}H_{15}CuO_{10}$) and $[Cu_2(L13)_2H_4]^{2+}$ ($C_{40}H_{30}Cu_2O_{20}$) complexes (lower panels).

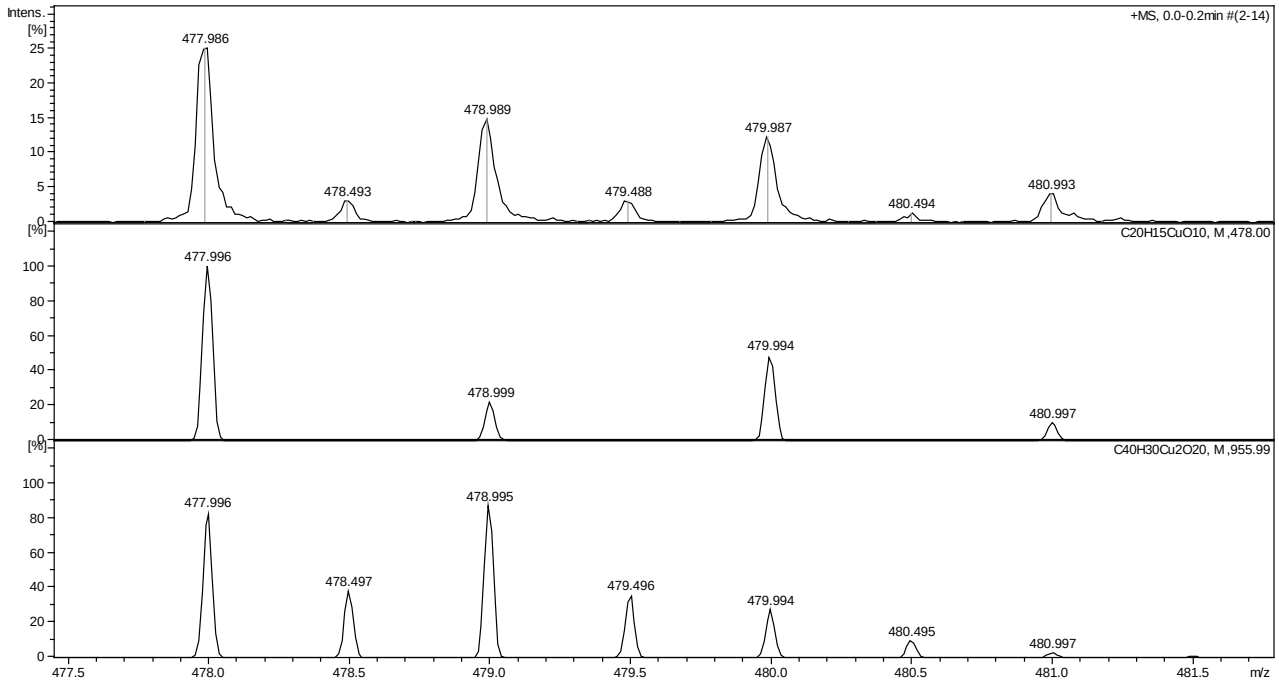

B) Experimental data for peak m/z = 954.960 are shown at the top of the panel and compared with the data calculated for the $[Cu_2(L13)_2H]^+$ ($C_{40}H_{29}Cu_2O_{20}$) complex (lower panel).

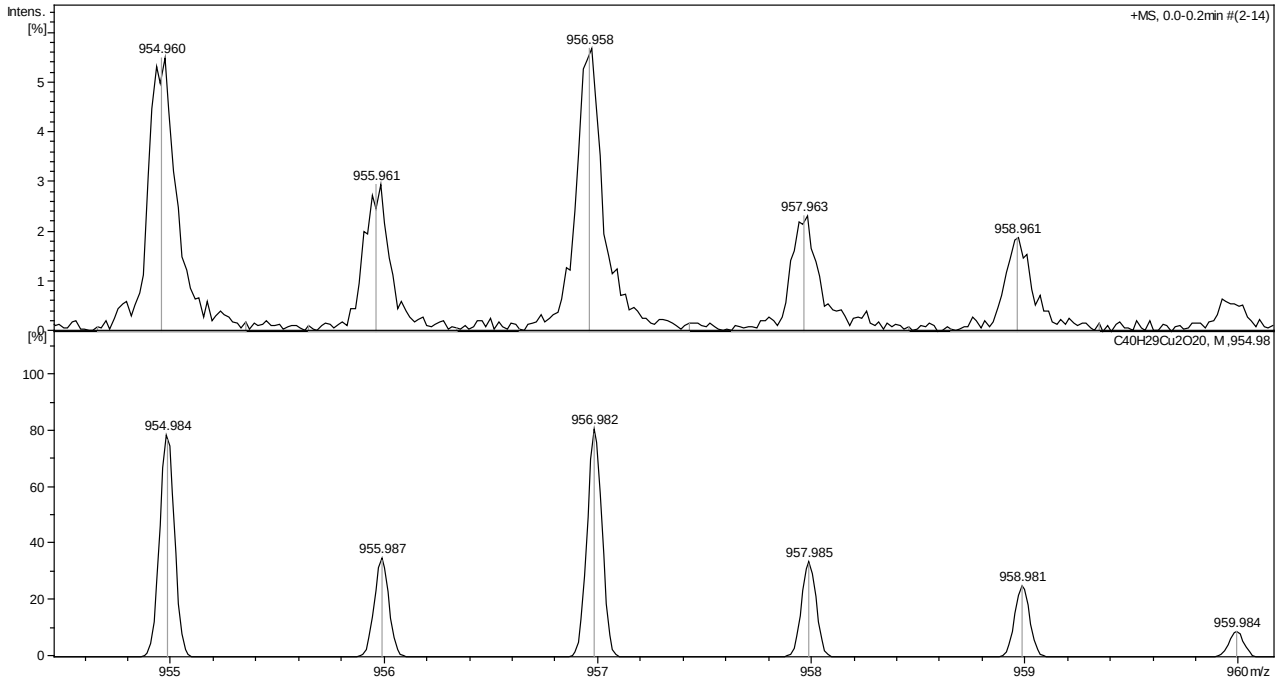

Figure A58. The full spectrum of L14 with Cu^{2+} solution in the molar ratio 1:1 in positive mode.

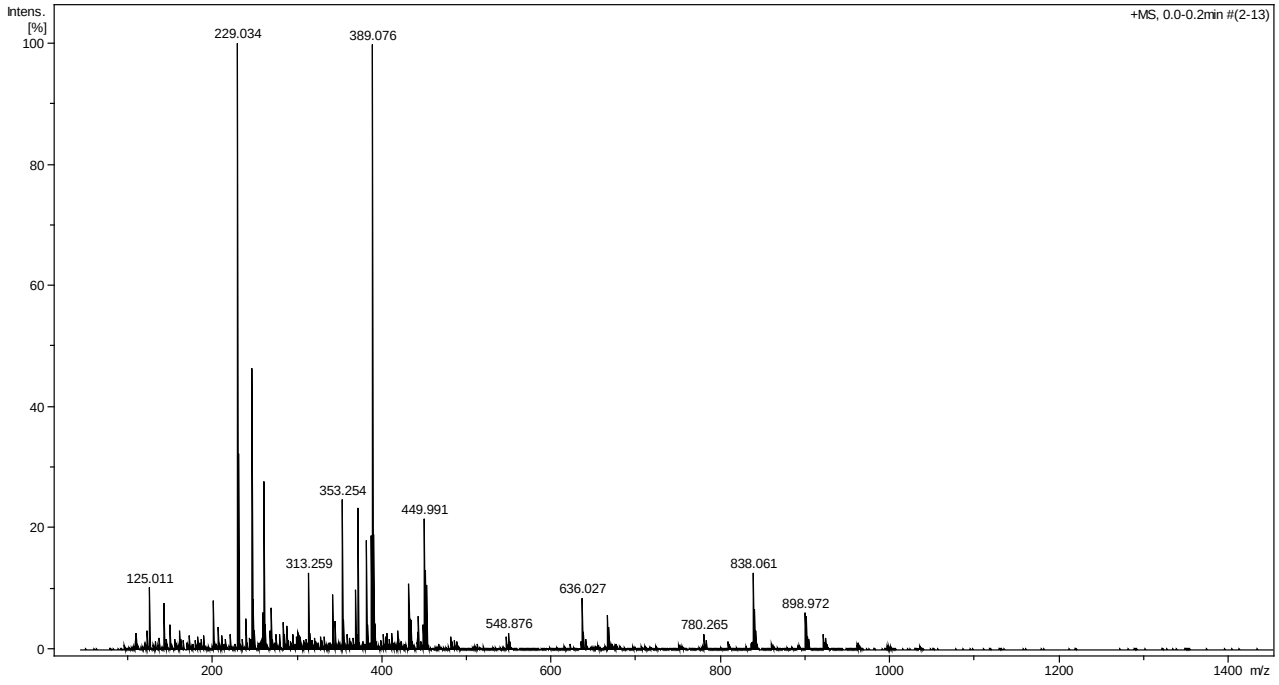

A) Experimental data for peak m/z = 449.991 are shown at the top of the panel and compared with the data calculated for the $[Cu(L14)H_2]^+$ ($C_{19}H_{15}CuO_9$) and $[Cu_2(L14)_2H_4]^{2+}$ ($C_{38}H_{30}Cu_2O_{18}$) complexes (lower panels).

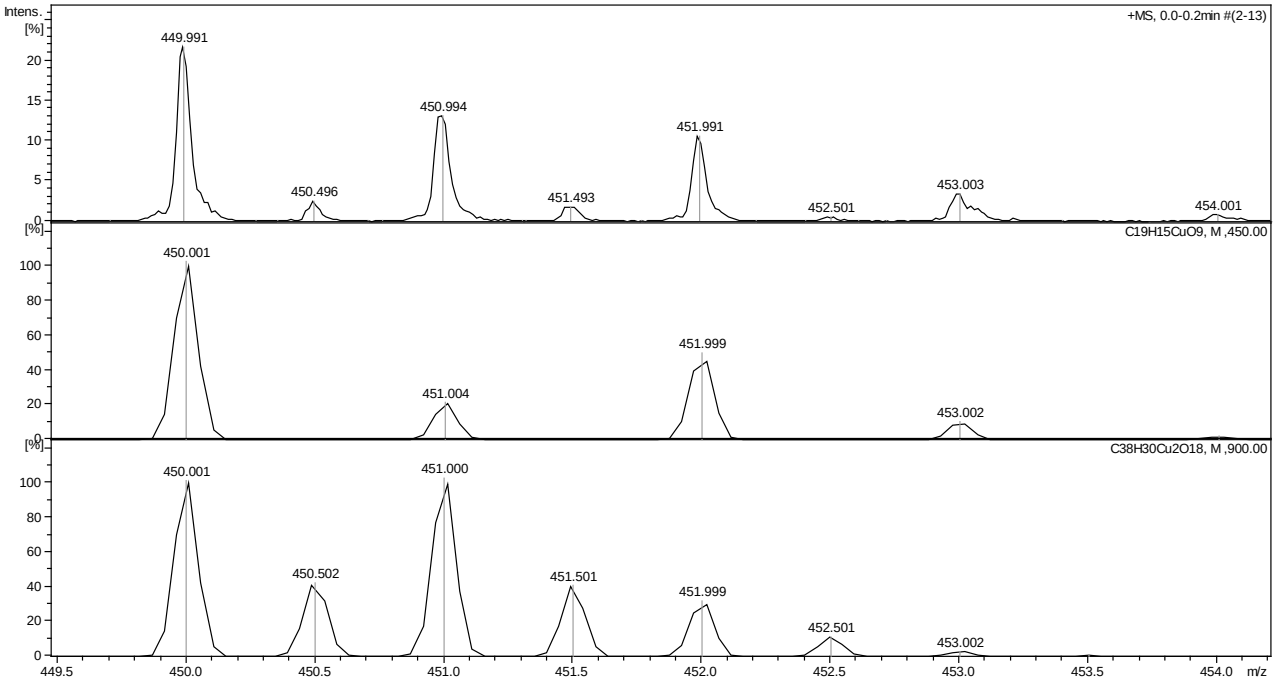

B) Experimental data for peak m/z = 838.061 are shown at the top of the panel and compared with the data calculated for the $[Cu(L14)_2H_5]^+$ ($C_{38}H_{31}CuO_{18}$) complex (lower panel).

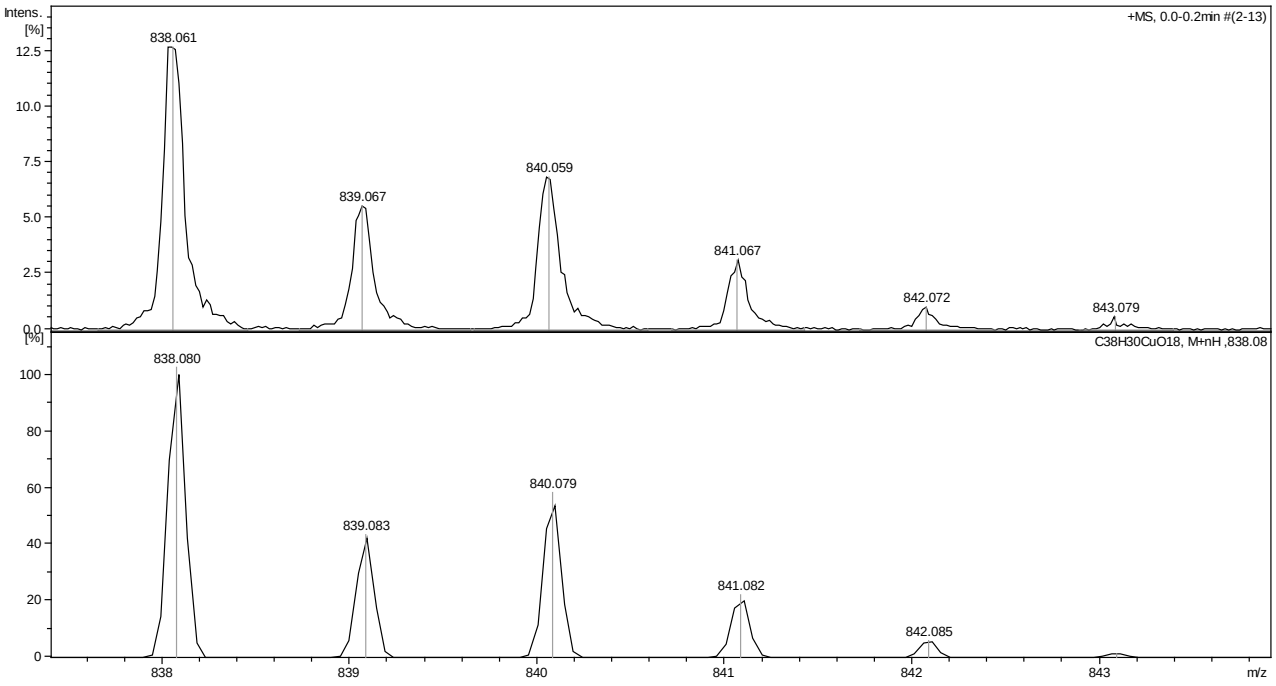

C) Experimental data for peak m/z = 898.972 are shown at the top of the panel and compared with the data calculated for the $[Cu_2(L14)_2H_3]^+$ ($C_{38}H_{29}Cu_2O_{18}$) complex (lower panel).

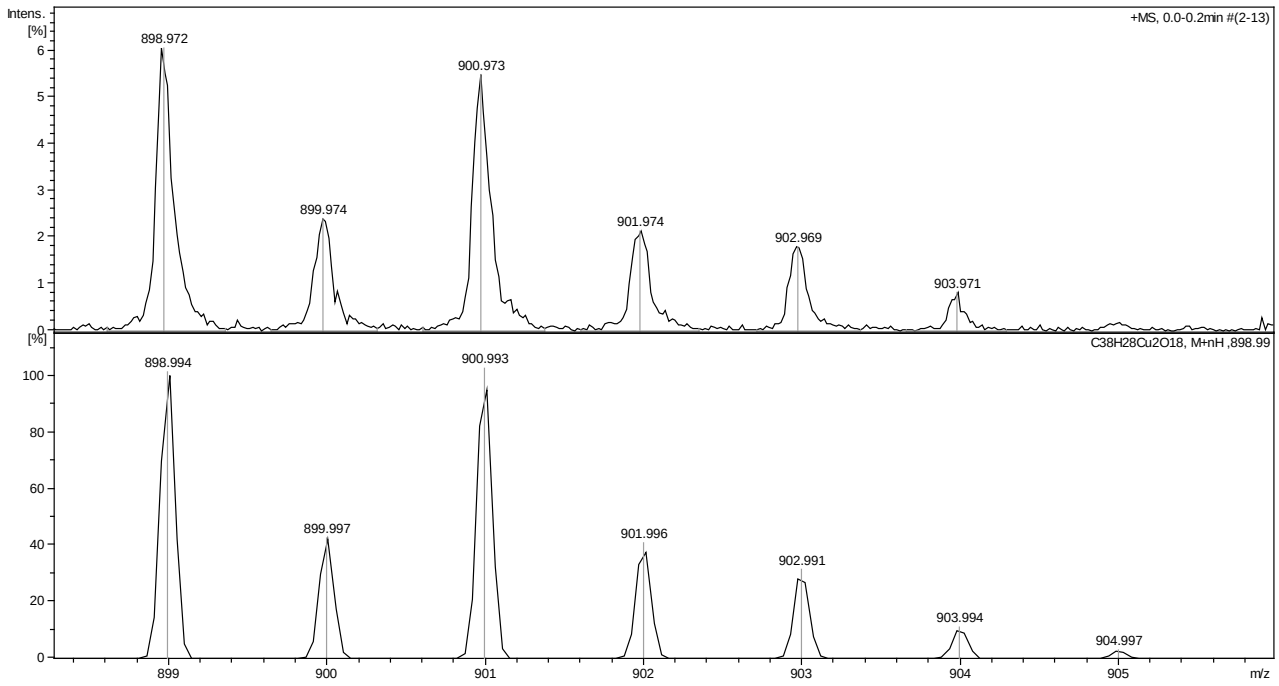

Figure A59. The full spectrum of L15 with Cu^{2+} solution in the molar ratio 1:1 in positive mode.

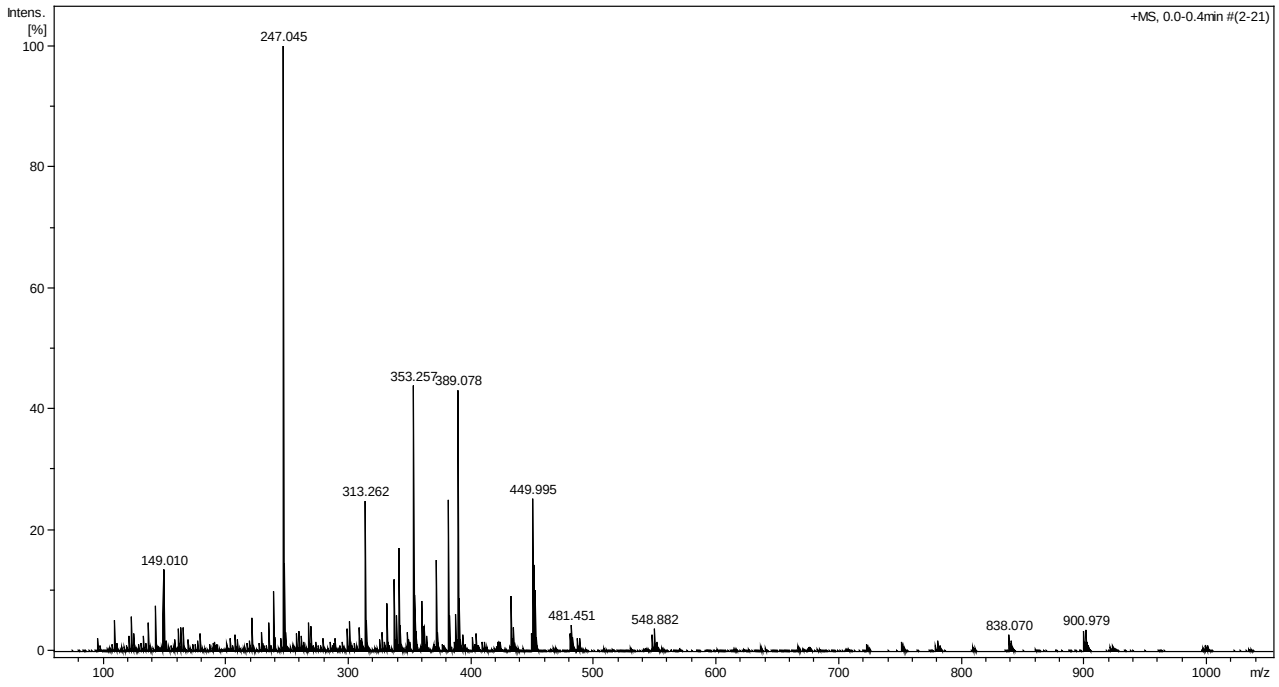

A) Experimental data for peak m/z = 449.995 are shown at the top of the panel and compared with the data calculated for the $[Cu(L15)H_2]^+$ ($C_{19}H_{15}CuO_9$) and $[Cu_2(L15)_2H_3]^{2+}$ ($C_{38}H_{30}Cu_2O_{18}$) (lower panels).

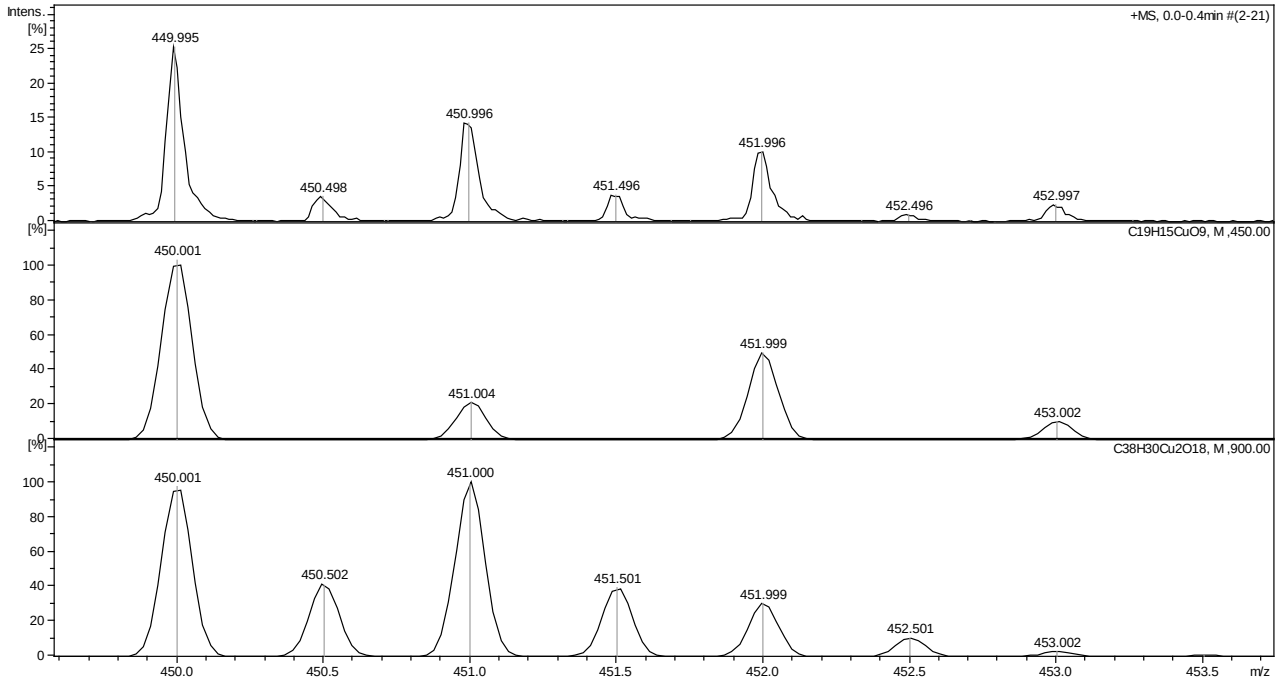

B) Experimental data for peak m/z = 898.983 and 920.976 are shown at the top of the panel and compared with the data calculated for the $[Cu_2(L15)_2H_3]^+$ ($C_{38}H_{29}Cu_2O_{18}$) and $[Cu_2(L15)_2H_2+Na]^+$ ($C_{38}H_{28}Cu_2O_{18}Na$) complexes (lower panels).

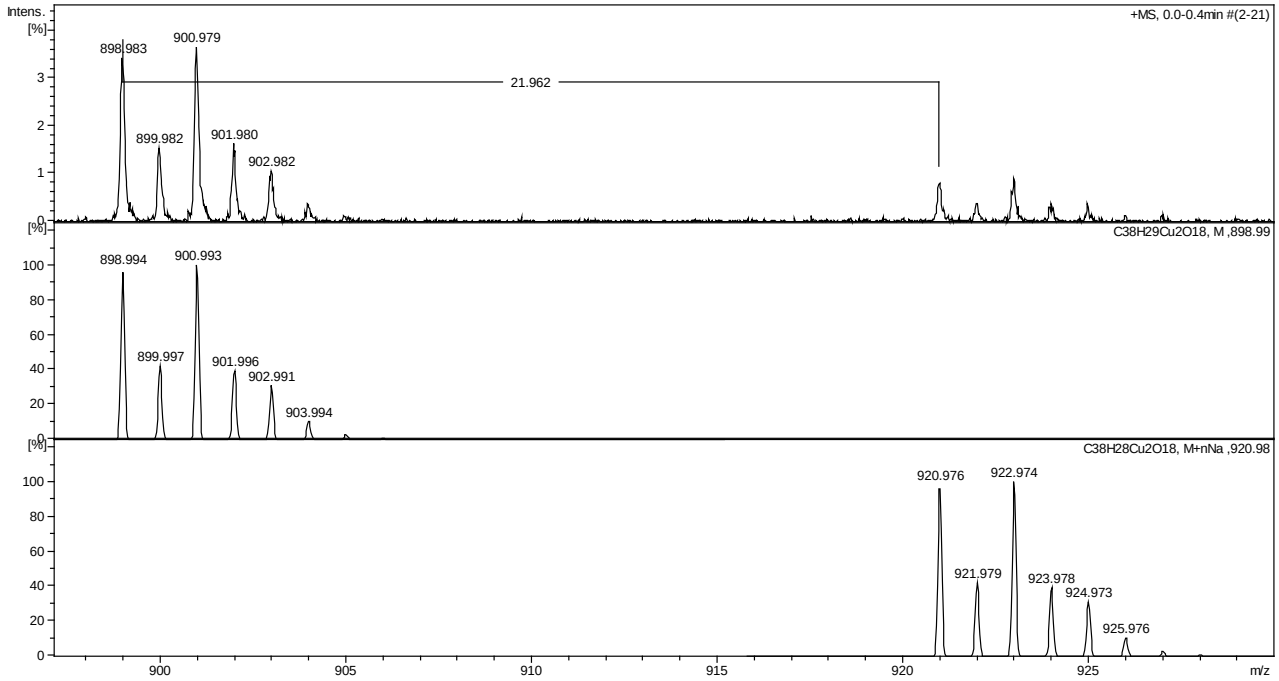

Figure A60. The full spectrum of L12 with Zn^{2+} solution in the molar ratio 1:1 in positive mode.

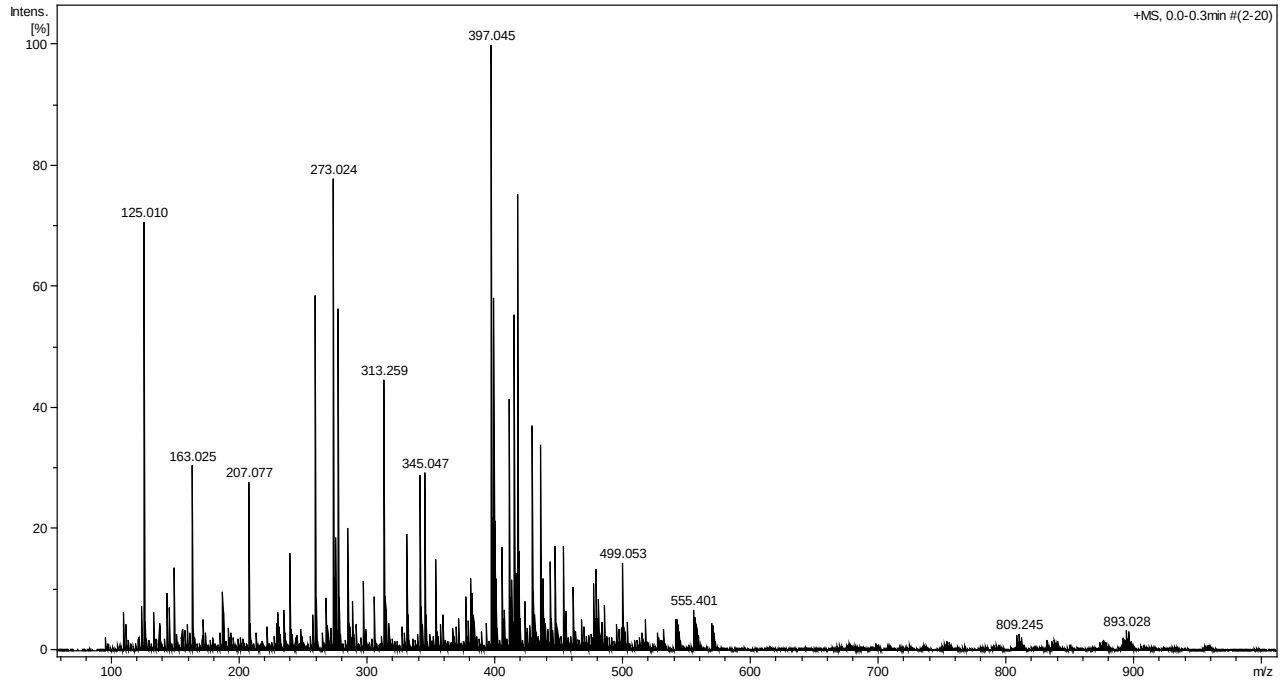

A) Experimental data for peak m/z = 476.972 and 478.979 are shown at the top of the panel and compared with the data calculated for the $[Zn(L12_{ox})H_2]^+$ ($C_{20}H_{13}ZnO_{10}$) and $[Zn(L12)H_2]^+$ ($C_{20}H_{15}ZnO_{10}$) complexes (lower panels).

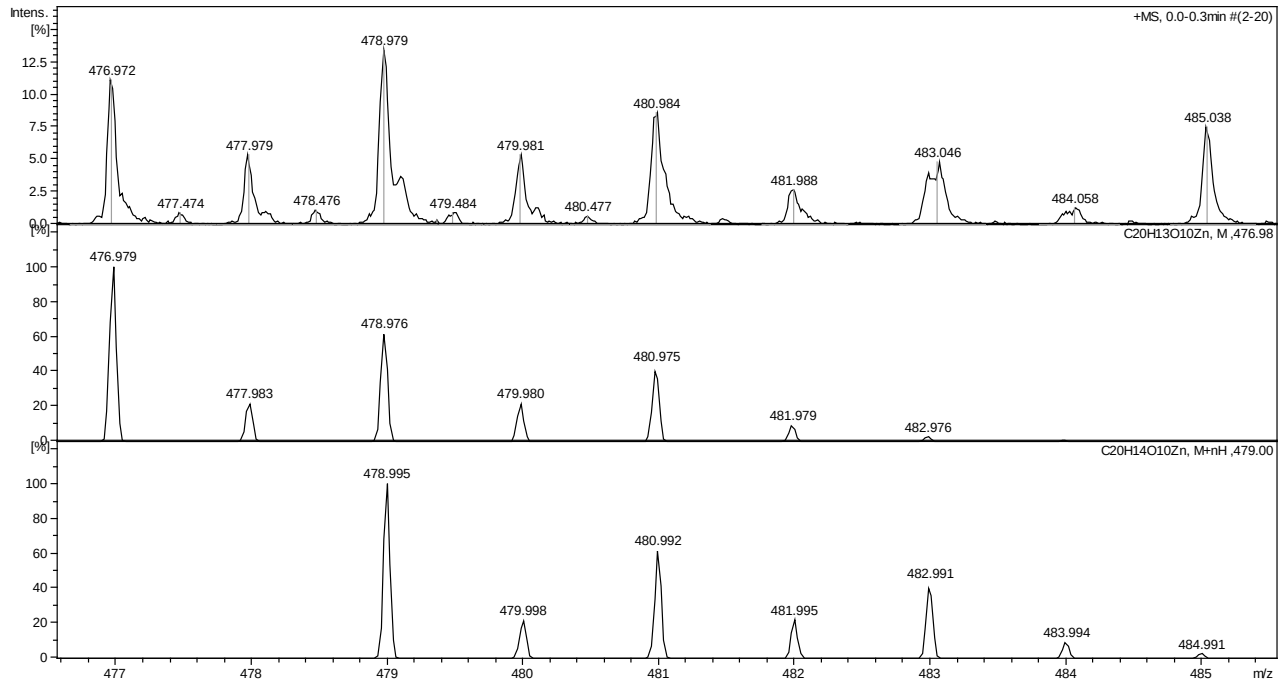

Figure A61. The full spectrum of L12 with Zn^{2+} solution in the molar ratio 1:1 in negative mode.

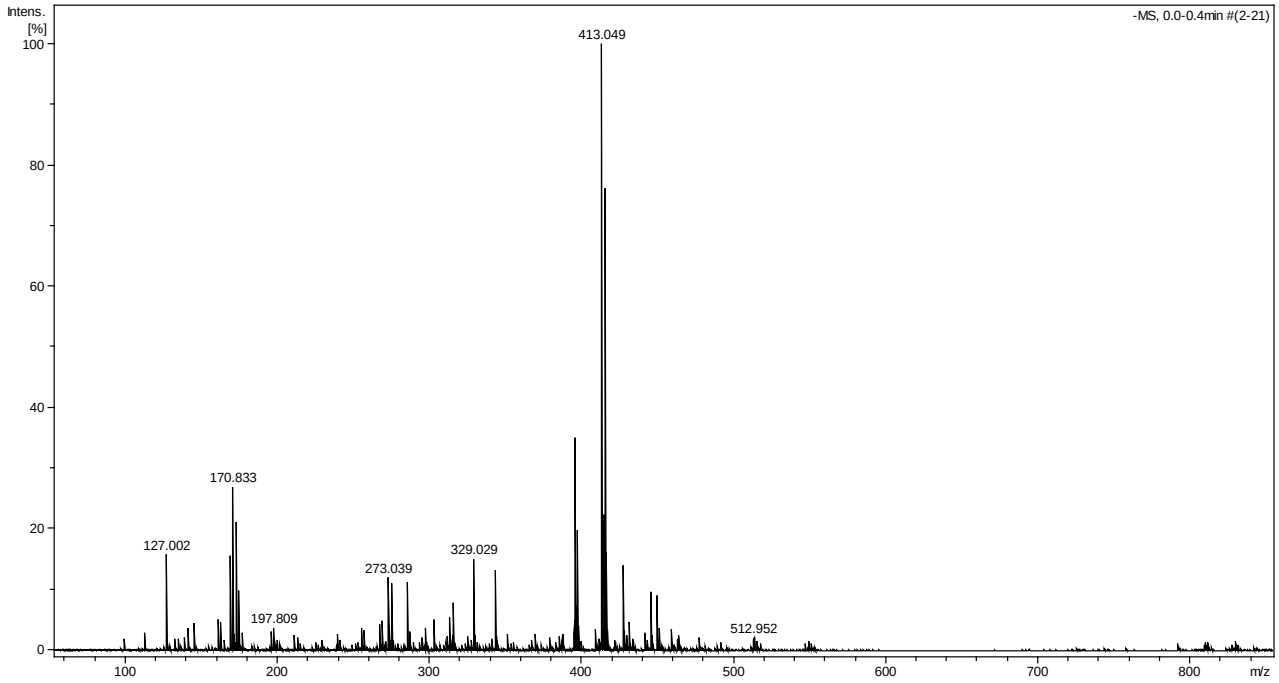

A) **Experimental data for peak m/z = 477.096 are shown at the top of the panel and compared with the data calculated for the $[Zn(L12)]^-$ ($C_{20}H_{13}ZnO_{10}$) complex (lower panel).**

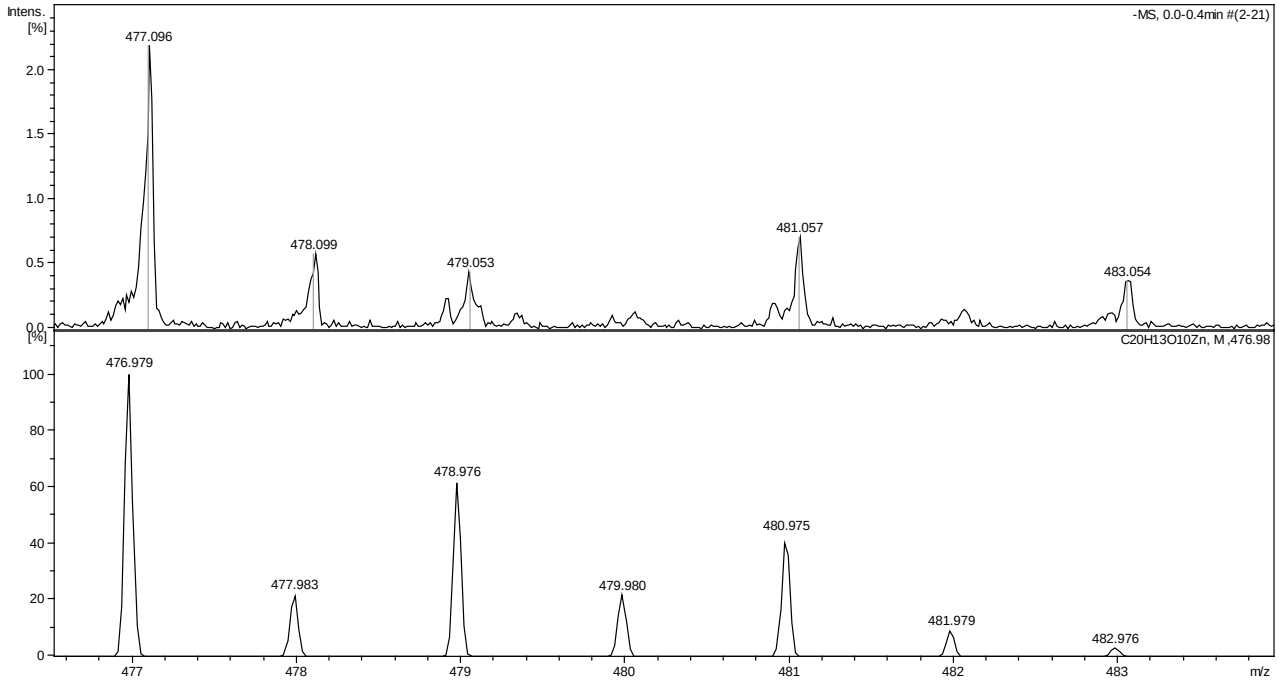

B) Experimental data for peak m/z = 512.952 are shown at the top of the panel and compared with the data calculated for the $[Zn(L12)H+Cl]^-$ ($C_{20}H_{14}ZnClO_{10}$) complex (lower panel).

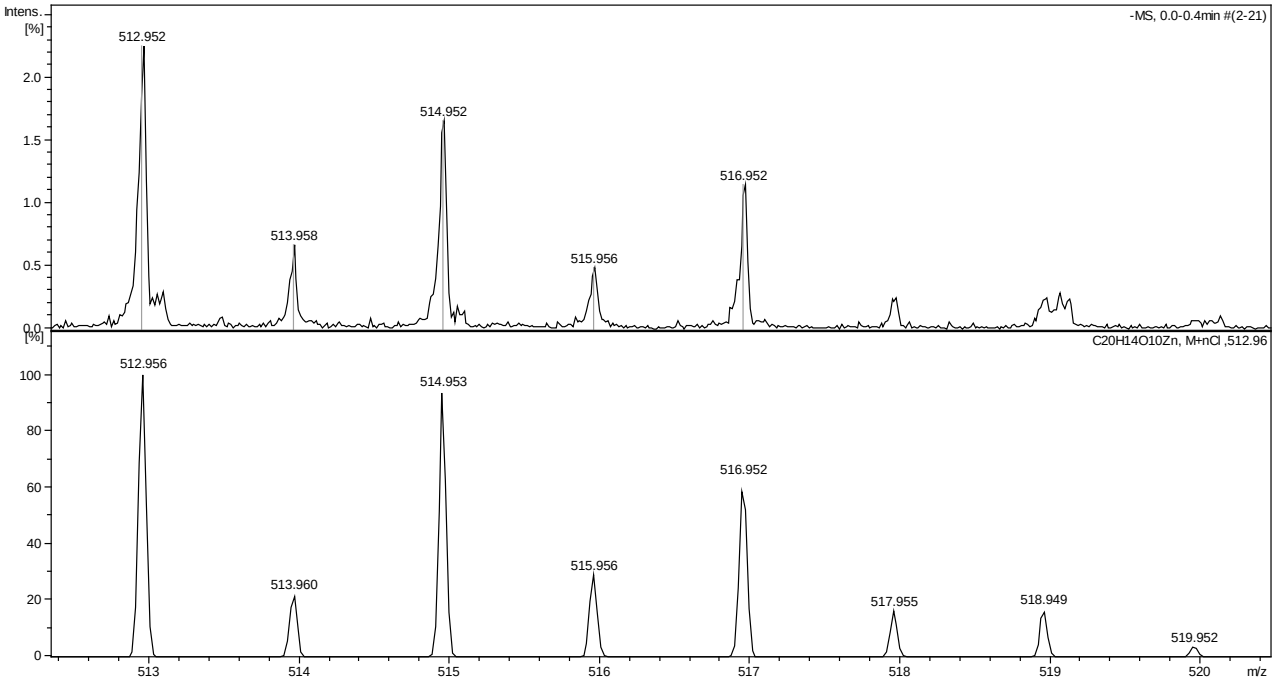

C) Experimental data for peak m/z = 548.920 are shown at the top of the panel and compared with the data calculated for the $[Zn(L12)H_2+2Cl]^-$ ($C_{20}H_{15}ZnCl_2O_{10}$) complex (lower panel).

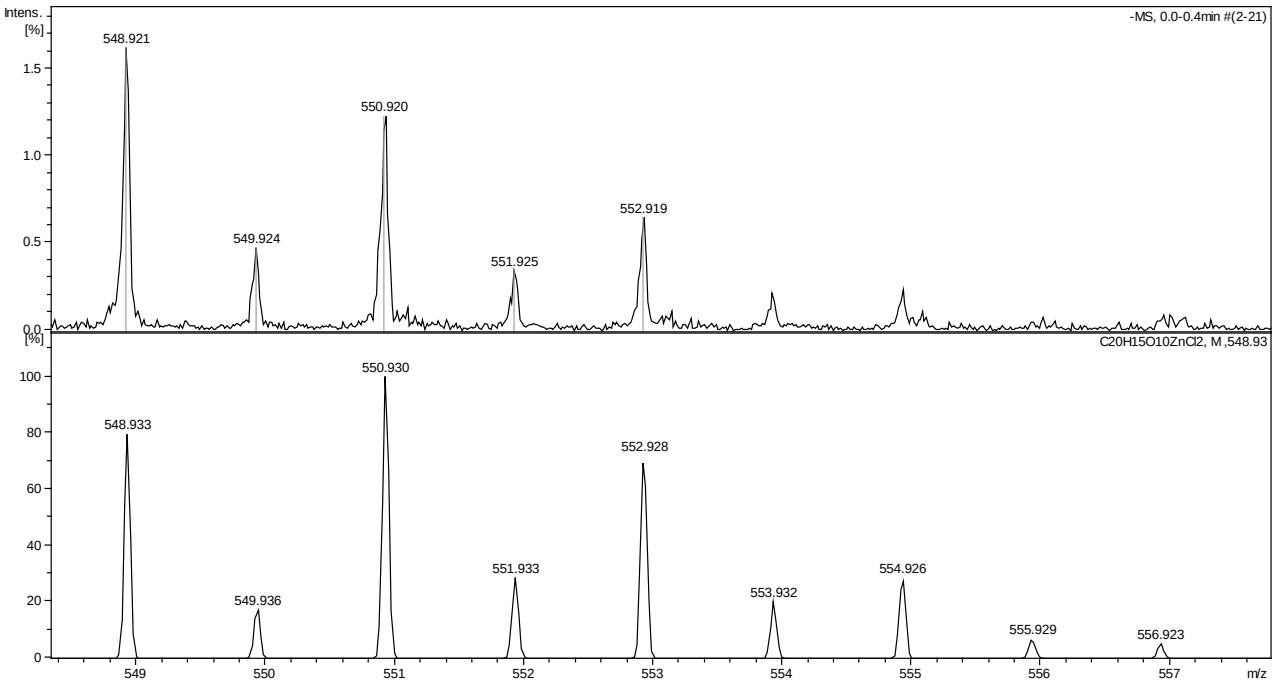

Figure A62. The full spectrum of L13 with Zn^{2+} solution in the molar ratio 1:1 in positive mode.

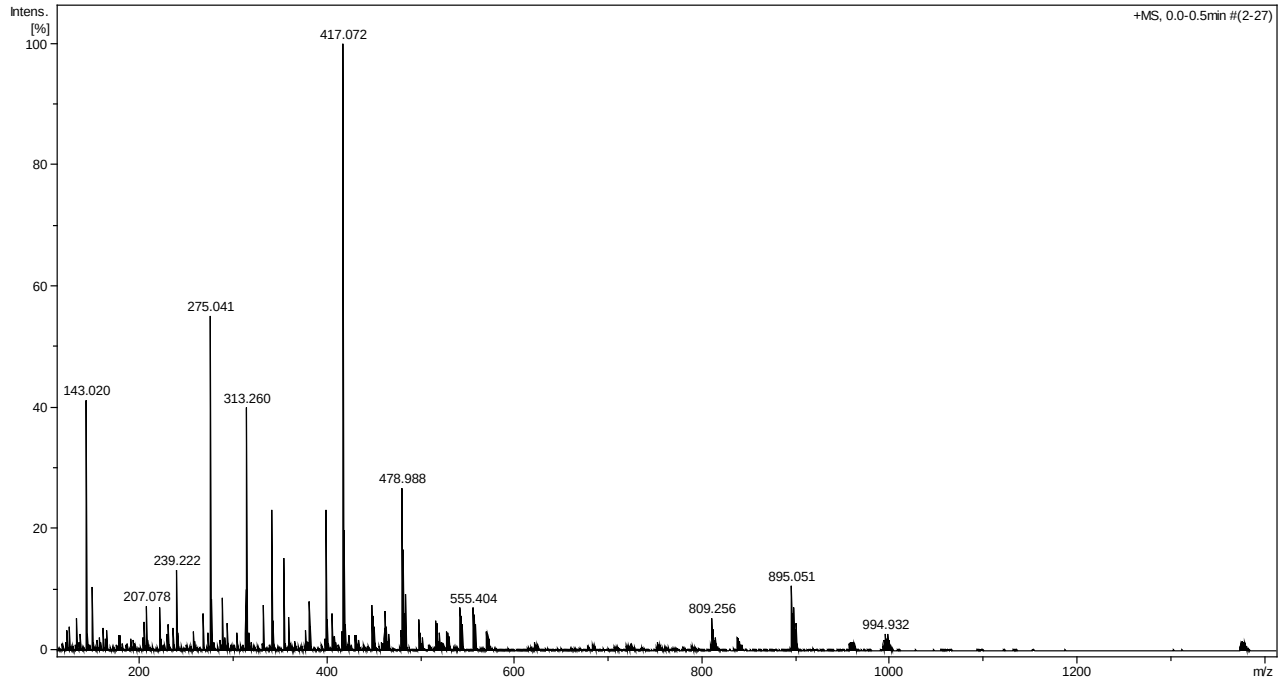

A) Experimental data for peak m/z = 478.988 are shown at the top of the panel and compared with the data calculated for the $[Zn_2(L13)_2H_4]^{2+}$ ($C_{40}H_{30}Zn_2O_{20}$) and $[Zn(L13)H_2]^{+}$ ($C_{20}H_{15}ZnO_{10}$) complexes (lower panels).

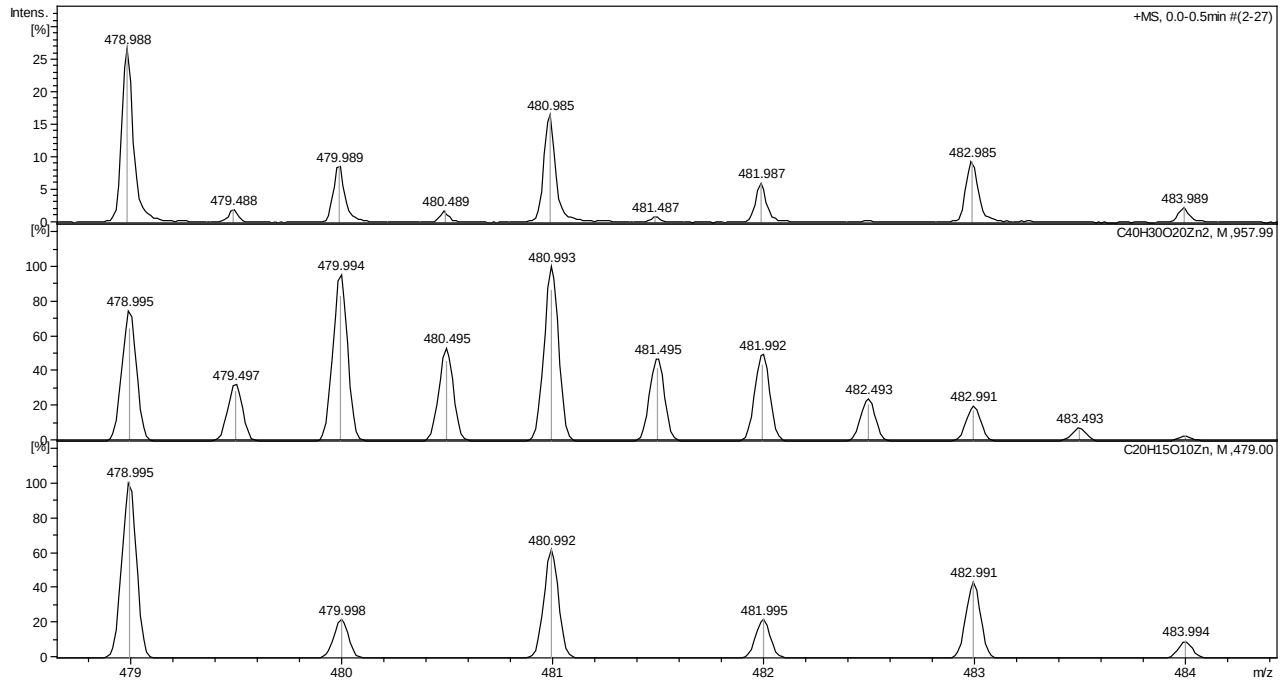

B) Experimental data for peak m/z = 496.998 and 514.977 are shown at the top of the panel and compared with the data calculated for the $[Zn(L13)H_2+H_2O]^+$ ($C_{20}H_{17}ZnO_{11}$) and $[Zn(L13)H_2+2H_2O]^+$ ($C_{20}H_{19}ZnO_{12}$) complexes (lower panels).

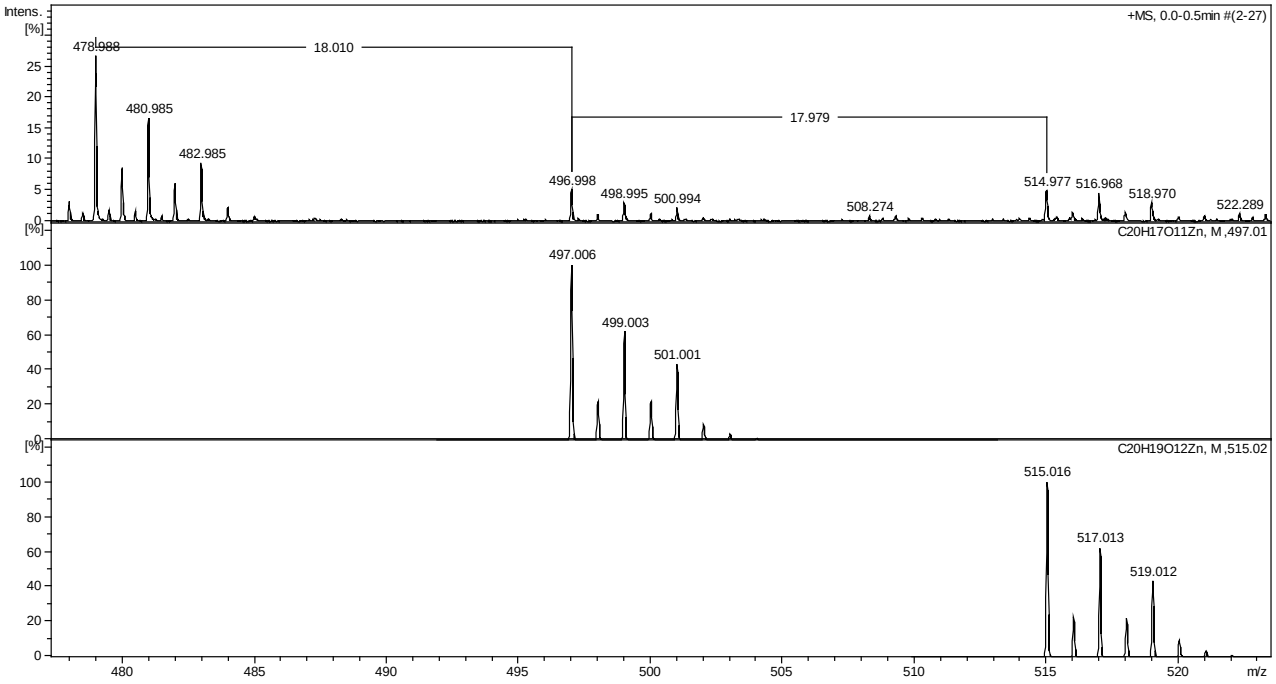

C) Experimental data for peak m/z = 956.964 are shown at the top of the panel and compared with the data calculated for the $[Zn_2(L13)_2H]^+$ ($C_{40}H_{29}Zn_2O_{20}$) and the $[Zn_4(L13)_4H_8]^{2+}$ ($C_{80}H_{58}Zn_4O_{40}$) complexes (lower panels).

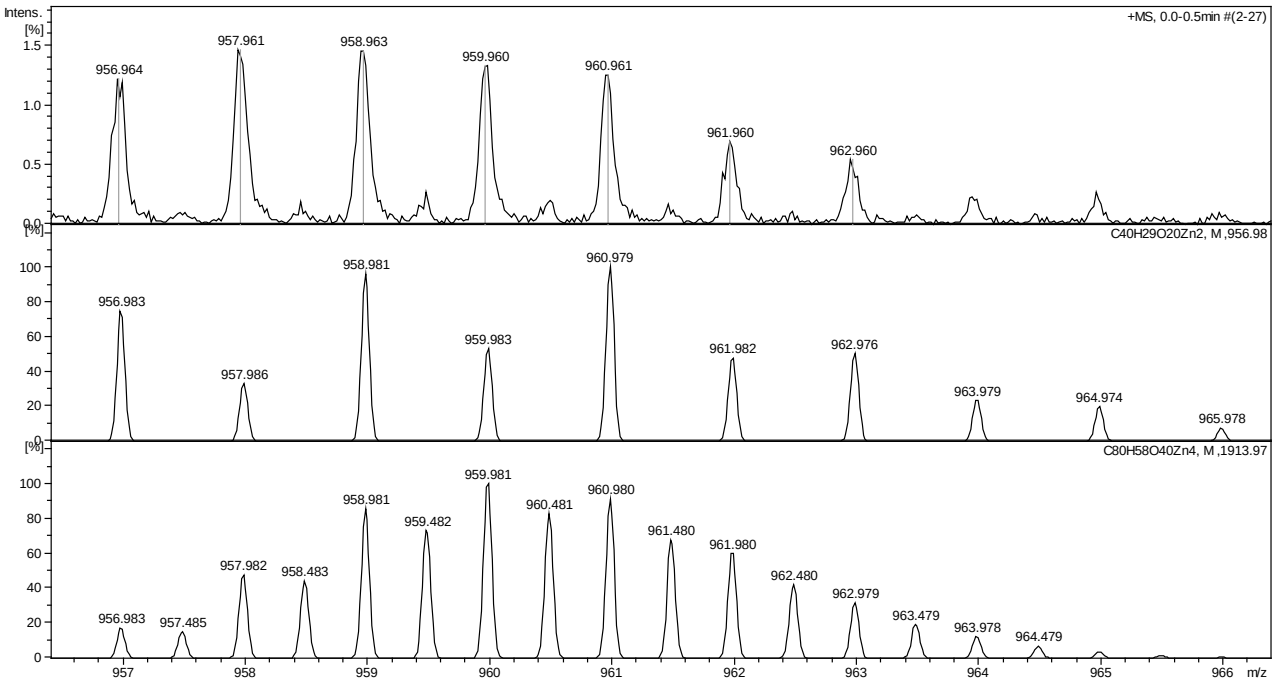

Figure A63. The full spectrum of L14 with Zn^{2+} solution in the molar ratio 1:1 in positive mode.

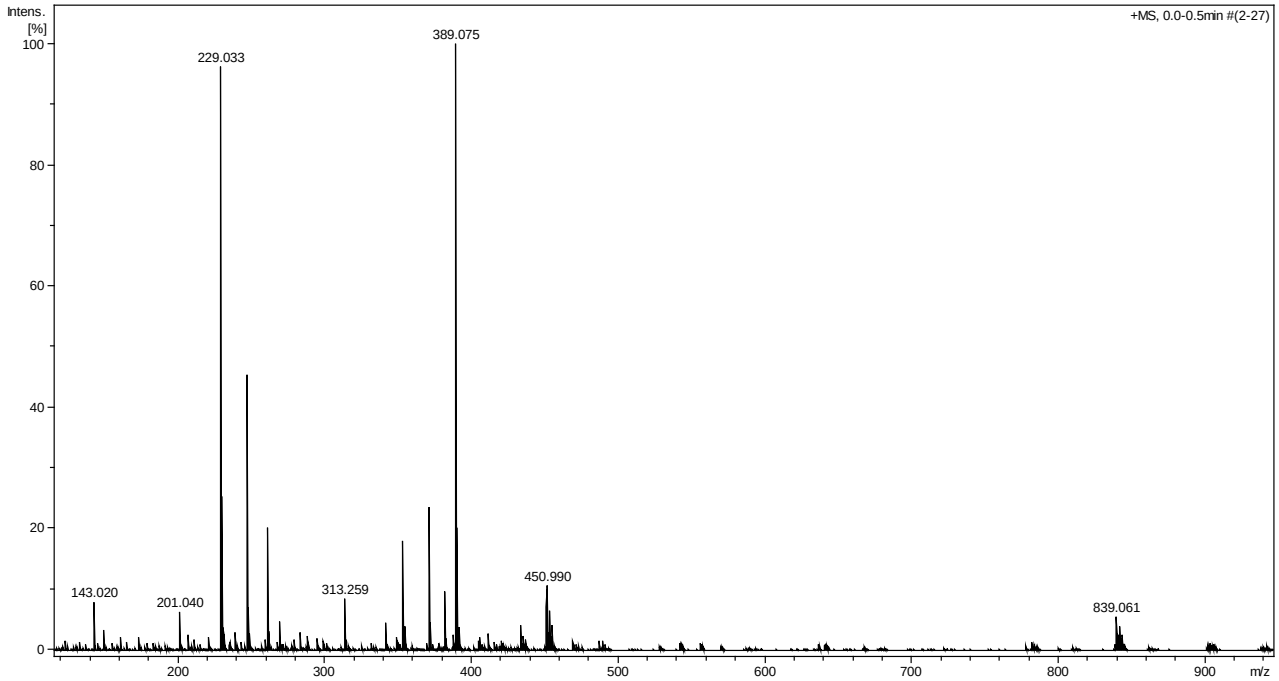

A) **Experimental data for peak m/z = 450.990 are shown at the top of the panel and compared with the data calculated for the $[Zn_2(L14)_2H_4]^{2+}$ ($C_{38}H_{30}Zn_2O_{18}$) and $[Zn(L14)H_2]^{+}$ ($C_{19}H_{15}ZnO_9$) complexes (lower panels).**

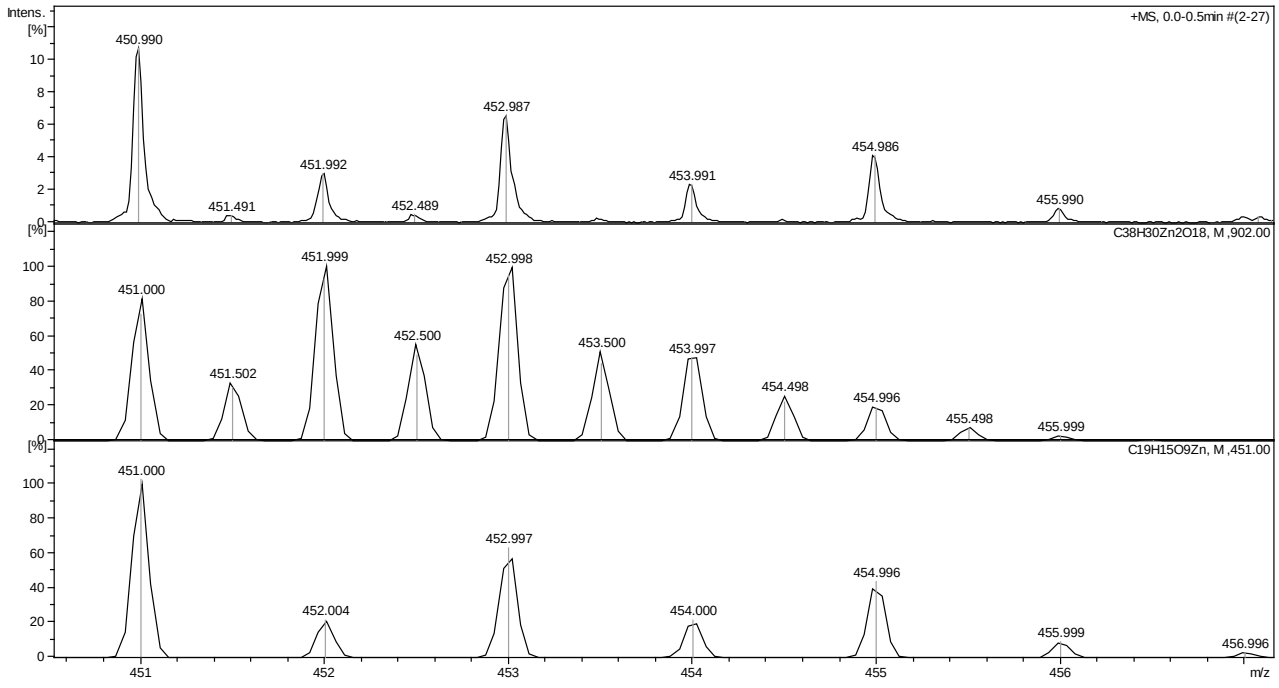

Figure A64. The full spectrum of L15 with Zn^{2+} solution in the molar ratio 1:1 in positive mode.

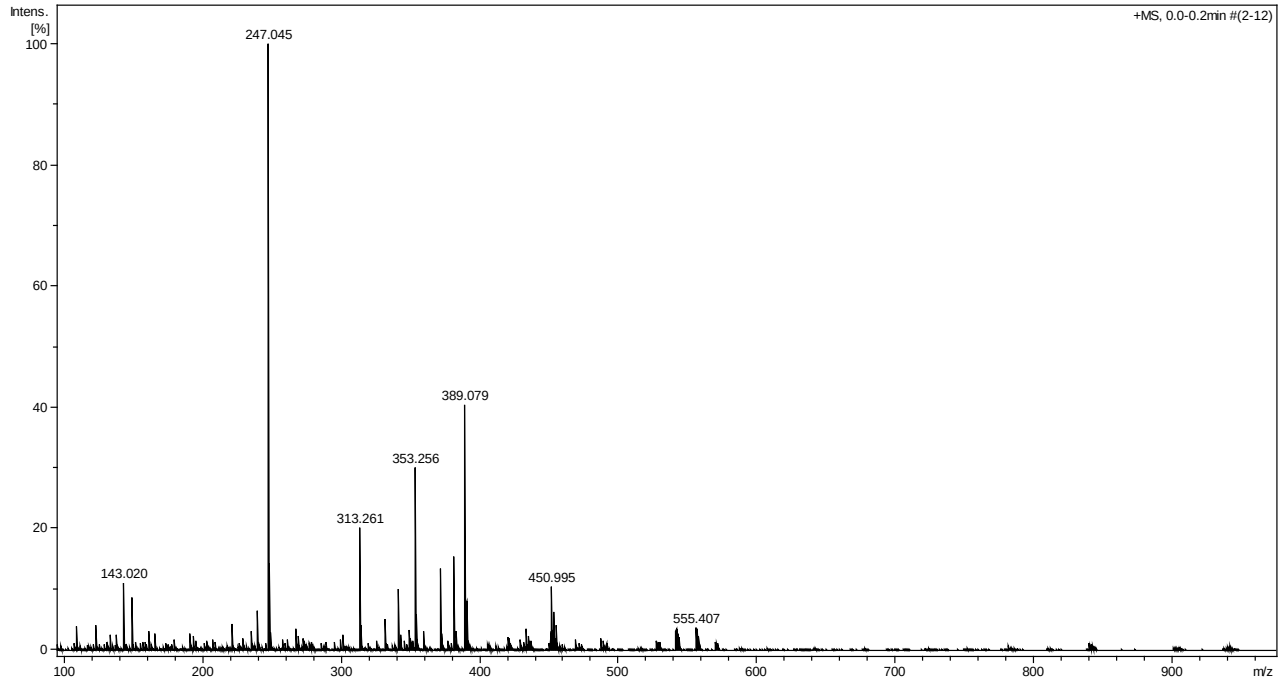

A) Experimental data for peak m/z = 450.995 are shown at the top of the panel and compared with the data calculated for the $[Zn(L15)H_2]^+$ ($C_{19}H_{15}O_9Zn$) and $[Zn_2(L15)_2H_4]^{2+}$ ($C_{38}H_{30}Zn_2O_{18}$) complexes (lower panels).

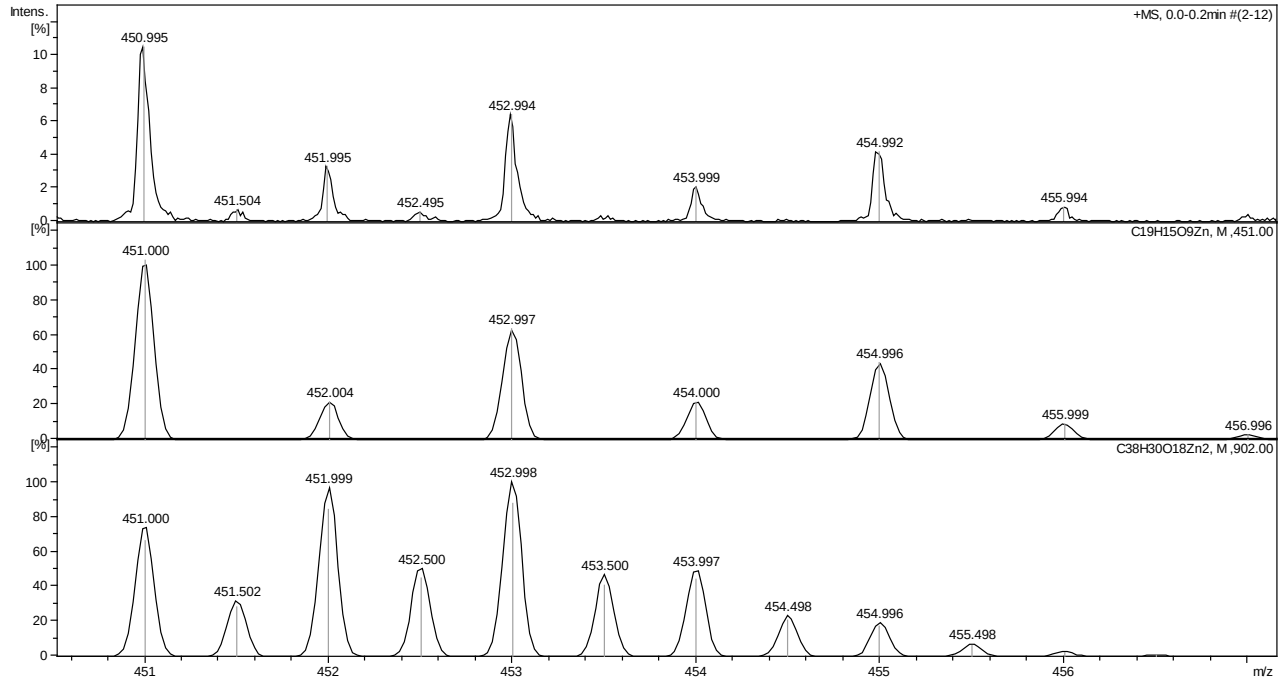

B) Experimental data for peak m/z = 469.006 and 486.977 are shown at the top of the panel and compared with the data calculated for the $[Zn(L15)H_2+H_2O]^+$ ($C_{19}H_{17}O_{10}Zn$) and $[Zn(L15)H_2+2H_2O]^+$ ($C_{19}H_{19}O_{11}Zn$) complexes (lower panels).